7th European Conference on Structural Control

Book of Abstracts and Selected Papers

Editors:

Jan Holnicki-Szulc, David Wagg and Łukasz Jankowski

Co-editors:

Bartłomiej Błachowski and Piotr Tauzowski

since 1993 eacs

INSTITUTE OF FUNDAMENTAL TECHNOLOGICAL RESEARCH
AND COMMITTEE ON MECHANICS
POLISH ACADEMY OF SCIENCES

7th European Conference on Structural Control

Book of Abstracts and Selected Papers

Editors:
Jan Holnicki-Szulc
David Wagg
Łukasz Jankowski

Co-editors:
Bartłomiej Błachowski
Piotr Tauzowski

WARSZAWA 2022

Preface

This e-book contains abstracts and selected papers accepted for presentation at the 7th European Conference on Structural Control (EACS 2022). The conference was held in Warsaw, Poland, on July 10-13, 2022. More details can be found on the conference website: http://eacs2022.ippt.pan.pl/

The European Conferences on Structural Control are a series of international conferences that was started in 1996 and progressed successfully over the years under the auspices of the European Association for the Control of Structures (EACS). Its previous editions have been organized in Barcelona (1996), Paris (2000), Vienna (2004), St. Petersburg (2008), Genoa (2012) and Sheffield (2016). This conference series provides a lively forum for presentation and discussion of current developments and trends in structural control and related fields. The conference topics cover a wide range of areas, including:

- Active, semi-active and hybrid structural control, passive structural control
- Structural dynamics and earthquake engineering
- Sensor and actuator technology, smart materials
- Structural health monitoring
- Applications to civil engineering, aerospace, marine and robotic systems
- Biological and bio-inspired systems

The 7th edition of the conference, originally planned for 2020 and postponed to 2022 due to COVID-19, was organized by the Institute of Fundamental Technological Research (IPPT PAN) and co-organized by the Committee on Mechanics, both of the Polish Academy of Sciences. The conference hosted 4 general lectures and 7 thematic sessions. A total of 92 researchers from 21 European and non-European countries (56% of them from outside Poland) attended the conference. They submitted and presented 77 abstracts.

Structural control is an area of active and dynamic research, which has also a large and obvious potential for important practical applications. The EACS conference series encompasses these new research directions and we foresee that this trend will continue to grow in the future.

Jan Holnicki-Szulc
David Wagg
Łukasz Jankowski
Chairs of EACS 2022

The 7th European Conference on Structural Control was organized by the Institute of Fundamental Technological Research and co-organized by the Committee on Mechanics, both of the Polish Academy of Sciences, under the auspices of the European Association for the Control of Structures.

International Scientific Committee

N. Alujević (*University of Zagreb, Croatia*)

B. Basu (*Trinity College Dublin, Ireland*)

O. S. Bursi (*University of Trento, Italy*)

F. Casciati (*Zhejiang University, China*)

S. Casciati (*SIART Srl, Italy*)

S. Cogan (*University of Franche-Comté, France*)

S. Dyke (*Purdue University, USA*)

S. Elliott (*University of Southampton, UK*)

L. Faravelli (*Zhejiang University, China*)

S. Fassois (*University of Patras, Greece*)

V. Gattulli (*University of L'Aquila, Italy*)

A. Del Grosso (*University of Genoa, Italy*)

J. Holnicki-Szulc (*IPPT PAN, Poland*)

T. Insperger (*Budapest University of Technology and Economics, Hungary*)

H. Irschik (*University of Linz, Austria*)

S. Krenk (*Technical University of Denmark, Denmark*)

M. Krommer (*Johannes Kepler University Linz, Austria*)

A. Martelli (*ENEA Centro Ricerche Bologna, Italy*)

J. Molinar (*JRC ISPRA, Italy*)

J. Mottershead (*University of Liverpool, UK*)

A. Myśliński (*Polish Academy of Sciences, Poland*)

S. Neild (*University of Bristol, UK*)

B. Öztürk (*Hacettepe University, Turkey*)

A. Pavic, (*University of Exeter, UK*)

F. Pozo (*Technical University of Catalonia, Spain*)

Z. Rakicevic (*Ss. Cyril and Methodius University in Skopje, N. Macedonia*)

J. Rodellar (*Technical University of Catalonia, Spain*)

D. Wagg (*University of Sheffield, UK*)

J. Warmiński (*Lublin University of Technology, Poland*)

M. Williams (*University of Oxford, UK*)

B. Wu (*Harbin Institute of Technology, China*)

Conference Chairs
J. Holnicki-Szulc (*IPPT PAN, Poland*)
D. Wagg (*University of Sheffield, UK*)
Ł. Jankowski (*IPPT PAN, Poland*)

Scientific Secretary
B. Błachowski (*IPPT PAN, Poland*)

Organizing Committee (*IPPT PAN, Poland*)

P. Tauzowski – *Technical Secretary*

K. Parkitna

M. Struska

C. Graczykowski

G. Mikułowski

Special sessions and their organizers

S1: **EACS 2022 special session: bridging to the future**
(Special session in honor of EACS founding fathers)
S. Casciati (*SIART s.r.l., Italy*), Ł. Jankowski (*IPPT-PAN, Poland*), M. Krommer (*TU Wien, Austria*),
F. Pozo (*Universitat Politècnica de Catalunya, UPC, Spain*)

S2: *[cancelled due to Covid-19]*

S3: **LIVE-I project session – lightweight gear transmission**
M. Ichchou (*Ecole Centrale de Lyon, France*), F. Franco (*University of Naples, Italy*),
S. Rinderknecht (*TU Darmstadt, Germany*), P. Kołakowski (*Adaptronica sp. z o.o., Poland*)

S4: **SMART-SPACE session**
J. Holnicki-Szulc, Z. Wołejsza (*IPPT PAN, Poland*), P. Kołakowski (*Adaptronica sp z o.o., Poland*)

S5: **Structural health monitoring and damage detection**
M. Rucka (*Gdansk University of Technology, Poland*), Y. An (*Dalian University of Technology, China*), B. Błachowski (*IPPT PAN, Poland*), N.G. Pnevmatikos (*University of West Attica, Greece*)

S6: **Optimization and optimal control approach in structural mechanics**
D. Pisarski (*IPPT PAN, Poland*), A. Myśliński (*Systems Research Institute, Poland*)

S7: **Adaptive shock-absorbers for mitigation of impact and vibration**
R. Zalewski (*Warsaw University of Technology, Poland*), C. Graczykowski (*IPPT PAN, Poland*)

S8: **Smart materials**
Tomasz G. Zieliński (*IPPT PAN, Poland*)

Abstracts

Selected full papers

Plenary lectures

Multidomain Synthesis of Vibration Suppression Systems

Jason Zheng Jiang

Department of Mechanical Engineering, University of Bristol, UK
e-mail: z.jiang@bristol.ac.uk

In this talk, the recent progresses will be introduced on the multidomain synthesis methodology of vibration suppression systems. Traditional vibration-absorber design approaches rely on introducing specific modifications to existing designs – this leaves huge performance possibilities unexplored. The developed synthesis-based methodology enables optimum designs to be constructed considering components from the mechanical, hydraulic, pneumatic, and electrical domains. The significant performance advantages will then be demonstrated via multiple application examples, for both vibration suppression and passive-active-combined motion control purposes.

Mitigation of vibrations with tuned mass damper with inerter

Przemysław Perlikowski

Department of Mechanical Engineering, Lodz University of Technology, Poland
e-mail: przemyslaw.perlikowski@p.lodz.pl

The idea of tuned mass dampers (TMD) has been developed since the beginning of the 20th century. The TMD is a device designed to reduce undesired oscillations of mechanical or structural systems. Frahm proposed the first solution in 1909. The simple device consisted of a mass and a spring. Its natural frequency was tuned to match the damped body's natural frequency. However, it was poorly efficient outside the narrow resonance zone. Den Hartog made the improvement by adding a dash-pot between the TMD and damped structure, which caused a significant increase in the TMD efficiency range. Alternative idea concerns interchanging the linear spring of TMD with the nonlinear one or with purely nonlinear characteristics. The other attempts include the application of multiple TMD instead of one. Recently, a novel concept of varying the tuned mass damper natural frequency has been applied using TMD with variable inertia. The variability of inertia is achieved by adding the inerter with the continuously variable transmission (CVT).

In this plenary presentation, we show the properties of the tuned mass damper with variable inertance (TMDVI) and compare its efficiency to existing TMDs. We proposed two possible variants of the TMDVI system. The first one is equipped with the belt-driven CVT, and the second one is with a variator. Mathematical models of both devices have been developed based on experimental data. Then, we derive the model of the main system with the TMDVI. We validate the new idea of the TMDVI with numerical simulations and experimental measurements. The proposed device is robust and works efficiently.

Structural Health Monitoring of Freight Railroad Bridges in North America

Billie F. Spencer Jr.

Department of Civil and Environmental Engineering, University of Illinois at Urbana-Champaign, USA
e-mail: bfs@illinois.edu

Railroads are one of the most critical components of the U.S. transportation system, accommodating transportation for 48% of the nation's total modal tonnage. Despite such vital importance, more than half of railroad bridges, an essential component of railroad infrastructure in maintaining the flow of the network, were built before 1920; as a result, bridges comprise one of the most fragile components of the railroad system. Current structural inspection practices do not ensure sufficient information for both short- and long-term condition assessment while keeping the operational costs sufficiently low for mandatory annual inspection. In this talk, we present the development of an autonomous, affordable system for monitoring railroad bridges using the wireless smart sensors. A complete end-to-end wireless monitoring solution can provide relevant information directly from the bridges to the end-users at a fraction of the cost of traditional monitoring solutions. The system's main contribution is to capture the train-crossing events efficiently and eliminate the need for a human-in-the-loop for remote data retrieval and post-processing. In the proposed system, an adaptive strategy combining an event-based and schedule-based framework is implemented. The wireless system addresses the challenges of continuous condition monitoring by completing the wireless data pipeline from smart sensors with edge computing capabilities to a scalable, cloud-based data management and visualization solution. To demonstrate the efficacy of this system, we present the results of a full-scale monitoring campaign on railroad bridges. By overcoming the challenges of monitoring railroad bridges wirelessly and autonomously, this system is expected to become an essential tool for bridge engineers and decision-makers.

Hybrid and data-based control of high-tech mechatronic system

Nathan van de Wouw

Department of Mechanical Engineering, Eindhoven University of Technology, The Netherlands
Department of Civil, Environmental and Geo-Engineering, University of Minnesota, Minneapolis, USA
e-mail: n.v.d.wouw@tue.nl

The motion dynamics of high-tech, mechatronic systems, such as for example electron microscope, semiconductor equipment or industrial printers, can generally be accurately described by linear dynamical models. Given this observation, state-of-practice motion controllers for such systems are also linear in nature. Nevertheless, fundamental limitations for linear control systems, e.g., due to the Bode sensitivity integral, limit the achievable positioning performance.

In this lecture, hybrid control strategies will be presented that yield superior positioning performance over linear controllers. In particular, variable-gain controllers will be discussed that strike a superior balance between low-frequency reference tracking and high-frequency measurement noise sensitivity. As a next step, we propose to use data-based performance optimization by extremum seeking control to optimally tune such hybrid controllers in the presence of uncertainties in the system dynamics. Finally, hybrid (reset) controllers are designed for motion system subject to friction to ensure superior positioning performance in point-to-point motions. The effectiveness of these hybrid controller design methodologies will be demonstrated through experimental and industrial case studies for electron microscopy and semi-conductor equipment.

Session S1

Bridging to the future
(Special session in honor of EACS founding fathers)

Organizers:
Sara Casciati (*SIART s.r.l., Italy*)
Łukasz Jankowski (*IPPT PAN, Poland*),
Michael Krommer (*TU Wien, Austria*),
Francesc Pozo (*Universitat Politècnica de Catalunya, UPC, Spain*)

COMPARING THE EFFICIENCY OF DIFFERENT STRUCTURAL SKELETONS FOR ISOLATED DOMES

S. Casciati[1]

[1]*SIART srl, Pavia, Italy*
e-mail: sara@dipmec.it

1. The problem

The structural concept of dome dates back to the Pantheon in Rome and it is used as cover of many churches and mosques all around the world. Light solutions with a well visible dome shaped truss skeleton are often preferred in modern architecture. Base isolation techniques can be adopted to mitigate the seismic effects [1]. The target of this contribution is to investigate the efficiency of different designs for the truss skeleton. To afford the problem, one has to assign the constraints, the materials and the geometry of the dome, its supporting structure, and the isolation devices (number, locations, type). Investigating the effects of different assumptions on the structural behaviour provides a better insight to the problem.

2. Alternatives to the geodesic option

Different mechanical models are studied in an effort to understand the stress distributions in the truss nodes: One first investigates the stress distribution across the structural members due to the gravity action and other operational loads. Different ground motions are then applied to the structure and, again, the stress state is estimated. The analyses are repeated with and without the isolation devices and their effectiveness are compared with reference to the considered truss options. In all the considered cases, the devices are idealized as orthotropic elastic volumes [1].

References

[1] B. Basu, et al., A European Association for the Control of Structures joint perspective. Recent studies in civil structural control across Europe, *Structural control & Health Monitoring*, 21 (12) , 2014, pp.1414-1436

A BISTABLE LOCALLY RESONANT METAFOUNDATION FOR SEISMIC PROTECTION OF PROCESS PLANT COMPONENTS

T. Guner[1], O.S. Bursi[1], and M. Broccardo[1]

[1]*Department of Civil, Environmental and Mechanical Engineering,*
University of Trento, Trento, Italy
e-mail: tugberk.guner@unitn.it

As a unique kind of nonlinearity, bistability has attracted great attention due to its intricate and advantageous dynamics. A simple bistable system can be created using a buckled column as shown see Fig. 1. More precisely, a bistable system can rapidly switch from one stable state to the other under a transverse force where the system stiffness in the transverse direction becomes negative. A well-known practice is the utilization of this snap-through motion for energy harvesting purposes, where the high-velocity motion is exploited. Another key consequence of this dynamic is the harmonic energy diffusion which simply corresponds to the distribution of input energy to multiple harmonics [1]. Recent years have seen various investigations on the topic of nonlinear periodic structures utilizing bistability to reveal their fascinating wave dynamics properties. As opposed to linear counterparts, the dynamics are sensitive to the wave amplitude, and various phenomena can be observed such as amplitude-dependent dispersion, nonreciprocity, chaos, and many others.
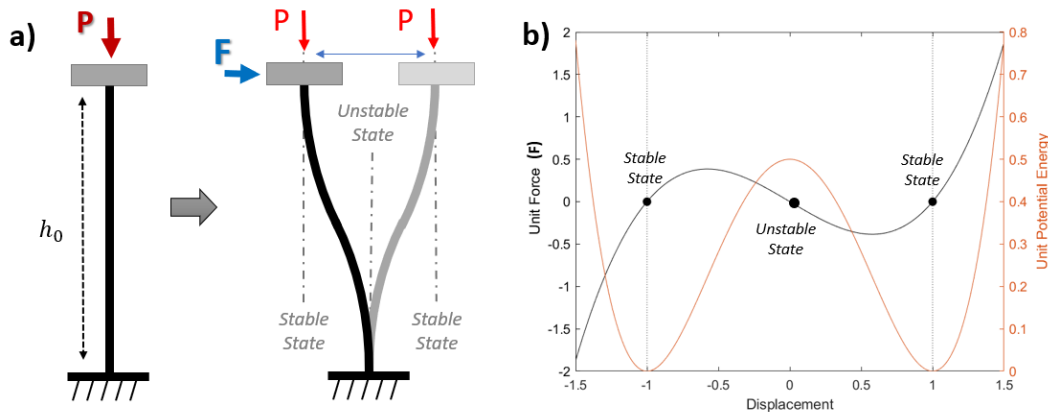
Figure 1. Simple bistable mechanism; (a) Fixed end − rotation fixed end buckled column; (b) transverse force − deformation and potential energy representation

Periodic systems can be utilized as acoustic metamaterial (AM) which can exhibit subwavelength band gaps due to their locally resonance ability. The application of AMs for seismic isolation, in structural media, is a new and developing application area [2]. As expected, the aim is to attenuate low-frequency waves engaging unit cells much smaller than the seismic wavelength and to prevent seismic waves to reach the superstructure. The proposed foundation employs the AM concept, so-called locally resonant metafoundation (LRM). An LRM simply comprises multiple mass-in-mass cells in a matrix form as a foundation where the main cell contains steel columns and a rigid slab [3]. The inner mass is employed by a reinforced concrete block, the so-called resonator. The resonator connects to the slab by wire ropes. The important aspect of the LRM is that, besides the AM advantages, the resonators work like a tuned mass damper and dissipate energy. Moreover, the columns reduce structural stiffness.

The aim of the study is to introduce bistability to the LRM and to get the benefit of the aforementioned dynamics. Explicitly, using the harmonic diffusion; reduction on structural responses, and using the energy harvesting advantages; increase in the energy dissipation of the resonators, are aimed. Accordingly, the bistable dynamics are introduced to the main columns of the LRM, see Fig. 2 in this respect, and 2-layer

bistable LRM for the slender water tank is designed and analyzed. The columns are designed such that the weight of the tank causes them to buckle in the weak direction while the strong axis of the columns resists the earthquake-induced forces and moments. By means of the finite element analysis, the elastic post-buckling range of the columns are determined.
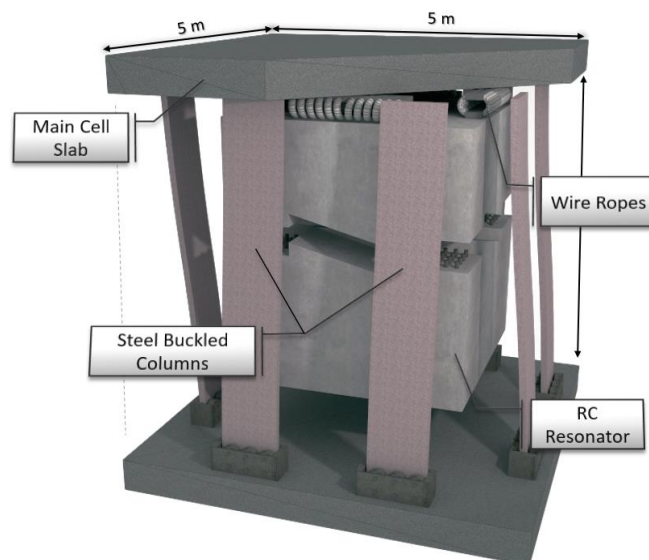
Figure 2. A bistable LRM cell

The optimization of the resonator parameters – stiffness and damping - are conducted in the time domain using the Kriging-based quadratic low-fidelity metamodeling technique. The metamodel is created by evaluating the resonator parameters that are selected by the central composite design (CCD) method. Subsequently, the optimized LRM is compared with the linear LRM using a set of ground motions records. The comparison is conducted in terms of the response parameters. The results showed that the bistable LRM exhibits an improvement in terms of energy dissipation and energy transmission to the superstructure. Explicitly, in specific cases, it was observed that bistable LRM isolated the superstructure such that the energy transferred to a storage tank is reduced up to 0.8% of the linear LRM case. In terms of median, a reduction of 67% is observed.

The bistable LRM single cell and periodic system dynamics are further investigated in the frequency domain. By means of sinusoidal input, the frequency content of the response is investigated. The extension of the harmonic diffusion to the anti-resonance effect of the resonators is observed. When we consider a periodic system, energy transfer behavior is explored. It is concluded that bistable LRM requires a significantly less number of cells to attenuate waves and transfer significantly less energy as the input duration increase. Using frequency response functions, the effect of bistability on periodicity and wave attenuation is studied. It is concluded that a bistable periodic system requires fewer cells – down to 2 cells- to create a band-gap structure at the targeted frequency range, while it also extends the band-gap lower boundary.

References

[1] R.L. Harne and K.W. Wang. *Harnessing Bistable Structural Dynamics: For Vibration Control, Energy Harvesting and Sensing.* Wiley, 2007
[2] D. Mu, H. Shu, L. Zhao, S. An. A Review of Research on Seismic Metamaterials, *Advanced Engineering Materials. 22 (2020). https://doi.org/10.1002/adem.201901148.*
[3] O.S. Bursi, F. Basone, M. Wenzel. Stochastic analysis of locally resonant linear and hysteretic metamaterials for seismic isolation of process equipment. *J. Sound Vib. 510 (2021) 116263, https://doi.org/10.1016/j.jsv.2021.116263.*

REINFORCEMENT LEARNING ALGORITHM FOR CONTROLLING THE TRANSIENT VIBRATIONS OF SEMI-ACTIVE STRUCTURES INDUCED BY UNKNOWN PERIODIC EXCITATION

D. Pisarski and Ł. Jankowski

Institute of Fundamental Technological Research of the Polish Academy of Sciences, Warsaw, Poland

e-mail: dpisar@ippt.pan.pl

1. Problem statement

The role of the adaptive control in the structural vibration problems is to guarantee a relevant adjustment of the control decisions as the environmental conditions or internal structural parameters are unknown or subject to changes. A typical approach to adapting the control functions is based on the model predictive control which employs repetitive solutions to an optimal control problem. This method exhibits high efficiency, nevertheless, due to the high computational burden, it is mostly dedicated to the applications in linear structural control problems (actively controlled structures) [2, 3]. To cope with the higher complexity of the dynamical systems concerned with semi-actively controlled structures, it is relevant to consider using iterative learning algorithms such as reinforcement learning (RL). Reinforcement learning control does not require complete information of the system [1] and the computational complexity concerned with successive iterations of the control policy is significantly lower than in the case of searching for the optimal solutions. In this work, we study the reinforcement learning actor-only algorithm for the problem of semi-active vibration control. The aim is to exploit the convergence property which is naturally inherited from the incorporated gradient descent method and to examine the stabilizing performance when compared to competitive control strategies.

We consider a class of semi-active vibrating structures described by the bilinear dynamical equation:

$$
(1) \qquad \dot{x}(t) = A\,x(t) + \sum_{j=1}^{m} u_j\,B_j\,x(t) + F(t)\,,\ \ x(0) = x_0\,.
$$

In (1), x, $u_1, ..., u_m$, and A, $B_1, ..., B_m$ stands respectively for the state vector, control functions, and constant matrices. The vector F stands for a repetitive short-time excitation defined be a periodic function with unknown amplitude and frequency (concerned for example with drilling processes). The aim is to design the control functions $u_j \in [u_{min}, u_{max}]$, $j = 1, ..., m$ (later referred to as the policy functions), and reinforcement learning algorithm that allows these functions to adjust their parameters (policy parameters) guaranteeing the best stabilization of the transient vibrations of the system (1) induced by the excitation F.

2. Design of the RL control

For the considered process time $t \in [0, T]$, for (1) we assume the switching state-feedback policy functions $u_1, ..., u_m$ defined as:

$$
(2) \qquad u_j(t) = \begin{cases} u_{min}, & x^T(t)K_j(t)x(t) \geq 0, \\ u_{max}, & x^T(t)K_j(t)x(t) < 0. \end{cases}
$$

In (2), K_j is the policy parameter and structured by two sub-parameters. The first one is K_j^*, iterated using the reinforcement learning actor-only algorithm for the time window $t \in [0, T_L]$ and then assumed for the time $t \in [0, T_F]$ ($T_F \geq T_L$) where the excitation force $F \neq 0$ is acting on a structure. The second sub-parameter is K_j^0, assumed for the free vibration for $t \in (T_F, T]$, i.e. when $F = 0$, and predefined based on the solution to the Lyapunov equation to guarantee the asymptotic stability of the autonomous form of the system (1) (see [5]). The aim of reinforcement learning is to minimize the cost functional J, defined as the integral of the structure's

energy computed for the learning time window $t \in [0, T_L]$:

$$(3) \qquad J(T_L) = \frac{1}{2} \int_0^{T_L} x^T(t) Q x(t) \, \mathrm{d}t \,, \quad Q \succ 0 \,.$$

For updating the policy parameter K_j^*, the reinforcement learning algorithm will use the following updating sequence and derivative of the cost functional:

$$(4) \qquad K_j^{*+} = K_j^* - \alpha_j \left(\frac{\mathrm{d}J}{\mathrm{d}K_j^*} \right)_{|K_j^*} \,, \quad \frac{\mathrm{d}J}{\mathrm{d}K_j^*} = (u_{max} - u_{min}) \sum_{i=1}^s p^T(\tau_i) \, B_j \, x(\tau_i) \, x(\tau_i) \, x^T(\tau_i) \,.$$

In (4), p and $\{\tau_i\}_{i=1,\ldots,s}$ denotes respectively the adjoint state associated to the cost functional (3) and the sequence of time instants $t \in [0, T_L]$ when $x^T(t) K_j^* x(t) = 0$. The sequence in (4) is initialized with K_j^0. The step size $\alpha_j > 0$ is selected by trial and error, to assure substantial decreases of the cost functional value.

3. Case study and results

We study an aluminum beam structure characterized by length $L = 1$ [m], moment of inertia $I = 0.7210^{-10}$[m^4]), mass per unit length $\mu = 0.2$[kg/m]), and simply supported at both ends with the additional support of the semi-active device mounted at the position $0.4L$. The structure is subjected to the periodic force acting at the location $0.6L$. For the semi-active supports, we assume the elastic and damping forces that they generate depend linearly on the control variable u. Using this assumption and the finite element model for the beam structure, we eventually represent the considered system in the form of (1). To perform the reinforcement learning algorithm based on (4), we repeat 500 excitations of the duration $T_F = 0.2$[s], frequency 25[Hz], and amplitude 200[N]. The scenario is repeated three times assuming the learning time windows $T_L = 0.4T_F$, $T_L = 0.75T_F$, and $T_L = T_F$. After the learning process, we compare the established RL control to the optimal, passive, and heuristic [4] strategies. Summarizing the simulation results (see Table 1), we conclude that the RL control in the cases of $T_L = 0.4T_F$ and $T_L = 0.75T_F$ provides suboptimal performance. The observed minor drop of the performance in the case of $T_L = T_F$ results from a slower convergence of the update sequence (4) that is concerned with the increased difficulty in the selection of the step size α. The observations remain intact when for the learning process we include relatively small random perturbations of the excitation frequency (up to 20%).

Passive strategy	RL control			Heuristic control	Optimal control
	$T_L = 0.4T_F$	$T_L = 0.75T_F$	$T_L = T_F$		
1.0000	0.6416	0.6412	0.6956	0.8186	0.6340

Table 1: Cost functional J values for the considered control cases (normalized to the passive case).

References

[1] C. Dengler C and B. Lohmann. Actor-critic reinforcement learning for the feedback control of a swinging chain. *IFAC Papers*, 51:378–383, 2018.

[2] G. Takacs G and B Rohal-Ilkiv. Model predictive control algorithms for active vibration control: a study on timing, performance and implementation properties. *J Vib Control*, 20(13):2061–2080, 2013.

[3] A. Oveisi, M. Hosseini-Pishrobat M, T Nestorovic, and J. Keighobadi. Observer-based repetitive model predictive control in active vibration suppression. *Struct Control Health Monit*, 25(5):e2149–1–23, 2018.

[4] D. Pisarski. Decentralized stabilization of semi-active vibrating structures. *Mech Syst Signal Process*, 100:694–705, 2018.

[5] D. Pisarski, T. Szmidt, and R. Konowrocki. Decentralized semi-active structural vibration control based on optimal system modelling. *Struct Control Health Monit*, 27(11):e2624–1–20, 2020.

Electromagnetically-controlled shape morphing composite

P. Bartkowski[1], F. Gawiński[1], Ł. Pawliszak[2]

[1]*Warsaw University of Technology Faculty of Automotive and Construction Machinery Engineering, Warsaw,*
[2]*Warsaw University of Technology Faculty of Materials Science and Engineering of Material Science, Warsaw*

e-mail: piotr.bartkowski@pw.edu.pl

Abstract

The electromagnetically-controlled shape morphing composite (e-morph) as a novel material for soft robotics is presented in this work. The structure is composed of a granular core and an outer shell made of silicon, with channels filled with liquid metal. Composite can change its shape in a controlled way by Lorentz forces, while the jamming mechanism allows the granules used in the core to maintain the desired shape. This work provides a detailed description of the composite, and empirical and simulation results of the samples tested.
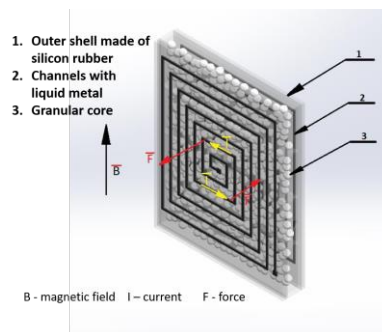
Fig. 1 Composite concept

Also the numerical simulation and potential applications of this material that can be used in the future are presented. At the end the conclusion and possible future work is presented.
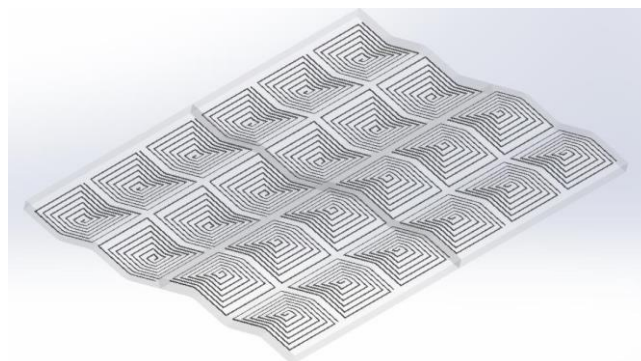
Fig. 2 Concept of a morphable plate

References

[1] Mao Guoyong, Drack Michael, Karami-Mosammam Mahya, Wirthl Daniela, Stockinger Thomas, Schwödiauer Reinhard, Kaltenbrunner Martin, "Soft electromagnetic actuators", Science Advances, vol. 6, no. 26, 2020.
[2] B. Jamil, G. Yoo, Y. Choi and H. Rodrigue, "Proprioceptive Soft Pneumatic Gripper for Extreme Environments Using Hybrid Optical Fibers", in IEEE Robotics and Automation Letters, vol. 6, no. 4, pp. 8694-8701, Oct. 2021.

ON THE DECOMPOSITION OF ACTUATION STRESSES FOR SHAPE CONTROL OF VISCOELASTIC SOLIDS AND STRUCTURES IN THE PRESENCE OF SHOCK AND ACCELERATION WAVES

H. Irschik[1], M. Krommer[1]

[1] *Institute of Technical Mechanics, Johannes Kepler University of Linz, Linz, Austria*

e-mail: hans.irschik@jku.at, michael.krommer@jku.at

1. Area of interest, basic assumptions and methods used

The present paper deals with eigenstrain-induced dynamic shape control of viscoelastic solids and structures. Linear viscoelastic bodies that are constitutively described by Boltzmann-type hereditary laws are studied under the action of transient forces and prescribed boundary conditions and with a given initial past history. We restrict to small deformations, thus dealing with a completely linear setting. Our goal of dynamic shape control is to find additional transient distributions of eigenstrain-induced actuation stresses such that the resulting total displacements of the body under consideration vanish. Quasi-static problems are included as special cases. The eigenstrains we have in mind for inducing actuation stresses are of the piezoelectric type, such as those used in smart materials and structures.

We are interested in analytic formulations for the necessary eigenstrain-induced actuation stresses; the question of restrictions on the allowable amount of the eigenstrains needed for producing the required actuation stresses will not be considered. Also without such restrictions, shape control represents an inverse problem, being ill-posed in the mathematical sense, but being of a high practical relevance also in the present linear setting, since engineering structures often are designed to operate in the linear range; due to linearity it turns out that solutions for this inverse problem do exist, and that they depend continuously on the input data, but these solutions need not to be unique. This gives freedom for minimizing the amount of eigenstrains.

Our contribution is organized as follows: Based on forthcoming own formulations [1], which extend older results of our group on shape control of transient smooth elastic vibrations, we first summarize the general conditions that must hold for the actuation stresses in order that the goal of shape control is satisfied also in viscoelasticity and when shock and acceleration wave fronts are present. These conditions are formulated in a three-dimensional setting and contain both, field conditions that must hold throughout the body outside the wave fronts, and jump conditions that must be satisfied across the locations of the fronts. We then treat the following question: Is it possible, also under situations, for which imposed transient forces and prescribed time-dependent boundary conditions would induce shock or acceleration waves, to decompose actuation stresses that are necessary for shape control into two portions, namely into a portion that is stress free, and a portion that is free of displacements? Again, in extension of older own results on transient smooth vibrations, we develop a positive answer to this question, and present corresponding conditions for the necessary decomposition of the eigenstrain-induced actuation stresses. A main theoretical result is that the decomposition conditions for shape control are not influenced by the hereditary behaviour of the material, but are the same as for the case of a purely elastic body. Our theoretical considerations are accompanied by examples from uniaxial wave propagation, giving evidence for the correctness of the derived field and jump conditions. The extended problem of displacement tracking, namely to find actuation stresses such that the resulting total displacements of the body under consideration do follow some prescribed trajectory, will be treated in a future study.

The mathematical notation of our contribution is motivated by the Encyclopedia-articles by Gurtin [2] on the linear theory of elasticity, and by Leitman and Fisher [3] on the linear theory of viscoelasticity. Methodologically, our derivation of necessary field and jump conditions for the actuation stresses utilizes some consequences of uniqueness theorems given by Edelstein and Gurtin [4]. The present contribution extends previous works on shape control and displacement tracking, which are shortly summarized below.

2. Some basic previous own works

Our group has been dealing with static and dynamic shape control and displacement tracking of solids and structures by eigenstrains since several decades. For reviews, including also works of others, see e.g. [5] and [6]. In statics, eigenstrains without deformations, so-called impotent or zero-displacement eigenstrains, were addressed by Mura [7] for elastic bodies. Within the same context, the ill-posedness of shape control problems as well as so-called nilpotent or zero-stress eigenstrains were discussed by Irschik and Ziegler [8]. In static thermoelasticity, Nyashin, Lokhov and Ziegler [9] showed that any static actuation stress in a linear elastic body can be uniquely decomposed into a zero-stress and a zero-displacement portion. The extension of this decomposition to viscoelastic bodies for dynamic shape control and displacement tracking of smooth displacements was given by Irschik and Krommer [10]. For elastic shape control and displacement tracking in the presence of smooth displacements, see [11]–[13] and the contributions cited there on structural applications. A first account on shape control in the presence of shock and acceleration waves in elastic bodies was given in [14] in the context of body force analogies. A more complete elastic study on displacement tracking in the presence of shock and acceleration waves was presented in [15]. Extension of this work to viscoelasticity will be published in a forthcoming paper [1]. In the present contribution, we add and exemplify a viscoelastic decomposition theorem for actuation stresses.

References

[1] H. Irschik and M. Krommer. *On the equivalence of force and eigenstrain induced displacements in linear visco-elastic solids and structures, with emphasis on the presence of singular waves.* Forthcoming.

[2] M. E.Gurtin. *The Linear Theory of Elasticity*. In: Encyclopedia of Physics (S. Flügge, Ed.), VIa/2; Springer: 1, 1972.

[3] Leitman, and G. M. C. Fisher. *The Linear Theory of Viscoelasticity*. In: Encyclopedia of Physics (S. Flügge, Ed.), VIa/3, Springer: 1, 1973.

[4] W. Edelstein and M. E. Gurtin: Uniqueness theorems in the linear dynamic theory of anisotropic viscoelastic solids. *Arch. Rat. Mech. Anal.*, 17: 47, 1964.

[5] H. Irschik. A review on static and dynamic shape control of structures by piezoelectric actuation. *Eng. Struct.*, 24: 5 2002.

[6] H. Irschik, M. Krommer et al. *Active and Passive Shape Control of Structures*. In: Proc. 5 th Europ. Conf. Struct. Contr. (EACS 2012, E. Del Grosso, P. Basso, Eds.), Paper No. 146, 2012.

[7] T. Mura. *Micromechanics of Defects in Solids, 2nd ed*. Kluwer, 1991.

[8] H. Irschik and F. Ziegler. Eigenstrain Without Stress and Static Shape Control of Structures. *AIAA Journal*, 39: 1985, 2001.

[9] V. Nyashin, V. Lokhov and F. Ziegler. Stress-free displacement control of structures. *Acta Mech.*, 175: 45, 2005.

[10] H. Irschik, M. Krommer. *Dynamic Displacement Tracking of Force-Loaded Linear Elastic or Viscoelastic Bodies by Eigenstrain-Induced Actuation Stresses*. In Proc. ASME IDETC/CIE Conf. 2005, Am. Soc. Mech. Eng., Paper No. DETC2005-84835: 681 (https://doi.org/10.1115/DETC2005-84835), 2005.

[11] H. Irschik and U. Pichler. Dynamic shape control of solids and structures by thermal expansion strains. *J. Thermal Stresses*, 24: 565, 2001.

[12] H. Irschik and U. Pichler. An extension of Neumann´s method for shape control of force-induced elastic vibrations by eigenstrains. *Int. J. Solids Struct.*, 41: 871, 2004.

[13] H. Irschik, M. Krommer and Ch. Zehetner. Displacement tracking of pre-deformed smart structures. *Smart Struct. Syst.*, 18: 139, 2016.

[14] H. Irschik, M. Krommer and U. Pichler. *A Body-Force Analogy for Dynamics of Elastic Bodies with Eigenstrains*. In: Modeling, Signal Processing and Control (Proc. SPIE's 12th Annual Int. Symp. Smart Mat. Struct., R.C. Smith, Ed.). SPIE - Am. Soc. Opt. Eng., Vol. 5757: 10, 2005.

[15] H. Irschik and A. Brandl. *On Control of Structural Displacements by Eigenstrains in the Presence of Singular Waves*. In: Contributions to Advanced Dynamics and Continuum Mechanics (H. Altenbach, H. Irschik and V. P. Matveenko, Eds.), Springer: 95, 2019.

SEMI-ACTIVE VIBRATION MITIGATION OF 2D FRAMES BY MEANS OF LOCAL NODAL RECONFIGURATION

B. Poplawski[1], G. Mikułowski[1], A. Mróz[2], and Ł. Jankowski[1]

[1]*Institute of Fundamental Technological Research, Polish Academy of Sciences, Warsaw, Poland*
[2]*Adaptronica sp. z o.o., Łomianki, Poland*

e-mail: bpop@ippt.pan.pl

1. Introduction

A semi-active control strategy has been developed that aims at mitigating vibrations in 2D slender, planar frame structures. It is anchored in the energy management strategy called Prestress Accumulation–Release (PAR) [1].

Structural slenderness is often the result of high expectations for minimum weight of the designed structures. Such problems are frequently encountered in the case of structures designed to serve in space, where every additional kilogram put into orbit costs thousands of dollars. This undesirable feature raises a number of problems, one of which is the low effectiveness of natural mechanisms of vibration damping. In such a case, once excited, vibrations can result in repeated large deformations of the structure and last for a prolonged time, which may lead to fatigue damage and stabilization problems.

We have designed a vibration damping system to be used especially in such structures, however not exclusively. It consists of dedicated, especially designed, semi-active nodes that are used for dynamic reconfiguration of the controlled structure. These nodes can change their state of operation from frame node connection to a truss-like connection in a controlled manner. Transition between operating states is achieved by piezoelectric stacks which uncouple the interacting friction surfaces, thereby eliminating the ability of the node to transmit bending moments. Proper arrangement of such nodes in the system allows for a momentary change of its mechanical characteristics in order to significantly increase the dissipation rate and vibration mitigation effectiveness [2]. In particular, it is possible to extract individual beams from the frame structure and change their state of operation, leading to a temporary change in the effective stiffness of the entire structure. Such an approach enables the possibility to control a relatively complex frame structures that consist of many elements. It should be emphasized that the semi-active nodes are fail-safe: they remain in their default frame mode of operation when the source of the electric energy, which powers the control system, fails.

The proposed control strategy works in a closed-loop manner, where the feedback signal is the strain energy of the controlled structure. It can be either the energy of the entire structure or just one of its elements. This distinguishes between the so-called global and local versions of the control strategy. The PAR methodology is embodied here by accumulating the strain energy and releasing it by switching the state of semi-active nodes for a very short period of time. Such a switch results in the immediate change of kinematic constraints of the entire structure. Accumulated strain energy induces then high modes of vibration, where the energy is dissipated at a very high rate by means of standard material damping capabilities. This approach was derived heuristically, relying on the bang-bang control methodology. Switching moments from frame to truss states of operation of the semi-active nodes are determined as the local maxima of the feedback signal. Intuitively, such a condition ensures the highest possible potential of transferring the energy into high-frequency vibration modes.

The equation of motion of a structure equipped with N described semi-active nodes can be presented as:

$$(1) \qquad \mathbf{M}\ddot{\mathbf{x}}(t) + (\mathbf{C} + \sum_{i=1}^{N} \gamma_i(t)\mathbf{C}_i)\dot{\mathbf{x}}(t) + \mathbf{K}\mathbf{x}(t) = \mathbf{f}(t)$$

where $\mathbf{M}$, $\mathbf{C}$ and $\mathbf{K}$ are global mass, damping and stiffness matrices, respectively, and $\mathbf{f}$ is the vector of possible external loading. The terms $\gamma_i(t)\mathbf{C}_i$ represent the coupling of rotational degrees of freedom (DOFs), which is modeled through a very high damping of the relative motion between the two selected DOFs. Here $\mathbf{C}_i$ is the matrix of the *i*th rotational damper, while $\gamma_i(t)$ is the corresponding damping coefficient that can be altered and serves as the control function that implements the derived control strategy.

In numerical simulations, parameters $\gamma_i(t)$ are changed in a bang-bang manner, based on the feedback signal:

$$\gamma_i(t) = \begin{cases} 0, & \text{at local maxima of } E_{\text{strain}} \\ \gamma^{\max}, & \text{otherwise} \end{cases} \tag{2}$$

In experimental work, the global strain energy has to be somehow approximated based on available sensor readings. Our approach employed laser measurements of in-plane displacements of the frame's free tip. We have chosen it as a good proxy for the strain energy changes associated with the eigenmodes which could possibly be controlled with our hardware. The local strain energy could be reliably measured using a set of strain gauges attached to the elements of interest. The length of the period in which the semi-active nodes remain in their truss-like state of operation can be determined in couple of ways. Numerically, the most effective condition seems to be based on the amount of the strain energy retained in the structure after the switch. However, a very simple time-based constraint is also sufficient and is preferable in experimental implementations.

2. Numerical and experimental results

The control strategy has been tested for an exemplary frame structure with two semi-active nodes shown in Fig. 1. Analyses were performed for the case of free and forced vibrations. Initial displacement conditions for the free vibration case were set correspondingly to the first and the second natural modes of vibration. In the case of forced vibrations we used harmonic and random force excitation. Exemplary results, presented in the form of time evolution of the normalized total mechanical energy (Fig. 1), demonstrate a very high effectiveness of the proposed strategy in mitigation of vibrations. For the first mode of vibration, the energy is dissipated almost completely after just two control switching cycles. For the second mode, the energy dissipation is less effective, however the control system enhances the natural dissipation abilities of the structure to a very large extent. Other results will be presented during the conference.
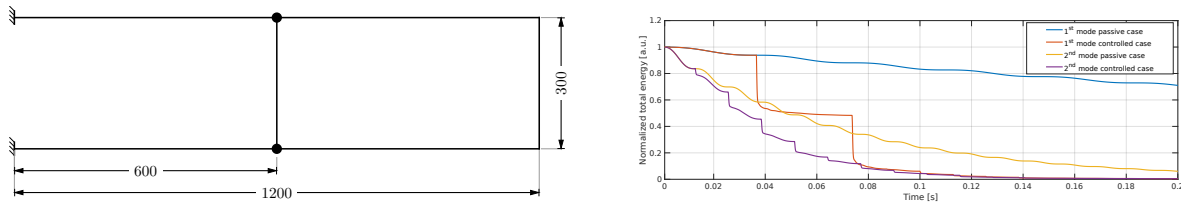
Figure 1: Exemplary frame structure (left) and the comparison of the total mechanical energy for the first and second natural modes of its free vibration (right)

3. Conclusions

The proposed vibration mitigation strategy has proven to be very effective in mitigating the vibrations of planar frame structures. Due to the difficulties in estimating the strain energy of the entire structure, its approximation must be used in experiments. Controlling the first few vibration modes could be successfully realized based on in-plane displacements of the frame free end or the related strain readings. This problem does not occur when the energy of individual elements is used.

References

[1] A. Mroz, A. Orlowska and J. Holnicki-Szulc. Semi-active damping of vibrations. Prestress Accumulation–Release strategy development. *Shock Vib* 17(2):123–36, 2010.

[2] B. Poplawski, G. Mikulowski, D. Pisarski, R. Wiszowaty and L. Jankowski. Optimum actuator placement for damping of vibrations using the Prestress Accumulation–Release control approach. *Smart Struct Syst* 24(1):27–35, 2019.

Session S3

LIVE-I project session – lightweight gear transmission

Organizers:

Mohamed Ichchou (*Ecole Centrale de Lyon, France*)

Francesco Franco (*University of Naples, Italy*)

Stephan Rinderknecht (*TU Darmstadt, Germany*)

Przemysław Kołakowski (*Adaptronica sp. z o.o., Poland*)

ASSESSMENT OF THE STATIC AND DYNAMIC BEHAVIOURS RESULTING FROM A GEAR BLANK WITH HOLES

F. Bejar[1], J. Perret-Liaudet[1], O. Bareille[1], M. Ichchou[1], and M. Fontana[2]

[1]*Ecole Centrale de Lyon,36 avenue Guy de Collongue, 69134 Ecully Cedex, France*
[2]*Powerflex s.r.l, via Campitiello 6, Benevento, 82030 Limatola, Italy*

e-mail: firas.bejar@ec-lyon.fr

1. Introduction

The development of car components is becoming more oriented towards lightweight design as the restrictions for greener technologies are growing stricter. However, lighter parts such as gears come with the additional risk of emitting more vibrations and consequently more noise. One of the main strategies for reducing the weight of gears is to apply some holes within the blank since a solid wheel can be considered to be over-designed vis-à-vis their main functionality. While this approach is popular, the understanding of the dynamic side effects is still shallow and not deeply investigated in literature. This study represents a basic assessment of the consequences of lightweight structures from a static and dynamic point of view.

2. Methodology

A simplified gearbox model consisting of gears, shafts, bearings and a housing was utilized for this study. The shafts were represented by modified Timoshenko beam elements while the gear bodies were represented by finite element structures since they allow to detect out-of-plane deformations. A sub-structuring method based on Craig-Bampton approach [2] was used to limit the number of degrees of freedom of the finite element components which are in this case the gear blanks and the housing. The bearing stiffness was calculated based on a steady state non-linear analysis taking into account parameters such as the loading conditions, internal geometries, clearances, etc. The gear model is inspired from the configuration of Singh et al. [4]. The gears are represented by their stiffness and inertia, and connected between them with a conceptual spring positioned along the line of action that represents the time varying mesh stiffness. The calculation of this latter is based on several iterative methods found in the literature [5–7] accounting for the microgeometry details of the teeth.

The bending and twisting movements are taken into consideration through the use of an embedded finite element representation of the stiffness inside the gear contact algorithm. Since the gear whine is of main interest in this study, the non-linear dynamic model of the gearbox is linearized around a static torque condition in order for a harmonic analysis to be possible. This will assume that the meshing stiffness between the gears is taken as the average stiffness and the mode shapes of the system will be calculated correspondingly. It should be mentioned that in these preliminary simulations, effects such as the time-varying misalignment, friction and damping have been overlooked. While this approach proved to be fairly accurate for standard gears, it lacked when it comes to modeling the real behaviour if geometrical cavities are being introduced as these latter are expected to cause the stiffness of the gears to be fluctuating in the circumferential direction. For this purpose, a quasi-harmonic approach was implemented instead that totally ignores the steady-state assumption [1].

3. Results

The model was first addressed in terms of its static transmission error (STE) which is considered to be as the principle source of excitation if the tonal noise is to be tackled [8]. The transmission error occurring due to the variation of the number of teeth in contact can be expressed in the form of a displacement along the line of action as the following:

$$(1) \qquad STE(\theta_1) = R_{b_2}\theta_2(\theta_1) - R_{b_1}\theta_1$$
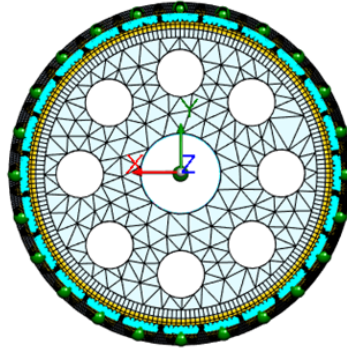
Figure 1: Graphical representation of an 8-hole gear

It is generally calculated for different rotational positions of the driving pinion. With this fact in mind, it can be assumed that the estimation of the TE value will depend on the local stiffness of the blank, in other words, whether the meshing region is located above a hole or a land position. The comparison between a normal and a modified gear shows that the STE increases in the second case. This can be fairly reasonable considering that a reduced local stiffness will induce additional deformation along the line of action. However, the static transmission error being speed-independent remains insufficient to evaluate the performance of the system under normal operating conditions. Thus, the dynamic mesh force (DMF) was addressed for this purpose [3]. The DMF calculation relies on isolating each side of the gear mesh and applying a unit transmission error in the line of action to determine the individual compliances from the pinion and wheel sides which are then summed up together to give the total compliance. The inverse of the total compliance gives the dynamic mesh stiffness which is then multiplied by the harmonics of TE to get the dynamic mesh forces associated to those individual excitations.

(2)
$$C_{mesh}(\omega) = C_p(\omega) + C_w(\omega)$$

(3)
$$D(\omega) = (C_{mesh}(\omega))^{-1}$$

(4)
$$F_i(\omega) = D(\omega) * \delta i$$

The comparison between the cases showed that the gear having the holes represent a lower overall mesh force. The reason for this is that the absence of material increases the compliance of the body which decreases the dynamic stiffness and hence the resulting mesh force. Furthermore, the holes are responsible for the appearance of sidebands with a particular order related to their number which are considered as additional excitations that are susceptible of increasing and spreading the response amplitude over larger frequency and speed ranges.

4. Conclusion

While the gear holes proved to reduce the overall amplitude of the main mesh harmonics, the undesired side-bands can represent a challenge when it comes to the dynamic tuning of the gears. This calls for a thorough optimisation regarding the amount of removed material that will guarantee a minimum dynamic response while still satisfying the basic static conditions.

References

[1] Yasuhiro Asai, Tokihito Nagae, and Yasuhide Hirabayashi. Time domain nv simulation with a/t assy model by modal synthesis method. Technical report, SAE Technical Paper, 2018.

[2] Roy R Craig Jr and Andrew J Kurdila. *Fundamentals of structural dynamics*. John Wiley & Sons, 2006.

[3] Andy Gale, Paul Langlois, and Owen Harris. Gear blank tuning.

[4] Ahmet Kahraman and Rajendra Singh. Non-linear dynamics of a spur gear pair. *Journal of sound and vibration*, 142(1):49–75, 1990.

[5] Paul Langlois, Baydu Al, and Owen Harris. Hybrid hertzian and fe-based helical gear-loaded tooth contact analysis and comparison with fe. *Gear Technology*, 6:54–57, 2016.

[6] Emmanuel Rigaud. *Interactions dynamiques entre dentures, lignes d'arbres, roulements et carter dans les transmissions par engrenages*. PhD thesis, Ecully, Ecole centrale de Lyon, 1998.

[7] Emmanuel Rigaud and Denis Barday. Modelling and analysis of static transmission error. effect of wheel body deformation and interactions between adjacent loaded teeth. In *4th World congress on gearing and power transmission*, volume 3, pages 1961–1972, 1999.

[8] DB Welbourn. Fundamental knowledge of gear noise: a survey. Technical report, 1979.

MATERIALS OPTIMIZATION OF LIGHTWEIGHT GEAR TRANSMISSION COMPONENTS

W. Masmoudi[1], J-L. Wojtowicki [2], G. Petrone[1], F. Franco[1], and S. De Rosa[1]

[1]Pasta-Lab, Universita degli Studi di Napoli Federico II, via Claudio 21, 80125 Napoli, Italy
[2]VIBRATEC SA, 69130 Ecully, France
e-mails: *masmoudi.wael@unina.it, jean-luc.wojtowicki@vibratec.fr, giuseppe.petrone@unina.it, francof@unina.it, derosa@unina.it,*

1. Abstract

Mass reduction is one of the main innovation drivers in several industrial sectors, including the automotive research and industry communities. The use of lightweight gearbox originated in the aerospace industry, where weight optimization has always been a key topic, and is recently extending to other sectors in the transportation such as automotive industry, where huge benefits are expected from mass reduction to enable products to comply with the ever-stricter regulations on fuel efficiency and emissions.
A more recent approach for weight reduction in mechanical systems and, specifically, in geared transmissions, is based on the exploitation of composite materials in a hybrid metal-composite design [1].

The authors propose a new configuration in which a combination between thin rim steel gears combined with composite multi-layered composite is studied. Figure 1 shows that gears teeth remain in steel and a high-modulus carbon fibre reinforced epoxy laminate will be placed in the web part. Since it is less solicited region, this strategy would be promising regarding mass reduction improvement and mechanical efficiency of the system.
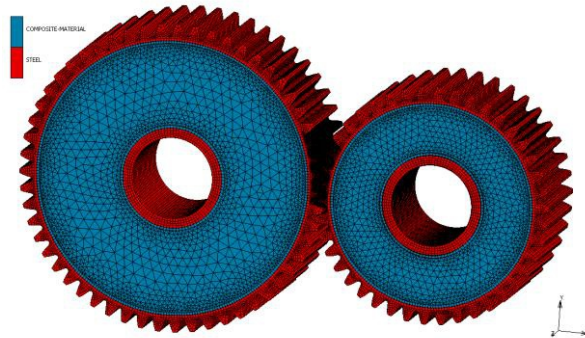
Figure 1. Hybrid gear pairs model

Moreover, developing such smart concepts must be always in accordance with vibroacoustic comfort, since whining noise corresponds to a large part of the noise perceived by passengers as well as the noise detected outside the vehicle: a common goal for improving NVH (Noise, Vibration and Harshness) is to obtain quiet gear systems by reducing the whining noise level.

The dynamic mesh force results mainly from the well-known static transmission error (STE) defined as the difference between the actual position of the output gear and the position it would occupy in case of perfect mate of the gear pair [2,3]. The STE is expressed along the line of action as:

(1)
$$\delta(\theta_1) = R_2\theta_2 - R_1\theta_1$$

θ_2 and θ_1 are respectively the angular position of the input wheel and the output gear. R_2 and R_1 are the base radii of the input wheel and the output gear.

A multibody analysis approach is considered using a Finite Element (FE) model in order to estimate an accurate and more realistic result of the STE curve for such a complex structure. The model is built by using the commercial software SIMSENTER SIMENS for model generation, and MARC as solver for non-linear contact analysis.

The STE obtained from conventional cases is first benchmarked with existing software's results namely ROMAX [4] and VIBRAGEAR. Then the hybrid gear pairs results are compared with conventional steel once.

The obtained results were promising, especially when compared to the common approach of gear lightening based on material removal from the gear body, such as "with-holes" or "thin-rim" gears, in which modulation of the STE and an increase in the amplitude were detected respectively.

Thus, the NVH of the transmission system is assessed starting from the STE excitations inducing dynamic excitations of the system. Where the hybrid structure results are compared with the conventional case.

Keywords: Lightweight, composite materials, FEA, NVH

References

[1]   Handschuh, R. F., Laberge, K. E., Deluca, S., & Pelagalli, R. (2017). Vibration and Operational Characteristics of a Composite-Steel (Hybrid) Gear. 13(December), 80–87.
[2]   Harris, S.L., 1958. Dynamic Loads on the Teeth of Spur Gears:. Proceedings of the Institution of Mechanical Engineers SAGE Publication- sSage UK: London, England.
[3]   Welbourn, D.B., 1979. Fundamental knowledge of gear noise: a survey. Number: IMechE-C117/79.
[4]   Romax Technology, Romax Designer User Manual, 2021.

Enhanced vibro-acoustic behavior of lightweight gearbox housing through the use of locally resonant metamaterials

D.R. Amaral[1], M. Ichchou[1], P. Kolakowski[2], P. Fossat[1], and M. Salvia[1]

[1]*LTDS, Laboratoire de Tribologie et Dynamique des Systems, Ecole Centrale de Lyon, France*
[2]*Adaptronica sp. z o.o., Łomianki, Poland*

e-mail: daniel.amaral@ec-lyon.fr

The reduction of the mass in vehicles represents an increase of its range and a reduction of greenhouse gases emission (and other noxious gases/particles) in the case of internal combustion engine (ICE) vehicles. This work is devoted to the lightening of the gearbox housing (GBH) and to the introduction of new paradigms in the early design of GBH using metamaterials.

Generally, the lightweight design in engineering applications gives rise to noise and vibration problems. Therefore, the automotive lightweight solutions must be developed in conjunction with innovation in the area of noise and vibration. The main focus of this work is to improve the vibro-acoustic behavior of the lightweight GBH through passive means, using vibro-acoustic metamaterials. Some automotive metamaterial solutions are found in the recent literature [1] [6] [4], however these concepts were never applied to GBHs. GBHs must follow specific requirements, namely provide support for the primary gearbox components, the selector mechanisms and actuators. The GBH must assure the correct gear meshing, respecting the assembly tolerances of the rotating components, and cope with system loading generated by the transmitted torque. Additionally, there are other requirements related with the protection of the gearbox inner components, enclosure of the lubricant, and heat dissipation. The mechanical loading at the bearing supports is dependent on the rotating components geometries, characteristics, and assembly configurations. The mechanical loading depends on the transmission ratio, the inclination angle of the gear teeth (in case of helical gears), the transmitted power, the input speed, and the distance between axes [7]. At the bearing support, loads are transferred from the shafts to the housing structure in radial and axial directions. In this work, a typical characteristic loading was applied in the GBH bearings'connection. GBHs are typically complex structures, whose geometry widely depends on the arrangement of the inner components, external connections and attached auxiliary components, such as actuators and electric units. Generally the gearbox housing has numerous openings, connections, patterns, and thickness changes over the surface. For ease of reference, a simpler gearbox housing geometry based in the works of Figlus et al. [3] [2] was considered.

The reduction of mass while preserving the benefits and strengths of the design is the core of the lightweight design approach. For this purpose, topology optimization methods can contribute, enabling multi-objective optimization of the housing geometry. In the literature, some works can be found on the topic of structural optimization of GBHs [7] [5]. A similar topology optimization process was followed in order to reduce the mass of the original GBH, optimizing the material distribution within a specified design space. The optimization objective was to maximize the stiffness of the structure, minimizing the structure compliance. Through numerical simulations, a sound power radiated comparison between the original GBH and the lightweight GBH was performed, see Figure 1. As visible in the Figure 1, the mass reduction shifts the peaks in the sound power to the lower frequencies. The objective of this work is to prove that it is possible to attenuate the low frequency peaks in the sound power radiated from lightweight GBHs through the use of vibro-acoustic metamaterials.

Metamaterials are a novel class of complex engineered materials. Generally, they take the form of unit cell (UC) assemblies of non-homogeneous material composition and/or topology. The most outstanding functionality of the vibro-acoustic metamaterials is the capability of enabling strong attenuation of vibration and noise in specific frequency ranges. These frequency ranges are called band gaps (BGs) or stop bands (SBs). There are two types of vibro-acoustic metamaterials: Phononic Crystals (PCs) which base the wave attenuation in the Bragg scattering phenomena, and Locally Resonant Metamaterials (LRMs) which rely on the internal resonances of the UCs. The LRMs prevail over PCs in the practical applications to attenuate low-frequency vibration, since the UC size and the spacing between the sub-size UCs are not required to be of the same order of the wave-
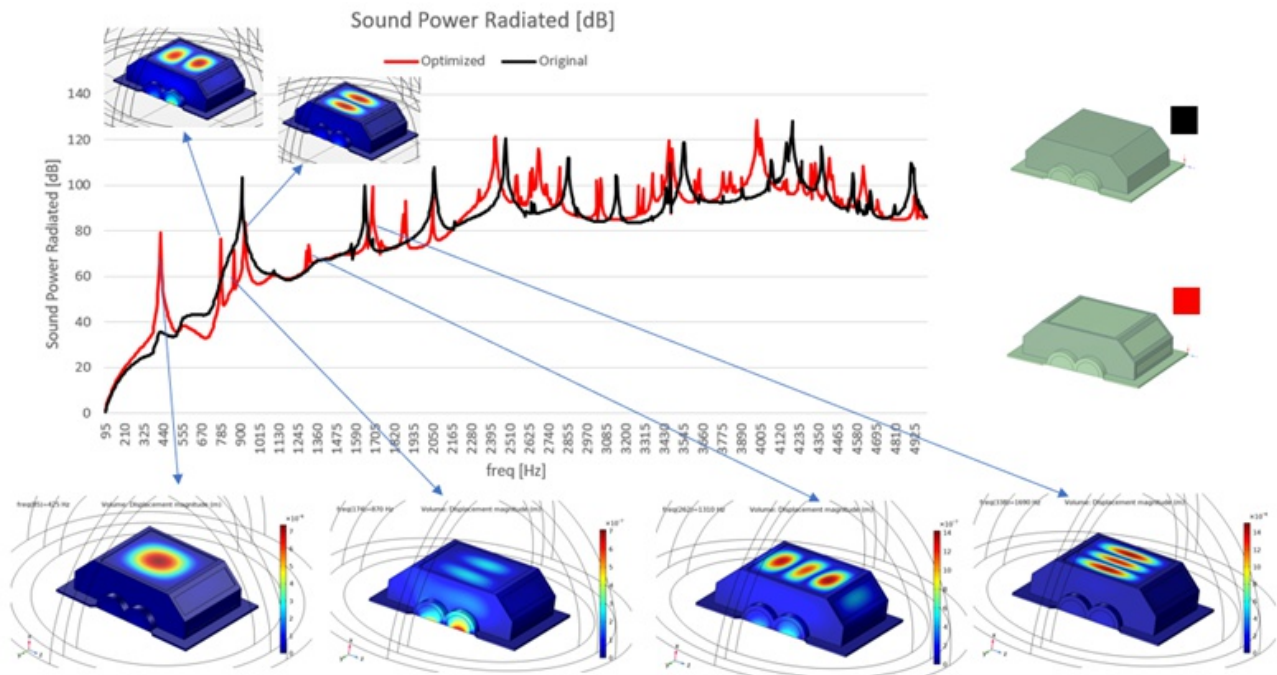
Figure 1: Sound power radiated comparison between a GBH (black) and a lightweight GBH (red)

length to target. This work aims not only to demonstrate that it is feasible to attenuate the low frequency peaks arising from the lightweight design, but it will also aim to prove broad noise attenuation is achievable over the lower frequency range through the correct tuning and modulation of the LRMs applied.

References

[1] N. G.R. de Melo Filho, C. Claeys, E. Deckers, and W. Desmet. Realisation of a thermoformed vibro-acoustic meta-material for increased STL in acoustic resonance driven environments. *Applied Acoustics*, 156:78–82, 2019.

[2] T. Figlus, M. Kozioł, and Ł. Kuczyński. Impact of application of selected composite materials on the weight and vibroactivity of the upper gearbox housing. *Materials*, 12(16):40–44, 2019.

[3] T. Figlus, M. Kozioł, and Ł. Kuczyński. The effect of selected operational factors on the vibroactivity of upper gearbox housings made of composite materials. *Sensors (Switzerland)*, 19(19), 2019.

[4] J. Jung, H. G. Kim, S. Goo, K. J. Chang, and S. Wang. Realisation of a locally resonant metamaterial on the automobile panel structure to reduce noise radiation. *Mechanical Systems and Signal Processing*, 122:206–231, 2019.

[5] L. Ling and Y. Huang. Topology optimization design of gearbox housing in electric bus. *Applied Mechanics and Materials*, 574:173–178, 2014.

[6] L. Sangiuliano, C. Claeys, E. Deckers, J. De Smet, B. Pluymers, and W. Desmet. Reducing Vehicle Interior NVH by Means of Locally Resonant Metamaterial Patches on Rear Shock Towers. *SAE Technical Papers*, 2019-June(June), 2019.

[7] S. Slavov and M. Konsulova-Bakalova. Optimizing weight of housing elements of two-stage reducer by using the topology management optimization capabilities integrated in SOLIDWORKS: A case study. *Machines*, 7(1), 2019.

MANUFACTURING MARGINS AND ROBUSTNESS OF NVH PREDICTION FOR LIGHTWEIGHT TRANSMISSIONS

R. Najib[1], J. Neufond[2], G. Petrone[1], F. Franco[1], and S. De Rosa[1]

[1]Pasta-Lab, Universita degli Studi di Napoli Federico II, 80125 Napoli, Italy
[2]VIBRATEC SA, 69130 Ecully, France
e-mails: ranim.najib@unina.it, jessica.neufond@vibratec.fr, giuseppe.petrone@unina.it, francof@unina.it,
derosa@unina.it,

1. Abstract

The static transmission error (STE) and gear mesh stiffness fluctuations are the main sources of gearbox excitations responsible for the radiated whining noise. The generated dynamic mesh forces are transmitted to the housing through wheel bodies, shafts, and bearings. The STE results from both tooth deflection and tooth micro-geometries (voluntary profile modifications and manufacturing errors). Optimizing the micro-geometry parameters is a solution to reduce the excitation at the source. This work has two targets: (i) to optimize gear geometry parameters taking into consideration the robustness aspect of the design and manufacturing uncertainties; (ii) the design of a lightweight gearbox. This work brings another contribution to gearbox design optimization in the context of NVH improvement and focuses on the impact of manufacturing uncertainties.

The author addresses the effect of microgeometry variables on reducing STE using an evolutionary algorithm to reduce the computational time needed to reach optimal solutions. The obtained results face robustness issues, for this reason, a sensitivity analysis is carried out on the manufacturing uncertainties of micro-geometry design parameters to define the related influence on STE responsible for meshing excitations. This approach allows the authors to define the tolerances ranges of tooth geometry. To validate the numerical results, an experimental analysis investigates the influence of adapted geometry corrections integrated with gear mounting deviations, misalignments, and operating conditions on the gearbox NVH response.

To meet these targets, the author used a meta-heuristic optimization algorithm based on the particle swarm optimization method (PSO) that proved to be well adapted to multi-parameters complex optimization problems [1]. It is integrated with the existing software *VibraGear* [2] that offers the potential to calculate the vibroacoustic response of the gear design, mainly the peak to peak static transmission error used to develop the fitness function of the optimization problem. *VibraGear* includes two main modules: (i) the first calculates the STE using a quadratic programming approach based on the resolution of contact equations. The chosen Ritz method [3] evaluates the tooth compliance matrix for STE computation. Another output is the mesh stiffness; (ii) the second calculates the dynamic response of the geared systems. This approach is a tool to minimize STE fluctuations considering the effect of geometric dispersions induced by manufacturing uncertainties.

The integration of the robustness aspect in the gear design is via sensitivity analysis. The applied approach is the Morris Method [4] which evaluates the global effects of microgeometry parameter variations in the design range, and parameter deviations in the corresponding tolerance intervals on the tested design objectives related to reducing STE in the gearbox. The adapted tolerance ranges are defined by the gear manufacturer. The contributions of this approach are of main importance. First, reduce the dimensions of design space by reducing the number of parameters considered in the gearbox robust optimization process. Second, reducing the computational time ensures faster convergence of the optimization algorithm towards the optimal design values for the considered gear pair and operational conditions, and also a faster estimation of the robustness indicators for the studied gear design variables (mean value and variance). Finally, the numerical results of the robust optimization problem are investigated experimentally by measuring the vibroacoustic response of conventional and optimized gear sets.

The test bench offers the ability to execute experimental investigations over a wide range of operating

conditions, and have access to both static and dynamic transmission errors. The gain on the optimized model shows the adapted approach's efficiency to enhance the NVH response of the conventional gearbox considering manufacturing uncertainties. Further investigations are to be carried out over hybrid gear pairs to estimate the impact of microgeometry modifications on lightweight gearbox design.

Keywords: Noise, vibration, microgeometry, robustness, Particle Swarm Optimization

References

[1]   A. Carbonelli, J. Perret-Liaudet, E. Rigaud, and A. Le Bot, "Particle swarm optimization as an efficient computational method in order to minimize vibrations of multimesh gears transmission," *Adv. Acoust. Vib.*, vol. 2011, 2011, doi: 10.1155/2011/195642.

[2]   J. Perret-Liaudet, A. Carbonelli, E. Rigaud, B. Nelain, P. Bouvet, and C. J. Vialonga, "Modeling of Gearbox Whining Noise," *SAE Tech. Pap. Ser.*, vol. 1, 2014, doi: 10.4271/2014-01-2090.

[3]   P. Garambois, J. Perret-Liaudet, and E. Rigaud, "NVH robust optimization of gear macro and microgeometries using an efficient tooth contact model," *Mech. Mach. Theory*, vol. 117, pp. 78–95, 2017, doi: 10.1016/j.mechmachtheory.2017.07.008.

[4]   M. D. Morris, "Factorial sampling plans for preliminary computational experiments," *Technometrics*, vol. 33, no. 2, pp. 161–174, 1991, doi: 10.1080/00401706.1991.10484804.

Uncertainty Propagation in Static and Dynamic Gear Whine Analyses through Neural Networks Surrogate Models

B. Z. Cunha[1,3], A. Zine[2], S. Foulard[3], C. Droz[4], and M. Ichchou[1]

[1] *Laboratoire de Tribologie et Dynamique des Systèmes, École Centrale de Lyon, Écully, France.*
[2]*Institut Camille Jordan, École Centrale de Lyon, Écully, France.*
[3]*Compredict, Darmstadt, Germany.*
[4]*Univ. Gustave Eiffel, Inria, Rennes, France.*

e-mail: barbara.zaparoli-cunha@ec-lyon

1. Abstract

Noise, Vibration, and Harshness (NVH) performance is a key aspect to evaluate passenger comfort in vehicles. At the gearbox level, the gear tooth profile deviations give rise to vibrations during the gear meshing process, which is the source of gear whine noise. Therefore, an NVH design should account for the uncertainties at the gear micro-geometry level, demanding several evaluations of the gearbox model. Our study introduces a gearbox surrogate model based on Neural Networks (NN) to create a fast and accurate copy of the static and dynamic gearbox simulations made in Romax software. An accurate surrogate model was built, enabling a reduction of uncertainty propagation analyses time by a factor 20, compared with traditional modeling by Romax.

2. Introduction

Gear whine is a tonal and annoying noise that originates in the gear meshing process in gear transmissions. The main cause of gear whine is the Static Transmission Error (STE), which accounts for the teeth profile deviations from an involute profile due to profile modifications, manufacturing errors, and elastic deflections [1]. The challenges to design a silent gearbox increase in the cases of lightweight gearbox design, a crucial requisite to more sustainable vehicles [5]. The lightweight gearboxes tend to be less stiff, leading to bigger misalignments and STE, as well as greater amplitudes of housing vibration and consequently radiate more noise.

Therefore, to achieve weight reduction while guaranteeing good NVH performance, it is crucial to carry out an appropriate assessment of whining noise. This includes evaluating the STE, the major excitation source, and applying it to evaluate the system dynamic behavior, which is closely correlated with the whining noise [5]. Besides that, the housing should also be included in the system model, allowing to directly quantify its walls vibration and to account for the coupling effects of it with the system. Finally, as profile errors are the source of system excitation, the effect of manufacturing errors cannot be neglected even for tight tolerances, and uncertainty propagation must be performed. [1].

To alleviate the computational burden of the numerous and costly evaluations involved in the static and dynamic analyses of the entire gearbox, we propose to create a surrogate model based on Neural Networks. The surrogate models or response surface methods are simple and efficient input-output maps of a more complex model with little loss of accuracy and are currently used to speed up in many engineering problems.

A surrogate model of the STE was developed by [4] using a parametric second-order regression to fit the model. However, Machine Learning methods usually have better generalization capabilities than parametric methods and could deliver better results. This can also be observed in the comparison of three different STE surrogates trained by [3]. To the author's knowledge, a surrogate to predict dynamic responses of an entire fully-coupled gearbox system has not been achieved so far. By implementing an automatic integration of *Python* with the Romax software, this work will enable to create a novel Neural Network-based surrogate model for the static and dynamic analysis of a complete gear transmission.

3. Methodology and Results

The first step to constructing a surrogate is to have a high-fidelity simulation model to be used as the ground truth. Therefore, we used ROMAX software to create a gearbox model including a pair of helical gears, shafts, bearings, and housing. The gear bodies are modeled as integral with the shafts using Timoshenko beam elements, while the bearings are modeled as [6x6] stiffness matrix by linearizing their behavior near the operational condition. The housing is modeled by a Finite Element (FE) model reduced with the Craig-Bampton method to decrease the computational cost resulting in a fully-coupled system of the gearbox [2].

First, a static analysis of the system is performed to each load condition to evaluate the system misalignment. This information is used in the tooth contact analysis, which also considers the tooth deflection and mesh stiffness using a FE model to evaluate the STE. The STE is then used as the excitation source of the dynamic analysis in the frequency domain that outputs results as the dynamic transmission error, bearing forces and housing accelerations across the operating speed range. Subsequently, a routine was implemented to allow the initialization and execution of Romax through *Python*.

Six tooth micro-geometry parameters were considered, namely the involute slope, lead crown and lead slope for both pinion and gear teeth. Latin hypercube sampling was used as sampling strategy to query 4000 samples due to its good space-filling properties. The resulting database was used to train several multilayer perceptron NN, one for each quantity of interest. The NNs implementation was done by using *Keras* library in *Python*. To illustrate the capabilities of the created surrogates, we use the example of the surrogate that predicts the vibration of one point of the housing, which presented a root mean squared error prediction of only 0.06 m/s^2.

Benefits of the surrogate model become evident when multiple evaluations are necessary, as in uncertainties propagation analysis, implemented in this work with the Markov chain Monte Carlo (MCMC) method. Figure 1 shows the confidence interval obtained with both Romax and the NN surrogate, showing the efficiency of the surrogate, which led to a 20-times reduction of the simulation time with negligible loss of accuracy.
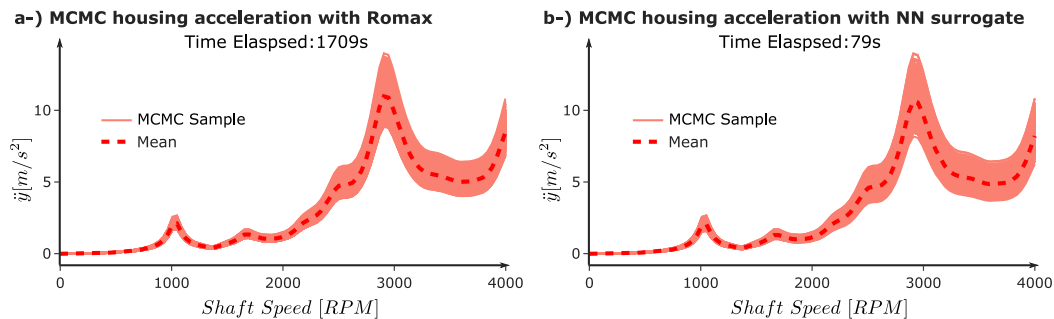
Figure 1: MCMC uncertainties propagation of the housing sidewall acceleration using Romax model (a) and NN surrogate (b).

References

[1] P. Garambois, J. Perret-Liaudet, and E. Rigaud. Nvh robust optimization of gear macro and microgeometries using an efficient tooth contact model. *Mechanism and Machine Theory*, 117:78–95, 2017.

[2] B. James, M. Douglas, and D. Palmer. Predicting the contact conditions for hypoid gear sets by analysis and a comparison with test data. *SAE Transactions*, 111:1489–1494, 2002.

[3] J.A. Korta and M. Domenico. Multi-objective micro-geometry optimization of gear tooth supported by response surface methodology. *Mechanism and Machine Theory*, 109:278–295, 2017.

[4] C.I.L. Park. Multi-objective optimization of the tooth surface in helical gears using design of experiment and the response surface method. *Journal of mechanical science and technology*, 24(3):823–829, 2010.

[5] M. Sun, C. Lu, Z. Liu, Y. Sun, H. Chen, and C. Shen. Classifying, predicting, and reducing strategies of the mesh excitations of gear whine noise: a survey. *Shock and Vibration*, 2020.

Optimal tuning of an adaptive vibration absorber
for vibration control of vehicle transmission system

S. Soleimanian[1,2], G. Petrone[1], A. Mroz[2], F. Franco[1*], P. Kolakowski[2], S. De Rosa[1]

[1]*University of Naples Federico II, Naples, Italy*
[2]*Adaptronica sp. z o.o., R&D company, Łomianki, Poland*

e-mail*: francof@unina.it

Noise and vibration in automotive transmission systems has been a concrete engineering problem for decades [1]. Few efforts have been made by experts and scholars to suppress vibrations of this kind with the help of vibration controllers following semi-active working principle [2]. In fact, the presence of large number of resonant modes and limited available energy make semi-active absorbers favorable in such applications. Semi-active systems require an online adaptation of their properties to the host structure response. To predict the adaptive points accurately, optimal tuning is helpful. The present research offers an optimal tuning of a vibration absorber (VA) to isolate the vibration of a transaxle Getrag DC T300. Since the ultimate objective is to reduce whine noise, the favorable frequency range is 2000 to 5000 Hz. The VA is supposed to be made of metal cushion which has a density dependant stiffness property providing the possibility to supress many modes of vibration. The main idea is to prevent force transmission from a middle plate to the rest of transaxle housing. The results revealed an efficient vibration reduction in a wide frequency band by implementing an optimally tuned VA relying on stiffness adaptability of metal cushion.

Figure 1(a) illustrates a transaxle gearbox model with one input shaft, one differential shaft and a lay shaft. The circular plate marked in red is the target structure which force transmission to the rest of housing is considered to be minimized. Figure 1(b) shows a dynamic model for the gearbox including the transverse plate fixed at the edge, with two mass points representing the mass of shafts and associated gears and bearings. This thin-walled plate is prone to vibration with out of plane modes which can be suppressed by a VA installed normal to the plate with a fixed end. A typical out of plane sinusoidal excitation of 500N amplitude is imposed at the plate centre.
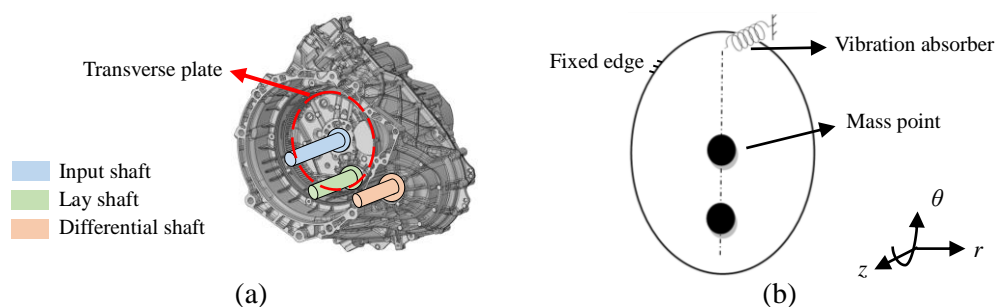
Figure 1. (a) transaxle Getrag DC T300, (b) dynamic model.

Considering metal cushion material for the VA, the stiffness property can be adjusted from 0.023×10^7 to 2.91×10^7 N/m which corresponds to a pre-compression range of 5 to 40% [3]. The numerical design procedure for the adaptive VA is given by the flowchart in Figure 2. The first stage is to identify the natural frequencies and corresponding mode shapes in the required frequency range. The next step is to evaluate the effect of absorber stiffness levels on the frequency response. For this purpose, it is required to design an experiment covering the potential range of stiffness as well as including Eigen resonances in the frequency domain. So that a set of harmonic analyses should be established in the wide frequency band of interest. In this work, the steady state forced vibration problem is solved based on mode superposition approach and defining the response and excitation by harmonic functions.

It should be noted that the required result for the present study is the *z* component of reaction force evaluated at the plate edge. Presenting this result in the frame of response surface can determine whether the VA is adaptable for the frequency range of requirement or not. In fact, the VA is adaptable if the frequency response demonstrates meaningful variations by changing the tuning variable, stiffness. If the VA works for the desired frequency band, the last step is to conduct narrow band optimizations to minimize the reaction force at specific frequencies.

Figure 2. Numerical design procedure of the VA.

References

[1] Y.H. Guan, M. Li, T.C. Lim, W.S. Shepard, Comparative analysis of actuator concepts for active gear pair vibration control, J. Sound Vib. 269:273, 2004.
[2] W. Li, X. Dong, J. Xi, X. Deng, K. Shi, Y. Zhou, Semi-active vibration control of a transmission system using a magneto-rheological variable stiffness and damping torsional vibration absorber, Proc. Inst. Mech. Eng. Part D J. Automob. Eng. 235:2679, 2021.
[3] S. Rieß, W. Kaal, Frequency-Adaptable Tuned Mass Damper Using Metal Cushions, Vibration. 4:77, 2021.

EXPERIMENTAL STUDIES ON THE INFLUENCE OF STATIC TORQUE IN A NOVEL GEARBOX TEST-RIG

S. Nampally[1], S. Okda[1], M. Fontana[2], R. Nordmann[1], and S. Rinderknecht[1]

[1]*Technical University of Darmstadt,Germany*
[2]*Powerflex SRL, Limatola, Italy*

e-mail: sneha_rupa.nampally@tu-darmstadt.de

1. Introduction

For gearboxes, the major source of vibration during operation, called gear whine arises from meshing of gear teeth. Structure-borne and air-borne noise are more significant due to implementation of lightweight materials, and this calls for smarter solutions to tackle this problem. The frequency range of 500-5000 Hz corresponds to majority of the gear mesh frequencies of an automotive gearbox, for which a feasible active vibration control solution has to be developed.

An economical test-rig is designed within the LIVE-I project, which is described in a complimentary paper submitted to this conference by authors. This test-rig employs a unique approach that replaces the traditional rotating drive machine with a piezoelectric stack actuator to establish a comparable and modular platform for vibration investigations. The aim of this work is to study the effect of static transmitted torque on the gearbox system vibration characteristics. This information is valuable in developing suitable control algorithms and actuator concepts for active vibration control. Challenges related to system behaviour at different static torques for frequencies higher than 1 kHz are dealt in this work.

2. Methodology and Preliminary Results

A first step in any Grey-Box identification method is to have some prior knowledge of the system we are dealing with. The test-rig is a close approximation to the free-free boundary condition, in order to avoid interactions with external environment. A Finite Element (FE) model of the test-rig is developed to calculate the natural frequencies and dominant vibration modes of the system. The modes relevant to the housing vibrations give a preliminary set of suitable sensor positions for vibration measurement as shown in Fig.1. According to [1], tests for system identification can be classified into two sets. First, the preliminary impulse tests to gain understanding of the primary system characteristics like number of poles or zeros (resonances and anti-resonances), linearity and time-invariance. These determine the system characteristics for potential actuator locations. The second category of tests is to understand the gearbox vibration behavior in operating conditions.
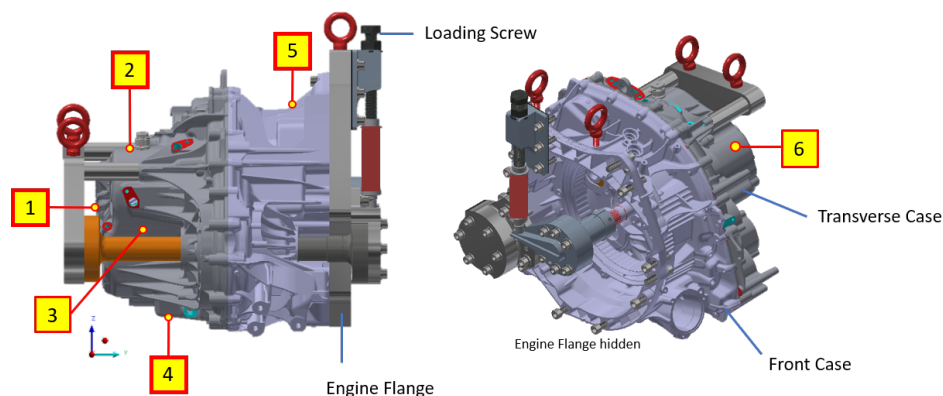
Figure 1: Test-rig schematic and six preliminary measurement points on gearbox housing

For the first type of test, an experimental modal analysis was therefore performed on the gearbox with a modal shaker upto 5 kHz. A good agreement with the FE calculations of major modes were seen. A static load given to the gear train via a loading screw arrangement, that simulates the input torque from a drive machine. This static torque gives rise to additional resonances and shifts the resonances at higher frequency ranges due to change in stiffness, as seen in Fig.2.
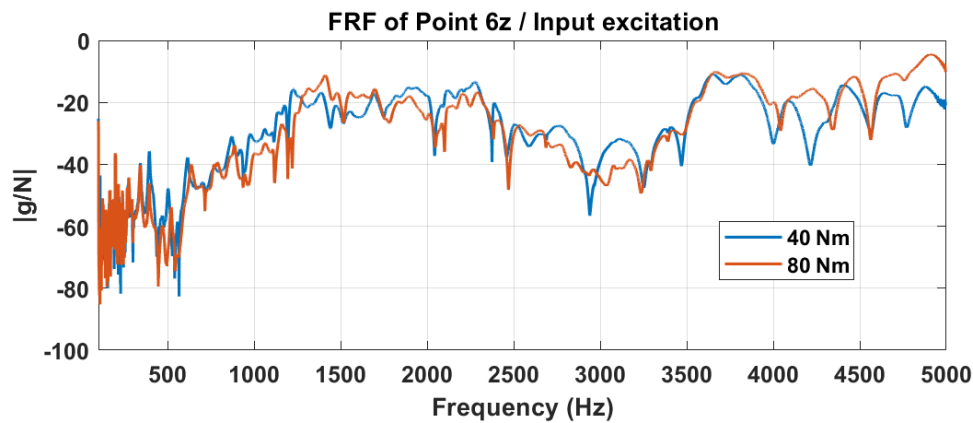
Figure 2: Influence of static torque on frequency response at sensor-6 from shaker excitation

For the operational behavior, the transmission excitation, which ideally comes from the drive machine in the vehicle is replaced by a piezoelectric stack actuator. This excitation mimics the dynamic torque fluctuations induced into the system at the input shaft of the transmission and the expected bandwidth of operation is 5 kHz. The system resonances are identified using sweep sine signals from the exciting actuator.

Typical challenges in proper dynamic identification of modes and system behavior lies in the high modal density in the chosen frequency range of the gearbox structure. These modes may pose as noise amplification zones for the gearbox in operational conditions. An optimal method is required to design an active control strategy for this range, which will be presented in detail in the paper.

3 . Outlook and Next Steps

Experimental methods for identification have been studied on various industrial gearboxes in the past [2], the excitation mechanisms were mostly shakers and electric motors. In this work, we develop requirements for the housing vibration reduction through experimental identification in the chosen frequency range of interest. Upon successfully identifying this model, work of this paper will be extended to perform HiL simulations [3] for implementation active vibration control and novel actuation strategies to mitigate gear whine in the frequency range up to 5 kHz.

References

[1] Lennart Andersson, Ulf T. Jönsson, Karl Henrik Johansson, and Johan E. Bengtsson. A manual for system identification. 2006.

[2] Mingfeng Li, Teik-Cheng Lim, William Steve Shepard, and Yuanhong Guan. Experimental active vibration control of gear mesh harmonics in a power recirculation gearbox system using a piezoelectric stack actuator. *Smart Materials and Structures*, 14:917–927, 2005.

[3] Dirk Mayer, Timo Jungblut, Jonathan Millitzer, and Stefan Wolter. Hardware-in-the-loop test environments for vibration control systems. 11 2015.

EXPERIMENTAL VIBRO-ACOUSTIC ANALYSIS OF GEARBOX BEHAVIOR USING PIEZOELECTRIC STACK ACTUATOR EXCITATION

S. Okda[1], S. Nampally[1], M. Fontana[2], S. Herold[3], R. Nordmann[3], S. Rinderknecht[1] and T. Melz[1,3]

[1]*Technical University of Darmstadt, Otto-Berndt-Str. 2, 64287, Darmstadt, Germany*
[2]*Powerflex s.r.l, via Campitiello 6, Benevento, 82030, Limatola, Italy*
[3]*Fraunhofer LBF, Bartningstraße 47, 64289, Darmstadt, Germany*

e-mail: sherif.okda@tu-darmstadt.de

1. Introduction

Due to the increasing demand to improve vibro-acoustic comfort, car manufacturers are concerned with the vibration and noise problems specially that are generated by gearboxes. In this paper, the vibro-acoustic behaviour of a dual-clutch gearbox (Magna-Getrag 7DCT300) is studied using a new method of excitation that is used to simulate the vibrations resulting from the gear whine without gear rotation. The aim of this work to introduce an economic yet realistic and a non-traditional setup that can be used to study gearbox vibrations. This test setup will be used in future to test an integrated active vibration control solution, for automotive transmission systems as a part of the LIVE-I project [1].

Previously, most of the researchers who used active vibration control solutions for transmission systems used traditional rotational test setups using motors and braking system or any kind of load as Rebbechi el al. [2] and Zech el al. [3]. In addition, others used different methods to excite the transmission systems as Dion el al. [4], who used an electrodynamic shaker to study the gear rattle effects.

2. Methodology

The proposed test setup consists of a simplified gear train of the dual-clutch transmission with two gear pairs engaged as well as the gearbox differential, while the rest of the gear pairs are removed, including the forks and synchronizers. The gearbox is excited through a piezoelectric stack actuator connected to the gearbox input driveshaft through a lever to induce a dynamic torque, the excitation mechanism can be shown in Fig. 1. In addition, the system is preloaded with a static load to have the same situation as for the rotating system with contact on the drive flanks, and this preload can be adjusted to study different stiffness situations in the bearings (non-linear effects) later on. The excitation takes the normal transfer path from the input shaft to the gears, bearings, then finally to the housing. The gearbox is fixed in a free-free boundary conditions by hanging it using rubber cords that are fixed to a steel frame. The test setup can be seen in Fig. 2. The excitation parameters (frequency, harmonics, amplitudes and phases) can be adjusted through a signal generator. The gearbox can be excited up to 5000 Hz, which can cover the most important harmonics of the gearbox. Several accelerometers are attached to the gearbox housing to measure the vibrations and a sound level meter is fixed near the gearbox to measure the sound pressure.

3. Results and Discussion

As it can be seen from Fig. 3, upon exciting the gearbox by a sine wave through the input shaft, harmonics of the input signal could be successfully captured by the accelerometers on the housing. The acceleration values are close to the real accelerations generated in a real rotating gearbox. These harmonics are generated due to mainly two reasons, the mechanical system of the gearbox with the gear contacts, and the piezo stack actuator nonlinearities which also induces harmonics to the system.
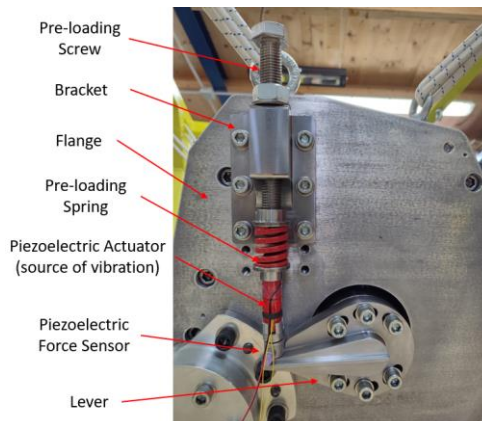
Figure 1: The excitation mechanism.
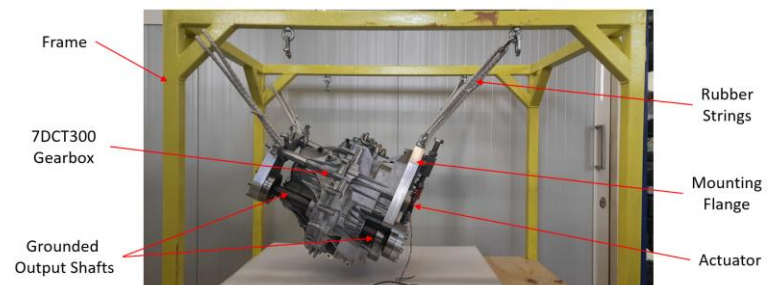
Figure 2: The test setup showing the 7DCT300.
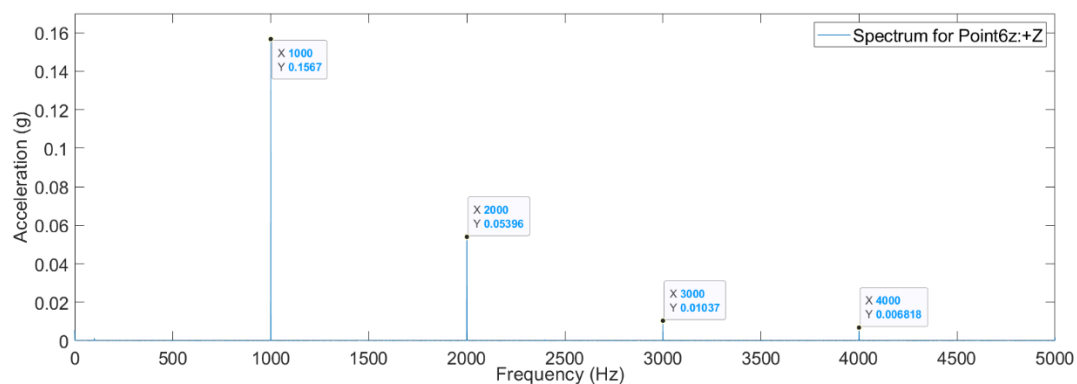
Figure 3: Acceleration spectrum showing harmonics captured with a 1000 Hz sine wave excitation.

4. Conclusion

A new proposed test setup is used to simulate the vibrations and noise of an automotive transmission system, by exciting the system using a piezo stack actuator. The vibrations and noise emitted through the gearbox housing include the harmonics of the exciting frequency, as well as amplitude values of acceleration close to the real running conditions. The exciting system shows great flexibility to induce excitations that simulate any running speed and meshing frequency with its harmonics. This finding will be useful to develop an active vibration control system to mitigate the noise and vibrations emitted from the system.

5. Acknowledgments

6. References

[1] É. C. d. Lyon, "LIVE-I," 2020. [Online]. Available: https://livei.fr/. [Accessed 01 01 2022].
[2] Rebbechi, Brian, Carl Howard, and Colin Hansen. "Active control of gearbox vibration." In INTER-NOISE and NOISE-CON Congress and Conference Proceedings, vol. 1999, no. 5, pp. 295-304.
[3] Zech, P., D. F. Plöger, T. Bartel, T. Röglin, and S. Rinderknecht. "Design of an inertial mass actuator for active vibration control of a planetary gearbox using piezoelectric shear actuator." In Proceedings of ISMA2018 International Conference on Noise and Vibration Engineering, pp. 203-215. 2018.
[4] Dion, Jean-Luc, Sylvie Le Moyne, Gaël Chevallier, and Hamidou Sebbah. "Gear impacts and idle gear noise: Experimental study and non-linear dynamic model." Mechanical Systems and Signal Processing 23, no. 8 (2009): 2608-2628.

Session S4

SMART-SPACE session

Organizers:

Jan Holnicki-Szulc (*IPPT PAN, Poland*)

Zbigniew Wołejsza (*IPPT PAN, Poland*)

Przemysław Kołakowski (*Adaptronica sp z o.o., Poland*)

CHALLENGES FOR SMART SPACE:
LTA (LIGHTER THAN AIR) AEROSTATS FOR GLOBE HEALTH MONITORING AND TELECOMMUNICATION

Z. Wolejsza, G. Mikułowski, J. Holnicki-Szulc

Institute of Fundamental Technological Research, Warsaw, Poland
e-mail: zbigniew.wolejsza@gmail.com , holnicki@ippt.pan.pl

There is clear need for development of the so-called Smart Space (complementary to satellite earth observation systems). It is motivated by the following factors and requirements:
- drastic cost reduction of earth observation and telecommunication services,
- stratospheric / tropospheric observation systems provide better image quality,
- stratospheric engineering for eco-cosmos (reduction of the cosmic trash problem).

Promising applications for monitoring aerostats might include:
- monitoring of forest heritage in Europe,
- monitoring of climate changes,
- agriculture monitoring.

This contribution will focus on and discuss a number of technological challenges that have to be solved for a successful development of Smart Space, including:
- option of economic hydrogen for LTA aerostats (vs. safe helium practice),
- photovoltaic energy supply for long-term stratospheric missions,
- innovative approach to short-term missions:
    - initial elevation (by warmed air balloon, aircraft, rocket, etc.),
    - controlled V-mobility and H-mobility,
- tethered LTA aerostats and their applications,
- Top-Drop – safe evacuation techniques for stratospheric / tropospheric wastes,
- SKYLAB (warmed air balloon) and testing technique for scaled aerostat models,
- various techniques for mitigation of impact born vibrations in ultra-light LTA structures.

DESIGN OF ADAPTIVE AEROSTATS FOR SHORT-TERM MISSIONS

A. Świercz[1], C. Graczykowski[1], L. Knap[2], G. Mikułowski[1], and J. Holnicki-Szulc[1]

[1]*Institute of Fundamental Technological Research, Polish Academy of Sciences, Pawińskiego 5B, 02-106 Warsaw, Poland*
[2]*Institute of Vehicles and Construction Machinery, Warsaw University of Technology,*
Narbutta 84, 02-524 Warsaw, Poland

e-mail: aswiercz@ippt.pan.pl

1. Introduction

Recent technological advances in the lighter-than-air vehicles allow for constructing bigger and bigger structures such as High-Altitude Pseudo-Satellites (HAPS), e.g., airplane Zephyr S developed by Airbus, Russian airship Berkut or autonomous, multi-mission, stratospheric, French airship Stratobus. Long-term missions require periodic replenishment of lifting gas losses using additional gas storage tanks due to lack of gas-tightness of aerostat shell. On the other hand, for the application in short-term missions particularly at low and medium altitudes (e.g. for aerial monitoring), the adaptive aerostats with controllable chamber volumes without gas accumulators can be applied. Such adaptive aerostats based on telescopic sections (see Fig. 1a) and supporting tensegrity-like structures (see Fig. 1b) are presented in [1] and [2, 3], respectively. Application of slightly over-pressurized chambers and adjustment of their volume allows to maintain constant aerostat altitude or change it in a controlled way, even in the case of small leakage of the lifting gas into the atmosphere.

Another type of adaptive aerostat reinforced by external coatings connected by inextensible belts (or tendons), is presented in Fig. 1c. The belts are elongated or shortened by remotely controlled electric devices. Excessive aerostat volume growth can be also restricted passively by application of belts with designed extensibility.
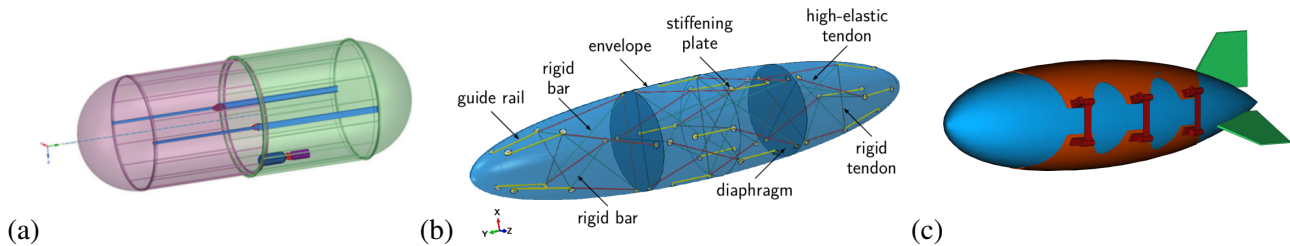
Figure 1: Schemes of adaptive aerostats controlled by: (a) telescoping sections, (b) tensegrity-like supporting structures and (c) belts connecting membrane reinforcement

2. Adaptive aerostats & volume measurement

The aerostat movement can be perturbed by different factors, e.g. diurnal temperature fluctuations and solar radiation, changes of wind speed and wind directions as well as lifting gas losses. The basic feature of adaptive aerostats is ability to change its shape and volume in order to control the motion in horizontal direction (H-mobility) and vertical direction (V-mobility). Therefore, the application of such aerostats is a very appealing solution. Generally, the volume V of the airship with telescopic-like sections, or with internal tensegrity-based structure, or with membrane reinforcement can be expressed by the volume control variable ε, defined differently for various types of adaptive aerostats. Equation of motion for the aerostat without propulsion system and constant total mass m_t can be written in the following form:

$$m_t \frac{d^2 x}{dt^2} = -Q_{dh} \cos(\alpha), \qquad m_t \frac{d^2 y}{dt^2} = -Q_{dh} \sin(\alpha), \qquad m_t \frac{d^2 h}{dt^2} = -Q_g + Q_b - Q_{dv},$$

where the coordinates (x, y, h) and resulting forces are illustrated in Fig. 2a. In the above equation, the subsequent terms denote:

- weight of the aerostat: $Q_g = m_t\, g(h)$, where $g(h)$ is the altitude-dependent standard gravity;
- buoyancy force: $Q_b = \rho_a(h)g(h)V(\varepsilon, h)$, where $\rho_a(h)$ is the altitude-dependent air density and the volume V depends on the volume control variable ε;
- vertical aerodynamic force $Q_{dv} = sgn(v_v)c_x(v_v, h)\rho_a(h)A_v(\varepsilon, h)\frac{v_v^2}{2}$, where v_v is the vertical velocity, c_x is aerodynamic drag coefficient and A_v is the horizontal cross-section of the aerostat which depends on the volume control variable ε;
- horizontal aerodynamic force $Q_{dh} = sgn(v_h)c_x(v_h, h)\rho_a(h)A_h(\varepsilon, h)\frac{v_h^2}{2}$, where v_h is the vertical velocity and A_h is the vertical cross-section of the aerostat which depends on the volume control variable ε.

The aerostat volume is one of the key features influencing its altitude in operational conditions. Therefore, in order to prepare a reliable numerical model, the preliminary laboratory tests aimed at volume changes measurements has to be performed. In conducted tests the whole extensible aerostat polyurethane membrane is reinforced by a textile material reducing its excessive deformations as presented in Fig. 2b. The volume measurement is conducted using non-contact, optical method – stereo photogrammetry based on triangulation principle. The hardware part is composed of two cameras recording double picture of the model covered with dedicated markers, in order to reconstruct the three-dimensional surface.
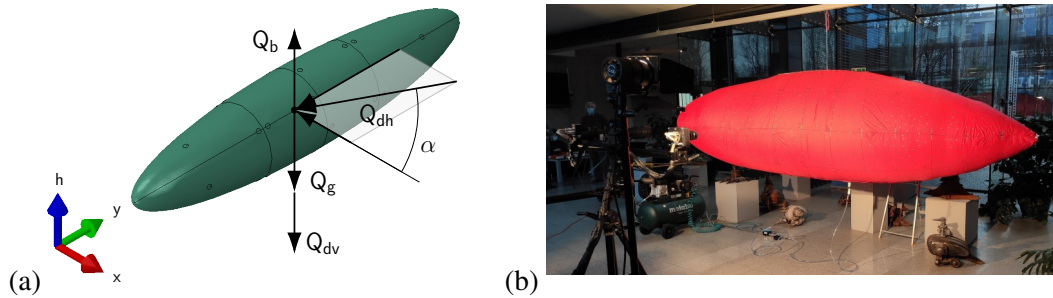
Figure 2: (a) Forces acting on the aerostat, (b) Model of the aerostat during volume optical measurement

3. Conclusions

In the article we discuss three types of adaptive aerostats with ability to control volume and shape using special construction and additional devices. Application of adaptive aerostats enables modification of the planned missions due to e.g. changing weather conditions, extension or shortening of mission duration or even enforced landing in emergency circumstances. Moreover, the applied additional devices facilitate hanging the payload and/or propulsion system. On the other hand, the added structures or devices contribute to the total mass of the airship which leads to decreasing payload or shortening of the operational time. The control mechanisms makes aerostat construction more complicated, and in the case of tensegrity structure may cause envelope damage, if one of bars is damaged or broken.

References

[1] L. Knap, C. Graczykowski, J. Holnicki-Szulc, and Z. Wołejsza. Strategies for reduction of energy consumption during ascending and descending process of modern telescopic HAPS aerostats. *Bulletin of the Polish Academy of Sciences: Technical Sciences*, 68(1):155–168, 2020.

[2] L Knap, A. Świercz, Graczykowski C., and J. Holnicki-Szulc. Self-deployable tensegrity structures for adaptive morphing of helium-filled aerostats. *Archives of Civil and Mechanical Engineering*, 21(4):1–18, oct 2021.

[3] L. Knap, A. Świercz, C. Graczykowski, and J. Holnicki-Szulc. Adaptive morphing of tensegrity-based helium-filled aerostats. In *AeroBest 2021, International Conference on Multidisciplinary Design Optimization of Aerospace Systems*, pages 3–13, Lisboa, 2021.

Semi-Active Interface (SAI) Technique for Suppressing of Impact Born Vibrations

A.Orłowska[1], L.Knap[2], J.Holnicki-Szulc[1]

[1]*Department of Intelligent Technologies, Institute of Fundamental Technological Research, Polish Academy of Sciences, Pawinskiego St. 5B, 02-106 Warsaw, Poland*

[2]*The Faculty of Automotive and Construction Machinery Engineering, Warsaw University of Technology, Narbutta St. 84, 02-524 Warsaw, Poland*

In the class of ultra-light structures (e.g. space structures) there is a strong need for innovative techniques allowing suppression of impact born vibrations (due to lack of sufficient material damping). Therefore, the objective of our SAI concept is to propose an effective technique, allowing suppression of impact born vibrations with zero mass added to the ultra-light structure and based on the following steps:

− design multi-layer structure with option for semi-active "delamination" control along the contact interfaces (slipping lines)
− apply an actuator realizing the on/off type of semi-active control for slipping lines' activation, playing the role of structural clutch (cf. the actuator in so-called PAR vibration suppression technique, [1-4]).
− apply various characteristics for the contact interfaces (friction coefficients)
− apply various control strategies for suppression of vibrations, depend on the case study and dynamic excitation.

Case study of two-layer beam dynamically excited shows significant effect on vibration suppression caused by their delamination and internal friction provoked. In case of random, impact born vibrations, proper initial prestressing can allow increasing of the final damping effect, due to stored additional slipping distortions available. In case of several potential slipping lines and various ways of dynamic excitations, more sophisticated algorithms for optimal solutions, like AI, can be applied for effective suppression of vibrations.

References

[1] A. Mroz, J. Biczyk, and J. Holnicki-Szulc. *Sterowalne sprzęgło oraz jego zastosowanie*. Patent PL230890, 2015.
[2] J. Holnicki-Szulc, A. Mroz, and J. Biczyk. *Półaktywny węzeł zwłaszcza do tłumienia drgań*. Patent PL 228141, 2014.
[3] A. Mroz, A. Orlowska, and J. Holnicki-Szulc. Semi-active damping of vibrations. Prestress Accumulation-Release strategy development. *Shock and Vibration* 17:123–136, 2010.
[4] A. Orlowska, A. Galęzia, A. Swiercz, and Ł. Jankowski. Mitigation of vibrations in sandwich-type structures by a controllable constrained layer. *Journal of Vibration and Control* 27(13–14):1595–1605, 2021.

MULTISPECTRAL IMAGERY OBTAINED WITH AN AEROSTAT AND THE POTENTIAL OF THEIR USE IN MONITORING OF AGRICULTURE, FORESTRY AND ENVIRONMENTAL PROTECTION

J. Januszewski[1], W. Fedorowicz-Jackowski[2]

[1]*GEOSYSTEMS Polska Sp. z o.o., Warsaw, Poland*
[2]*GEOSYSTEMS Polska Sp. z o.o., Warsaw, Poland*
e-mail: jarek.januszewski@geosystems.pl

Abstract

Development of unmanned aerial vehicle (UAV) technologies contributed at the same time quite significantly to the development of the imaging technologies. Running alongside with the progressive miniaturization of the electronic circuits and the use of new materials in optics, ultra-light, compact and more and more advanced devices for recording static or video images have been developed and are currently widely applied for remote detection of various phenomena and processes occurring the geographical environment.

An interesting alternative to drones, the most commonly used UAVs, seems to be an aerostat. It can be seen as a developmental platform for raising various types of imaging instruments above the surface of the Earth. This text presents a review of the first experiences related to the operational use of the MoniKite aerostat to obtain multispectral remote sensing images using the MicaSense Altum camera, their photogrammetric processing and the possibility of obtaining reliable indicators/indices/metrics such as NDVI or NDRE derived during digital processing of multispectral imagery.

These experiences have been collected during the activities carried out under the NCBiR research program, TANGO 4, entitled *Adaptive aerostats, stretched on the SDT (Self Deployable Tensegrity) support structure, as a platform for multi-thematic monitoring of the Earth's surface (Aero-SDT)*. The works are carried out by a research and implementation consortium led by the Institute of Fundamental Technological Research of the Polish Academy of Sciences, and technological partners of ADAPTRONICA Sp. z o.o. and GEOSYSTEMS Polska Sp. z o.o.

CAPSULES FOR SAFE AIRDROP AND EFFICIENT TOUCHDOWN MITIGATION

C.Graczykowski[1], L. Knap[2], R. Faraj[1] and J. Holnicki-Szulc[1]

[1]*Institute of Fundamental Technological Research, Warsaw, Poland*
[2]*Warsaw University of Technology, Warsaw, Poland*
e-mail: cezary.graczykowski@ippt.pan.pl

1. Introduction

Novel systems for specialised airdrop operations are still elaborated and used in military, commercial, rescue and humanitarian applications. Each application implies different requirements for the system construction and its performance. Moreover, the touchdown conditions can significantly vary, and the airdrop system should be robust to possible disturbances. This paper discusses development of a new general-purpose airdrop capsule. The proposed system guarantees efficient mitigation of impact during capsule touchdown and enables efficient protection of the transported cargo.

2. The concept of adaptable absorber

According to the analysis presented in [1-2] an efficient reduction of the loading transmitted to the airdrop capsule can be obtained by using adaptable pneumatic shock-absorber. The concept is based on application of two concentric cylinders (Fig. 1a) - the upper with vent of optimized shape and the lower with narrow longitudinal slot. During touchdown the relative cylinders' motion provides compression of the gas and initial increase of reaction force, while overlapping of the slot and the vent provides proper release of gas and maintaining constant reaction force level (Fig. 1b). As a result, the obtained change of generated force enables stopping vertical motion of the capsule with minimal value of deceleration. Adaptation of the system to various loading conditions is executed with the use of specially adjusted shutters [3], which change both the compression distance and the vent shape.
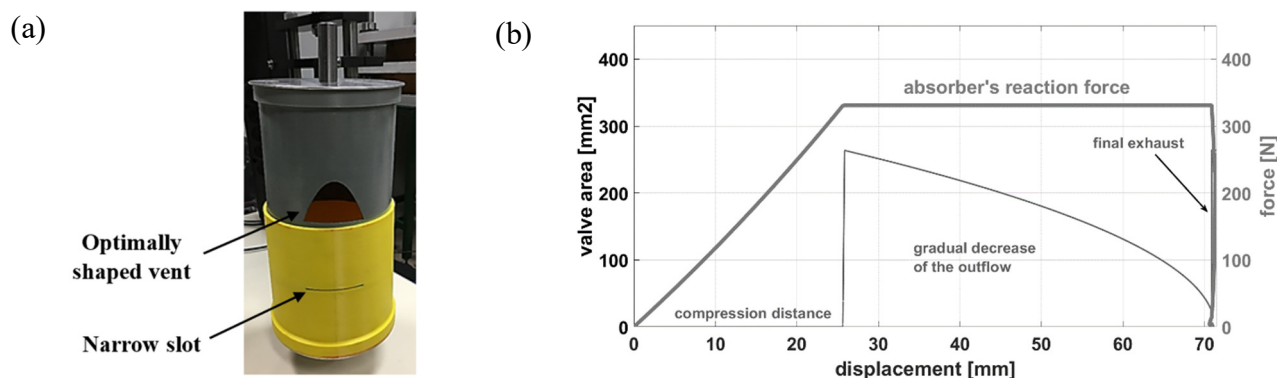
Figure 1: a) adaptable pneumatic shock-absorber, b) basic characteristics of the adaptable absorber

3. The airdrop capsule with adaptable valve

In another solution based on a similar operating principle, the airdrop capsule is equipped with a parachute, self-deployable airbag with highly elastic internal skeletal structure and adaptable valve (Fig. 2a). The airbag is deployed and inflated just before touchdown using gas from external accumulator or ambient air flowing through specially designed holes located in the envelope. The adaptable valve is used to control the outflow of air from the airbag during touchdown in a predefined manner. The valve is composed of external housing with

an optimally designed vent and a mobile piston (Fig. 2b). The motion of the piston, which is driven by pressure of internal gas, causes gradual overlapping of the vent and change of the gas outflow area. Due to appropriate shape of the vent in the valve housing, it is possible to obtain desired change of gas pressure inside the airbag and maintain constant value of total reaction force acing on the capsule.

The adaptation to various touchdown conditions can be provided by modification of valve characteristics before the touchdown process. This can be achieved by change of stiffness of the spring supporting the valve piston, adjustment of the mass of the valve piston or modification of the friction force acting between the valve piston and the housing. In an alternative solution, the supporting spring can be replaced by micro-actuator, which allows to obtain semi-active system with full control of the gas outflow and wide range of system adaptivity to different touchdown conditions.
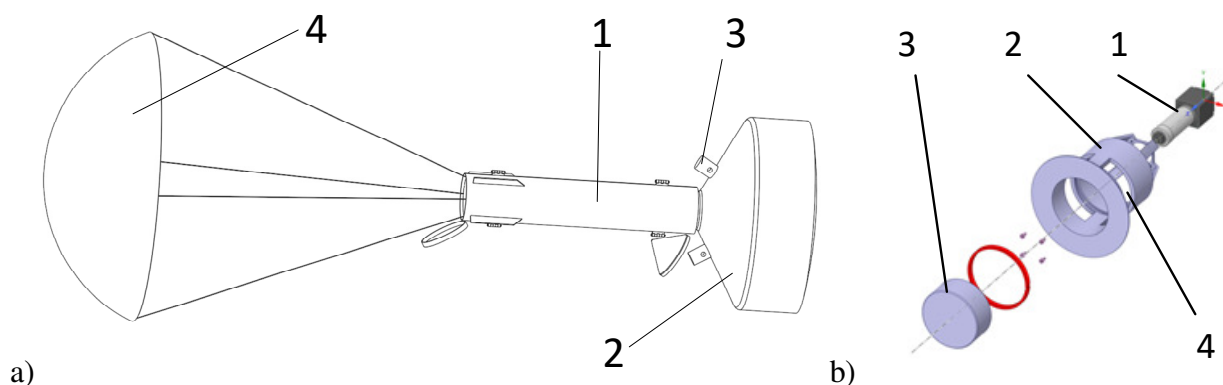
Figure 2: a) airdrop system composed of: capsule (1), airbag (2), adaptable valves (3) and parachute (4), b) components of the discharge valve in a version with micro-actuator: (1) micro-actuator, (2) valve housing, (3) valve piston with a sealing, (4) optimally shaped vent

The paper presents numerical analyses aimed at optimal design of the shock-absorption system for the airdrop capsule. The special attention will be paid to the adaptable valve which can be considered as a crucial component in providing efficient touchdown mitigation. The proposed mathematical model of the airdrop system will be used to determine optimal change of gas outflow from the airbag for various capsule mass and touchdown velocity. Further, the model of the adaptable valve will be applied to compute optimal shape of the vent for the assumed range of touchdown scenarios. Finally, we will present the results of system adaptation obtained by modification of valve spring stiffness, valve piston mass and piston-housing friction coefficient.

4. Conclusions

The paper discusses the innovative airdrop system equipped with airbag and discharge valve. The authors propose novel design of the shock-absorption system based on adaptable valve with optimally shaped vent and methodology of its adaptation to different touchdown scenarios. The proposed solution is expected to ensure safety of the touchdown process and efficient protection of the cargo.

References

[1] R. Faraj, C. Graczykowski, J. Holnicki-Szulc, Adaptable pneumatic shock absorber, *J. Vib. Contr.*, 25 (3), 2018.
[2] R. Faraj, C. Graczykowski, J. Holnicki-Szulc, polish patent no. 234219, WUP 01/20 2020-01-31.
[3] R. Faraj, High performance pneumatic shock-absorbers for aeronautical applications, 31st Congress of the International Council of the Aeronautical Sciences, ICAS 2018.

Small sensors in atmospheric aerosols profiling

M. A. Posyniak[1], A. Szkop[1], and K. M. Markowicz[2]

[1]*Institute of Geophysics Polish Academy of Sciences, Księcia Janusza 64, 01-452 Warszawa, Poland*
[2]*University of Warsaw, Faculty of Physics, Institute of Geophysics, Pasteura 5, 02-093 Warszawa, Poland*
e-mail: mpos@igf.edu.pl

To broaden the knowledge of aerosol optical and microphysical properties, researchers have employed both remote sensing techniques and in situ methods using various atmospheric probing platforms. Modern miniature equipment measuring the concentration of particulate matter (PM2.5 and PM10), and the equivalent black carbon (eBC) concentration can be mounted on tethered balloons, UAVs, and cable cars to perform vertical profiles of atmosphere. This work presents a methodology for obtaining vertical profiles of aerosol properties using different measurement platforms and a combination of measurement techniques.

One part of the presented data were obtained under the iAREA (Impact of absorbing aerosols on radiative forcing in the European Arctic) campaigns conducted in Ny-Ålesund (Spitsbergen) during the Arctic haze seasons of 2015 and 2016. Black carbon (BC) concentration profiles were made using a micro-aethalometer AE-51 mounted under a tethered balloon. Results were obtained in an altitude range from about 400 m up to 1600 m a.s.l. and for cases with increased aerosol load. The main results consist of the observation of increasing values of equivalent black carbon (eBC) and absorption coefficient with altitude, and the opposite trend for aerosol concentration for particles larger than 0.3 mm [1].

In 2018 a three-week research experiment was organised in the Mt. Szyndzielnia area (the Silesian Beskids). Smog in Bielsko-Biala (southern Poland) during the winter season was examined. The main objective of this study was to understand the vertical variability of aerosol optical and microphysical properties under different meteorological conditions. An AE-51 micro-aethalometer and PMS7003 and OPC-N2 optical particle counters were mounted on the cable car and used to measure the profiles of eBC, the concentration and aerosol size distribution [2].

Miniature sensors for determination of aerosol size distribution were also tested on the MoniKite airborne platform. Test flight was made in June 2022 in Jabłonna (near Warsaw). Vertical profiles of concentrations aerosol particles were determined using a aerosol particles counter SPS30. This method allowed multiple profiling in boundary layer up to approximately 250 m.

Tests conducted in the Institute of Geophysics Polish Academy of Sciences on UAVs show that to obtain acceptable results of measurements from small sensors, special measurement techniques should be applied. Due to fluctuations of measured values, an averaging of data should be done. It can be done in post processing by dividing profile into layers, but also by making the profile itself. Stopping for a certain time on specified levels every e.g. 10 or 50 m gives better results than making multiple profiles in short time.

References

[1] K. M. Markowicz, C. Ritter, J. Lisok, P. Makuch, I. S. Stachlewska, D. Cappelletti, M. Mazzola, and M. T. Chilinski. Vertical Variability of Aerosol Single-Scattering Albedo and Equivalent Black Carbon Concentration Based on in-Situ and Remote Sensing Techniques during the iAREA Campaigns in Ny-Ålesund. *Atmospheric Environment* 164: 431-447. 2017

[2] M. A. Posyniak, K. M. Markowicz, D. Czyzewska, M. T. Chilinski, P. Makuch, O. Zawadzka-Manko, S. Kucieba, et al. Experimental Study of Smog Microphysical and Optical Vertical Structure in the Silesian Beskids, Poland. *Atmospheric Pollution Research*, 12 (9), 2021.

Session S5

Structural health monitoring and damage detection

Organizers:

Magdalena Rucka (*Gdansk University of Technology, Poland*)

Yonghui An (*Dalian University of Technology, China*)

Bartłomiej Błachowski (*IPPT PAN, Poland*)

Nikos G. Pnevmatikos (*University of West Attica, Greece*)

Data interpretation challenges in Structural Health Monitoring

Z. Dworakowski[1]

[1]*AGH University of Science and Technology, Al. A. Mickiewicza 30, 30-059 Krakow, Poland*

e-mail: zdw@agh.edu.pl

1. Introduction

Data-driven approaches obtained a prominent place in industrial data interpretation problems. A vast amount of applications rely on some form of autonomous decision making or data processing to facilitate the work of human experts or enable the processing of large-scale datasets gathered in contemporary industrial environments. These approaches are commonly divided into natural optimization, machine learning, and fuzzy-logic-based solutions [3].

However, despite the enormous progress made in artificial intelligence-related areas in recent years, several pitfalls and challenges undermine the practical implementation of autonomous decision-making systems in mechanical systems research. Structural Health Monitoring (SHM) suffers particularly from this issue [1, 2].

This work describes a selection of these challenges with practical examples of dedicated solutions or requirements that need to be met while designing reliable monitoring methods. The list includes possible sources of data leakage undermining the final efficiency of the decision systems, design of unbiased system testing procedures, challenges related to the acquisition of representative datasets, moving the monitoring systems from laboratory to real-life conditions, and transferability of obtained results to other problems of a similar type. Several approaches to addressing these problems are proposed. Finally, an overview of the most promising future research directions is given.

2. Structural Health Monitoring as a source of data

A typical SHM system is built with a clear goal in mind: To detect (and possibly: classify) future damage in a given structure early enough, so proper maintenance decisions can be made ahead of time. To this end, such a system should first be given relevant data to learn to properly recognize general classes of undamaged and damaged systems. Since gathering examples representing different damage states on the structure that is to be monitored is usually infeasible, we usually get such training information from similar structures in the hope that they are *similar enough* so the generalization can be achieved. Several approaches for generalization can be distinguished here:

Numerical simulation, where we design a numerical simulation of the monitored object with and without damages

Artificially introduced damage, where we use monitored object but artificially introduce *removable damage* - that is: simulated faults that can be introduced and deleted without affecting long-term structural health

Historical data from similar objects, where we assume that all objects from the same family share detectable reaction to early damage

While these three general approaches come with their own set of challenges in terms of providing enough similarity so that the generalization can be performed, the most important issue is that usually, neither of them is efficient in terms of large datasets generation. Numerical simulations are time-consuming, Artificially introduced damage requires costly experiments and a lot of human effort, and the historical database can only be gathered if a monitoring system is already operational in the first place. As a result, datasets used in SHM are often not general and diverse enough and should be perceived as more challenging than it is commonly done.

3. Data processing and interpretation challenges

3.1. Decision systems constraints

Data leakage in ML happens if the training and testing procedures use information that would not be available in practice when the system is at its production stage. This phenomenon may be caused by errors in data acquisition, sampling, augmentation, or splitting into subsets and is often concealed by improper (not-rigorous-enough) testing stage. What is more, many decision systems contain many hyperparameters that significantly affect the outcome. Their selection can be made using a subset of training data, with an unfortunate trade-off: The more data we spend for designing the decision system's structure, the less data we have for the training of this system. However, suppose we spend too few data samples for hyperparameter setup or use any of the other data subsets to this end. In that case, we risk having a system that overfits and simply remembers proper answers for a given set of testing data.

3.2. SHM requirements

Structures are built to endure. For this reason, it is orders of magnitude more likely that the structure at any given point in time is healthy than that it is damaged. Consequently, if an SHM system has any chance of producing false positive indications, it will produce almost entirely false calls from the operator's point of view. The methods should then be configured in such a way as to reduce the false positive rate to 0 - often rendering their damage-detection capabilities to be crippled as well. Moreover, SHM systems are intended to operate in variable operational and environmental conditions. The structures are subjected to variable loading and temperature; they age, gather dust, suffer from harsh weather, and are operated in a sub-optimal way. The same stress is usually put on the sensors and data-acquisition units. As a result, gathered data are often noisy. At the same time, the decision systems should be general and robust enough, so the early damage cases are detected reliably under a majority of possible circumstances. This problem is orders of magnitude more challenging than a reliable laboratory setup where all the parameters can be measured and taken care of. For this reason, successful testing of a monitoring concept in a laboratory marks only a beginning of a long road towards real-life implementation.

4. Future research directions

The future work suggestions emerging from this paper are mainly aimed at bridging the gaps that render SHM datasets not diverse enough and cause the described challenges to arise. In the author's opinion, the SHM community would benefit from researching better similarity estimates between structures, more rigorous testing procedures that would be able to pinpoint data leakage and overfitting cases and development of a general benchmark datasets that span over large families of similar structures to develop population-based and Deep Learning approaches.

References

[1] Jérôme Antoni. A Critical Overview of the "Filterbank-Feature-Decision" Methodology in Machine Condition Monitoring. *Acoustics Australia*, 49(2):177–184, 2021.

[2] Peter Cawley. Structural health monitoring : Closing the gap between research and industrial deployment. *Structural Health Monitoring*, 17(5):1225–1244, 2018.

[3] Keith Worden, Wieslaw J. Staszewski, and James J. Hensman. Natural computing for mechanical systems research: A tutorial overview. *Mechanical Systems and Signal Processing*, 25(1):4–111, jan 2011.

ENSEMBLE OF FEATURE EXTRACTION METHODS TO IMPROVE THE STRUCTURAL DAMAGE CLASSIFICATION IN A WIND TURBINE FOUNDATION

J. X. Leon-Medina[1,2], N. Parés[3], M. Anaya[4], D. A. Tibaduiza[5], and F. Pozo[1,6]

[1]*Control, Modeling, Identification and Applications (CoDAlab), Department of Mathematics, Escola d'Enginyeria de Barcelona Est (EEBE), Campus Diagonal-Besòs (CDB), Universitat Politècnica de Catalunya (UPC), Eduard Maristany 16, 08019 Barcelona, Spain;*
[2]*Programa de Ingeniería Mecatrónica, Universidad de San Buenaventura, Carrera 8H 172-20, Bogota, Colombia*
[3]*Laboratori de Càlcul Numèric (LaCàN), Department of Mathematics, Escola d'Enginyeria de Barcelona Est (EEBE), Campus Diagonal-Besòs (CDB), Universitat Politècnica de Catalunya (UPC), Eduard Maristany 16, 08019 Barcelona, Spain*
[4]*MEM (Modelling-Electronics and Monitoring Research Group), Faculty of Electronics Engineering, Universidad Santo Tomás, Bogotá 110231, Colombia*
[5]*Departamento de Ingeniería Eléctrica y Electrónica, Universidad Nacional de Colombia, Cra 45 No. 26-85, Bogotá 111321, Colombia*
[6]*Institute of Mathematics (IMTech), Universitat Politècnica de Catalunya (UPC), Pau Gargallo 14, 08028 Barcelona, Spain*

e-mail: jersson.xavier.leon@upc.edu

Abstract

The condition monitoring of offshore wind power plants is an important topic that remains open. This monitoring search to lower the maintenance cost of this plants. One of the main components of the wind power plant is the wind turbine foundation. This study describes a data driven structural damage classification methodology applied in a wind turbine foundation. A vibration-response was captured in the structure using an accelerometer network. After arranged the obtained data a feature vector of 58,008 features was obtained. An ensemble approach of dimensionality reduction methods was applied to obtain a new set of features that is used to train a machine learning based classification model. Four different damage scenarios were applied in the structure. Therefore, considering the healthy structure, there are 5 classes in total that were correctly classified. As a result, 100% of classification accuracy was obtained after applying the damage classification methodology in a wind-turbine offshore jacket-type foundation benchmark structure.

1. Introduction

Structural health monitoring (SHM) of wind turbine foundations can consider the effects that marine waves and wind exert on the structure. In this study a vibration response generated by a shaker in a wind turbine foundation is acquired by accelerometers located strategically according to a modal study [4]. 24 sensors in total acquired signals with a sampling frequency of 275 Hz during 8.789 s obtaining 2417 data points per sensor. These 24 signals are arranged following an unfolding procedure to finally obtain a feature vector in every experiment of 58008 features. This high dimensionality must be treated in order to reduce the size of the feature matrix. The experiments were performed following a number of replicas for every structural state 2460 for the healthy structure and 820 for every one of the four types of damages applied to a link of the wind turbine foundation

2. Damage classification methodology

A feature extraction-based approach using manifold learning algorithms is developed to improve the classification accuracy in a wind turbine foundation structural damage classification problem. The developed signal processing methodology is composed of four stages: data unfolding, normalization using the mean centered unitary group scaling method (MCUGS) [5], ensemble feature extraction and classification through a XGBoost [3] model. This study aims to use an ensemble of feature extraction algorithms among which are principal component analysis (PCA) [2] as linear feature extraction method and laplacian eigenmaps [1] as nonlinear manifold

learning algorithm. A low dimensional representation of the first three dimensions for PCA and Laplacian Eigenmaps are showed in Figures 1 and 2 respectively. A sensitivity study of the parameters of the feature extraction algorithms is performed. A data set of five different structural states in a wind turbine foundation is used to validate the proposed methodology. A 5-fold cross validation procedure was applied to obtain the final confusion matrix in the classification problem. This confusion matrix representing a classification accuracy of 100% is illustrated in Table 1.
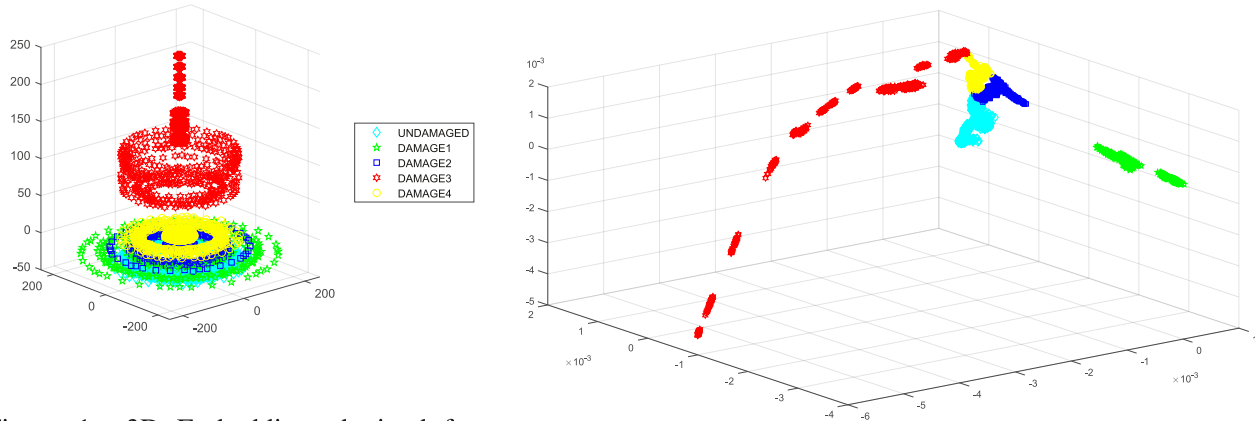
Figure 1: 3D Embedding obtained from PCA method, first three components are plotted.

Figure 2: 3D Embedding obtained from the laplacian eigenmaps method, first three dimensions are plotted.

Table 1: Confusion matrix obtained with the ensemble PCA+ Laplacian eigenmaps using XGBoost classifier method.

		Predicted Class				
		UNDAMAGED	DAMAGE 1	DAMAGE 2	DAMAGE 3	DAMAGE 4
Actual Class	UNDAMAGED	2460	0	0	0	0
	DAMAGE 1	0	820	0	0	0
	DAMAGE 2	0	0	820	0	0
	DAMAGE 3	0	0	0	820	0
	DAMAGE 4	0	0	0	0	820

References

[1] Mikhail Belkin and Partha Niyogi. Laplacian eigenmaps for dimensionality reduction and data representation. *Neural computation*, 15(6):1373–1396, 2003.

[2] Rasmus Bro and Age K Smilde. Principal component analysis. *Analytical methods*, 6(9):2812–2831, 2014.

[3] Tianqi Chen and Carlos Guestrin. Xgboost: A scalable tree boosting system. In *Proceedings of the 22nd acm sigkdd international conference on knowledge discovery and data mining*, pages 785–794, 2016.

[4] Jersson X Leon-Medina, Maribel Anaya, Núria Parés, Diego A Tibaduiza, and Francesc Pozo. Structural damage classification in a jacket-type wind-turbine foundation using principal component analysis and extreme gradient boosting. *Sensors*, 21(8):2748, 2021.

[5] Jersson X Leon-Medina, Núria Parés, Maribel Anaya, Diego A Tibaduiza, and Francesc Pozo. Data classification methodology for electronic noses using uniform manifold approximation and projection and extreme learning machine. *Mathematics*, 10(1):29, 2022.

THE PROBLEM OF GEOTHERMAL POWER INSTALLATION ON BUILDINGS: STRUCTURAL BUILDING MONITORING AND ASSESSMENT DURING DRILLING ACTIVITIES

D. Bortoluzzi[1], S. Casciati[1] and M. Francolini[2]

[1] *SIART Srl, via dei Mille 73, Pavia, Italy*

[2]Formerly *SIART Srl, via dei Mille 73, Pavia, Italy*

e-mail: danielebortoluzzi.ing@gmail.com

1. Abstract

The European project GEOFIT (Deployment of novel GEOthermal systems, technologies and tools for energy efficient building retrofitting) is gathering more than 20 partners from all around Europe. Its main objective is to deploy and to integrate advanced methods of worksite inspection, ground research, and building structural monitoring, drilling and worksite characterization into advanced geothermal based retrofitting methods.

This paper reports the results achieved within GEOFIT in terms of standard accelerometric measurements pre- and during drilling operations at the location of specific case studies.

2. Introduction

The current European Union (EU) policy aims to increase the use of "green" energies within the more than 20 European Countries forming the Union, to reduce in the next years the carbon footprint. Within this strategy, the exploitation of the geothermal energy is a well promising approach. Due to some technical issues related to the implementation of the geothermal technology, standard application refers only to isolated buildings far from urban nuclei. Nevertheless, the installation itself requires to drill close to the building. The source of vibrations caused by this activity may result dangerous for the target building.

The project GEOFIT [1] planned to implement structural monitoring in some pilot locations within the Consortium. The purpose of this paper is to present and discuss the health assessment of the bulging pre- and post- drilling operation based on the results acquired during an experimental campaign, to avoid any traumatic event (building damages) and develop a methodology for a rapid building assessment during worksite activities.

3. Case study: Pins del Vallès School located in Sant Cugat (Barcelona - ES)

Structural Monitoring (SM) is widely recognized as the basis for any sort of diagnostics in assessing the operating conditions of structures and infrastructures. Through the continuous technological development of data collection and processing tools, SM allows one to evaluate the structural characteristics and the level of damage of any structural system, giving the technicians the ability to predict the structural response deterioration along time.

The buildings under study is called *Pins del Vallès School* and it is located in Sant Cugat (Barcelona - SPAIN). The building has a rectangular-shaped plan and in elevation consists of columns, beams, walls in c.a. and standard hybrid scheme floors (see Figure 1). The monitoring system designed for the purpose of this paper is series of a tri-axial *EPISENSOR Model FBA ES-T* accelerometers [2] coupled with a wireless acquisition system designed in [3-4] and tested during several test applications [5-6]. The main advantages of using these sensors are: very-low self-noise, resulting in 155 dB dynamic range; user-selectable full g-scale range: from ±0.25g to ±4g; user-selectable full output range: from ±2.5V to ±20V, differential; wide frequency response: from DC to 200 Hz.

Figure 1: Site location.

3.1 Monitoring campaign

The monitoring campaign has been developped in five different days:
- **day 1**: general inspection to identify any evident structural and non-structural damges -if any;
- **day 2**: data acquisition due to environmental loads (no drilling) – BUILDING #2 (Figure 1);
- **day 3**: environmental vertical tests (no drilling) – BUILDING #1 (Figure 1);
- **day 4**: environmental floor tests (no drilling) – BUILDING #2 (Figure 1);
- **day 5**: data acquisition during drilling activities (Figure 2) – BUILDING #2 (Figure 1).

Figure 2: Data acquisition system on site.

References

[1] Geofit. "https://geofit-project.eu/"
[2] Kinemetrics. " https://kinemetrics.com/post_products/episensor-es-t/"
[3] Casciati, S., Z. Chen. 2011. "A multi-channel wireless connection system for structural health monitoring applications" *Structural Control & Health Monitoring*, Volume: 18 Issue: 5 Pages: 588-600.
[4] Casciati, S., L. Faravelli, Z. Chen. 2012. "Energy harvesting and power management of wireless sensors for structural control applications in civil engineering" *Smart Structures and* Systems, Volume: 10 Issue: 3 Pages: 299-312.
[5] Chen, Z., S. Casciati, L. Faravelli. 2015. "In-Situ Validation of a Wireless Data Acquisition System by Monitoring a Pedestrian Bridge" *Advances in Structural Engineering*, Volume: 18 Issue: 1 Pages: 97-106.
[6] F. Casciati, S. Casciati, A. Colnaghi and L. Faravelli, "Geothermal Power: Monitoring the Building Response During Installation," in *Proceedings IWSHM*, Stanford, California, USA, 2019.

INNOVATIVE MONOLITHIC DFOS SENSOR FOR TEMPERATURE AND MECHANICAL STRAIN MEASUREMENTS

R. Sieńko[1], Ł. Bednarski[2], T. Howiacki[1,3], and K. Zdanowicz[4]

[1]*Faculty of Civil Engineering, Cracow University of Technology, Krakow, Poland*
[2]*Faculty of Mechanical Engineering and Robotics, AGH University of Science and Technology in Krakow, Poland*
[3]*Nerve-Sensors, Krakow, Poland, www.nerve-sensors.com*
[4]*Faculty of Geoengineering, University of Warmia and Mazury in Olsztyn, Poland,*
e-mail: tomasz.howiacki@nerve-sensors.com

1. Distributed fibre optic sensing

Distributed fibre optic sensing (DFOS), in contrast to conventional spot gauges, allows the measurements to be performed continuously along the entire measurement path. Thanks to that approach, the profile of measurand (e.g. strain or temperature) is obtained with extremely high spatial resolution [1] instead of a single number. This is the essential feature of this technology and its most significant advantage at the same time, as local damage detection is now truly possible. However, to utilise the benefits coming from DFOS, both appropriate measurement tools (sensors) and installation procedures must be applied.

2. Distributed fibre optic fibres and conventional cables

Usually, the standard telecom optical fibre in the primary coating has a diameter up to 250 µm. It could be used as distributed sensor under laboratory conditions. It is too fragile for civil engineering and geotechnical applications. That is why several different types of sensing cables [2] are produced using the technologies known from telecommunication, i.e. including many intermediate layers (Fig. 1a). These layers protect the fibre against mechanical and environmental influences, but they also can disturb the strain transfer mechanism [3] due to the random (uncontrolled) slippage between the layers. What is more, steel or plastic components significantly limit the high elastic range of the optical fibre itself. It is much more beneficial to use materials with decreased elastic modulus [4] as it is easier for the sensor to reflect the actual structural behaviour of the monitored component.
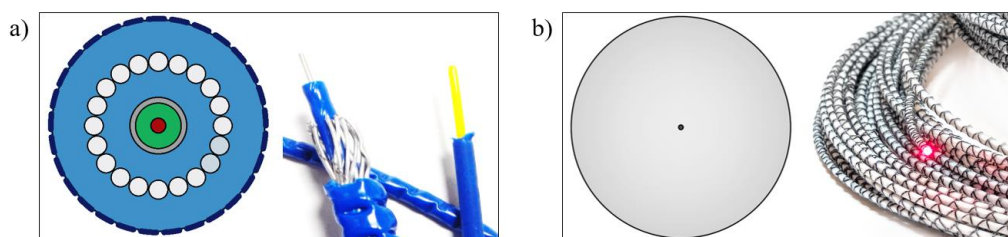
Figure 1: Cross-section and the view of the example: a) conventional layered cable; b) innovative composite DFOS strain sensor with a monolithic cross-section.

3. Innovative sensor for temperature and strain measurements

The new quality is provided by composite and monolithic sensors, which overcame the existing limitations of layered cables. First of all, they are produced in the pultrusion process, which fully integrates the fibre inside a monolithic core (without any layers) [5]. Application of high-elastic composite provides extremely high strain range, even up to ±40 000 µε (±4%). So, the sensors can be successfully used to monitor cracking in the concrete [6] or yielding in the steel. They are also durable and fully resistant to corrosion, which is extremely important in terms of long-term structural health monitoring. Outer braid (Fig. 1b) provides perfect bonding properties with the surrounding material.

Composite DFOS sensors can also be successfully used for temperature monitoring. Thanks to their monolithic cross-section, they are characterised by the linear thermal coefficient for strain results compensation in the form of a single multiplier. Appropriate additives added during production, significantly increase thermal conductivity so that the sensor's response to temperature changes is as fast as possible. On the other hand, multiple layers in conventional cables are made of materials with different thermal expansion coefficients. This results in their mechanical interactions distorting the correct temperature measurements. Their datasheets do not define the coefficient needed for thermal compensation of the strain readings.

4. Example application

The high-quality performance of monolithic and composite sensors was proved in the lab and many field applications, including challenging geotechnical conditions. Fig. 2 shows one of the highest road embankments in Poland equipped with innovative DFOS sensors along its base. The purpose of the measurements was to obtain temperature profiles along the entire length (Fig. 2b) to compensate for the results from other techniques. Unique data show that temperature gradients can reach up to 10°C over a distance of 15 m, depending on actual weather conditions, sun exposition and geometry of the slopes.
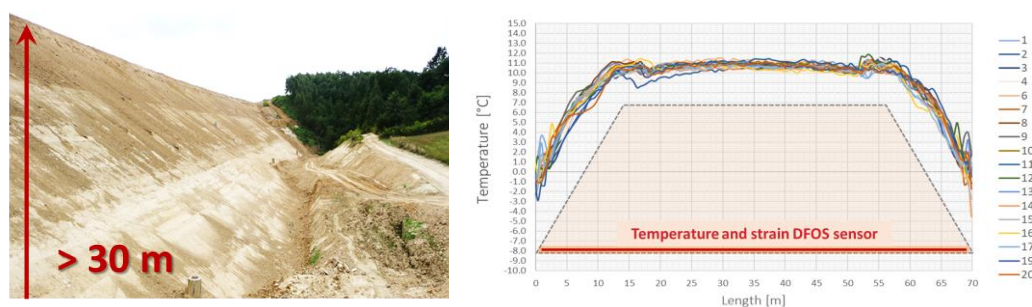
Figure 2: The view of the road embankment and example temperature profiles measured at its base [7]

6. Summary

Innovative composite sensors with monolithic cross-sections can create an auto-diagnostic system integrated with the monitored structure, detecting minor changes in the measurand (strains or temperatures) with extremely high precision and accuracy. Together with a DFOS-based datalogger, such a system can be compared to the nervous system in the human body, informing about any threats at any point of the structure.

References

[1] L. Palmieri and L. Schenato. Distributed Optical Fiber Sensing Based on Rayleigh Scattering. *The Open Optics Journal* 7, (Suppl-1, M7): 104-127, 2016.
[2] M. F. Bado and J. R. Casas. A Review of Recent Distributed Optical Fiber Sensors Applications for Civil Engineering Structural Health Monitoring. *Sensors* 2021, 21(5), 1818; https://doi.org/10.3390/s21051818.
[3] F. Falcetelli, L. Rossi, R. Di Sante and G. Bolognini. Strain Transfer in Surface-Bonded Optical Fiber Sensors. *Sensors* 2020, 20(11), 3100; https://doi.org/10.3390/s20113100.
[4] L. Meng, L. Wang, Y. Hou and G. Yan. A Research on Low Modulus Distributed Fiber Optical Sensor for Pavement Material Strain Monitoring. Sensors 2017, 17(10), 2386; https://doi.org/10.3390/s17102386.
[5] M. Kulpa, T. Howiacki, A. Wiater, T. Siwowski and R. Sieńko R. Strain and displacement measurement based on distributed fibre optic sensing (DFOS) system integrated with FRP composite sandwich panel. *Measurement* 175(15):109099, 2021.
[6] T. Howiacki. *Analysis of cracks in concrete structures with the use of distributed optical fibre measurements*. PhD dissertation. Faculty of Civil Engineering, Cracow University of Technology, Poland, 2022 (in press).
[7] Nerve-Sensors, *www.nerve-sensors.com/projects*, last accessed 2022/03/21.

FULLY AUTONOMOUS POST-EARTHQUAKE VISUAL INSPECTION OF RAILWAY BRIDGES: PROTOTYPE DEVELOPEMENT

Y. Narazaki[1], Wendong Pang[1]

[1]*Zhejiang University/University of Illinois at Urbana-Champaign Institute, Zhejiang University, Haining, China*
e-mail: narazaki@intl.zju.edu.cn (Y. N.), wendong.21@intl.zju.edu.cn (W. P.)

Abstract

This research envisions a fully autonomous system for rapid post-earthquake visual inspection of railway bridges. The system is designed to mimic the behavior of human inspectors during the entire inspection process, from data collection to data post-processing. The proposed system consists of four subsystems: bridge component recognition and localization, vision-based robotic navigation, image post-processing for structural assessment, and synthetic environments as testbeds for the prototype development. This research develops a prototype autonomous structural inspection system working in the synthetic environment, followed by the discussions of roadmap for extending the system to the field environment. The developed prototype system is expected to be a key step toward the effective rapid post-earthquake response activities through enhanced degree of autonomy.

1. Introduction

Rapid post-earthquake structural inspection is critical during the initial phase of disaster response to minimize the negative impact to people's lives and business. Currently, such inspections are performed mainly by human inspectors, whose main roles are accessing, observing, and assessing critical parts of target structures in the complex environments. The process is time-consuming, because available human resources are often limited due to damage to homes, transportation/communication systems, etc. The inspection process even becomes unsafe if the significant extent of damage is expected for the structures in the affected area. These limitations hinder structural inspections required for effective planning and execution of emergency response activities after an earthquake.

This research envisions a fully autonomous system that mimics the behavior of human inspectors to facilitate the entire process of post-earthquake visual inspection of railway bridges, from data collection to data post-processing. First, a robotic "inspector" (e.g., an unmanned aerial vehicle) navigates nearby and obtains initial partial understanding of the target structure, as well as a clear idea of where the first few critical structural components are located. The inspector then navigates to the identified components to collect close-up images suitable for structural assessment. Moreover, the inspector's understanding of the target structure is improved progressively by experiencing additional viewpoints during that navigation process. After inspecting the first critical structural component, the inspector transition to the inspection of next critical component based on the updated understanding of the target structure. After this process, the collected close-up images of target surfaces are post-processed to derive the structure's inspection rating.

The autonomous system consists of four technical components: synthetic environments as testbeds for the prototype development, bridge component recognition and localization, vision-based navigation, and image post-processing for structural assessment. Investigation of those subsystems leads to the development of a prototype system working in the synthetic environment. Finally, the roadmap for extending the system to the field environment is discussed.

2. Fully autonomous system for rapid post-earthquake visual inspection of railway bridges

The components of the envisioned autonomous inspection system are illustrated in Figure 1. To facilitate the system development, large-scale synthetic environments of reinforced concrete (RC) railway bridges, also called viaducts, are created (Figure 1(a)). A total of 2,000 viaduct models are generated randomly and programmatically, following the actual design procedure adopted by the Tokaido Shinkansen, one of the Japanese high-speed railway lines. Moreover, the viaduct columns exhibit various damage scenarios, such as concrete damage and exposed rebar, enabling the simulation and training data generation closely aligned with the target application scenario. Narazaki et al. (2021) [1] discusses the details of the synthetic environments, with examples of training deep learning methods to perform inspection subtasks automatically.

Supported by the synthetic environments, an autonomous subsystem that recognizes and localizes critical structural components (viaduct columns in this research, Figure 1(b)) and navigates to those components to collect close-up images (Figure 1(b)) is investigated [2]. Here, the "inspector" processes the input image stream on-line to detect viaduct columns represented by square prismatic shapes (pairs of rectangles). The viewpoints suitable for inspection image collection are determined relative to the identified shapes.

Finally, the collected images are post-processed to assess the structural conditions. This step is formulated as a semantic segmentation problem that parses input images into structural component/damage categories. The synthetic data is used effectively to train deep networks that can perform complex damage detection tasks aitpmatically.

| (a) | (b) | (c) | (d) |
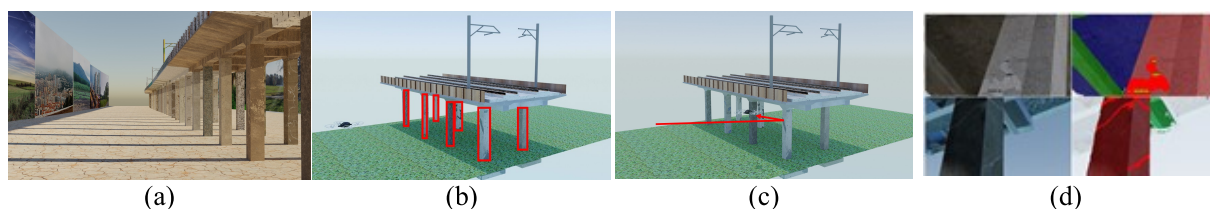
Figure 1. Steps of envisioned autonomous system for post-earthquake structural inspection. (a) synthetic environment, (b) bridge component recognition and localization, (c) vision-based navigation, (d) image post-processing for structural assessment.

3. Concluding remarks

This research developed a prototype fully autonomous post-earthquake visual inspection system for railway viaducts that collects inspection images based on the understanding of the target structure, and post-processes the collected images for structural assessment. The proposed system is designed to mimic human inspectors' behavior during inspection, and the perception of the inspectors (structural components and damage) is implemented by deep learning methods trained using the large-scale synthetic dataset. The prototype system is tested in the synthetic environments, and the roadmap for extending the prototype system to the field environment will be discussed during the presentation.

References

[1] Y. Narazaki, V. Hoskere, K. Yoshida, B. F. Spencer and Y. Fujino. Synthetic environments for vision-based structural condition assessment of Japanese high-speed railway viaducts. *Mechanical Systems and Signal Processing*, 160, 107850, 2021.
[2] Y. Narazaki, V. Hoskere, G. Chowdhary and B. F. Spencer. Vision-based navigation planning for autonomous post-earthquake inspection of reinforced concrete railway viaducts using unmanned aerial vehicles. *Automation in Construction*, in press, 2022.

Comparison of the accuracy of computer vision-based methods for estimation of structural displacements using synthetic video data

Mariusz Ostrowski[1], Bartlomiej Blachowski[1], Mateusz Zarski[2,3], Bartosz Wojcik[2,3], Piotr Tauzowski[1], and Lukasz Jankowski[1]

[1]*Institute of Fundamental Technological Research, Polish Academy of Sciences, Warsaw, Poland*
[2]*Silesian University of Technology, Gliwice, Poland*
[3]*Institute of Theoretical and Applied Informatics, Polish Academy of Sciences, Gliwice, Poland*

e-mail: mostr@ippt.pan.pl

1. Introduction

Despite significant advances in structural health monitoring (SHM), the design of contact sensor networks and their power supply for large-scale structures is still expensive and difficult [2]. Due to the recent progress in computer vision (CV) it is possible to monitor structural components or even whole structures with the aid of digital cameras that allow to avoid the use of the contact sensors [4]. However, CV-based measurements have a significantly lower accuracy than the techniques based on the contact sensors. Moreover, the amount of benchmark data available for development, testing and comparison of CV-based methods is limited. This problem has been partially overcome in recent years by the use of the physics-based graphical models (PBGM) in generation of synthetic but realistic video data [3].

In this work, a comparison of two popular methods of CV-based object tracking applicable in SHM is discussed. PBGM-based videos used in this study are a part of *"The 2nd International Competition for Structural Health Monitoring"* [1]. Exact structural displacements are available due to the fact that PBGM-based video are generated using the structural model. Hence, calculation of the error metrics is straightforward and reliable. The PBGM-based videos show a spatial truss subjected to an unknown excitation (Fig. 1).

2. Computer vision-based methods of estimation of the dynamic displacements

Two popular methods are tested on the PBGM-based video:

Normalised cross-correlation-based template matching (NCCTM). Template matching is one of the most accurate and popular methods of object tracking due to its relatively high accuracy. Displacements of the joints are estimated as the position of the template, including tracked truss node, that is matched with a sub-region of a usually larger region of interest (ROI) in the currently processed video frame. In this case matching is obtained by maximization of the normalized cross-correlation (NCC) between the template and the ROI. In order to achieve a sub-pixel precision, the NCC is interpolated with an eight times denser mesh.

Kanade–Lucas–Tomasi algorithm with repetitive correction (KLT-RC). In this case, the problem of the estimation of the nodal displacements can be divided into three parts. The first part is the initiation of the algorithm by extraction of the corner points in manually selected ROIs (Fig. 1) with the Harris–Stephens detector.
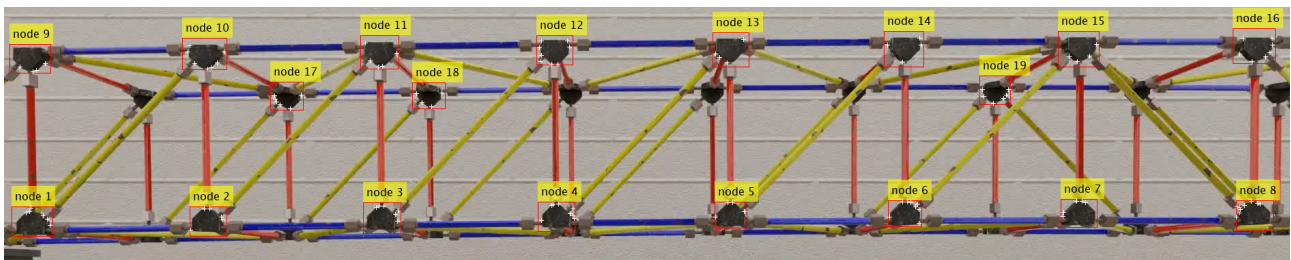
Figure 1: Frame of a PBGM-based video showing the investigated truss structure, manually selected truss nodes (marked by the red rectangles) and extracted corner points (marked by the white crosses "+")
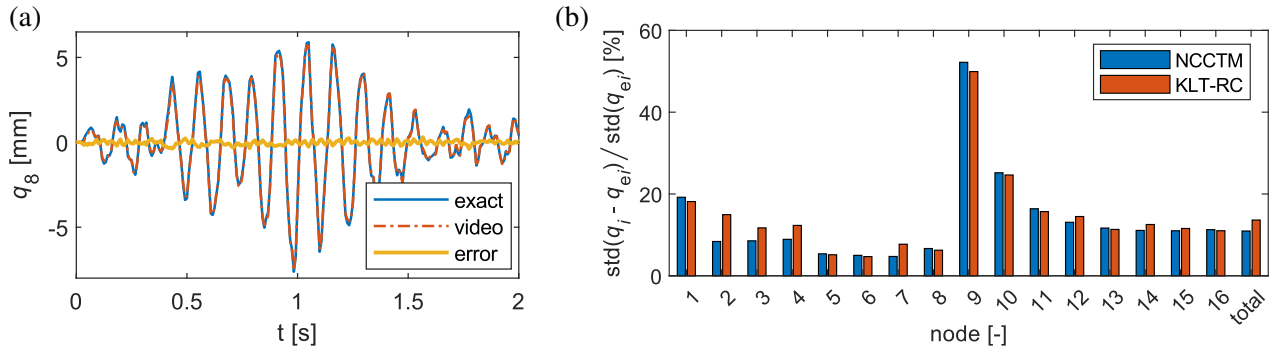
Figure 2: (a) vertical displacements of the 8th node obtained with the KLT-RC method and (b) comparison of the standard deviation of the estimation error in relation to the standard deviation of the exact displacements, q_i – vertical displacements of ith node, q_{ei} – corresponding exact displacements

The second part is tracking the points with Kanade-Lucas-Tomasi (KLT) algorithm that minimizes the sum of the squared differences between the subsequent movie frames in the neighborhood of the extracted corner points. Estimated displacement between subsequent frames is added to the total displacement of the truss node. Such an incremental approach results in error accumulation during long-term tracking. Thus, in the third part of the algorithm, a repetitive correction of the nodal position with the aid of feature matching is employed.

3. Results of comparison

The PBGM-based video with full-HD resolution and the frame rate (equivalent of the sampling frequency) of 120 fps are used for object tracking. Exact vertical displacements of the nodes 1–16 are known. As an example, the vertical displacement extracted from the video for node 8 with the KLT-CR method is compared with the exact value in Fig. 2a. Relative estimation errors for each node and for all nodes are shown in Fig. 2b.

Averaged error for the NCCTM is 10.1 %, whereas for the KLT-RC it is 13.6 %. The estimation error is significantly greater for the nodes close to the structure supports (1st and 9th node, Fig. 1). The reason is the fact that smaller displacements result in a greater sensitivity of the tracking to disturbances. Moreover, the response of these nodes has a relatively larger participation of higher order modes. The NCCTM is less efficient in terms of the tracking frame rate which is 3.6 fps, while the KLT-CR achieves the frame rate of 100 fps.

4. Conclusions

Both tested methods, NCCTM and KLT-RC, achieve comparable accuracy for the tested PBGM-based video. The NCCTM is more accurate (10.1 % vs 13.6 % of the noise level) but much slower (3.6 fps vs. 100 fps). Thus, the choice depends on the application of the CV-based measurement.

References

[1] The 2nd international competition for structural health monitoring (IC-SHM, 2021).

[2] T. Nagayama and B. F. Spencer. *Structural Health Monitoring Using Smart Sensors*. The Newmark Structural Engineering Laboratory, University of Illinois at Urbana-Champaign, 2007.

[3] Y. Narazaki, F. Gomez, V. Hoskere, M. D. Smith, and B. F. Spencer. Efficient development of vision-based dense three-dimensional displacement measurement algorithms using physics-based graphics models. *Structural Health Monitoring*, 20:1841–1863, 2021.

[4] B. F. Spencer, V. Hoskere, and Y. Narazaki. Advances in computer vision-based civil infrastructure inspection and monitoring. *Engineering*, 5:199–222, 2019.

MONITORING FLEXURAL STIFFNESS DROP OF REINFORCED CONCRETE STRUCTURES USING ROTATION RATE SENSORS

P. Bońkowski[1], P. Bobra[1], Z. Zembaty[1]

[1]*Opole University of Technology, Opole, Poland*

e-mail: p.bonkowski@po.edu.pl

1. Introduction

Vibration based damage detection is a challenging problem of modern engineering. In particular in civil engineering the approach using evolution of natural frequencies with damage often do not properly reflect local, though substantial, stiffness losses. These difficulties in proper implementation of SHM methods are can be particularly observed when dealing with reinforced concrete beams and frames where very sophisticated methods are involved in damage monitoring (e.g. [1]). On the other hand, the stiffness losses are better reflected in the variations of spatial derivatives of the translational modes (rotational and curvature modes) than in the translational modes themselves. For some time new techniques emerged to directly measure angle variations with increasing accuracy (e.g. Meydan [2], Yang & Yang [3]).

Thus, in addition to transversal accelerations, it is now possible to measure angle variations along the bar axis during vibrations of the structures. This way, the average changes in curvature of the axes of the bars can be obtained almost directly even when the structure beam is a cracked reinforced concrete (r/c) beam. Numerical simulations demonstrated many potential advantages for these new angular measurements of axes of beams and rods of frames. This is illustrated in Figure 1, where by using two rotation rate sensors measuring time changes of their relative angle $\Delta\varphi = \varphi_1 - \varphi_2$, conclusions about curvature changes $1/\rho$, can be drawn.
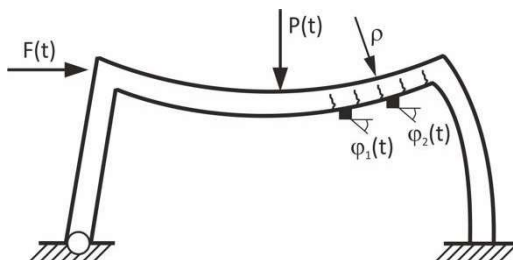
Figure 1: Rotation rate sensors (shown as little squares) applied to monitor vibrations of a cracked r/c frame

2. Description of experimental program of r/c beam stiffness "reconstruction"

Recently a research program aiming at monitoring flexural stiffness *EJ* variations of r/c beams including beams made of Ultra High Performance Concrete was undertaken in the laboratory of the Faculty of Civil Engineering & Architecture, Opole University of Technology, with partial support of Polish National Science Centre (NCN). The main purpose of this research program is to undertake difficult tasks of stiffness "reconstruction" of r/c beams based on measuring their vibrations. This can be done using e.g. minimization techniques described in detail in papers by Kokot & Zembaty [4], Zembaty et al. [5], [6]. The typical experimental set up (with damages unevenly distributed in form of cracks of the beam) is shown in Figure 2.

The damaged beam is induced by modal hammer and respective translational and rotational modes as well as eigenvalues are obtained by the means on experimental modal analysis. The results are used to build a functional (eq. 1) which (minimized) can lead to compute coefficients α_1, α_2, ..., α_i of stiffness losses describing the actual stiffness drops $\alpha_i EJ$ of sections of the analysed beam:

(1) $$J(\boldsymbol{\alpha}) = \sum_i \sum_j \left(\phi_{ij}^{ref} - \phi_{ij}^d(\boldsymbol{\alpha}) \right)^2 + \sum_k \left(\lambda_k^{ref} - \lambda_k^d(\boldsymbol{\alpha}) \right)^2,$$

where ϕ_{ij} = value of translational or rotational i normalised natural mode in j node, $\lambda_k = k$ eigenvalue, superscripts *ref* and *d* = reference FEM and damaged structure respectively, $\boldsymbol{\alpha}$ = vector describing stiffness losses in the selected areas of the analysed beam.
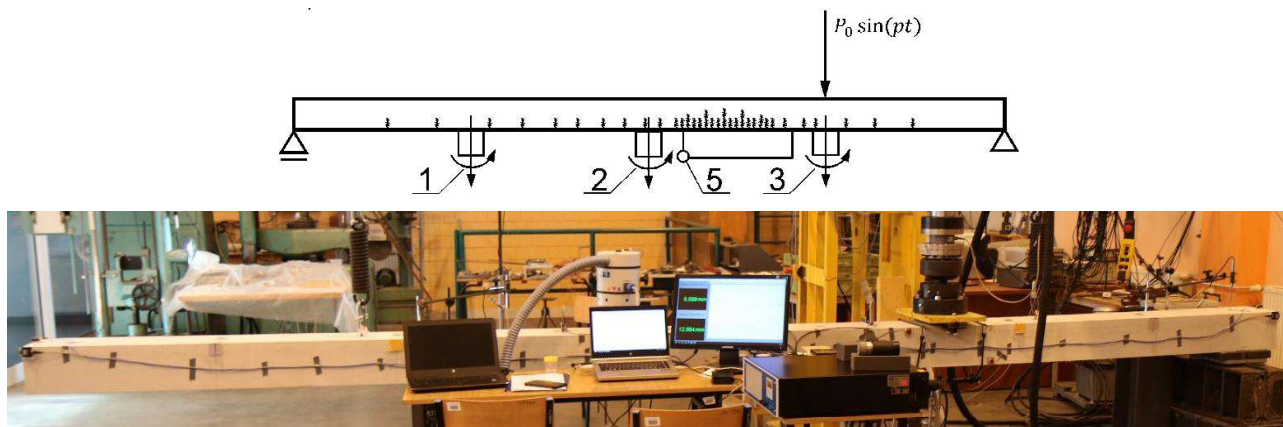
Figure 2. Simple sketch and actual experimental set up used to monitor stiffness variations of an UHPC beam under harmonic excitations and measured by translational accelerometers, rotation rate sensors (1, 2, 3) and using extensometer (5) for comparison

The purpose of the planned presentation during the EACS2022 Conference is to report results of the experiment carried out on 6 m UHPC with traditional steel reinforcing bars and additional content of glass and steel fibers and r/c beams. The beams have been damaged using static actuator in a number of stages: from the moment when only 1-2 cracks where barely visible to the yielding of reinforcing steel bars. After each stage the beams were hanged in free-free conditions and their translational and rotational vibrations induced by a modal hammer have been measured. Measurements were later used to find average stiffness losses of the beams and compared with measurements during static load an observed crack pattern. To help finding optimal solution for finding minima of eq. (1), genetic algorithms were used. Our preliminary results show that by using rotation rate sensors one can improve determination of flexural stiffness losses in ordinary r/c or UHPC beams.

References

[1]   Y. Goldfeld and A. Klar, 'Damage Identification in Reinforced Concrete Beams Using Spatially Distributed Strain Measurements', *Journal of Structural Engineering*, vol. 139, no. 12, Dec. 2013, doi: 10.1061/(ASCE)ST.1943-541X.0000795.

[2]   T. Meydan, 'Recent trends in linear and angular accelerometers', *Sensors and Actuators A: Physical*, vol. 59, no. 1, pp. 43–50, Apr. 1997, doi: 10.1016/S0924-4247(97)80146-X.

[3]   B. Yang and Y. Yang, 'A new angular velocity sensor with ultrahigh resolution using magnetoelectric effect under the principle of Coriolis force', *Sensors and Actuators A: Physical*, vol. 238, pp. 234–239, Feb. 2016, doi: 10.1016/j.sna.2015.12.021.

[4]   S. Kokot and Z. Zembaty, 'Vibration based stiffness reconstruction of beams and frames by observing their rotations under harmonic excitations — Numerical analysis', *Engineering Structures*, vol. 31, no. 7, pp. 1581–1588, Jul. 2009, doi: 10.1016/j.engstruct.2009.02.032.

[5]   Z. Zembaty, S. Kokot, and P. Bobra, 'Application of rotation rate sensors in an experiment of stiffness "reconstruction"', *Smart Materials and Structures*, vol. 22, no. 7, p. 077001, 2013.

[6]   Z. Zembaty, P. Bobra, P. A. Bońkowski, S. Kokot, and J. Kuś, 'Strain sensing of beams in flexural vibrations using rotation rate sensors', *Sensors and Actuators A: Physical*, vol. 269, pp. 322–330, Jan. 2018, doi: 10.1016/j.sna.2017.11.051.

OPTIMAL SENSOR PLACEMENT FOR STRUCTURAL HEALTH MONITORING

T. Ercan[1] and C. Papadimitriou[1]

[1]*University of Thessaly, Department of Mechanical Engineering Volos, Greece*

e-mail: ercan@uth.gr, costasp@uth.gr

1. Abstract

Optimal sensor placement (OSP) strategies are important for health monitoring of civil engineering systems. The OSP should account for modeling uncertainties that arise from system operational conditions, as well as uncertainties associated with the excitation characteristics. A Bayesian OSP method for parameter estimation [1] in linear and nonlinear models is extended to take into account the modelling and input uncertainties. The optimal sensor locations are selected to maximize the information gained from the sensors for evaluating the system parameters representative of its healthy and/or deteriorating condition over a monitoring period. Such information gain is defined as the Kulback-Leibler divergence between the prior and posterior distribution of the model parameters estimated using Bayesian inference. To design an optimal sensor configuration robust to system modeling and input uncertainties, the utility function is taken as the expected information gain over all possible data that would arise under all possible model and input realizations. Asymptotic approximations are proposed for estimating part of the multidimensional integrals arising in the utility formulation in terms of the sensitivities of model responses at the measured locations with respect to the estimated parameters. The remaining multidimensional integrals over the prior distribution of the model parameters, the modeling uncertainties and input variabilities arising in the formulation are estimated by using Monte Carlo methods.

Keywords: Bayesian Optimal Sensor Placement, Parameter Estimation, Stochastic Excitation, SHM.

2. OSP for parameter estimation considering model and input uncertainties

The robust OSP design for estimating the model parameters $\underline{\theta}$ maximizes the expected information gain over all possible data that can be obtained over all possible values of the model parameters and the input realizations. Let $\underline{\varphi}$ be a parameter set containing the uncertain non-updatable model parameters, the model prediction error parameter and the uncertain input parameters accounting for the stochastic nature of the input. Let also $\underline{\delta}$ be the sensor configuration. It can be shown that asymptotically for the large number of data and small prediction errors, the expected utility function to be maximized with respect to the sensor configuration $\underline{\delta}$ is given by the multi-dimensional integral:

$$(1) \qquad U(\underline{\delta}) = -\frac{1}{2} \int_\Theta \int_\Phi \ln \frac{\det[Q(\underline{\delta}; \underline{\theta}, \underline{\varphi}) + Q_\pi(\underline{\varphi})]}{\det Q_\pi(\underline{\varphi})} p(\underline{\theta}) \, p(\underline{\varphi}) d\underline{\theta} \, d\underline{\varphi}$$

where $Q_\pi(\underline{\varphi})$ is the inverse of the covariance matrix of the Gaussian prior distribution and $Q(\underline{\delta}; \underline{\theta}, \underline{\varphi})$ is the Fisher information matrix, a semipositive definite matrix given by:

$$(2) \qquad Q(\underline{\delta}; \underline{\theta}, \underline{\varphi}) = \sum_{k=1}^{n_d} \nabla_{\underline{\theta}} g(\underline{\theta}; \underline{\delta}, \underline{\varphi})^T \, \Sigma_e(\underline{\theta}; \underline{\varphi}) \, \nabla_{\underline{\theta}}^T g(\underline{\theta}; \underline{\delta}, \underline{\varphi})$$

$\nabla_{\underline{\theta}} = [\partial/\partial\theta_1, \cdots, \partial/\partial\theta_{n_\theta}]$ is the gradient operator and $g(\underline{\theta}; \underline{\delta}, \underline{\varphi})$ is the vector of model response time histories related to the sensor locations. Σ_e is the covariance matrix of the prediction error, which is assumed as the sum of model and measurement error. $p(\underline{\theta})$ and $p(\underline{\varphi})$ are postulated prior distribution of the model and nuisance parameters, respectively. A Monte Carlo sampling estimate is used to evaluate the multi-dimensional integrals. Heuristic sequential sensor placement algorithms [1] are used to solve the optimization problem.

3. Application

The effectiveness of the method is demonstrated on a 20-DOF shear model of a MDOF system subjected to earthquake excitation modelled by a stochastic process. Here, the Kanai-Tajimi (KT) spectrum is considered. The Kanai-Tajimi filter parameters are selected as constants: $\zeta = 0.64$ and $\omega_g = 15$ rad/sn [2]. The white noise sequence used as the input to the KT spectrum constitutes the parameter set $\underline{\varphi}$. To consider the white noise input uncertainty, the expectation over 100 different white noise inputs is calculated. Optimal locations of the acceleration sensors are found for reliable estimation of the stiffness parameters of the first 10 stories ($\theta \sim N(1, 0.1)$). The standard deviation of the model prediction error is selected to correspond to 1% model prediction error and $\sim 10\%$ measurement error. The portion of the response that is included in the utility estimation corresponds to the time interval from 5–10 seconds. The best sensor locations and the normalized maximum and minimum utility values are presented in Figure 1. According to the best location result, the first 4 sensors are placed on the first 4 floors, the fifth sensor is placed at the 9-th floor in order to reliably estimate the model parameters of the lowest 10 floors. As observed from the utility values, there is a significant information gain when the first sensor is optimally placed in the system to estimate the model parameters since this sensor accounts for 81% of the maximum information that can be obtained by placing acceleration sensors in all floors. Each additional sensor provides some extra information for estimating the model parameters.
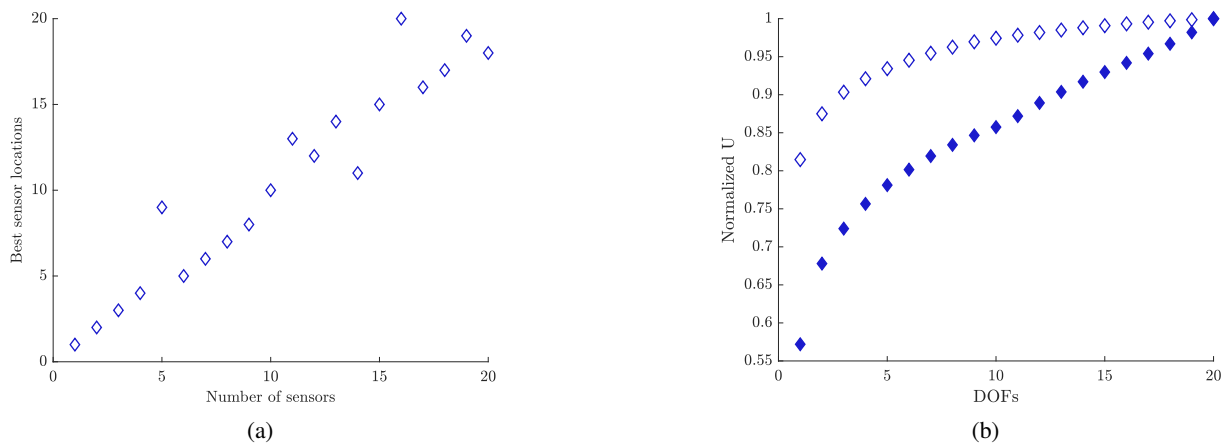
Figure 1: OSP (left); Maximum and minimum normalized utility values (right).

4. Conclusions

The proposed Bayesian OSP framework is general, applicable to a wide variety of linear/nonlinear systems encountered in structural health monitoring applications. The OSP design is extended in this study to handle the realistic case of uncertain temporal variability of the input, such as earthquake excitation, often modelled by stochastic processes. The optimal sensor configuration designs are demonstrated to be robust to uncertain temporal variability of the input.

References

[1] T. Ercan and C. Papadimitriou. Optimal Experimental Design Methodology for Parameter Estimation of Nonlinear Models. In *Proceedings of 10th International Conference on Structural Health Monitoring of Intelligent Infrastructure, SHMII 10*, pages 689–693. Universidade do Porto, 2021.

[2] T. Neckel and F. Rupp. *Random differential equations in scientific computing*. De Gruyter Open Poland, 2013.

3D SEISMIC NETWORK IN URBAN ENVIRONMENT

A. Bogdanovic[1], Z. Rakicevic[1], J. Bojadzieva[1], V. Sheshov[1], K. Edip[1]A. Poposka[1], F. Manojlovski[1], A. Shoklarovski[1], I. Markovski[1], D. Filipovski[1]and N. Naumovski[1]

[1]Ss. Cyril and Methodius University in Skopje-UKIM, Institute of Earthquake Engineering and Engineering Seismology, Skopje-IZIIS, N. Macedonia
e-mail: saska@iziis.ukim.edu.mk

1. Introduction

Continuous safe and low-cost operation of structures extensively depends on their proper maintenance and management. To apply optimal management strategies for the existing structures, accurate assessment of their present and future safety is important and crucial. In order to study local site effect on the modification of strong ground motions and dynamic response of structural systems a three-dimensional seismic network at Ohrid Lake basin is developed in the 80's (Petrovski et al., 1995) with support from USGS (United States Geological Survey). This 3d strong motion array is consisted of three free field sites (Fig. 1) with one surface and three downhole instruments each, up to 125 meters to the bedrock; one nine story building site with two instruments on the building, 4 instruments at the foundation level and one outcropping rock site with one instrument (location Tower). The characteristics of the instruments at the locations are presented in Figure 2 and Table 1.

Figure 1. 3-dimensional seismic network in Ohrid

Table 1. Specification of the instruments at the 3d Ohrid seismic network

	Location – 1- Tower In situ laboratory	Location - 2	Location - 3	Location - 4
Site type	Instrumented building	Free field	Free field	Rock -outcrop
Instruments at building structure	2 (6th and 9th story)			
Instruments at foundation structure	4			
Instruments at soil surface	1	1	1	1
Instruments in soil profile	2 (13.0m, 22.9m)	2 (9.5m, 22m)	2 (9.0m, 21.5m)	
Instruments at bedrock	1	1	1	1
Total number of instruments	10	4	4	1

2. General information of the system and software

During planning and installation of the Ohrid Lake Seismic network in late 70's entire network was composed of most successful instruments produced by Kinemetrics Inc., Pasadena, California. In the time period between 2020-2021 extensive revitalizations process has begun replacing analogue to digital
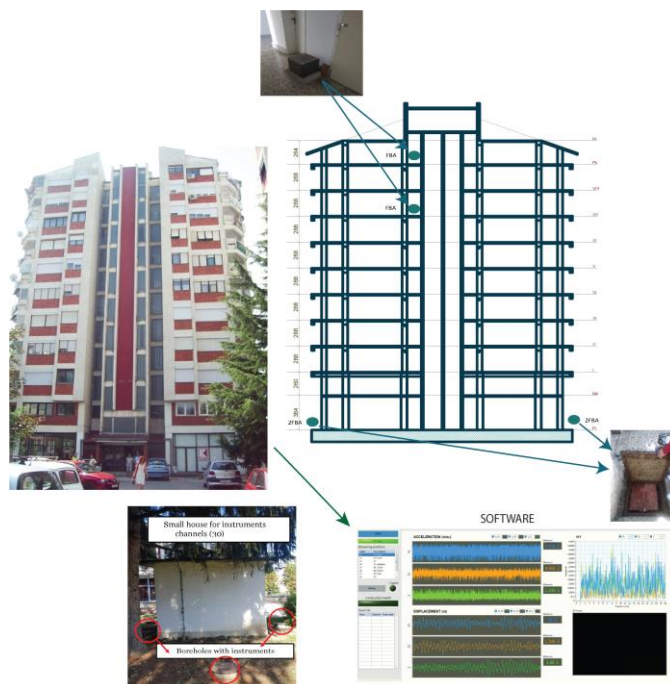
Figure 2. Instrumentation at the location Tower; The building structure; Small house for instrumentation for real time recordings; Software

conversion device which enables recording of real time earthquake events and thus structural and health monitoring system at the Location Tower. The behaviour of the structure is monitored in serviceability conditions, during and after seismic effects (if any during the considered period). The recorded data is analysed by different methodologies for system identification for the purpose of obtaining necessary data on the structure and its performances. Processing of the acquisitioned data is done by mathematical and software solutions and methodologies developed at UKIM-IZIIS. The monitoring software is developed in LabView. The software allows defining a limit level (trigger) for each measuring channel individually. The trigger can be in terms of acceleration or displacement level. After exceeding this level, the software creates a record in TMDS format which can then be further analyzed or processed in other data processing and analysis software. In the background, the software constantly performs a basic analysis of the measured data and based on previously determined parameters displays the condition of the structure, expressed by a traffic light indicator (green - the construction is OK, yellow - caution and additional checks are needed, red - the construction is not safe. From March 2021 three more significant earthquake events has proven the functionality of the installed instruments and provided important data for further investigation at the location including numerical model verifications and analysis.

4. References

[1] Petrovski J. et al.(1995). Characteristics of earthquake ground motions obtained on the Ohrid lake three dimensional strong motion array in the Republic of Macedonia.10th European Conference on Earthquake Engineering, Duma (ed.) © 1995 Balkema, Rotterdam, ISBN 90 5410 528 3.

[2] Aydin E.,Öztürk B., Noroozinejad Farsangi E, Bogdanovic A., Dutkiewicz M. (2020) New Trends and Developments on Structural Control & Health Monitoring, Front. Built Environ., 29 April 2020 | https://doi.org/10.3389/fbuil.2020.00053 (2020), (available online)

[4] Ehsan Noroozinejad Farsangi, Aleksandra Bogdanovic, Zoran Rakicevic, Angela Poposka and Marta Stojmanovska, Ambient Vibration Testing and Field Investigations of Two Historical Buildings in Europe, Structural Durability & Health Monitoring, Vol.14, No.4, 2020, pp.283-301, Tech Science Press DOI:10.32604/sdhm.2020.010564

[5] Julijana Bojadjieva, Vlatko Sheshov, Kemal Edip, Jordanka Chaneva, Toni Kitanovski, Dejan Ivanovski (2019). "GIS based assessment of liquefaction potential for selected earthquake scenario". Earthquake geotechnical engineering for protection and development of environment and constructions. Proceedings of the 7th International Conference of earthquake geotechnical engineering. 7th ICEGE, Rome, Italy, 17-20th, June, 2019.

COMPARISON OF EXPERIMENTALLY DETERMINED STRUCTURAL DYNAMIC CHARACTERISTICS ON A SHAKE TABLE TESTED MODEL BY DIFFERENT METHODS

A. Kwiecień[1], Z. Rakicevic[2], J. Chełmecki[1], A. Bogdanovic[2], M. Tekieli[1], M. Gams[3], Ł. Hojdys[1], P. Krajewski[1], F. Manojlovski[2], A. Soklarovski[2], O.F. Halici[4] and A. Sapalidis[5]

[1]*Cracow University of Technology, Cracow, Poland*
[2]*IZIIS, Ss. Cyril and Methodius University, Skopje, Republic of North Macedonia*
Faculty of Civil and Geodetic Engineering, University of Ljubljana, Ljubljana, Slovenia
[3]*Istanbul Technical University, Istanbul, Turkey*
[4]*Democritus University of Thrace, Xanthi, Greece*
e-mail: akwiecie@pk.edu.pl

1. Model tested on a shake table

The present study base on experimental results of the "INfills and MASonry structures protected by deformable POLyurethanes in seismic areas" (INMASPOL) project within the SERA, Horizon 2020. INMASPOL investigates the efficiency of innovative PUFJ protection at the frame-infill interface for RC frames with brick infills [1]. Further, PUs are used for bonding of glass fiber grids to the weak masonry substrate to form FRPU as emergency repair [2]. The methods are applied on full-scale infilled RC building tested on shake table under simulated seismic excitations. The seismic tests validated the improved in-plane and out-of-plane infill performance when modified or repaired with PUFJ and FRPU systems.

The tested structure is a fully symmetrical 3D frame of one storey with 4 RC columns, 4 beams, a slab and 4 infill masonry walls, all designed according to current Eurocodes. The real scale building has plane dimensions of 3.8x3.8m and height of 3.3m (foundation and column extensions included). The one storey RC frame building with infills has 1:1 scale. The floor plan dimensions of the frame were 2.7 x 2.7 m, and the 20 x 20 cm columns had height of 2.5 m (to the top of the slab). The height of infills in the building was 2.3 m (Fig. 1). On top of the columns a RC slab with thickness of 20 cm was constructed. The slab, was extended beyond the frame beams to serve as additional mass and to attach the additional masses in the form of steel massive elements.

a)   b)
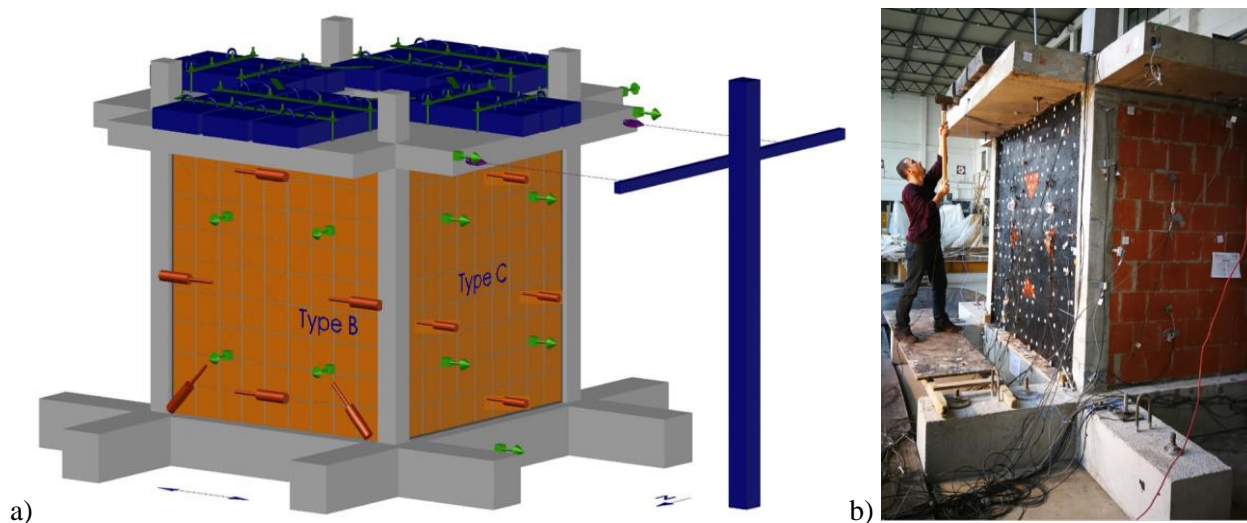
Table 1: Experimental model with a scheme of instrumentation (a) and dynamic excitation using a modal hammer (b).

2. Shake table excitation

The shake table tests have been performed in the laboratory for dynamic testing in the Institute of Earthquake Engineering and Engineering Seismology in Skopje (IZIIS), Republic of North Macedonia. Operational since the year 1980, the shake table is 5.0 m by 5.0 m pre-stressed concrete waffle slab weighing 33.0 tons with payload up to 40 tons. Five degrees of freedom are provided by 2 lateral and 4 vertical MTS hydraulic pistons, controlled by MTS Digital Controller 469D. National instruments PXI modular system has been used as data acquisition for the three different types of transducers: 23 accelerometers, 10 linear variable differential transformers and 2 linear potentiometers (Fig. 1a).

For the purpose of the experimental investigations two types of tests have been performed, i.e. dynamic shake table tests and tests for determination of dynamic characteristics. The dynamic shake table tests comprised of gradually increasing input intensity level from 3% to 77% of the adopted earthquake Kefallonia E-W component. Maximum applied load level was depended on the induced damage of the RC frame and infill walls as well as on the limit state of the shake table (considering the weight of the specimen and the additional load). A total of 23 seismic tests were performed.

3. Structural dynamic characteristics determined by different methods

Resonant frequency tests were examined after selected shake table tests regarding the observed damage. Sine-sweeps and white noise 0.02g low intensity tests were performed, confirming the gradual degradation of the bearing elements and infill softening. These dynamic diagnosis methods are classically using in all shake table tests. However, significantly damaged structures being about to collapse are in many cases too vulnerable to dynamic excitation, especially those generating resonance frequencies (sine-sweeps and white noise). One of proposed dynamic diagnosis methods used during the INMASPOL tests is modal analysis of dynamic structural response recorded by accelerometers to impact excitation with a 5 kg modal hammer. This method introduces in the weakened structure less energy, protecting it against developing additional damages and gives reasonable information about dynamic characteristics. Additional diagnostic information is provided by an inertance function, determined in frequency domain. This function allows also evaluating damping properties (half-power bandwidth method) throughout testing procedure.

Other diagnostic method tested in the SERA project was DIC (Digital Image Correlation) method, applied to dynamic measurements. Efficiency of this method was tested using two different optical devices: video camera Manta MG-235B and photo camera Nikon D7500. Pictures obtained from these optical devices were analysed by DIC software CivEng Vision [3]. Determined dynamic characteristics were compared with results obtained from sine-sweeps, white noise and modal hammer. Difference in the resolution of these methods were discussed.

References

[1] Kwiecień, A. 2019. Reduction of stress concentration by polymer flexible joints in seismic protection of masonry infill walls in RC frames. Materials Science and Engineering Vol. 474, pp. 1-7.
[2] Viskovic, A., Zuccarino, L., Kwiecień, A., Zając, B. & Gams, M. 2017. Quick seismic protection of weak masonry infilling in filled framed structures using flexible joints. Key Engineering Materials 747, pp. 628-637.
[3] Tekieli M., De Santis S., de Felice G., Kwiecień A., Roscini F.: Application of Digital Image Correlation to composite reinforcements testing. Composite Structures 160 (2017), pp. 670–688.

DAMAGE DETECTION OF STRUCTURE SUBJECTED TO EARTHQUAKE EXCITATION BASED ON MULTIFRACTAL ANALYSIS AND WAVELET LEADERS

N. Pnevmatikos[1], B. Blachowski[2], S Papatzani[3] F. Konstandakopoulou[4] and P. Broukos[5]

[1]*Department of Civil Engineering, School of Engineering, University of West Attica, Athens, Greece, e-mail: pnevma@uniwa.gr*

[2] *Institute of Fundamental Technological Research, Polish Academy of Sciences, Warsaw, Poland, e-mail: bblach@ippt.pan.pl*

[3]*Department of Surveying and Geoinformatics Engineering, School of Engineering, University of West Attica, Athens, Greece, e-mail: spapatzani@uniwa.gr*

[4] *School of Science and Technology, Hellenic Open University, Patras, Greece; e-mail: konstantakopoulou.foteini@ac.eap.gr*

[5]*Imperial College London, Department of Chemical Engineering, Urban Energy Systems, e-mail: p.broukos11@imperial.ac.uk*

1. Introduction

This work deals with the application of multifractal analysis for damage detection in structures subjected to earthquake excitation. Specifically, a robust signal processing technique known as multifractal wavelet leader (MFWL) is used. The multifractal analysis is used to calculate fractal properties and scaling behaviour of the time history structural response excited by an earthquake. The singularity spectrum is obtained from the Legendre-transformation to Holder exponents. In this paper a parameter which is based on the shape of singularity spectrum and can identify the damage in the structure is proposed. The proposed method is an output-only damage detection method. Non-linear dynamic analysis has been performed and acceleration response at each story are obtained which are, in turn, used as simulation data. Damage in the structure was introduced due to hysteretic behaviour of the elements. Since the dynamic behaviour of an inelastic structure subjected to an earthquake excitation is a non-stationary process, the above procedure of multifractal wavelet leader is suitable to retrieve the simulation response data. The numerical results indicate that the MFWL is an appropriate method for structural damage detection.

2. Theoretical background

Fractal systems can be classified into one of two categories: either monofractal or multifractal. They are characterized with the power law with real scaling exponents. Monofractal systems are described by a singular unique scaling exponent, in contrast to the multifractal systems that are labelled by a continuum of scaling exponents. The multifractal wavelet leader technique has been developed by Jaffard et al. [1]. Wendt et al. [2], proposed a new multifractal formalism based on wavelet leaders (MFWL). The coefficients of a 2D Discrete Wavelet Transform(DWT) are used to constructed the wavelet leaders and hence take benefits from low computational costs and a simple implementation. Di Matteo et al., [3], used multifractality to investigate developing and developed markets since the second order of the Hurst exponent can predict the development level of a market. Morales et al., [4], used the multifractal characterstics as an indicator of financial crises proposing that as the second order of the Hurst exponent increases when the financial crise begins. In signal analysis the wavelet leader, $w(i, s)$, is calculated as the convolution of the signal, $u(t)$. The wavelet leader represents the supremum of the wavelet coefficient. Based on wavelet leader the scaling function, $S_w(q, s)$, is then calculated, where q is the order of the wavelet leader. Following the work on multifractral analysis introduced by Mukli et al, [5], where Holder exponents, h, are related with the multifractal Hurst exponents, H, and scaling exponents, s, one can apply a Legendre-transformation to the Holder exponents to obtain the singularity spectrum. Such a singularity spectrum is shown in Figure 1. As one can observe this spectrum is a concave function with a parabolic shape. The width and the shape of the spectrum curve contain characteristic information of the signal to be represented. The parameter $2h_{max} f_{whm}/3F_{max}$ is a combination of the Holder exponent at the maximum multifractal spectrum and the full width at half maximum of the spectrum. This parameter is used to distinguish the activity of the signal data and can serve as the damage index indicator.

3. Numerical case study

The above singularity spectrum has been calculated for the numerical model of the three-storey building

represented as a dynamical system with concentrated mass and stiffness parameters and its properties shown in Figure 2a.
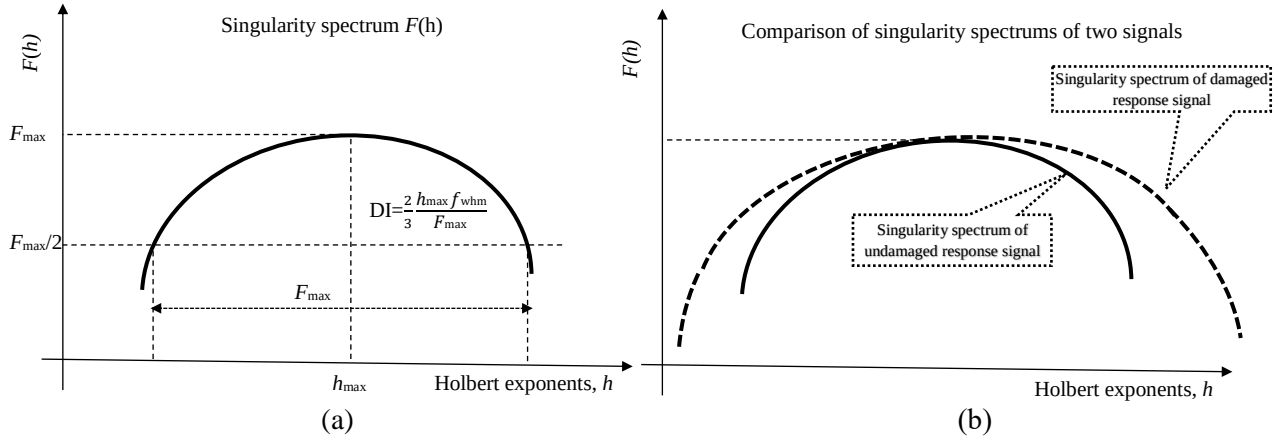
Figure 1: Characteristic parameters of singularity spectrum for calculating the damage indicator, (a), and singularity spectrum of damaged and undamaged structural response signal, (b).

Hysteretic plastic kinematic model was used for simulation the non-linear behaviour of columns. Athens 1999 earthquake record was applied at the base of the structure and the response, $u(t)$, at the top was calculated. The non-linear dynamic analysis has been executed using the software programme SAP2000nl. With appropriate scale of the earthquake excitation signal, the linear or undamaged (healthy), $u_{healthy}(t)$ and non-linear, damaged (unhealthy), $u_{unhealthy}(t)$, acceleration response were calculated. The multifractal spectrum or the singularity spectrum for the damaged and undamage response signal at the third floor has been calculated using MATLAB software. Aditionally, the damage indicator DI is also calculated for each case and shown in Figure 2b.
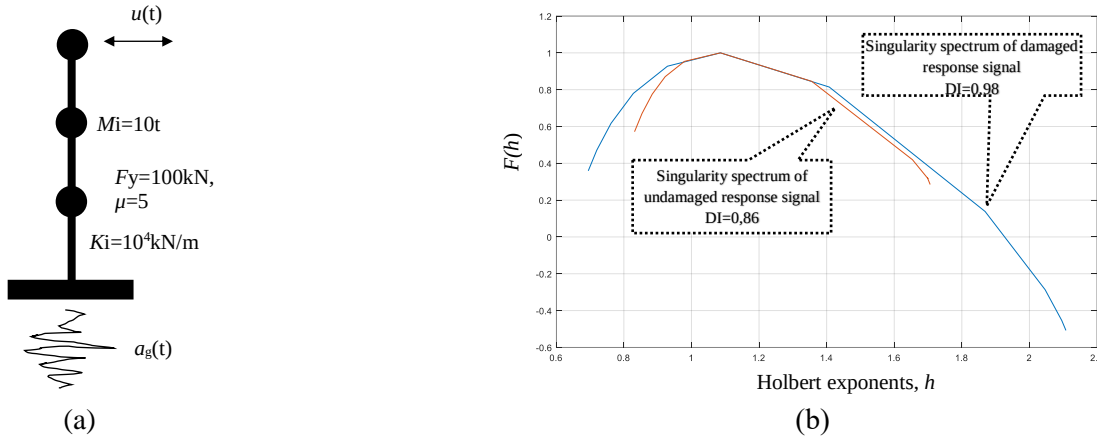
Figure 2: Characteristic parameters of singularity spectrum for calculating the damage indicator (a), and singularity spectrum of damaged and undamaged structural response signal, (b).

3. Conclusions

An application of MFWL, on damage detection in structures subjected to earthquake excitation has been performed. A parameter which is based on the shape of singularity spectrum and can identify the damage or not to the structure is proposed. The proposed method is an output-only damage detection method. The numerical results indicate that the, MFWL, is an appropriate method for structural damage detection.

4. References

[1] S. Jaffard, B. Lashermes, and P. Abry, Wavelet leaders in multifractal analysis, *Wavelet Analysis and Applications,* Springer, pp. 201–246, 2006.

[2] H.Wendt, S.G. Roux, P. Abry, and S. Jaffard., Wavelet leaders and bootstrap for multifractal analysis of images, Signal *Process*, vol. 89, pp. 1100–1114, 2009.

[3] T. Di Matteo, T. Aste, and M. M. Dacorogna, Long-term memories of developed and emerging markets: Using the scaling analysis to characterize their stage of development, *J. Banking Finance* 29(4): 827–851, 2005.

[4] R. Morales, T. Di Matteo, R. Gramatica, and T. Aste, Dynamical generalized Hurst exponent as a tool to monitor unstable periods in financial time series, *Physica A* 391(11): 3180–3189, 2012.

[5] P. Mukli, Z. Nagy, and A. Eke, Multifractal formalism by enforcing the universal behavior of scaling functions, *Physica A* 417: 150–167, 2015.

NON-CONTACT NONLINEAR WAVE MIXING RESPONSE OF NARROWBAND LAMB WAVES GENERATED BY MAKING A LASER BEAM WITH LINE LASER ARRAY SOURCCES

Santhakumar Sampath[1], and Hoon Sohn[1]

[1]*Department of Civil & Environmental Engineering, KAIST, 291 Daehakro, Yuseong-gu, Daejeon 34141, Republic of Korea*
e-mail: hoonsohn@kaist.ac.kr

1. Background

A nonlinear ultrasonic wave mixing approach has recently been used to identify damage in plate-like materials. A damaged structure is subjected to two input Lamb waves in this method. Nonlinear mixed components at the sum and difference of the input frequencies are produced by the interaction between these waves [1]. However, the applicability of contact method to damage detection of plates is challenges mainly for the following three main reasons [2]. To begin with, it requires a coulpling medium which adds an additional nonlinearity to the output response. Second, it may not applicable under hazardous environments (e.g., high temperature). Third, it is challenging to acquire high spatial resolution (less than μm) enough to identify damage when the transducer can only be installed in a few distinct points.

2. Objective

In this study, a non-contact nonlinear Lamb wave mixing technique based on laser line-array excitation was developed for non-contact generation and detection of the nonlinear mixed components in plates. Specifically, a pulsed laser with a line-array pattern (LAP) source was created to generate two narrowband Lamb waves with distinctive frequencies; then, a laser Doppler vibrometer (LDV) was used to measure the corresponding ultrasonic responses. The uniqueness of this study is as follows: (1) A completely non-contact laser ultrasonic system equipped with a Sagnac interferometer was created for the generation of narrowband Lamb waves; additionally, an LDV was used to identify the mixed components.; (2) the proposed system allows two Lamb waves with different frequencies to be made at the same time by using a single pulse laser source; (3) it is possible to implement Lamb wave mode at a specific input frequency by simply altering an optical lens; and (4) unlike the slit mask method, the Sagnac interferometer produces laser LAP sources with sufficient energy (at least 80%) to generate input waves in structures.

3. Introduction

The nonlinear Lamb wave mixing technique has been widely used for nondestructive evaluation because of its advantages of a long propagation distance and high sensitivity to microstructural heterogeneity (e.g., microcrack) [3, 4]. These advantages include a long propagation distance and high sensitivity to microstructural heterogeneity (e.g., microcrack). In a nutshell, the nonlinearity of microcrack can be recognized by applying incident Lamb waves; this characteristic can then be used to detect microcracks. The detectable nonlinear effects are commonly exploited for applications in harmonics [5] and wave mixing [1] techniques, amongst other things. In the case of harmonics technique, the self-mixing of a single Lamb wave generates the harmonic components; alternatively, the wave mixing technique entails cross-mixing between two Lamb waves to generate the mixed components. In the case of the harmonics approach, the harmonic components are generated by the self-mixing of a single Lamb wave; in the case of the wave mixing technique, the mixed components are generated by the cross-mixing of two Lamb waves. Wave mixing has the following advantages over harmonics: I the amplitudes of the mixed components are only averaged within the wave mixing zone, which provides it with higher spatial resolution [6]; (ii) it is less sensitive to nonlinearity introduced by instruments such as transducers and coupling media [7]; and (iii) the transmitter and receiver can remain fixed in place, as microcrack position detection is achieved by scanning the wave mixing zone [8]. As a result of these factors, the nonlinear Lamb wave mixing technique has gained popularity in recent years.

3. Nonlinear ultrasonic Lamb wave mixing

Figure 1. Illustration of non-contact nonlinear ultrasonic wave mixing. (a) Linear structure and (b) nonlinear structure.

When two input waves a and b traveling at distinct frequencies f_a and f_b ($f_b < f_a$), respectively, are applied to a linear (ideal) structure, the structural response contains only the linear components corresponding to the input frequencies, as shown in Figure 1(a). Once the structure behaves nonlinearly (i.e., in the presence of a damage), the structural response undergoes a change that, in addition to the presence of the linear components and their harmonic components (i.e., $2f_a$ and $2f_b$), there is some indication of the presence of mixed components (i.e., $f_a \pm f_b$) (see Figure 1(b)) [7, 9]. Because these mixed components occur only if nonlinear sources exist, it can be considered an indication of the damage [6].

4. Developed laser non-contact Lamb wave mixing

Figure 2 depicts a schematic representation of the newly designed laser ultrasonic system, which is comprised of emission and sensor components. When generating laser LAP sources, the emission unit employs a Sagnac interferometer and laser beam polarization, which are both implemented in the emission unit. A Nd:YAG laser source produces a pulsed laser beam when it is turned on. In the first step, the laser beam is directed toward a quarter wave plate (QWP), which modifies the polarization components (s-polarized and p-polarized) of the incident laser beam. A 50/50 beam splitter divides a laser beam in half, resulting in two beams. A Lamb wave a is generated by the first laser beam and is referred to as Laser beam 1; an excited Lamb wave b is generated by the second laser beam and is referred to as Laser beam 2. The first polarized beam splitter divides laser beam 1 into s-polarized and p-polarized components, resulting in a total of two polarized components (PBS1). Following that, the p- and s-polarized components are transferred to the M2 and M4 amplifiers, respectively. After that, they are recombined using PBS1. PBS1 produces a laser LAP in accordance with the Fresnel-Arago equations, which is formed as a result of a polarization component interaction between two other polarization components [10]. The outputs from PBS1 are coupled to a beam expander (BE1), which generates a narrowband Lamb wave a on the surface of the specimen using the outputs from PBS1. BEs are utilized to change the size of the laser LAP in this instance. The designs of PBS1, M2, M3, and M4 are very similar to those of a Sagnac interferometer setup in terms of functionality. The setup for the Laser beam 2-derived creation of a laser LAP for the excitation of Lamb wave b at PBS2 is the same as it is for the excitation of Lamb wave b at PBS1.

5. Results

The performance of developed laser ultrasonic system is demonstrated experimentally by non-contact damage detection against an aluminum plate with varying damage sizes. The amplitude of mixed components obtained from the experiments is used to quantify the damage of test specimen. The test results indicate that the damaged specimen exhibits a larger amplitude value of mixed components than the intact specimen does.

Figure 2. Optical design of non-contact wave mixing. QWP- Quarter wave plate; BS- Beam splitter; PBS- Polarized beam splitter; M- Mirror; BE- Beam expander.

6. Conclusion

In this study, a fully noncontact laser ultrasonic system was developed for generation and measurement of mixed components in an aluminum plate. With the help of developed laser-based optical Sagnac interferometer system, the location of the damage in an aluminum plate can be successfully detected.

References

[1] D.J. Lee, Y. Cho, W. Li, A feasibility study for Lamb wave mixing nonlinear technique, AIP Conference Proceedings, American Institute of Physics2014, pp. 662-666.

[2] L. Sun, S.S. Kulkarni, J.D. Achenbach, S. Krishnaswamy, Technique to minimize couplant-effect in acoustic nonlinearity measurements, The Journal of the Acoustical Society of America, 120 (2006) 2500-2505.

[3] N. Hosoya, T. Katsumata, I. Kajiwara, T. Onuma, A. Kanda, Measurements of S mode Lamb waves using a high-speed polarization camera to detect damage in transparent materials during non-contact excitation based on a laser-induced plasma shock wave, Optics and Lasers in Engineering, 148 (2022) 106770.

[4] X. Sun, G. Shui, Y. Zhao, W. Liu, N. Hu, M. Deng, Evaluation of early stage local plastic damage induced by bending using quasi-static component of Lamb waves, NDT & E International, 116 (2020) 102332.

[5] K.H. Matlack, J.-Y. Kim, L.J. Jacobs, J. Qu, Review of second harmonic generation measurement techniques for material state determination in metals, Journal of Nondestructive Evaluation, 34 (2015) 273.

[6] M. Sun, Y. Xiang, M. Deng, J. Xu, F.-Z. Xuan, Scanning non-collinear wave mixing for nonlinear ultrasonic detection and localization of plasticity, NDT & E International, 93 (2018) 1-6.

[7] J. Jingpin, M. Xiangji, H. Cunfu, W. Bin, Nonlinear Lamb wave-mixing technique for micro-crack detection in plates, Ndt & E International, 85 (2017) 63-71.

[8] S. Sampath, H. Sohn, Detection and localization of fatigue crack using nonlinear ultrasonic three-wave mixing technique, International Journal of Fatigue, (2021) 106582.

[9] A.J. Croxford, P.D. Wilcox, B.W. Drinkwater, P.B. Nagy, The use of non-collinear mixing for nonlinear ultrasonic detection of plasticity and fatigue, The Journal of the Acoustical Society of America, 126 (2009) EL117-EL122.

[10] M. Mujat, A. Dogariu, E. Wolf, A law of interference of electromagnetic beams of any state of coherence and polarization and the Fresnel–Arago interference laws, JOSA A, 21 (2004) 2414-2417.

CODA WAVE INTERFEROMETRY FOR MONITORING THE FRACTURE PROCESS OF CONCRETE BEAMS UNDER BENDING TEST

M. Knak, E. Wojtczak, and M. Rucka

Department of Mechanics of Materials and Structures, Faculty of Civil and Environmental Engineering, Gdańsk University of Technology, Narutowicza 11/12, 80-233, Gdańsk, Poland;
e-mail: magdalena.knak@pg.edu.pl (M.K.); erwin.wojtczak@pg.edu.pl (E.W.); magdalena.rucka@pg.edu.pl (M.R.)

1. Introduction

Concrete elements such as beams are widely used in engineering structures. For safe use, is important to verify the material condition, detect existing damage and prevent its future growth. An essential aspect to mention is the observation of micro-cracks, which indicate incipient damage. Non-destructive testing (NDT) techniques give the possibility to observe the current state of a structure. Digital image correlation (DIC) is a method gaining popularity among scientists. It allows localizing structural damage (e.g., cracks) by observing the changes of local strains and displacements. DIC is based on the comparison between photographs of a specimen [1-3]. Another promising diagnostics approach is coda wave interferometry (CWI). An increasing number of researchers are using CWI to effectively detect emerging structural damage [3-5]. The technique allows the detection of flaws using the decorrelation between guided wave signals collected at different states of structure. In this work, the implementation of CWI is used for early-stage damage detection. The results of NDT measurements are verified by the DIC technique.

2. Background

The experimental analysis was carried out on concrete beams with dimensions $4 \times 4 \times 16$ cm^3. The specimens were notched in the central part (Figure 1a) to induce the crack formation in the region of interest. During the three-point bending tests (performed by Zwick/Roell Z10 universal testing machine – UTM), the fracture process was characterized using DIC and CWI methods (Figure 1b). The photographs of the samples were taken each 1 s by Aramis Professional system. The ultrasonic signals were registered using the same time interval by five piezoelectric transducers. One of them was actuator (A) while the others (B – D) acted as sensors. The excitation was a wave packet composed of a 5-cycle sine wave modulated by the Hann window. The signals were further processed by CWI. The so-called decorrelation coefficient (DC) was calculated for each signal, with respect to equation (1), in which $s_r(t)$ is the reference signal and $s_n(t)$ is the current signal registered during degradation.

$$(1) \qquad DC^{(s)} = 1 - \frac{\int_{t_1}^{t_2} s_r(t) \cdot s_n(t)\, dt}{\sqrt{\int_{t_1}^{t_2} s_r^2(t)\, dt \cdot \int_{t_1}^{t_2} s_n^2(t)\, dt}}.$$
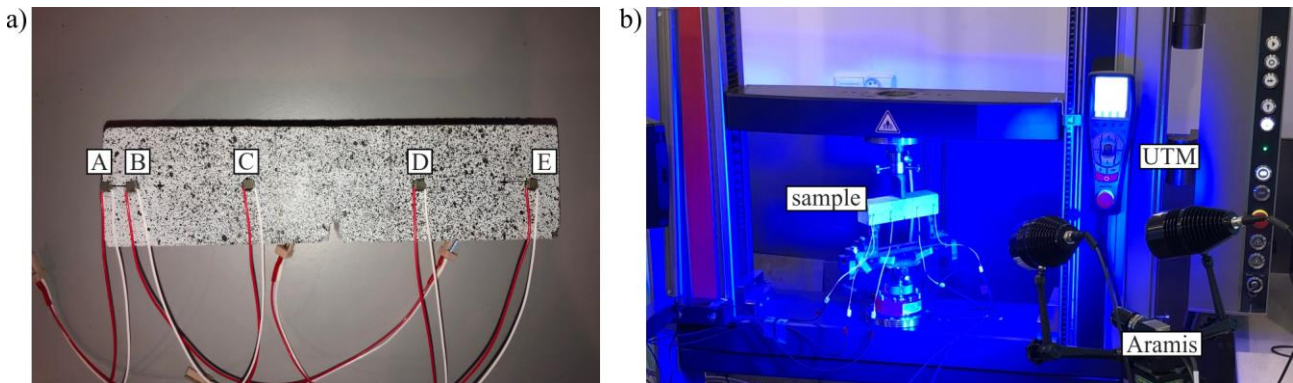
Figure 1: Experimental setup: a) example of specimen and location of transducers, b) specimen under test.

3. Results

The illustrative results are given in Figure 2. The major strain field obtained using DIC at the time of maximum load for $t = 337$ s (Figure 2a, three-sigma rule scaling used) allows localizing the crack initiation zone before the destruction of the specimen. Figure 2b shows the load-time curve (red line marks the time of maximum load). Figure 2c presented the changes of decorrelation for each sensor during the whole bending test. The calculations were performed for the part of signals in the time range of 0.2 – 0.5 ms. It can be seen that DC values are relatively low in the first stage of the test (until 337 s, before peak load) for all sensors. What is important, an increase of decorrelation is visible, even though no damage is observed on the object. This growth is caused by the reconfiguration of concrete grains at the micro-level, leading to changes in scattering characteristics and, in turn, subtle differences in ultrasonic signals. Thanks to them, the damage state could be detected before fracture and the appearance of macro-cracks, causing catastrophic consequences. When the maximum load is reached, a significant jump in DC values occurs, triggered by the formation of macro-cracks, which change the medium geometry. At this stage, the development of fracture can be observed. The results for all sensors are comparable. The leading conclusion of the performed work is that the CWI technique is successful in the early-stage damage detection, despite the location of sensors.
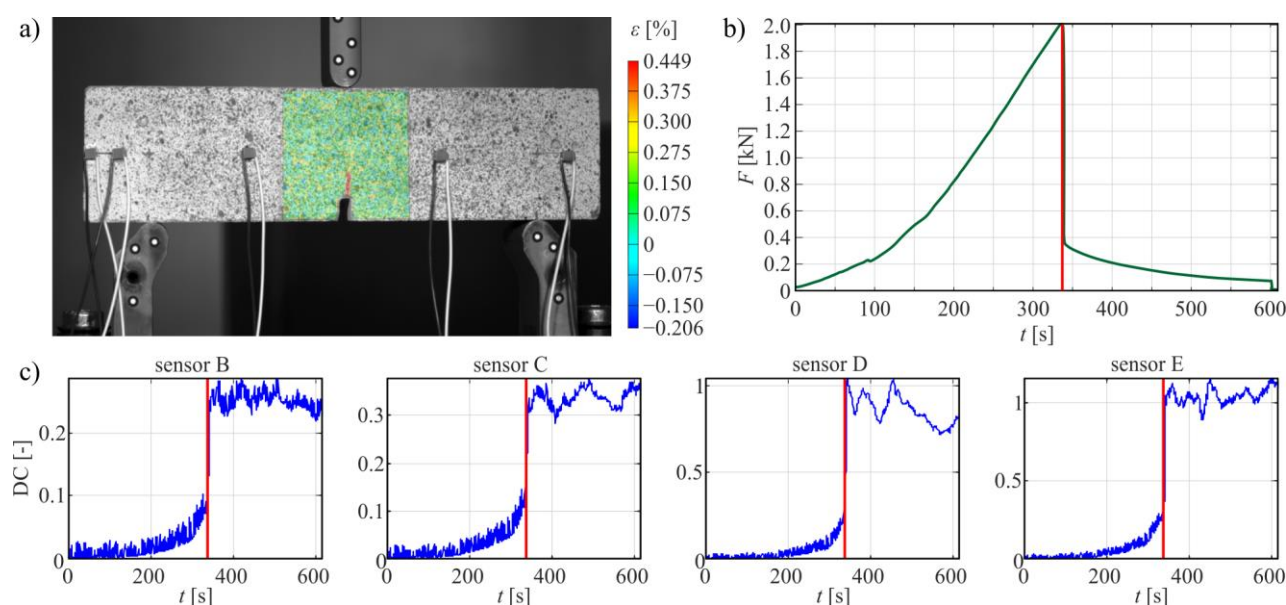
Figure 2: Illustrative results: a) snapshot of major strains from DIC at maximum load, b) load vs. time chart, b) CWI for sensors B – E.

References

[1] M. Rucka, E. Wojtczak, M. Knak, and M. Kurpińska. Characterization of fracture process in polyolefin fibre-reinforced concrete using ultrasonic waves and digital image correlation. *Construct. Build. Mater.*, 280:122522, 2021. https://doi.org/10.1016/j.conbuildmat.2021.122522.

[2] B. Gencturk, K. Hossain, A. Kapadia, E. Labib, and Y. L. Mo. Use of digital image correlation technique in full-scale testing of prestressed concrete structures. *Meas. J. Int. Meas. Confed.*, 47:505–515, 2014. https://doi.org/10.1016/j.measurement.2013.09.018.

[3] E. Wojtczak, M. Rucka, and Ł. Skarżyński. Monitoring the fracture process of concrete during splitting using integrated ultrasonic coda wave interferometry, digital image correlation and X-ray micro-computed tomography. *NDT E Int.*, 126:102591, 2022. https://doi.org/10.1016/j.ndteint.2021.102591

[4] Q. Zhu, K. Yu, H. Li, H. Zhang, Y. Ding, D. Tu. A loading assisted diffuse wave inspection of delamination in a unidirectional composite. *Appl Acoust*, 177:107868, 2021. https://doi.org/10.1016/j.apacoust.2020.107868.

[5] D. P. Schurr, J. Y. Kim, K. G. Sabra, L. J. Jacobs. Monitoring damage in concrete using diffuse ultrasonic coda wave interferometry. *AIP Conf. Proc*, 1335:1283–1290, 2011. https://doi.org/10.1063/1.3592081.

Low velocity impact identification and damage assessment of composite structures based on embedded PZT sensors

M. Dziendzikowski[1], K. Kowalczyk[1], P. Niedbała[1], A. Kurnyta[1],

J. Biczyk[2], K. Sekuła[2], K. Kaźmierczak[2], P. Kolakowski[2],

[1]*Instytut Techniczny Wojsk Lotniczych, ul. Ks. Boleslawa 6, Warszawa, Polska*
[2]*Adaptronica Sp. z o.o., ul. Szpitalna 32, Lomianki, Polska*

e-mail[1]*: michal.dziendzikowski@itwl.pl, e-mail*[2]*: janek.biczyk@adaptronica.pl*

1. General

One of the major issues which could increase safety of aircraft operation is automated early detection of different damage modes of composite structures [1, 2]. The following damage types can affect the performance and durability of composite structures: debonding, delamination, foreign object inclusion and porosity [3]. Composites are vulnerable to impacts, even of low energies, which can introduce in the structure the so called Barely Visible Impact Damage (BVID) [4]. BVID can decrease the stiffness and durability of a composite due to multiple delaminations and transverse cracks of its layers (Fig. 1) [5, 6]. The most commonly used non-destructive technique for BVID detection is ultrasonic testing. This method allows for precise damage localization and sizing [7], however its use is possible only during the ground aircraft maintenance.
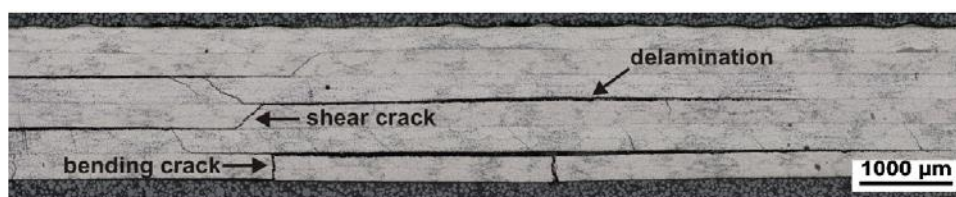
Figure 1: An example of BVID of composite structure [6]

2. Structural Health Monitoring based on guided waves

Conventional non-destructive testing techniques are nowadays supposed to be complemented by systems of structure integrated sensors continuously monitoring its health, i.e. Structural Health Monitoring systems. Application of such technology would definitely increase the safety, especially when considering hardly accessible 'hotspots', but also it could save up to 50% of necessary inspections time depending on the aircraft type [8]. One of the ideas for structural health monitoring systems built is based on the measuring of the mechanical properties of materials used for aircraft structural elements. The approach is based on analysis of small displacements propagation excited in the element by a network of PZT piezoelectric actuators [9, 10]. Solution for small deformation dynamics of the medium strongly depends on the boundary conditions, in particular the geometry of the object and its distortions caused by discontinuities and deformations. Structural damages can thus result in observable changes of the signal generated by the network sensors. The state of a monitored structure is assessed based on chosen signal characteristics called the Damage Indices (DIs). The acquired signals can be also influenced by factors other than damages thus posing a risk of false indications. Therefore DI's used for the structure assessment needs to be balanced between sensitivity to damages and stability under varying working conditions of transducers.

3. Experiment description

In the paper efficiency of PZT sensors for impact event detection and BVID damage assessment in compact structures is investigated. The performance of a SHM system based on PZT network is rooted in two distinct

areas of the technology development, that is: the hardware and the signal analysis. The first include the type of transducers used to build a network and the way of their integration with a monitored structure. For efficiency comparison the following parameters were considered:

- type of PZT sensors;
- parameters of the excited elastic waves (frequency, duration);
- sensors integration technology with a host structure.

Three different types of sensors integration with the structure were developed:

- adhesive joint of sensor and the structure;
- sensor embedding in the internal structure of the composite;
- sensor embedding in additional "technological" layer near composite surface.

Sensor networks were placed in composite specimen in the same hot-spots and maintaining the same geometry of the network, therefore efficiency of different type of sensors integration with host structure can be directly compared.
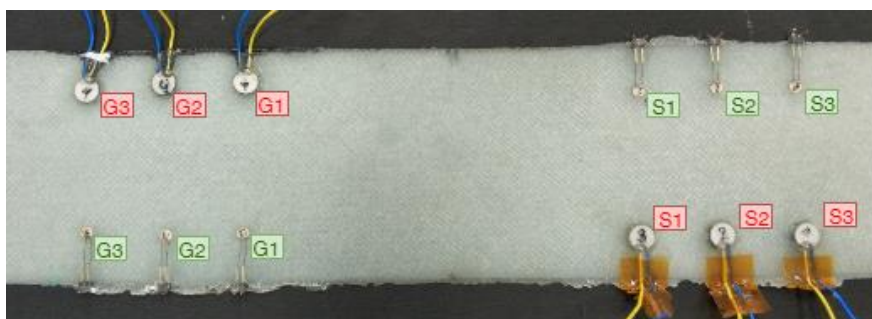
Figure 2: Example of a specimen with surface attached and structure embedded sensors

Detailed description of sensors integration technologies used, as well as its impact on the performance of PZT sensors in passive and active monitoring methods of composite structures will be delivered in the paper.

References

[1] M. Sohn, X. Hu, J. Kim, L. Walker, Impact damage characterisation of carbon fibre/epoxy composites with multilayer reinforcement, *Composites Part B: Engineering 31(8)*: 681-691, 2000.

[2] S.-X. Wang, L.-Z. Wu, L. Ma, Low-velocity impact and residual tensile strength analysis to carbon fiber composite laminates, *Materials &Design 31(1)*: 118-125, 2010.

[3] R. Adams, P. Cawley, A review of defect types and nondestructive testing techniques for composites and bonded joints, *NDT international 21(4)*: 208-222, 1988.

[4] C. Poon, T. Benak, R. Gould, Assessment of impact damage in toughened resin composites, *Theoretical and Applied Fracture Mechanics 13(2)*: 81-97, 1990.

[5] C. Li, N. Hu, Y. Yin, H. Sekine, H. Fukunaga, Low-velocity impact induced damage of continuous fiber-reinforced composite laminates. Part I. An FEM numerical model, *Composites Part A: Applied science and manufacturing 33(8)*: 1055-1062, 2002.

[6] J. Bienias, P. Jakubczak, B. Surowska, K. Dragan, Low-energy impact behaviour and damage characterization of carbon fibre reinforced polymer and aluminium hybrid laminates, *Archives of Civil and Mechanical Engineering 15(4)*: 925-932, 2015.

[7] R. Smith, L. Jones, B. Zeqiri, M. Hodnett, Ultrasonic C-scan standardisation for fibre-reinforced polymer composites: minimising the uncertainties in attenuation measurements, Insight 40(1): 34-43, 1998.

[8] W. J. Staszewski, C. Boller, G.R. Tomlinson, Health Monitoring of Aerospace Structures, John Wiley&Sons Ltd, 2004.

[9] V. Giurgiutiu, Structural health monitoring with piezoelectric wafer active sensors, Academic Press, 2007.

[10] Z. Su, L. Ye., Identification of damage using lamb waves: from fundamentals to applications, Springer, 2009.

IDENTIFICATION OF VEHICLE FREQUENCY RESPONSE FUNCTION BASED ON TIKHONOV REGULARIZATION METHOD

Xinhao An[1], Jilin Hou[1], Qingxia Zhang[2], and Łukasz Jankowski[3]

[1]School of Civil Engineering, Dalian University of Technology, 116023 Dalian, China y
[2]School of Civil Engineering, Dalian Minzu University, 116600 Dalian, China
[3]Institute of Fundamental Technological Research, Polish Academy of Sciences, 02-106 Warsaw, Poland

houjilin@dlut.edu.cn

Abstract

The vehicle frequency response function reflects the relationship between the vehicle response and different road surface excitations, and it has a very important practical significance.

Frequency domain response can be applied to identify structural parameters [1,2] and structural damage [3-5]. In addition, it can also be used to identify vehicle or road conditions. Zhao et al. [6,7] identified the vehicle parameters of a four-degree-of-freedom (DOF) half-car model. Zhang et al. [8] used the vehicle frequency response function to identify road roughness.

However, during experimental tests with real vehicles, many singularities may appear in the frequency response function, which turn out to be numerical artefacts that do not conform to the actual situation. Therefore, a method based on Tikhonov regularization is proposed to obtain a reliable frequency response function of the vehicle. The method can remove the singularities to make the results more accurate.

Firstly, according to the displacement of the vehicle and the road contact point, the vehicle frequency response function is derived to establish the relationship between the frequency response function, the vehicle response and the road profile in the frequency domain. Then, the vehicle frequency response is directly estimated by using the vehicle response when driving over road bumps of a known size. Finally, Tikhonov regularization method is employed to remove the singular data directly calculated for the vehicle frequency response and to update the estimated vehicle frequency response.

Keywords: frequency response function, Tikhonov regularization, vehicle response.

References

[1] J. Guo, L. Wang and I. Takewaki. Frequency response-based damage identification in frames by minimum constitutive relation error and sparse regularization. *J. Sound Vib.*, 443:270, 2019.
[2] A. Esfandiari, M.S. Nabiyan and F.R. Rofooei. Structural damage detection using principal component analysis of frequency response function data. *Structural Control and Health Monitoring*, 27:1, 2020.
[3] U. Lee and J. Shin. A frequency response function-based structural damage identification method. *Comput. Struct.*, 80:117, 2002.
[4] S.M. Seyedpoor and N. Pahnabi. Structural Damage Identification Using Frequency Domain Responses and a Differential Evolution Algorithm. *Iranian Journal of Science and Technology, Transactions of Civil Engineering*, 45:1253, 2021.
[5] S. Wang and X. Long. Damage Identification for Underground Structure Based on Frequency Response Function. *Sensors-Basel*, 18:3033, 2018.
[6] B. Zhao and T. Nagayama. IRI Estimation by the Frequency Domain Analysis of Vehicle Dynamic Responses and Its Large-scale Application. *Adjunct Proceedings of The 13th International Conference on Mobile and Ubiquitous Systems: Computing Networking and Services (Mobiquitous 2016)*, 41, 2016.
[7] B. Zhao and T. Nagayama. Vehicle Model Calibration in the Frequency Domain and its Application to Large-Scale IRI Estimation. *Journal of Disaster Research*, 12:446, 2017.
[8] Q. Zhang and J. Hou. Road Roughness Estimation Based on the Vehicle Frequency Response Function. *Actuators*, 10:89, 2021.

COMPARISON OF MODE MATCHING AND BAYESIAN APPROACH FOR PARAMETRIC IDENTIFICATION OF FRAMES WITH BOLTED CONNECTIONS

M. Ostrowski, B. Blachowski, G. Mikulowski, Ł. Jankowski

Institute of Fundamental Technological Research, Polish Academy of Sciences, Warsaw, Poland
e-mail: mostr@ippt.pan.pl

Nowadays engineering studies require the use of the sophisticated finite element (FE) models consisting of hundreds if not thousands of degrees of freedom. However, using only such models does not allow for accurate reproduction of physical properties of real structures. To overcome this problem usually model updating (MU) techniques are employed.

MU usually has one of two goals:
1) modification of some parameters of the model in order to minimize error between output of the FE model and experimental data obtained from the real system, and
2) identification of some properties of the real system using both experimental data and updated FE model.

The former case relates to finding the model for performing simulations of the behaviour of the real system. In the later case MU can be applied in damage assessment process. Due to modelling uncertainties minimization of the error between measured and model output does not always provides the most accurate parametric identification.

In this research unknown parameters describing rotational stiffness of bolted connections in a frame structure are estimated. Effectiveness of the two competitive model updating methods are compared. The first is based on modal sensitivities and minimizes error between numerical and experimental modal data. It requires matching of the numerical modes with the experimental ones, hence it is often called mode matching. The second is based on probabilistic Bayesian framework. In this approach maximum a posteriori (MAP) estimate of the unknown parameters is searched. It provides an augmented optimization allowing for model updating without mode matching. Moreover, this method is intended for parametric identification and explicitly includes the modelling errors into the problem formulation. In this study vibration modes are obtained from laboratory-scale frame with uncertain bolted connections. It is shown that assembly imperfections have significant influence on the mode shapes of the frame. The results also show that the two methods for model updating provide significantly different values of the identified stiffness parameters for the investigated bolted connections.

Session S6

Optimization and optimal control approach in structural mechanics

Organizers:
Dominik Pisarski (*IPPT PAN, Poland*)
Andrzej Myśliński (*Systems Research Institute, Poland*)

PERFORMANCE IMPROVEMENTS IN AN IN-WHEEL MOTOR SYSTEM INCORPORATING INERTERS

N. J. Wills[1], *Y-Y. Li*[1], *J. Z. Jiang*[1], *T. L. Hill*[1], *S. A. Neild*[1], and *M. Dhaens*[2]

[1]*Department of Mechanical Engineering, University of Bristol, Bristol, UK*
[2]*Tenneco, Sint-Truiden, Belgium*

e-mail: z.jiang@bristol.ac.uk, yiyuan.li@bristol.ac.uk, mdhaens@tenneco.com

1. Introduction

This study explores a fully passive vibration absorbing method, whereby an optimal inerter-based absorber network configuration is incorporated into the traditional damping system of an in-wheel motor (IWM). This method is applied to the suspension strut and the bushes. The structure-immittance approach is used to identify optimal network topologies [7]. This study addresses some of the issues inherent to the IWM system (worsened ride comfort and handling due to an increase in unsprung mass) using passive inerter-based absorbers.

An important factor when considering the IWM is the magnetic gap deformation (MGD), and is defined as the deflection between the motor rotor and stator. This deflection leads to an unbalanced radial magnetic force, (URMF). This is a destructive input to the system in addition to the existing road input [6]. Restricting MGD is essential to reduce this URMF, and permits a simplified model where the URMF is neglected (as in [5]). Therefore, MGD is constrained to be no worse than the default system in this study.

2. Assumptions and Methods

The IWM model studied here represents the suspension strut as generic network $H(s)$ in parallel with a static stiffness k_2, and the bushes as $G(s)$ and $Y(s)$ (with static stiffnesses k_{31} and k_{32}). The default properties and physical system parameters are obtained from [1]. The static stiffnesses are not optimised in this procedure. This is because the static stiffness determines the performance characteristics of the system, and hence must be kept constant in order for the optimised results to be compared to the default.

In this study, body vertical acceleration J_1 and tyre dynamic load J_3 are used as objective functions (and are metrics for ride comfort and handling respectively). These are described in [4], and shown as follows:

$$J_1 = 2\pi (V\kappa)^{\frac{1}{2}} \left\| sT_{\hat{x}_0 \to \hat{x}_2} \right\|_2 \tag{1}$$

$$J_3 = 2\pi (V\kappa)^{\frac{1}{2}} \left\| \frac{1}{s} T_{\hat{x}_0 \to k_1(\hat{x}_1 - \hat{x}_0)} \right\|_2 \tag{2}$$

the displacement of the masses from the equilibrium position is denoted by x. The subscripts 0, 1, 2, 31, 32 and 33 refer to the road, unsprung mass, sprung mass, hub and brake caliper, stator, and rotor and rim masses respectively. Here, V is vehicle velocity, κ is the road surface roughness, and k_1 is the tyre stiffness. An equivalent performance metric for MGD can also be derived using the same method.

Road velocity profiles are often assumed to be a white noise input [3], with the power spectral density of the road surface described using the work of [2]. Hence the road surface input is assumed to be a white noise here.

Benchmark performance values are obtained for J_1, J_3 and MGD, and used as constraints in the optimisations:

$$J_1 = 1.4915 \text{m/s}^2, \qquad J_3 = 953.87 \text{N}, \qquad J_m = 7.4361 \mu\text{m} \tag{3}$$

Optimisation of the system is undertaken in the frequency domain, and using MATLAB. The first step of the optimisation uses the 'particleswarm' optimisation method, with the initial conditions logarithmically spaced
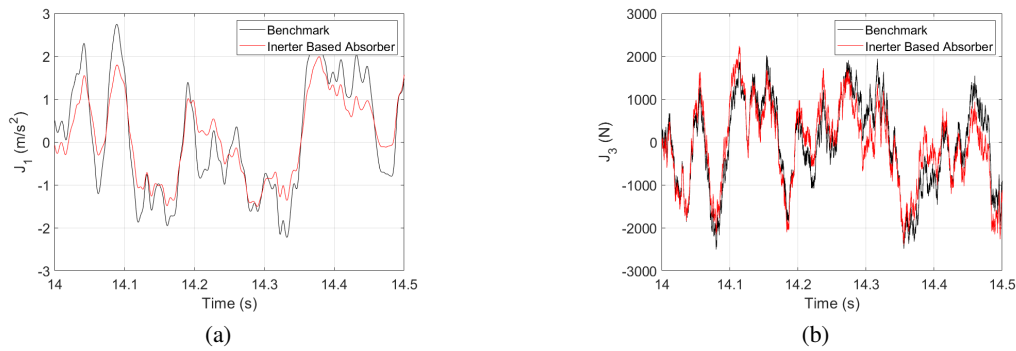
Figure 1: Time domain plots with all networks optimised together for a white noise input for (a) J_1 and (b) J_3.

through the boundaries provided, and the static stiffnesses fixed to default. These solutions are passed to 'patternsearch', then 'fminsearch', with the solution getting finer and closer to a global minimum with each step.

3. Results

Minimal improvement is possible when the strut alone is optimised for J_1 and J_3 (4.26% and 1.28% respectively), this is because the constraints on the value for MGD kept being breached. Hence, in order to further improve the performance of J_1 and J_3, the bushes would need to be included in this optimisation.

Where the strut and both bushes are optimised for J_1 and J_3, the respective improvements over the default are 21.3% and 8.66%. These improvements can be seen in the time domain plots in Figure 1. Therefore, the key finding from this study is that both ride comfort and handling can be improved in an in-wheel motor system using inerters without compromising MGD. Moreover, the ride comfort improvement is the most significant.

4. Conclusions

In their most optimal cases, J_1 and J_3 are improved by 21.3% and 8.66% respectively. These improvements show that the inclusion of inerter-based absorbers is worthwhile in an IWM. They help to mitigate the negative effects that the IWM can have on the vehicle dynamic performance due to the increase in unsprung mass.

References

[1] Yutao Luo and Di Tan. Study on the dynamics of the in-wheel motor system. *IEEE Transactions on Vehicular Technology*, 61:3510–3518, 2012.

[2] J. D. Robson. Road surface description and vehicle response. *International Journal of Vehicle Design*, 1(1):25–35, 1979.

[3] Werner Schiehlen. White noise excitation of road vehicle structures. *Sadhana*, 37(4):487–503, 2006.

[4] Malcolm C. Smith and Fu-Cheng Wang. Performance benefits in passive vehicle suspensions employing inerters. *Vehicle System Dynamics*, 42:235–257, 2004.

[5] Qiang Wang, Rui Li, Youfeng Zhu, Xianbin Du, and Zongfeng Liu. Integration design and parameter optimization for a novel in-wheel motor with dynamic vibration absorbers. *Journal of the Brazilian Society of Mechanical Sciences and Engineering*, 42:459, 2020.

[6] Yanyang Wang, Pingfei Li, and Guizhou Ren. Electric vehicles with in-wheel switched reluctance motors: Coupling effects between road excitation and the unbalanced radial force. *Journal of Sound and Vibration*, 372:69–81, 2016.

[7] S. Y. Zhang, J. Z. Jiang, and S. A. Neild. Passive vibration control: a structure–immittance approach. *Proceedings of the Royal Society A*, 473(2201):20170011, 2017.

CUBIC FREQUENCY FORMAT FOR VISCOUS DAMPER
ON A FLEXIBLE STRUCTURE

Steen Krenk

Mechanical Engineering, Technical University of Denmark, Kongens Lyngby, Denmark

e-mail: sk@mek.dtu.dk

1. General

Many studies have been carried out over the last two decades on local damping by a root-locus analysis of the combined system of either non-resonant form [1] form, exemplified by a local damper, or of resonant form [2], corresponding to a tuned mass or inerter device. The resonant devices add an extra degree of freedom to the system, and the analysis is conveniently based on the corresponding complex quartic characteristic equation. Most contributions dealing with the local non-resonant damper have included a linearization, whereby the idealized characteristic equation of the resonant mode is reduced to quadratic form. This permits a very simple analytical formulation yielding a 'universal curve' for the resulting damping as function of a suitably normalized damping parameter. The present paper skips the linearization and retains at a cubic characteristic equation with several remarkable properties, similar to those of the resonant systems, e.g. a root-locus curve built up from points and their inverse points in a circle centered at the origin. With suitable normalization of the damping parameter inverse points, having equal damping ratio, correspond to reciprocal values of the damping parameter, and much of the simplicity of the quadratic approximation is retained, while extending the accuracy of the results to damping ratios up to critical damping.

2. The cubic root-locus format

The theory is concerned with resonant frequency response of a discrete linear system, governed by the equation of motion

$$(1) \qquad \left[\mathbf{K} - \omega^2 \mathbf{M}\right] \mathbf{u} + \mathbf{f}_{\mathrm{d}} = \mathbf{f}_{\mathrm{e}},$$

where $\mathbf{K}$, $\mathbf{M}$ and $\mathbf{f}_{\mathrm{e}}$ are the stiffness matrix, mass matrix and the external load, respectively. $\mathbf{u}$ is the displacement vector, and $\mathbf{f}_{\mathrm{d}}$ is the device force defined in terms of the connectivity vector $\mathbf{w}$ as

$$(2) \qquad \mathbf{f}_{\mathrm{d}} = \mathbf{w} f_{\mathrm{d}}, \qquad u = \mathbf{w}^T \mathbf{u},$$

with $\mathbf{w} = [0, \cdots, 1, \cdots, 0]^T$ for single-point fixture of the device and $\mathbf{w} = [0, \cdots, 1, -1, \cdots, 0]^T$ for relative motion of two points. The device is assumed to be linear, $f_{\mathrm{d}} = H_{\mathrm{d}}(\omega) u$ with the device frequency function $H_{\mathrm{d}}(\omega)$.

The displacement across the terminals of the device is given both by the structural response and by the device characteristic, and equating these provides the characteristic equation of the combined system. In this equation the non-resonant terms are eliminated by assuming that they can be approximated by their value at the frequency $\tilde{\omega}_r$ corresponding to resonance with the device locked. This corresponds to representing the contributions from all the non-resonant terms by a constant, determined by the locking frequency $\tilde{\omega}_r$, leading to the ampproximate characteristic equation

$$(3) \qquad \left(\omega^2 - \omega_r^2\right) = \frac{\omega_r^2}{\tilde{\omega}_r^2 - \omega_r^2} \frac{H_{\mathrm{d}}(\omega)}{k_r} \left(\tilde{\omega}_r^2 - \omega^2\right)$$

For a linear viscous damper $H_{\mathrm{d}}(\omega) = i\omega c_{\mathrm{d}}$ this equation is cubic.

The root-locus format (3) is conveniently described in terms of the geometric mean frequency ω_0 and a non-
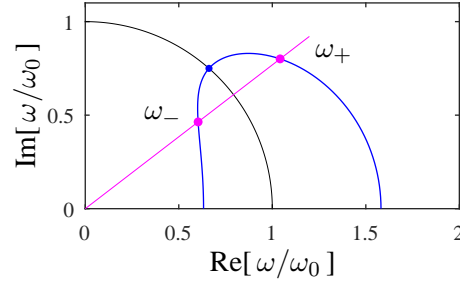
Figure 1: Normalized root-locus curve with inverse points ω_- and ω_+ for $\tilde{\omega}_r/\omega_r = 2.5$.

dimensional damping parameter η_0,

$$(4) \qquad \omega_0^2 = \omega_r \tilde{\omega}_r \,, \qquad \eta_0 = \frac{\omega_0^3}{\tilde{\omega}_r^2 - \omega_r^2} \frac{c_{\mathrm{d}}}{k_r} \,.$$

In terms of these parameters the root-locus curve consists of inverse points with magnitudes $\omega_+\omega_- = \omega_0^2$ as shown in Fig. 1, corresponding to $\eta_0^+ = 1/\eta_0^-$. It follows that the maximum damping ratio is attained for $\eta_0 = 1$,

$$(5) \qquad \zeta_{\mathrm{max}} = \frac{1}{2}\left(\frac{\tilde{\omega}_r}{\omega_r} - 1\right) = \frac{\tilde{\omega}_r - \omega_r}{2\omega_r} \,.$$

The root-locus curve reaches bifurcation at the imaginary axis for $\tilde{\omega}_r > 3\omega_r$.

3. Example

The importance of using the cubic frequency format (3) increases with increasing relative frequency difference $(\tilde{\omega}_r - \omega_r)/\omega_r$ as suggested by Fig. 1. The effect of the cubic format is illustrated in Fig. 2, showing the root-locus curves and the damping ratio as function of the non-dimensional parameter η_0. The figure shows the results for the lowest six modes of a system consisting of a simply supported beam with viscous rotation springs at the ends. This system has been studied in [3] in connection with earthquake response and in [4] in connection with complex modes. The cubic format (curves) captures the full solution (crosses) well, even for the fairly large damping ratio $\zeta_{\mathrm{max}} = 0.65$ of the lowest mode.
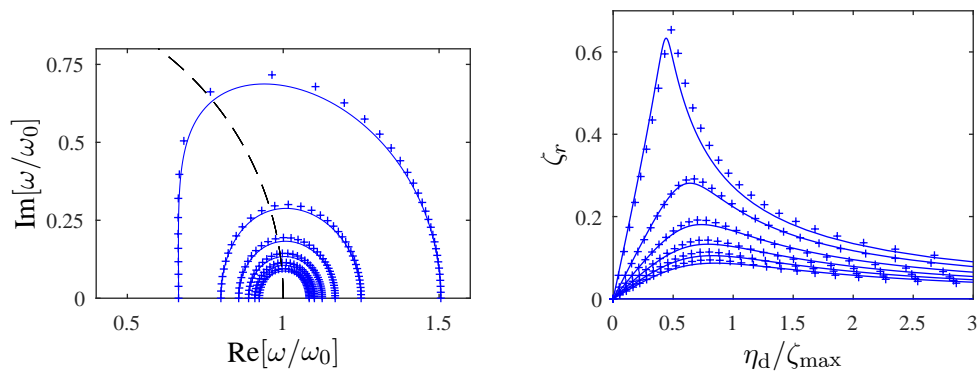
Figure 2: a) Normalized root locus diagram, and b) damping ratio of first six modes.

References

[1] J. A. Main and S. Krenk. Efficiency and tuning of viscous dampers on discrete systems, *Journal of Sound and Vibration*, 286:97, 2005.

[2] S. Krenk. Frequency analysis of the tuned mass damper, *Journal of Applied Mechanics*, 72:936, 2005.

[3] G. Oliveto, A. Santini and E. Tripodi. Complex modal analysis of a flexural vibrating beam with viscous end conditions, *Journal of Sound and Vibration*, 200:327, 1997.

[4] S. Krenk. Complex modes and frequencies in damped structural vibrations, *Journal of Sound and Vibration*, 270:981, 2004.

MRD Based Semi-active Robust H$_\infty$ Control of Civil Structures with Parametric Uncertainties

Vedat SENOL[1], Gürsoy TURAN[1], Anders HELMERSSON[2], and Vortechz ANDERSSON[3]

[1]*Izmir Institute of Technology, Urla, Izmir, Turkey*
[2]*Linköping University, Linkoping, Sweden*
[3]*Vortechz Research, Norrkoping, Sweden*

e-mail: vedatsenol@iyte.edu.tr

1. Abstract

In developing a mathematical model of a real structure, the model's simulation results may not match the real structural response. This issue is a general problem that arises during the dynamic motion of the structure, which may be modeled using parameter variations in the stiffness, damping, and mass matrices. These changes in parameters need to be estimated, and the mathematical model to be updated to obtain higher control performances and robustness. In this study, a linear fractional transformation (LFT) is utilized for uncertainty modeling. Further, a general approach to the design of a H_∞ control of a magneto-rheological damper (MRD) for vibration reduction in a building with mass, damping, and stiffness uncertainties is presented.

2. General

As it is known today, structures are exposed to static loads and horizontal seismic loads, such as earthquakes and strong winds. These loads can disturb the civil structures and cause vibrations. Since [1] first proposed the *concept of structural control* for civil engineering, many studies have been done on structural vibration attenuation.

The civil structures can be modeled as second-order systems. However, this approach does not fully represent physical systems and their behaviors. Hence, uncertainties should be considered in modeling so that the simulation behaviors get close to physical ones. For that reason, [2] inquired about the robust control approach with uncertainties in system matrices and control input matrices. Moreover, [3] designed a robust controller based on the state-feedback control with a modified Kalman filter. Nevertheless, the parametric uncertainties were implemented as an increment of state-space representation matrices. Thus, uncertainties cannot be recognized whether those are in mass, damping, or stiffness matrices. [4] modeled these uncertainties as distinguishable with reasonable percentages. Thanks to the LFT work of [5], upper linear fractional transformation (LFT) can be applied to civil structures uncertainties.

3. Main Contrubitions

In this study, the magneto-rheological damper (MRD) device will be implemented to stabilize the civil structure given below.
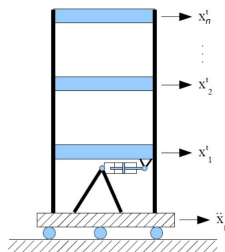
Figure 1: Shear building model having MRD with n floors

Different from the previous works, while designing the robust controller, we take into account parametric uncertainties in mass, stiffness, and damping matrices, as depicted in Figure 2.
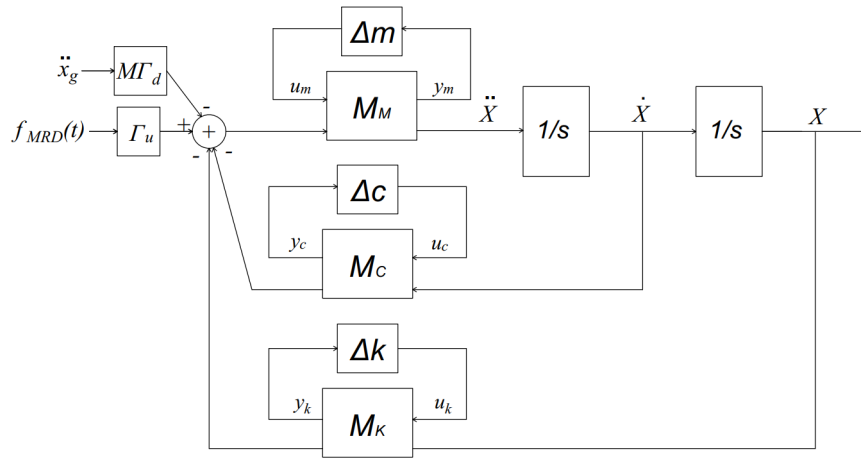
Figure 2: Block diagram of the control system with uncertainties.

In the discussion part, the performance of the designed controller and the nominal controller will be compared.

References

[1] J. Yao, "Concept of structural control," *Journal of the Structural Division*, vol. 98, no. st 7, 1972.

[2] I. N. Kar, T. Miyakura, and K. Seto, "Bending and torsional vibration control of a flexible plate structure using h_∞-based robust control law," *IEEE Transactions on Control Systems Technology*, vol. 8, no. 3, pp. 545–553, May 2000.

[3] S.-G. Wang, "Robust active control for uncertain structural systems with acceleration sensors," *Journal of Structural Control*, vol. 10, no. 1, pp. 59–76, 2003.

[4] L. Huo, C. Qu, and H. Li, "Robust control of civil structures with parametric uncertainties through d-k iteration," *The Structural Design of Tall and Special Buildings*, vol. 25, no. 3, pp. 158–176, 2016.

[5] K. Zhou and J. C. Doyle, *Essentials of robust control.*   Prentice hall Upper Saddle River, NJ, 1998, vol. 104.

NON-RECIPROCAL VIBRATION TRANSMISSION THROUGH ABSOLUTE POSITION AND VELOCITY FEEDBACK

N. Alujević[1], M. Jalšić[2], Srećko Arandia-Krešić[1], and I. Ćatipović[1]

[1]*Faculty of Mechanical Engineering and Naval Architecture, University of Zagreb, Ivana Lučića 5, Zagreb, Croatia*
[2]*INETEC, Dolenica ul. 28, Lučko, Croatia*

e-mail: nalujevic@fsb.hr

In this study, the effect of reciprocity loss in vibration transmission of active structures is studied. This effect can be achieved by using a non-collocated absolute velocity feedback to drive a reactive force actuator. The theoretical background for this approach has been given in a recent short communication, [1], and is briefly discussed next. Active structure S equipped with a direct velocity feedback loop is shown in Figure 1. It is assumed that the structure is linear elastic. Velocity sensor is placed at point 2 of the structure and its output is fed back via a negative gain $-g$ to the control actuator reacting between points 2 and 1.
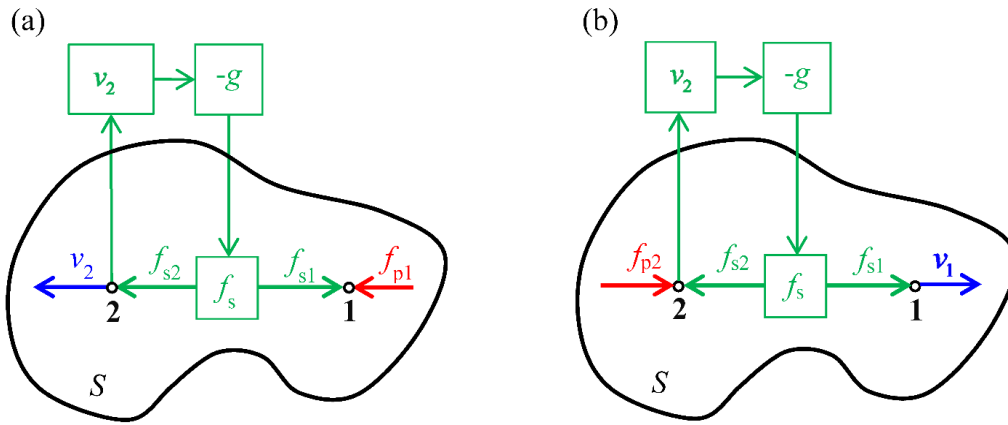
Figure 1: An active liner elastic structure (a) excited from point 1 and responding at point 2. (b) excited from point 2 and responding at point 1.

Provided that the feedback loop is stable, velocity response v_2 at point 2, due to the primary forcing f_{p1} at point 1, can be calculated as the sum of contributions from the primary force and the secondary (control) forces f_{s1} and f_{s2}:

$$(1) \qquad v_2 = Y_{2,1} f_{p1} + Y_{2,2} f_{s2} + Y_{2,1} f_{s1} \,.$$

$Y_{2,1}$ is the transfer mobility of the passive system between points 2 and 1, and $Y_{2,2}$ is the driving point mobility of the passive structure at point 2. The secondary forces f_{s1} and f_{s2} generated by the control actuator are given by the control law:

$$(2) \qquad f_{s2} = -g v_2 \,,$$

$$(3) \qquad f_{s1} = g v_2 \,.$$

Substituting (2) and (3) into (1) and isolating for v_2, yields the transfer mobility function of the active structure S between the force f_{p1} and the velocity v_2:

$$(4) \qquad Q_{2,1} = \frac{Y_{2,1}}{1 + g\left(Y_{2,2} - Y_{2,1}\right)} \,.$$

Considering now the situation shown in Figure 1b, where the structure S is excited by the primary force f_{p2} at point 2, and assuming again a stable controller, velocity v_2 can be calculated using (2) and (3) as:

(5) $$v_2 = Y_{2,2} f_{p2} - Y_{2,2} g v_2 + Y_{2,1} g v_2 ,$$

whereas velocity v_1 is given by:

(6) $$v_1 = Y_{1,2} f_{p2} + Y_{1,1} g v_2 - Y_{1,2} g v_2 .$$

$Y_{1,2}$ is the transfer mobility of the passive structure S between points 1 and 2, and $Y_{1,1}$ is the driving point mobility of the passive structure S at point 1.

Eliminating v_2 from equations (5) and (6) yields the transfer mobility function of the active structure between the force f_{p2} and the velocity v_1:

(7) $$Q_{1,2} = \frac{g\left(Y_{1,1} Y_{2,2} - Y_{2,1}^2\right) + Y_{2,1}}{1 + g\left(Y_{2,2} - Y_{2,1}\right)} .$$

As can be seen by comparing equations (4) and (7), $Q_{1,2} \neq Q_{2,1}$ unless $g=0$, thus the reciprocity principle does not hold if the system is made active. The above formulation is valid if the active system is stable.

However, this approach results in an amplitude difference between transfer mobility pairs describing vibration transmission in two opposite directions to increase with frequency. At low frequencies, the effect is rather small and drops to zero in the static case. In an attempt to increase the effect at low frequencies, absolute position and velocity of the structure at one of the two force actuator footprints are combined into the error signal. Relations between the proportional and integral feedback gains which are necessary to keep the system stable are determined. It is then shown that the reciprocity loss can now be induced also at low frequencies. Finally, it is shown that the two spectra after control are rather similar in shape but different in their amplitudes. Therefore the structure blocks vibration transmission in one direction and enhances it in the opposite one in broad frequency bands. The theoretical findings are verified on an experimental test rig and a very good agreement is found. The 3D-printed experimental setup is shown in Figure 2.
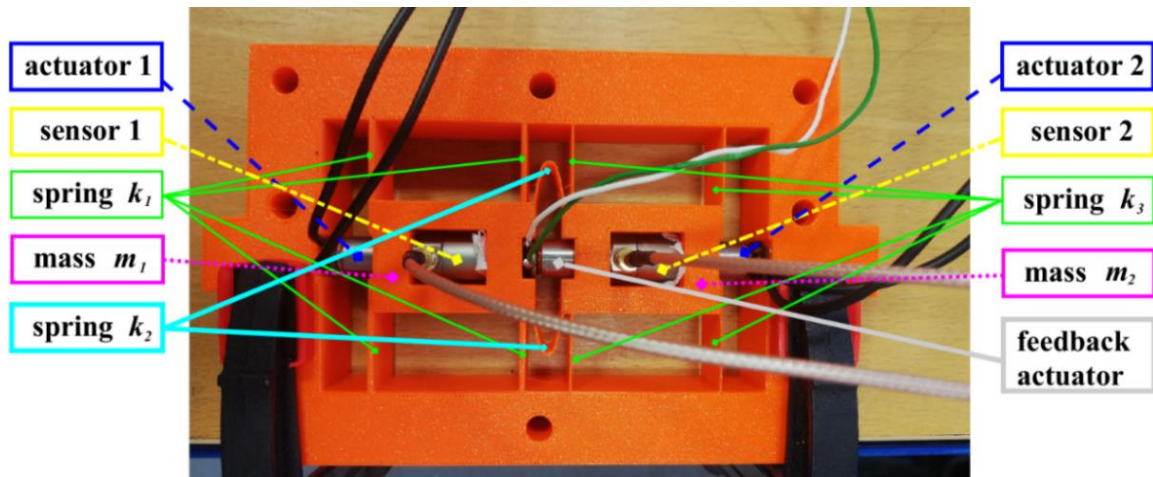
Figure 2: Active flexible structure for non-reciprocal vibration transmission

References

[1] N. Alujević, I. Senjanović, I. Ćatipović, and N. Vladimir. The absence of reciprocity in active structures using direct velocity feedback. *J. Sou. Vib.,* 438, 251–256, 2018.

Towards an automated physics-regularized model updating strategy applied to the monitoring of civil engineering structures in low-frequency dynamics

M. Diaz[1], P.-É. Charbonnel[2], and L. Chamoin[1,3]

[1]*Université Paris-Saclay, ENS Paris-Saclay, CentraleSupelec, CNRS, LMPS - Laboratoire de Mécanique Paris-Saclay, Gif-sur-Yvette, France*
[2]*Service d'Études Mécaniques et Thermiques (SEMT), CEA, Université Paris-Saclay, Gif-sur-Yvette, France*
[3]*IUF, Institut Universitaire de France, Paris, France*

e-mail: matthieu.diaz@ens-paris-saclay.fr

Keywords: *Data assimilation, Kalman filtering, modified Constitutive Relation Error, Low-frequency dynamics, Shaking-table experiments, Earthquake Engineering*

As most of modern systems are now equipped with numerous sensing devices, the integration of experimental data in model-based approaches provides new techniques for monitoring the occurrence and propagation of structural damage in a structural health monitoring context. In particular, the dialogue between physics-based models and experimental data has become of major importance in the last two decades with the emergence of new paradigms such as *Digital Twins* [6] or *Dynamic Data-Driven Application Systems* (DDDAS) [1, 3]. The latter consists in establishing a close online interaction between models and measurements with a dual objective: (i) exploiting model predictions for decision-making operations on the experimental system such as model-based control and, (ii) updating the numerical model using data assimilated in real-time.

For earthquake engineering applications, the CEA/TAMARIS facility carries out seismic tests using shaking-tables moved by high-power hydraulic actuators. However, controlling the hydraulic actuators of the shaking-tables is still a challenging task that emphasizes the need of establishing a DDDAS framework. Indeed, the modal signature of damaging specimens can suddenly change under seismic loading conditions [2]. As modal signature is the key input-feature for linear control law design, the initial control strategy may become inadequate when damage occurs, leading to unstable experiments.

In this context, this work aims at contributing to the integration of Finite Element (FE) models in control loop of shaking-tables by resorting to a dynamical data-to-model interaction. In this talk, we will essentially focus on the identification/update loop of FIG. 1 from sparse and noisy measurements acquired in low-frequency dynamics. A new numerical framework is presented for data assimilation able to operate in real-time, robust to measurement noise as well as easily handleable by non-expert users.
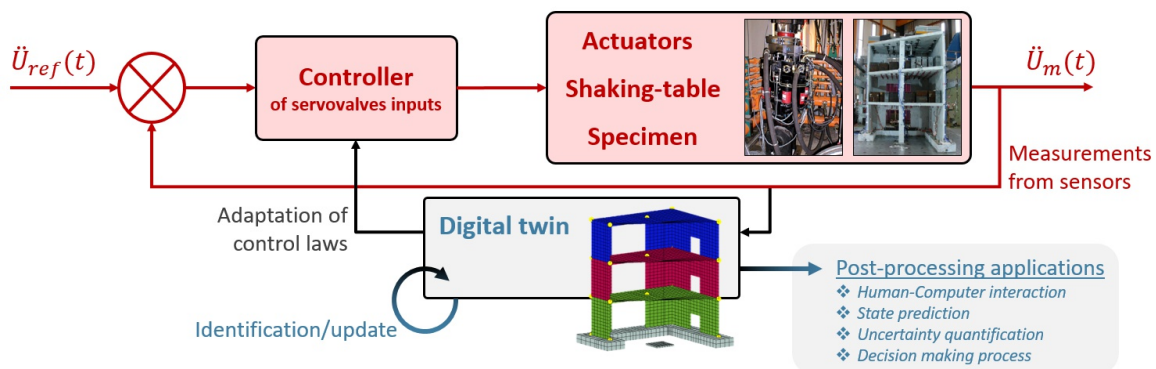
Figure 1: DDDAS framework for the control of shaking-tables - Introduction of a numerical model in the feedback loop for adaptative control law design.

Considering the model updating problem itself, low signal-to-noise ratio measurements from seismic inputs may be hard to integrate for correcting FE models properly. Alternatively to standard deterministic or stochastic model updating techniques, a strategy based on the minimization of a *modified Constitutive Relation Error* functional (mCRE) has been recently tailored to low-frequency dynamics in [4]. Built as a Hermitian data-

to-model distance written in the frequency domain enriched with a CRE residual accounting for model bias, the mCRE functional has shown extended robustness to measurement noise and the ability to process strongly nonlinear datasets (due to occurence of damage) with reasonably low computational effort. Besides, the mCRE-based model updating algorithm has been made independent of any expert user's *a priori* knowledge: automated procedures permit to define all mCRE internal parameters and the model parametrization itself is adaptively tuned to identify damage at best according to the available measurements.

In order to adapt this model updating algorithm to online structural monitoring applications, following the strategy initiated in [5], we integrate the mCRE as new observation operator within a dual Unscented Kalman filter, leading to a new *Modified Dual Kalman Filter* algorithm (MDKF). It differs from classical nonlinear Kalman filtering techniques for parameter estimation as the metric of the measurement update equation allows to confront indirectly model predictions with measurements, meaning that optimal parameters are sought as mCRE minimizers. Although this new framework seems more complex to operate, general guidelines based on physical meaning and engineering judgement are provided regarding the calibration of internal tuning parameters. In particular, noise covariance error matrices can be quickly and efficiently chosen.

After being validated using synthetic data, the methodology successfully processed actual measurements of the SMART2013 shaking-table test campaign in a real-time context. In the latter, the possibility to perform real-time monitoring of complex structures undergoing nonlinear phenomena is emphasized (see FIG. 2). The good correlation with former identification results [2,4] illustrates the relevance of this new approach for online structural monitoring and suggests promising use of MDKF for adaptive control design purposes.
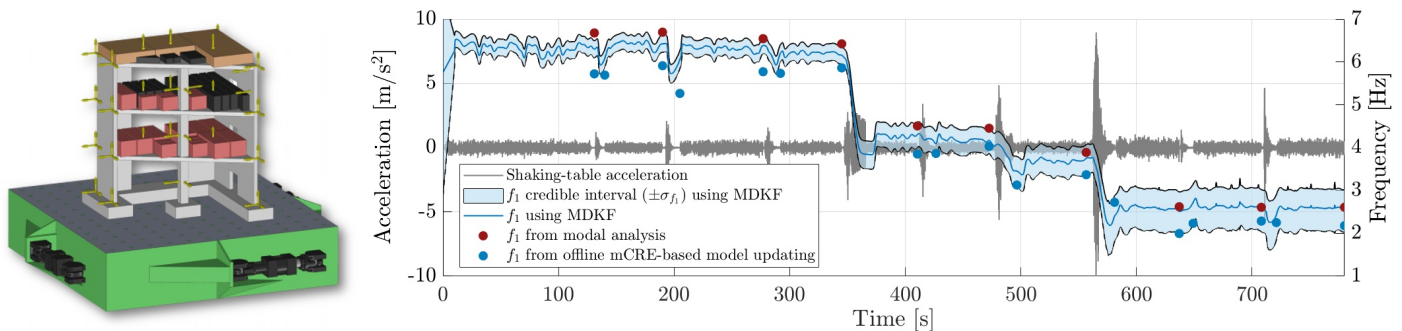
Figure 2: SMART2013 - Tracking the first eigenfrequency of the specimen using MDKF. Former reference identification results are given for comparison purposes: [4] in blue dots, [2] in red dots. An accelerometer measurement is also shown to relate inputs with structural state evolution.

References

[1] Ludovic Chamoin. Merging advanced sensing techniques and simulation tools for future structural health monitoring technologies. *The Project Repository Journal*, 10(1):124–127, September 2021.

[2] P.-É. Charbonnel. Fuzzy-driven strategy for fully automated modal analysis: Application to the SMART2013 shaking-table test campaign. *Mechanical Systems and Signal Processing*, 152:107388, May 2021.

[3] Frederica Darema. Dynamic Data Driven Applications Systems: A New Paradigm for Application Simulations and Measurements. In Marian Bubak, Geert Dick van Albada, Peter M. A. Sloot, and Jack Dongarra, editors, *Computational Science - ICCS 2004*, Lecture Notes in Computer Science, pages 662–669, Berlin, Heidelberg, 2004. Springer.

[4] M Diaz, P.-É Charbonnel, and L Chamoin. Robust energy-based model updating framework for random processes in dynamics: application to shaking-table experiments. *Computers and Structures*, 2022. Available at hal-03528432.

[5] Basile Marchand, Ludovic Chamoin, and Christian Rey. Real-time updating of structural mechanics models using kalman filtering, modified constitutive relation error, and proper generalized. *International Journal For Numericals Methods in Engineering*, pages 1102–1119, 2015.

[6] D. J. Wagg, K. Worden, R. J. Barthorpe, and P. Gardner. Digital Twins: State-of-the-Art and Future Directions for Modeling and Simulation in Engineering Dynamics Applications. *ASCE-ASME Journal of Risk and Uncertainty in Engineering Systems Part B Mech. Engrg.*, 6(3):030901, September 2020.

EFFECT OF TUNED MASS DAMPERS ON DISPLACEMENT RESPONSE BEHAVIOR OF STRUCTURES UNDER HARMONIC LOADING

E. Aydin[1], B. Ozturk[2,*], H. Cetin[1], F.M. Tugrul[1], Y.E. Bozkurt[1], T. Celik[1] and M. Akcakoyunluo[1]

[1]*Nigde Omer Halisdemir University, Dept.of Civil Engineering, Nigde, Turkey*
[2]*Hacettepe University, Dept.of Civil Engineering, Ankara, Turkey*

e-mail: bakiozturk@hacettepe.edu.tr

In this study, the effect of tuned mass dampers (TMDs) on controlling the displacement response behaviour of structures under harmonic loading was investigated theoretically. The structural model was defined in the Mathematica program; and the pendulum lengths and weights of the TMDs used were programmed to change. The pendulum symbolizes and refers to TMDs in this research. Afterwards, a harmonic sinusoidal load, defined in the program, was applied to the structure.

A theoretical structural model is introduced for the evaluation of numerical examples. The formulation of a 3-storey structural model is provided both for model without pendulum and model with pendulum cases. The harmonic sinusoidal load is introduced. The models for both no TMD and TMD application cases are compared. Structural behaviour of models with damping and no damping are also investigated, and the results are compared.

Considering the application of TMDs, combinations of 12 different masses and 18 different lengths are defined in the Mathematica program. For the structure with TMD, various L/m ratios are examined, and the calculated maximum displacement response values are obtained. The variation of L/m values and the corresponding maximum displacement response values are discussed. It is observed that as L/m ratios converge to 1 optimum maximum displacement response values are obtained. This proves that regardless of length or weight of TMD when L/m ratios converge to 1 optimum displacement values are obtained. As a result of this research, it is observed that when TMDs with certain L/m ratios are used in the structures, improvements are obtained in their displacement response behaviours.

Key Words: Tuned Mass Damper, Structural Control, Passive Control, Energy Dissipation Devices

MOTION TRACKING OF A RIGID-FLEXIBLE LINK ROBOTIC SYSTEM IN AN UNDERACTUATED CONTROL MODE

Elżbieta Jarzębowska[1], Krzysztof Augustynek[2], Andrzej Urbaś[3]

1. Warsaw University of Technology, 00-665 Warsaw, Nowowiejska 24, Poland, [0000-0003-1407-7546]
2. University of Bielsko-Biala, 43-309 Bielsko-Biala, Willowa 2, Poland, [0000-0001-8861-4135]
3. University of Bielsko-Biala, 43-309 Bielsko-Biala, Willowa 2, Poland, [0000-0003-0454-6193]

1. The paper aim and contribution

The paper presents its contribution to tracking control design of mechanical systems in an underactuated mode conditions, i.e. when the number of actuators is less than the number of possible control inputs. Fully actuated mechanical systems are quite well researched and controller designs are well developed for them as well. However, in applications, due to costs, weight, design and performance regimes or due to an actuator failure, the underactuated control mode is required. With the aid of the computational procedure for constrained dynamics (CoPCoD), reference motion dynamics and tracking control in an underactuated mode is designed for an example of a three link planar manipulator model with rigid and flexible links. A dynamic optimization problem is formulated to obtain optimal time courses of manipulator joint coordinates in underactuated mode conditions in order to apply them to a manipulator driving links controller.

2. Introduction

Mechanical control systems like robots, aircraft, satellites and space platforms, underwater vehicles and human servicing systems are designed to perform work and services, participate in exploration, rescue, military and other missions. These tasks and missions require high performance levels, durability and reliability of these systems. There are domains where failure is not an option, like in space missions or health related operations, and control actions have to be as good as possible. Also, some system functionalities or mission demands require cost, weight or size reductions. These two factors, failure avoidance and specific operation demands, lead to active research in dynamics, nonlinear and optimal control of underactuated control systems. A fully actuated system, i.e. the one enjoying the number of control inputs equal to the number of degrees of freedom, does its mission as long as the actuators work properly. In case of failure, questions arise of how to minimize risks and danger of damages to the workplace and continue a predefined task up to bringing the system to some safe rest position. In case of an intentional underactuated design, a controller has to be dedicated to the system and its mission. Controls for underactuated systems are usually driven by two main design approaches, i.e. by attempts to control underactuated system models using current control techniques or by designing new ones that can support reliability problems in practice. These approaches motivate a lot of current research in underactuated control systems. The literature on underactuated control systems is quite vast, see e.g. [1]. Most of these papers tackle work conditions where there are no other motion limitations and demands, i.e. constraints. The constrained underactuated control systems dynamics are presented in [2,3] for rigid models of underactuated systems. In [4] a dynamics approach to modeling, i.e. the automated computational procedure for constrained dynamics (CoPCoD) is presented. It works for rigid and flexible multibody systems which are fully actuated. Tracking control of USM is still a challenge topic, see e.g. [5-7].

3. Mathematical model of a rigid-flexible link manipulator

A model of a three link planar manipulator is presented in Fig.1a. It is assumed that link 2 can be treated as rigid or flexible. The flexible link is discretised using the Rigid Finite Element Method (RFEM). Motion of the manipulator is forced by means of three driving torque controllers. The aim of the paper is to propose an algorithm for control the manipulator when the system becomes underactuated due to failure or its

intentional design. Based upon our previous experience [2-4], underactuated systems require specific control approach. In our work, the dynamic optimization problem is formulated, in which optimal drives displacements in underactuated mode conditions are calculated. The proposed optimization algorithm is implemented in the following steps (Fig. 1b):

- calculation of reference time courses of joint coordinates according assumed programmed constraints, which specify the work regime using the CoPCoD method,
- application of the results from the previous step as a starting point for the optimization procedure,
- solution of the nonlinear optimization problem with constraints for the manipulator with the second drive non-working using the Nelder-Mead algorithm with the penalty method,
- verification of the obtained optimal solutions $\psi_{opt}^{(1)}, \psi_{opt}^{(3)}$.
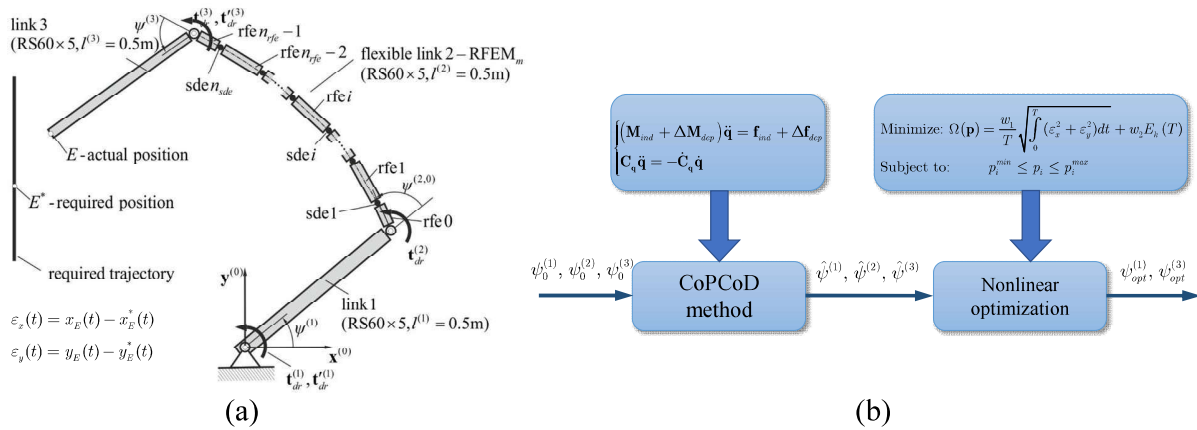
Figure 1: The three-link manipulator (a), the proposed optimization procedure (b)

The objective function takes into account a trajectory tracking error and the kinetic energy of the system at its final configuration. The simulation is performed for the manipulator with the rigid and flexible second link. Due to the long computation time, in further work the results obtained from the optimization task will be used as the training set for the artificial neural network that can be used in a real-time controller.

4. References

[1] Y. Liu, and H. Yu. A survey of underactuated mechanical systems. *IET Control Theory & Applications*, **7**(7):921–935, 2013.

[2] E. Jarzębowska and A. Szewczyk. An Emergency tracking controller design for a manipulator after its actuator failure, *Proc. ASME, IDETC/CIE*, August 2-5, 2015, Boston, MA, USA. https://doi.org/10.1115/DETC2015-47304.

[3] E. Jarzębowska. Tracking control design for underactuated constrained systems. *Robotica*, 24(5):591-593, 2006.

[4] E. Jarzębowska, A. Urbaś and K. Augustynek. Analysis of influence of a crane flexible supports, link flexibility, and joint friction on vibration associated with programmed motion execution. *Journal of Vibration Engineering & Technologies*, **8**:337–350, 2020.

[5] S. G. Nersesov, H. Ashrafiuon and P. Ghorbanian. On the stability of sliding mode control for a class of underactuated nonlinear systems. *Proc. of the 2010 American Control Conference*, Baltimore, USA, 3446–3451, 2010.

[6] J. Zhong-Ping. Controlling Underactuated Mechanical Systems: A Review and Open Problems. *in Lecture Notes in Control and Information Sciences book series* 2010, 407: 77-88.

[7] B. He, S. A. Wang and Y. Liu. Underactuated robotics: A review. *International Journal of Advanced Robotic Systems* 2019, https://doi.org/10.1177/1729881419862164.

Optimal Structural Control by Using Active and Semi-active Devices Concurrently

Ido Halperin and Yuri Ribakov

Department of Civil Engineering, Faculty of Engineering, Ariel University, Ariel, Israel

e-mail: idoh@ariel.ac.il

For many years, the concept of hybrid structural control has been interpreted as controlling a structure by a mixed set of passive and active actuators [1, 5, 8, 9]. Recently published studies presents a new concept for hybrid systems by utilizing active and semi-active control devices in parallel [2, 6]. In the present study, an optimal control is computed and performance is evaluated for such hybrid control strategy, i.e. one that combines active and semi-active control devices.

The dynamic properties of a structure, controlled by a hybrid controller of the above type, are modeled by the following, second order ODE:

$$(1) \qquad \mathbf{M}\ddot{\mathbf{z}}(t) + \mathbf{C}_d\dot{\mathbf{z}}(t) + \mathbf{K}\mathbf{z}(t) = \mathbf{F}^a\mathbf{w}^a(t) + \mathbf{F}^b\mathbf{w}^b(t) + \mathbf{p}(t); \quad \forall t \in (0, t_f); \quad \mathbf{z}(0), \dot{\mathbf{z}}(0)$$

It describes the relation between the inherent inertial, damping and stiffness properties, in direction of the structure's dynamic degrees of freedom; the control forces input and the external excitation. Here $\mathbf{z} : \mathbb{R} \to \mathbb{R}^{n_d}$ is a trajectory of the structure's dynamic degrees of freedom; $\mathbf{w}^a : \mathbb{R} \to \mathbb{R}^{n_{ua}}$ is a control forces trajectory generated by the active control devices; $\mathbf{w}^b : \mathbb{R} \to \mathbb{R}^{n_{ub}}$ is a control forces trajectory generated by the semi-active dampers and $\mathbf{p} : \mathbb{R} \to \mathbb{R}^{n_d}$ is an external excitation. $\mathbf{M}, \mathbf{C}_d, \mathbf{K} \in \mathbb{R}^{n_d \times n_d}$ are the mass, damping and stiffness matrices, respectively. $\mathbf{F}^a \in \mathbb{R}^{n_d \times n_{ua}}$ and $\mathbf{F}^b \in \mathbb{R}^{n_d \times n_{ub}}$ are the active and semi-active control forces distribution matrices, respectively.

Additionally, in the addressed problem, restrictions are imposed on the controller, as follows. The peak control forces in the active devices are bounded by a $\mathbf{w}^a_{max}$. The control forces in the semi-active dampers must follow the next constraints.

- The semi-active force can only resist the relative motion of damper's anchors.

- The peak semi-active control force must not exceed certain bound—$\mathbf{w}^b_{max}$.

The optimal control problem is defined to a performance index that weighs the states response and the mechanical power in the active control devices.

A solution to this problem is suggested by enhancing recently published works, concerning optimal control design for semi-active controlled structures [3, 4]. Those are founded on Krotov's method, a.k.a *Successive Global Improvements of Control*. It is a successive method that is aimed at solving optimal control problems by taking advantage of Krotov's theory [7]. According to this method, the key to the problem is formulating a sequence of functions with special properties. Once such sequence was found, it allows computing a sequence of processes that converges monotonously to a candidate optimum.

Here the optimization is carried out by tailoring the previous results [3, 4] to match the characteristics of the addressed physical problem. The optimal response of different combinations of active and semi-active devices are compared for different external excitations.

References

[1] Petrina Bogdan, Pasca Stefania, and Ioana Muresan. Active, semi-active and hybrid control systems properties and applications. *Acta Technica Napocensis: Civil Engineering & Architecture*, 54(2):153–161, 2011.

[2] Demetris Demetriou and Nikolaos Nikitas. A novel hybrid semi-active mass damper configuration for structural applications. *Applied Sciences*, 6(12), 2016.

[3] I. Halperin, G. Agranovich, and Y. Ribakov. *Design of Optimal Feedback for Structural Control*. CRC Press, 2021.

[4] Ido Halperin, Grigory Agranovich, and Yuri Ribakov. Multi-input control design for a constrained bilinear biquadratic regulator with external excitation. *Optimal Control Applications and Methods*, 40(6):1045–1053, 2019.

[5] G.W. Housner, L.A. Bergman, T.K. Caughey, A.G. Chassiakos, R.O. Claus, S.F. Masri, R.E. Skelton, T.T. Soong, B.F. Spencer Jr., and J.T.P. Yao. Structural control: Past, present and future. *Journal of Engineering Mechanics*, 123(9):897–971, 1997.

[6] Irfan Ullah Khan, David Wagg, and Neil D Sims. Improving the vibration suppression capabilities of a magneto-rheological damper using hybrid active and semi-active control. *Smart Materials and Structures*, 25(8):085045, jul 2016.

[7] V. F. Krotov. *Global Methods in Optimal Control Theory*. Chapman & Hall/CRC Pure and Applied Mathematics. Taylor & Francis, 1995.

[8] Yoshihiro Nitta and Akira Nishitani. Hybrid structural control combining active mass driver and hysteretic damper systems. In *Proceedings of the Twelfth World Conference on Earthquake Engineering*, page 1897, Auckland, New Zealand 2000, January 2000.

[9] T. T. Soong and B. F. Jr Spencer. Active, semi-active and hybrid control of structures. In *Proceedings of the Twelfth World Conference on Earthquake Engineering*, page 2834, Auckland, New Zealand 2000, January 2000.

Experimental studies of rotor blades vibration control

A. Mitura[1] and J. Warminski[1,]

[1]*Faculty of Mechanical Engineering, Department of Applied Mechanics, Lublin University of Technology, Nadbystrzycka 36, Lublin, Poland*
e-mail: a.mitura@pollub.pl

1. Introduction

The rotating components are essential parts of many systems. Examples of such objects are blades of a helicopter rotors, wind turbines or airplane engines. Non-constant rotational speed of the rotor, variable pitch of the blades and many other factors can cause undesirable blades vibrations. Therefore, scientists try to develop so-called active blade. The active structure with embedded sensor and actuator should enable the vibration reduction. Several suggestions for such solutions can be found in the literature. A mathematical model of a rotating beam represented by ordinary differential equations obtained from Galerkin's method is presented in article [1]. This model was extended with an additional differential equation used for the Positive Position Feedback (PPF) controller. The analysis demonstrated the control efficiency analytically, by the multiple timescale (MTS) method, and numerically. In paper [2] the structure was studied with another control algorithm - Nonlinear Saturation Control (NSC). The authors again limited the research to an analytical and numerical approach. However, they suggested that the Macro Fiber Composites (MFC) elements to be used as actuators.

In both mentioned above control algorithms (PPF and NSC) the additional control differential equation must be solved together with the equations of the plant. A simpler control strategies was used in work [3]. In two control variants the supplied voltage of a MFC piezoelectric patch was proportional to the sensor signal (linear control- LC) or to the third power of the sensor signal (cubic control - CC). Dynamics of the complete active rotating beam was described by partial differential equations and the solution was found analytically by MTS method. Obtained results showed that the approach was also effective in the case of the rotating beam vibrations suppression.

In the present research the experimental rotor blades vibration control are studied. Based on the articles [1-3] four control algorithms are selected for their practical implementation: LC, CC, PPF, NSC. Analysis of the controllers in the practical laboratory setup is presented.

2. Object and scope of research

The object of the study is an experimental setup composed of the three-blade rotor, DC motor as a source of energy supply and a system to measure blades vibrations and a control system enabling testing various control algorithms. In the rotor hub three adjustable grips are embedded. These grips allow fixing the blades under different preset angles. The blades are beams made of unidirectional graphite-epoxy prepreg material. The MFC actuator and strain gauge are glued on the opposite sides of each beam nearby clamping. The laboratory setup is equipped with two control systems. The first is used to control the rotor rotation $\varphi(t)$ and to change the angle according to the following formula:

$$(1) \qquad\qquad \varphi(t) = \omega_C t + \varphi_0 \sin(\omega_V t),$$

where ω_C describes constant angular rotor speed, while the oscillation level is defined by amplitude φ_0 and frequency ω_V. During rotor operation the vibrations of blades can be excited. The beams responses are measured using by strain gauges. The signals $u_{i,sensor}$ from these sensors are used as inputs to the second control system – the digital signal processing (DSP) studio in which selected controller can be applied. In the DSP different algorithms are written separately for each beam using. The proposed control algorithms

can be written in the following forms:

the proportional control

(2)
$$u_{i,MFC} = \gamma_{linear,i} u_{i,sensor} + \gamma_{cubic,i} u_{i,sensor},$$

the PPF control method

(3a)
$$\ddot{u}_{i,control} + \omega^2_{control} u_{i,control} + 2n_{control} \dot{u}_{i,control} = \gamma_{1,i} u_{i,sensor},$$

(3b)
$$u_{i,MFC} = \gamma_{2,i} u_{i,control},$$

and the NSC method

(4a)
$$\ddot{u}_{i,control} + \omega^2_{control} u_{i,control} + 2n_{control} \dot{u}_{i,control} = \gamma_{1,i} u_{i,sensor} u_{i,control},$$

(4b)
$$u_{i,MFC} = \gamma_{2,i} u^2_{i,control},$$

where i is beam index, u_{sensor} is signal from sensor (controller input), $u_{control}$ is controller variable and u_{MFC} is a voltage (controller output) supplied to the MFC actuator. Coefficients $\omega_{control}$ and $n_{control}$ are controller parameters, natural frequency and damping, respectively. Whereas γ_1, γ_2, γ_{linear}, γ_{cubic} are control gains. Second order ordinary differential equation (3a or 4a) is solved numerically in the controller processor using fourth order Runge-Kutta method.

The experimental tests consist of two parts. Firstly, the rotor dynamics without control activation are tested to find regions with significant blades vibrations. Next, for the selected cases, the proposed control algorithms (2-4) are used to reduce vibrations. The experimental investigations are used to evaluate the effectiveness of these algorithms in applications related to the rotating beams.

References

[1] Y.S. Hamed, A. Kandil and J.T. Machado. Utilizing macro fiber composite to control rotating blade vibrations, *Symmetry*, 12: 1-23, 2020.
[2] Y.S. Hamed and A. Kandil. Influence of time delay on controlling the non-linear oscillations of a rotating blade, *Symmetry*, 13: 1:17, 2021.
[3] J. Warminski, L. Kloda, J. Latalski, A. Mitura and M. Kowalczuk. Nonlinear vibrations and time delays control of an extensible slowly rotating beam, *Nonlinear Dyn.*, 103: 3255-3281, 2021.

ACTIVE CONTROL OF TORSIONAL VIBRATIONS IN ROTATING SYSTEMS BY MEANS OF THE DRIVING ASYNCHRONOUS MOTOR

P. Hańczur[1,2], T. Szolc[1*], and R. Konowrocki[1]

[1]*Institute of Fundamental Technological Research of the Polish Academy of Sciences, Warsaw, Poland*
[2]*Schneider Electric Polska Sp. z o.o, Warsaw, Poland*

e-mail: tszolc@ippt.pan.pl

1. Abstract

Majority of industrial machinery and several mechanisms are driven by asynchronous motors. Such electro-mechanical systems are often affected by detrimental torsional vibrations, suppression of which is commonly performed by more or less effective passive, semi active and active dampers. In this paper there is proposed an alternative method of attenuation of torsional vibrations in such objects. Here, an asynchronous motor under the proper vector control can simultaneously operate as a source of drive and actuator. Using this approach, transient and steady-state torsional vibrations of the driven mechanical system can be effectively suppressed as well as its precise operational motion can be assured. The theoretical investigations are carried out by means of an advanced structural mechanical model of the drive system and circuit model of the asynchronous motor controlled using two methods: the direct torque control (DTC-SVM) and the rotational velocity controlled torque method (RVCT) originally developed in this paper. In the computational examples performed for three representative drive systems torsional vibration control ability is analyzed for various dynamic properties of the mechanical part and several parameters of the asynchronous motor control. From the obtained results it follows that for majority of tested parameters, transient torsional vibrations excited by step-wisely disturbed loadings of the driven object are successfully attenuated using both abovementioned vector control strategies. However, a suppression effectiveness of resonant steady-state torsional vibrations by means of these methods depends on the specific case of an asynchronous motor with a given electromagnetic stiffness in the stable operational range of its static characteristics.

2. Introduction and description of the problem

From among various kinds of vibrations occurring in mechanisms and structures the torsional ones are very important as naturally associated with their rotational motions. Torsional vibrations are a source of additional oscillatory angular displacements superimposed on the nominal rotational motions of objects in question. On the one-hand-side, this phenomenon results in severe dynamic overloads leading to dangerous material fatigue of the most heavily affected and responsible elements of these mechanical systems and structures, e.g. shaft segments, joints and couplings, in too fast wear of gear stage teeth as well as in harmful noise generation and unexpected loss of transmitted energy.

In the presented paper an attenuation of torsional vibrations of machines driven by an asynchronous motor is going to be carried out using an active control. The investigations will be performed by means of structural hybrid mechanical models of the machine drive systems, wherein geometrical dimensions and material constants of the shaft line segments are thoroughly taken into consideration. These systems are driven by various asynchronous motors equipped with control units of a cascade structure consisting of the electromagnetic torque inner loop control and the rotational speed outer loop control. Contrary to the methods of active control of asynchronous motors applied so far, the motors of the tested systems are powered using power electronic converters with the 6-transistor IGBT bridge systems, which directly control the electromagnetic moment of the electric motors using the DTC-SVM control strategy. Alternatively, the standard DTC-SVM method will be properly modified using an additional driven machine input rotational speed control loop, which leads to a cascade and branched control structure containing two major control

loops. Namely, the standard DTC-SVM approach is realized by the inner control loop performing motor torque regulation, and is cascaded by the outer loop providing in this way an additional rotational velocity control according to a given reference value. This modified approach will be called further "the method of rotational velocity controlled torque" (RVCT).

3. Results of investigations

In the computational examples an influence of dynamic properties of the driven mechanical system and characteristics of driving motor on a vector control effectiveness will be tested. The abovementioned vector control methods are going to applied for three different electromechanical systems consisting each of an asynchronous motor driving a machine by means of an elastic coupling and transmission shaft segments. The examined static characteristics of such motor differ in a more or less stiff stable operation part, as "soft", "medium" and "stiff" shown in Fig. 1a. In turn, the driven mechanical object can be relatively more massive or "lighter" than the driving motor, which has been expressed by different fundamental eigenforms depicted
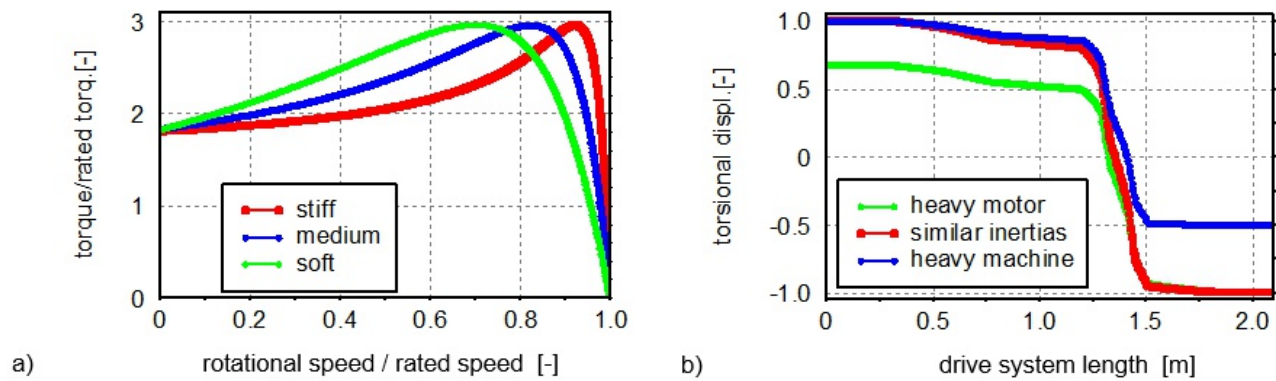
Figure 1: Static characteristics of the asynchronous motor (a) and variants of the fundamental torsional eigenmode of the drive system (b).
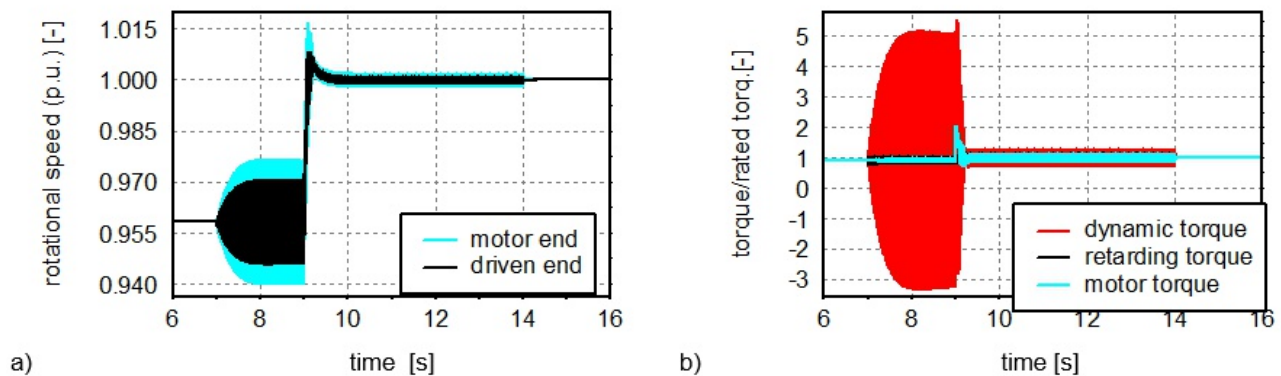
Figure 2: Controlled torsional response due to resonant harmonic excitation in the form of time histories of the system rotational speeds (a) and electromagnetic, retarding and dynamic torque (b).

in Fig. 1b. Here, the driven objects are loaded by step-wisely variable torques and harmonically oscillating torques with resonant frequencies. When assessing the simulation results, the main focus will be on ensuring that both vector control methods enable the best possible precision of steady-state movement and the highest degree of attenuation of resonant vibrations. In Fig. 2 there are plotted exemplary time-histories of the effectively controlled resonant response of one of the electromechanical systems under study in the form of rotational speeds respectively on the motor end and the driven end (Fig. 2a) as well as dynamic, electromagnetic and retarding torques transmitted by the drive system (Fig. 2b). Summing up, it should be stated that the both mutually compared approaches of vector control of the asynchronous motors are promising, but they require experimental verifications in order to be successfully used in an industrial practice.

Bi-objective optimal design of the energy harvesting enabled tuned mass damper inerter (EH-TMDI) for vibration mitigation and energy harvesting in stochastically excited multi-degree-of-freedom structures

K. Rajana[1], A. Giaralis[1]

[1]*Department of Civil Engineering, City, University of London, Northampton Square, London EC1V 0HB, UK.*
E-mail: Agathoklis.Giaralis.1@city.ac.uk

Extended Abstract

The energy-harvesting enabled tuned mass damper inerter (EH-TMDI) has been introduced by Salvi and Giaralis [1,2] as a dual-functional passive dynamic vibration absorber (DVA) capable of simultaneously harvesting energy and mitigating structural vibrations. The EH-TMDI configuration couples an electromagnetic motor (EM) with a tuned mass damper inerter (TMDI) [3]. The latter is a generalization of the conventional tuned mass damper which includes an inerter element that links the secondary mass to a different location of the primary structure from the one that the secondary mass is attached to via a linear spring in parallel with a dashpot. In the EH-TMDI configuration, the EM is connected in series between the inerter element and the secondary mass. In this regard, the EH-TMDI has richer dynamics than the TMD(I) as it effectively becomes a two degree of freedom (2-DOF) DVA, while the inerter simultaneously amplifies the dynamical effects of both the secondary mass and the EM [1,2]. In this respect, it was recently shown [4] that by increasing the inertance property of the EH-TMDI, improved energy generation and vibration suppression can be simultaneously achieved. This is a notable attribute of the EH-TMDI as inertance can readily scale-up at little additional monetary cost and weight [5-7], while in most regenerative DVAs, energy harvesting and vibration control do not necessarily improve simultaneously [8-10]. Nevertheless, the EH-TMDI in [4] have only been sub-optimally tuned for vibration mitigation which allow only relative comparisons between performances.

In this regard, this paper pursues the optimal bi-objective design of EH-TMDI for minimising structural dynamic response and maximising energy generation in white-noise base-excited multi degree of freedom (MDOF) structures. In this respect, the herein work extends recent efforts in [11] to address optimal design of regenerative inerter-based DVAs by treating MDOF primary structures in which the inerter is not necessarily grounded as opposed to single degree of freedom (SDOF) primary structures with grounded DVAs and by allowing for any desirable balance between the two studied objectives to be accounted in the optimal EH-TMDI tuning. To this aim, the adopted bi-objective optimisation approach utilizes weighting factors between the two objectives, represented by carefully normalized performance indices, gauging displacement response statistics of the primary structure and energy generation at the EM, which can be predefined at will. Further, a reduced-order 3-DOF mechanical model is used to expedite the optimization, derived from first principles such that it faithfully represents the fundamental mode dynamics of a MDOF primary structure equipped with an EH-TMDI any connectivity, that is, primary structure locations where the inerter and where the spring-dashpot are connected to. This is achieved by extending the formulations in [12,13], which treated the TMDI case, to the EH-TMDI case. In the thus derived 3-DOF model, the fundamental modal coordinates of the two different locations that the EH-TMDI is attached to the structure are explicitly accounted. This is an important consideration as it has been recently shown that the difference of these two modal coordinates, $\Delta\varphi$, which depends on the average modal curvature [13], significantly affects the vibration suppression efficacy of the TMDI.

In this context, in the numerical part of the work, special attention is focused on highlighting the relative importance of $\Delta\varphi$ to the dual performance of the EH-TMDI, namely vibration suppression and energy generation, for different predefined weighting factors in the definition of the objective function of the

optimization problem, as well as on the assumed EH-TMDI properties. It is numerically shown that by increasing $\Delta\varphi$ while keeping inertance fixed, both the energy dissipation by the EM and the vibration suppression efficacy improve. In addition, the influence of the inertial EH-TMDI properties (i.e. inertance and secondary mass ratio) on vibration suppression efficacy and energy generation are also assessed parametrically. Overall, numerical data provided demonstrate that the EH-TMDI is a promising configuration for bona fide dual purpose DVAs, effectively supported by the herein developed bi-objective optimal design framework.

References

[1] Salvi, J. and Giaralis, A., 2016. Concept study of a novel energy harvesting-enabled tuned mass-damper-inerter (EH-TMDI) device for vibration control of harmonically-excited structures. *Journal of Physics: Conference Series*, 744, p.012082.

[2] Salvi, J. and Giaralis, A. 2016. Performance assessment of the novel Energy Harvesting-enabled Tuned Mass Damper-Inerter (EH-TMDI) for simultaneous vibration suppression and energy scavenging in white noise excited structures. In: *Proceedings of the 6th European Conference on Structural Control- EACS2016* (July 11-13, 2016, Sheffield, UK), paper #151, p.12.

[3] Marian, L. and Giaralis, A., 2014. Optimal design of a novel tuned mass-damper–inerter (TMDI) passive vibration control configuration for stochastically support-excited structural systems. *Probabilistic Engineering Mechanics*, 38, pp.156-164.

[4] Giaralis, A. 2021. An inerter-based dynamic vibration absorber with concurrently enhanced energy harvesting and motion control performances under broadband stochastic excitation via inertance amplification. *ASCE-ASME Journal of Risk and Uncertainty in Engineering systems, Part B: Mechanical Engineering*, 7, p.010909.

[5] Brzeski, P., Lazarek, M., and Perlikowski, P. 2017. Experimental study of the novel tuned mass damper with inerter which enables changes of inertance. *Journal of Sound and Vibration*, 404, pp. 47–57.

[6] Pietrosanti D, De Angelis M and Giaralis A 2020. Experimental shaking table study of nonlinear SDOF system equipped with tuned mass damper inerter (TMDI) under harmonic excitation. *International Journal of Mechanical Sciences*, 184, p. 105762.

[7] Gonzalez-Buelga, A., Clare, L., Cammarano, A., Neild, S., Burrow, S. and Inman, D., 2014. An optimised tuned mass damper/harvester device. Structural Control and Health Monitoring, 21(8), pp.1154-1169.

[8] Shen, W., Zhu, S., and Zhu, H. 2019. Unify energy harvesting and vibration control functions in randomly excited structures with electromagnetic devices. *Journal of Engineering Mechanics, ASCE*, 145, p. 04018115.

[9] Liu, X., Jiang, J.Z., Titurus, B., and Harrison, A. 2018. Model identification methodology for fluid-based inerters, *Mechanical Systems and Signal Processing*, 106, pp. 479-494.

[10] Cai, Q. and Zhu S. 2022. The nexus between vibration-based energy harvesting and structural vibration control: A comprehensive review. *Renewable and Sustainable Energy Reviews*, 155, p.111920.

[11] Joubaneh, E.F., and Barry O.R. 2019. On the improvement of vibration mitigation and energy harvesting using electromagnetic vibration absorber-inerter: Exact H2 optimization. *Journal of Vibrations and Acoustics*, 141 p. 061007.

[12] Pietrosanti, D., De Angelis, M. and Basili, M., 2020. A generalized 2-DOF model for optimal design of MDOF structures controlled by Tuned Mass Damper Inerter (TMDI). International Journal of Mechanical Sciences, 185, p.105849.

[13] Wang, Z. and Giaralis, A., 2021. Enhanced motion control performance of the tuned mass damper inerter through primary structure shaping. Structural Control and Health Monitoring,.

EXPERIMENTAL VERIFICATION OF DEPLOYMENT STRATEGIES FOR A SIMPLEX TENSEGRITY COLUMN

A. Al Sabouni-Zawadzka[1] and A. Zawadzki[2]

[1] *Warsaw University of Technology, Faculty of Civil Engineering, Al. Armii Ludowej 16, 00-637 Warsaw, Poland*
[2] *Warsaw University of Technology, Faculty of Automotive and Construction Machinery Engineering, Narbutta 84, 02-524 Warsaw, Poland*

e-mail: anna.zawadzka@pw.edu.pl

1. Introduction

In recent years, a growing interest in adaptive systems has been observed. Such structural systems can be designed for the use in space, as well as on Earth, where they find numerous applications within mechanical and civil engineering. Deployable structures should be lightweight, compact when stowed and should have a good stiffness-to-mass ratio.

Tensegrities are pin jointed systems that consist of cables (elements in tension) and struts (compressed members) [2]. Thanks to the infinitesimal mechanisms, which are balanced with self-stress states, tensegrity structures are suitable for the application in adaptive systems with adjustable properties. Tensegrities have a high stiffness-to-mass ratio and are prone to structural control through an adjustment of self-stress forces [3]. While designing a deployable tensegrity structure, one should focus on large shape and geometry changes with the simultaneous assurance of the stability, stiffness and desired load carrying capacity of the deployed system.

In the present paper, the authors focus on a deployable tensegrity column aimed at civil engineering applications. The main aim of this study is to experimentally verify the deployment strategies of the proposed two-module simplex tensegrity column. The laboratory results are compared with numerical simulations of the column, examples of which were already presented by the authors in [4, 6].

2. Tensegrity column

The deployable tensegrity column considered in this study was constructed from two three-strut simplex modules, connected via common cables of the triangular middle base. Each module has three struts made of aluminium tubes with an outer diameter of 10 mm and a wall thickness of 1 mm, and nine cables made of polyarylate super fibres with a diameter of 0.8 mm. The total height of the deployed column is 2 m. In both modules the same level of self-stress was adopted.

The model of the column is equipped with 15 actuators and 36 sensors. Self-stress values are controlled using the readings from 21 strain gauges. Displacements of the cables are controlled using 15 magnetic encoders. The signals are processed in a microcontroller and control signals are fed to the actuators.

Figure 1 shows three stages of the column deployment: at first both modules are flat and the deployment of the bottom module occurs, then the bottom module is fully deployed and the deployment of the upper module is conducted and at the end, the whole column is fully deployed.

3. Control strategies

In the previous papers [4, 6] the authors analysed theoretical possibilities to deploy a tensegrity column in various ways. That research was conducted with an assumption that the model was described by the formulas that are valid for tensegrity structures. Such an approach is called a model based control, where the stability of the mechanical system is assured by assuring that the lengths of cables, struts and self-stress values are as it results from the geometry configuration changing in time.
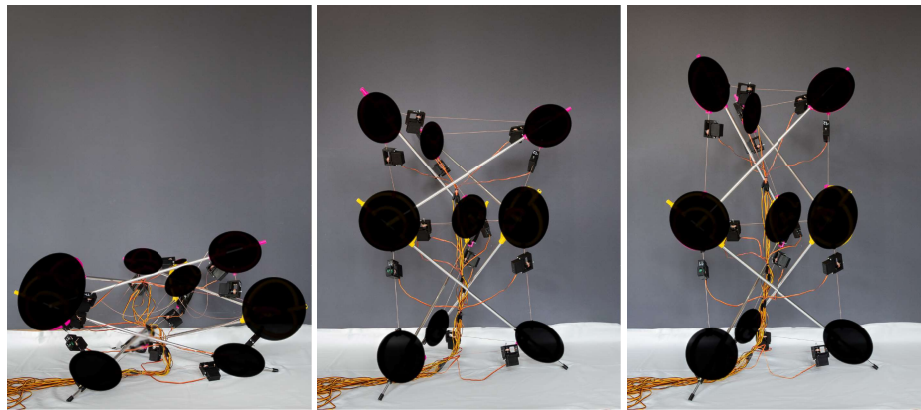
Figure 1: Deployment of the column (*the joints are hidden due to the on-going patent procedure, the photos will be replaced before the conference once the documents are in the patent office*).

The model based control is safe because it gives us a full control of structural behaviour [5]. However, in this specific application it has a couple of major disadvantages. If during the deployment process the structure is not meant to behave as tensegrity, the control will have to use additional decision algorithms, what can be problematic if e.g. varying loads are to be applied. The next problem is strictly technical, as each actuator must be directly controlled with a feedback loop from the position sensors and self-stress measuring sensors. It makes the structure complicated and therefore, the advantage of tensegrity simplicity is lost.

Due to the above mentioned disadvantages, the authors compare the model based control with a proportional-integral (PI) control. Such controllers are widely used in industrial control systems, where the positioning accuracy is the main goal. The PI control is widely described in the literature [1] and therefore, it should only be mentioned that it is based on analysing an error signal (difference between the set value and the actual value) of the controlled parameter using a negative feedback loop.

4. Summary

The presented study was aimed at experimental verification of selected control strategies used for the deployment of a two-module simplex tensegrity column. Firstly, analyses of a single module were carried out using different loading scenarios: constant vertical load (e.g. the structure acts as a support), constant horizontal load, variable horizontal load (e.g. the structure subjected to wind load). Secondly, the obtained results were compared with an experiment conducted on a scale model to verify mechanical behaviour and to analyse the influence of friction in joints, contact between struts and cables, especially in the minimum-height position and additionally, the entanglement risk. Afterwards the whole process was repeated for the two-module column.

References

[1] K. Ang, G. Chong, and Y. Li. Pid control system analysis, design, and technology. *IEEE Transactions on Control Systems Technology*, 13(4):559–576, 2005.

[2] Rene Motro. *Tensegrity: Structural Systems for the Future*. Kogan Page Science, London, UK, 2003.

[3] A. Al Sabouni-Zawadzka and W. Gilewski. Inherent properties of smart tensegrity structures. *Applied Sciences*, 8:787, 2018.

[4] A. Al Sabouni-Zawadzka and A. Zawadzki. Simulation of a deployable tensegrity column based on the finite element modeling and multibody dynamics simulations. *Archives of Civil Engineering*, 66(4):543–560, 2020.

[5] F. A. Steven. *Control Theory Tutorial: Basic Concepts Illustrated By Software Examples*. Springer Open, 2018.

[6] A. Zawadzki and A. Al Sabouni-Zawadzka. In search of lightweight deployable tensegrity columns. *Applied Sciences*, 10(23), 2020.

Tuned Liquid Column Damper Inerter (TLCDI) for vibration control of base-isolated structures

A. Di Matteo[1], C. Masnata[1], and A. Pirrotta[1]

[1]*Department of Engineering, University of Palermo, viale delle Scienze, 90128 Palermo, Italy*
e-mail: alberto.dimatteo@unipa.it

Abstract

In this study the use of a novel passive control device referred to as Tuned Liquid Column Damper Inerter (TLCDI) coupled with a base isolation system is investigated with the aim to mitigate the seismic response of base-isolated structures. The TLCDI optimal parameters for pre-design purposes are obtained by means of a statistical linearization technique and an optimization procedure which considers the minimization of the base structural displacement variance and a white noise process as base excitation. The reliability of the proposed approach is assessed by a comparison with a more accurate and computationally complex numerical optimization procedure. Finally, the control performance of the base-isolated TLCDI-controlled structure is investigated and comparisons with the structural responses of the uncontrolled structure are presented.

1. Introduction

In the field of passive vibration control, seismic base-isolation (BI) is recognized as one of the most effective seismic protection strategies to prevent or minimise damage to buildings, widely employed especially for those structures built in regions prone to earthquakes. BI systems lead to a decoupling of the motion of the building from the ground motion by introducing a layer with low lateral stiffness between the structure and the foundation so the superstructure essentially behaves like a rigid body. In this manner, the majority of displacements occurs within the BI system, while interstory drift and accelerations of the main structure are greatly reduced. To this aim, innovative combined control strategies have been recently conceived for the enhancement of the dynamic performance of isolated structures by reducing the large and undesirable displacements which BI systems may undergo during earthquakes. Among the several alternatives analysed in the literature, a possible solution to reduce base displacements concerns the idea to combine the BI system with other types of passive control systems, such as Tuned Mass Damper (TMDs) [1] and Tuned Liquid Column Dampers (TLCDs) [2]. However, these devices may require large masses to be efficient. Consequently, additional mass amplifying mechanisms such as inerter-based devices, have gained increasing interest as lightweight solutions [3]. On this basis, following the logical flow which led to the development of the Tuned Mass Damper Inerter (TMDI) [4] as a more efficient strategy compared to the classical TMD, the recently introduced Tuned Liquid Column Damper Inerter (TLCDI) [5] is here proposed, for the first time applied to isolated systems, as a promising passive control device which exploits the synergetic beneficial features of the inerter and the TLCD. TLCDIs, being simple U-shaped liquid tanks, show greater versatility and architectural adaptability due to their easy installation, little maintenance needed and, furthermore, the liquid inside may be used for both water supply and firefighting purposes.

3. Optimal design of the TLCDI: Results and Discussion

The present work focuses on the development of closed-form formulas for the optimal TLCDI parameters to obtain the best mitigation effect of the structural response of a single degree of freedom (SDOF) base-isolated structure subjected to a seismic base acceleration (Fig. 1 (a)). The TLCDI is supposed to be able to

translate through a sliding support and is linked to the BI system by a linear spring and a damper and to the ground by an inerter. In this manner, the TLCDI allows the displacement demand of the BI system to be reduced by means of a combined action which involves the vertical motion of the liquid and the horizontal motion of the container. Notably, since the governing equations of the TLCDI are nonlinear, as shown in Eq. (1), the optimal design process may be time consuming and computationally complex. Thus, for a simplifying treatment of the problem, as customary in the literature, the nonlinear system can be replaced with an equivalent linear one by resorting to the so-called Statistical Linearization Technique (SLT).

(1)
$$M_s \ddot{x}_b(t) + M_s \ddot{x}_s(t) + C_s \dot{x}_s(t) + K_s x_s(t) = -M_s \ddot{x}_g(t)$$
$$M_{tot} \ddot{x}_b(t) + M_s \ddot{x}_s(t) + C_b \dot{x}_b(t) + K_b x_b(t) - c_2 \dot{y}(t) - k_2 y(t) = -M_{tot} \ddot{x}_g(t)$$
$$(\rho AL + M_c + b)\ddot{y}(t) + (\rho AL + M_c + b)\ddot{x}_b(t) + \rho AL_h \ddot{u}(t) + c_2 \dot{y}(t) + k_2 y(t) = -(\rho AL + M_c)\ddot{x}_g(t)$$
$$\rho AL_h \ddot{x}_b(t) + \rho AL_h \ddot{y}(t) + \rho AL \ddot{u}(t) + \frac{\rho A}{2}\xi|\dot{u}(t)|\dot{u}(t) + 2\rho Agu(t) = -\rho AL_h \ddot{x}_g(t)$$

The effectiveness of the TLCDI is quantified by the reduction in the base displacement variance of the BI system due to the presence of the proposed device. Therefore, in order to find a tool to promptly compute the steady state response statistics and the optimal parameters some simplifying hypothesis are introduced. Notably, by assuming a white noise excitation and that the entire base isolated structure can be modelled as a SDOF system (Fig. 1 (b)) pertinent analytical expressions for the optimal TLCDI parameters are provided by neglecting damping effects. Finally, the accuracy of the proposed optimization procedure is assessed through a comparison with the optimal values obtained by performing a more computationally demanding numerical procedure on the original system and the control performance of TLCDI is discussed for base isolated structures and compared with uncontrolled systems.
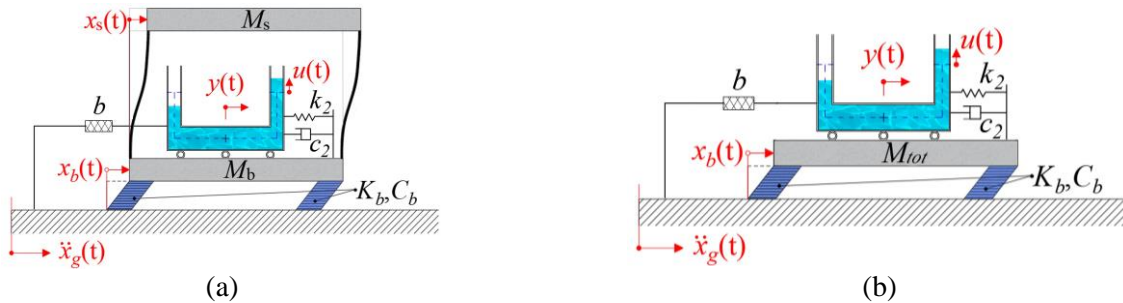
Figure 1: Analysed systems: (a) base-isolated TLCDI-controlled SDOF structure; (b) simplified model of base isolated rigid structure equipped with TLCDI.

References

[1] Yang J.N., Danielians A., & Liu S.C., (1991), "Aseismic hybrid control systems for building structures", Journal of Engineering Mechanics, vol. 117, pp. 836-853.
[2] Di Matteo A., Furtmuller T., Adam C., & Pirrotta A., (2017), "Optimal design of tuned liquid column dampers for seismic response control of base-isolated structures", Acta Mechanica, pp. 1-18.
[3] Smith, M.C., (2002), "Synthesis of mechanical networks: The Inerter", IEEE Transactions in Automatic Control, vol. 47(10), pp. 1648-1662.
[4] Di Matteo, A., Masnata, C., and Pirrotta, A. (2019). "Simplified analytical solution for the optimal design of Tuned Mass Damper Inerter for base isolated structures". In: Mechanical Systems and Signal Processing 134, p. 106337.
[5] Di Matteo, A., Masnata, C. Adam, A. Pirrotta, A (2022), "Optimal Design of Tuned Liquid Column Damper Inerter for vibration control", Mechanical Systems and Signal Processing, 167 108553.

THE PARAMETRIC PREDICTIVE CONTROL ALGORITHM
IN THE MAGNETIC SUPPORT SYSTEM OF A HIGH-SPEED MACHINE

P. Kurnyta-Mazurek[1], T. Szolc[2], M. Henzel[1] and K. Falkowski[1]

[1]*Faculty of Mechatronics, Armament and Aerospace, Military University of Technology, 00-908, Warsaw, Poland*
[2]*Institute of Fundamental Technological Research, Polish Academy of Science, Warsaw, 02-106, Poland*

e-mail: paulina.mazurek@wat.edu.pl, tszolc@ippt.pan.pl, maciej.henzel@wat.edu.pl, krzysztof.falkowski@wat.edu.pl

Abstract

In recent years, magnetic bearing technology has been implemented in many practical applications. In comparison with mechanical bearings, the magnetic ones have decreased stiffness coefficients and increased damping coefficients of radial bearings reducing the critical rotor speeds, [1]. These features are given the magnetic bearings a considerable potential to become a key element in rotating machines, like jet engines, turbo-compressors, generators and many others, [2]. Active magnetic bearings allow precise control of a rotor position and enable "online" monitoring, diagnosing, and identifying high-speed machines, [3].

The magnetic bearings are structurally unstable. Namely, an effective control system with a proper controller ought to be designed to ensure defined control quality indicators. In general, control systems of magnetic bearings are mostly restricted for using proportional-integral-derivative (PID) controllers. However, robust and slide control methods are also used in similar systems**,** [4]. Some predictive control algorithms were implemented in the analyzed AMB control loop [1].

The paper presents the research results of a parametric predictive control algorithm implemented in a high-speed rotor machine's magnetic bearing support system. The theoretical and experimental analyses of the control system with the Extended Horizon Adaptive Control (EHAC) algorithm are presented using an AutoRegressive with eXogenous input (ARX) model. A laboratory model of the magnetic suspension system consists of two active radial magnetic bearings and one axial (thrust) active magnetic bearing. The levitated rotor displacement in air-gaps and control current signals in control loops were measured for various rotor speeds and several parameters of the control algorithm, and they were presented in the form of time histories. Moreover, the power consumption of the magnetic bearing system with the predictive control algorithms was analysed, and the influence of a tuning factor and control horizon on rotor dynamic properties were determined. The theoretical studies were carried out using Matlab and Simulink software, whereas the experimental studies were performed using an appropriately dedicated test rig.

References

[1] Kurnyta-Mazurek P., Szolc T., Henzel M., Falkowski K.: „Control system with nonparametric predictive algorithm for the high-speed rotating machine with magnetic bearings", *Bulletin of the Polish Academy of Sciences: Technical Science*, 2021

[2] Brusa: "Semi-active and active magnetic stabilisation of supercritical rotor dynamics by contra-rotating damping", *Mechatronics* 24, 2014, pp. 500–510, //doi.org/10.1016/j.mechatronics.2014.06.001.

[3] R. Siva Srinivas, R. Tiwari, Ch. Kannababu: "Application of active magnetic bearings in flexible rotordynamic systems – A state-of-the-art review", *Mechanical Systems and Signal Processing*, 106, 2018, pp. 537-572

[4] A. Tonoli, A. Bonfitto, M. Silvagni, and L. D. Suarez, "Rotors on Active Magnetic Bearings: Modeling and Control Techniques", in Advances in Vibration Engineering and Structural Dynamics. London, United Kingdom: IntechOpen, 2012 [Online]. Available: https://www.intechopen.com/chapters/41670 doi: 10.5772/51298

ACTIVE BAYESIAN VIBRATION MITIGATION OF NONLINEAR SYSTEMS WITH UNCERTAIN DYNAMICS

V.K. Dertimanis[1], S.F. Masri[2], and E.N. Chatzi[1]

[1]*Institute of Structural Engineering, ETH Zurich, Stefano-Franscini-Platz 5, 8093 Zurich, Switzerland*
[2]*Viterbi School of Engineering, University of Southern California, University Park, Los Angeles, CA 90089, USA*

e-mail: v.derti@ibk.baug.ethz.ch, masri@usc.edu, chatzi@ibk.baug.ethz.ch

Abstract

Despite the substantial progress made over the last decades on the problem of structural vibration control [1], there exist topic areas that are still not thoroughly investigated. Among others, there's an increasing interest on the vibration attenuation of structures that feature nonlinear characteristics. Such structures, usually described by nonlinear differential equations with fixed parameters, are oftentimes further exposed to some degree of uncertainty [2], in the sense that these parameters are partially known, time-varying, or even completely unknown. Within this context, the effective mitigation of vibration remains an issue that is largely unexplored.

The linear subproblem, although still open to research, has been already treated to a large extent, both in a active [3] and semi-active [5,6] setting. There, it has been shown that the use of an appropriate Bayesian filter that can effectively account for all parametric uncertainties in *real-time* can provide a certain flexibility. It's extension to nonlinear systems is not, nevertheless, directly applicable. This is mainly due to the additional complexity that is being imposed by the nonlinear dynamics, which render the design of a controller a rather difficult task.

We explore this problem and introduce an active nonlinear vibration control framework that is simple, straightforward and implementable in real-time. Following the encouraging results of the linear case [3], we propose the architecture of Fig. 1. The measured structural excitations and responses, $\mathbf{u}[k]$ and $\mathbf{y}[k]$, respectively, are being fed to an unscented Kalman filter (UKF), which is implemented for adaptive joint state and parameter estimation, while the estimated states $\boldsymbol{\xi}[k]$ and parameters $\boldsymbol{\theta}$ are then forwarded to the controller.

The adopted control law consists of two tasks: the former applies feedback linearization for canceling the nonlinear dynamics of the system, while the latter operates on the linearized state equation and allows for any conventional linear strategy to be integrated, i.e., the addition of damping, LQR control, etc. The combined control forces $\mathbf{f}[k]$ accordingly serve as additional excitations to the system, while are further "copied" to the UKF, in order to ensure consistency between the closed-loop dynamics and the Bayesian observer.

Our framework is validated via a Duffing oscillator with light damping and uncertain nonlinear parameter. In specific, we investigate the transient and the steady-state behaviour of the closed loop dynamics under harmonic and stochastic disturbance, and we comment on the behaviour of the UKF with respect to the uncertain parameter. Since our main aim herein is to assess the feasibility of our approach, no rigorous stability, convergence, or robustness results are reported. We do include, however, an algebraic test for the discrete-time observability of the augmented state-parameter vector [4], since this property is crucial for both the observer and the controller. The assessment of the underlying simulations suggests that the proposed Bayesian approach for nonlinear vibration control is quite promising and provides a competitive layout for handling uncertain systems.

References

[1] B. Basu, O. S. Bursi, F. Casciati, S. Casciati, A.E. Del Grosso, M. Domaneschi, L. Faravelli, J. Holnicki-Szulc, H. Irschik, M. Krommer, M. Lepidi, A. Martelli, B. Ozturk, F. Pozo, G. Pujol, Z. Rakicevic, and J. Rodellar. A european association for the control of structures joint perspective. recent studies in civil structural control across europe. *Structural Control and Health Monitoring*, 21(12):1414–1436, 2014.

[2] E.N. Chatzi, A.W. Smyth, and S.F. Masri. Experimental application of on-line parametric identification for nonlinear hysteretic systems with model uncertainty. *Journal of Structural Safety*, 32(5):326 – 337, 2010.
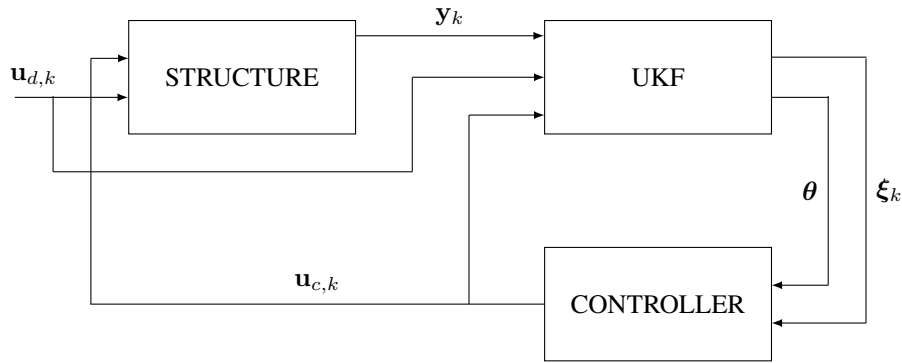
Figure 1: Layout of the proposed nonlinear vibration control scheme.

[3] V.K. Dertimanis and E.N. Chatzi. LQR-UKF active comfort control of passenger vehicles with uncertain dynamics. *IFAC-PapersOnLine*, 51(15):120–125, 2018.

[4] V.K. Dertimanis, E.N. Chatzi, S. Eftekhar Azam, and C. Papadimitriou. Input-state-parameter estimation of structural systems from limited output information. *Mechanical Systems and Signal Processing*, 126:711–746, 2019.

[5] V.K. Dertimanis, E.N. Chatzi, and F. Weber. LQR-UKF Semi-Active Control Of Uncertain Structures. In *EACS 2016-6th European Conference on Structural Control*, page Paper No. 161, Sheffield, UK, 2016.

[6] M.S. Miah, E.N. Chatzi, V.K. Dertimanis, and F. Weber. Real–time experimental validation of a novel semi-active control scheme for vibration mitigation. *Structural Control and Health Monitoring*, 24(3):e1878, 2017.

Distributed modular semi-active controller for suppression of vibrations and energy harvesting

D. Pisarski[1], R. Konowrocki[1], and T. Szolc[1]

[1]*Institute of Fundamental Technological Research, Polish Academy of Sciences, Warsaw, Poland*

e-mail: dpisar@ippt.pan.pl

Distributed controllers have been widely developed for a variety of engineering applications, taking advantage of their robustness, functionality and computing capabilities. The purpose of this work is to design a distributed state-feedback controller that can be perceived as a 'plug and play' device, allowing effortless integration with a structure and providing simplicity in assembly, replacement, or reconfiguration. Our controller is based on a set of individual subcontrollers each one of which is associated with a subsystem representing part of a vibrating structure. Each subcontroller relies on state measurements of the adjacent subsystem's sensors to carry out global vibration suppression and energy harvesting tasks. Additionally, we assume that the neighboring subcontrollers exchange some state information to estimate a prediction of the coupling forces. The incorporated computational procedures for the subcontrollers are uniform which allows for designing a modular architecture that is cheap to build and easy to maintain. One of the essential benefits of the proposed distributed controller is that the subcontrollers perform the computing in parallel, which compared to standard centralized approaches significantly reduces the computational burden and allows for an adaptive implementation to large-scale structures subjected to changes in the parameters and excitation.

The majority of the distributed controllers designed for structural control have been based on the idea of isolated subsystems conforming to the parts of a vibrating structure and designing a set of local state-feedback controllers, where each relies solely on the state information of its adjacent subsystem [1, 3, 5, 6]. In our work, we suggest using the communication between the neighboring subcontrollers and building an evolutionary model that allows for short-time prediction of the coupling forces between subsystems. For the control we assume a stabilizing state-feedback switching law [4]. The selection of the parameters of this control law enables compromising antagonistic vibration suppression and energy harvesting objectives [2]. The validation of the method is carried out by experiments on a specially designed semi-active modular vibrating platform equipped with a set of electromagnetic control devices, displacement laser sensors and a real-time control system. We investigate a series of free-vibration scenarios assuming different selections of the distributed controller's architecture. The performance of the proposed method is tested by comparisons with standard centralized controller and passive damping strategy.

References

[1] L. Bakule. Decentralized control: An overview. *Annual Reviews in Control*, 32:87–98, 2008.

[2] K. Kecik. Simultaneous vibration mitigation and energy harvesting from a pendulum-type absorber. *Communications in Nonlinear Science and Numerical Simulation*, 92:105479, 2021.

[3] Y. Lei and D. T. Wu. A new decentralized control approach for the benchmark problem. *Procedia Engineering*, 14:1229–1236, 2011.

[4] G. Leitmann. Semiactive control for vibration attenuation. *Journal of Intelligent Material Systems and Structures*, 5(6):841–846, 1994.

[5] D. Pisarski and A. Myśliński. Suboptimal distributed state-feedback control of semi-active vibrating systems. *Journal of Sound and Vibration*, 443:637–651, 2019.

[6] B. Popławski, G. Mikułowski, A. Mróz, and Ł. Jankowski. Decentralized semi-active damping of free structural vibrations by means of structural nodes with an on/off ability to transmit moments. *Mechanical Systems and Signal Processing*, 100:926–939, 2018.

Human-induced force reconstruction using a non-linear electrodynamic shaker applying ANN-based iterative learning controller

C. Peláez[1,2], A. Magdaleno[2], and A. Lorenzana[2]

[1]*Universidad de Alcalá, Spain*
[2]*Universidad de Valladolid, Spain*

e-mail: cesar.pelaez@uah.es, cesar.pelaez@alumnos.uva.es

1. General

Recent advances in structural technologies have promoted a trend toward designing stylish, lighter and more slender structures with fewer nonstructural elements. This causes these structures to be significantly more affected by the presence of human activity when compared to past constructions. Human activity upon the structures may be divided into passive and active. While passive humans may influence the dynamic response of the structure by modifying its modal parameters [1], active human activities can bring the structure into vibration [2]. Excessive vibration may occur if the motion frequency of the humans is close to some natural frequency of the structural system, and once the structure starts vibrating beyond a certain limit, serviceability problems may occur. Therefore, structures with low natural frequencies should be inspected for human-induced vibration to assess their serviceability and adopt appropriate actions to mitigate these vibrations if necessary. The major challenge in conducting these tests on structures resides in the lack of repeatability associated with tests performed by humans. Pedestrian induced excitation is defined in terms of ground reaction forces (GRF).

The approach adopted in this paper aims to provide a solution to this problem by using an electrodynamic shaker to recreate the forces generated by humans. This shaker consists of an inertial actuator, which works by generating inertial forces on the structure on which it is placed, but it is also inherently a nonlinear electro-mechanical system [3]. In addition, it is not necessary to use a model of the walking force pattern, as the temporal force signal measured with instrumented insoles is replicated.

Hence, this paper deals with the development of a robust control system in order to achieve a high fidelity signal reproduction with the electrodynamic shaker, addressing the inverse problem of obtaining a temporal output that presents the least possible error compared to the reference signal. This problem belongs to a wide class of ill-posed inverse problems [4]. One of the strategies for dealing with this type of problem is the use of optimal control techniques, which are efficient alternatives to adapt controller parameters for dynamic systems, to deal with the system nonlinearities and to enhance the tuning process of the controller without causing system divergence or instability.

The control system developed consists of an iterative learning control system (ILC), which is a control method that identifies the shaker model and iteratively modifies the drive signal offline to make the inertial force output of the shaker consistent with the desired signal (Figure 1). As we are dealing with a non-invertible model of the shaker dynamics, the problem becomes more difficult leading to highly non-trivial control design. To prevent this, instead of adopting a traditional approach to obtain the inverse model of the system [5], a black box system based on an artificial intelligence algorithm has been developed. Thus, a neural network approach is proposed to address the solution to this inverse problem. The approach followed in this paper consists of implementing a unique ANN as a substitute for the inverted model of the shaker dynamics in the ILC scheme, as the direct model of the shaker has been satisfactorily obtained in previous works [6].

16 experimental force measurements were performed using a pair of wireless instrumented insoles recently

developed by Novel Gmbh (Munich, Germany) [7] for different movement conditions at different frequencies and amplitudes focusing on those motion types in which there is always at least one foot touching the ground (bouncing, walking, random excitation), in order to facilitate the replication of these signals with the shaker. Since the shaker can only apply forces in a single location, it was decided to replicate the sum of the forces exerted by each foot, corresponding to the total force applied by the pedestrian on the ground.

The accuracy of the resulting signals obtained compared to the reference signals has been evaluated for the 16 experiments performed, both in the time domain and by evaluating the frequency content of both signals, proving that both have a very similar frequency content (Figure 2). Hence, when introducing these forces as excitation in a structure, a similar response will be produced, which is precisely the goal of this paper.
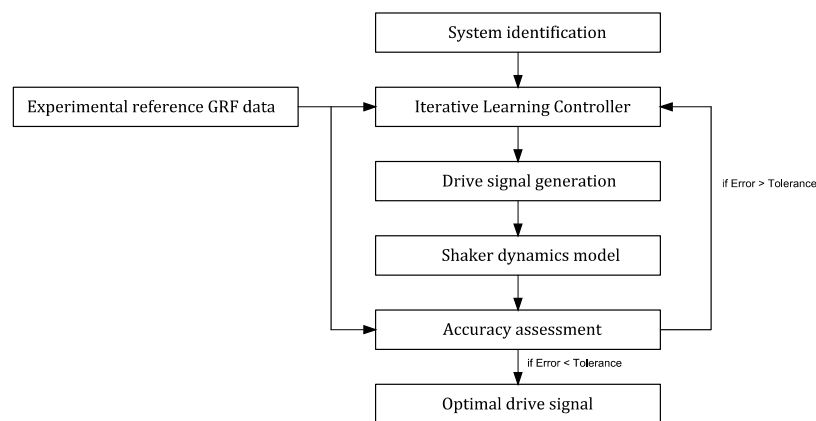
Figure 1: Operation scheme of the proposed iterative control system
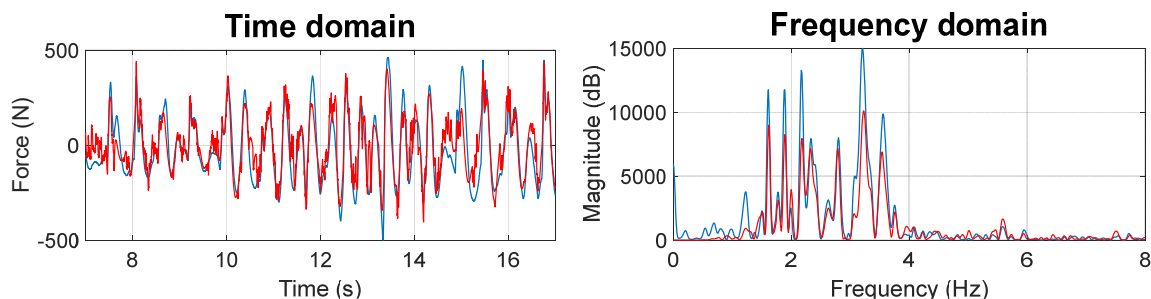
Figure 2: Experimental results. Blue signal represents the reference force while red signal represents the experimental force achieved with the inertial shaker

References

[1] G. Busca et al., Quantification of changes in modal parameters due to the presence of passive people on a slender structure., Journal of Sound and Vibration 333:5641–52.

[2] Zivanovic S., Díaz I. M. and Pavic. A., Influence of walking and standing crowds on structural dynamic properties., Proceedings of the 27th Conference Exposition on Structural Dynamics (IMAC '09)

[3] Abhishek S. and Tiwari N. Modeling and study of nonlinear effects in electrodynamic shakers. "Mechanical Systems and Signal Processing Volume 85, 15 February 2017, Pages 162-176

[4] Bakushinsky A. and Goncharsky A. Ill-posed problems: Theory and applications. Mathematics and Its Applications. Kluwer: Dordrecht, The Nederlands, 1994. Volume 301

[5] Widrow B. and Bilello M. Adaptive Inverse Control. Conference: Intelligent Control, 1993., Proceedings of the 1993 IEEE International Symposium on Intelligent Control. Chicago, Illinois, USA, August 1993

[6] Casado C. et al. Implementation of passive and active vibration control on an in-service footbridge. Structural Control and health monitoring 20, Pages 70-87

[7] Peebles A. et al. Using force sensing insoles to predict kinetic knee symmetry during a stop jump. Journal of Biomechanics Volume 95, 11 October 2019, 109293

Study of the interaction phenomena between a slender structure and its passive mitigation devices

A. Magdaleno[1,2], J. Naranjo[2,3], A. Iglesias-Pordomingo[1], C. Peláez[1] and I. M. Díaz[2]

[1]*Escuela de Ingenierías Industriales, Universidad de Valladolid, Spain*
[2]*E.T.S. de Caminos, Canales y Puertos, Universidad Politécnica de Madrid, Spain*
[3]*Escuela Técnica Superior de Ingeniería, Universidad de Sevilla, Spain*

e-mail: alvaro.magdaleno@uva.es

A Tuned Mass Damper (TMD) is a device that is installed on a slender structure which is prone to oscillate under the effect of dynamic loading [1]. It is basically composed of a moving mass, m_t, and an elastic member that joins the mass to the structure, k_t, conferring it a certain natural frequency, ω_t, as shown in Figure 1. The main purpose of a TMD is to reduce the vibration level of the structure on which it is installed for a certain range of excitation frequencies. To do so, the TMD also has a damper, c_t, between the moving mass and the structure, in parallel with the elastic member, which helps to dissipate part of the energy it receives and provides a robust performance for the TMD. For the device to be efficient, the motion of both systems (TMD and structure) must be mechanically coupled. This is achieved by designing its elements (m_t, k_t, c_t) so the natural frequency of the TMD ($\omega_t^2 \approx k_t/m_t$) is close to the natural frequency of the structure to be mitigated [2]. When this happens, the TMD is said to be tuned to that specific structural mode so its contribution to the structural response is notably reduced.
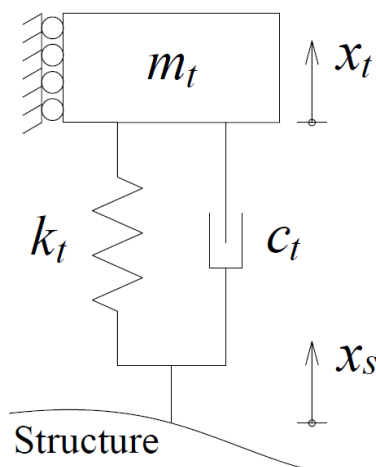
Figure 1. Schematics of a TMD installed on a structure [3]

One TMD can only efficiently mitigate the effect of a single mode at a time. If more than one structural mode is of concern, then several TMDs must be installed or another type of approach must be considered (active, semi-active, hybrid, etc.). In any case, the properties and position of each TMD can be determined in different ways, depending on which structural response parameter is to be reduced (displacement, acceleration, etc.). Each criterion leads to a different set of properties which are only valid for a relatively narrow frequency band, i.e., if the modal properties of the structure slightly change, or the natural frequency of the TMD is slightly modified, its efficiency may be drastically affected [4]. It is known that larger values of moving masses (m_t) lead to more robust designs which work efficiently in wider frequency bands. In addition, the amount of moving mass is directly related to the maximum attainable efficiency of the device, since more mass implies greater mitigation levels.

In this work, the interaction effects between different TMDs and between the TMDs and the structure are investigated. It is known that once a TMD is installed on the structure, its properties are modified. The modal properties of the mode being affected by the TMD are obviously drastically changed, since another mode appears due to the mechanical coupling between both. This affects not only the natural frequency and damping ratio, but also the generalized mass of the affected mode in the point and direction where the TMD is placed. This is due to several reasons, like the mass

addition caused by the non-moving parts of the TMD, the influence of the elastic member and the presence of the moving mass itself. The generalized mass being affected has a several impact on the tuning properties and the efficiency of the device, since it is that mass the one that is used as a reference for the different computations, instead for example of the total mass of the structure. Additionally, although less significantly, the presence of a TMD also affects other modes of the structure. If the other modes are close enough, this phenomenon may determine the properties of other TMDs installed to mitigate their effect. In other words, the design of a second TMD must include the effect of the first TMD and, ideally, both must be designed simultaneously to precisely take into account the mentioned interaction phenomena.

References

[1] S. Elias and V. Matsagar. Research developments in vibration control of structures using passive tuned mass dampers. *Annu. Rev. Control*, 44, 129:156, 2017. DOI: 10.1016/j.arcontrol.2017.09.015

[2] J. Ormondroyd and J.P. Den Hartog. The theory of the dynamic vibration absorber. *J. Appl. Mech.*, 50, 9:22, 1928.

[3] A. Magdaleno, C. Pelaez, A. Iglesias-Pordomingo and A. Lorenzana. On the estimation of the moving mass of a TMD installed on a lively structure. Appl. Sci., 11, 4712, 2021. DOI: 10.3390/app11104712

[4] F. Rahimi, R. Aghayari and B. Samali. Application of Tuned Mass Dampers for Structural Vibration Control: a state-of-the-art review. *Civ. Eng. J.*, 6, 1622:1651, 2020. DOI: 10.28991/cej-2020-03091571.

Session S7

Adaptive shock-absorbers for mitigation of impact and vibration

Organizers:

Robert Zalewski (*Warsaw University of Technology, Poland*)

Cezary Graczykowski (*IPPT PAN, Poland*)

Recent developments in inerter-based devices for vibration mitigation

David Wagg[1]

[1]*Department of Mechanical Engineering, University of Sheffield, Sheffield, United Kingdom*

e-mail: david.wagg@sheffield.ac.uk

1. Abstract

Unwanted vibrations occur in a range of important engineering application areas. For example, in civil engineering, tall buildings and structures can suffer from vibrations caused by earthquakes, tsunamis or strong winds. In the most severe cases, the human and economic consequences can be devastating. One of the most useful state-of-the-art techniques engineers can use to guard against this type of problem is called the tuned-mass-damper[1]. It is based on an idea patented by Hermann Frahm in 1909. Although many modifications and minor improvements to Frahm's idea have been suggested, nothing fundamentally changed until the advent of the *inerter*. The term inerter was first coined by Malcolm Smith [7] to represent a mechanical device that produced an inertia force from a relative acceleration. In fact, these type of devices had previously been known about for a range of other mechanical and civil engineering applications, but by different names.

In automotive and aerospace applications inerter-like devices have been used primarily as a vibration isolators, for example in engine mounts of cars, and helicopters since the 1960s — see [4] for details of this historical context and references. This included both mechanical and fluid based devices (for example hydramounts), that are used to try and minimise the amount of unwanted vibration that is transmitted to a passenger cabin — a technology that is still the state-of-the-art today. In the early 2000s, Smith and co-workers also developed the inerter concept for automotive applications, particularly suspension systems, with McLaren Formula-1 to great success, and mechanical inerters are now available commercially for performance motorsport [1].

The application of the inerter for vibration suppression has been intensively developed in recent years. This has been primarily based on devices made from three basic elements: inerter, damper, and spring, arranged in different configurations. There are three device configurations that have emerged as the most important for applications. The first to be introduced was the tuned-viscous-mass-damper (TVMD), described in detail in Ikago *et al.* [3]. The device consists of a parallel-connected inerter-viscous damper in series with a spring element, and at least one version of this device has been put into service in a real structure in Japan [8].

The second type of device is the tuned-inerter-damper (TID) which was proposed by Lazar *et al.* [5]. This device consists of a parallel connected spring and viscous damper in series with an inerter — an arrangement that is similar to that of a tuned-mass-damper with the mass element being replaced by an inerter. The third device was proposed is by Marian and Giaralis [6] and is called a tuned-mass-damper-inerter (TMDI). This device consists of a traditional tuned-mass-damper with an inerter attached to the mass element.

All these devices have been proven to have similar or better performance to the traditional tuned-mass-damper in terms of reducing the displacement amplitudes around the targeted resonance. In addition there are additional benefits compared to the TMD, e.g. the large reduction in mass ratio needed to achieve optimum performance.

These, and other points are detailed in the references cited above, and related literature. In this paper, we will focus on some of the more recent developments carried out at the University of Sheffield. Specifically, we will describe, the living hinge inerter [4], which is a solid-state device designed to eliminate all frictional elements (although not all energy loss). This device has been demonstrated on a vibration isolation experiment, and sample results are shown in Fig. 1. We will also discuss the development of a magnetorheological fluid inerter device [9] that is in the early stages of development. In addition, we will give insights into a new type of inerter device for suppression of machine tool vibration and chatter [2].

Finally, we will describe some recent results using a pivoted-flywheel inerter to suppress seismic excitations of a 3-storey frame structure. This device was constructed using gel-damper elements so that the damping

---

[1]It can also be called "tuned-vibration-absorber" or "tuned dynamic absorber".

behaviour was hysteretic rather than viscous. As a result, it is now possible to verify what type of behaviour occurs in practice when hysteretic rather than viscous damping is present in the system

In summary, the introduction of the inerter is the most exciting thing to happen in the passive vibration research field for 100 years! In this presentation, we will discuss the history and development of the inerter, including applications to a range of engineering problems. Specifically, we will discuss the three key inerter based devices. We will also describe recent work in developing new types of inerter systems, including recent experimental results.
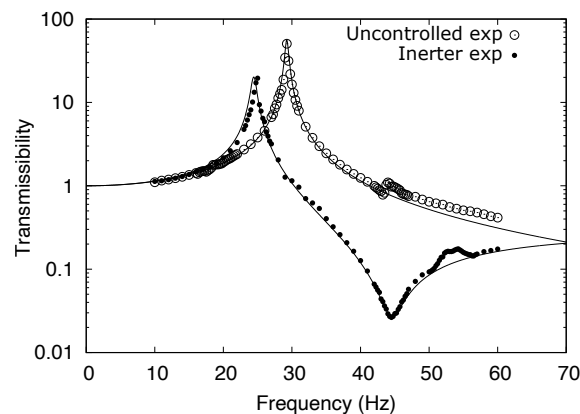
Figure 1: Example results from the living hinge inerter configured as a vibration isolation problem. The solid lines show the theoretical predictions of the transmissibility of the uncontrolled system and the system with inerter added. The experimental results are shown by open circles for uncontrolled, and solid black circles for the system plus inerter. The anti-resonance created by the inclusion of the inerter is clearly visible close to 43Hz.

References

[1] M.Z.Q. Chen, C. Papageorgiou, F. Scheibe, F-C. Wang, and M. C. Smith. The missing mechanical circuit element. *IEEE Circuits and Systems Magazine*, 9(1):10–26, 2009.

[2] H. Dogan, N. D. Sims, and D. J. Wagg. Investigation of the inerter-based dynamic vibration absorber for machining chatter suppression. In *Journal of Physics: Conference Series*, volume 1264, page 012030. IOP Publishing, 2019.

[3] K. Ikago, K. Saito, and N. Inoue. Seismic control of single-degree-of-freedom structure using tuned viscous mass damper. *Earthquake Engineering & Structural Dynamics*, 41(3):453–474, 2012.

[4] E. D. A. John and D. J. Wagg. Design and testing of a frictionless mechanical inerter device using living-hinges. *Journal of the Franklin Institute*, 356:7650–7668, 2019. https://doi.org/10.1016/j.jfranklin.2019.01.036.

[5] I. F. Lazar, S. A. Neild, and D. J. Wagg. Using an inerter-based device for structural vibration suppression. *Earthquake Engineering & Structural Dynamics*, 43(8):1129–1147, 2014. DOI: 10.1002/eqe.2390.

[6] L. Marian and A. Giaralis. Optimal design of a novel tuned mass-damper-inerter (tmdi) passive vibration control configuration for stochastically support-excited structural systems. *Probabilistic Engineering Mechanics*, 38:156–164., 2014.

[7] M. C. Smith. Synthesis of mechanical networks: the inerter. *IEEE Transactions on Automatic Control*, 47(10):1648–1662, 2002.

[8] Y. Sugimura, W. Goto, H. Tanizawa, K. Saito, and T. Nimomiya. Response control effect of steel building structure using tuned viscous mass damper. In *Proceedings of the 15th World Conference on Earthquake Engineering*, 2012.

[9] M. Tipuric, D. Wagg, and N. Sims. Magnetorheological bypass valve design for a semi-active inerter. In *Active and Passive Smart Structures and Integrated Systems XII*, volume 10967, page 109671L. International Society for Optics and Photonics, 2019.

ENERGY HARVESTING AND VIBRATION CONTROL USING ADAPTIVE SUSPENSION OF A PENDULUM TUNED MASS DAMPER

K. Kecik[1] and K. Serwin[1]

[1]*Department of Applied Mechanics, Lublin University of Technology, Lublin, Poland*

e-mail: k.kecik@pollub.pl

1. General

Typical dynamic vibration absorber (DVA) consists of a single degree of freedom system that is attached to the main structure to vibration control. A particular type of absorber is the so-called pendulum vibration absorber (known as pendulum tuned mass damper, PTMD) in which the oscillating secondary mass is a pendulum [1]. The natural frequency of PTMD is influenced by the pendulum parameters, and the pendulum's length is an additional tuning parameter. The main problem of using DVA is that the operating conditions or changes in excitation frequency may result in a mistuning of their natural frequency. One solution to this problem is to use an adaptive vibration absorber taht improves the vibration attenuation performance by adjusting its resonant frequency .

Simultaneous vibration control and energy harvesting (regenerative vibration control [3]) look attractive for potential applications. Mechanisms s used in energy harvesters (EH). Therefore, it is naturally using the same device for both effects. As we can see previously, the harvester added to the PTMD does not reduce the effectiveness of vibration reduction. However, the recovered energy is relatively low. The semi-active suspension of PTMD has the potential to improve the efficiency of the vibration control/energy harvesting effect by increasing the useful frequency bandwidth and output power [2].

The paper presents a dual-functional system by integrating the PTMD and EH lead to pendulum tuned mass damper energy harvester (PTMDEH). To improve the effectiveness the adaptive suspension consists of the magnetorheological damper and SMA spring is used. The numerical results have been verified by experiment tests.

2. Description of the PTMDEH

The key idea of the PTMDEH is shown in Fig. 1. The system consisted of the host structure (main system) with added the pendulum harvester. The design of the harvester is based on the two ring fixed magnets (top and bottom) and the oscillating magnet consists of stacked magnets. All magnets are mounted on the non-magnetic rod teflon coated. This concept reduces the friction problem and the magnet's rotation effect compared to our previous concepts. Magnets are arranged to produce repellant forces of each other. The use of multiple mag-
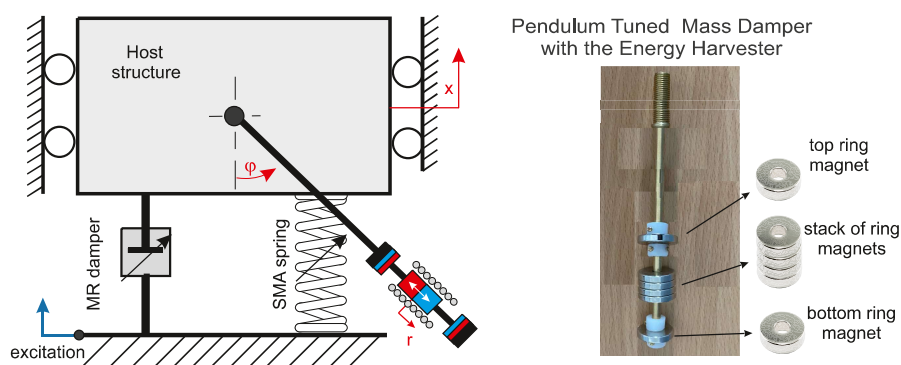
Figure 1: Pendulum tuned mass damper energy harvester

nets or change in the magnet distances influences the repulsive forces and natural frequency of the oscillating magnet.

The PTMDEH can be modelled as the nonlinear oscillators, the pendulum absorber and the electrical circuit. To improve the effectiveness of proposed system, the adaptive (semi-active) suspension consists of the SMA spring and MR damper is proposed. The SMA Ikuta's model is used to describe the behaviour of the theoretical stiffness, while the modified Bingham's model is applied for the MR damper. The influence of electromechanical coupling and semi-active elements on vibration mitigation and energy harvesting is studied in detail.

3. Results

Figure 2 shows the exemplary resonance curve for the host structure, the pendulum, and the recovered current. The case of response for the stable solution is marked by the solid line, while the unstable corresponds to the dashed line. The activation of the pendulum absorber (red line) causes oscillation of the host structure. The black line denotes the semi-trivial solution,i.e. the host structure and the magnet oscillate, but the pendulum is at rest. The vibration mitigation effect occurs for a frequency of 37-50 rad/s.
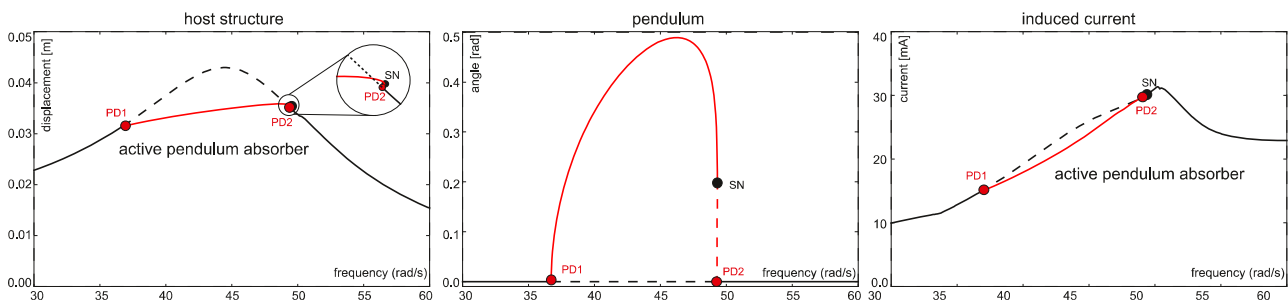
Figure 2: Frequency response curve (FRC) of the main system, the pendulum absorber and the induced current. PD means the period doubling bifurcation and SN denotes saddle-node bifurcation points.

However, if the pendulum absorber operates, the induced current is also reduced. The application of adaptive suspension and modification in electromechanical coupling can be used to extend the frequency bandwidth and improve the induced energy.

References

[1] Gino Bertollucci Colherinhas, Francesco Petrini, Marcus Vinícius Girao de Morais, and Franco Bontempi. Optimal design of passive-adaptive pendulum tuned mass damper for the global vibration control of offshore wind turbines. *Wind Energy*, 24(6):573–595, 2021.

[2] Krzysztof Kecik. Numerical study of a pendulum absorber/harvester system with a semi-active suspension. *ZAMM - Journal of Applied Mathematics and Mechanics / Zeitschrift für Angewandte Mathematik und Mechanik*, 101(1):e202000045, 2021.

[3] Xiudong Tang and Lei Zuo. Simultaneous energy harvesting and vibration control of structures with tuned mass dampers. *Journal of Intelligent Material Systems and Structures*, 23(18):2117–2127, 2012.

EXPERIMENTAL VALIDATION OF VIBRATION CONTROL PERFORMANCE AND SENSOR PLACEMENT IN A FRAME STRUCTURE WITH SEMI-ACTIVE JOINTS

G. Mikułowski[1], B. Popławski[1], and Ł. Jankowski[1]

[1]*Institute of Fundamental Technological Research, ul. Pawińskiego 5B, Warsaw, Poland*
e-mail: gmikulow@ippt.pan.pl

1. Scope

This contribution presents a study dedicated to performance assessment of a vibration mitigation system designed for a frame structure equipped with semi-active joints. The joints allow for a controllable transfer of bending moments between the frame members. The control approach belongs to the class of Prestress-Accumulation Release algorithms [1]. The investigation is based on an experimental approach and is carried out on a laboratory demonstrator. The rendered issues discussed in the study comprise topics related to the optimal control signal synchronisation, sensor placement and performance assessment of the system.

2. Semi-active joint

An important part of the described approach is a semi-active joint concept [2] dedicated for slender frame structures (Fig. 1). The design of the device allows for connecting three neighbouring beams of a frame. One of the connectors allows for a short-lasting controllable limitation of the transferred moments, while the remaining two transfer them continuously in a passive manner. It is assumed that the joints are activated with a time delay short enough to allow for synchronisation of the control system with the dynamic response of the structure. In practice, the effect could have been achieved by utilization of piezoelectric stacks as actuators.
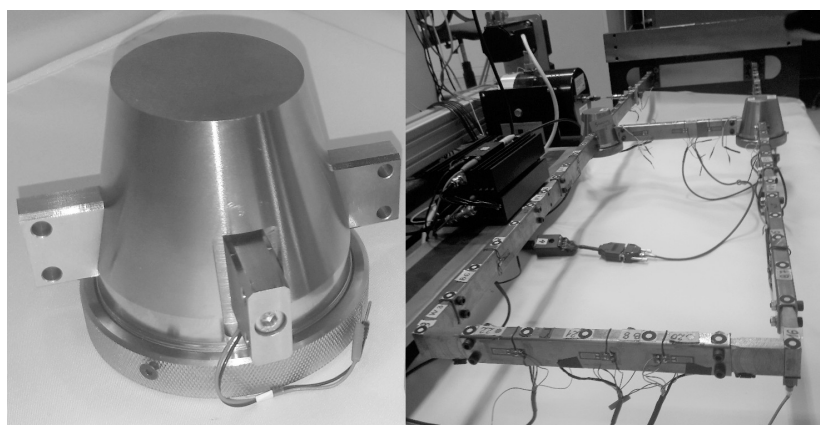
Figure 1: Semi-active joint (left) and the demostrative frame (right)

3. Control approach

A synchronous application of structural reconfiguration is the aim of the presented control approach. The control algorithm assumes synchronisation between the control signal application and the dynamic response of an object [3]. The objective of the strategy is to minimise the strain energy level in the structure and obtain an effect of transferring the vibration energy towards the higher frequency range. The high frequency structural eigenmodes are effectively mitigated with passive means of damping (e.g., material damping,

polymer layers). Therefore, the aim here is to mitigate the low frequency dynamic responses of the structures, which are recognised as the most challenging in reduction. The application of a short lasting decrease of the bending moment transmission in the joints results in decreasing the level of the accumulated internal energy related to deformation. A conducted optimisation procedure has shown that the optimal time instant for the reconfiguration takes place at the maximum of the internal energy.

4. Methodology

The study is based on an experimental investigation conducted on a laboratory demonstrator in the form of a cantilever frame (Fig. 1). The demonstrator is equipped with a pair of the described semi-active joints and a feedback controller allowing for application of the procedure in real-time. The study consists of a modal identification of the object and its spectral testing in a variety of conditions. The obtained frequency response functions have been calculated from the data acquired under free and forced excitations as well as in passive and in semi-active modes of operation.

5. Results

The conducted investigation validates the theoretically derived control strategy, reveals a significant effectiveness of the system in mitigation of vibrations and verifies the methods for sensor placement dedicated to the considered case.
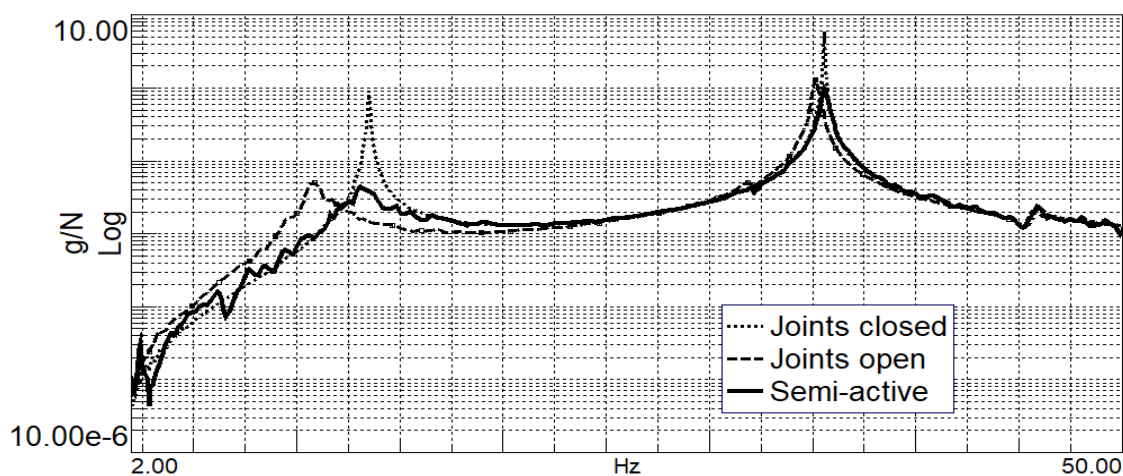
Figure 2: Dynamic responses of the demonstrator under random forced excitation in three modes of operation: joints closed, joints open, semi-active.

References

[1] Z. Marzec, J. Holnicki-Szulc, Strategy of impulse release of strain energy for damping of vibration, in: Proc. of NATO Advanced Research Workshop "Smart Structures", pp. 111–114, 1998.

[2] B. Popławski, G. Mikułowski, A. Mróz, Ł. Jankowski, Decentralized semi-active damping of free structural vibrations by means of structural joints with an on/off ability to transmit moments, *Mechanical Systems and Signal Processing*; 100:926–939, 2018.

[3] G. Mikułowski, B. Popławski, Ł. Jankowski, Semi-active vibration control based on switchable transfer of bending moments: study and experimental validation of control performance, *Smart Materials and Structures*, 30:045005(14pp), 2021.

THE PROTOTYPE, MATHEMATICAL MODELLING AND OPTIMIZATION OF ADAPTIVE TUNED PARTICLE IMPACT DAMPER

M. Żurawski[1], C. Graczykowski[2], and R. Zalewski[1]

[1]*Institute of Machine Design Fundamentals, Warsaw University of Technology, Warsaw, Poland ,*
[2]*Institute of Fundamental Technological Research, Polish Academy of Sciences, Warsaw, Poland*

e-mail: Mateusz.Zurawski@pw.edu.pl

1. Introduction

The contribution presents a short description of the novel controllable device called Adaptive Tuned Particle Impact Damper (ATPID). Such device allows to effectively reduce mechanical vibrations of the beam element under various types of excitations. The whole construction can be considered as an extension of the classical Particles Impact Damper (PID) [1, 2, 3], in which container height can be changed (in real time) by the movement of the ceiling controlled by a simple electromechanical system. The ATPID operation is determined by particle flight time and particle-container contact duration [4], which depend on actual container height. Therefore, control of the damper height is crucial from the vibration mitigation point of view.

2. ATPID construction and modelling

The conducted research consists of experimental and numerical part. The experimental part concerns construction and prototype of the proposed ATPID damper (Fig. 1a). The specially designed test stand (Fig. 1b) allows to study response of the beam vibration under harmonic excitation of a wide frequency range.

Fig. 1 a) ATPID model, **b)** Experimental test stand, **c)** Scheme of the ATPID construction

The numerical part of research is devoted to mathematical modelling, sensitivity analysis and optimization of the ATPID damper. The scheme of the ATPID construction (Fig. 1c) is used to derive governing equations, which take the form:

(1)
$$m_s \ddot{x}_s + F_{ext} - F_{ATPID}(x_s, x_g, \dot{x}_s, \dot{x}_g, h, \dot{h}) + Q_s = 0$$

(2)
$$m_g \ddot{x}_g + F_{ATPID}(x_s, x_g, \dot{x}_s, \dot{x}_g, h, \dot{h}) + Q_g = 0$$

where: m_s - mass of the base system, m_g - mass of the grain, F_{ext} - harmonic excitation, F_{ATPID} - the total force forces generated by the ATPID, x_s - displacement of base system, x_g - displacement o the grain, h - height of the damper, Q_s and Q_g - gravity forces acting on the system and grain, respectively. The total force generated by the ATPID damper F_{ATPID} depends on forces exerted during impacts of the grain against cylinders walls (Eq. 3). Both these forces are modelled using soft contact theory [5 and 6] and nonlinear viscoelastic model of impact (Eqs. 4 and 5):

(3)
$$F_{ATPID}(x_s, x_g, \dot{x}_s, \dot{x}_g, h, \dot{h}) = -F_{c_1}(x_s, x_g, \dot{x}_s, \dot{x}_g) + F_{c_2}(x_s, x_g, \dot{x}_s, \dot{x}_g, h, \dot{h})$$

$$(4) \qquad F_{c_1}(x_s, x_g, \dot{x}_s, \dot{x}_g) = k_c \xi_{c_1}{}^{3/2} + c_c \dot{\xi}_{c_1} \xi_{c_1}{}^{1/4}$$

$$(5) \qquad F_{c_2}(x_s, x_g, \dot{x}_s, \dot{x}_g, h, \dot{h}) = k_c \xi_{c_2}{}^{3/2} + c_c \dot{\xi}_{c_2} \xi_{c_2}{}^{1/4}$$

In the mathematical model the moveable ceiling is implemented by using time-dependent function of the damper height $h(t)$ defined by Eq. 6. Such parameter is described by initial minimal value of the height h_{min} (diameter of the grain), the controllable range Δh and control function $\psi(t)$:

$$(6) \qquad h(t) = h_{min} + \Delta h \psi(t)$$

The proposed ATPID model is validated against experimental results. Moreover, the model allows to disclose the principles of the ATPID operation, investigate the influence of the selected parameters on the damping ability and to conduct optimization process of ATPID parameters.

The change of damping effectiveness of the proposed device is revealed by displacements of the beam under resonant excitation, corresponding to five different controllable ranges of the damper heights (Fig. 2). The obtained results show the increase of damping ability with an increase of the maximal absorber height. In particular, in considered case, the vibration reduction of up to 90 % can be observed for the height $h(t) = 0.212\ m$. The larger container heights result in rumble effect, which decreases vibration mitigation ability.
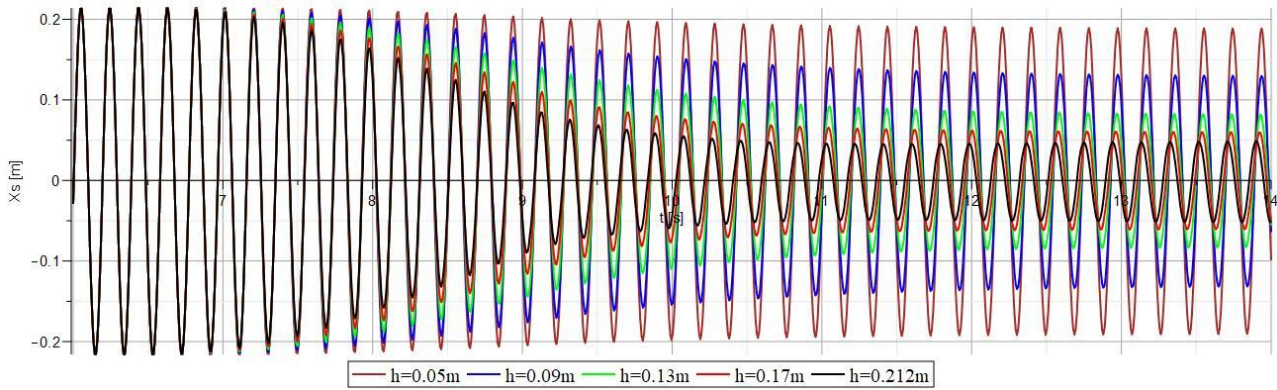
Fig. 2 Beam displacements for various maximal container heights

3. Conclusions

The proposed ATPID damper with controllable container height provides high damping effectiveness for a wide range of harmonic excitations of various frequencies and amplitudes. Therefore, it can be considered as promising solution mitigation of vibrations of various engineering structures. The further research in this field will be dedicated to development of various control algorithms and application of the ATPID damper in multi-degree of freedom systems.

References

[1] L. Gagnon, M. Morandini, and G. Ghiringhelli, A review of particle damping modelling and testing. Journal of Sound and Vibration, 2019, doi: 10.1016/j.jsv.2019.114865.
[2] Z. Lu and Z. Wang and Y. Zhou and X. Lu, Nonlinear dissipative devices in structural vibration control: A review. Journal of Sound and Vibration, 2018, doi: 10.1016/j.jsv.2018.02.052.
[3] Binoy M.Shah et al., Semi-active particle-based damping systems controlled by magnetic fields. Journal of Sound and Vibration, 2011, doi: 10.1016/j.jsv.2010.08.009.
[4] M.R. Duncan and C.R. Wassgren and C.M. Krousgrill, The damping performance of a single particle impact damper. Journal of Sound and Vibration, 2005, doi: 10.1016/j.jsv.2004.09.028
[5] A. Di Renzo and F. P. Di Maio., Comparison of contact-force models for the simulation of collisions in DEM-based granular ow codes. Chemical Engineering Science, 2004, doi: 10.1016/j.ces.2003.09.037.
[6] H. Kruggel-Emden et al., Review and extension of normal force models for the Discrete Element Method. Powder Technology, 2007, doi: 10.1016/j.powtec.2006.10.004.

Concept of smart multiaxial vacuum packed particles impact damper

P. Bartkowski[1], R. Zalewski[1]

[1]*The Institute of Machine Design Fundamentals, Warsaw, Poland*

e-mail: piotr.bartkowski@pw.edu.pl

Abstract

The conceptual design of smart crash energy absorber made of Vacuum Packed Particles (VPP) is presented in this work. The absorber can change the flexural stiffness and as a result the amount of dissipated energy depending on the impact conditions. Since VPP have the properties that allow to reverse the plastic deformation the absorber can be used many times in a different working modes.

The term Vacuum Packed Particles (VPP) [1, 2] refers to a structure that is composed of a plastomer granular material with granules having a diameter of about 1−5mm. They are typically semi-finished products used in the production of packaging of liquid beverages or plastic cutlery. The loose granules are enclosed in a hermetic, flexible sleeve and when air is pumped out of it, by a suitable valve mounted on the body surface, an underpressure is generated causing controllable changes in the mechanical and rheological properties of the system. A VPP typically behaves as a plastic material at the atmospheric pressure and as a solid when the underpressure is greater. They feature typical properties of a solid, such as tensile or compressive and shear strengths, damping capacity, internal "intergranular" friction and the ability to absorb energy under impact. These are all non-linear functions of the internal underpressure. It is of importance to note that all the physical and mechanical or rheological changes induced by the underpressure are fully reversible upon restoring atmospheric pressure. Indeed, such a material can almost instantaneously, only depending on the rate of the vacuum pump, be solidified and plasticized by supplying and removing air. The example of sample made of VPP is presented on fig. 1.

Fig. 1 Sample made of VPP

In this paper the numerical and experimental results of VPP impact absorber are presented. At the beginning the basic results of VPP are presented. In the next part Authors show the concept of absorber that was tested in laboratory. Parallel to experimental test the modelling work were performed. The examples of the numerical results are shown on figure 2.
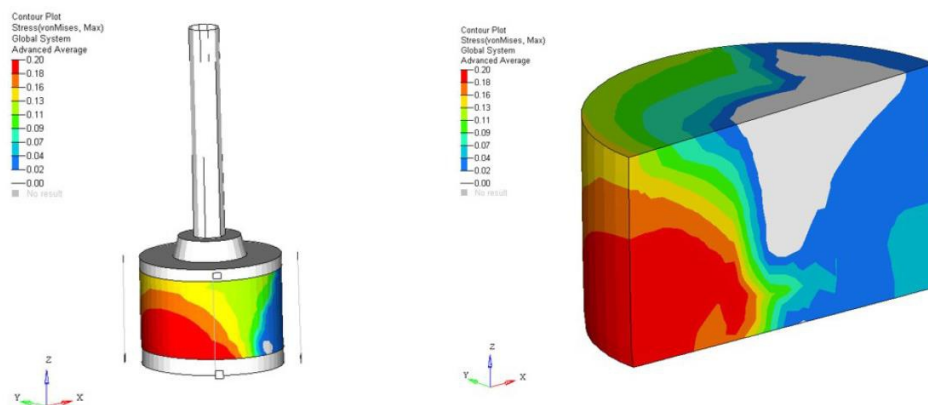
Fig. 2 Results of numerical simulation

In the final stage of the paper Authors proposed to used absorber as a smart parking post. The simulation crash tests with a vehicle were conducted and it was confirmed that it is possible to change to interaction between the vehicle and absorber by changing the underpressure.

The issues presented in this paper proved that it is possible to implement VPP into active energy absorbers and to control their response by changing the underpressure value. Due to the simplicity of the VPP structures and the controlling devices it can be concluded that the active VPP absorbers can be an attractive alternative to the commonly available devices.

References

[1] Bajkowski, J. M., Dyniewicz, B., and Bajer, C. I. (2015). Damping properties of a beamwith vacuum-packed granular damper. *Journal of Sound and Vibration*, 341:74 – 85.
[2] Zalewski, R. and Szmidt, T. (2014). Application of special granular structures for semiactive damping of lateral beam vibrations. *Engineering Structures*, 65:13–20.

HYBRID CONTROL OF SMART BASE-ISOLATED STRUCTURES UNDER MULTI-HAZARD SCENARIOS

D. H. Zelleke[1], and V. A. Matsagar[2]

[1]*Indian Institute of Technology* (*IIT*) *Delhi, Hauz Khas, New Delhi* – 110 016, *India.*
e-mail: daniel.habtamu@alumni.iitd.ac.in
[2]*Indian Institute of Technology* (*IIT*) *Delhi, Hauz Khas, New Delhi* – 110 016, *India.*
e-mail: matsagar@civil.iitd.ac.in

1. Introduction

The base isolation technique has proved to be an effective strategy for earthquake protection of structures. Although there are numerous studies on the earthquake response control of structures using base isolation, there is limited research on the performance of the base isolation technique under non-seismic excitations. Notably, some researchers [1,2] have studied the behavior of base-isolated buildings under blast-induced ground motion (BIGM) and shown that base isolation could be used to mitigate the response of structures under BIGM. However, a recent study [3] has shown that the behavior of structures equipped with passive elastomeric and sliding bearings could be different under earthquake ground motion (EQGM) and BIGM. Studies performed considering wind excitation have also shown that the increased flexibility introduced due to the isolators could make base-isolated buildings vulnerable under wind load (WL) [3].

The applications of passive hybrid base isolation systems (e.g., simultaneous application of base isolation and tuned mass damper (TMD)) for the response control of structures have been studied by some researchers. However, the response of base-isolated structures equipped with semi-active tuned mass dampers (SATMDs) under multi-hazard scenarios is not investigated yet. Therefore, this study investigates the application of a hybrid response control strategy composed of elastomeric base isolators and SATMDs for the multi-hazard response mitigation of structures.

2. Multi-story structure equipped with hybrid base isolation system

This study considers a multi-story structure equipped with laminated rubber bearings (LRBs) and SATMDs. The idealized mathematical model of the smart base-isolated structure is shown in Figure 1. The SATMD used in this study is considered to be equipped with a variable orifice viscous damper whose damping can be adjusted in real-time using a semi-active response control algorithm. The equations of motion of the structure equipped with the semi-active hybrid isolation system are given in the state-space form as

$$
(1) \quad \begin{Bmatrix} \dot{\bar{X}} \\ \ddot{\bar{X}} \end{Bmatrix} = \begin{bmatrix} \bar{\mathbf{0}} & I \\ -\bar{M}^{-1}\bar{K} & -\bar{M}^{-1}\bar{C} \end{bmatrix} \begin{Bmatrix} \bar{X} \\ \dot{\bar{X}} \end{Bmatrix} + \begin{bmatrix} \bar{\mathbf{0}} \\ -\bar{M}^{-1} \end{bmatrix} \begin{Bmatrix} -f_b \\ \mathbf{0}^T \\ 0 \end{Bmatrix} + \begin{bmatrix} \bar{\mathbf{0}} \\ -\bar{M}^{-1} \end{bmatrix} \begin{Bmatrix} f_d \\ \mathbf{0}^T \\ -f_d \end{Bmatrix} + \begin{bmatrix} \bar{\mathbf{0}} \\ \bar{M}^{-1} \end{bmatrix} \bar{F}_{exc} .
$$

Here, the force in the laminated rubber bearing is given as $f_b = c_b \dot{x}_b + k_b x_b$, where k_b and c_b, respectively, are the stiffness and damping constant of the isolator. Moreover, x_b and $\dot{x}_b$, respectively, are the displacement and velocity of the base mass with respect to the ground, and $\bar{F}_{exc}$ is the excitation vector.

3. Multi-hazard response of smart base-isolated structures

The semi-active component of the control force in the TMD at a time instant can be computed in real-time as $f_d = c_d \dot{x}_d$, where c_d is the damping constant of the variable orifice damper and $\dot{x}_d$ is the velocity of the TMD mass with respect to the base mass. In this study, a recently developed semi-active control algorithm, i.e., the energy-based predictive (EBP) algorithm [4,5], is adapted to control the semi-active damper in the

smart base isolation system. Accordingly, the instantaneous TMD damping constant ($c_{d,i}$) is given as

$$(2) \qquad c_{d,i} = c_{d,Max} H \left(E_{m,p2} - E_{m,p1} \right),$$

where $H(\bullet)$ is the Heaviside step function; $c_{d,Max}$ is the maximum damping constant that the variable orifice damper can provide; and $E_{m,p1}$ and $E_{m,p2}$ are the predicted mechanical energies of the base-isolated building corresponding to $c_d = c_{d,Max}$ and $c_d = 0$, respectively.

A deterministic response assessment of the smart base-isolated structure is conducted under independent multi-hazard scenarios involving EQGM, BIGM, and WL. The effectiveness of the presented smart base isolation strategy in controlling the response of the structure under the three hazards is evaluated in comparison with that of the passive base isolation system. Moreover, a stochastic investigation is performed considering uncertainties in the hazards to study the fragility of the base-isolated structures under the considered multi-hazard scenarios. The results of the study show that the proposed smart base isolation strategy reduces the response of the multi-story structure more compared to the passive base isolation systems. Furthermore, the comparisons of the fragilities of the base-isolated structures indicate that the smart base isolation strategy leads to reduced probabilities of failure compared to the passive isolation system.
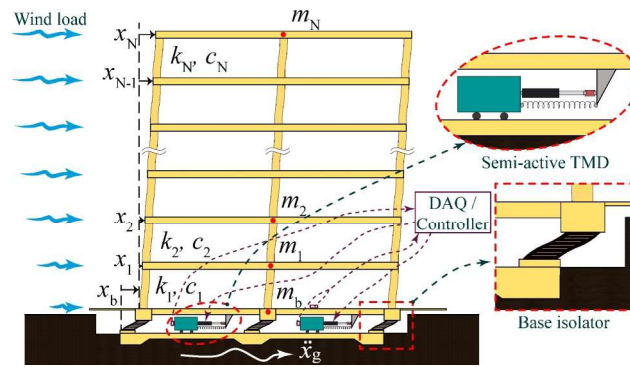
Figure 1: The mathematical model of a multi-story structure equipped with hybrid base isolation under ground motion and wind force.

4. Conclusions

The hybrid smart base isolation strategy is superior in reducing the response of the structure under the multi-hazard scenarios compared to both the passive hybrid isolation system and passive base isolation system without TMD. Furthermore, the implementation of the smart base isolation strategy reduces the fragility of the structure. Importantly, the semi-active control strategy enhances the multi-hazard performance, and it is especially useful in catering to the contradicting effects of the different hazards.

References

[1] P. D. Mondal, A. D. Ghosh, and S. Chakraborty. Performance of N-Z systems in the mitigation of underground blast-induced vibration of structures. *Journal of Vibration and Control*, 20(13):2019-2031, 2013.

[2] P. D. Mondal, A. D. Ghosh, and S. Chakraborty. Performances of various base isolation systems in mitigation of structural vibration due to underground blast-induced ground motion. *International Journal of Structural Stability and Dynamics*, 17(04):1750043, 2017.

[3] D. H. Zelleke, S. K. Saha, and V. A. Matsagar. Multi-hazard response control of base-isolated buildings under bi-directional dynamic excitation. *Shock and Vibration*, 2020:1-24, 2020.

[4] D. H. Zelleke and V. A. Matsagar. Semi-active algorithm for energy-based predictive structural control using tuned mass dampers. *Computer-Aided Civil and Infrastructure Engineering*, 34(11):1010-1025, 2019.

[5] D. H. Zelleke and V. A. Matsagar. Energy-based predictive algorithm for semi-active tuned mass dampers. *The Structural Design of Tall and Special Buildings*, 28(12):e1626, 2019.

Nonlinear Adaptive Inverse Control for Real Time Hybrid Simulation

T. Simpson[1], V. Dertimanis[1], and E. Chatzi[1]

[1]*Chair of Structural Mechanics and Monitoring, Institute of Structural Engineering, Department of Civil, Environmental and Geomatic Engineering, ETH Zurich, Switzerland*

e-mail: {simpson, v.derti, chatzi}@ibk.baug.ethz.ch

1. Introduction

Real-time hybrid simulation has been an experimental framework of considerable interest to research in the last 20 years. Whilst RTHS has great potential for capturing the full complexity, notably with regards to rate dependency, of nonlinear physical subsystems in hybrid testing, it also brings with it a host of difficulties [2]. The constraint of real-time solution of the system, requires that the numerical system be solvable within the chosen control time step, resulting in challenges with regards to model order reduction. With regards to the physical substructure, the real-time aspect results in considerable challenges regarding accurate control of the actuators used for excitation.

This control problem is the principle interest of this work, the accurate reconstruction of the control signal at the actuators. The hard real-time constraint considerably increases the difficulty of this problem compared to a traditional pseudo-dynamic hybrid simulation. Issues arise as a result of the dynamics of the control system itself as well as the control-structure interaction. These effects must be compensated for in order to accurately reconstruct the control signal and to eliminate time delay from the control signal. This problem is only exacerbated when we consider nonlinearity in the physical specimen and the development of a robust control regime for RTHS is an area of intensive research.

Virtual RTHS (vRTHS) provides a convenient framework for the development and testing of novel hybrid simulation algorithms at low cost and preparation time. In previous work by the authors, a vRTHS framework was used to demonstrate the utility of adaptive inverse control (AIC) methods for the problem of actuator dynamics compensation in hybrid simulation [5]. It was demonstrated on a benchmark problem, that AIC demonstrated good performance in compensating for controller and controller/structure dynamics, and exhibited robustness to various input signals, partitioning schemes and parametric uncertainties. The method demonstrated also has the advantage of being purely data-driven, no models of the plant are required and only a small number of hyper-parameters must be tuned for good performance. This work, however, was limited in scope to a linear plant model and linear finite impulse response (FIR) filters for the control scheme. In this work, we demonstrate a nonlinear AIC method for the control of a nonlinear plant model within a vRTHS framework.

2. Methodology

In traditional linear AIC, we face the problem of identifying an FIR filter $G^{-1}(z)$ of the form

$$(1) \qquad G^{-1}(z) = \sum_{i=0}^{N} g_i z_{n-i}$$

which when cascaded with the plant, $G(z)$, and a pure delay, $z^{-\Delta}$, results in a unitary transfer function, i.e.,

$$(2) \qquad z^{-\Delta} G^{-1}(z) G(z) = 1$$

In nonlinear AIC, the linear FIR filters used to approximate the forward and inverse plant models, are replaced by nonlinear functions. Such an extension of AIC to the nonlinear domain was demonstrated by Widrow et al. [4], in which neural networks are used as nonlinear estimators in replacement of the FIR filters. Concretely the response of the inverse controller, in the linear version expressed by the FIR filter in equation 1, is now
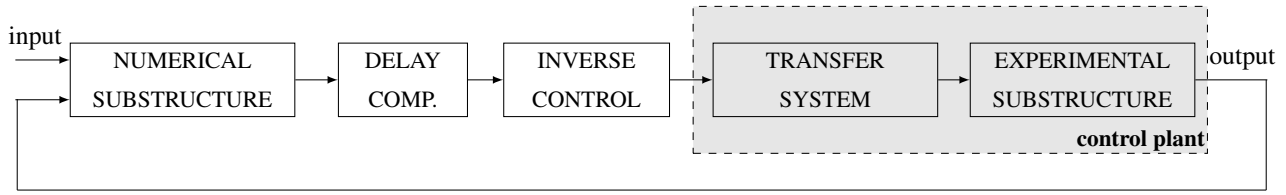
Figure 1: The RTHS loop

expressed by a neural network as

$$(3) \qquad g(z) = f(W^T z + b)$$

The output of the nonlinear filter, $g(z)$, is calculated by the matrix multiplication of a trainable weights matrix W with the vector of previous input values, z, with the addition of a trainable bias vector, b. A nonlinear "Activation function" is then applied to this. Such a neural network model has been shown to be incredibly powerful for the modelling of nonlinear systems [3], especially with the use of "deep neural network" architectures [1] wherein this procedure of matrix multiplication followed by application of a nonlinear function is repeated multiple times before the output is predicted.

3. Application

In this work, we demonstrate the use of nonlinear adaptive inverse control in a vRTHS framework featuring a nonlinear plant model exhibiting a hysteretic type nonlinearity. The scheme consists of a 2 DOF shear frame structure model, where the lower story is considered as the numerical substructure, to which excitation is applied in the form of seismic input. The upper story is considered to be the physical substructure, while both the lower and upper stories exhibit nonlinearity in the form of Bouc-Wen hysteresis. For the purpose of the vRTHS all physical components of the system, including actuators and analog-to-digital and digital-to-analog converters, as well as the two substructures themselves, are taken into account, as depicted in figure 1. The performance and robustness for the nonlinear AIC control scheme is assessed for various inputs with regards to recreation of the control signal at the actuator.

References

[1] Yoshua Bengio and Yann Lecun. *Scaling learning algorithms towards AI*. MIT Press, 2007.

[2] P. Benson Shing. *Real-Time Hybrid Testing Techniques*, pages 259–292. Springer Vienna, Vienna, 2008.

[3] J. Park and I. W. Sandberg. Universal approximation using radial-basis-function networks. *Neural Computation*, 3(2):246–257, 1991.

[4] G.L. Plett. Adaptive inverse control of linear and nonlinear systems using dynamic neural networks. *IEEE Transactions on Neural Networks*, 14(2):360–376, 2003.

[5] Thomas Simpson, Vasilis K. Dertimanis, and Eleni N. Chatzi. Towards data-driven real-time hybrid simulation: Adaptive modeling of control plants. *Frontiers in Built Environment*, 6, 2020.

ALGORITHM FOR REAL-TIME IDENTIFICATION OF FAULTS IN SEMI-ACTIVE SUSPENSION

M. Makowski[1], L. Knap[1], C. Graczykowski[2]

[1]*Institute of Vehicles and Construction Machinery, Warsaw University of Technology,*
Narbutta 84, 02-524 Warsaw, Poland
[2]*Institute of Fundamental Technological Research, Polish Academy of Sciences,*
Pawińskiego 5B, 02-106 Warsaw, Poland

e-mail: michal.makowski1@pw.edu.pl

1. Introduction

In recent years semi-active and active suspensions are more often used in automotive vehicles, which contributes significantly to driving comfort and safety of users. The key component of semi-active vehicle suspension is a controllable damper and an electronic controller, which allows for the generation of control signals and changes of damper characteristics. In order determine the correct values of the control signals, the dedicated algorithms taking into account assumed control criterion and the signals from a number of sensors are used. Generally, two opposing control criteria are adopted: comfort and safety. The first one is based on minimization of vehicle body acceleration, while the second one is based on minimization of variation in vertical wheel forces acting on the road surface. With the control occurring up to 1000 times per second, the vehicle's semi-active or active suspension system can be to some extent resistant to disturbances caused by damper's damage. Therefore, one of the most important problems in vehicle diagnostics is to detect and recognize different types of dampers' damages adequately early in order to prevent dangerous traffic incidents.

2. Suspension fault identification algorithm

In this paper we investigate the possibility of identifying the changes in parameters of vehicle suspension while driving. Such assessment of the vehicle's suspension state enables detection of potential dampers' faults and allows the driver to consider the need for service. The preliminary results indicate that based on well-tuned mathematical model of the suspension and measurements of selected physical quantities, we are able to assess the suspension condition in real-time. The basic scheme of suspension parameters identification algorithm is shown in Figure 1.
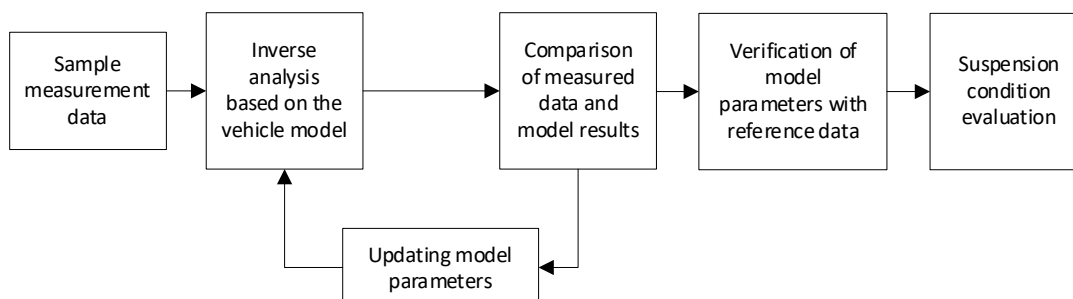
Figure 1. General algorithm for evaluating vehicle suspension condition.

The method assumes that it is possible to develop a mathematical model of the undamaged suspension (e.g., for a new vehicle) and identify a range of acceptable values of its parameters. In particular, it is possible to determine the values of parameters describing vehicle's mass and damping forces generated by the applied

dampers. The algorithm starts with measurement of selected physical quantities, including suspension deflection, vehicle body's and wheel's acceleration. Based on measurement data and developed suspension model it is possible to conduct inverse analysis providing preliminary identification of model parameters. This allows to compare the values of deflections and accelerations from the model with measured data, and to update model parameters accordingly. After final identification of the actual values of the model parameters, the algorithm compares them with the preliminarily determined range of acceptable parameters. In the case of differences exceeding the permissible variance, it informs a driver about a damage to the vehicle suspension and its severity.

The operation of the proposed algorithm for identification of the faults in semi-active suspension will be demonstrated using hydraulic damper with a piezoelectric valve [1], presented on experimental test stand in Figure 2a. The results of exemplary numerical tests conducted using developed mathematical model indicate significant difference in damper response resulting from changes in damping coefficient and stroke clearance (Figure 2b). As it will be shown, such results can be effectively used for precise identification of the changes in damper parameters and detection of damper faults. In addition, we will present the simplified version of the identification algorithm which does not require full numerical model of the damper.
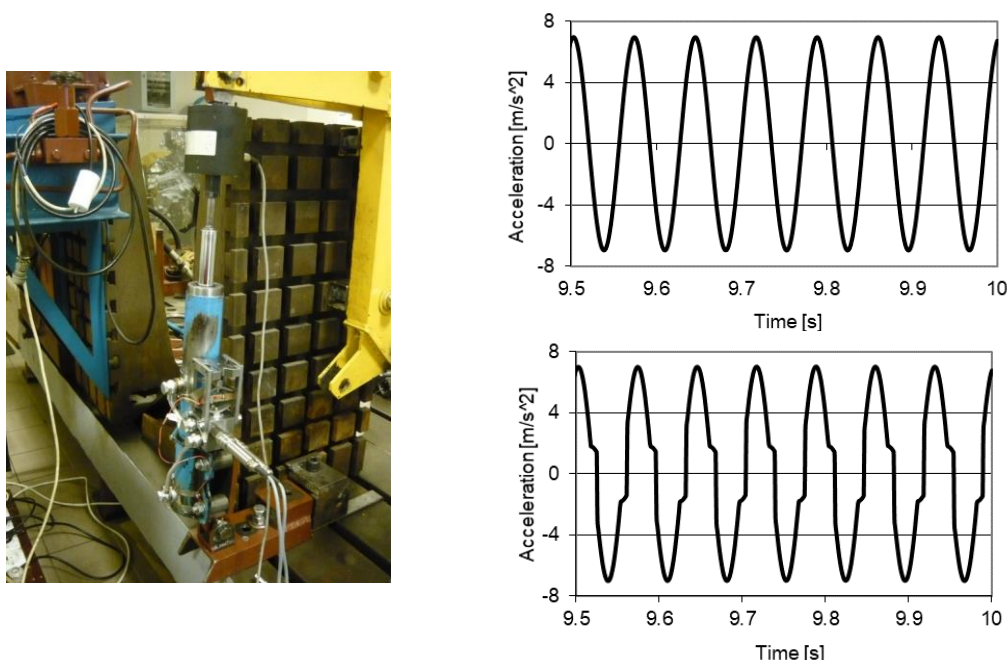
Figure 2. a) View of the PZD damper with the piezoelectric valve on experimental test stand, b) exemplary numerical results presenting vehicle body accelerations in case of damping coefficient $\gamma=0.2$ and two different values of clearance: top – clearance $\Delta=0$ m, bottom - clearance $\Delta=0,002$m.

3. Conclusions

In this contribution we propose a novel algorithm for the identification of the parameters of dampers used in vehicle's suspensions. We show that proposed algorithm is operates effectively and can be successfully used to diagnose the actual state and the potential faults of vehicle suspension while riding.

References

[1] M. Makowski, L. Knap. Study of a Controlled Piezoelectric Damper. *Sensors, Vol. 21 (10)*, 1:20, 2021.

ANALYSES OF THE RESCUE CUSHION DESIGN – SENSITIVITY STUDY

R. Faraj[1], B. Popławski[1], D. Gabryel[1], T. Kowalski[1] and K. Hinc[1]

[1]*Institute of Fundamental Technological Research, Warsaw, Poland*
e-mail: rfaraj@ippt.pan.pl

1. Introduction

The contribution presents analyses of a rescue cushion, the system which is based on an airbag (Fig. 1a) and is used by Fire Brigades for evacuation of people from high altitudes. A person landing on the airbag compresses the air enclosed in its volume, what results in an increase of the pneumatic force. The compressed gas is simultaneously released by a number of vents located on the side surfaces of the rescue cushion. As a result, the impact corresponding to touchdown is significantly reduced and its harmful effects are limited. Two types of rescue cushions are available on the market. The first type, which is a subject of presented research, is a system based on the inflatable frame. The second alternative is represented by a group of constantly powered rescue cushions, which are inflated with a use of special fans. Impact absorption effectiveness of the latter devices is typically higher than for the frame-based systems. On the other hand, they are less compact and more complicated from a technical point of view. Because of that, the rescue cushions inflated by fans are mainly used in geographical areas where the heights of buildings exceed 20 m.
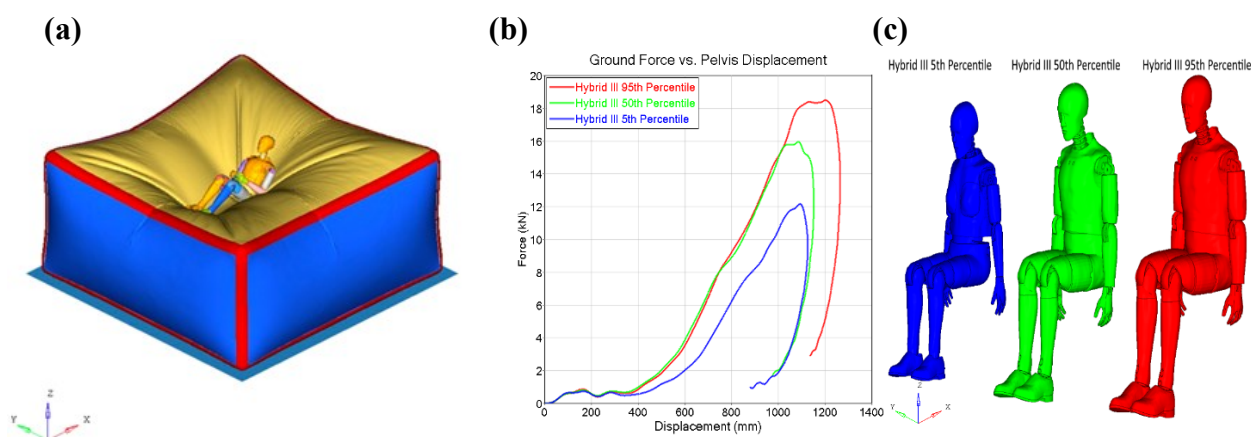
Figure 1: a) dummy landing on the airbag – visualization of the numerical model, b) force responses of the rescue cushion, c) models of dummies used for computation of the system response [3].

2. Possible improvements of the rescue cushion

Every rescue cushion introduced to the market has to meet a number of functional, operational and legal requirements. Moreover, efficiency of the impact mitigation is evaluated by drop tests, during which strictly specified reduction of decelerations acting on a head, chest and pelvis has to be ensured [1]. The construction of currently used rescue cushions with inflatable frame is based on the idea introduced over 30 years ago by Peter Lorsbach in his patent [2]. All requirements mentioned above make the process of rescue cushion design very challenging. Probably, this is the reason why a number of solutions available on the market is limited.

Within this contribution the influence of selected system parameters is investigated and the possibilities for improvement of the rescue cushion's performance are analysed. The discussion is based on numerical simulations conducted in LS-DYNA and ABAQUS software environments, where the models of the airbag with inflatable frame are implemented. Results of the parametric study are used to elaborate concepts for

system adaptation. The effectiveness of adaptation methods is evaluated with the use of appropriately selected impactors and models of dummies (Fig. 1c), which relates to 5th, 50th and 95th percentile in terms of people height and weight [3]. According to the conducted analyses, significant reduction of the impact loading can be obtained for all considered cases. Discussed results include simulations in case of different heights of evacuation as well as different masses of the landing person.

3. Conclusions

The presented work concerns the analyses of the rescue cushion, which is equipped with the inflatable frame. Using the results of numerical simulations the selected adaptation mechanisms are proposed. As a result, the response of the airbag can be improved for the range of impact conditions. The effectiveness of proposed solutions is evaluated with the use of different models of dummies, which are dropped from various heights. Based on presented results it can be concluded that the concept of adaptive rescue cushion has been introduced and it provides adaptation to both the height of evacuation and the mass of landing person.

References
[1] DIN 14151-3, Rescue cushions - Part 3: Jumping cushion type 16 - Requirements, testing, 2016-08.
[2] Lorsbach P., Jump Rescue Aparatus, patent US4875548, 1986-04-24.
[3] Mohan P., Park C.-K., Marzougui D., Kan C.-D.,Guha S., Maurath C., and Bhalsod D., "LSTC/NCAC Dummy Model Development", 11th International LS-DYNA Conference, Dearborn, Michigan, June 2010.

New strategy for the safety and comfort of the passengers and aircraft crew during atmospheric turbulence

Daniela Enciu, Ioan Ursu, George Tecuceanu

INCAS – National Institute for Aerospace Research "Elie Carafoli"
220 Iuliu Maniu Bd., 061126 Bucharest, Romania
e-mail: enciu.daniela@incas.ro

Abstract

An airplane trip can be psychological terrifying for any traveler. If, during the flight, the airplane meets a turbulent air front, then the scenario is perfect for a Hollywood movie, and the panic among passengers increases proportionally with the severity of the turbulence. In this paper, a new approach of the turbulence mitigation methodology is proposed based on a solid background using an active control vibration. The experimental model is represented by a realistic, elastic airplane wing model controlled by an electric linear servoactuator. The mathematical model is completed by numerical simulations and experiments in the subsonic wind tunnel upgraded with a turbulence generator. The qualification of an emergent technology of this type will have double impact: for the passengers – safety and mental comfort increasing given by the significant reduction of the dynamic effects produced by the turbulent field; for the airplane – weight optimization based on the loads control generated by the atmospheric turbulence.

Keywords:

atmospheric turbulence, clear-air turbulence, subsonic wind, turbulence generator, active control, vibration mitigation, smart wing, aileron control

1. Introduction

The current context of climate change is a difficult challenge for humanity and brings major modifications in the way the activities are conducted in various fields, including aeronautics. Thus, the destruction of the ozone layer, the rising temperatures, sudden changes in temperature lead to imbalances in the air masses that are reflected in aircraft infrastructure damage and performance deterioration leading to flight cancellations, delayed or rerouting of flights, increased fuel consumption, and high costs dedicated to aircraft maintenance [1,2]. Some of the most significant changes are taking place in tropopause area where the jet streams are meet and where the most of the civil aircraft fly. The jet streams underlie the appearance of areas with atmospheric turbulence, especially of Clear-Air Turbulence (CAT) [3, 4]. The specific character of CAT is that it is found in areas without clouds, in areas where no turbulence can be detected by the usual methods, e.g. LIDAR, being a surprise element for pilots. Such accidents caused by turbulence are more and more common. No less than 91 CAT events were recorded between 01 April 2018 and 25 June 2021, https://www.spacescience.ro/projects/contur/index_en.html.

Although CAT is a phenomenon studied in the literature, no methods have yet been found to warn that the aircraft is entering such an area. Therefore, it is necessary to develop active control methods to attenuate the effect of vibrations.

2. Experimental set-up and results

The experimental set-up consisted in the design and manufacture of an intelligent wing, in obtaining a turbulence generator, and in the synthesis of an adequate active control law. The specific case of the wing is given by the realistic and elastic model, unlike the models found in the literature. The wing is composed of a longeron covered by an aerodynamic layer. The electric broadband servoactuator is represented by a moving coil linear actuator whose role is to convert the linear motion of the actuator into an incomplete rotational movement of the aileron hinge in both directions.

The implemented control algorithm was based on the emerging technology of synthesis of the mathematical model of the wing by experimental identification and by the LQG and robust $\mathcal{H}_\infty$ control laws. The control algorithms have as a starting point the identification of the transfer functions in the wind tunnel, for several air speeds.

Significant results for the performance of active control laws for vibration attenuation are summarized in Fig. 1 and Fig. 2. A reduction of about 18 dB at the basic modal frequency 5 Hz, for both laws, for the air speed of $V = 25$ m/s, can be seen in Fig. 1. Here, AC and UC means active control, and un-controlled, respectively, for both control laws $\mathcal{H}_\infty$ and LQG. Vibration attenuation in the event of a turbulent atmospheric environment is shown in Fig. 2.
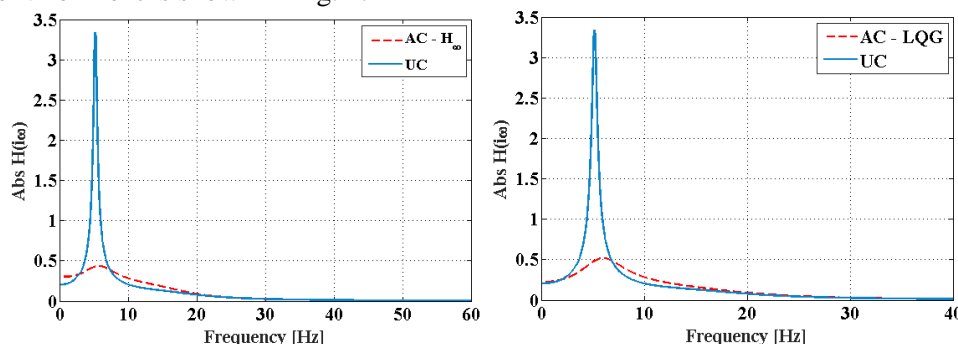
Fig. 1. Attenuation of approx. 18 dB of the first spectral frequency. Left: robust $\mathcal{H}_\infty$ control law; right: LQG control law
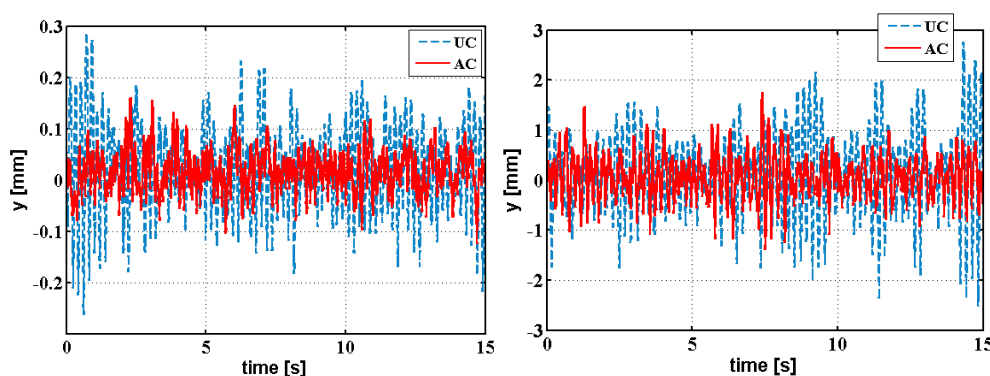
Fig. 2. Left: aileron displacement in the subsonic tunnel, at the air velocity of $V = 25$ m/s, clear air, for robust $\mathcal{H}_\infty$; right: the same set-up, but with turbulence

3. Conclusion

The active control applied to the wing reduces the load and the bending moments being a suitable method, along with a proper design of the wing, for vibration attenuation and flight envelope expansion. Moreover, the effect of turbulence in the wind tunnel is increased by an order of magnitude compared with the low level of vibrations in the absence of the turbulence generator.

References

[1] European Aviation Environmental Report TO-01-18-673-EN-N, 2019. http://dx.doi.org/10.2822/309946
[2] E. Coffel, R. Horton. Climate change and the impact of extreme temperatures on aviation. *Weather Clim Soc* 2015;7(1):94-102. https://doi.org/10.1175/WCAS-D-14-00026.1
[3] G.P. Ellrod, A. Knox, P.F. Lester, L.J. Ehernberger. *Clear Air Turbulence*. In North GR, Pyle J, Zhang F, editors. Encyclopedia of atmospheric sciences: Elsevier; 2015;1:177-186. http://dx.doi.org/10.1016/B978-0-12-382225-3.00104-3
[4] P.D. Williams. Increased light, moderate, and severe Clear-Air Turbulence in response to climate change. *Adv Atmos Sci* 2017;34: 576-586. https://doi.org/10.1007/s00376-017-6268-2

OPTIMAL AND PREDICTIVE CONTROL OF SEMI-ACTIVE FLUID-BASED DAMPERS UNDER IMPACT EXCITATION

C. Graczykowski[1], R. Faraj[1]

[1]*Institute of Fundamental Technological Research, Polish Academy of Sciences, Warsaw, Poland*

e-mail: cezary.graczykowski@ippt.pan.pl

1. Introduction

Semi-active fluid-based dampers consist of two chambers filled with hydraulic or pneumatic fluid and connected by the orifice, which is equipped with fast-operating valve controlling the actual rate of fluid flow. The most often used types of fluid-based shock-absorbers are semi-active hydraulic and pneumatic dampers with fast electro-mechanical or piezoelectric valves. These devices can be used in both vibration suppression problems and impact mitigation problems. Although many control strategies have been successfully developed for protection against vibration, the problem of optimal impact absorption has not gained sufficient attention of researchers and has not been completely solved so far.

2. General formulation of the impact mitigation problem

In the considered impact absorption problem the damper is subjected to the impact of a rigid object of mass M moving with initial velocity v_0 and external force $F_{ext}(t)$, as shown in Fig. 1a. The objective of the control problem is to find the change of valve opening in time $A_v(t)$, which provides absorption and dissipation of the entire impact energy with minimal value of total discrepancy between force generated by the absorber F_{abs} and its theoretical optimal value F_{abs}^{opt}, see Fig. 1b (black and red lines, respectively).
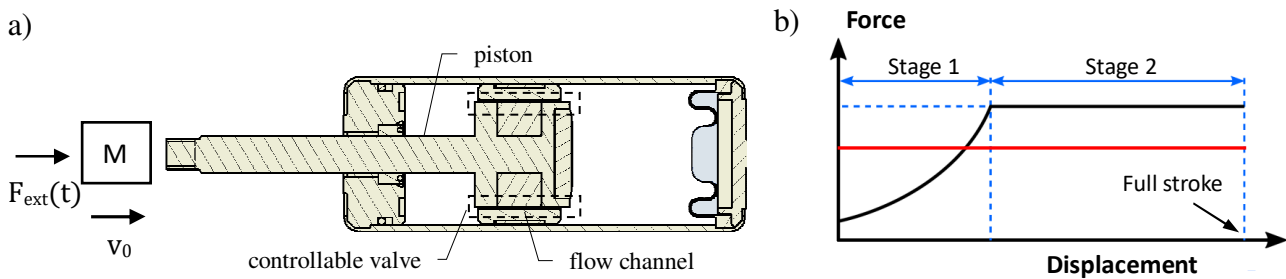
Fig. 1: a) The problem considered: damper subjected to the impact excitation, b) force-displacement characteristics: red – theoretical optimal force, black – schematic optimal change of force obtained using pneumatic damper

The direct mathematical formulation of the impact mitigation problem, which has been studied in detail by the authors reads:

(1a) $\quad$ Minimize: $\int_0^T \left(F_{abs}(A_v(t),t) - F_{abs}^{opt} \right)^2 dt$

(1b) $\quad$ With respect to: $A_v(t) \geq 0$

(1c) $\quad$ Subject to: $\int_d \vec{F}_{abs} d\vec{s} = E_{imp}^0 + E_{imp}^{ext} = \frac{1}{2} M v_0^2 + \int_d \vec{F}_{ext} d\vec{s}$

The solution of the above control problem is straightforward (and for pneumatic damper assumes the form shown in Fig. 1b) only in a very special case when: a) no limitations on maximal valve area and valve operation speed are considered, b) the impact excitation is a priori known and the theoretical value of optimal force F_{abs}^{opt} can be directly calculated. In the opposite situation, the solution of the impact mitigation problem requires application of the advanced methods of control theory. In particular, the control problem with valve operation constraints requires the optimal control methods, while the control problem with unknown excitations and disturbances requires the paradigm of Model Predictive Control.

3. Optimal control of dampers with valve operation constraints

The exact solution of the impact mitigation problem taking into account valve operation constraints can be found when impact excitation (impacting object mass, its initial velocity and time-history of external force) are entirely known before the process. In such a case, the theoretical optimal value of force F_{abs}^{opt} equals:

$$(2) \qquad F_{abs}^{opt} = \frac{Mv_0^2}{2d} + \frac{\int_d \vec{F}_{ext} d\vec{s}}{d}$$

where d is absorber stroke. Consequently, the problem of optimal impact absorption takes the form:

$$(3a) \qquad \text{Minimize: } \int_0^T \left[F_{abs}(A_v(t), t) - \left(\frac{Mv_0^2}{2d} + \frac{\int_d \vec{F}_{ext} d\vec{s}}{d} \right) \right]^2 dt$$

(3b)   With respect to: $A_v(t)$ such that $A_v(t) \in \langle A_v^{min}, A_v^{max} \rangle$ and $\frac{dA_v(t)}{dt} \leq V_v^{max}$

(3c)   Subject to: condition of energy absorption (1c)

The above formulation constitutes classical optimal control problem, which can be solved using the Pontryagin's maximum principle and direct methods based on discretization of the control function in time and conversion to the classical optimization problem. Implementation of both methods entails different challenges, which will be briefly analyzed and discussed.

4. Predictive control of dampers subjected to unknown impact excitation

In the situation when the external excitation is not a priori known, the above force-based formulation and the corresponding optimal control methods cannot be directly applied. Instead, the problem has to be reformulated into its kinematic version, the so called *state-dependent path-tracking*, based on minimization of the actual and currently optimal value of deceleration, which is continuously updated during the process:

$$(4a) \qquad \text{Minimize: } \int_0^T \left[\ddot{u}(A_v(t), t) + \frac{\dot{u}(t)^2}{2(d - u(t))} \right]^2 dt$$

(4b)   With respect to: $A_v(t)$ such that $A_v(t) \in \langle A_v^{min}, A_v^{max} \rangle$ and $\frac{dA_v(t)}{dt} \leq V_v^{max}$

(4c)   Subject to: condition of energy absorption (1c)

In such a case, the efficient approach is application of Model Predictive Control, which assumes repetitive solving of the control problems defined at finite time horizons of arbitrary length Δt:

$$(5) \qquad \text{Minimize: } \int_{t_i}^{t_i + \Delta t} \left[\ddot{u}(A_v(t), t) + \frac{\dot{u}(t_i)^2}{2(d - u(t_i))} \right]^2 dt$$

The approximate solution of this problem can be based on the proposed by the authors methods including Hybrid Prediction Control (HPC) [1] and Adaptive Model Predictive Control (AMPC) [2]. The HPC provides efficient impact mitigation by using system kinematics measurements, prediction of the valve operation mode and prediction of the required change of valve opening. In turn, the AMPC additionally utilizes equivalent model parameters which compensate the presence of disturbances in order to improve system performance at each control step. Both these methods will be discussed in detail during presentation.

References

[1] R. Faraj and C. Graczykowski. Hybrid prediction control for self-adaptive fluid-based shock-absorbers. *Journal of Sound and Vibration*, 449:427 – 446, 2019.

[2] C. Graczykowski and R. Faraj. Adaptive Model Predictive Control of semi-active shock-absorbers under impact excitation, under review.

EXPERIMENTAL VERIFICATION OF THE KINEMATIC CONTROL FOR PNEUMATIC IMPACT ABSORBER

R. Wiszowaty[1], R. Faraj[1], G. Mikułowski[1], and C. Graczykowski[1]

[1]*Institute of Fundamental Technological Research Polish Academy of Sciences, Pawińskiego 5B, Warszawa, Poland*

e-mail: rwisz@ippt.pan.pl

1. Scope of investigations

The subject of this contribution is a pneumatic absorber developed for protection of mechanical systems under impact excitation. The absence of oil evaporation as well as the reduction of environmental pollution makes dry pneumatic systems attractive in selected industrial applications [1] [2]. Therefore their development may occur to be advantageous.

The presented results concern the method of braking objects that are initially in motion. Investigated technique of bringing to stop the body of mass M involves the use of pneumatic cylinder equipped with piezoelectric valve (fig. 1). The purpose of the valve application is to enable control of the flow from the space being contracted with the piston movement inside the sleeve to the expanded space. This flow is regulated to minimize top value of the reaction force.
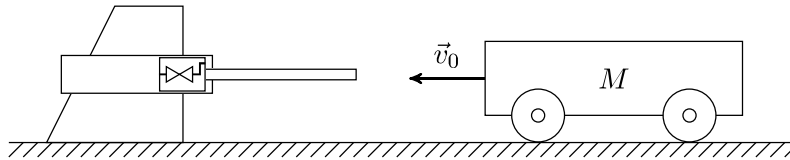
Figure 1: Mode of operation of the pneumatic cylinder applied as a bumper

Presented results cover both the theoretical investigations and the laboratory verification of the impact energy dissipation with adaptation to different values of the impact parameters.

2. Dynamic-based and kinematic-based adaptation to the impact

Control of the absorber may by performed in two ways [4] [3]:

- estimation of the initial kinetic energy of moving body and maintaining the adequate force vs distance travelled dependency,

- estimation of the velocity of moving body and maintaining the adequate deceleration.

Both these methods are based on the demand of utilization the whole admissible piston stroke. In order to make them resistant to unexpected perturbations during the braking process, real-time measurements of the system kinematics and relevant force control are required.

The presented work is focused on the latter method – fully kinematic problem.

3. Control method

The data including the object velocity v and the remaining distance x_{rem} of the piston inside the sleeve is sufficient to compute the required object deceleration: $|\ddot{x}_{req}| = \frac{v^2}{2x_{rem}}$. This value is compared with the measured deceleration and the controller opens or closes the valve – dependently on the result of this comparison. Here no assumptions about the friction or contact element rheological properties are required because the controller

does not use the model of the system. The main assumption taken, both in the numerical simulation and in the controller-implemented algorithm, is the absence of mechanical shock effects at the very first period of collision. During system modelling any vibrations are neglected while in the real system the data supplied to the controller was filtered.

4. Configuration of the set-up and the main results

The method of adaptive impact energy dissipation with the use of the controllable pneumatic absorber was investigated on drop test stand (fig. 2). In each experiment the carriage supported on vertical linear guide system was dropped and braked by the absorber attached to it. Tests were executed by various drop heights and carriage masses. Also remaining distance x_{rem} in the controller-implemented algorithm was modified. The

Figure 2: Experimental set-up
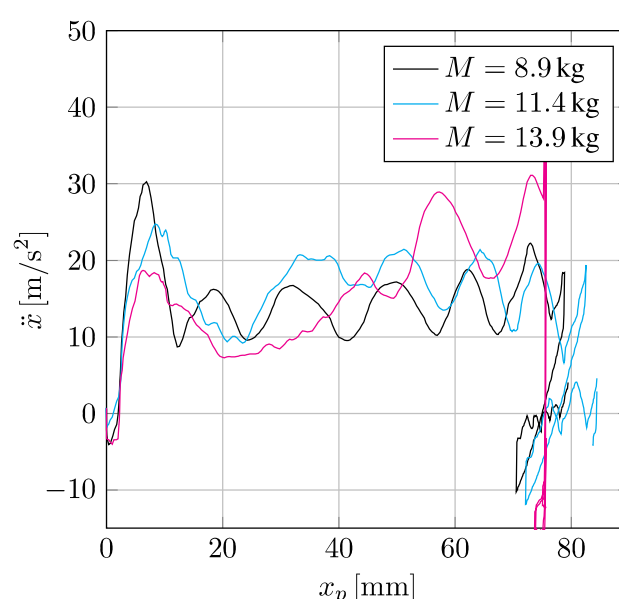
Figure 3: Exemplary dependencies of carriage deceleration vs piston displacement

exemplary results of deceleration control are depicted in fig. 3. In these cases the carriage was equipped with various weights; drop height was equal to $150\,\text{mm}$. The oscilations around the desired deceleration value visible on each plot are the result of compliance of the contact element and delays in the valve response to the digital control: each rising slope responds to the force increase caused by gas compression with piston movement inside the sleeve. During experimental series was stated the absorber robustness to variability of rubber or foam separator placed between coliding elements.

References

[1] BOGE Kompressoren. Sprężone powietrze w przemyśle spożywczym. *Pneumatyka*, (2/39):12–13, 2003.

[2] Konrad Cempel and Waldemar Skorczyk. Metal Work dla przemysłu spożywczego – technika KANIGEN. *Pneumatyka*, (3/52):12–13, 2005.

[3] Rami Faraj and Cezary Graczykowski. Hybrid prediction control for self-adaptive fluid-based shock-absorbers. *Journal of Sound and Vibration*, 449:427 – 446, 2019.

[4] Cezary Graczykowski and Rami Faraj. Development of control systems for fluid-based adaptive impact absorbers. *Mechanical Systems and Signal Processing*, 122:622 – 641, 2019.

THE USE OF CONTROLED DAMPER WITH THE PIEZOELECTRIC VALVE IN CONTROL OF VEHICLE VIBRATIONS

L. Knap[1], M. Makowski[1]

[1]*Institute of Vehicles and Construction Machinery, Warsaw University of Technology,*
Narbutta 84, 02-524 Warsaw, Poland
e-mail: lech.knap@pw.edu.pl

1. Introduction

Although vehicles have been designed and built for many years, the emergence of new materials, technologies as well as fast and efficient electronic measurement and control systems cause that design of vehicles, and their components is constantly improved. One of the main vehicle systems which affects the safety and comfort of passengers is the vehicle suspension. More and more vehicles are equipped with different types of semi-active suspensions, which allows to change driving characteristics depending on the current road conditions. The operation of this type of suspension requires the use of controlled dampers. Key to the effective and efficient operation is application of the dampers with a sufficiently short response time to the control signal and large range of changes in damping force.

2. Controlled damper with piezoelectric valve (PZD)

In the article we present selected problems related to the design and investigation of a hydraulic damper equipped with a valve controlled by a piezoelectric actuator. The presented results are a continuation of the previous research on the design of laboratory dampers [1]. Thanks to the appropriate construction of the designed and built valve and short response time of the piezoelectric element it is possible to quickly change the size of the gap through which oil flows between the chambers of the damper. A change in the size of the gap causes a change in flow resistance, which corresponds to a change in the generated damping force. The PZD damper with piezoelectric valve mounted in the Ford Transit suspension is shown in Fig. 1, while Fig. 2 shows the achieved characteristics of the controlled damper and the range of variation of the damping forces.

Figure 1. View of the PZD damper with the piezoelectric valve and its installation in the suspension of a Ford-Transit vehicle.
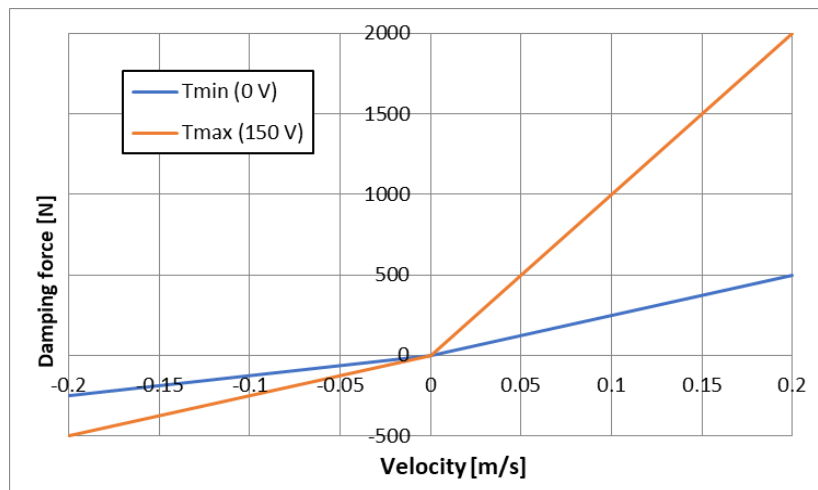
Figure. 2 Characteristics of silencer PZD installed in Ford Transit: T_{min} – no supply, T_{max} - voltage 150 V.

3. Road experimental tests

The above-mentioned Ford Transit with PZD dampers was subjected to a series of road tests During the tests, the damper control algorithm (with the comfort criterion) presented in [2] and [3] were used. The road tests were conducted on two different road sections at different speeds. Moreover, different strategies of damping force control were used to compare the effectiveness of the developed semi-active suspension with original passive suspension. In the Table 1 the results of the tests in relation to the requirements of the ISO 2631 standard - which defines acceptable exposition times (maximum time allowed) at the criterion of comfort, inconvenience, or harmfulness - are summarized and compared.

Speed [km/h]	Allowed time of exposition (hours)					
	Original damper			PZD damper with control		
	Comfort	Inconvenience	Harmfulness	Comfort	Inconvenience	Harmfulness
45	0h 58'	8h 37'	24h 00'	2h 24'	21h 44'	24h 00'
60	0h 20'	2h58'	11h 48'	0h 33'	5h 01'	20h 07'
90	0h 15'	2h 08'	8h 30'	0h 13'	1h 59'	7h 59'

Table 1: Allowed time of exposition according to the standard ISO 2631.

The road test results show that the developed damper with piezoelectric valve allows for a significant increase in the exposition time associated with vehicle body vibration and the influence on the driver and passenger (?) at 45 and 60 km/h. However, it is apparent that the developed control algorithm slightly deteriorates the driving conditions at 90 km/h. This disadvantage could be avoided by implementing sensors for road roughness recognition in front of the vehicle and adequate control the dampers' properties in advance. Another way to improve the efficiency of the damper with piezoelectric valve can be extension of the control characteristics range shown in Figure 2.

References

[1] M. Makowski, L. Knap. Study of a Controlled Piezoelectric Damper. *Sensors, Vol. 21 (10)*, 1:20, 2021.
[2] M. Makowski, L. Knap. Investigation of an off-road vehicle equipped with magnetorheological dampers. *Advances in Mechanical Engineering, Vol. 10 (5)*, 1:11, 2018.
[3] M. Makowski, L. Knap. Reduction of wheel force variations with magnetorheological devices. *Journal of Vibration and Control, Vol. 20 (10)*, 1552:1564, 2014.

Optimal vibration-absorber network identification: an approach based on graph theory

H. He[1], Y. Li[1], J. Z. Jiang[1], S. G. Burrow[2], S. A. Neild[1], and A. T. Conn[1]

[1]*Department of Mechanical Engineering, University of Bristol, Bristol, UK*
[2]*Department of Aerospace Engineering, University of Bristol, Bristol, UK*

e-mail: z.jiang@bristol.ac.uk, yuan.li@bristol.ac.uk

1. Introduction

Passive vibration absorbers, traditionally comprising springs, dampers and masses, play a vital role in improving the dynamic performance of mechanical structures, e.g., enhancing vehicle riding quality, reducing noise from the engine and minimizing track wear induced by rail-wheel interactions. In 2002, a new passive element termed 'inerter' was introduced [1]. It fundamentally enlarges the network possibilities of passive absorbers, but also arises a question: how to identify the optimum one among them?

Traditional absorber designs (e.g., [2]) first propose a network layout and then tune parameter values of each element for a better performance. The advantage is the complexity of the network topology can be pre-determined. However, despite there are countless possible network layouts, only one can be covered at a time by this approach. Another design approach (e.g., [3]) can identify the optimal one without restricting the networks in a few possibilities, whereby one first obtains the positive-real immittance function providing the optimum performance, and then uses the network synthesis to identify the corresponding network layout and element values. The problem is unrealisable networks, such as one with excessive number of components or unfeasible component parameter values, could be obtained. A new design method [4] enables the identification of the optimum one among all network possibilities with a given complexity, which preserves the advantages of both two traditional approaches. However, only series-parallel networks can be covered (bridge networks are not covered), and most importantly there is no programmatic implementation, which means the network generation cannot be automated. To this end, this paper proposes an automated process based on graph theory to generate the full set of networks given a pre-determined number for each element type (not restricted to series-parallel ones). Genetic optimization algorithms, e.g., patternsearch, can then be adopted to identify the optimal one within the full set.

2. Methodology

In the proposed approach, the network of the absorber will be presented by a *graph*, where the connection point of elements is modelled as a *vertex* and the element as an *edge* between two vertices. To distinguish two physical terminals with other internal nodes, the vertices representing the physical terminals are labelled *red* while others are labelled *blue*. The element type is presented by giving each edge with different weights. For example, the weights of springs, dampers, and inerters are one, two and three respectively in this study.

In graph theory, the *simple graph* is a graph that does not have more than one edge between any two vertices and no edge starts and ends at the same vertex. The *multigraph* is a graph permitted to have multiple edges between two vertices but no edge starts and ends at the same vertex. The *weighted multigraph* is a multigraph where each edge is assigned with a weight. With these definitions, the enumeration of absorber networks with a pre-determined number for each element type can be converted to the enumeration of a set of weighted multigraphs with a fixed number of edges. There are three nested loops in the enumeration process as shown in Figure 1, where the inner loop enumerates all simple graphs with N_e edges and two vertices are labelled red, the intermediate loop enumerates all multigraphs with N edges by adding parallel edges to the obtained graphs, and the outer loop enumerates all weighted multigraphs with N edges by assigning properties to each edge. In each loop, the isomorphism will be checked to reduce the redundancy. Besides, some network constraints, such as no self loops and the edges with the same weight cannot be in series, will also be checked.
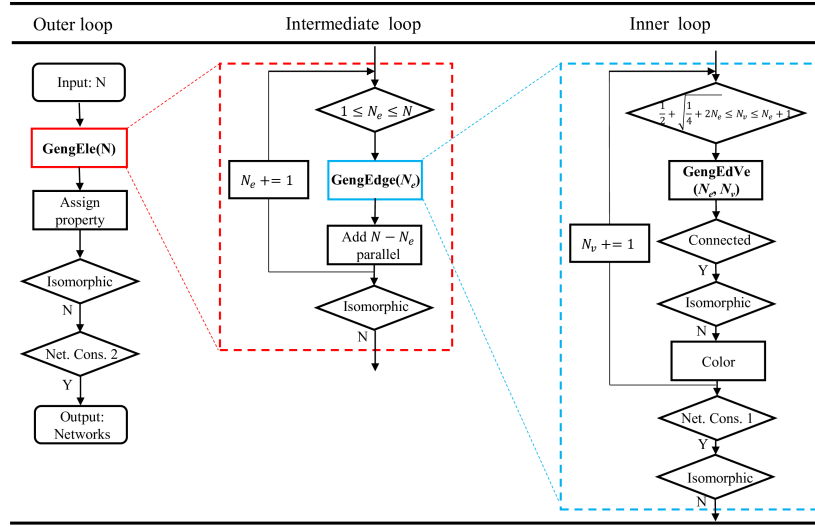
Figure 1: The programmatic approach to enumerate all networks with a given number of each element type.
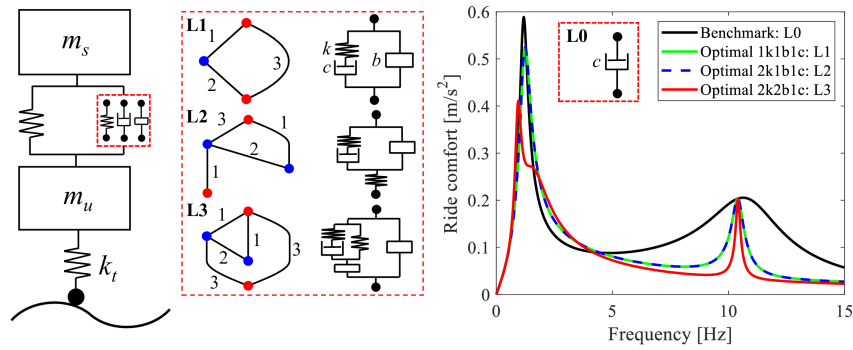
Figure 2: Quarter-car model, optimal networks with graph representations, and obtained optimal ride comfort.

3. Results and Conclusions

To compare with the existing approach in [4] (which cannot be automated), the same example is studied here as shown in Figure 2. For the 1k1b1c (one spring, one damper and one inerter) and 2k1b1c cases, there are in total 8 and 18 network possibilities respectively, which are the same as [4]. However, for the 2k2b1c case there are 9 (out of 85) bridge networks which cannot be covered by [4]. Then, via the genetic optimization the optimum one in each case is identified. Compared with the benchmark layout L0, using the optimal 1k1b1c layout L1 and the optimal 2k2b1c layout L3 can improve the vehicle ride comfort by 15% and 28%, respectively.

References

[1] M. C. Smith. Synthesis of mechanical networks: the inerter. *IEEE Trans. Automat. Contr.*, 47(10):1648–1662, 2002.

[2] M. C. Smith and F. C. Wang. Performance benefits in passive vehicle suspensions employing inerters. *Vehicle Syst. Dyn.*, 42(4):235–257, 2004.

[3] J. Z. Jiang and M. C. Smith. Regular positive-real functions and five-element network synthesis for electrical and mechanical networks. *IEEE Trans. Automat. Contr.*, 56(6):1275–1290, 2011.

[4] S. Y. Zhang, J. Z. Jiang, and S. A. Neild. Passive vibration control: a structure-immittance approach. *Proc. Math. Phys. Eng. Sci.*, 473(2201):20170011, 2017.

Session S8

Smart materials

Organizer:
Tomasz G. Zieliński (*IPPT PAN, Poland*)

Parameter Optimization of a Magnetic Coupled Piezoelectric Energy Harvester: numerical analysis and experimental study

A. Koszewnik[1a], D. Oldziej[1b]

[1]*Bialystok University of Technology, Department of Robotics and Mechatronics, Bialystok, Poland*
e-mail: a.koszewnik@pb.edu.pl , d.oldziej@pb.edu.pl

1. Abstract

Piezoelectric energy harvesting is a promising way to develop self-sufficient systems. Structural design and nonlinear parameter optimization of this system are key issues to improve performance in applications. This paper presents a magnetic coupled piezoelectric energy harvester to increase the output and bandwidth. A lumped parameter model considering the static position is established and various modes are simulated. The paper is focused on the low frequency repulsion mode for structure shown in Fig.1 that is complex with two beams containing Macro-Fiber Components (MFC) with homogenous material and thin cylinder magnets located close to free end of each of them. The optimization process of some key parameters, such a magnets spacing, optimal impedance matching and flux density is carried out. The results show that there is a corresponding optimal spacing for each flux density, which is positive correlated. With the optimized parameter design, the system achieves peak electrical power of 2.45 mW under the harmonic excitation of $3m/s^2$.
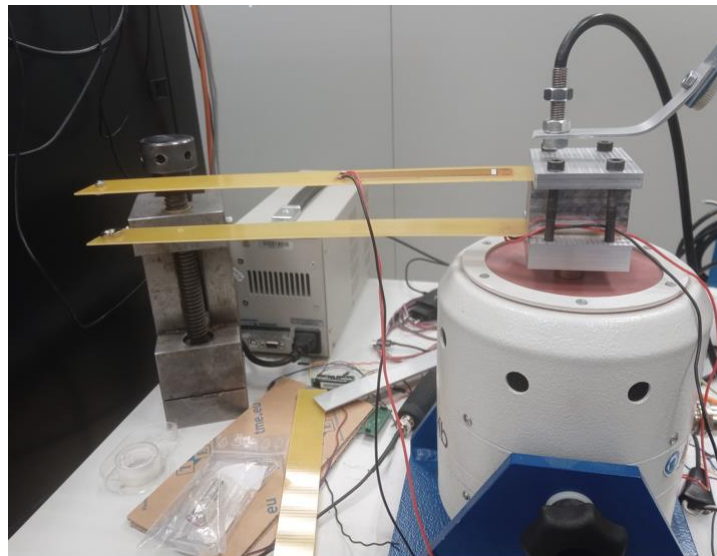
Fig.1. The view of real laboratory stand during test.

MODELLING OF TWO ANTAGONISTIC SHAPE MEMORY ALLOY WIRES

B. Stępniak[1], K. Falkowski[1]

[1] *Faculty of Mechatronics, Armament and Aerospace, Military University of Technology,*
ul. Gen. Sylwestra Kaliskiego 2,00-908 Warsaw, Poland
e-mail: bartlomiej.stepniak@wat.edu.pl

Shape memory alloys (SMAs) are materials which can be classified as functional materials. The feature which distinguishes them from the other materials in this group is a shape memory effect. The forementioned effect is connected with the direct and reverse martensitic transition. It means that the shape of an element which is made of that alloy can significantly change during these processes. The phenomenon has already been successfully used in engineering and medicine where a part of applications are linear and rotary actuators. Such designs are driven by one, two or more shape memory alloy elements (in some cases with a bias spring or springs additionally applied). There is some particular case where the antagonistic work of two SMA elements is used.

There are a number of models of the behaviour of shape memory alloys which can be used to simulate SMA elements' actuation. They can be divided into three groups, as follows: thermal models, phase transition models and mechanical models. This paper presents some of the models belonging to three aforementioned groups. These considerations are followed by the author's approach to modelling of mechanical behaviour of antagonistic pair of shape memory alloy wires.

MAGNETICALLY CONTROLLED SOUND ABSORPTION BY MEANS OF A COMPOSITE ADDITIVELY MANUFACTURED MATERIAL

Kamil C. Opiela, Robert Konowrocki, and Tomasz G. Zieliński

Institute of Fundamental Technological Research, Polish Academy of Sciences, Pawiński ego 5B, 02-106 Warsaw, Poland

e-mail: kopiela@ippt.pan.pl

Abstract

A composite additively manufactured material for controlled sound absorption is proposed. The operation of the material is based on its changeable microgeometry with steel balls that modify propagation of acoustic waves when subject to an external magnetic field. Both numerical predictions and experimental verification is provided.

1. Introduction

Porous materials are known for their exceptional acoustic properties. In rigid foams the energy of acoustic waves is dissipated due to a visco-thermal interaction between air particles and a solid skeleton. Given the microgeometry of a conventional porous material, the acoustic characteristics like sound absorption and insulation are dependent solely on the material thickness for the same excitation conditions. However, the concept of an adaptable additively manufactured sound absorber was introduced and discussed in [1, 2]. The idea is based on the modification of material microstructure, keeping its outer dimensions unchanged. It turned out possible by designing a specific periodic shape of a rigid skeleton and inserting to the pores small steel balls that redirect air-flow to wide or narrow internal channels by gravity or centrifugal forces. In this way, one affects the intensity of visco-inertial and thermal phenomena resulting in different sound absorption spectra.

This contribution is an extension to the previous work and presents another method for a controlled steel ball relocation. Instead of gravity or centrifugal forces, a neodymium magnet is applied to influence the position of balls trapped in the pores. Two configurations studied in the previous papers [1, 2] are obtained by placing the magnet close to the bottom or lateral sides of a square 3D printed impedance tube extension containing the adaptable material sample and hung vertically on a wall: vertical state V—with balls clogging the wide channels in the direction of incidence and forcing more tortuous air-flow through narrow oblique channels, and horizontal state H—with balls closing wide channels perpendicular to the direction of incidence and allowing less tortuous air-flow mainly through wide channels parallel to the direction of incidence to happen. In addition to these two extreme situations, the proposed magnetic relocation technique opens new possibilities in achieving intermediate absorption states.

2. Methods

The research was conducted using the cuboidal material sample and the square impedance tube extension (see Figure 1) produced in the SLA and FDM additive manufacturing technologies, respectively [3]. A Brüel & Kjær equipment was utilised to perform measurements. The hybrid multiscale modelling technique [4] was applied to evaluate homogenised equivalent-fluid properties based on a periodic unit cell (see Figure 1) representative for the material. Two Helmholtz problems were solved in the $30 \times 30 \times 60$ mm rectangular domain using the homogenised properties to calculate the sound absorption coefficient resulting from the V and H states. The finite-element analyses were run in the open-source FEniCS software [5].

3. Results

Figure 1 presents the experimental and computational sound absorption coefficient values obtained for two material states H and V. In general, the higher the values, the more energy of acoustic waves is dissipated within the material. A substantial difference in performance is observed between the states, and the state V with a higher microstructural tortuosity is shown to yield better overall absorption. However, if applicably controlled, the material offers sound absorption at the level of 0.7 and higher for frequencies ranging from about 550 Hz to 1.1 kHz and from 1.9 kHz to 6.4 kHz, as confirmed by the measurements.
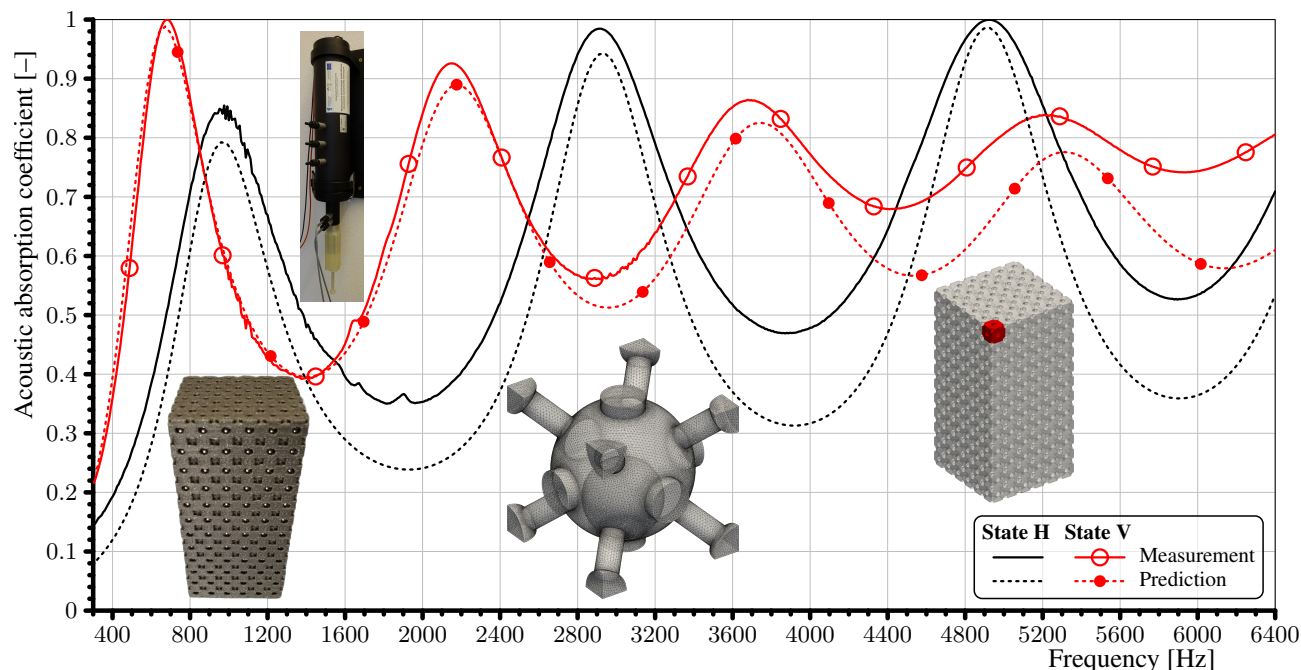
Figure 1: Normal incidence sound absorption coefficient spectra for a 60 mm-thick material layer in both V and H ball configurations. The insets in the figure show (from left to right): the additively manufactured sample, the impedance tube with the square 3D printed extension, the periodic unit cell used in calculations, the computer model of a sample with a single periodic skeleton component highlighted.

4. Conclusions

A composite material for magnetically controlled sound absorption was presented. Its cuboidal sample was additively manufactured and tested in an impedance tube. The normal incidence measurements of acoustic pressure indicate that the sound absorption spectrum in the material depends on the position of steel balls within its microstructure. The balls were moved by placing the sample in an external magnetic field. Two extreme states were investigated in which the balls were attracted in two mutually perpendicular directions: along as well as transversely across the direction of incidence. The experimental results were predicted with good accuracy using multi-scale modelling.

References

[1] K. C. Opiela, M. Rak, and T. G. Zieliński. A concept demonstrator of adaptive sound absorber/insulator involving microstructure-based modelling and 3D printing. In: W. Desmet, B. Pluymers, D. Moens, and W. Rottiers, eds, *Proc. of ISMA2018 International Conference on Noise and Vibration Engineering/USD2018 International Conference on Uncertainty in Structural Dynamics*, pp. 1091–1104, 2018.

[2] K. C. Opiela and T. G. Zieliński. Microstructural design, manufacturing and dual-scale modelling of an adaptable porous composite sound absorber. *Compos. Part B-Eng.*, 187:107833, pp. 1–13, 2020.

[3] T. G. Zieliński, K. C. Opiela, P. Pawłowski, N. Dauchez, T. Boutin, J. Kennedy, D. Trimble, H. Rice, B. Van Damme, G. Hannema, R. Wróbel, S. Kim, S. Ghaffari Mosanenzadeh, N. X. Fang, J. Yang, B. Briere de la Hosseraye, M. C. J. Hornikx, E. Salze, M.-A. Galland, R. Boonen, A. Carvalho de Sousa, E. Deckers, M. Gaborit, and J.-P. Groby. Reproducibility of sound-absorbing periodic porous materials using additive manufacturing technologies: Round robin study. *Addit. Manuf.*, 36:101564, pp. 1–24, 2020.

[4] T. G. Zieliński, R. Venegas, C. Perrot, M. Červenka, F. Chevillotte, and K. Attenborough. Benchmarks for microstructure-based modelling of sound absorbing rigid-frame porous media. *J. Sound Vib.*, 483:115441, pp. 1–38, 2020.

[5] K. C. Opiela and T. G. Zieliński. Predicting sound absorption in additively manufactured porous materials using multiscale simulations in FEniCS. In: I. Baratta, J. S. Dokken, C. Richardson, and M. W. Scroggs, eds, *Proc. of FEniCS 2021*, p. 370, 2021.

Flywheel proof mass actuator for active vibration control

A. Kras[1], and P. Gardonio[2]

[1]*Silencions, Bierutowska 57-59, 51-315 Wrocław, Poland*
[2] *DPIA, Università di Udine, Via delle Scienze 206, 33100, Udine, Italy*
e-mail: aleksander@silencions.com

1. Introduction

This paper presents experimental tests carried out on a flywheel proof mass actuator used for the implementation of velocity feedback control loops to reduce the flexural vibration of a thin plate. The classical proof mass actuators used in vibration control systems are formed by an electromagnetic linear transducer [1]. As shown schematically in Figure 1a, the transducer, is formed by a magnetic inner element, acting as a base mass m_b, and an external coil-armature component, acting as a proof mass M_a, which is suspended to the inner element via two springs of stiffness k. The air in the small gap between the inner and outer elements generates a damping effect characterised by the damping factor c. The interaction between the magnetic field produced by the inner magnet and the current flow in the coil i_a produces a pair of forces F_a proportional to the voltage u_a through the transduction coefficient ψ_a. The coil is characterised by inductance L and resistance R effects [2].

Figure 1b shows the classical transducer used in this study for the experimental implementation of the velocity feedback control loops. At frequencies above the fundamental resonance frequency of the spring-coil-armature assembly, this actuator generates a constant force in phase with the driving voltage, which can be used to implement point velocity feedback control loops [3]. However, the internal dynamics of the spring-coil-armature assembly limits the stability, and thus control performance of the feedback loop. Moreover, when exposed to shocks, the soft suspension springs may cause undesired stroke saturation effects, which lead to instability of the feedback loops [4].

Thus, to improve stability and obtain higher control gains of the velocity feedback control loops this paper proposes to use a flywheel proof mass actuator, whose functioning is based on the concept of the inerter [5].
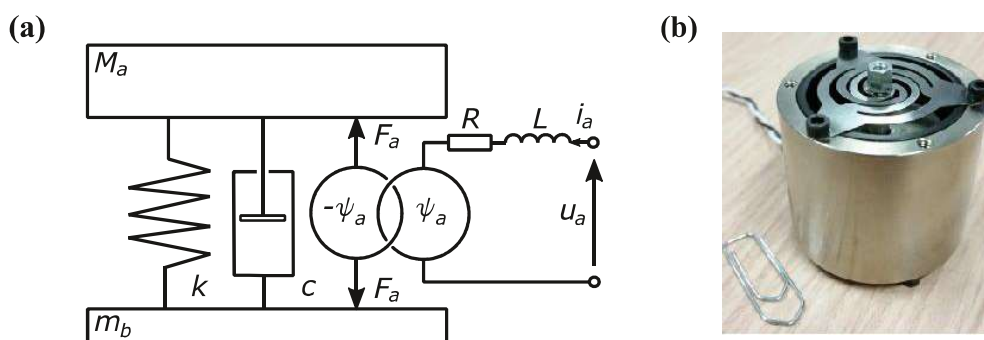
Figure 1: Scheme (a) and picture (b) of classical proof mass actuator for velocity feedback control applications.

2. Flywheel proof mass actuator

As shown in Fig. 2, the flywheel proof mass actuator presented in this paper consists in the classical coil-magnet proof mass actuator equipped with a flywheel element, which increases the inertia effect of the proof mass [6]. As shown schematically in Figure 2a, the additional flywheel element is composed by a circular

wheel with polar moment of inertia I_w and mass m_w that adds to the inertial mass M_a. The flywheel element was suspended with two flexural bearings of torsional stiffness k_w to a bracket attached to the coil armature. A third frictionless pivot bearing connects the flywheel element with the inner magnet of the actuator via a small stinger mounted with an offset r_w from the flywheel horizontal axis of rotation. To keep the whole actuator in balance, this assembly was set to intersect the vertical axis of the coil-magnet transducer. In this way, the relative axial motion between proof mass and the base mass of the actuator produces rotational oscillations of the flywheel too, and thus creates an additional inertia at the base and proof mass of the actuator.

Experimental and simulation tests have shown that the flywheel element can be effectively used to reduce the fundamental resonance frequency of the actuator without increasing its total mass. This is an important result, which indicates the flywheel actuator can be suitably used to implement velocity feedback control units with increased stability and, consequently, control properties.
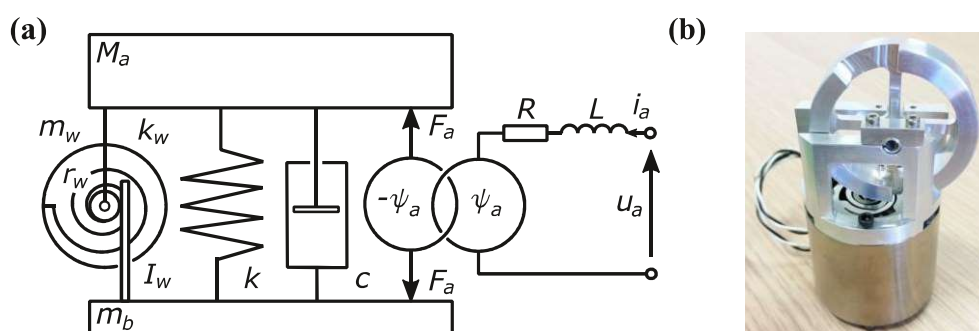
Figure 2: Scheme (a) and picture (b) of flywheel proof mass actuator prototype.

3. Active vibration control

The paper presents both simulations and experimental results that contrast the stability and control performance of velocity feedback loops equipped with the classical proof mass actuator and the proposed flywheel proof mass actuator mounted on a thin plate excited in bending by a random point force. The simulation and experimental results show that, the new flywheel proof mass actuator can be effectively used to implement a more stable and robust velocity feedback loop. As a result higher feedback control gains can be implemented in the loop, which generate larger vibration control effects. The experimental testes matched well the numerical results for both types of actuators.

References

[1] D.W. Miller, E.F. Crawley, Theoretical and experimental investigation of space-realizable inertial actuation for passive and active structural control, Journal of Guidance, Control, and Dynamics 11 (5) (1988) 449–458.

[2] F. Fahy, P. Gardonio, Sound and structural vibration. Radiation, Transmission and Response, 2nd ed., Academic Press, Oxford, 2007.

[3] D.C. Zimmerman, D.J. Inman, On the nature of the interaction between structures and proof mass actuators, Journal of Guidance, Control, and Dynamics 13 (1) (1990) 82–88.

[4] D.K. Lindner, G.A. Zvonar, D. Borojevic, Performance and control of proof-mass actuators accounting for stroke saturation, Journal of Guidance, Control, and Dynamics 17 (5) (1994) 1103–1108.

[5] M.C. Smith, Synthesis of mechanical networks: the inerter, IEEE Transactions on automatic control 47 (10) (2002) 1648–1662.

[6] A. Kras, P. Gardonio, Velocity feedback control with a flywheel proof mass actuator, Journal of Sound and Vibration 402 (2017) 31–50.

LASER MICRO BENDING MECHANISM
FOR HIGH-PRECISION ADJUSTMENT IN MECHATRONIC SYSTEMS

J. Widłaszewski[1]

[1]*Institute of Fundamental Technological Research PASc, A. Pawińskiego 5 B, Warsaw, Poland*
e-mail: Jacek.Widlaszewski@ippt.pan.pl

1. Introduction

Application of laser technology makes it possible to perform highly accurate adjustment of components, which are difficult to access using traditional tools and are sensitive to mechanical forces. The energy input by the laser beam into the work-piece can be easily and precisely controlled. Adjustment of critical dimensions with micrometer or milliradian accuracy in small metallic components is applied during assembly stage in mass-production and it allows relatively large tolerances in the preceding production stages [1]. The potential of a laser beam as a means of energy transport for optothermal microactuation is intensively investigated to expand practical applications of micro-opto-electro-mechanical systems (MOEMS) [2].

Presented paper reports experimental and numerical investigations of a thermal micro-bending mechanism, which enables deformation either towards or away from the laser beam (a heat source), dependent on the applied processing parameters. A 3D finite element method (FEM) model has been developed to study the behaviour of a cantilever stainless steel beam heated by a laser beam. Experimentally-validated numerical model allowed an analysis of temperature, strain and stress fields during the heating and cooling cycle.

2. Experiments

Samples of dimensions 50 x 4.05 x 0.55 mm made of 18-8 type stainless steel, clamped in the cantilever arrangement, were heated with a stationary Nd:YAG laser beam (Fig. 1).
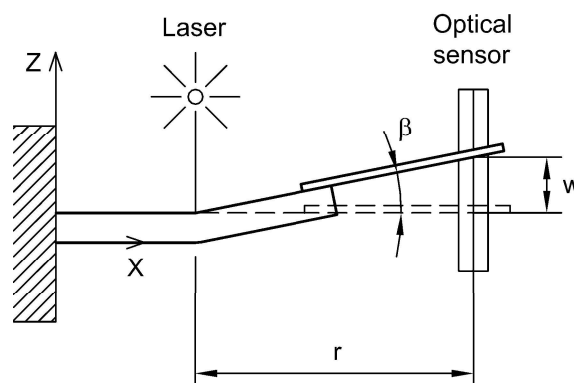
Fig. 1. A schematic of the laser bending experimental setup.
The definition of the positive angular deformation $\beta > 0$.

Non-contact deformation measurements were performed with a high-accuracy laser micrometer. In order to achieve a high accuracy of optical measurements, an additional element of high-quality surface and low mass was attached to the sample. Its displacement was measured and recorded during laser heating and after cooling down the sample to the initial material temperature. Angle β of the bending deformation induced by the laser pulse was calculated from the linear vertical displacement w (Fig. 1) measured with the micrometer.

3. Numerical simulation

Numerical simulations were conducted using the Finite Element Method (FEM). The thermal-mechanical sequentially coupled analysis was conducted in two separate steps: (1) determination of temperature field under prescribed heat load and boundary conditions, and (2) elastic-plastic incremental analysis of stress and strain due to the calculated temperature field. The calculations were performed with the ABAQUS system. Energy input from the laser beam was treated as a surface heat source, since the absorption of the infrared radiation by metals is typically confined to a layer several tens of nanometers thick.
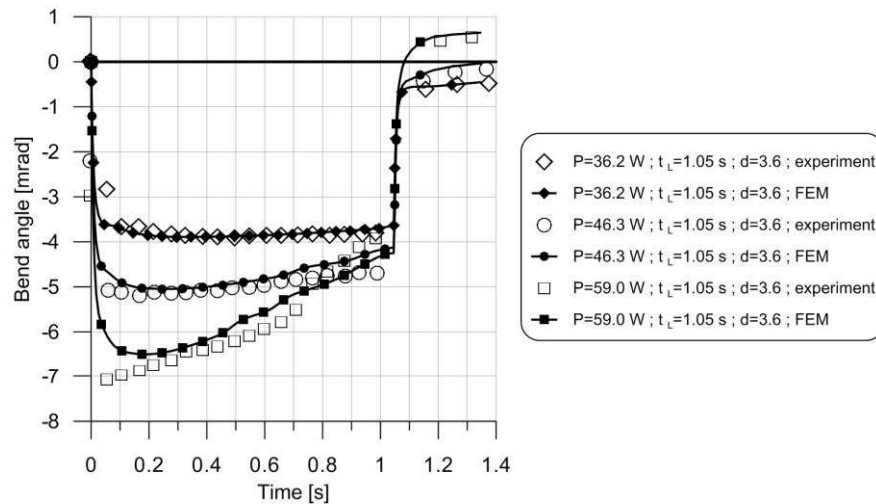
Fig. 2. A comparison of experimental and numerical time-runs of the angle of bend for various laser power P, time of laser heating 1.05 s and laser spot diameter 3.6 mm.

Thermal dependences of the following material properties were taken into consideration: thermal conductivity, specific heat, thermal expansion coefficient, Young's modulus, yield stress, Poisson's ratio and density. The Huber-Mises-Hencky yield criterion was employed.

4. Conclusions

Experimentally validated simulations explained the mechanism of laser-induced deformation. The studied mechanism of bending involves a significant positive longitudinal plastic strain in the edge regions of the beam. The deformation results from a considerable temperature gradient across the width of the beam, with some contribution of the temperature gradient in the thickness direction. Application of the mechanism opens up new opportunities for the laser-based micro-adjustment technology, particularly when the processed component is accessible from one side only.

References

[1] W. Hoving, *Accurate manipulation using laser technology*, in: M. Geiger, A. Otto (Eds.), Proceedings of the 3rd LANE 2001 (Laser Assisted Net Shape Engineering 3, International Conference) Meisenbach Bamberg, 2001, pp. 113-124.

[2] X. Han, H. Zhang, R. Xu, S. Wang, C. Qin, *Theoretical model of an optothermal microactuator directly driven by laser beams*. J. Micromech. Microeng. 25(7) (2015) 075012. DOI: 10.1088/0960-1317/25/7/075012.

Selected full papers

Enhanced vibro-acoustic behavior of lightweight gearbox housing through the use of locally resonant metamaterials

D.R. Amaral[1], M. Ichchou[1], P. Kolakowski[2], P. Fossat[1], and M. Salvia[1]

[1]*LTDS, Laboratoire de Tribologie et Dynamique des Systems, Ecole Centrale de Lyon, France*
[2]*Adaptronica sp. z o.o., Łomianki, Poland*

e-mail: daniel.amaral@ec-lyon.fr

1. Abstract

Reducing the vehicles' mass increases its range and reduces the emission of polluting gases in the case of internal combustion engine (ICE) vehicles. This work is devoted to the lightening of the gearbox housing (GBH) and to the introduction of new paradigms in the early design of GBH using metamaterials. Generally, the lightweight design in engineering applications gives rise to noise and vibration problems. Therefore, automotive lightweight solutions must be developed in conjunction with innovation in the area of noise and vibration. The main focus of this work is to improve the vibro-acoustic behavior of the lightweight GBH through passive means, using vibro-acoustic metamaterials, in particular locally resonant metamaterials (LRMs). This work aims not only to demonstrate that it is feasible to attenuate the low frequency peaks arising from the lightweight design, but also demonstrate that broad noise attenuation is achievable over the lower frequency range through the correct tuning and modulation of the LRM solutions applied.

2. Introduction and Problem Definition

Nowadays, there is an urgent need for solutions to mitigate the human influence on climate change. Transportation and mobility represent a significant part of our impact on the environment. The reduction of the weight of vehicles constitutes a clear benefit for reducing the environmental impacts of transport and mobility, providing more energy efficient solutions and, in the case of ICE vehicles, fewer emissions of greenhouse gases and other noxious gases and particles.

Automotive manufacturers also seek to provide the market with silent vehicles, for two main reasons: stricter noise emission regulations and fulfillment of customer expectations. For these reasons, better Noise, vibration, and harshness (NVH) control solutions are in high demand.

The laws of physics reveal that, as a general rule, lightweight components radiate more noise due to their higher stiffness to mass ratio. Hence, these two conflicting design objectives need to be addressed with novel solutions, and one of the solutions is the use of vibro-acoustic metamaterials.

2.1. Introduction to Metamaterial NVH Solutions

In general, metamaterials are a novel class of complex engineered materials. As a rule, they take the form of unit cells assemblies of non-homogeneous material composition and/or topology. The topic generated enthusiasm in the scientific community since they can be designed to exhibit unconventional electromagnetic, mechanical or vibro-acoustic properties. The physics of the metamaterials and their interactions with all kinds of waves can be highly counter-intuitive, which induced a burst of new research [26] [1]. The most outstanding functionality of the vibro-acoustic metamaterials is the strong attenuation of vibration and noise in specific frequency ranges. These frequency ranges are called band gaps (BGs). There are essentially two types of vibro-acoustic metamaterials. The first type are the Phononic Crystals (PCs), which rely on interference-based attenuation and depend on the periodicity of the arrangement. The second are the Locally Resonant Metamaterials (LRMs), for which the vibration attenuation is generated by the sub-wavelength resonant inclusions or additions. Since the LRMs do not depend on the periodicity of the arrangement and the resonating structures are sub-wavelength sized,

their implementation is more feasible in engineering applications, especially in the low frequency region where the wavelength is higher. Moreover, the resonating structures can be tuned to reduce the vibration and noise emission in distinct frequency zones. For these reasons, we considered LRM solutions as a mean to reduce the noise emission from the GBH while maintaining a lightweight and compact design, and give a particular emphasis to LRMs physics and their modeling. As stated before, noise reduction is important not only to respect the established noise regulations, but also to provide the best acoustic comfort for the people inside and outside the vehicles.

Although some automotive metamaterial solutions can be found in the recent literature [9] [28] [17], to our knowledge, there is no application of these concepts to GBHs. GBHs must follow specific requirements, namely provide support for the primary gearbox components, the selector mechanisms and actuators. The GBH must ensure the correct gear meshing, respecting the assembly tolerances of the rotating components, and cope with system loading generated by the transmitted torque. Additionally, there are other requirements related with the protection of the gearbox inner components, enclosure of the lubricant, and heat dissipation.

2.2 . Considered GBH Loading

The mechanical loading at the GBH's bearing supports depends on the rotating components' geometries, characteristics, and assembly configurations. The mechanical loading depends on the transmission ratio, the inclination angle of the gear teeth (in case of helical gears), the transmitted power, the input speed, and the distance between axes [30]. At the bearing support, loads are transferred from the shafts to the housing structure in radial and axial directions. In this work, a typical characteristic loading was applied in the GBH bearings'connection, in the bearings areas according to Figure 2. The considered bearings' loading was extracted from a simple gearbox with helical gears. The loading for each of the four bearings is shown in Figure 1.
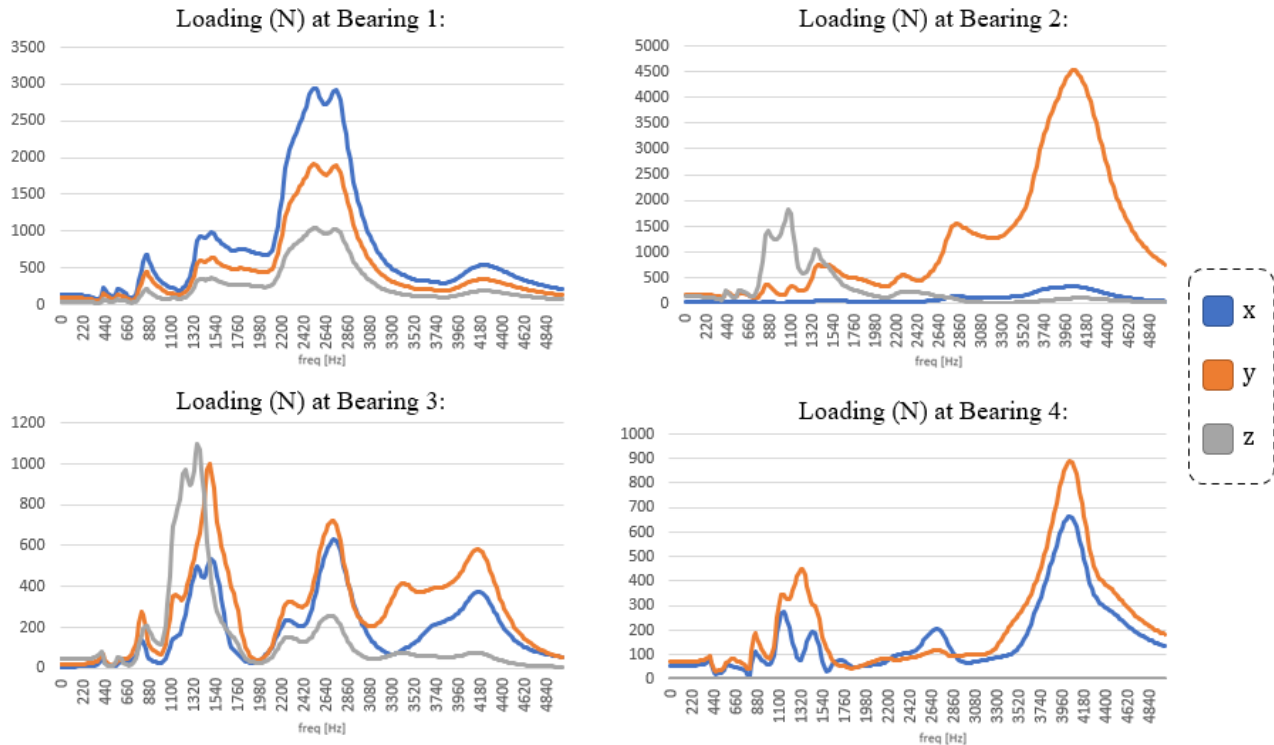
Figure 1: Loading for each of the four bearings in x (side), y (upwards) and z (axial) directions.
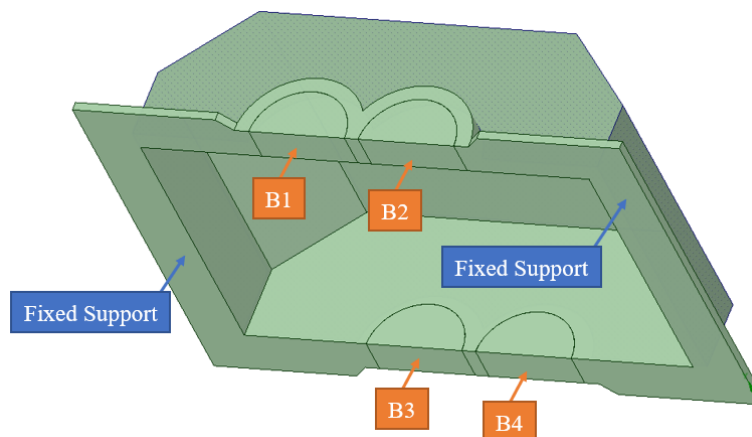
Figure 2: Location of the excitation for each bearing: Bearing 1 (B1), Bearing 2 (B2), Bearing 3 (B3), Bearing 4 (B4); and the Fixed Support Boundary Conditions.

2.3 . Considered GBH Geometry

GBHs are typically complex structures, whose geometry widely depends on the arrangement of the inner components, external connections and attached auxiliary components, such as actuators and electric units. Generally, the gearbox housing has numerous openings, connections, patterns, and thickness changes over the surface. For ease of reference, a simpler gearbox housing geometry based on the works of Figlus et al. [14] [13] was considered. In order to simplify the study, solely the top part of the GBH was considered in the analysis.

2.4 . GBH Lightweight Design

The reduction of mass while preserving the benefits and strengths of the design is the core of the lightweight design approach. For this purpose, topology optimization methods can contribute, enabling multi-objective optimization of the housing geometry. In the literature, some works can be found on the topic of structural optimization of GBHs [30] [21]. A similar topology optimization process was followed in order to reduce the mass of the original GBH, optimizing the material distribution within a specified design space. The optimization objective was to maximize the stiffness of the structure, minimizing the structure compliance. After topology optimization studies, material was removed in areas that contribute less to the global stiffness of the GBH. Figure 3 illustrates this process. The thickness of the top plate and the four smaller side plates was reduced from 6 mm to 2 mm generating a lightweight version of the GBH. The mass of the original steel GBH is 8.92 kg, and the lightweight version of the GBH is 6.81 kg. In other words, an absolute mass reduction of 2.10 kg is attained, representing a 24% relative mass reduction.

Figure 3: Illustration of the followed topology optimization process.

2.5. Initial Sound Power Radiated Assessments

The sound power radiated, over the frequency domain, is obtained by integrating the far-field intensity over a hemispherical surface centered on the structure [12], as written in Equation 1. Sound Power Levels are indicated in decibels, by the following formula stated in Equation 2, where the reference power $P_0 = 10^{-12}W$.
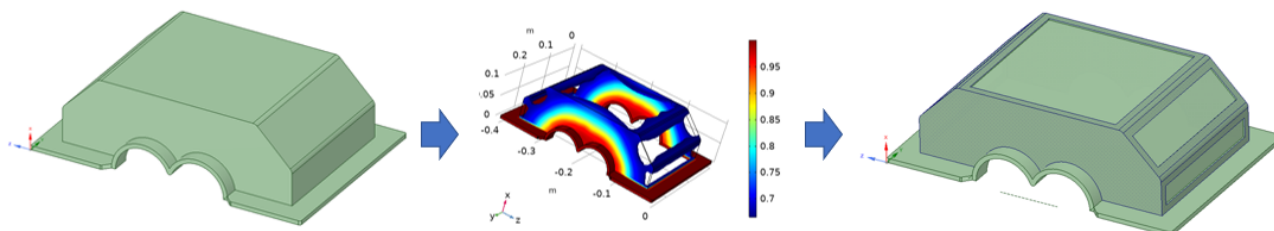
$$(1) \qquad P_{radiated}(\omega) = \int_S I(\theta, \phi, \omega)\, dS = \int_0^{\pi/2} \int_0^{2\pi} I(\theta, \phi, \omega) r^2 sin(\theta)\, d\theta\, d\phi$$

$$(2) \qquad L_w = 10 \cdot log\left(\frac{P_{radiated}(\omega)}{P_0}\right)$$

Through numerical simulations, performed in the commercial software COMSOL Multiphysics (version 5.6), a sound power radiated comparison between the original GBH and the lightweight GBH was performed, see Figure 4. The model was solved in the frequency domain using the solid mechanics and pressure acoustics modules, with an acoustic-structure boundary within COMSOL Multiphysics. The considered steel material has the following properties: Density of 7850 $[kg/m^3]$, Young's modulus of 200e9 $[Pa]$, Poisson's ratio of 0.3 and isotropic structural loss factor of 0.1%. A hemispherical acoustic air domain of 0.4 m radius was set outside the top part of a GBH. The considered air material properties depend on the ambient pressure p_A and temperature T. The speed of sound c and the density ρ are defined through the ideal gas law (assuming adiabatic behavior), according to Equation 3 where R stands for universal gas constant ($R = 8.3144621[J/(molK)]$), γ stands for the ratio of specific heats ($\gamma = 1.4$) and the M_n is the molar mass $M_n = 0.02897[kg/mol]$. The considered ambient pressure and temperature were 1 atm and 20ºC (293.15 [K]), respectively.

$$(3) \qquad c^2 = \frac{R}{M_n}T \qquad \rho = \frac{M_n p_A}{RT}$$

A Perfectly Matched Layer (PML) was set between the radius of 0.35 m and 0.4 m to represent the open environment [2]. The maximum element size was set as the speed of sound divided by the five times the highest frequency to be modelled. The structural-acoustic model for the original GBH was constituted by 810509 elements, with an average and minimum quality of 67% and 18%, respectively. As for the model for the lightweight GBH was constituted by 852208 elements, with an average and minimum quality of 65% and 14%, respectively. The integration of the sound power radiated was made at a radius of 0.3 m. The model structural loading was the bearings' loading described in Figure 1, and its application was made in the geometry areas stated in Figure 2. Since this study focus exclusively on the top part of the GBH, a fixed support was considered in the connection interface to the other half of the GBH, as indicated in Figure 2.

As visible in Figure 4, the mass reduction shifts the peaks in the sound power to the lower frequencies. It is also perceptible by the housing deformation shapes that the sound power radiated peaks generally correspond to the eigenmodes of the structure, most of them correspondent to the local eigenmodes of the top plate. In order to normalize the power results, the sound power radiated results were divided by the power injected in the structure. The total power injected is calculated by the summation of the power injected in each bearing, see Equation 4. The power injected for each bearing is calculated according to the integral over the area of load application stated in Equation 5, where $\boldsymbol{f}$ and $\boldsymbol{v}$ denote the applied force and velocity complex amplitudes in the loading area, respectively, ^{H} is the complex transpose conjugate operator [32]. The ratio of the sound power radiated to the power injected in the structure, see Equation 6, is depicted in Figure 5 for the original GBH and the lightweight GBH. It is possible to observe the same trend in the normalized results as in the nominal results for the sound power radiated. The main objective of this work is to prove that it is possible to attenuate the low frequency peaks in the sound power radiated from lightweight GBHs through the use of vibro-acoustic

metamaterials.
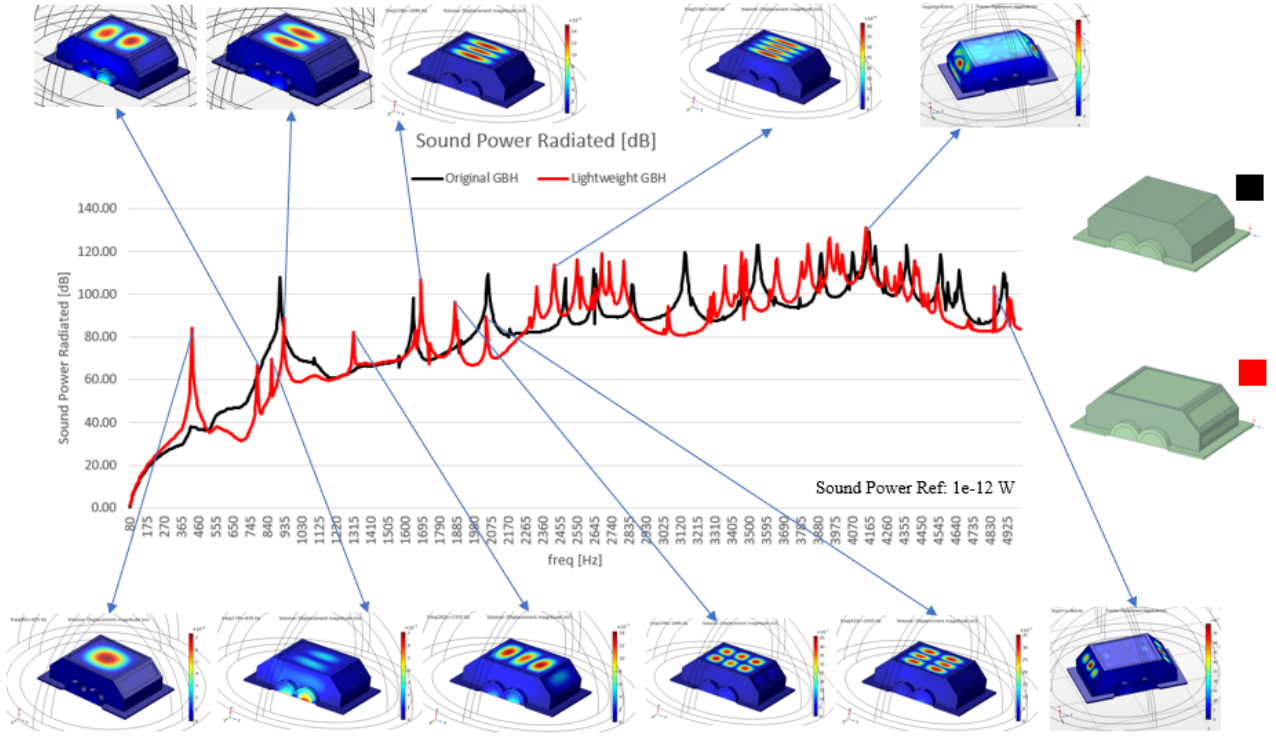
Figure 4: Sound power radiated comparison between the original GBH (black) and the lightweight version of the GBH (red), complemented with a number of housing deformation shapes.

$$(4) \qquad P_{injeted\,total}(\omega) = P_{injeted\,B1}(\omega) + P_{injeted\,B2}(\omega) + P_{injeted\,B3}(\omega) + P_{injeted\,B4}(\omega)$$

$$(5) \qquad P_{injeted}(\omega) = \frac{1}{2}\int_A \Re e\{\boldsymbol{v}(\omega)\boldsymbol{f}(\omega)^H\}\,dA$$

$$(6) \qquad Power\,Ratio(\omega) = \frac{P_{radiated}(\omega)}{P_{injeted\,total}(\omega)}$$

3. GBH Locally Resonant Metamaterial Solutions

As seen in Figure 4 and in Figure 5, the sound power radiated peaks in the lower frequency region are due to the vibration of the top plate of the lightweight GBH. Therefore, in this study, an LRM solution was applied in the top plate. The peak at 425 Hz in particular corresponds to the first local eigenmode of the top plate. The attenuation of this peak is hard to achieve by conventional means [15]. For that reason it should be attenuated by the LRM solution. Ideally, the LRM solution should also provide a broad band attenuation of vibration and noise emission, the broad band attenuation is originated from the structural damping in the LRM [33] [31] [8] [15].

For the first LRM solution to apply in the Lightweight GBH, a unit cell size of 20 mm x 20 mm was considered. The top plate dimensions are 204 x 190 mm, so it is able to fit 90 UCs in a rectangular pattern. There are several types of micro-resonator designs in the bibliography with different geometries and based in different

Figure 5: Ratio between the sound power radiated and the power injected in the structure of the original GBH (black) and the lightweight GBH (red).

resonant mechanisms [27] [7] [35] [29] [34] [11] [5] [28]. In this case, a simple micro-resonator geometry was considered, based on the same resonant mechanism of the micro-resonators presented in [7] [29] [34] [11] [5], see Figure 6. The micro-resonator consists of a flexible acrylic part and a steel mass on the top. The up-and-down vert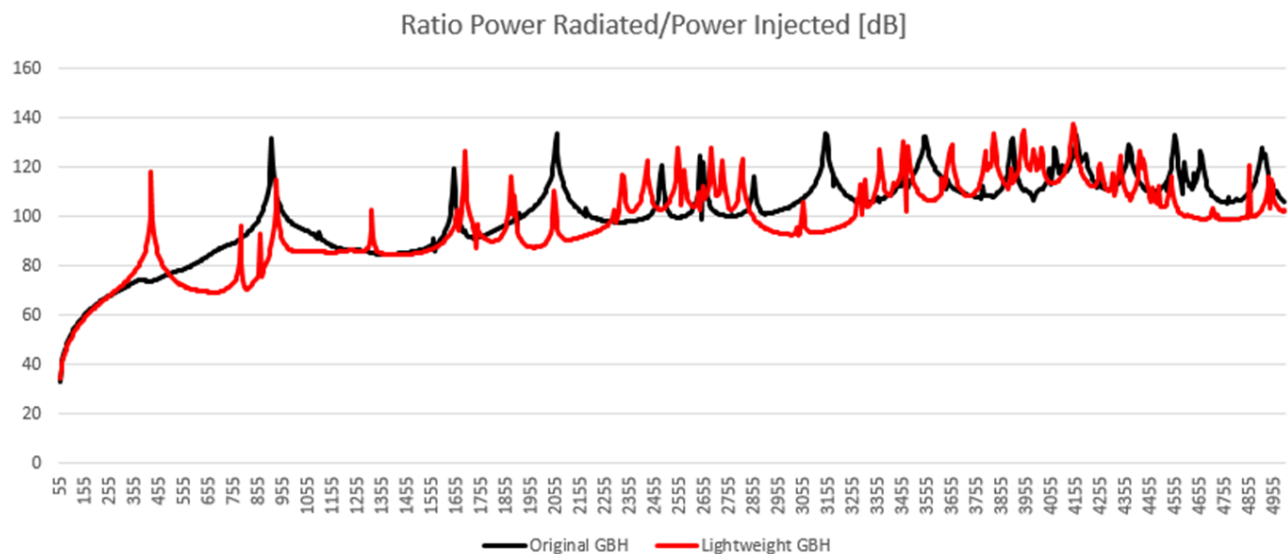ical movement of the micro-resonators mass will dynamically absorb the vibrational energy of the host structure, dampening the bending waves on the structure. The acrylic material properties considered in this study are the following: Density of 1190 $[kg/m^3]$, Young's modulus of 3.2e9 $[Pa]$, Poisson's ratio of 0.35 and isotropic structural loss factor 5%. Even for a micro-resonator with a simple geometry, there are several design variables to be controlled [27] [20] [35]. In the case of the selected micro-resonator design, several dimensional parameters must be defined, such as its width, the length/thickness of the flexible part and the dimensions of the mass part.

The proposed UC has the advantage of easy frequency tuning. The frequency tuning of a micro-resonator is performed using the relation between the natural frequency and parameters of a vibration system. The micro-resonator spring part affects mainly the stiffness (k), and the concentrated mass part affects the mass (m). The following methods can be used to decrease the stiffness of micro-resonator: decrease the thickness of the micro-resonator spring part; increase the length of micro-resonator spring part; change the shape of micro-resonator spring part, for example, by inclusion of slits in the micro-resonator spring part. Opposite methods can be used to increase the stiffness of the micro-resonator. The mass of the micro-resonator can be adjusted simply by changing the concentrated mass (changing the mass dimensions or changing the material). Using these relations, it is possible to tune the frequency band where the vibration is highly attenuated.

Jung et al. [17] and Claeys et al. [6] stated additional properties that an LRM should have in practical engineering applications, for example its manufacturability, its compatibility and its sub-wavelength scale characteristics. Regarding the manufacturability, the proposed micro-resonator spring part can be to manufactured by 3D printing/additive manufacturing, and the mass part of the micro-resonator can be bonded to the spring part by adhesive bonding. The micro-resonator design can also be easily adapted for mass production as shown in 2019 by Yu et al. [34], they proposed a resonant structure, for industrial applications, manufactured by injection molding with the metal part already placed in, ensuring that the plastic part and steel are permanently attached.

The resonator was tuned by changing its dimensions, within the design limits, taking into consideration the following objectives:

1. Tuning the 1st eigenfrequency (bending mode) of the micro-resonator to the desired hard-to-tackle low frequency;

2. Maximize the ratio of the modal mass for the micro-resonator's 1st eigenmode by the total mass of the micro-resonator;

3. Minimize the nonessential mass addition, since lightweight design is the goal, the total mass added by the micro-resonator should be minimized (e.g., minimize the mass of the bending beam part of the micro-resonator).

Aiming for the previously stated objectives, and defining the tuning eigenfrequency of 425 Hz, a micro-resonator width of 16 mm was defined, the acrylic base was defined as a square cross-section of 4×4 mm, the acrylic beam was defined with a thickness of 1 mm and a length of 14.547 mm, and finally the steel mass was defined as a square cross-section of 4×4 mm.
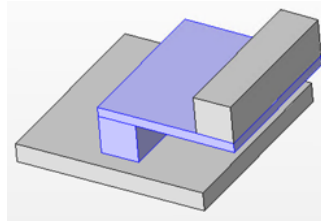
Figure 6: UC with micro-resonator: acrylic part (blue) and steel part (grey).

Even though LR structures can be applied in non-periodic ways, striving to simplify the analysis of LRMs in the majority of the cases, in the current literature, assume an infinite periodic distribution of LR structures [16] [19] [22]. In this way, a full representation of the LRM can be obtained using a unit cell (UC) and Floquet–Bloch boundary conditions. A schematic representation of a two-dimensional periodic structure is shown in Figure 7. The periodic structure is a repetition of a generic unit cell in two directions, being $\mathbf{d}_x$ and $\mathbf{d}_y$ the basis vectors of the unit cell. Given that the structure is periodic, any point P in the structure can be expressed with respect to a corresponding point U in the unit cell, translated n_x cells along $\mathbf{d}_x$ and n_x times along $\mathbf{d}_y$, see Equation 7 [8].
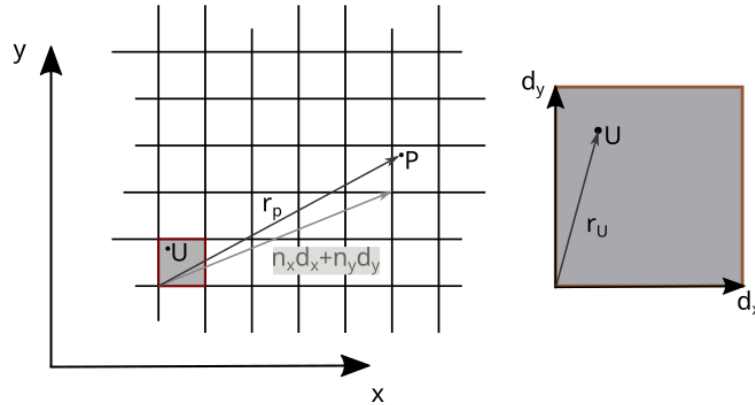
Figure 7: Schematic presentation of an infinite periodic structure (left). A unit cell of the structure(right).

(7)
$$\mathbf{r}_P = \mathbf{r}_U + n_x\mathbf{d}_x + n_y\mathbf{d}_y$$

The theorem of Bloch states that the response of a two-dimensional periodic system can be expressed in terms of the response of a reference unit cell. The amplitude and phase change of a wave propagating in an infinite periodic structure may be defined by an exponential term, see Equation 8 [3] [8], where the '·' indicated a scalar product.

(8)
$$u(\mathbf{r}_P, \omega) = u_{ref}(\mathbf{r}_U, \omega)e^{\mathbf{k} \cdot (n_x \mathbf{d}_x + n_y \mathbf{d}_y)}$$

The wave vector $\mathbf{k} = (k_x, k_y)$ defines the amplitude and phase change. In infinite periodic structures, the propagation vector $\boldsymbol{\mu}$, defined in Equation 9, expresses the complex phase shifts when in motion within a cell in the $\mathbf{d}_x$ and $\mathbf{d}_y$-directions.

(9)
$$\boldsymbol{\mu} = (\mu_x, \mu_y) = (\mathbf{k} \cdot \mathbf{d}_x, \mathbf{k} \cdot \mathbf{d}_y) = \mathbf{k} \cdot \mathbf{d}$$

Employing this notation to rewrite the Bloch theorem, Equation 10 is reached, where $\mathbf{n}$ is a vector indicating the amount of cells moved in each direction in relation to the reference UC.

(10)
$$u(\mathbf{r}_P, \omega) = u_{ref}(\mathbf{r}_U, \omega)e^{\boldsymbol{\mu} \cdot \mathbf{n}}$$

Using the infinite periodic structure theory allows the study of wave propagation in LRM, without the necessity of full-scale finite-structure vibro-acoustic numerical models [16] [8]. The distinctive vibro-acoustic performance of LRMs is assessed by the presence of BGs in the dispersion curves. Dispersion curves display the relation between frequency and wavenumbers.

The lattice shapes may adopt different geometrical shapes. Focusing on the simple example of a 2D rectangular lattice, the periodic zone in the wave domain, called a Brillouin zone, can be circumscribed in $[-\pi, \pi]$ in both principal directions. Employing the UC symmetries, the area to study can be further reduced, in what is called irreducible Brillouin zone (IBZ). The IBZ is dependent on the shape and symmetries of the UC [18]. There is a common practice of assessing the abovementioned BGs in the LRM dispersion curves, by the calculation of the dispersion curves exclusively on the IBZ boundaries, also known as irreducible Brillouin contour (IBC) [3] [16] [17]. For the purpose of calculating the dispersion curves of LRM infinite periodic structures and representing its constitutive UC, several methods can be applied. The modelling methods present in the literature are lumped parameter modelling, the plane wave expansion (PWE) method, the multiple scattering (MS) method, finite difference (FD) methods and finite element (FE) methods. Conversely, to the other mentioned methods, which are restricted to simple UC topologies and geometries [4], the FE method allows the analysis of wave propagation in more complex structures, owing to its modelling versatility. For that reason, the undamped FE approach is used to model the UC in several recent works, specially in works regarding LRM applications [5] [11] [6] [34] [29] [26] [7] [17] [10]. There are a few strategies to analyze the LRM periodic structures. The most common strategy is through the discretization of the UC using the FE method and the definition of Bloch-Floquet boundary conditions on the UC boundaries to obtain a dispersion eigenvalue problem. This is known as the wave finite element (WFE) method [23] [24]. The WFE was developed in the seventies [25], aiming to enable faster calculations, and it was originally based on the wave propagation along one-dimensional periodic elastic structures.Since the main focus of this work is to investigate LRMs in a real application, the LRM UCs should be assessed in the most detailed way as possible to capture the LRM real behavior. For that reason, the FE based UC modelling comes as the best method to model the UCs.

Generally there are two modelling approaches to get the dispersion curves, one is the inverse or $\omega(\boldsymbol{\mu})$ approach in which the real propagation constants $\boldsymbol{\mu}$ are defined and the dispersion eigenvalue problem is solved to frequencies ω, and the other is the direct or $\boldsymbol{\mu}(\omega)$ approach which imposes the real frequencies ω and solves the dispersion eigenvalue problem to propagation constants $\boldsymbol{\mu}$ [16]. The $\boldsymbol{\mu}(\omega)$ approach is suitable for 1D periodic structures, however its application to 2D periodic structures more complicated [16]. In this work, an inverse approach was followed, spanning through the values of k_x and k_y, and obtaining the eigenfrequencies. The Irreducible Brillouin Contour (IBC) was established according to the diagram in the top right of Figure 8. An auxiliary variable k was defined, varying from 0 to 4 while spanning all the IBC. For k varying from 0 to 1,

the wave vector $\mathbf{k} = (k_x, k_y)$ spans from $(0,0)$ to $(\pi/al, 0)$, where al is the UC side length. For k varying from 1 to 2, the wave vector $\mathbf{k} = (k_x, k_y)$ spans from $(\pi/al, 0)$ to $(\pi/al, \pi/al)$. For k varying from 2 to 3, the wave vector $\mathbf{k} = (k_x, k_y)$ spans from $(\pi/al, \pi/al)$ to $(0, \pi/al)$. For k varying from 3 to 4, the wave vector $\mathbf{k} = (k_x, k_y)$ spans from $(0, \pi/al)$ to $(0, 0)$. On the right side of Figure 8 the dispersion curves for the LRM UC are shown, and on the left side of Figure 8 the dispersion curves for a simple plate case with the same dimensions for comparison. One can notice the bending and shear wave propagation present in both graphs. The presence of the micro-resonator in the UC introduces BGs in the bending wave propagation, the BGs are pointed out in the left part of Figure 8. The most relevant BG is the one between 425 Hz and 474 Hz, which is created by the up-and-down movement of the micro-resonator mass, which dampens the vibration of the structure, as mentioned before.
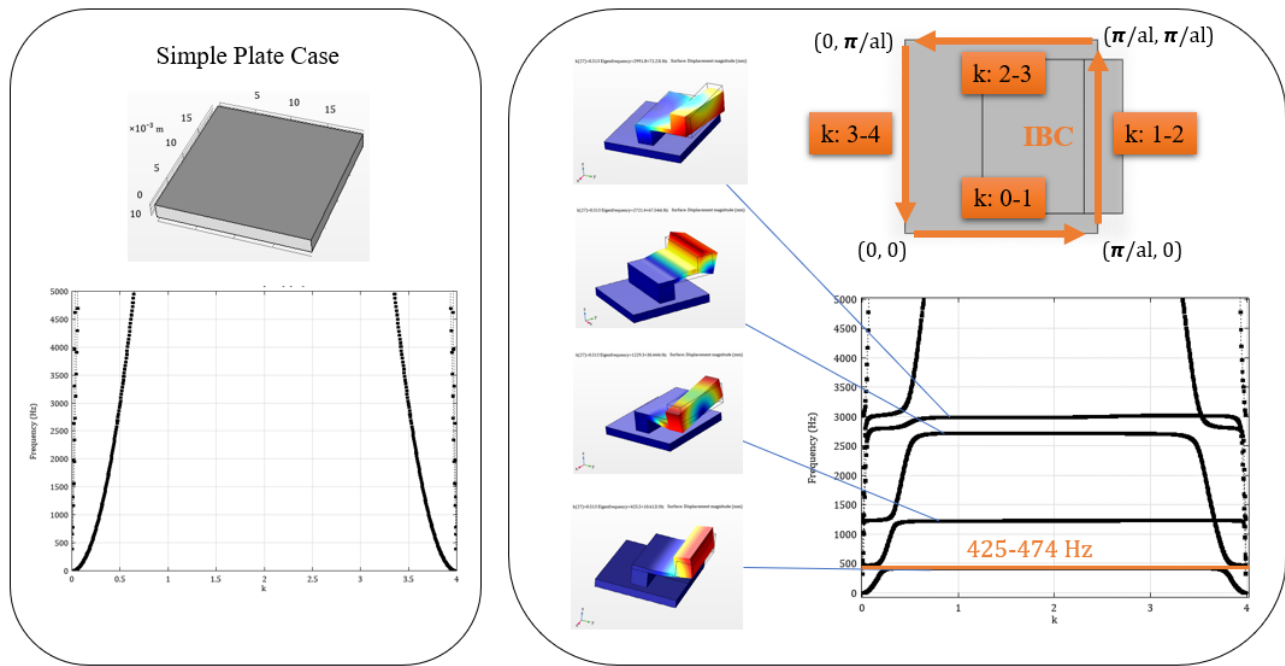

Figure 8: Dispersion curves for the LRM UC (right) and for a simple plate with the same dimensions (left), including the IBC definition (top right).

In Figure 9 the lightweight GBH with the LRM solution applied is shown, zoom was made to clearly show the presence of the micro-resonators presence in the LRM assembly.

For the purpose of sensing the mass addition quantities, the mass of the original GBH is 11 kg (including the bearings part), while the mass of lightweight GBH is 8.87 kg (including the bearings part), which represents a reduction of 2.10 kg (20% reduction). The added mass added from all micro-resonators in this LRM solution is only 0.232 kg (2.6% increase relative to the lightweight GBH mass). The LRM introduction represents a very slight mass addition compared to the previously obtained mass reduction.

A computation of the sound power radiated by the lightweight GBH with the LRM solution, subject to the same loading, was made through numerical simulations with the same setup described previously in the Section 2.5. The structural-acoustic model for the lightweight GBH with the LRM solution was constituted by 982855 elements, with an average and minimum quality of 64% and 15%, respectively. The results' comparison between the GBH, the lightweight version of the GBH and the lightweight GBH with the LRM solution applied can be seen in Figure 10. The results confirm the attenuation from the predicted BG between 425 Hz and 474 Hz. The introduction of the LRM solution in the housing provides an attenuation of the first sound power radiated peak at 425 Hz, a type of attenuation similar to a tuned mass damper (TMD) behavior. The presence of the micro-resonators reduces the original peak at 425 Hz and introduces two other smaller peaks in the vicinity, one at 330 Hz and another at 575 Hz. Moreover, as discussed before, the LRM Solution provide also a broad attenuation
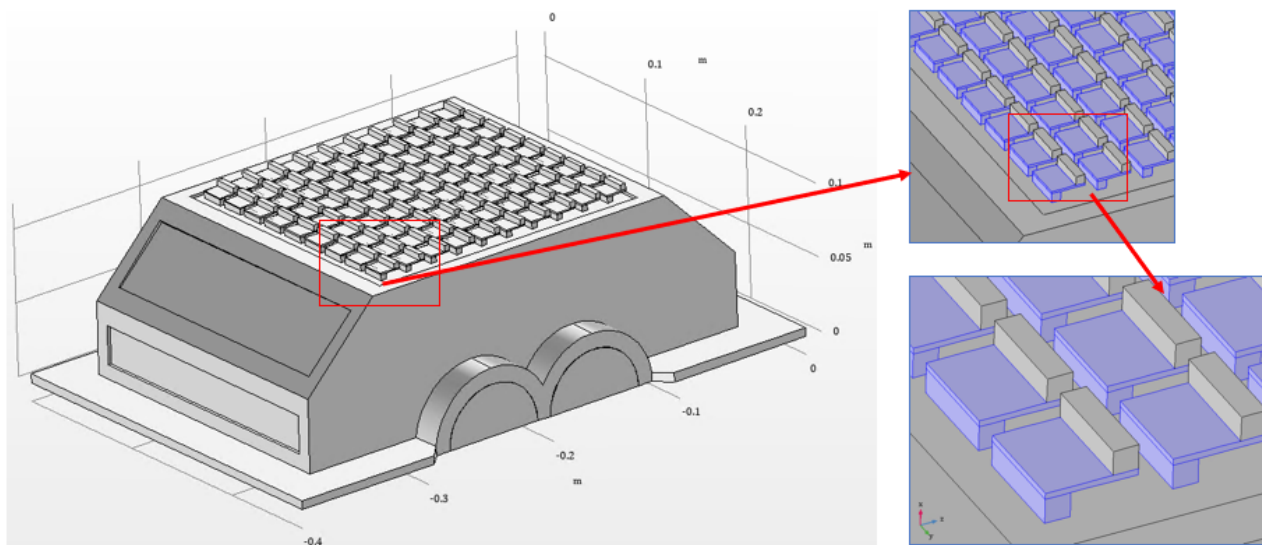
Figure 9: Lightweight GBH with LRM solution applied in the top plate.

of the sound power radiated over the considered spectrum, a significant reduction of the sound radiation peaks is noticeable in Figure 10.

Figure 10: Sound power radiated comparison between the original GBH (black), the lightweight version of the GBH (red) and the lightweight GBH with the LRM solution applied (green).

The ratio of the sound power radiated to the power injected in the structure was also calculated for the lightweight GBH with the LRM solution applied, its comparison with the results from the original GBH and the lightweight GBH depicted in Figure 15. It is possible to observe the same trends in the normalized results as in the nominal results for the sound power radiated.

A second LRM solution was idealized, consisting of an LRM with two groups of micro-resonators intercalated. One group is constituted by micro-resonators similar to the one already mentioned, see Figure 6. The second group is constituted by micro-resonators with similar geometry but this different dimensions, so that the micro-resonators have its 1st eigenfrequency (bending mode) tuned to another low frequency, in this case a frequency of 870 Hz was chosen to create another BG coinciding with the other peaks in the lower frequency. The dimensional changes were the following: the acrylic beam length was changed to 12 mm and the steel

Figure 11: Ratio between the sound power radiated and the power injected in the structure of the original GBH (black), the lightweight GBH (red) and the lightweight GBH with the LRM solution applied (green).

mass cross-section was change to 3(length)× 2.6953(height) mm. Following the same dispersion curve analysis method described previously in this section, the relevant BG is achieved between 870 Hz and 925 Hz. The two groups of resonators were assembled in intercalated lines, see Figure 12. The total mass added with the two groups of the micro-resonators was 0.185 kg, which corresponds to a 2.1% mass increase relative to the lightweight GBH mass.

Another computation of the sound power radiated by the lightweight GBH with the second LRM solution, subject to the same loading, was made through numerical simulations with the same setup described previously. The structural-acoustic model for the lightweight GBH with the second LRM solution was constituted by 975256 elements, with an average and minimum quality of 64% and 8%, respectively. The results can be seen in Figure 13. Comparing both LRM solutions, the LRM solution with two types of micro-resonators combined shows a higher attenuation of the sound power radiated in the frequency region where the new group of micro-resonators were tuned for, attenuating the peaks in the vicinity. Complementing this remark, the peak at 930 Hz present in the sound power radiated for the first LRM solution is attenuated, and as can be seen in Figure 14 that attenuating is due to the movement of the masses of the micro-resonators in the second group. Additionally, the second LRM solution, reduced the second peak in the low frequency region (around 500 Hz). In the higher frequencies, both LRM solutions follow a similar attenuation trend. However. it can be observed that the solution with a single group of micro-resonators has slightly higher attenuations in some frequencies, and the solution with two groups of micro-resonators has slightly higher attenuations in the other frequencies regions.

The ratio of the sound power radiated to the power injected in the structure was again calculated according to Equation 6 for all the configurations. The ratio is depicted in Figure 15 for the original GBH, the lightweight GBH, the lightweight GBH with one group of micro-resonators LRM solution applied and the lightweight GBH with two groups of micro-resonators LRM solution applied. It is possible to observe the same trends in the normalized results as in the nominal results for the sound power radiated.

4 . Conclusions and Future Work

This paper presents the application of locally resonant metamaterials to attenuate the noise emitted by a lightweight version of a GBH. The results from the numerical simulations display that a significant noise reduction is achievable with the application of LRM solutions to GBHs. The presented LRM solutions are pas-

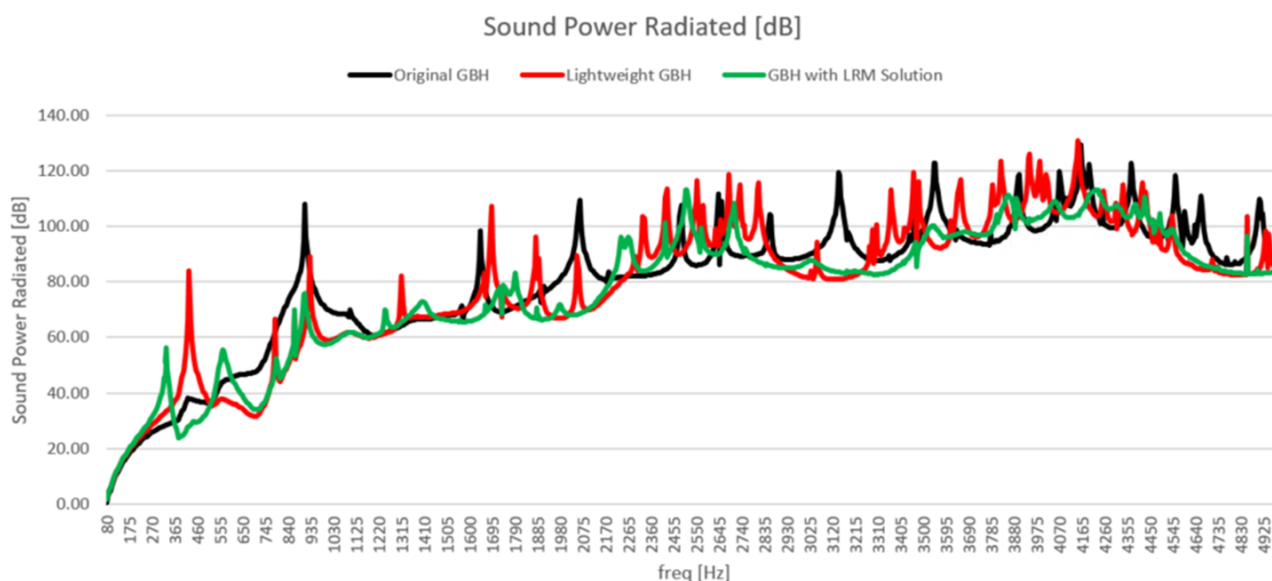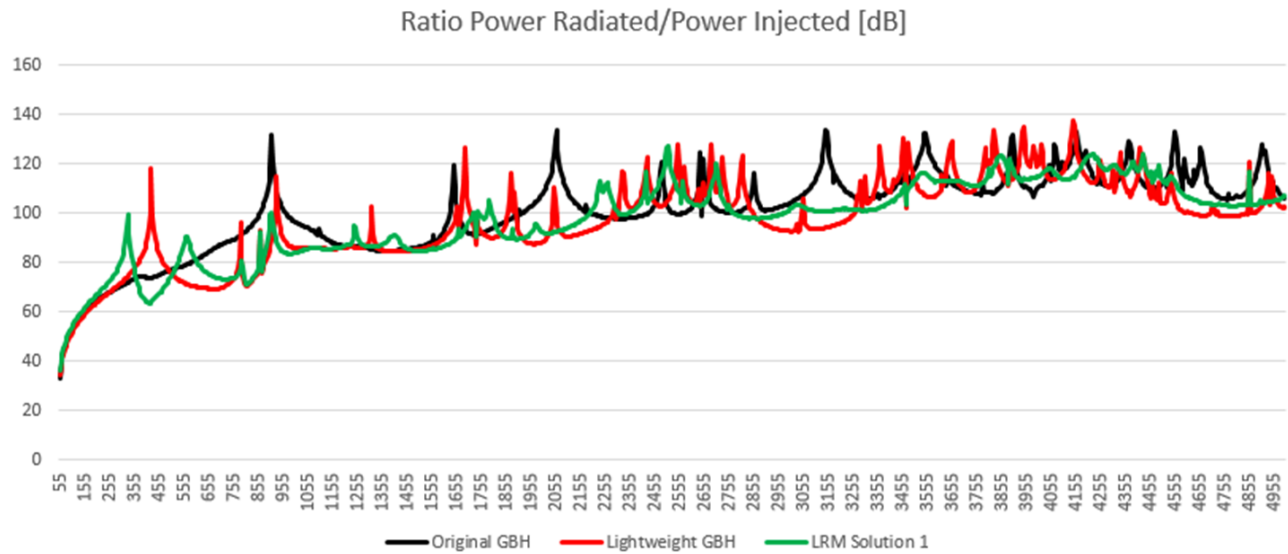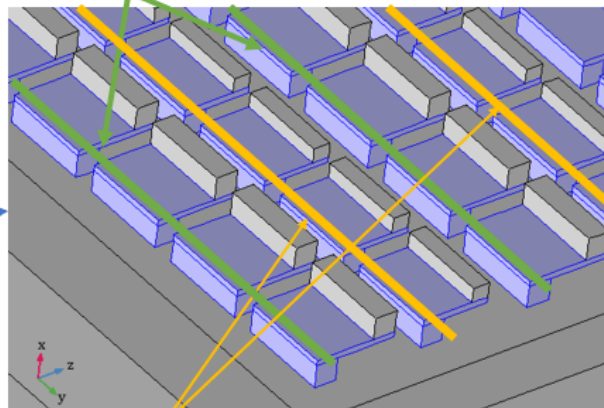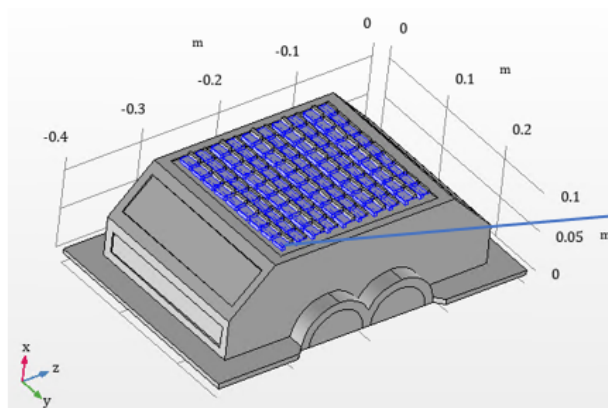Figure 12: Lightweight GBH with LRM solution with 2 groups of micro-resonators applied in the top plate.
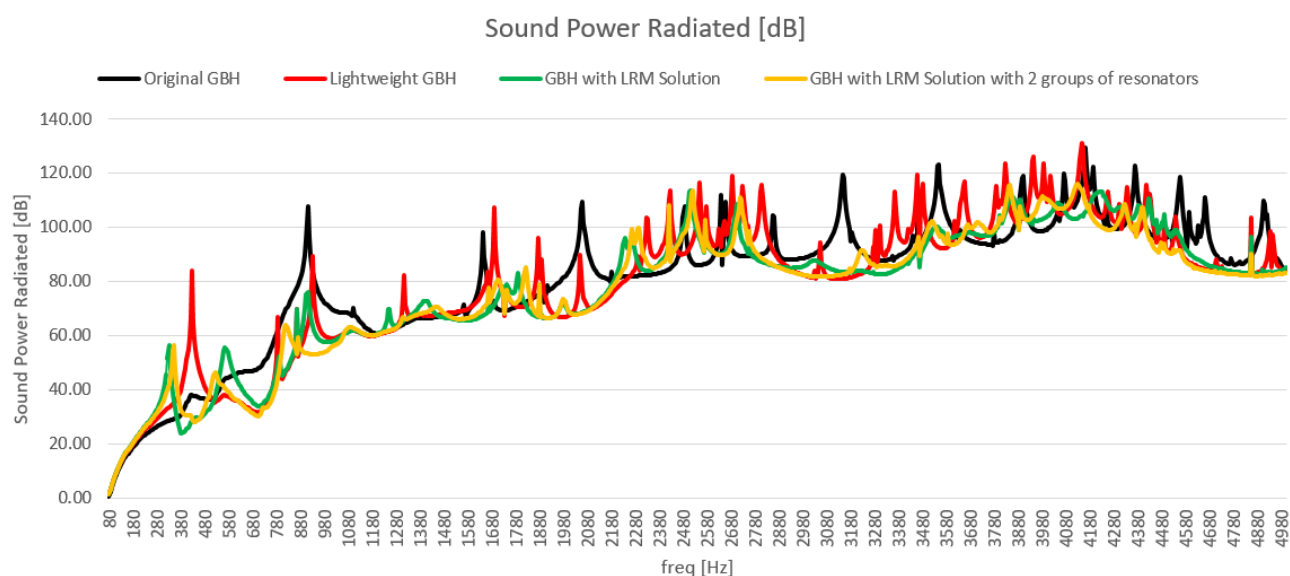

Figure 13: Sound power radiated comparison between the original GBH (black), the lightweight version of the GBH (red), the lightweight GBH with the LRM solution applied (green) and the lightweight GBH with the LRM solution with 2 groups of micro-resonators applied (yellow).
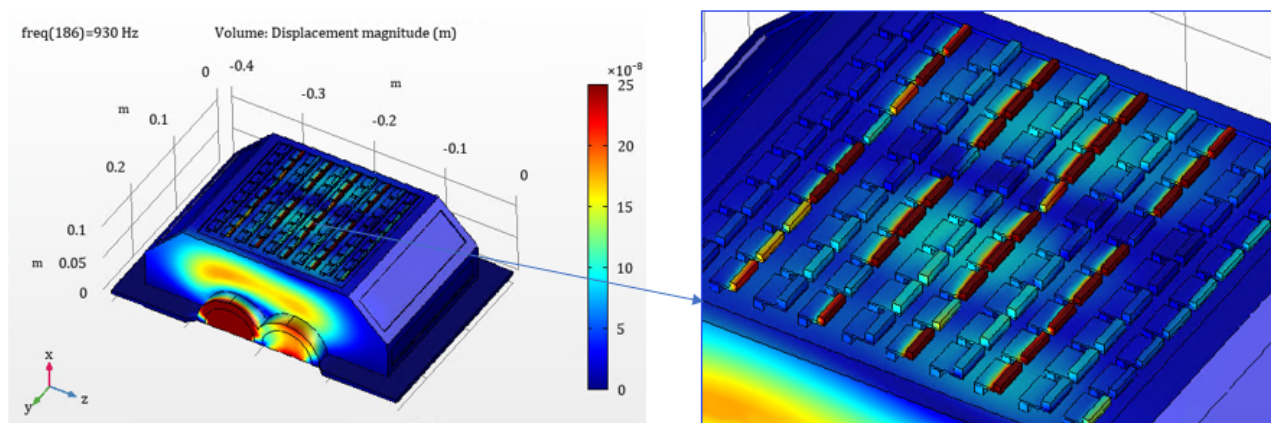

Figure 14: Displacement of the lightweight GBH with the LRM solution with 2 groups of micro-resonators at 930 Hz.
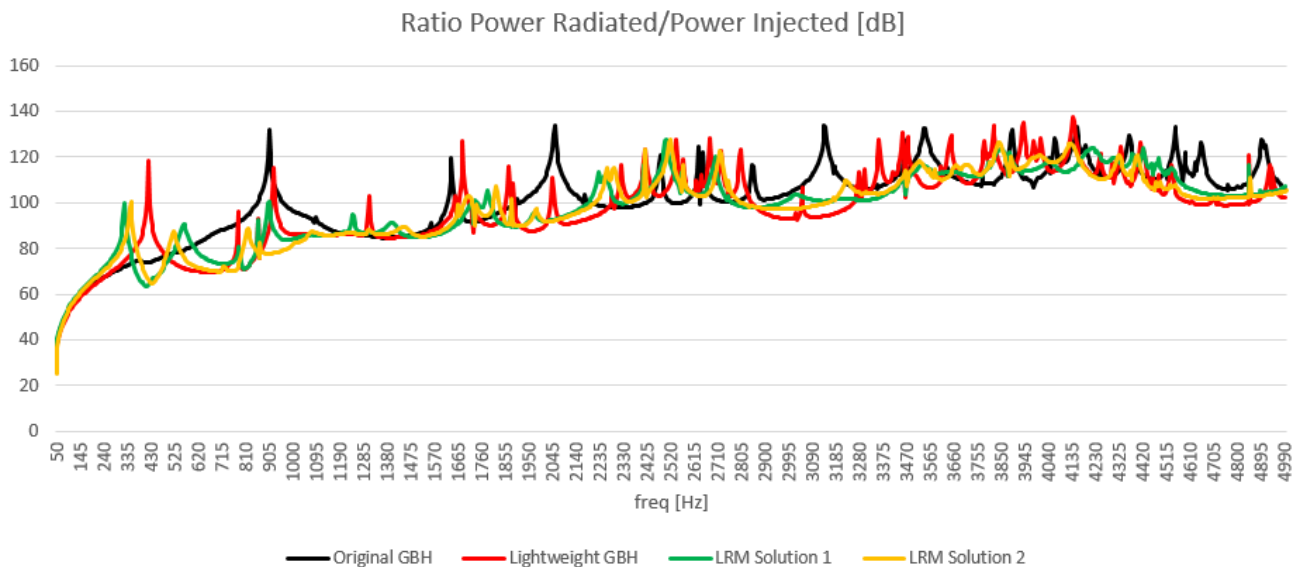
Figure 15: Ratio between the sound power radiated and the power injected in the structure of the original GBH (black), the lightweight GBH (red), the lightweight GBH with one group of micro-resonators LRM solution applied (green) and the lightweight GBH with two groups of micro-resonators LRM solution applied (yellow).

sive low-cost solutions that can be implemented in GBHs for enhancing its NVH characteristics, attenuating its vibration and the noise emission peaks across the low frequency spectrum. These solutions do not require a control system, only a proper early design according to the defined process. The increase in mass from the introduction of the micro-resonators belonging to the metamaterial solution is residual, a relative mass addition between 2% and 3% (depending on the designed solution) comparing to the mass of the host structure. The results also revealed that the use of multi micro-resonators groups can be beneficial to achieve a broader attenuation of noise and vibration, when comparing with the solution constituted by just one group of resonators. For real applications in GBHs, the material used for the micro-resonators manufacturing could be switched to high temperature polyamides, since high temperatures can be reached in the outside part of the GBHs.

Experimental validation would be beneficial to corroborate the results obtained in the numerical simulations presented in this work. Moreover, further investigation can be made regarding the distribution of the groups of resonators. As observable in Figure 12, the two groups of resonators were assembled in intercalated lines, however other distribution configurations are possible, for example diagonal distributions or even distribute the resonators according to the structure eigenmodes shapes.

Deeper research can be made on the effects of the frequency tuning of the micro-resonators in the performance of the LRM solution. In this work, the micro-resonators were tuned for frequencies corresponding to specific noise emission peaks in the sound power radiated assessments. Additional studies can be made on the effects of the frequency tuning of the micro-resonators by not deliberately tuning the LRM solution from the main noise peaks in the lower frequency, to assess if generic solutions are possible to achieve. This further investigation would allow assessing the performance dependence from the tuning of the LRM solutions in real applications. The definition of a general method for application of LRM solutions in gearbox housings might also be a future contribution.

References

[1] Arnab Banerjee, Raj Das, and Emilio P. Calius. Waves in Structured Mediums or Metamaterials: A Review. *Archives of Computational Methods in Engineering*, 26(4):1029–1058, 2019.

[2] Jean-Pierre Berenger. A perfectly matched layer for the absorption of electromagnetic waves. *Journal of Computa-*

tional Physics, 114(2):185–200, 1994.

[3] L. Brillouin. Wave Propagation in Periodic Structures, 1946.

[4] Alejandro Cebrecos, Dimitri Krattiger, Victor J. Sánchez-Morcillo, Vicent Romero-García, and Mahmoud I. Hussein. The finite-element time-domain method for elastic band-structure calculations. *Computer Physics Communications*, 238:77–87, 2019.

[5] Kyoung Jin Chang, Noé Geraldo Rocha de Melo Filho, Lucas Van Belle, Claus Claeys, and Wim Desmet. A study on the application of locally resonant acoustic metamaterial for reducing a vehicle's engine noise. *INTER-NOISE 2019 MADRID - 48th International Congress and Exhibition on Noise Control Engineering*, 2019.

[6] C. Claeys, E. Deckers, B. Pluymers, and W. Desmet. A lightweight vibro-acoustic metamaterial demonstrator: Numerical and experimental investigation. *Mechanical Systems and Signal Processing*, 70-71:853–880, 2016.

[7] Claus Claeys, Noé Geraldo Rocha de Melo Filho, Lucas Van Belle, Elke Deckers, and Wim Desmet. Design and validation of metamaterials for multiple structural stop bands in waveguides. *Extreme Mechanics Letters*, 12:7–22, 2017.

[8] Claus C. Claeys, Karel Vergote, Paul Sas, and Wim Desmet. On the potential of tuned resonators to obtain low-frequency vibrational stop bands in periodic panels. *Journal of Sound and Vibration*, 332(6):1418–1436, 2013.

[9] N. G.R. de Melo Filho, C. Claeys, E. Deckers, and W. Desmet. Realisation of a thermoformed vibro-acoustic meta-material for increased STL in acoustic resonance driven environments. *Applied Acoustics*, 156:78–82, 2019.

[10] N. G.R. de Melo Filho, C. Claeys, E. Deckers, and W. Desmet. Metamaterial foam core sandwich panel designed to attenuate the mass-spring-mass resonance sound transmission loss dip. *Mechanical Systems and Signal Processing*, 139:106624, 2020.

[11] Christophe Droz, Olivier Robin, Mohamed Ichchou, and Noureddine Atalla. Improving sound transmission loss at ring frequency of a curved panel using tunable 3D-printed small-scale resonators. *The Journal of the Acoustical Society of America*, 145(1):EL72–EL78, 2019.

[12] F J Fahy and P Gardonio. *Sound and Structural Vibration: Radiation, Transmission and Response*. EngineeringPro collection. Elsevier Science, 2007.

[13] Tomasz Figlus, Mateusz Kozioł, and Łukasz Kuczyński. Impact of application of selected composite materials on the weight and vibroactivity of the upper gearbox housing. *Materials*, 12(16):40–44, 2019.

[14] Tomasz Figlus, Mateusz Kozioł, and Łukasz Kuczyński. The effect of selected operational factors on the vibroac-tivity of upper gearbox housings made of composite materials. *Sensors (Switzerland)*, 19(19), 2019.

[15] C. R. Fuller and R. L. Harne. Advanced passive treatment of low frequency sound and vibration. *Annual Conference of the Australian Acoustical Society 2009 - Acoustics 2009: Research to Consulting*, (November):161–167, 2009.

[16] Mahmoud I. Hussein, Michael J. Leamy, and Massimo Ruzzene. Dynamics of phononic materials and structures: Historical origins, recent progress, and future outlook. *Applied Mechanics Reviews*, 66(4):1–38, 2014.

[17] Jaesoon Jung, Hyun Guk Kim, Seongyeol Goo, Kyoung Jin Chang, and Semyung Wang. Realisation of a locally resonant metamaterial on the automobile panel structure to reduce noise radiation. *Mechanical Systems and Signal Processing*, 122:206–231, 2019.

[18] Charles Kittel. *Introduction to Solid State Physics*. John Wiley & Sons, New York, 8th editio edition, 2004.

[19] A. O. Krushynska, V. G. Kouznetsova, and M. G.D. Geers. Towards optimal design of locally resonant acoustic metamaterials. *Journal of the Mechanics and Physics of Solids*, 71(1):179–196, 2014.

[20] Yinggang Li, Tianning Chen, Xiaopeng Wang, Yanhui Xi, and Qingxuan Liang. Enlargement of locally resonant sonic band gap by using composite plate-type acoustic metamaterial. *Physics Letters, Section A: General, Atomic and Solid State Physics*, 379(5):412–416, 2015.

[21] Ling Ling and Yong Huang. Topology optimization design of gearbox housing in electric bus. *Applied Mechanics and Materials*, 574:173–178, 2014.

[22] Z. Liu, X. Zhang, Y. Mao, Y. Y. Zhu, Z. Yang, C. T. Chan, and P. Sheng. Locally resonant sonic materials. *Science*, 289(5485):1734–1736, 2000.

[23] Brian R. Mace, Denis Duhamel, Michael J. Brennan, and Lars Hinke. Finite element prediction of wave motion in structural waveguides. *The Journal of the Acoustical Society of America*, 117(5):2835–2843, 2005.

[24] Brian R. Mace and Elisabetta Manconi. Modelling wave propagation in two-dimensional structures using finite element analysis. *Journal of Sound and Vibration*, 318(4-5):884–902, 2008.

[25] D. J. Mead. A General Theory of Harmonic Wave Propagation in Linear Periodic Systems with Multiple Coupling. *Journal of Sound and Vibration*, 27(2):235–260, 1973.

[26] Noé F. Melo, Claus Claeys, Elke Deckers, Bert Pluymers, and Wim Desmet. Dynamic Metamaterials for Structural Stopband Creation. *SAE International Journal of Passenger Cars - Mechanical Systems*, 9(3), 2016.

[27] Mourad Oudich, Yong Li, Badreddine M. Assouar, and Zhilin Hou. A sonic band gap based on the locally resonant phononic plates with stubs. *New Journal of Physics*, 12, 2010.

[28] Luca Sangiuliano, Claus Claeys, Elke Deckers, Jasper De Smet, Bert Pluymers, and Wim Desmet. Reducing Vehicle Interior NVH by Means of Locally Resonant Metamaterial Patches on Rear Shock Towers. *SAE Technical Papers*,

2019(June), 2019.

[29] Luca Sangiuliano, Claus Claeys, Elke Deckers, Bert Pluymers, and Wim Desmet. Force Isolation by Locally Resonant Metamaterials to Reduce NVH. *SAE Technical Papers*, 2018(June):1–7, 2018.

[30] Stoyan Slavov and Mariya Konsulova-Bakalova. Optimizing weight of housing elements of two-stage reducer by using the topology management optimization capabilities integrated in SOLIDWORKS: A case study. *Machines*, 7(1), 2019.

[31] Lucas Van Belle, Claus Claeys, Elke Deckers, and Wim Desmet. On the impact of damping on the dispersion curves of a locally resonant metamaterial: Modelling and experimental validation. *Journal of Sound and Vibration*, 409:1–23, 2017.

[32] Thomas Weisser, Emmanuel Foltête, Noureddine Bouhaddi, and Luc Olivier Gonidou. A power flow mode approach dedicated to structural interface dynamic characterization. *Journal of Sound and Vibration*, 334:202–218, 2015.

[33] Yong Xiao, Jihong Wen, Gang Wang, and Xisen Wen. Theoretical and experimental study of locally resonant and bragg band gaps in flexural beams carrying periodic arrays of beam-like resonators. *Journal of Vibration and Acoustics, Transactions of the ASME*, 135(4), 2013.

[34] Junmin Yu, Can Nerse, Giseok Lee, Semyung Wang, and Chang Kyoung-Jin. Mass production applicable locally resonant metamaterials for NVH applications. In *Proceedings of the 26th International Congress on Sound and Vibration, ICSV26*, Montreal, 2019.

[35] S. Zouari, J. Brocail, and J. M. Génevaux. Flexural wave band gaps in metamaterial plates: A numerical and experimental study from infinite to finite models. *Journal of Sound and Vibration*, 435:246–263, 2018.

IDENTIFICATION OF VEHICLE FREQUENCY RESPONSE FUNCTION BASED ON TIKHONOV REGULARIZATION METHOD

Xinhao An[1], Jilin Hou[1], Qingxia Zhang[2], and Łukasz Jankowski[3]

[1]School of Civil Engineering, Dalian University of Technology, 116023 Dalian, China
[2]School of Civil Engineering, Dalian Minzu University, 116600 Dalian, China
[3]Institute of Fundamental Technological Research, Polish Academy of Sciences, 02-106 Warsaw, Poland

e-mail: houjilin@dlut.edu.cn

Abstract

The vehicle frequency response function (FRF) reflects the relationship between the vehicle response and different road surface excitations, and it has a very important practical significance. The direct inverse computation of vehicle FRF usually have many singularities due to the noise pollution or insufficient measured data in practice. Therefore, a method based on Tikhonov regularization is proposed to obtain a reliable vehicle FRF. The method can remove the singularities to make the results more accurate. Firstly, according to the displacement of the vehicle and the road contact point, the vehicle frequency response function is derived to establish the relationship between the frequency response function, the vehicle response and the road profile in the frequency domain. Then, the vehicle frequency response is directly estimated by using the vehicle response when driving over road bumps of a known size. Finally, Tikhonov regularization method is employed to remove the singular data existing in the direct calculation of the vehicle FRF and to update the estimated vehicle FRF

Keywords: frequency response function, Tikhonov regularization, vehicle response.

1.Introduction

Structural frequency response function (FRF) reflects the relationship between system responses and external excitations, and it has a very important practical significance in structural dynamic analysis. It can be used for modal identification [1] and parameter identification [2-5], structural damage identification [6-9] and model modification [10,11].

Based on the characteristic of FRF, vehicle FRF is widely used on the identification of vehicle parameters and road conditions. Thite et al.[12] proposed a method to identify vehicle suspension parameters in the frequency domain based on four-column bench test data. Zhao et al.[13,14] identified the vehicle parameters of a four-degree-of-freedom (DOF) half-car model via vehicle FRF. Zhang et al.[15] and Liu et al.[16] used the vehicle FRF to identify road roughness.

Theoretically, the FRF can be directly calculated by measured excitation signal and response signal. However, due to noise pollution in the measured signal, singular points usually exist in the direct calculation of FRF. While it is possible to remove or reduce singularities by measuring multiple sets of data and averaging the measured data, however, this requires more experimental work. Hostettler et al.[17]proposed a maximum likelihood estimation method for FRF under similar impulse excitation. Peumans et al.[18] obtained accurate FRF for a lightly damped mechanical system by using BootStrapped total least squares. The local polynomial method [19,20] and the local rational method [21,22] are also proposed respectively, which approximate the FRF locally by polynomial or rational function in the frequency domain, so as to obtain the exact estimate of the nonparametric FRF. This study tries to use a simpler method to obtain reliable FRF.

Tikhonov regularization is an improved least square estimation method, which has a better fitting effect on ill-conditioned data. Zhang et al.[23] solved the ill-posedness of damage recognition based on sensitivity by

Tikhonov regularization method. Wang et al.[24] used the improved Tikhonov regularization method for structural damage identification, which was more accurate under noise conditions. Li et al.[25] proposed an adaptive Tikhonov regularization method to solve parameter correction of nonlinear model, which is more accurate than the traditional method under high noise conditions. Wang et al.[26] used the iterative Tikhonov regularization method to identify the load size outside the structure and prove its stability

In this study, the vehicle FRF is regarded as a continuous function in frequency domain, and Tikhonov regularization method is used to fit it for the elimination of singular points. In the second part, the expression method of vehicle acceleration FRF and Tikhonov regularization correction method are introduced. In the third part, the feasibility of the proposed method is verified by numerical simulation.

2. Identification of Vehicle Frequency Response Function

2.1 Vehicle model

A four-DOF half-car model adopted in this paper is shown in Figure 1, which is a simplified mass-spring and damping model. The model can represent the mechanical characteristics of the vehicle suspension and the unsprung part. Here $u_1(t)$, $u_2(t)$, $u_3(t)$ and $u_4(t)$ of the model respectively represents the vertical displacement of the vehicle body, the pitching rotation of the body, the vertical displacement of the front wheel and the vertical displacement of the rear wheel.
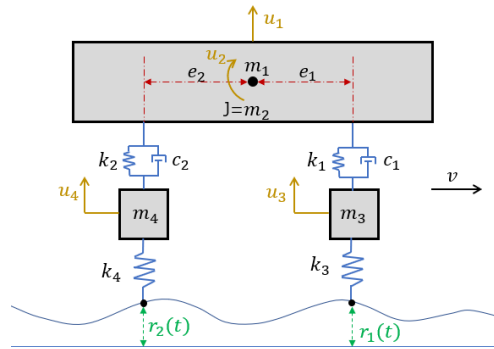

Figure 1:Half-car model of vehicle

The parameters used to represent the vehicle body refer to body mass m_1, body pitch moment of inertia m_2, distance respectively from the centroid of the vehicle to front and rear wheel e_1 and e_2. The parameters of the suspension include front and rear suspension stiffness k_1 and k_2, front and rear suspension damping coefficients c_1 and c_2. The parameters of the wheels -- unsprung part include mass of front and rear wheel m_3 and m_4 and the stiffness coefficients k_3 and k_4 of front and rear wheels.

Assume the vehicle travels on a rigid road surface, so that the coupled vibration of the vehicle and road can be ignored. The vibration differential equation of the vehicle can be obtained by system dynamic force analysis. Its matrix form is shown in Eq. (1) where **M**, **C** and **K** respectively represents the vehicle mass matrix, damping matrix and stiffness matrix. Respectively denote $r_1(t)$ and $r_2(t)$ as the road profile corresponding to the wheel and ground contact displacement. **F** represents the excitation generated by the road roughness of the vehicle, which can be calculated by the stiffness of wheels and the road profile, as show in Eq. (2). The detailed elements in matrices of Eq. (1) are expressed as Eq. (3) ~ Eq.(8).

(1) $$\mathbf{M}\ddot{u}(t)+\mathbf{C}\dot{u}(t)+\mathbf{K}u(t)=\mathbf{F}(t)$$

(2) $$\mathbf{F}(t) = \mathbf{K_t}\mathbf{r}(t)$$

(3) $$\mathbf{M} = \begin{bmatrix} \mathbf{m_1} & & & \\ & \mathbf{m_2} & & \\ & & \mathbf{m_3} & \\ & & & \mathbf{m_4} \end{bmatrix}$$

(4)
$$K = \begin{bmatrix} k_1 + k_2 & k_2 e_2 - k_1 e_1 & -k_1 & -k_2 \\ k_2 e_2 - k_1 e_1 & k_1 e_1^2 + k_2 e_2^2 & k_1 e_1 & -k_2 e_2 \\ -k_1 & k_1 e_1 & k_1 + k_3 & 0 \\ -k_2 & -k_2 e_2 & 0 & k_2 + k_4 \end{bmatrix}$$

(5)
$$C = \begin{bmatrix} c_1 + c_2 & c_2 e_2 - c_1 e_1 & -c_1 & -c_2 \\ c_2 e_2 - c_1 e_1 & c_1 e_1^2 + c_2 e_2^2 & c_1 e_1 & -c_2 e_2 \\ -c_1 & c_1 e_1 & c_1 & 0 \\ -c_2 & c_2 e_2 & 0 & c_2 \end{bmatrix}$$

(6)
$$K_t = \begin{bmatrix} 0 & 0 \\ 0 & 0 \\ k_3 & 0 \\ 0 & k_4 \end{bmatrix}$$

(7)
$$r = \begin{bmatrix} r_1 \\ r_2 \end{bmatrix}$$

(8)
$$u = \begin{bmatrix} u_1 \\ u_2 \\ u_3 \\ u_4 \end{bmatrix}$$

2.2 Frequency response function of vehicle

Perform Fourier transform on both sides Eq. (1), and the vehicle dynamic equation in the frequency domain can be obtained, which is shown in Eq. (9) as follows:

(9)
$$-\omega^2 MU(\omega) + \omega j CU(\omega) + KU(\omega) = K_t R(\omega)$$

The vehicle responses $U(\omega)$ in frequency domain can be obtained from Eq. (9), as shown in Eq. (10):

(10)
$$U(\omega) = (-\omega^2 M + \omega j C + K)^{-1} K_t R(\omega)$$

When only acceleration sensors are used to measure the responses in practice, the measured responses can be written as in Eq. (11), where C_0 is the observation matrix.

(11)
$$Y(\omega) = -\omega^2 C_0 U(\omega)$$

By substituting Eq. (10) into Eq. (11), the measured responses can be expressed in the term of FRF and road roughness in frequency domain, as shown in Eq. (12):

(12)
$$Y(\omega) = H_{yr}(\omega) R(\omega)$$

The vehicle FRF between road surface and vehicle acceleration is shown in Eq. (13):

(13)
$$H_{yr}(\omega) = -\omega^2 C_0 (-\omega^2 M + \omega j C + K)^{-1} K_t$$

2.3 Estimation of vehicle FRF using Tikhonov regularization method

FRF can be estimated directly according to Eq. (14).

(14)
$$H_{yr}(\omega) = Y(\omega) R^{-1}(\omega)$$

The amplitude of road roughness $R(\omega)$ is close to 0 at some frequency values, which results in the singularity of the frequency response at these values. According to the relationship expressed in Eq. (1), the Tikhonov regularization method is used to establish the objective function for the estimation of the vehicle frequency response function $H_{yr}(\omega)$, as shown in Eq. (15).

(15)
$$\min(\mathbf{f}) \Rightarrow \sum \left\| \mathbf{H_{yr}}(\omega_i)\mathbf{R}(\omega_i) - \mathbf{Y}(\omega_i) \right\|_2^2 + \lambda \sum \left\| \mathbf{H_{yr}}(\omega_i) - \mathbf{H_{yr}}(\omega_{i-1}) \right\|_2^2$$

where λ represents the regularization coefficient.

3 Numerical Simulation

To verify the validity of the proposed theory, a four-DOF half vehicle model is used for numerical simulation of the vehicle driving over the bump at a certain speed. The vehicle model is shown in Figure 1.

3.1 Parameters of vehicle model and bump

The values of the vehicle parameters are shown in Table 1. In addition, the distances between the centroid of the vehicle and the front and rear wheels respectively is $e_1 = 1.5\text{m}$ and $e_2 = 1.6\text{m}$.

Model parameters	Values
m_1	1400 kg
m_2	2000 kg·m²
m_3	75 kg
m_4	70 kg
k_1	26000 N/m
k_2	25000 N/m
k_3	184000 N/m
k_4	154000 N/m
c_1	3000 N·s /m
c_2	3000 N·s /m

Table 1: Vehicle parameters

The height of the bump is 0.02m with length of 0.5m, and the shape of its profile is shown in Figure 2. In the simulation, the vehicle passes the bump at two speeds, i.e. 9 m/s and 5 m/s respectively. In cases of different driving speeds, the corresponding excitation generated by the bump in frequency domain is shown in Figure 3.

According to Eq. (13) , via the measured vehicle responses, the vehicle FRF can be calculated if the profile of the road surface is known. Therefore, a field test of a vehicle driving over a bump of known shape is designed, where the profile of the bump is taken as the known road profile with the designed shape shown in Eq. (16):

(16)
$$r(x) = \frac{h(1 - \cos(\frac{2\pi x}{l}))}{2} \quad 0 \le x \le l$$
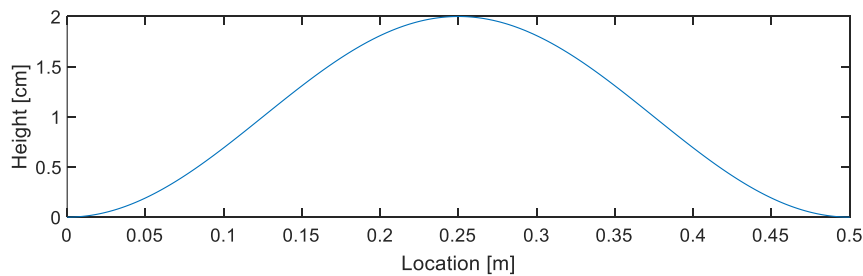
Figure 2: Bump profile
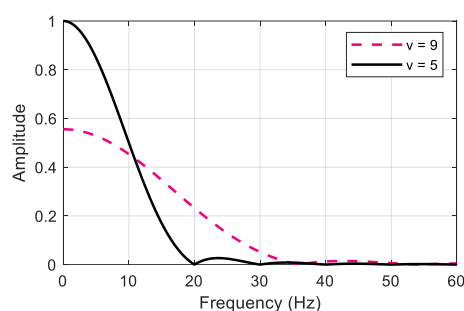
Figure 3: the excitation generated by the bump in frequency domain in case of different driving speeds

3.2 The simulated measured vehicle responses

Acceleration sensors were employed to measure the vertical responses, which are respectively located along the DOF of body $u_1(t)$, front wheel $u_3(t)$ and rear wheel $u_4(t)$, and recorded as s_1, s_2 and s_3. To improve the calculation accuracy, let the vehicle pass over the bump at a constant speed of 9 m/s and 5m/s respectively. 5% gaussian white noise is added in the simulated measurement signal to simulate the noise pollution in practice. The time histories of the measured acceleration responses by sensors s_1, s_2 and s_3 at different speeds are respectively shown in Figure 4~Figure 6. By Fourier transform, the measured responses in frequency domain are respectively shown in Figure 7~Figure 9.
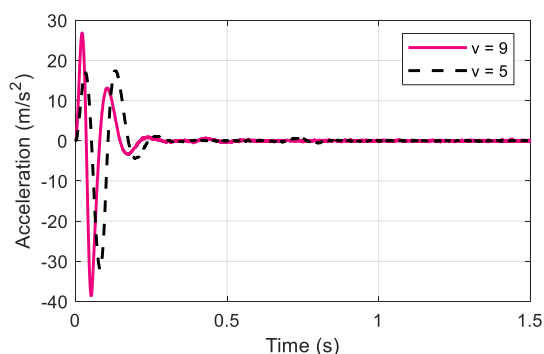
Figure 4:Accelerations of the front wheel measured by s_2 with velocities of 9 m/s and 5 m/s, respectively
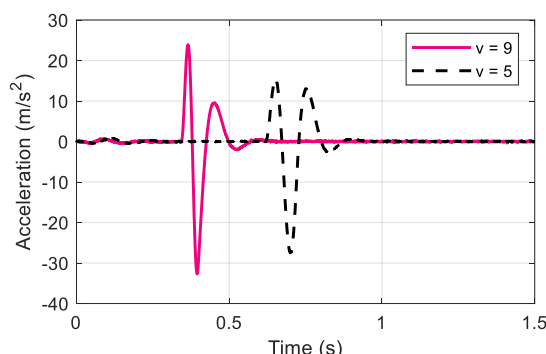
Figure 5:Accelerations of the rear wheel measured by s_3 with velocities of 9 m/s and 5 m/s, respectively
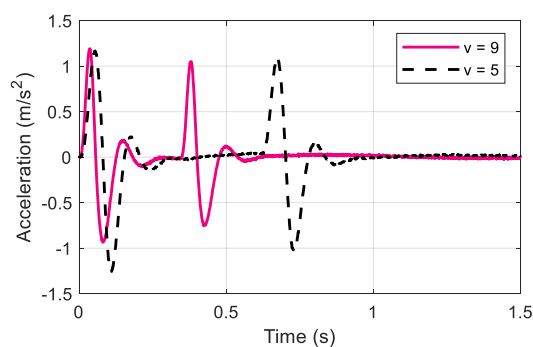
Figure 6: Accelerations of the vehicle body measured by s_1 with velocities of 9 m/s, and 5 m/s, respectively
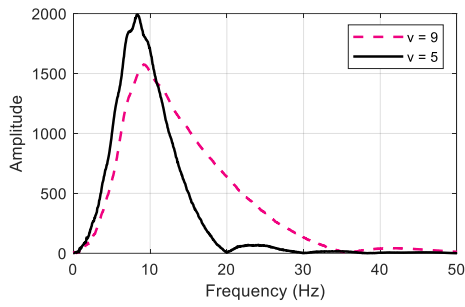
Figure 7: Acceleration of the front wheel measured by s_2 with velocities of 9 m/s and 5 m/s respectively in frequency domain
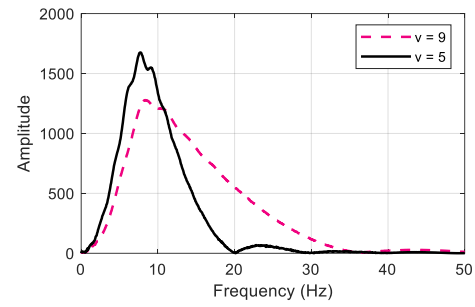
Figure 8: Acceleration of the rear wheel measured by s_3 with velocities of 9 m/s and 5 m/s respectively in frequency domain
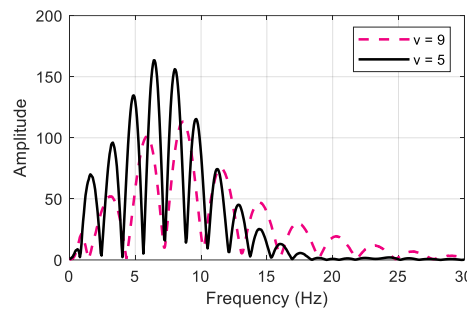
Figure 9: Acceleration of the vehicle body measured by s_1 with velocities of 9 m/s and 5 m/s respectively in frequency domain

3.3 Estimation of FRF using the direct calculation

Via Eq. (14), the acceleration FRF of different DOF to the displacement of wheel contact point can be calculated directly as shown in Figure 10~Figure 15.
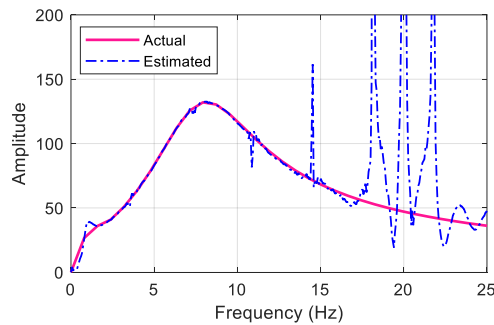
Figure 10: Estimated vehicle FRF along DOF u_1 to the unit displacement of the front wheel contact point
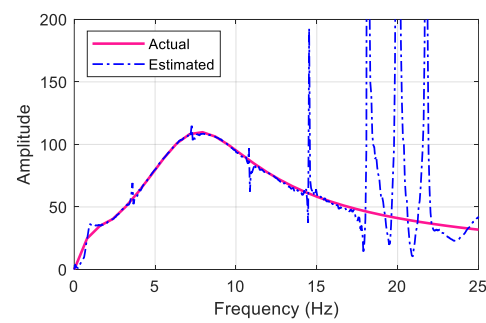
Figure 11: Estimated vehicle FRF along DOF u_1 to the unit displacement of the rear wheel contact point
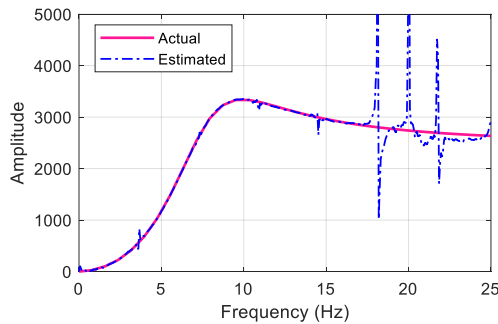
Figure 12: Estimated vehicle FRF along DOF u_3 to the unit displacement of the front wheel contact point
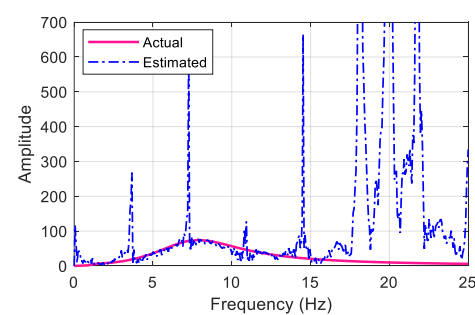
Figure 13: Estimated vehicle FRF along DOF u_3 to the unit displacement of the rear wheel contact point
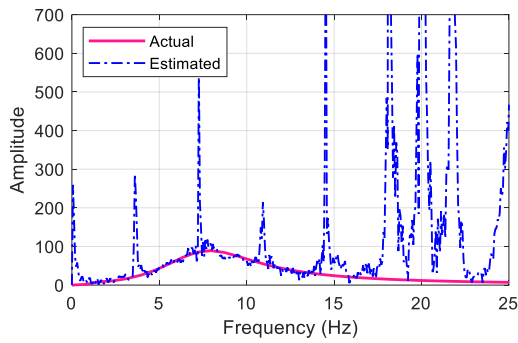
Figure 14: Estimated vehicle FRF along DOF u_4 to the unit displacement of the front wheel contact point
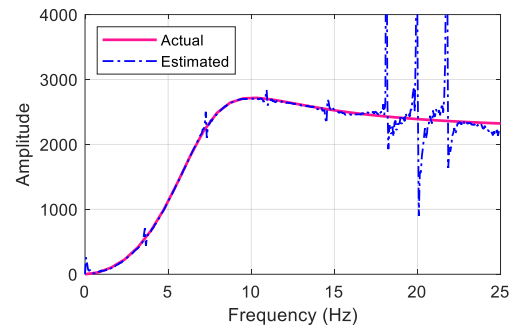
Figure 15: Estimated vehicle FRF along DOF u_4 to the unit displacement of the rear wheel contact point

From Figure 10~Figure 15, it can be seen that there are singular points existing in the frequency response function calculated using only data from a few times of tests. In the curve of the estimated FRF, several singular points exist especially after 15 Hz, and thus it will cause large errors in the further application of FRF.

3.4 Updating of FRF using Tikhonov regularization

In the above analysis, due to noise pollution or lack of measured data, there are obvious singular values in the direct estimation of vehicle FRF. The Tikhonov regularization method is used to update the estimated FRF. Set the regularization coefficient λ=0.0025 in Eq. **Błąd! Nie można odnaleźć źródła odwołania.** .
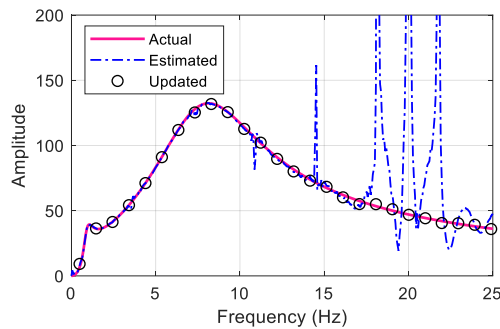
Figure 16: The updated vehicle FRF along DOF u_1 to the unit displacement of the front wheel contact point
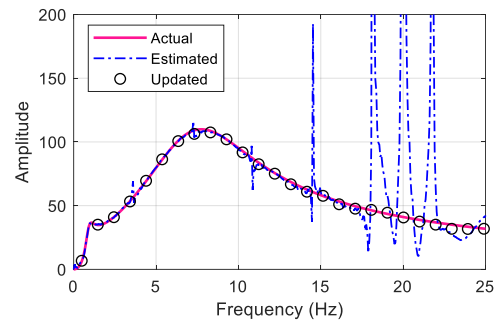
Figure 17: The updated vehicle FRF along DOF u_1 to the unit displacement of the rear wheel contact point
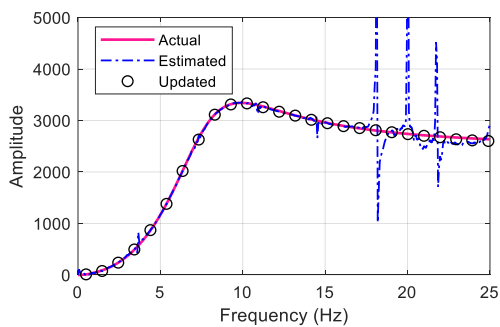
Figure 18: The updated vehicle FRF along DOF u_3 to the unit displacement of the front wheel contact point
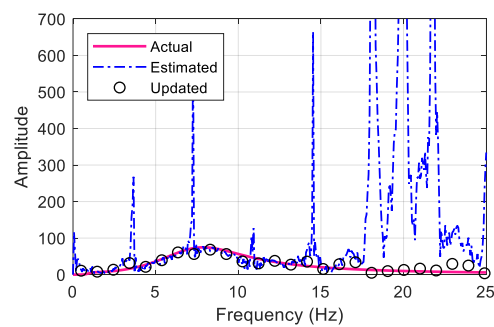
Figure 19: The updated vehicle FRF along DOF u_3 to the unit displacement of the rear wheel contact point
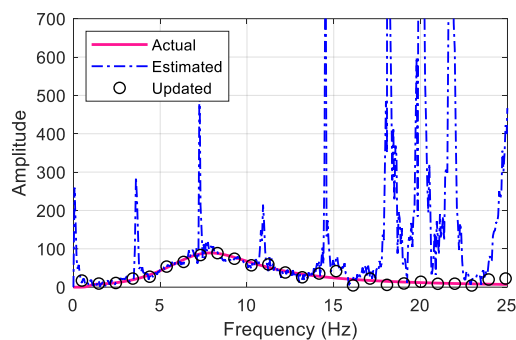
Figure 20: The updated vehicle FRF along DOF u_4 to the unit displacement of the front wheel contact point
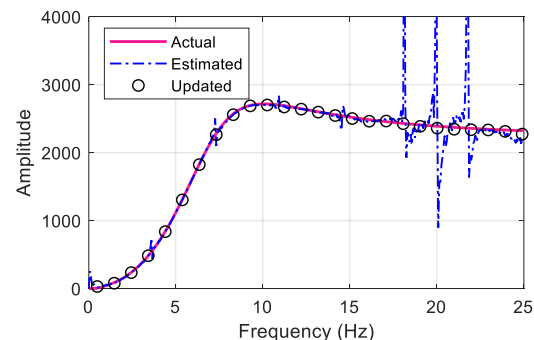
Figure 21: The updated vehicle FRF along DOF u_4 to the unit displacement of the rear wheel contact point

5. Conclusion

A method for the estimation of vehicle FRF was proposed based on Tikhonov regularization. The validity of the method was verified by numerical simulation of vehicle driving tests, and the main conclusions are as follows:

(1) Although the vehicle acceleration FRF can be estimated theoretically via the measured response of the vehicle passing over a bump with known shape, there are many singular values in the obtained results, especially in the part of high frequencies.

(2) Tikhonov regularization method can be used to update the estimated frequency response function, and then the vehicle FRF with higher accuracy can be obtained, which help realize the further potential application of vehicle FRF.

References

[1] F. Shen and M. Zheng. Using the Cross-Correlation Technique to Extract Modal Parameters On Response-Only Data. *J. Sound Vib.*, 259:1163, 2003.

[2] J. Guo, L. Wang and I. Takewaki. Frequency Response-Based Damage Identification in Frames by Minimum Constitutive Relation Error and Sparse Regularization. *J. Sound Vib.*, 443:270, 2019.

[3] A. Esfandiari, M.S. Nabiyan and F.R. Rofooei. Structural Damage Detection Using Principal Component Analysis of Frequency Response Function Data. *Structural Control and Health Monitoring*, 27:1, 2020.

[4] M. Dalenbring. Damping Function Estimation Based On Measured Vibration Frequency Responses and Finite-Element Displacement Modes. *Mech. Syst. Signal Pr.*, 13:547, 1999.

[5] H.Y. Hwang. Identification Techniques of Structure Connection Parameters Using Frequency Response Functions. *J. Sound Vib.*, 212:469, 1998.

[6] U. Lee and J. Shin. A Frequency Response Function-Based Structural Damage Identification Method. *Comput. Struct.*, 80:117, 2002.

[7] S.M. Seyedpoor and N. Pahnabi. Structural Damage Identification Using Frequency Domain Responses and a Differential Evolution Algorithm. *Iranian Journal of Science and Technology, Transactions of Civil Engineering*, 45:1253, 2021.

[8] S. Wang and X. Long. Damage Identification for Underground Structure Based On Frequency Response Function. *Sensors-Basel*, 18:3033, 2018.

[9] S.M. Seyedpoor and N. Pahnabi. Structural Damage Identification Using Frequency Domain Responses and a Differential Evolution Algorithm. *Iranian journal of science and technology. Transactions of civil engineering*, 45:1253, 2020.

[10] M.H. Jalali and D.G. Rideout. Frequency-Based Decoupling and Finite Element Model Updating in Vibration of

Cable–Beam Systems. *J. Vib. Control*, 1802289651, 2021.

[11] Y. Hong and Q. Pu. Model-Updating with Experimental Frequency Response Function Considering General Damping. *Adv. Struct. Eng.*, 21:82, 2017.

[12] A.N. Thite and S. Banvidi. Suspension Parameter Estimation in the Frequency Domain Using a Matrix Inversion Approach. *Vehicle Syst. Dyn.*, 49:1803, 2011.

[13] B. Zhao and T. Nagayama. Vehicle Model Calibration in the Frequency Domain and its Application to Large-Scale Iri Estimation. *Journal of disaster research*, 12:446, 2017.

[14] B. Zhao and T. Nagayama. Iri Estimation by the Frequency Domain Analysis of Vehicle Dynamic Responses and its Large-Scale Application, 2016, 2016.

[15] Q. Zhang and J. Hou. Road Roughness Estimation Based On the Vehicle Frequency Response Function. *Actuators*, 10:89, 2021.

[16] S.W. Liu and X. Zhang. Relationship Between International Roughness Index and Power Spectral Density of Asphalt Pavements in China. *Advanced Materials Research*, 742:104, 2013.

[17] R. Hostettler, W. Birk and M. Lundberg Nordenvaad. Maximum Likelihood Estimation of the Non-Parametric Frf for Pulse-Like Excitations. *Ieee T. Automat. Contr.*, 61:2276, 2016.

[18] D. Peumans and A. De Vestel. Accurate Estimation of the Non-Parametric Frf of Lightly-Damped Mechanical Systems Using Arbitrary Excitations. *Mech. Syst. Signal Pr.*, 130:545, 2019.

[19] R. Pintelon and J. Schoukens. Estimation of Nonparametric Noise and Frf Models for Multivariable Systems—Part I: Theory. *Mech. Syst. Signal Pr.*, 24:573, 2010.

[20] R. Pintelon and J. Schoukens. Estimation of Nonparametric Noise and Frf Models for Multivariable Systems—Part Ii: Extensions, Applications. *Mech. Syst. Signal Pr.*, 24:596, 2010.

[21] T. Mckelvey and G. Guérin. Non-Parametric Frequency Response Estimation Using a Local Rational Model1. *IFAC Proceedings Volumes*, 45:49, 2012.

[22] R. Voorhoeve, A. van der Maas and T. Oomen. Non-Parametric Identification of Multivariable Systems: A Local Rational Modeling Approach with Application to a Vibration Isolation Benchmark. *Mech. Syst. Signal Pr.*, 105:129, 2018.

[23] C.D. Zhang and Y.L. Xu. Comparative Studies On Damage Identification with Tikhonov Regularization and Sparse Regularization. *Structural Control and Health Monitoring*, 23:560, 2016.

[24] J. Wang and Q.S. Yang. Modified Tikhonov Regularization in Model Updating for Damage Identification. *Struct. Eng. Mech.*, 44:585, 2012.

[25] X.Y. Li and S.S. Law. Adaptive Tikhonov Regularization for Damage Detection Based On Nonlinear Model Updating. *Mech. Syst. Signal Pr.*, 24:1646, 2010.

[26] L. Wang, H. Cao and Y. Xie. An Improved Iterative Tikhonov Regularization Method for Solving the Dynamic Load Identification Problem. *International journal of computational methods in engineering science and mechanics*, 16:292, 2015.

THE PROBLEM OF GEOTHERMAL POWER INSTALLATION ON BUILDINGS: STRUCTURAL BUILDING MONITORING AND ASSESSMENT DURING DRILLING ACTIVITIES

D. Bortoluzzi[1], S. Casciati[1] and M. Francolini[2]

[1] *SIART Srl, via dei Mille 73, Pavia, Italy*

[2]Formerly *SIART Srl, via dei Mille 73, Pavia, Italy*

e-mail: danielebortoluzzi.ing@gmail.com

1. Abstract

The current European Union (EU) policy aims to increase the use of "green" energies, and within this strategy the exploitation of the geothermal energy is a well promising approach. The European Horizon2020 project GEOFIT (Deployment of novel GEOthermal systems, technologies and tools for energy efficient building retroFITting) aims among the others to deploy and to integrate advanced methods of worksite inspection, ground research, and building structural monitoring, drilling and worksite characterization into advanced geothermal based retrofitting methods.

When dealing with "plants of power production", one needs to develop a Life Cycle Analysis and to apply a Life Cycle Assessment (LCA) for evaluating any environmental aspects and potential influences throughout the whole life cycle of a product or process or service. The paper first provides a preliminary discussion on this aspect. Then it focuses attention on a pilot site made available within the GEOFIT Consortium. The results from a structural monitoring campaign in this pilot site before and during the drilling operations associated to the implementation of the geothermal power system are presented discussed.

2. Introduction

The authors are currently engaged in the European Horizon2020 project GEOFIT (Deployment of novel GEOthermal systems, technologies and tools for energy efficient building retroFITting). It aims, among others goals, to deploy and to integrate advanced methods of worksite inspection, ground research, and building structural monitoring, drilling and worksite characterization into advanced geothermal based retrofitting methods [1]. One of the pillars of the ongoing investigation is the exploitation of Life Cycle Analysis and Life Cycle Assessment (LCA), according to the definitions in ISO 14040 [2], toward the rationalization of the design. It is a technique for evaluating environmental aspects and potential impacts throughout the life cycle of a product or process or service through:

- the compilation and inventory of the significant inputs and outputs of the system;
- the assessment of the potential impacts associated with these inputs and outputs;
- the interpretation of the results of the inventory and evaluation phases, in relation to the objectives of the study.

When focusing on plants of power production, LCA is often adopted for comparing solutions exploiting different sources. A deep study was produced by the US Department of Energy in 2010 [3]. More recently an updated review was published in 2017 in [4]. All these studies report on large-size plants (see Figure 1). Section 3 discusses these aspects for smal size applications. The further sections illustrate the expertise caugth in monitoring the implementation stages.

3. Life Cycle Assessment outcome for small size geothermal plants

Any geothermal plant shows interfaces with the external world at the source and at the output levels. Under

the assumption that no disturbance is left at any time at the source level, a regular performance of the plant does not offer impacts at the output level. By contrast, any stop obliges the user to move to the power offered by the power company of reference. The associated global costs become losses originated by each stop of the geothermal plant and they strongly depend on the time of unavailability.
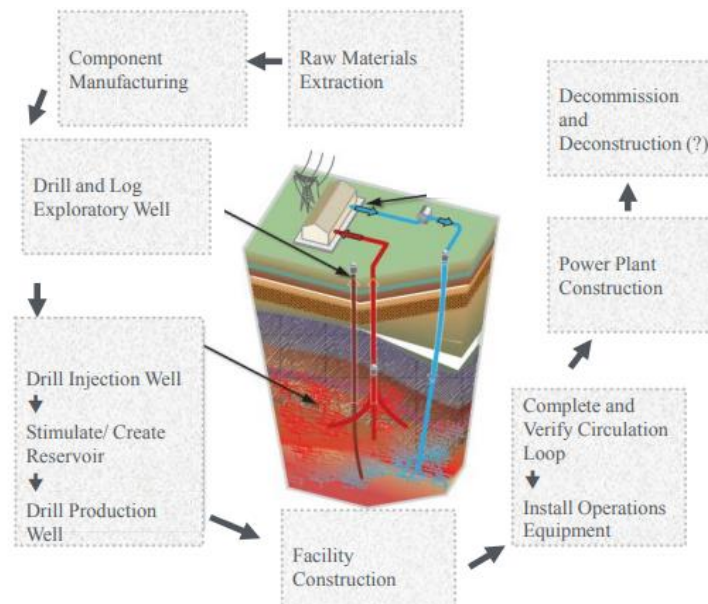
Figure 1 – The plant sketch considered by the US Department of Energy.

In the specific case of GEOFIT, the attention is focused on rural buildings or small size town buildings being "geothermal retrofitted". Thus, one of the expected goals covers the optimization of the plant design. This is the specific target pursued in this section.

When approaching LCA analysis and studies, the possibility to deal with redundancy system is fundamental to compute the reliability of the resulting system. As a first step one needs to idealize whether the system is classifiable as [5-7] :

- *Series systems* that also are non-repairable: the system works if and only if all components work (*non-redundant system*);

- *Parallel system*s that also are non-repairable: the system works even if some components are not working (*redundant system*).

Once the plant is idealized as the series/parallel assemblage of components, the target is to compute the reliability of the resulting system, characterized by a number of redundancies to be optimized. These redundancies are better adopted for those components whose replacement requires more time. The actual economic options, however, can only be caught when data on the costs encountered after a system failure are made explicit.

As well outlined in the GEOFIT research activity progresses, three classes of component characterize a geothermal plant: the pipe, the pump and the conversion device (i.e. single redundancy). In the following table the reliability versus time for systems with single redundancy as obtained by CARDINAL [8] are presented. The selected redundancy degree influence the extent of the drilling the implementation of the power system requires.

Redundancy	1 year	5 years	10 years	20 years
borehole	1 - 0.1045	1 - 0.4237	1 - 0.6700	1 - 0.8933
geothermal pump	1 - 0.0526	1 - 0.2894	1 - 0.5505	1 - 0.8449
radiant panel	1 - 0.0837	1 - 0.3650	1 - 0.6134	1 - 0.8668
Double:bor.&pump	**1 - 0.0409**	**1 - 0.2474**	**1 - 0.4990**	**1 – 0.8114**

Table 1 – Reliability vs. time for systems with single and double redundancy as obtained by CARDINAL

4. Pilot case: The "Pins del Vallès School in Sant Cugat"

The case under study covers "Els Pins del Vallès" School, which is located in Sant Cugat, about 25km North-West of the town of Barcelona (Spain) (see Figure 2). The building under study consists of three reinforced concrete elements:

1. School main building;
2. Administrative building (see Figure 3);
3. Pavilion building.
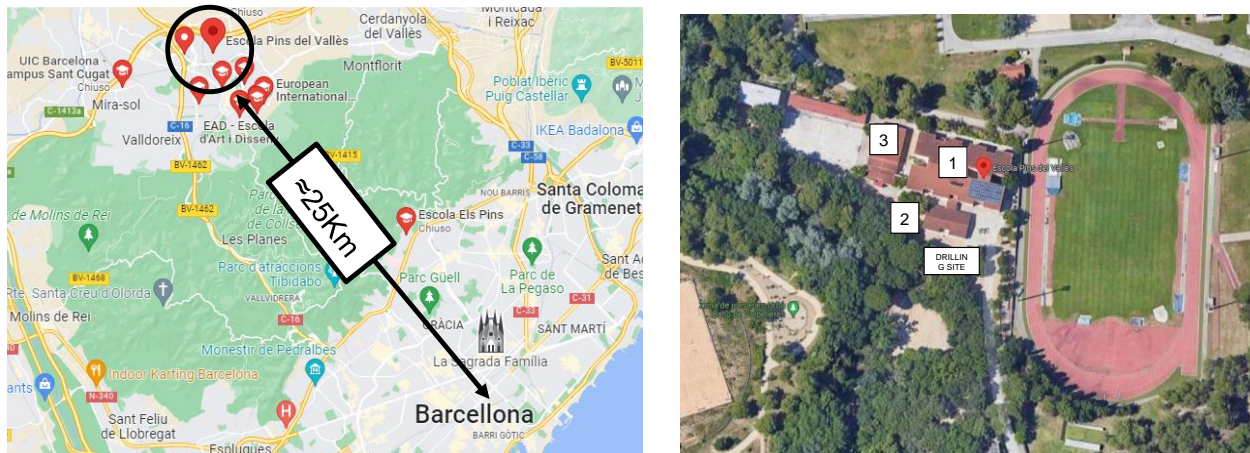
Figure 2: Pilot site location.

The building investigated in this paper is the administrative building (building #2 in Figure 2), i.e., the closest to the selected drilling site. From a structural point of view, its scheme consists of reinforced concrete (RC) columns, beams and walls. Geometrically speaking the building has a rectangular-shaped plan: about 23.70 by 12.75 m. It has only one floor above the ground and a double-pitch roof. The inter-floor height varies in the range from 2.50 to 3.50 m (see Figure 3).
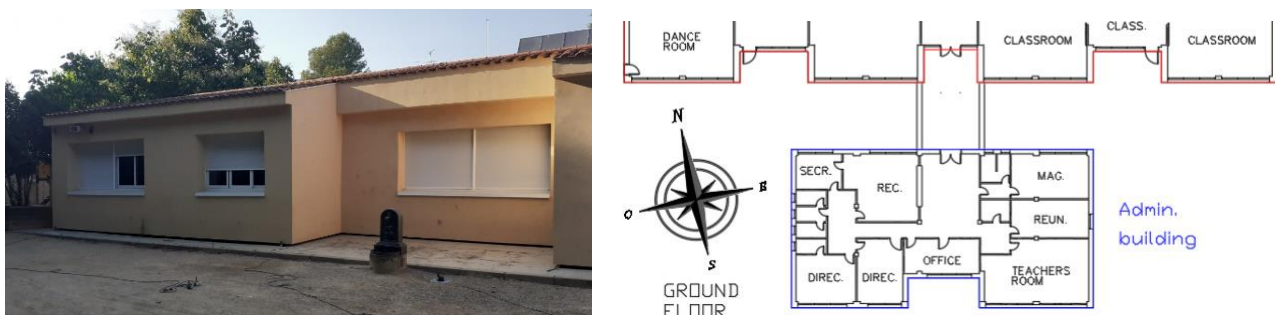
Figure 3: Administrative building: frontal view (left); plant (right).

Due to some technical issues related to the implementation of the geothermal technology, and in particular due to the vibration caused during drilling activities, standard application refers only to buildings in isolated locations, i.e., far from urban nuclei. Nevertheless, the installation itself requires to drill close to the building. The source of vibrations caused by this activity may result dangerous for the target building. Thus, a careful Structural Monitoring (SM) on site, during excavation activities, has to be planned to prevent from any sort of structural damage [9].

5. The experimental campaign

A dedicate monitoring campaign based on the acquisition of acceleration data of sensitive points along the administrative building under environmental loads and under drilling activities has been designed and

implemented. This campaign had a double purpose:

1. To identify the dynamic behaviour of the building in the original state (pre-drilling) and during the drilling activities;

2. To customize and to validate a "building monitoring strategy when implementing geothermal power system" in an existing building.

The tests carried out on site has been organized as follows:
   A. a preliminary visual investigation of the building to determine the current state of the structure in its operational state and the detection of possible anomalies and/or damage.
   B. *environmental loads survey campaign* carried out by the acquisition of accelerometric signals to assess the building dynamic behaviour in the pre-drilling phase;
   C. *drilling phase survey campaign* to cover the collection of accelerometric data during the installation of the geothermal energy system (i.e. drilling activities).

The monitoring system designed for the above purpose is made by a set of tri-axial *EPISENSOR Model FBA ES-T* accelerometers [10] coupled with a Wireless Data Acquisition, collection and transmission System (WDAS) designed in [11-12] and tested during several test applications [13-14]. The main advantages of using these sensors are: very-low self-noise, resulting in 155 dB dynamic range; user-selectable full g-scale range: from ±0.25g to ±4g; user-selectable full output range: from ±2.5V to ±20V, differential; wide frequency response: from DC to 200 Hz (Figure 4).

When using wireless sensor units for the data transmission and collection there is the risk of data losses during transfer. The workstations adopted in the test come with the option of storing not only the received data but also the history of the transmission. This allows the operator to detect if data lost occurred as well as if some workstations received more points than others did. Therefore, in selecting the test among the several replicates carried out at the same sensor locations, the criterion of having the same number of recorded points was adopted. In other words, the elaborations cover reliable data only.

All recorded data have been gathered in terms of "*Volts*" and then converted into acceleration "*m/s²*" simply multiplying "Volts" by the factor "1/2.5" according to the technical specification of the accelerometers (SEE Figure 5).

Figure 4: Device equipment. Left: EPISENSOR Model FBA ES-T accelerometers; Right: Wireless Data Acquisition, collection and transmission System (WDAS)

During the fourth day (*drilling activities phase*), in order to identify the drilling-machine working frequencies for further and easier data elaboration and discussion, a data acquisition test focused on the drilling machine, was carried out by installing an *Episensor FBA* accelerometer directly on the machine (Figure 6).
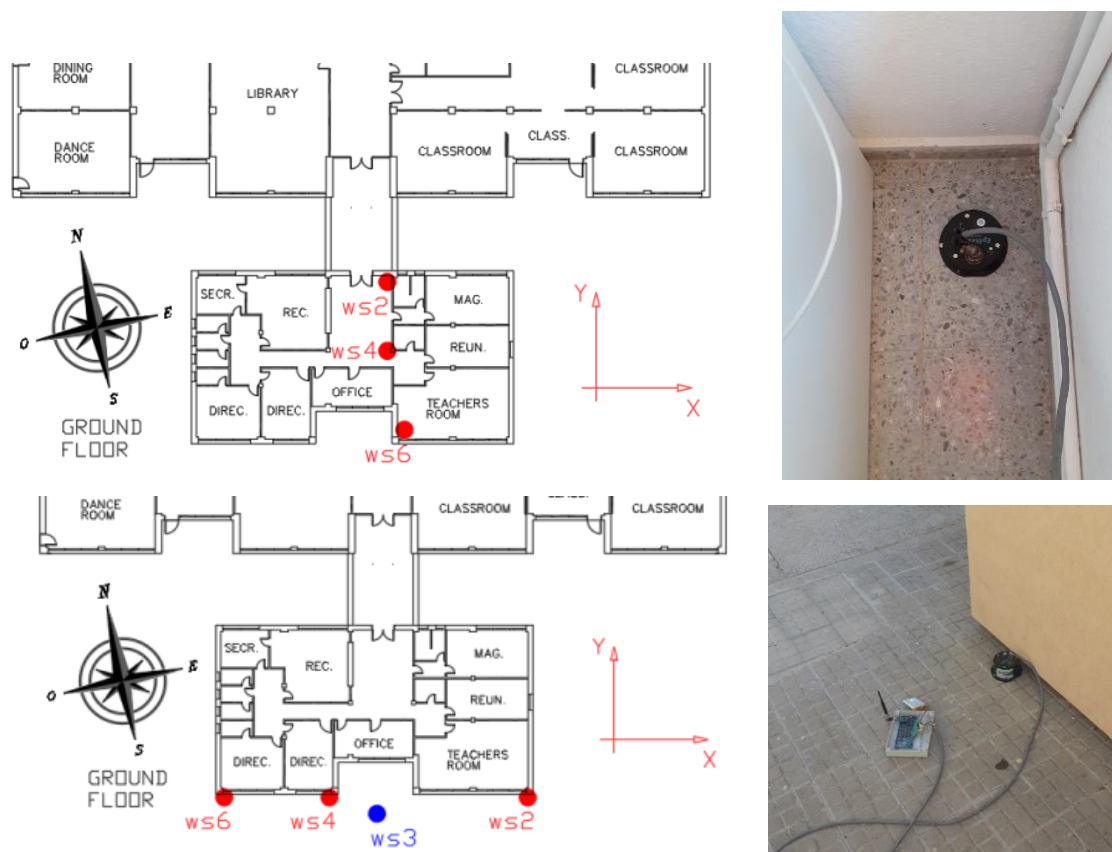
Figure 5: Devices configurations

Fig. 6 Drilling machine (left); The accelerometer on the drilling machine (right)

6. Some results

In this section the signal data elaborations (accelerations) gathered during the monitoring campaigns is presented. The data analysis used the tools offered by the *MatLab environment* (www.mathworks.com) and plotted in terms of *periodograms*. One estimates such periodogram in two alternative ways:

1. either by plotting the square of the absolute value of the signal's *Fast Fourier Transform* (*FFT*) multiplied by the time step (0.01s for all the recorded signals) and divided by the numbers of recorded points. The covered frequency range is from 0 to 50Hz, for a time step of 0.01s, and the frequency step results from the division of the higher frequency value, 50, divided by one half of the number of available recording times.

2. or by estimating the power spectral density of the signal for a given frequency step.

Option "1" was used to analyse the dynamic behaviour of the drilling machine as shown in Figure 7, mainly due to the wish of exploiting the entire reliable parts of the recorded signals.
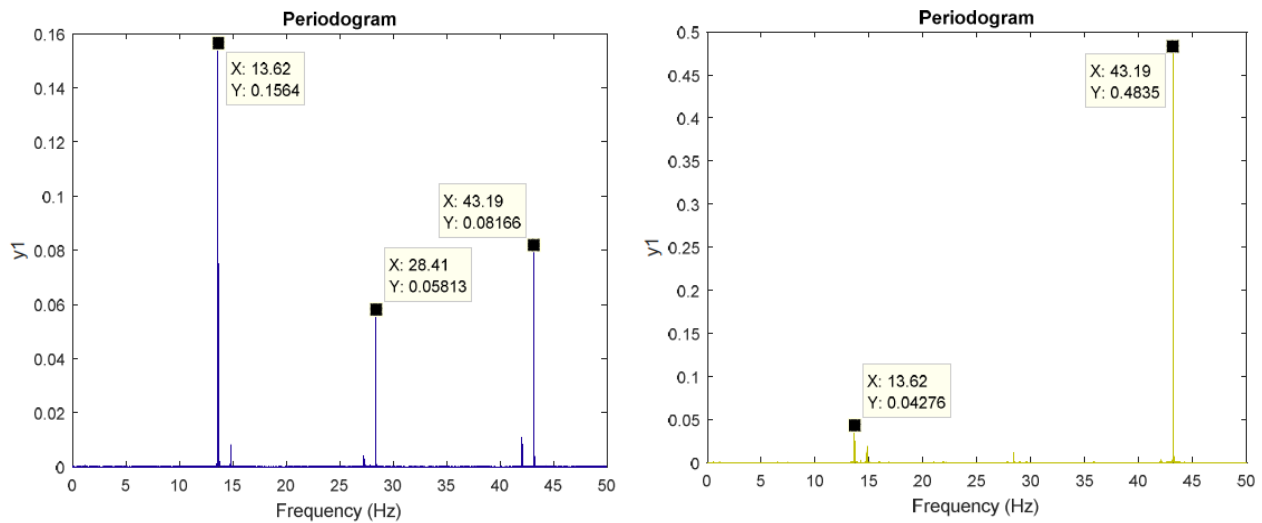
Figure 7. Dynamic characterization of the drilling machine. Periodograms for the signals recorded along the directions *X* (left) and gravity (*Z*) (right).

Option "2" was selected to analyse the administrative building response pre- and during-drilling activities (see sections 5). A discretization of the range 0-50 Hz in 512 points has been adopted. This scheme works on windows of the signal of 1024 points and keep the mean over the available windows. To preserve the same degree of accuracy not the entire signals are compared but segments of the same length, multiple of 1024 points, i.e., 2 to power 10. In particular, segments of length 32,768 (2 to power 15) were retained. For any selected set of data, the mean is first removed. Then a band-pass filter covering the window 0.8 – 50 Hz filters the signal. The plots give the periodograms achieved by a Power Spectral Density (*PSD*) estimate on windows of 2^10 (=1,024) points.

The data plotted in Figure 8 and Figure 9 come from the elaboration of the data recorded at WS3 along directions *Z* and *X* respectively. The left column covers the "pre-drilling" tests; the right column those during the drilling activities. The work station unit WS3 is located on a manhole nearby the building (see Figure 5). The signals collected in that location represents the incoming ground vibration for the building.
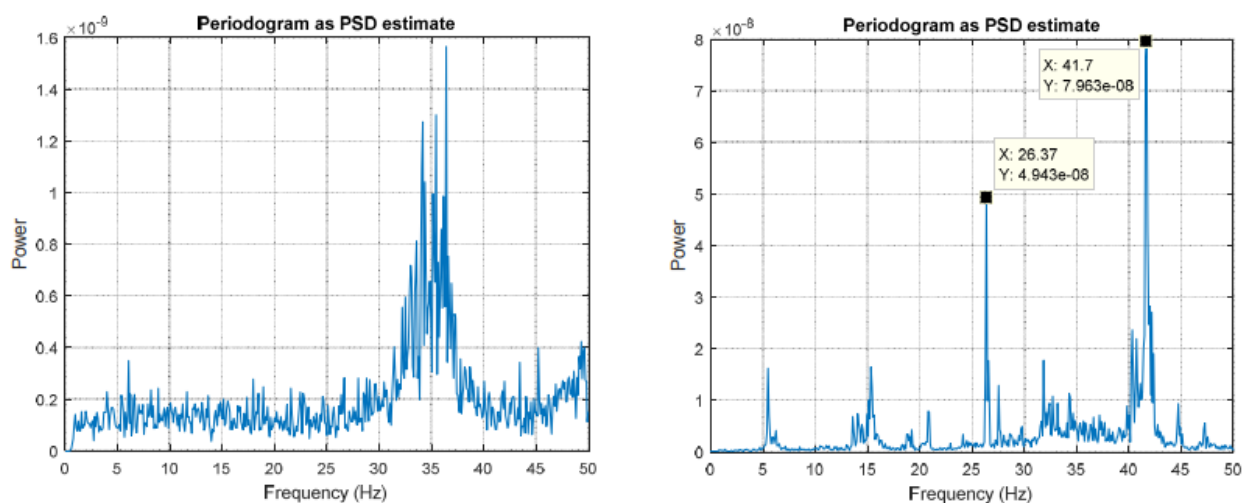
Figure 8. WS3: PSDs of the signals collected along gravity direction (*Z*): left "pre-drilling"; right "during the drilling"
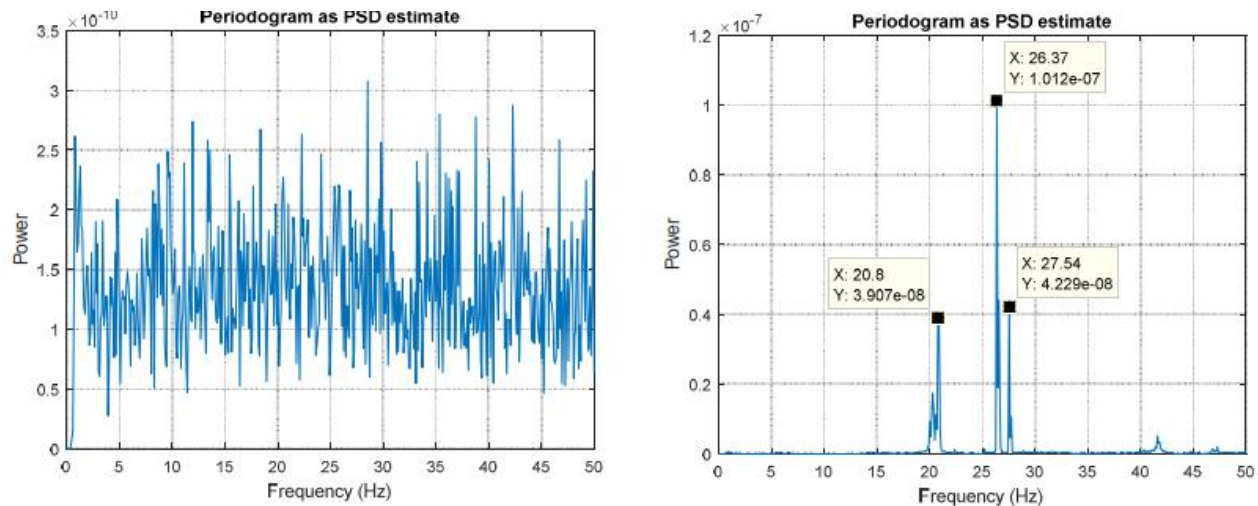
Figure 9. WS3: PSDs of the signals collected along horizontal direction (X): left "pre-drilling"; right "during the drilling"

As shown in Figure 7 the drilling machine itself generates three main frequencies, around 13 Hz, 28 Hz and 43 Hz. Moreover, the workstation on the manhole labelled as WS3 (Figure 5) shows that there is an external input when the drilling machine is active, input that was absent in the previous days when drilling activities was not carried out (Figure 7 and Figure 8).

7. Conclusions

In this paper the data gathered in a RC single-story building located in San Cugat (Barcelona-Spain), a pilot case within GEOFIT Project, have been collected, elaborated, presented, discussed and implemented within a LCA (Life Cycle Assessment) process to validate a "building monitoring strategy when implementing geothermal power system" in an existing building.

The basic steps of LCA, as introduced in Section 3, showed out the main role of the "system redundancy". The estimates in Table 1 outline the role of redundancy on the system reliability. Nevertheless, one cannot ignore the role of reparability and availability in the decision process.

Regarding the "building monitoring strategy" scope of the "pilot case" experience, one could extract the following items in view of guidelines for an automatic implementation of a geothermal power system in an existing building:

- define the dynamic behaviour of the "drilling machine" (by direct data acquisition);
- test the propagation of the vibration from the drilling location to the existing building;
- replicate the test at different depth of excavation, to understand the different response at the basement;
- produce the building signature to identify the frequencies sensible to nearby vibrations.

The experience carried out shown as the whole data acquisition process could easily be implemented in a consultation assistant and would be easily implemented in the field by technicians in thermo-technique, also without any background in vibration mechanics.

References

[1]   Geofit. "https://geofit-project.eu/"

[2]   https://www.iso.org/

[3]   https://www.energy.gov/sites/default/files/2014/02/f7/analysis_wang_lifecycle_analysis.pdf

[4]   C. Tomasini-Montenegro; E. Santoyo-Castelazo; H. Gujba; R.J. Romero; E.Santoyoad; "Life cycle assessment of geothermal power generation technologies: An updated review". *Applied Thermal Engineering* Volume 114, 5 March 2017, Pages 1119-1136

[5]   G. Augusti, A. Baratta, F. Casciati, 1984, *Probabilistic Methods in Structural Engineering*, 1984, Chapman & Hall.

[6]   R.E. Melchers, 1987, *Structural reliability analysis and prediction*, R. E. Ellis Horwood, Chichester.

[7]   F. Casciati, L. Faravelli, 1991, *Fragility Analysis of Complex Structural Systems*, Research Studies Press, Taunton.

[8]   CARDINAL User's manual

[9]   C. Yan; M. Sepideh; R. Shervin; G. Aria; B. Fateme; B. Shahrizan; H. Pedram; A. Hamid. "Economic application of structural health monitoring and internet of things in efficiency of building information modelling". *Smart Structures and Systems* - Volume 26 Issue 5 / Pages.559-573 / 2020 / 1738-1584(pISSN) / 1738-1991(eISSN) - Techno-Press

[10] Kinemetrics. " https://kinemetrics.com/post_products/episensor-es-t/"

[11] S. Casciati, Z. Chen, 2011. "A multi-channel wireless connection system for structural health monitoring applications" *Structural Control & Health Monitoring*, Volume: 18 Issue: 5 Pages: 588-600.

[12] S. Casciati, L. Faravelli, Z. Chen, 2012. "Energy harvesting and power management of wireless sensors for structural control applications in civil engineering" *Smart Structures and* Systems, Volume: 10   Issue: 3   Pages: 299-312.

[13] Z. Chen, S. Casciati, L. Faravelli, 2015. "In-Situ Validation of a Wireless Data Acquisition System by Monitoring a Pedestrian Bridge" *Advances in Structural Engineering*, Volume: 18   Issue: 1   Pages: 97-106.

[14] F. Casciati, S. Casciati, A. Colnaghi and L. Faravelli, "Geothermal Power: Monitoring the Building Response During Installation," in *Proceedings IWSHM*, Stanford, California, USA, 2019.

Neural Network-based Surrogates of Gear Whine Noise for Uncertainty Propagation

B. Z. Cunha[1,2], C. Droz[3], A. Zine[4], M. Ichchou[1], and S. Foulard[2]

[1] *Laboratoire de Tribologie et Dynamique des Systèmes, École Centrale de Lyon, Écully, France.*
[2] *Compredict, Darmstadt, Germany.*
[3] *Univ. Gustave Eiffel, Inria, COSYS/SII, I4S team, Rennes, France.*
[4] *Institut Camille Jordan, École Centrale de Lyon, Écully, France.*

e-mail: barbara.zaparoli-cunha@ec-lyon.fr

1. Abstract

Noise, Vibration, and Harshness (NVH) performance is a key aspect to evaluate passengers' comfort in vehicles. At the gearbox level, the gear tooth profile deviations give rise to vibrations during the gear meshing process, which is the source of gear whine noise. Therefore, an NVH design should account for the uncertainties at the gear micro-geometry level, demanding several evaluations of the gearbox model. Our study introduces a gearbox surrogate model based on Neural Networks (NN) to create a fast and accurate copy of the static and dynamic gearbox simulations made in Romax software. An accurate surrogate model was built, enabling a reduction of uncertainty propagation analyses time by a factor of 380, compared with traditional modeling by Romax.

2. Introduction

Gear whine is a tonal and annoying noise that originates in the gear meshing process in gear transmissions. The main cause of gear whine is the Static Transmission Error (STE), which can be defined as the difference between the actual contact position of the output teeth and its theoretical position in a perfect conjugated contact [16] accounting for deviations from an involute profile due to profile modifications, manufacturing errors, misalignments, and elastic deflections [4]. The challenges to designing a silent gearbox increase in the cases of lightweight gearbox design, a crucial requisite to more sustainable vehicles [14], as lightweight gearboxes tend to be more flexible, leading to more misalignments, higher STE, and greater amplitudes of housing vibration, radiating more noise.

The proper evaluation of the whining noise includes the evaluation of the STE and, subsequently, the application of the STE as a source of excitation of the system to evaluate its dynamic behavior, which closely correlates with the whining noise [14]. Åkerblom [1] provided a review of the methodologies used to model the STE and the gear transmission dynamic analysis. Guo et al. [6] showed that the housing should be included in the system model, allowing to account for the coupling effects of it with the system and to quantify the housing vibration. Besides, the effect of manufacturing errors and other uncertainties in the gear teeth profile cannot be neglected, once the profile errors are the cause of the system excitation, and, therefore, micro-geometry uncertainty propagation must be performed even for tight tolerances [4].

To alleviate the computational burden of the numerous and costly evaluations involved in the uncertainty propagation of the static and dynamic analyses of the entire gearbox, this paper proposes to create a surrogate model based on Neural Networks (NN). The surrogate models or response surface methods are simple and efficient input-output maps of a more complex model with little loss of accuracy and are currently used to speed up many engineering problems [2, 13].

A surrogate model of the STE was developed by Park [11] using a parametric second-order regression to fit the model. However, Machine Learning (ML) methods usually have better generalization capabilities than parametric methods and can deliver better prediction results. This statement is supported by the results from the comparison of three different STE surrogates done by Korta and Mundo [8]. To the author's knowledge,

the development of a surrogate to predict dynamic responses of an entire fully-coupled gearbox system has not been achieved so far. By implementing an automatic integration of *Python* with the Romax software [12], this work will enable the creation of a novel NN-based surrogate model for the static and dynamic analysis of complete gear transmission. The present paper adds to the current state of the art as it analyzes a surrogate of a complete gearbox model, including housing and dynamic effects.

3. Construction of the Surrogate Model of the Gear Whine Analyses and Uncertainty Propagation Methodology

The first step in building a surrogate is to have a high-fidelity simulation model being used as the ground truth. Therefore, a complete model of gearbox with gears, shafts, bearings and housing was built in Romax software. The gear bodies are modeled as integral with the shafts using Timoshenko beam elements, while the bearings are modeled as [6x6] stiffness matrix by linearizing their behavior near the operational condition. The housing is modeled by a Finite Element (FE) model reduced with the Craig-Bampton method to decrease the computational cost of the simulations while still taking into account the dynamic behavior, which results in a fully-coupled system of the gearbox [7].

First, a static analysis of the system is performed on each load condition to evaluate the system elastic deflection, which includes bearing displacements and the deformations of the shafts, gears, and housing and results in the gear mesh misalignment. The FE-based model of the tooth contact provides the tooth compliance matrix C, the mesh stiffness k and tooth deflection in relation to the input angular position θ [4]. The tooth compliance matrix accounts for tooth bending, root rotation and translation, Hertz deformation, and radial deformations. Then, STL can be evaluated simultaneously with the static load distribution in the contact line p for a given static force transmitted F, by solving:

$$(1) \qquad \begin{cases} C(\theta)p(\theta) = STE(\theta) - e(\theta) \\ \sum_i p_i(\theta) = F \end{cases}$$

where, e is the vector with the initial gap between the teeth at each discrete point, including the effects of the micro-geometric modifications, manufacturing errors, and gear mesh misalignment.

The STE displacement multiplied by the system compliance at the gear mesh location results in the force resulting from the transmission error. This force is then applied as the excitation source of the system in the dynamic analysis. In this paper, the dynamic system is modeled by a linear analysis with constant mesh stiffness approximated to its average value and it is solved in the frequency domain. The resulting frequency response functions (FRF) allow evaluating, e.g., the bearing forces and housing responses across the operating speed range.

Using the physics-driven gear transmission model, M pairs of input-outputs are sampled based on Latin Hypercube Sampling (LHS) to create a database of supporting points in the design space of interest. The LHS results in an informative database, with good space-filling properties and allows capturing the effects of the iterations among the variables. The *Python* routine integrated with Romax enables to perform the sampling by running the gear transmission model with the parameters defined by the LHS.

A fully-connected NN is used to create the surrogate model in this paper and it can be trained to predict all static and dynamic quantities of interest related to the gear whine at once. The inputs of a fully-connected NN are combined through a sequence of arithmetic operations that depend on the NN parameters called weights and biases. In supervised training, as in this paper, the NN outputs are compared with the reference outputs from the physical-driven model and an assessment of the error between them defines the NN loss function. The training process consists of optimizing the weights and biases of the NN to minimize the loss function. In order

to improve the NN performance and the optimization convergence, the inputs and outputs are scaled before training, in the data preprocessing stage.

The ML performance is evaluated in the remaining samples of the database, known as the test dataset. The workflow for the construction of the surrogate model is presented in Figure 1 and further details on the implementation of NN can be found at [5, 10]. Once trained, the surrogate model can predict the gearbox static and dynamic results with little loss of accuracy and with low computational cost.
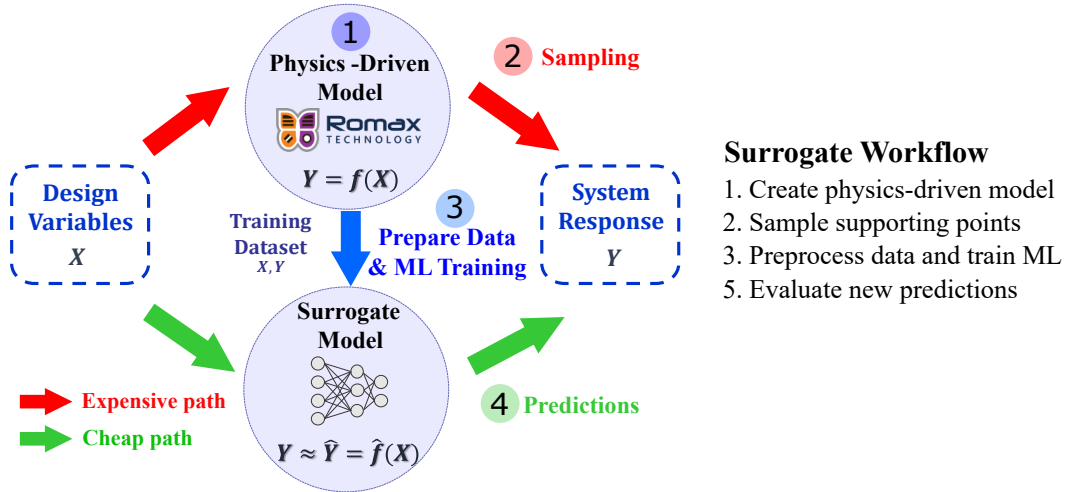
Figure 1: Workflow for the construction of the surrogate model of the gear transmission.

Hence, surrogate models are widely used in analyses that demand a large number of evaluations of the same function, as in uncertainty propagation analyses. These analyses provide the output uncertainties given the input uncertainties and are necessary to develop robust and reliable designs. Popular and accurate uncertainty propagation methods are based on Monte Carlo (MC) simulation methods [9], which generate random samples from the input statistical distribution and evaluate the deterministic response of each sample. The ensemble of all deterministic responses converges towards the stochastic response as the number of samples tends to infinity.

MC methods are convenient as they use the non-modified deterministic model, but are computationally costly as they demand numerous evaluations of this model. Thus, the joint use of MC with surrogates is advantageous and, therefore, largely used in the literature [3], as it enables fast evaluations of the deterministic model, optimized simultaneous evaluation of large sets of samples by using batch prediction and automatic parallelization of the solution.

4. Gear Whine Static and Dynamic Uncertainty Propagation Results via the Surrogate Model

This section presents the results of the investigation of the use of the NN-based surrogate model to propagate the effects of micro-geometry errors on static and dynamic indicators of gear whine noise. The analyses were carried out using a single-stage gear transmission with helical gears with module equals two, face width of $20\,mm$ and having 55 and 49 teeth in the wheel and pinion, respectively. Figure 2a shows the main dimensions of the gearbox used and Figure 2b shows the Romax model with the position where the housing acceleration was evaluated. The results were obtained for a load case with $50\,Nm$ of input torque. All analyses were carried out using a desktop with 4 cores with $3.6GHz$ and an NVIDIA Quadro P400 GPU.

The gear micro-geometry parameters illustrated in Figure 3 were considered as inputs, namely the involute crowning C_α, the lead crowning C_β and lead slope $C_{H\beta}$, for both pinion and wheel teeth, implying a six-dimensional design space. Table 1 presents the design space of interest considered for the input variables, from where $M = 1000$ input-output pairs were sampled using the Latin hypercube sampling method with Romax, which took 1891.85 seconds. Any output of the high-fidelity model can be used to train the surrogate model.

(a) Top view of 2D drawing.

(b) Model in Romax with red arrow indicating the position where the housing acceleration was evaluated.
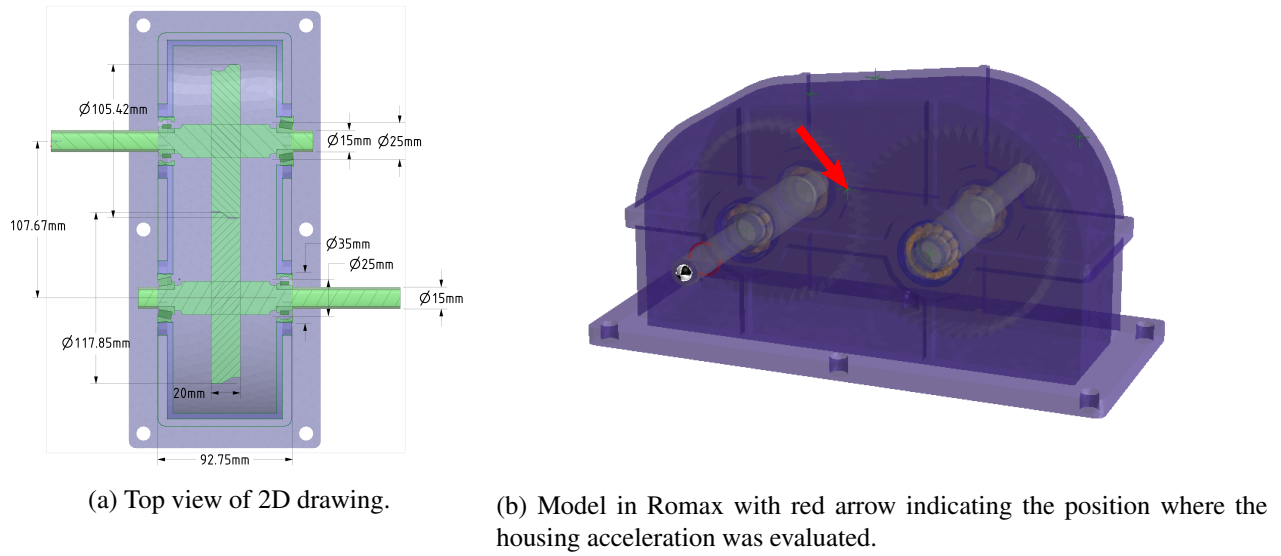
Figure 2: Single stage gear transmission.

Table 1: Design space of the gear teeth micro-geometry input variables. The ranges apply to both pinion and gear micro-geometries.

	$C_{H\alpha}$ [μm]	C_β [μm]	$C_{H\beta}$ [μm]
Lower Bound	0	0	-20
Upper Bound	15	15	20

In this paper, the peak-to-peak transmission error (PPTE) and the housing acceleration at the position indicated by the red arrow in Figure 2b were chosen as the static and dynamic indicators of the gear whine performance, respectively.
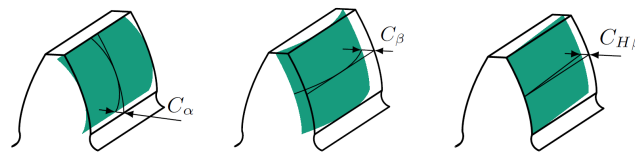
Figure 3: Gear tooth micro-geometry parameters used: involute crowning C_α, lead crowning C_β and lead slope $C_{H\beta}$. Source: [15].

4.1. NN-based Surrogate Accuracy

The surrogate model is based on a fully-connected NN with one input layer with six neurons, four hidden layers with 16 neurons each, and 101 neurons in the output layers, which correspond to the number of evaluated output results for each design, that is the PPTE and the housing acceleration evaluated at 100 different frequencies input shaft speed ranging from 0 to 4000 rpm, as illustrated in Figure 4. The neural units use the *sigmoid* function as activation function, excepted by the output layer that uses *softmax* function. The *Adam* optimizer is used to optimize the *mean squared error* during the NN training, which takes place in 3000 epochs with batches of 16 samples. The database was divided into 200 samples for the test database and 800 samples for the training dataset, from which 80 samples are used as the validation dataset. The inputs and the outputs were

scaled using respectively *StandardScaler* and *MinMaxScaler* from *scikit-learn* library and are fitted solely in the training dataset. The NN implementation was done with *Keras* library in *Python*.
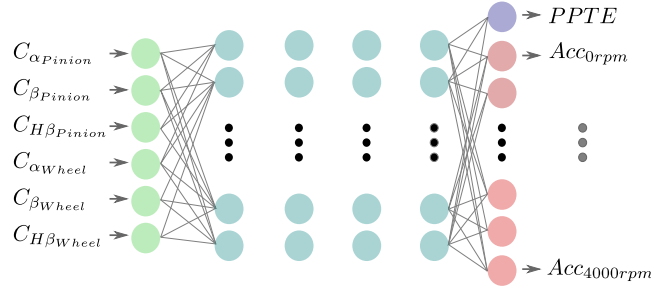
Figure 4: Representation of the Neural-Network used to implement the surrogate model.

The NN training took 434.84 seconds and the final surrogate achieved a root mean squared error (RMSE) in the test database of $0.08 \ \mu m$ for the PPTE and $0.08 \ m/s^2$ for the housing acceleration at any frequency. Figures 5a and 5b shows the scatter plot of the true values and the prediction values in the test dataset for PPTE and housing acceleration, respectively. Figure 5c shows the good agreement between the true and the predicted curve for the housing acceleration for an illustrative design sample from the test dataset. Once the NN-based surrogate is trained, it can predict new results in a negligible time.
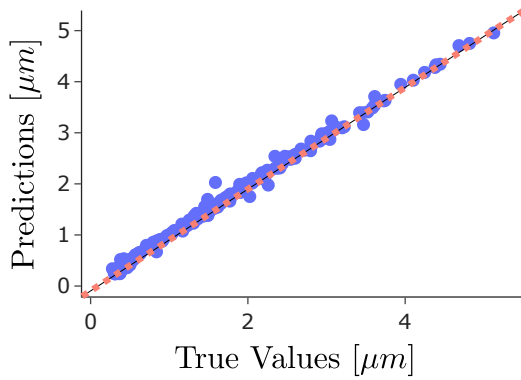
(a) Scatter plot of testing data of true observations versus surrogate predictions of PPTE with $RMSE = 0.08 \ \mu m$.
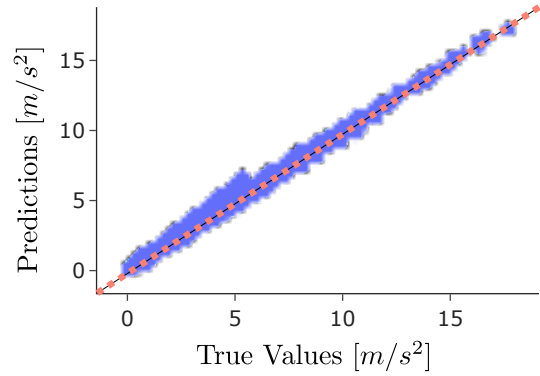
(b) Scatter plot of testing data of true observations versus surrogate predictions of housing acceleration with $RMSE = 0.08 \ m/s^2$.
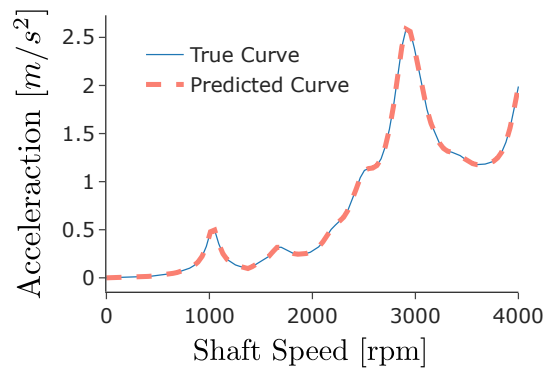
(c) True and predicted housing acceleration curves for one design in the test dataset.

Figure 5: Accuracy of the Neural Network-based surrogate model.

4.2. Uncertainty Propagation

Table 2: Design space of the gear teeth micro-geometry.

		$C_{\alpha_{Pinion}}$ μm	$C_{\beta_{Pinion}}$ μm	$C_{H\beta_{Pinion}}$ μm	$C_{\alpha_{Wheel}}$ μm	$C_{\beta_{Wheel}}$ μm	$C_{H\beta_{Wheel}}$ μm
Design 1	μ_1	5	5	0	7	5	-3
Design 2	μ_2	11	8	14	7	2	5
Design 3	μ_3	3	10	-10	2	10	-5
Tolerance	$\Delta_{1,2,3}$	1	1	1	1	1	1

The use of surrogate models becomes beneficial when multiple evaluations are necessary, as in the uncertainties propagation analysis by the MC method. The Monte Carlo simulation is performed for the three micro-geometry designs in Table 2 using both Romax and the surrogate in order to illustrate the time-saving capabilities of the surrogate. The input distribution is given by a uniform distribution $\mu \pm \Delta$, where μ is the design mean and Δ is the tolerance, and $M = 2500$ random samples from this distribution are evaluated in order to evaluate the output distributions, leading to an MC error of the order of 0.02 [17].

The time spent propagating the uncertainties for each design averages $4751.8\ s$ with Romax and $12.5\ s$ with the surrogate model, that is, the surrogate is 380 times faster than Romax. The sampling time ($1891.85\ s$) and the training time ($434.84\ s$) must be considered once since after creating the surrogate it can be used to propagate uncertainties of all designs contained in the defined space of interest.

Figure 6 shows the PPTE confidence interval obtained with both Romax and with the NN-based surrogate for the three designs. It is observed that the results obtained with the NN-based surrogate model are very close to those obtained with Romax, being that only the propagation of uncertainties of design 3 presents a visible difference in Figure 6, which is still acceptable. Figure 7 shows the $M = 2500$ housing acceleration curves of the MC estimator for design 1 obtained with Romax and with the surroate model.

Both static and dynamic results show a good agreement between Romax and surrogate results, therefore, the proposed NN-based surrogate model was successfully used to speed-up uncertainty propagation analyses of gear whine. Any other quantity of interest of the gear transmission model could be added to the NN training to be predicted by the surrogate.
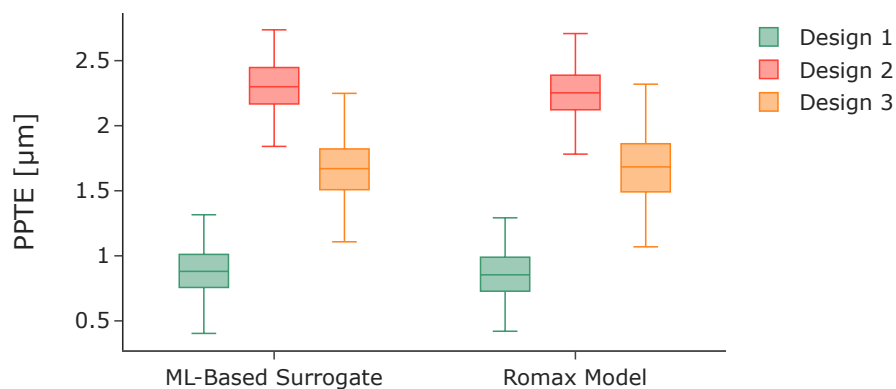
Figure 6: Comparison of the peak to peak transmission error uncertainty propagation using a Romax model and the correspondent surrogate model for three different gear micro-geometry designs.

(a) Results with Romax model.

(b) Results with ML-based surrogate.
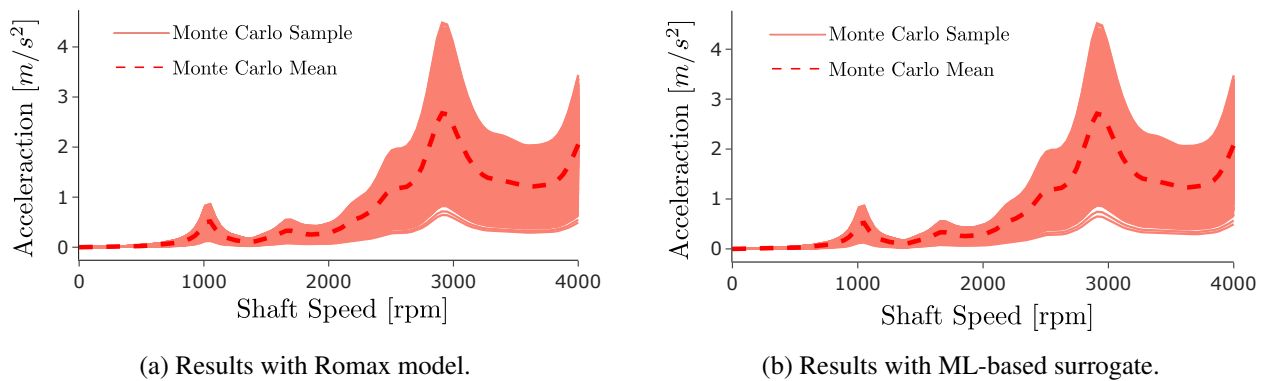
Figure 7: Uncertainty propagation results of the housing acceleration curve using Monte Carlo method for the Design 1.

5. Conclusion

This paper investigates the use of Neural-Network (NN) based surrogate models applied to gear whine problems and its application to robust design modeling. An NN-based surrogate was constructed to predict the housing acceleration for several shaft speeds and the peak-to-peak transmission error (PPTE) regarding the gear micro-geometry parameters, namely lead crowning, lead slope, and profile crowning of wheel and pinion teeth. The surrogate uses a high-fidelity physical simulation modeled with Romax software as ground truth, including gears, shafts, bearings, and housing.

The NN-based surrogate has reasonable accuracy, with root mean square errors of $0.08m/s^2$ for the housing acceleration and $0.08\mu m$ for the PPTE. It was shown that the proposed surrogate is suitable to perform uncertainty propagation using methods like Monte Carlo, which relies on several evaluations of the model. The uncertainty propagation results with the surrogate are computed 308 times faster than with the high-fidelity model and present minor precision loss.

Therefore, the proposed surrogate model is adequate to assist the robust design of the gear micro-geometries considering static and dynamic results, making an extensive exploration of the design space feasible. Further work could use the proposed surrogate in a robust optimization analysis.

References

[1] Mats Åkerblom. Gear noise and vibration: a literature survey. 2001.

[2] Ágnes Bárkányi, Tibor Chován, Sándor Németh, and János Abonyi. Modelling for digital twins—potential role of surrogate models. *Processes*, 9(3):476, 2021.

[3] Daniel A DeLaurentis and Dimitri Mavris. Uncertainty modeling and management in multidisciplinary analysis and synthesis. In *38th Aerospace sciences meeting and exhibit*, page 422, 2000.

[4] P. Garambois, J. Perret-Liaudet, and E. Rigaud. Nvh robust optimization of gear macro and microgeometries using an efficient tooth contact model. *Mechanism and Machine Theory*, 117:78–95, 2017.

[5] Ian Goodfellow, Yoshua Bengio, and Aaron Courville. *Deep learning*. MIT press, 2016.

[6] Yi Guo, Tugan Eritenel, Tristan M Ericson, and Robert G Parker. Vibro-acoustic propagation of gear dynamics in a gear-bearing-housing system. *Journal of Sound and Vibration*, 333(22):5762–5785, 2014.

[7] B. James, M. Douglas, and D. Palmer. Predicting the contact conditions for hypoid gear sets by analysis and a comparison with test data. *SAE Transactions*, 111:1489–1494, 2002.

[8] J.A. Korta and M. Domenico. Multi-objective micro-geometry optimization of gear tooth supported by response surface methodology. *Mechanism and Machine Theory*, 109:278–295, 2017.

[9] Nicholas Metropolis and Stanislaw Ulam. The monte carlo method. *Journal of the American statistical association*, 44(247):335–341, 1949.

[10] Michael A Nielsen. *Neural networks and deep learning*, volume 25. Determination press San Francisco, CA, USA,

2015.

[11] C.I.L. Park. Multi-objective optimization of the tooth surface in helical gears using design of experiment and the response surface method. *Journal of mechanical science and technology*, 24(3):823–829, 2010.

[12] Romax Technology Ltd. Romax spectrum.

[13] András Sobester, Alexander Forrester, and Andy Keane. *Engineering design via surrogate modelling: a practical guide*. John Wiley & Sons, 2008.

[14] M. Sun, C. Lu, Z. Liu, Y. Sun, H. Chen, and C. Shen. Classifying, predicting, and reducing strategies of the mesh excitations of gear whine noise: a survey. *Shock and Vibration*, 2020.

[15] Jan Troge, Eric Hensel, Sebastian Zumach, and Jan Bräunig. Acoustical optimization of a train gearbox based on overall system simulation. In *INTER-NOISE and NOISE-CON Congress and Conference Proceedings*, volume 253, pages 1–10. Institute of Noise Control Engineering, 2016.

[16] DB Welbourn. Fundamental knowledge of gear noise: a survey. Technical report, 1979.

[17] Jiaxin Zhang. Modern monte carlo methods for efficient uncertainty quantification and propagation: A survey. *Wiley Interdisciplinary Reviews: Computational Statistics*, 13(5):e1539, 2021.

OPTIMAL TWO-TERMINAL VIBRATION-ABSORBER IDENTIFICATION: AN APPROACH BASED ON GRAPH THEORY

H. He[1], Y. Li[1], J. Z. Jiang[1], S. G. Burrow[2], S. A. Neild[1], and A. T. Conn[1]

[1]*Department of Mechanical Engineering, University of Bristol, Bristol, UK*
[2]*Department of Aerospace Engineering, University of Bristol, Bristol, UK*

e-mail: z.jiang@bristol.ac.uk, yuan.li@bristol.ac.uk

Abstract: The passive vibration absorber is a commonly-used technique in industrial applications where vibration suppression is required. Traditionally, it contains springs, dampers and masses. Since the introduction of a new element termed 'inerter', the network possibilities of passive vibration absorbers have been greatly enlarged. The previous structure-immittance approach can already identify the optimal solution from all network possibilities with a controlled complexity. However, the inability to automate the the step of network enumeration limits its wide application. To this end, a novel design approach based on graph theory is proposed in this paper. The approach has been implemented with a program, which can automatically generate the full set of two-terminal networks with any pre-determined number of each element type (such as springs, dampers and inerters in a mechanical absorber). Then, genetic optimization is used to identify the optimal one within the full set. The suspension design problem for a standard quarter-car model is adopted as a case study. The results show that, compared with the traditional spring-damper layout, the identified network can achieve up to 28.4% ride comfort improvement.

Keywords: vibration absorber, graph theory, optimal design, programmatic implementation, vehicle suspension

1. Introduction

Passive vibration absorbers, traditionally comprising springs, dampers and masses, play a vital role in improving dynamic performance of mechanical structures, e.g., enhancing vehicle riding quality, reducing noise from the engine and minimizing track wear induced by rail-wheel interactions. In 2002, a new passive element termed 'inerter' was introduced [1]. Contrasting with the mass element, the generated force of an inerter is proportional to the relative acceleration across its two terminals. Its introduction fundamentally enlarges the network possibilities of two-terminal passive absorbers. To identify a beneficial absorber network, there are three traditional approaches that can be used: the structure-based approach, the immittance-based approach and the evolutionary-based approach.

The structure-based approach (e.g., [2, 3]) first proposes a network layout and then tunes the parameter of each element according to performance criteria. The advantage is that the complexity of the network topology can be pre-determined. However, despite the fact that there are countless possible network layouts, only one can be covered at a time by this approach. This inevitably limits the achievable performance of the system. The immittance-based approach (e.g., [4, 5]) can identify the optimal one without restricting the network to a few specific topology arrangements. With this approach, one first obtains the positive-real immittance function providing the optimum performance, and then uses network synthesis [6, 7] to identify the corresponding network layout and element values. Unfortunately, unrealisable networks, such as one with an excessive number of components or unfeasible component parameter values, could be obtained. For example, a series-parallel network with nine elements is required to synthesis the obtained positive-real bi-quadratic immittance [6]. In the evolutionary-based approach (e.g., [8, 9]), an initial set of candidate networks is generated and iteratively updated through metaheuristics and stochastic operators. While this approach can automatically produce a network layout with good performance, there is no guarantee that the obtained network is the optimal one, and similar to the immittance-based approach the network could be too complex to be manufactured.

To control the network complexity while achieving the optimal performance of a vibration absorber, the structure-immittance approach was proposed [10]. In this approach, the full set of series-parallel network possibilities with a pre-determined number of each element type was formulated first. Then, by evaluating the vibration-suppression effect of each network the optimal one could be identified. While promising results have

been shown in different application area [11, 12], there are two main limitations with this approach. One is that networks not formed by series and parallel connections, such as bridge networks, cannot be covered. The other and more important is that there is no programmatic implementation of the key step 'network enumeration', which will limit its wide application.

To solve these two problems simultaneously, a novel design approach based on graph theory is proposed in this paper. The approach has been implemented with a program, which can automatically generate the full set of two-terminal networks with a pre-determined number of each element type (such as springs, dampers and inerters in a mechanical absorber). All types of networks including both series-parallel and bridge ones can be covered. Genetic optimization is then adopted to identify the optimal one within the full set. The idea of using graph theory in network enumeration is inspired by references [13, 14], where the mechanical network is represented by an undirected labelled graph. The difference lies in how the elements and their connection points in the network are represented in the corresponding graph. The approach in [13, 14] is not suitable for the aim of this paper: automatically generating the full set of networks with a certain element number. This is because besides the element quantity, the number of junctions where three or more edges are connected together also needs to be specified.

The remainder of the paper is structured as follows. Section 2 introduces the network enumeration based on graph theory. Section 3 explains the procedures for redundancy elimination, and then verifies the approach by comparing the enumeration results with existing literatures. In Section 4, the suspension design problem for a standard quarter-car model is adopted as a case study to show the advantage of the approach. Finally, conclusions are drawn in Section 5.

2. Network enumeration based on graph theory

2.1. Graph representation of networks

The design approach proposed in this paper aims at generating and evaluating the full set of two-terminal networks with a pre-determined number for each element type. Fundamental to this approach is representing the network by a *graph*, where the connection point of elements is modelled as a *vertex* and the element is modelled as an *edge* between two vertices. There are two types of vertices in this graph representation: (1) the terminal vertices to denote physical terminals of the absorber connecting with the hosting system, and (2) the internal vertices to denote the inner connection points of the absorber. To distinguish these two types of vertices, they are labelled with different colours. For example, in this paper the terminal vertices are labelled *red* while the internal vertices are labelled *blue*. Different elements are represented by different weights of edges. In this paper, the weights for springs, dampers, and inerters are one, two and three respectively. Based on these definitions, two example networks and their graph representations are given in Figure 1. It should be noted that while a mechanical absorber is adopted here to demonstrate the proposed approach, it is also applicable to other domains, such as the passive analog filter in the electrical domain.

There are other graph representations of networks. A more common representation is to represent elements as vertices and their connections as edges [13, 14]. Since in this representation the number of edges adjacent to the vertex has to equal the number of element terminals, some additional vertices are required to represent the junctions where three or more edges are connected together. If we need to generate the full set of networks with a pre-determined number for each element type, the number required for this type of vertices needs to be determined first, which will complicate the enumeration process. By contrast, these vertices are not needed in the chosen representation.

2.2. Network enumeration

Before describing the enumeration process, we need to introduce two basic graphs commonly used in the graph theory: the simple graph and the multigraph [15]. The simple graph is a graph that does not have more than
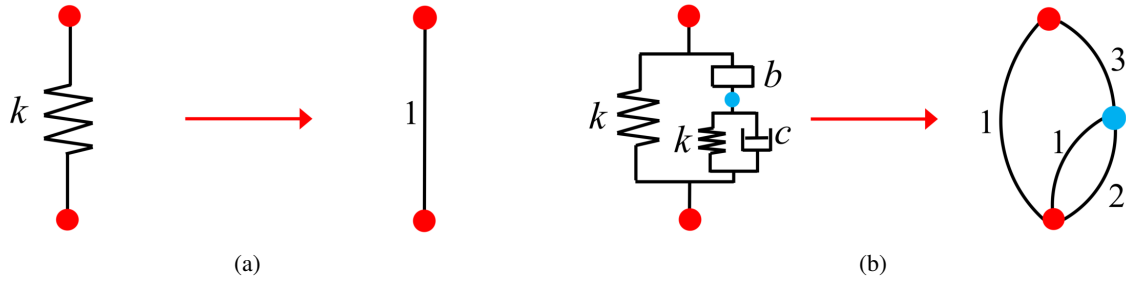
Figure 1: The graph representation of (a) a spring and (b) an inerter-based layout.

one edge between any two vertices and no edge starts and ends at the same vertex. The multigraph is a graph permitted to have multiple edges between two vertices but no edge starts and ends at the same vertex. If each edge in these two graphs is assigned with a numerical weight, they can be further termed as weighted simple (or multi) graphs [15]. Similarly, if each vertex in these two graphs is assigned with a colour, they will be termed as coloured simple (or multi) graphs. Because as introduced in Section 2.1 each edge in the graph has a weight to represent its element type, each vertex has a colour to show whether it is a terminal or internal vertex and there could be parallel elements, the network is actually a weighted and coloured multigraph. Therefore, the enumeration of absorber networks with a pre-determined number for each element type can be converted to the enumeration of a set of weighted and coloured multigraphs with a fixed number of edges. This target is realized by the following three nested steps:

1. To generate the totality of weighted and coloured multigraphs with N edges, the coloured multigraphs with N edges and two vertices coloured red could be enumerated first, and then the edges are assigned with a set of weights with a pre-determined number for each element type. Note that to cover all the possibilities of weight assignment, the mathematical permutation of the given set of weights into N edges is used. There are $N!$ possibilities in total.

2. To generate the totality of coloured multigraphs with N edges, the coloured simple graphs with N_e ($1 \leq N_e \leq N$) edges and two vertices coloured red could be enumerated first, and then the remaining $N - N_e$ edges are added in parallel with existing edges. Each remaining edge could be placed in parallel with N_e different edges, so there are $N_e^{N-N_e}$ possibilities for all remaining edges. By repeating the above procedures for N_e from 1 to N, all coloured multigraphs can be covered.

3. To generate the totality of coloured simple graphs with N_e edges, the simple graphs with N_e edges could be enumerated first, and then two vertices are selected to colour red while keeping others blue. There could be N_v vertices in the graph, where N_v is within the range of

(1)
$$\frac{1}{2} + \sqrt{\frac{1}{4} + 2N_e} \leq N_v \leq N_e + 1$$

For each graph, by using the combinatorial mathematics there will be $C_{N_v}^2 = N_v(N_v - 1)/2$ colouring possibilities.

A three-layer enumeration process summarizing the above three steps are shown in Figure 2. It can be noted that, in each layer besides the explained procedures for network generation, there are several additional procedures for redundancy elimination, such as network structure constraints (NSCs) and an isomorphism check, which will be explained in the next section. Without these procedures, the totality of networks with a given number for each element type can still be covered, but there would be many redundant networks, leading to a higher computational cost. Therefore, it is necessary to reduce the redundancy as much as possible.
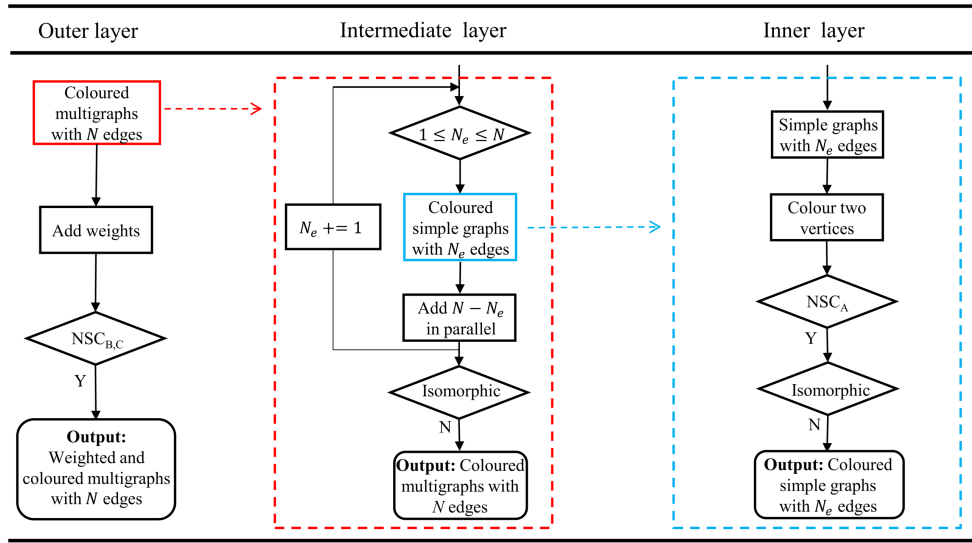
Figure 2: A three-layer network enumeration process.

3. Redundancy elimination and approach verification

3.1. Redundancy elimination

To eliminate the redundancy, three network structure constraints (NSCs) and the isomorphism check are introduced in the enumeration process, as shown in Figure 2 and described as below:

NSC$_A$: *Every vertex in the graph can be passed through by at least one path connecting two terminal vertices (In the graph theory, a path is a walk in which neither vertices nor edges are repeated and a walk is a sequence of vertices and edges of a graph [15]).* In the inner layer, the result of the second step 'Colour two vertices' is a set of simple graphs with N_e edges and two vertices coloured red, which may include those with self loops or isolate vertices. These graphs should be eliminated as the elements in the self loop or connecting with isolate vertices do not function in the networks built from these graphs. Figure 3 gives two examples of $N_e = 4$ where the left one includes a self loop (highlighted in the red dashed circle), and the right one has an isolate vertex. It is clear that both of them do not satisfy NSC$_A$ and will be eliminated.
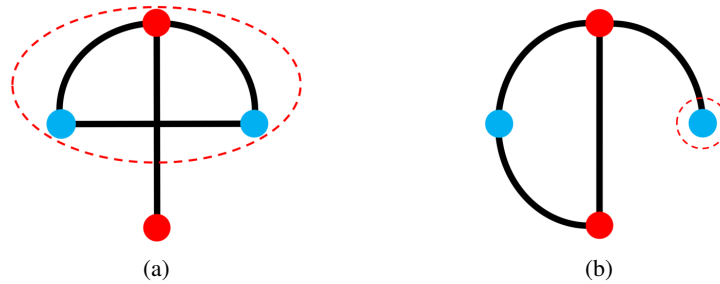
Figure 3: The coloured simple graph with (a) a self loop and (b) an isolate vertex.

NSC$_B$: *For edges with the same weight, they cannot be in series or parallel; For edges with different weights, if they are in series or parallel, they should follow a specific ordering.* In the outer layer, the result of the second step 'Add weights' is a set of weighted and coloured multigraphs with N edges, which may include the following two sets of redundant graphs: (1) the graphs having series or parallel edges with the same weight; and (2) the graphs formed by permuting different weights into series or parallel edges. The first set of redundant graphs should be eliminated as they can be simplified to a graph with fewer edges. In the second set of graphs, we only keep those with a specific ordering of series or parallel connections and eliminate the others, as swapping

series or parallel elements will only generate equivalent networks. As when storing a graph in the computer every edge has an unique index 'idx', the adopted ordering here is that the edge with a higher index should have more weight. Figure 4 gives two examples to be eliminated which belong to the first and second set of redundant graphs, respectively. Figure 4(b) does not satisfy NSC$_B$ because for the two parallel edges the weight of the edge with a higher index $idx = 4$ is lower than that of the other edge $idx = 3$.
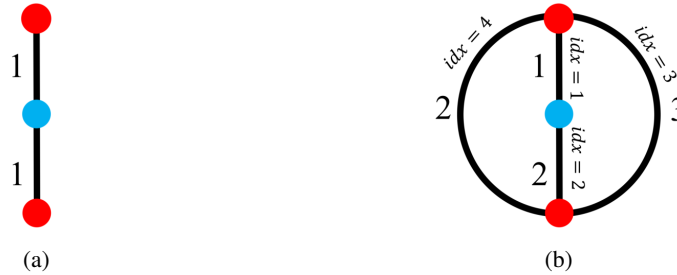
Figure 4: The redundant multigraph of (a) the first set and (b) the second set.

NSC$_C$: *Impedance functions for any two networks built from weighted and coloured graphs cannot be the same.* In the outer layer, after implementing NSC$_B$ there is still redundancy that can be further eliminated. The networks built from some resulted graphs have the same impedance, which means that although they may present different structures they have the same dynamic performance, so only one of them needs to be kept and all the others should be eliminated. As an example, the networks built from the two graphs in Figure 5 have the same impedance as just by swapping the part in the red dashed curve with the part in the blue dashed curve, Figure 5(b) can be generated from Figure 5(a). One of them should be eliminated to ensure the least redundancy.
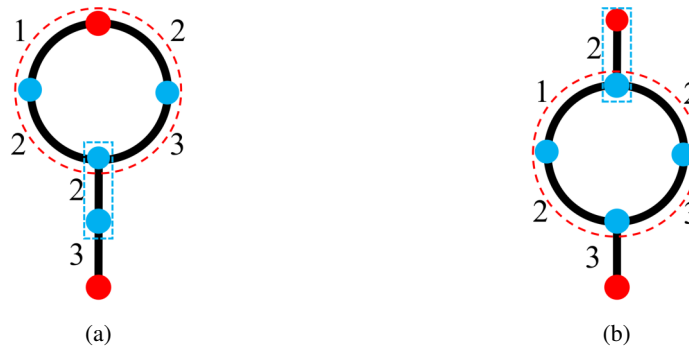
Figure 5: Two example weighted and coloured graphs with the same impedance.

In the inner and intermediate layers, besides NSCs there is also an isomorphism check to further eliminate the redundant graphs. Isomorphism is a basic concept in graph theory, which is used to express the equivalence relation on graphs [15]. If two graphs G_1 and G_2 are isomorphic, then there is a mapping from the vertices of G_1 to the vertices of G_2 such that the vertex colour and edge weight are preserved. This concept applies to all types of graphs, such as simple graphs, multigraphs and those with weights or colours. Two example isomorphic graphs are shown in Figure 6, and one of them should be eliminated. It can be noted that there is no isomorphism check in the outer layer. This is because the networks built from isomorphic graphs have the same impedance, and by implementing NSC$_C$ all resulted graphs will become non-isomorphic.

The three-layer network enumeration process integrated with redundancy elimination as shown in Figure 2 has been automatically implemented via a program. Due to space limitations, only the algorithm for the inner layer is provided in the Appendix as an example.
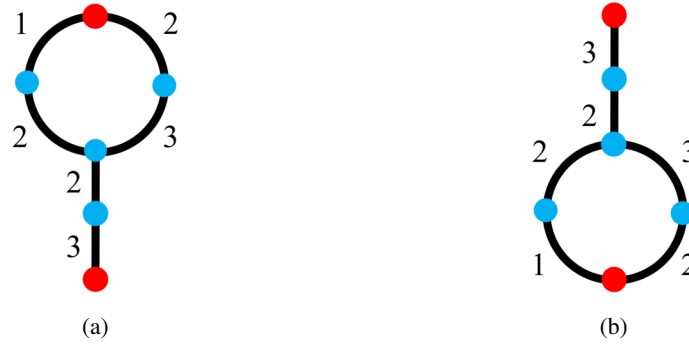
Figure 6: Two isomorphic weighted and coloured graphs.

3.2. Approach verification

Through the above NSCs and isomorphism check, the enumeration process as shown in Figure 2 not only covers the totality of networks with a pre-determined number for each element type but also removes as many redundant graphs as possible. To verify the correctness of the approach, we first take the case of 1k1b1c (one spring, one damper and one inerter, $N = 3$) for example. The resulted graphs for each step of the enumeration process is shown in Figure 7, where each row corresponds to the graph development from a simple graph with a specific number of edges N_e. Via this approach, eight unique networks are obtained, which is the same with the result from [10, 16, 17]. The second example is in the electrical domain and with more elements. The famous Ladenheim catalogue [18] has shown a set of 148 essentially distinct two-terminal RLC networks with five elements or less, of which at most two are reactive (inductors and capacitors). With our approach, the same networks are automatically obtained, indicating the correctness of the approach and its ability to reduce redundancy automatically. It should be noted that in these networks there may still be some equivalent networks which cannot be simplified to a network with fewer elements but can be converted to each other via the Zobel transformation [18, 19]. Some examples of the Zobel equivalence can be seen from the case given in the following section.

As the enumeration approach has been verified, the generated networks can be used as candidate layouts for passive vibration absorbers. The genetic optimization algorithm, such as 'patternsearch' [20] will then be adopted to evaluate the networks according to performance criteria and to identify the optimal one.

4. Case demonstration via a quarter car

The suspension design problem in a standard quarter-car model is adopted as an example here. As shown in Figure 8(a), the quarter-car model consists of a sprung mass m_s, an unsprung mass m_u, a tire modelled as a spring with stiffness k_t and a suspension. Specifically, the suspension is composed of a static spring k_s and a passive absorber with a pre-determined number of springs, dampers and inerters. The total element number of the passive absorber is denoted by N. The displacements of the sprung mass, the unsprung mass and the road profile are denoted as x_s, x_u and x_r respectively, with their positive directions shown in the figure. The suspension stiffness together with other quarter-car parameters including the sprung mass, the unsprung mass, and the tire stiffness are listed in Table 1. These are typical values for passenger cars [21, 22].

In line with [21], the road disturbance is assumed to be a white noise. The power spectra density (PSD) of the road velocity is expressed by $S_{\dot{x}_r} = 4\pi^2 \kappa V$ where the road roughness parameter is selected as $\kappa = 5 \times 10^{-7}$ m³/cycle and the vehicle velocity is $V = 25$ m/s. The ride comfort index J_r is assumed as the main dynamic performance metric to be optimized here. For the considered quarter-car model, the index J_r can be expressed as [21]:

(2) $$J_r = 2\pi\sqrt{\kappa V}\|H_{\dot{x}_r \to \ddot{x}_s}(j\omega)\|_2$$
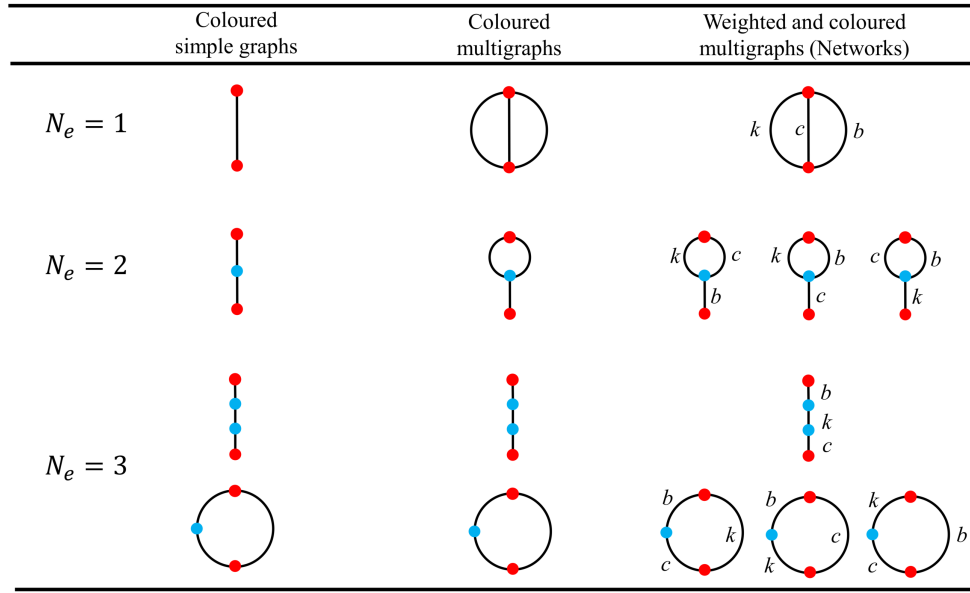
Figure 7: The three-step network enumeration for $N = 3$.

where $H_{\dot{x}_r \to \ddot{x}_s}(j\omega)$ is the transfer function from the road velocity $\dot{x}_r$ to the sprung mass acceleration $\ddot{x}_s$.

The proposed design approach aims at identifying the network which can achieve the optimal ride comfort of the vehicle. Given a number of springs, dampers, and inerters, the full set of networks will be enumerated first and then evaluated one by one. For a fair comparison, the benchmark passive absorber is a damper as shown in Figure 8(b). Five sets of networks with different element numbers N are considered: (1) $N = 2$: a damper and an inerter, denoted as 1b1c, with 2 possibilities; (2) $N = 3$: a spring, a damper and an inerter, denoted as 1k1b1c, with 8 possibilities; (3) $N = 4$: 2k1b1c, 1k2b1c and 1k1b2c with 54 possibilities; (4) $N = 5$: 2k2b1c, 2k1b2c and 1k2b2c with 255 possibilities; (5) $N = 6$: 2k2b2c with 558 possibilities. Note that for the set of $N = 5$ there are 27 bridge networks that cannot be covered by [10], and this number will be more with increasing N. The optimal ride comfort for each set and the corresponding networks are summarised in Figure 9. It can be seen that with rising number of elements N, the ride comfort keeps improving until $N = 5$ the ride comfort no longer changes. The maximum improvement reaches 28.4%. It is also found that for the case of $N = 4$, the two networks in the purple square have the same optimal ride comfort as they can be converted to each other via the Zobel transformation [18, 19]. Similarly, for $N = 5$ the optimal ride comfort can be achieved by four different networks which are also Zobel equivalent. For $N = 6$, to save space only one of the equivalent networks is shown in the grey square. It is found that one damping in this network tends to infinity, which means that the network actually degrades to one with only five elements so there is no more improvement when $N = 6$.

Parameter	Value
Sprung mass m_s	250 kg
Unsprung mass m_u	35 kg
Tire stiffness k_t	150 kN/m
Suspension stiffness k_s	15 kN/m

Table 1: Parameters of the quarter-car model [21, 22].
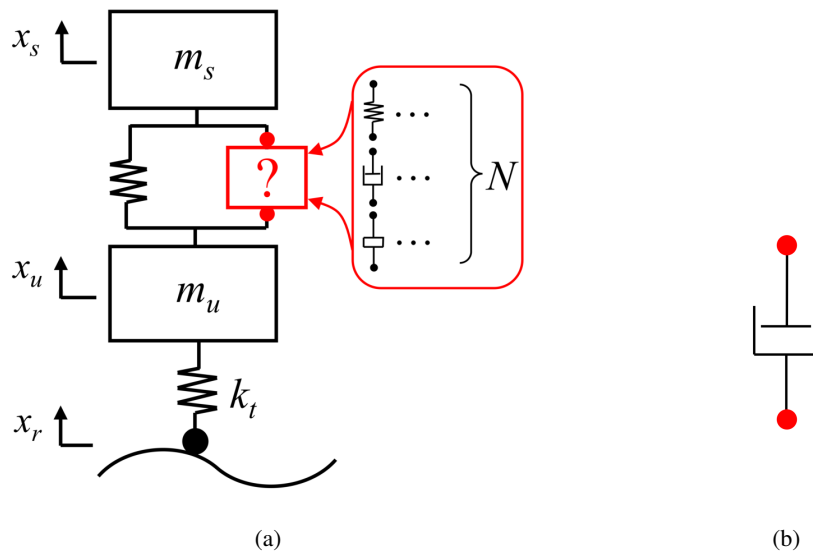
Figure 8: (a) The quarter-car model, (b) the benchmark passive absorber.
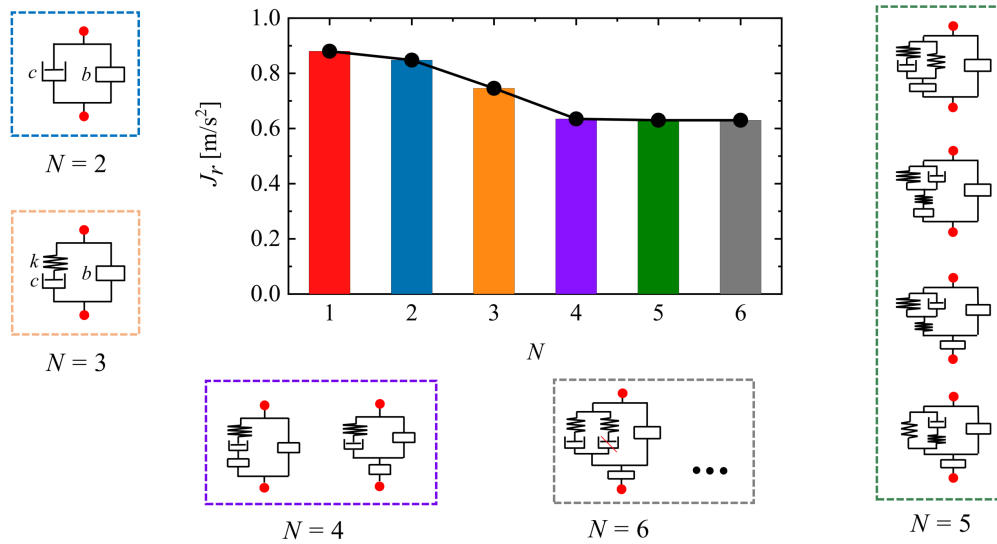
Figure 9: The optimal ride comfort and corresponding networks for $N = 1, 2, ..5$.

5. Conclusions

In this paper, a novel design approach for passive vibration absorbers has been proposed. Compared with the structure-immittance approach [10] and the approach based on perfect matching [13, 14], it not only allows the generation of the full set of network possibilities given a pre-determined number of each element type, covering both series-parallel networks and bridge networks, but also automates this process via a three-layer enumeration algorithm. In the enumeration process, three network structure constraints (NSCs) and an isomorphism check are introduced to reduce the redundancy automatically. The approach has been verified by comparing with the existing network totality of two examples: networks with 1k1b1c and RLC networks with no more than five elements. To show the advantage of the approach, the suspension design problem for a standard quarter-car model is adopted as a case study. Five sets of networks with up to six elements are studied. The results show that, compared with the traditional spring-damper layout, the ride comfort keeps improving with rising element quantity and when $N = 5$ the maximum improvement 28.4% is achieved.

References

[1] M. C. Smith. Synthesis of mechanical networks: the inerter. *IEEE Trans. Automat. Contr.*, 47(10):1648–1662, 2002.

[2] M. C. Smith and F. C. Wang. Performance benefits in passive vehicle suspensions employing inerters. *Veh. Syst. Dyn.*, 42(4):235–257, 2004.

[3] I. F. Lazar, S. A. Neild, and D. J. Wagg. Using an inerter-based device for structural vibration suppression. *Earthq. Eng. Struct. D.*, 43(8):1129–1147, 2014.

[4] J. Z. Jiang and M. C. Smith. Regular positive-real functions and five-element network synthesis for electrical and mechanical networks. *IEEE Trans. Automat. Contr.*, 56(6):1275–1290, 2011.

[5] Y. Li, J. Z. Jiang, S. A. Neild, and H. Wang. Optimal inerter-based shock-strut configurations for landing-gear touchdown performance. *J. Aircr.*, 54(5):1901–1909, 2017.

[6] R. Bott and R. J. Duffin. Impedance synthesis without use of transformers. *J. Appl. Phys.*, 20(8):816–816, 1949.

[7] O. Brune. Synthesis of a finite two-terminal network whose driving-point impedance is a prescribed function of frequency. *J. Math. Phys. Camb.*, 10(1-4):191–236, 1931.

[8] Z. Gan, Z. Yang, T. Shang, T. Yu, and M. Jiang. Automated synthesis of passive analog filters using graph representation. *Expert Syst. Appl.*, 37(3):1887–1898, 2010.

[9] S. Chang, H. Hou, and Y. Su. Automated passive filter synthesis using a novel tree representation and genetic programming. *IEEE Trans. Evol. Comput.*, 10(1):93–100, 2006.

[10] S. Y. Zhang, J. Z. Jiang, and S. A. Neild. Passive vibration control: a structure-immittance approach. *Proc. Math. Phys. Eng. Sci.*, 473(2201):20170011, 2017.

[11] T. D. Lewis, Y. Li, G. J. Tucker, J. Z. Jiang, Y. Zhao, S. A. Neild, M. C. Smith, R. Goodall, and N. Dinmore. Improving the track friendliness of a four-axle railway vehicle using an inertance-integrated lateral primary suspension. *Veh. Syst. Dyn.*, 59(1):115–134, 2019.

[12] S. Y. Zhang, M. Zhu, Y. Li, J. Z. Jiang, R. Ficca, M. Czechowicz, R. Neilson, S. A. Neild, and G. Herrmann. Ride comfort enhancement for passenger vehicles using the structure-immittance approach. *Veh. Syst. Dyn.*, 59(4):504–525, 2019.

[13] D. R. Herber and J. T. Allison. A problem class with combined architecture, plant, and control design applied to vehicle suspensions. *J. Mech. Design*, 141:101401, 2019.

[14] D. R. Herber, T. H. Guo, and J. T. Allison. Enumeration of architectures with perfect matchings. *J. Mech. Design*, 139:051403, 2017.

[15] R. J. Wilson. *Introduction to graph theory*. Addison Wesley Longman Limited, fourth edition, 1996.

[16] J. Riordan and C. E. Shannon. The number of two-terminal series-parallel networks. *J. Math. Phys.*, 21:83–93, 1942.

[17] Z. A. Lomnicki. Two-terminal series-parallel networks. *Adv. Appl. Prob*, 4(1):109–150, 1972.

[18] A. Morelli and M. C. Smith. *Passive network synthesis: an approach to classification*. Society for Industrial and Applied Mathematics, 2019.

[19] O. J. Zobel. Theory and design of uniform and composite electric wave-filters. *Bell Syst. Tech. J.*, 2(1):1–46, 1923.

[20] C. Audet and J. E. Dennis. Analysis of generalized pattern searches. *SIAM J. Optim.*, 13(3):889–903, 2002.

[21] F. Scheibe and M. C. Smith. Analytical solutions for optimal ride comfort and tyre grip for passive vehicle suspensions. *Veh. Syst. Dyn.*, 47(10):1229–1252, 2009.

[22] H. He, Y. Li, J. Z. Jiang, S. Burrow, S. Neild, and A. Conn. Using an inerter to enhance an active-passive-combined vehicle suspension system. *Int. J. Mech. Sci.*, 204:106535, 2021.

Appendix

Algorithm 1: Generate all coloured simple graphs with N_e edges

---

Input: N_e – number of edges
Output: G_s – set of coloured simple graphs

1   $G_s \leftarrow \varnothing$

2   **for** $N_v \leftarrow \frac{1}{2} + \sqrt{\frac{1}{4} + 2N_e} : N_e + 1$ **do**
3      $G \leftarrow$ GengEdVe (N_e, N_v)
4   **for** $i \leftarrow 1 : length(G)$ **do**
5         $idx \leftarrow$ Find combinations of 2 from N_v elements
6   **for** $j \leftarrow 1 : length(idx)$ **do**
7            $g \leftarrow$ Mark two nodes $idx(j)$ of $G(i)$ in red
8            $NSC_A \leftarrow$ Check if g satisfies the Network Structure Constraint A
9   **if** NSC_A *is true* **then**
10               $IsIso \leftarrow$ false
11   **for** $k \leftarrow 1 : length(G_s)$ **do**
12                  $IsIso \leftarrow$ Check if g and $G_s(k)$ are isomorphic
13   Terminate loop is $IsIso$ is true, otherwise continue
14   **end**
15   **if** *IsIso is false* **then**
16                  $G_s(end + 1) \leftarrow g$
17   **end**
18   **end**
19   **end**
20   **end**
21 **end**

/* The function to generate all simple graphs with N_e edges and N_v vertices   */

22 **Function** GengEdVe (N_e, N_v)**:**
23      $K_{N_v} \leftarrow$ Generate the complete graph with N_v vertices
24      $idx \leftarrow$ Find combinations of N_e from $N_v(N_v - 1)/2$ elements
25      $G \leftarrow \varnothing$
26   **for** $i \leftarrow 1 : length(idx)$ **do**
27         $g \leftarrow$ Generate the graph with edges $idx(i)$ of K_{N_v}
28         $IsCon \leftarrow$ Check if g is connected
29   **if** *IsCon is true* **then**
30            $IsIso \leftarrow$ false
31   **for** $j \leftarrow 1 : length(G)$ **do**
32               $IsIso \leftarrow$ Check if g and $G(j)$ are isomorphic
33   Terminate loop is $IsIso$ is true, otherwise continue
34   **end**
35   **if** *IsIso is false* **then**
36               $G(end + 1) \leftarrow g$
37   **end**
38   **end**
39   **end**
40   **return** G

EXPERIMENTAL STUDIES ON THE INFLUENCE OF STATIC TORQUE IN A NOVEL GEARBOX TEST-RIG

S. Nampally[1], S. Okda[1], M. Fontana[2], R. Nordmann[1], and S. Rinderknecht[1]

[1]*Technical University of Darmstadt,Germany*
[2]*Powerflex SRL, Limatola, Italy*

e-mail: sneha_rupa.nampally@tu-darmstadt.de

Abstract

In the trend of light weighting of automotive gearboxes, structure-borne and air-borne noise are more significant, and this calls for smarter solutions to tackle this problem. Most vibrations from the gearbox arise from the gear meshing, which could go up to several kilohertz in frequency and can be detrimental to comfort of passengers. Active solutions to control vibrations related to the gear meshing under operation is the central theme of this research. As a first step in the experimental investigations, the behavior of the gearbox in modal and experimental conditions is studied to evaluate the parameters affecting the vibration response of the housing. The objective is to monitor the influence of these parameters on the system's response in the frequency range of 1000-5000 Hz, which is the frequency range of interest for this study. Effect of transmitted load on the gearbox housing vibration level is studied using a non-rotational set-up to achieve comparable results with a rotating test-bench.

1. Introduction

Gearbox noise in lightweight transmissions is a matter of great concern as this determines the comfort and vibration transfer characteristics to the vehicle compartment. Generally, such a problem is treated with active mounts or a variety of passive solutions that generally render good performance for high frequency noise and vibration control. The gear meshing forces in a gearbox arise from the periodic contact between the gear teeth. At high frequencies, the higher harmonics of gear meshing tend to have greater impact on noise levels produced. This calls for effective solutions with active and adaptive characteristics in higher frequency ranges.

Several examples of active vibration control have been demonstrated for lower frequencies below 1000 Hz. In recent times, active control techniques have been implemented in the higher frequency ranges up to 4500 Hz [7] [9]. In our case, the focus lies in the domain of 1000-5000 Hz to build a dedicated active vibration control solution for an automotive gearbox housing.

For this frequency range, adaptive feed forward control in general provides effective solutions to minimise vibrations. As a prerequisite to the development of the control mechanism, it is important to evaluate the system characteristics of the gearbox under test. In this study, behavior of the gearbox housing of prime focus and its modal characteristics are examined. The areas of the housing, most responsive to incoming load, are targeted as the preliminary locations to evaluate the vibration response and quantify the performance of the planned development of active vibration control system.

This study aims to evaluate the relevance of the transmitted torque on the vibration characteristics of the housing. A lot of relevant literature exists where the influence of input torque has been studied on dynamic behavior of a gearbox, mainly through developed lumped parameter models using the mesh stiffness as the parametric excitation. The influence of input torque on a gear-train has been studied in [3]. It was determined that an increase in load increased the overall vibration level. This is mainly due to change of tooth engagement process which had a direct influence on the meshing stiffness for different torque levels. This influences the dynamic response of the system.

The main drawback of these models is that they tend to terminate the discussion at the locations of the bearing as the inclusion of housing dynamics is complicated to model and realize through lumped parameter models. It is also hard to evaluate specific regions of the housing that would be more responsive compared to others in complex geometries. Such a limitation calls for experimental investigations, which are much easier to setup

and can be easily validated with finite element modeling. There have also been experimental investigations studying the influence of transmitted torque on the vibration characteristics of the gearbox in high speeds, in the similar frequency range of out interest [8]. However, the effects of the load have been mainly studied on the input shaft with an accelerometer mounted on a rotation disc, which is still rather upstream in the vibration path. Consequences of this torque has been seldom addressed in downstream components such as bearings and gearbox housing through experimentation.

Through this study, the phenomenon and factors affecting the load transfer in rather downstream components like the gearbox housing will be explored. This also determines the level of vibration transferred to the car body. Another special consideration in the work presented here, is the use of a more economical gearbox set-up without any rotation of components. Harmonics of steady state input can be achieved with this set-up, which is analogous to the gear-meshing phenomenon in an automotive gearbox running with real operating scenarios. To characterize the gearbox vibration and the control, two major paths are defined in active vibration control development: Primary path and secondary path. The primary path refers to the main transfer path causing the vibration response in the system. In this case, it is from the excitation mechanism to the housing responses measured. This path determines the actuator requirements in terms of amount of force to be delivered to control the vibrations. The secondary path corresponds to the path with the control mechanism influencing the incoming vibrations. Behavior of this path in this challenging frequency range is useful in deciding the actuator design limits and optimal locations for their placement.

2 . Methodology

The current study is based on the test-rig that has been described in a complimentary paper submitted to this conference by the authors within the LIVE-I project [5]. This test-rig employs a unique approach that replaces the traditional rotating drive machine with a piezoelectric stack actuator to establish a comparable and modular platform for vibration investigations. A pilot study on a complete transmission, in a rotational set-up, with a drive motor at the input and a brake at the output was conducted at IMS CONNECT, TU Darmstadt [4].

2.1 . Finite Element Analysis (FEA) description

A finite element model of the test-rig is constructed including the relevant parts of the test-rig. The contacts and materials are set to be linear and the boundary conditions are set to be free-free. The main objective is to study the local modes of the gearbox housing, which remain unaffected with this free-free condition compared to the as-installed condition in the car. The contacts are defined conservatively with bonded elements. The finite element model serves as a directional guide to select the most susceptible positions on the gearbox housing in the vibration transfer using modal strain as an evaluation parameter.

2.2 . Experimental methodology

The regions of suspected high modal strain from the FE analysis are equipped with triaxial accelerometers (Model : PCB 356A16). For the operational behavior, the transmission drive excitation, which ideally comes from the drive machine in the vehicle is replaced by a piezoelectric stack actuator. A quasi-static force sensor (Model : Kistler 9001a), is placed below the exciting actuator, that measures the input torque into the system. The static torque is given with the help of a loading screw and the superimposed dynamic torque is due to the piezoelectric forces generated by the actuator. The input torque schematic is described in Figure 1. The gearbox is designed for 300 Nm load at the input shaft. An unloaded test-case would be a candidate for gear rattle, which is not in the scope of this study. Hence, the experimental set-up is always operated under an imposed static torque to ensure the contact between gear teeth is established to evaluate the gear whine phenomenon. Input loads up to 80 Nm were applicable to avoid tilting of the exciting piezoelectric stack actuator which is crucial for proper load transfer. Using the proposed set-up, a static load of 80 Nm superimposed with a dynamic load of up to 8 Nm amplitude can be achieved. The effective dynamic excitation at a particular static

torque, depends on the speed of operation of a gearbox. In the case of the test-rig, dynamic torque variation depends on the frequency of excitation of the piezoelectric stack actuator. The cumulative excitation mimics the dynamic torque fluctuations induced into the system at the input shaft of the transmission case of an automotive transmission in rotational operation that was measured on IMS CONNECT test-rig as shown in Figure 1(right).
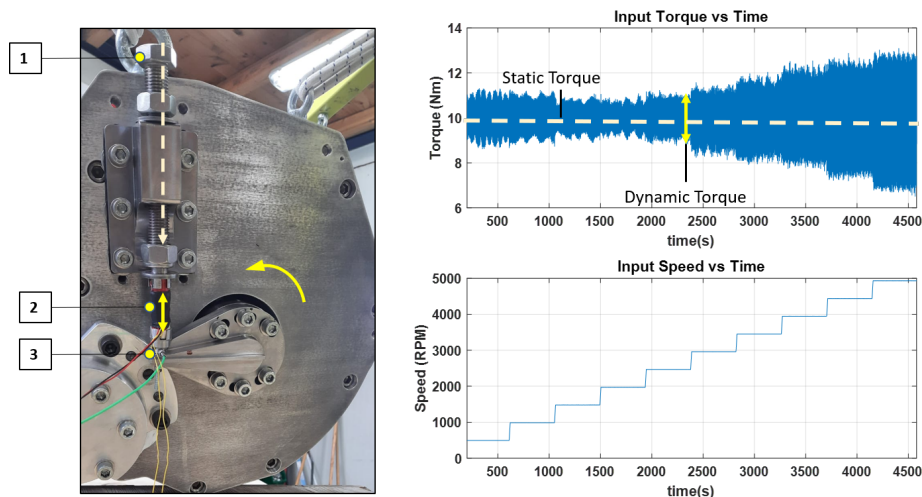

Figure 1: Left : Input Torque arrangement in the proposed gearbox test-rig showing the static loading screw (1), the piezoelectric stack-actuator (2) and the load cell measuring the transmitted torque (3). Right: Torque profile over varying input speed of gearbox in rotational set-up measured on IMS CONNECT

The piezoelectric actuator is excited with swept-sine signals or chirps from 0 - 5000 Hz to study the path of vibration transfer. The frequency responses to these excitation signals we recorded at various input levels of static torque corresponding to the levels seen in a gearbox in operation. It was noted that the total time of sweep or sweep rate does not affect the frequency response of the gearbox. Two load levels are discussed here; 40 Nm and 80 Nm. Each measurement was repeated ten times to reduce influence of random disturbances by averaging.

3. Results and Discussion

3.1. Identification of Housing Responses using FEA

The frequency response measurements obtained from the accelerometers were used to derive the natural frequencies of the gearbox. A comparison was made with finite element calculations of the natural frequencies. The finite element model was developed with rigid contacts; hence a good correlation can be established with experiments conducted with a higher applied static torque.

Table 1 shows the comparison of some identified frequencies related to the vibrating modes of the gearbox housing and the poles identified by using 'RKFit'; an open source modal curve fitting algorithm as described in [2] using the frequency response of accelerometers obtained from the 80 Nm test. A visual representation of the modal strains corresponding to these housing vibration modes can be seen in Figure 2. At frequencies higher than 3000 Hz, the vibrations on the housing tend to become more localized with higher order mode shapes.

A set of locations of interest on the gearbox was chosen based on the areas with high modal strains extracted from the relevant mode shapes of the housing in the frequency range of interest. The locations are illustrated in Figure 3. Position 1 corresponds to the location of the bearing seated in the housing supporting the input shaft. This position can directly evaluate the effects of the load transfer path rather upstream in the gear-train.

	Experimental		FEA
	40 Nm	80 Nm	
1	1020.8	1015.1	1020.0
2	1898.9	1896.2	1926.6
3	2394.4	2388.4	–
4	2708.5	2714.2	2746.6
5	3561.2	3680.8	3727.9
6	3815.5	3982.9	4033.8
7	3893.3	4041.2	4123.1
8	4038.6	4145.7	4231.6

Table 1: Frequencies corresponding to Housing Vibrations in Hz
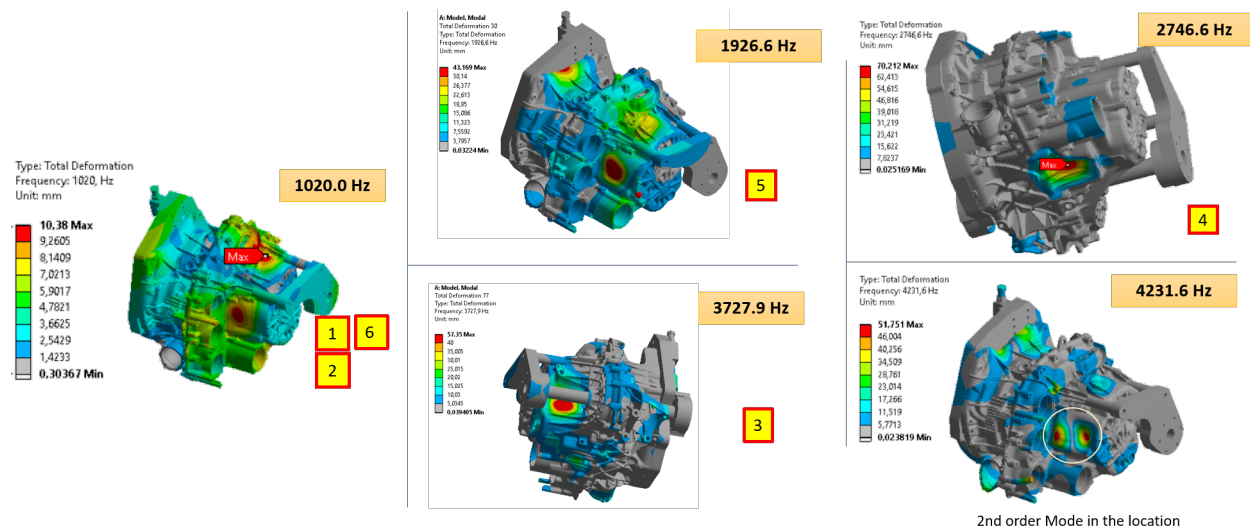

Figure 2: Gearbox vibrating modes indicating regions of high modal strains. Numbers in yellow boxes indicate the sensor mounting points shown in Figure 3

The gearbox housing is composed of two cases - front case and the transverse case. The transverse case is more flexible compared to the front case, as the latter is rigidly supported by the engine flange as shown in Figure 3 These locations are used to quantify the gearbox vibrations, which will later help us in bench-marking the requirements for the control actuator.
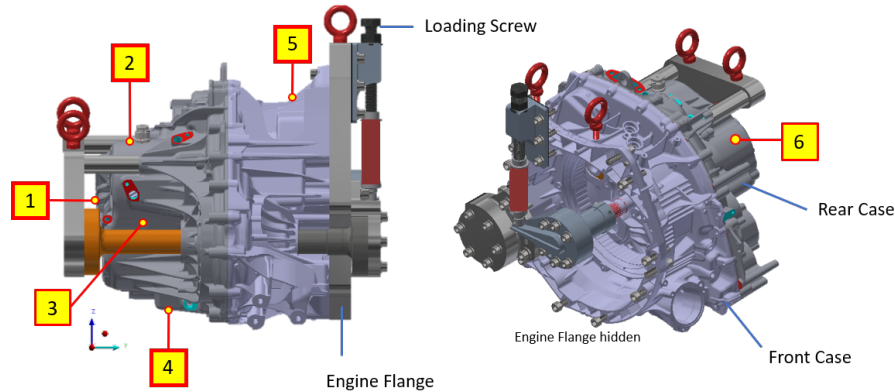
Figure 3: Gearbox schematics with locations of high response of housing vibrations

3.2 . General effect of static torque on the vibration responses

To evaluate the effect of input torque on the vibration transmission characteristics of the primary path, the total vibration level is illustrated is studied. Figure 4 (left) shows the cumulative vibration level obtained from all the accelerometers on the gearbox housing at two input torque levels 40 Nm and 80 Nm. A significant observation that can be made is that the level of vibration is higher at 80 Nm in the regions 1300 - 1800 Hz and also in the regions above 3500 Hz. The underlying cause of such an increase in response can be explained by increase in contact area between gear teeth and increase bearing stiffness [1].
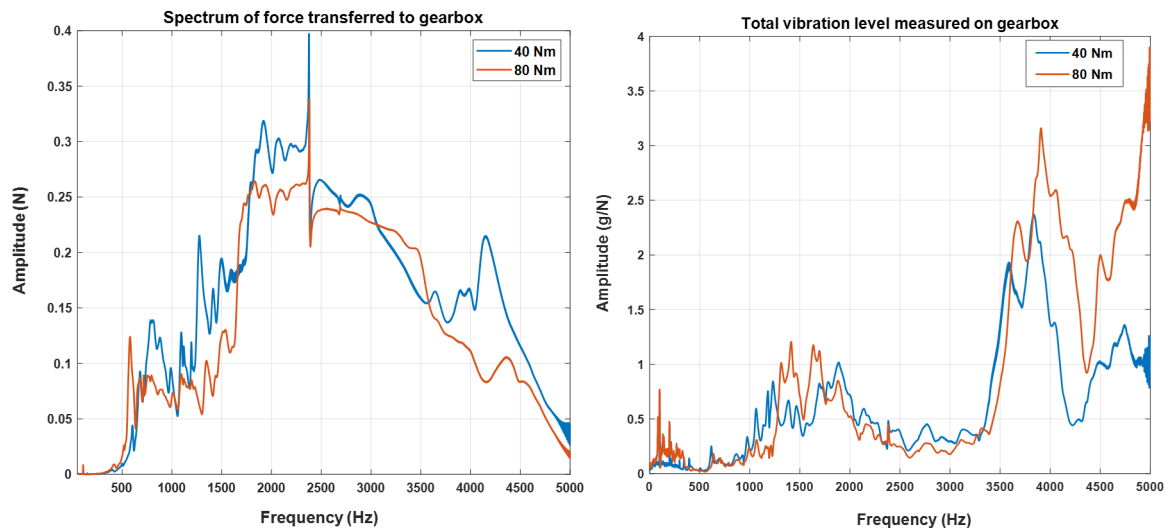
Figure 4: Left : Spectrum of dynamic input force applied using the piezoelectric stack actuator ; Right: Total vibration level per unit dynamic input force measured at two static torque values

It is also evident that peaks corresponding to the resonance of the gearbox have a rightward shift denoting an increase in natural frequencies. The comparison of poles extracted from the curve fitting at both torque levels is shown in Table 1. There is relatively greater shift in natural frequencies in the range above 3300 Hz among the two load levels along with an increase in vibration level denoted in Figure 4 (right). The anisotropic stiffening
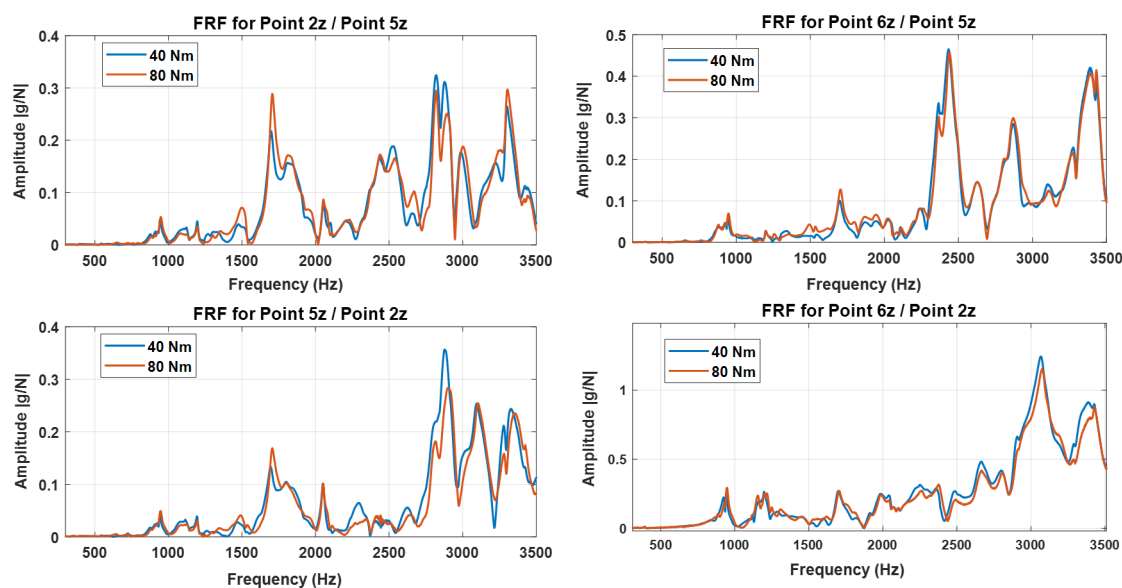
Figure 5: Top Left: Frequency Response at transverse case (Point 2) due to hammer impulse at front case (Point 5).Bottom Left : Frequency Response at front case (Point 5) due to excitation at transverse case (Point 5). Right: Frequency response at Point 6 due to hammer impulses in front case (Top Right) and transverse case (Bottom right) of gearbox housing.

of the bearings and contacts in the load transfer path is also demonstrated in the model by [3]. It is also observed that the peaks in the vibration response tend to become sharper indicating a reduction in damping. Reduction in damping combined with increase in vibration at higher loads demands an actuator delivering more force to compensate the disturbances actively.

The dynamic input force delivered to the gearbox varies greatly in frequency. The eigen-dynamics of the input arrangement, consisting of the piezo stack actuator and the static loading screw, influence this force delivered. Figure 4 (left) depicts the spectrum of input load transferred to the gearbox input shaft due to the piezoelectric excitation of the actuator on the lever to the input shaft as seen in Figure 1. Clear peaks in the spectrum of input force indicate the resonances of the loading mechanism, specifically at 2380 Hz. The resonance frequencies tend to show up as zeros in the frequency response functions of accelerometers placed in position 6 and 2. Resonances of the exciting mechanism can also be seen distinctly in the total vibration level corresponding to two static load levels as seen in Figure 4 (right) (for example at 2380 Hz).

3.3. Effect of static load on secondary path

For the control of vibrations, the primary choice of actuator locations are the points on the housing with high modal strains.Each measurement point is equipped with a triaxial accelerometer to record the housing vibrations. The z-direction records the vibration normal to the housing structure. Exploration among the selected points using an impact hammer determines the degree of influence of a potential actuator on the vibration level of the housing. Bandwidth of uniform input of the impact hammer is valid in the range up to 3500 Hz. The vibration response of the gearbox housing evaluated between the front case and the transverse case. Point 2 on the transverse case and point 5 on the front case have been used to impact with a hammer. The effect of hammer force one side (Point 5 - front case) of the gearbox to another (Point 2 - transverse case) and vice versa, remains unaffected with the change in applied static torque as seen in Figure 5 (left). The influence is also explored at point 6 on the transverse case (refer Figure 3) due to a potential actuator location on the front and transverse cases of the housing. Point 6 lies in the vicinity of the meshing gear pair of interest in the reduced transmission. The hammer responses indicate that the stiffness of the gearbox housing remains unaffected due to the static

load applied to the system. This eliminates the need to incorporate static transmitted torque as a parameter for secondary path modeling for controller development.

4. Conclusion and Future Work

In this work, we can conclude that there is a clear influence of the input torque on the vibration response of the gearbox. In rotating experimental set-ups of gearboxes, the change in dynamic response with transmitted torque can be attributed to changes in Dynamic Transmission Error (DTE), torsional stiffness of shaft and bearing stiffness. Comparable influences of change in responses have also been established here in a non-rotating system. Resonances of the input excitation mechanism determines the amount of dynamic torque transferred into the system. The secondary paths or the possible actuator impact locations showed no change in responses because of the change in transmitted torque, making the control development independent of this parameter. The work of this paper will be extended to benchmark actuator concepts in the development of the mechanism for active vibration control. HiL simulations [6] for implementation active vibration control and novel actuation strategies to mitigate gear whine in the frequency range up to 5 kHz.

References

[1] Mats Åkerblom and Ulf Sellgren. Gearbox noise and vibration: Influence of bearing preload, 2008.

[2] Mario Berljafa and Stefan Güttel. The rkfit algorithm for nonlinear rational approximation. *SIAM Journal on Scientific Computing*, 39(5):A2049–A2071, 2017.

[3] A. Fernandez del Rincon, P. Garcia, A. Diez-Ibarbia, A. de Juan, M. Iglesias, and F. Viadero. Enhanced model of gear transmission dynamics for condition monitoring applications: Effects of torque, friction and bearing clearance. *Mechanical Systems and Signal Processing*, 85:445–467, 2017.

[4] Institute for Mechatronic Systems – TU Darmstadt. IMS Connect. https://www.ims.tu-darmstadt.de/institut/aktuelles_6/ims_connect_1.en.jsp.

[5] LIVE-I H2020. Lightening and innovating transmission for improving vehicle environmental impacts, 2020. https://livei.fr/.

[6] Dirk Mayer, Timo Jungblut, S Wolter, and J Millitzer. Hardware-in-the-loop test environments for vibration control systems. In *NAFEMS Seminar Practical Aspects of Structural Dynamics, Deutschland, Wiesbaden*, 2015.

[7] Gerald T. Montague, Albert F. Kascak, Alan Palazzolo, Daniel Manchala, and Erwin Thomas. Feedforward control of gear mesh vibration using piezoelectric actuators. *Shock and Vibration*, 1:959651, 1994.

[8] Milosav Ognjanovic and Fathi Agemi. Gear vibrations in supercritical mesh-frequency range caused by teeth impacts. *Strojniški vestnik - Journal of Mechanical Engineering*, 56(10):653–662, 2010.

[9] P Zech, DF Plöger, T Bartel, T Röglin, and S Rinderknecht. Design of an inertial mass actuator for active vibration control of a planetary gearbox using piezoelectric shear actuator. In *Proceedings of ISMA2018 International Conference on Noise and Vibration Engineering*, pages 203–215, 2018.

EXPERIMENTAL VIBRO-ACOUSTIC ANALYSIS OF GEARBOX BEHAVIOR USING PIEZOELECTRIC STACK ACTUATOR EXCITATION

S. Okda[1], S. Nampally[1], M. Fontana[2], S. Herold[3], R. Nordmann[3], S. Rinderknecht[1] and T. Melz[1,3]

[1]*Technical University of Darmstadt, Otto-Berndt-Str. 2, 64287, Darmstadt, Germany*
[2]*Powerflex s.r.l, via Campitiello 6, Benevento, 82030, Limatola, Italy*
[3]*Fraunhofer LBF, Bartningstraße 47, 64289, Darmstadt, Germany*

e-mail: sherif.okda@sam.tu-darmstadt.de

Abstract

In this paper, a new test-rig is designed to study the vibro-acoustic behavior of a simplified automotive transmission system. The aim is to experimentally reproduce the gear whine phenomenon in the gearbox, which is caused due to the transmission error without the need of rotating elements. Instead, an innovative method of excitation is proposed using a piezoelectric actuator. The test rig is designed to be an economical solution to otherwise complicated setups. Experimental investigations of the gearbox housing accelerations and noise emission are done, and the setup successfully captures the accelerations with its associated harmonics, with values that are very close to the state of a real rotating gearbox. In addition, a correlation is found between the housing accelerations and the emitted noise in certain frequency ranges. This setup will be used in future to test and integrate an active vibration control solution, to mitigate the generated vibrations and noise.

Keywords: Gearbox; Vibrations; Noise; Piezoelectric; Actuator; Test-rig; Active Vibration Control

1. Introduction

For the past few years automotive manufacturers have been focusing on car weight reduction, to decrease the fuel consumption and gas emissions. One of the most significant components of the vehicles, that contribute to the weight, is the transmission system of the vehicle. However, decreasing the weight of the transmission system can lead to an increase in the vibrations and noise emitted. Due to the increasing demand to improve the vibro-acoustic comfort, the manufacturers are also concerned with the vibration and noise problems specially that are generated by the gearboxes.

The main source of the gear vibrations is the transmission error which induces a periodic source of excitation. The excitaion is transferred from the gears to the shafts, bearings, and then to the gearbox housing. This excitation creates a noise that is mostly tonal in nature, as the noise frequency spectrum mainly consists of sinusoidal components at certain frequencies, which are equal to the product of the gear rotational speed and the number of teeth, that is referred to the gear meshing frequencies GMF. In addition, there are also the harmonics which are the multiples of the gear meshing frequencies [1]. The developed test-rig aims to simulate the meshing frequency and its associated harmonics, so that these frequencies can be controlled later on using the active vibration control system.

In this paper, the vibro-acoustic behaviour of a dual clutch transmission (Magna 7DCT300) is studied using a novel method of excitation, to simulate vibrations resulting from gear mesh without rotational input. The aim of this work to introduce an economic yet realistic and a non-traditional setup that can be used to test gearbox housing vibrations. This test setup will be used in future to test an integrated active vibration control (AVC) solution. The AVC solution will be used for automotive transmission systems as a part of the European MC project LIVE-I [2]. The experimental and numerical AVC development in the project will be performed by

means of two test-rigs and in several steps, before testing it in a full car will be possible. In a first step, a simplified test-rig which is presented in this paper will be used, that consists of a separated reduced transmission system. The first test-rig is designed to be economic, hence an artificial test environment had to be developed with static and dynamic input torques in order to obtain the same dynamic behavior of the transmission system as in case of real operation. The existing second test-rig IMS CONNECT [3] will allow the full operation of the complete transmission with a drive motor at the input and a Brake at the output. In this test rig all operating data regarding speed, power, torques, etc. can be realized. This test-rig will be used to evaluate the AVC system with all components after its development on the first test-rig.

Previously, most of the researchers, who used active vibration control solutions for transmission systems, used traditional rotational test setups using a motor and a braking system, such as Rebbechi el al. [4], Guan el al. [5], Sopouch el al. [6], Zech el al. [7], and Wang el al. [8]. In addition, others used different methods to excite the transmission systems, such as Dion el al. [9], who used an electrodynamic shaker connected to a rod, and transformed translational oscillations into angular oscillations to the main shaft. Moreover, Barthod el al. [10], used an electrodynamic translation exciter that was connected to the gearbox input shaft through a crank. Both Dion and Barthod used these non-traditional setups to study the gear rattle effects. However, in this paper the focus lies on studying the gear whine rather than rattle. In addition, a new type of exciter is used to induce the vibrations into the system, which is a piezoelectric stack actuator. The piezo actuators are known of their high efficiency at high frequencies, which can excite the same range of the gear meshing frequency and its associated harmonics. In the next section, the test setup is described in more details and the measurements done are defined.

2. Methodology

The proposed test setup consists of a simplified gear train of the dual-clutch gearbox (Magna 7DCT300), where two gear pairs are only engaged, along with the gearbox differential gears. While the rest of the gear pairs are detached, including the forks and synchronizers. As mentioned before, there is no rotation in the gearbox setup, thus the lubrication is absent. The gearbox is excited through a piezoelectric stack actuator (P-016.40P) from Physik Instrumente (PI), the actuator is connected to the gearbox input driveshaft through an intermediate lever, that is used to induce a dynamic torque. The excitation takes the normal transfer path from the input shaft to the gears, bearings, then finally to the housing. A schematic is shown in Fig. 1 showing the load transfer path. In addition, the system is preloaded with a static load by a screw, to have the same situation as for the rotating system with contact on the drive flanks, and this preload can be adjusted to study different stiffness situations in the bearings (non-linear effects) later on. The excitation mechanism is shown in Fig. 2. Furthermore, the gearbox is fixed in a free-free boundary conditions by hanging it using rubber cords, that are fixed to a steel frame. The free-free boundary condition is chosen for the test-rig to keep the natural frequency of the foundation away and from the operating frequency range, the test setup can be seen in Fig. 3.

Six 3-axis ICP accelerometers of model (356A16) from PCB Piezotronics are attached to the gearbox at critical points to measure the vibration levels of the housing. In addition, an PCB Piezotronics ICP microphone of model (378C20) is used to measure the sound pressure. LMS SCADAS SC-310 data acquisition system is used to adjust the excitation parameters (frequency, harmonics, amplitudes and phases) and record the measured accelerations and sound pressure level. The gearbox can be excited up to 5000 Hz, which can cover the most important harmonics of the gearbox.
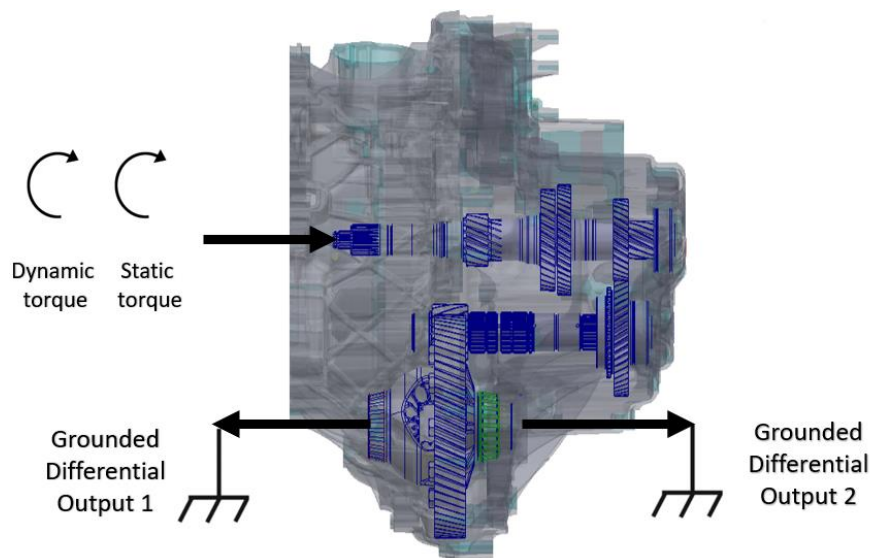
Figure 1: Schematic drawings of the load transfer path in the simplified 7DCT300 gearbox.
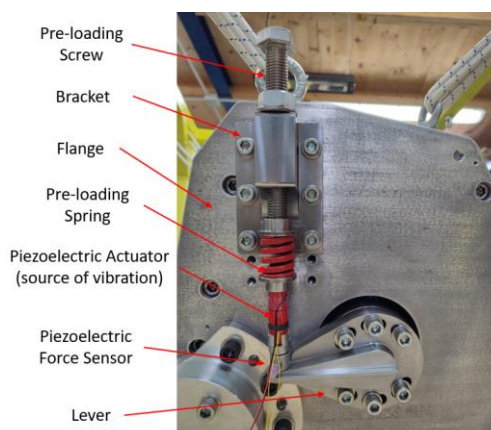
Figure 2: The excitation mechanism used to excite the gearbox.
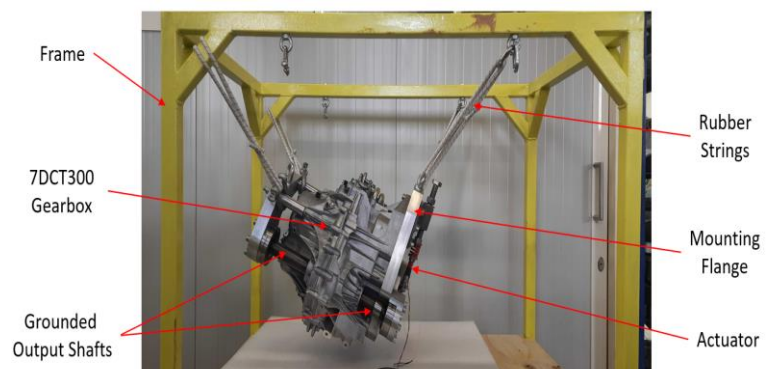
Figure 3: The test setup showing the 7DCT300 fixed in a free-fee boundary condition using rubber strings.

The aim of the acceleration measurements is to prove that the new excitation system can generate acceleration profiles, that are close to the real conditions. The acceleration profiles should include the excitation frequency and its associated harmonics. In addition, the housing accelerations values should be comparable to the real conditions. Preliminary measurements were performed in the IMS CONNECT test bench previously in TU-Darmstadt with the 7DCT300 gearbox, with all the internal components included and running at the real operating conditions. The acceleration values measured were used as a benchmark, the values were of the same order for the gear meshing frequency and its first three harmonics. The acceleration values are used to settle the input voltage to the piezo stack actuator so that similar accelerations are generated in the developed test-rig. In addition, the acoustic measurements are carried out to study the relationship between the excited housing accelerations and the sound emitted. This data will be used in the future in the development of the active vibration control system, to distinguish which frequencies contribute to the noise generated by the housing. The sound pressure level is measured inside one of the holes in the housing, as shown in Fig. 4.
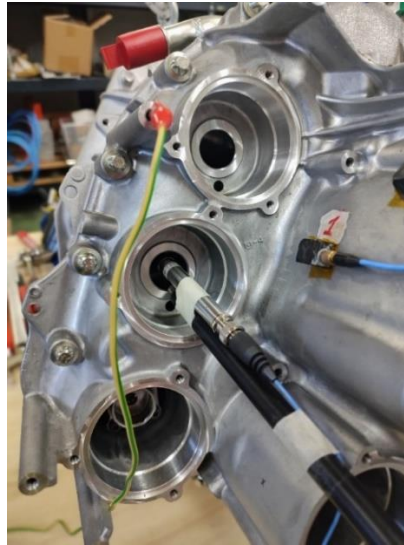
Figure 4: The microphone position used for the sound pressure measurements.

3. Results and Discussion

The piezo electric actuator is first excited with a harmonic signal, and as it can be seen from Fig. 5, by exciting the gearbox by a 1000 Hz sine wave through the input shaft, the harmonics of the input signal can be successfully captured by the accelerometers on the housing. By setting the input voltage given to the actuator by the power amplifier, the acceleration values can be set to have the same order as the real accelerations generated in a real rotating gearbox (IMS CONNECT test bench). In Fig.6, a sample of the measurements done using the IMS CONNECT Test Bench is shown. The acceleration spectrum of the same point on the housing that is loaded by the same torque is shown. The meshing frequency was equal to 1381 Hz, and it can be seen the first two harmonics are observable up to the range of 5000 Hz, and the acceleration values have the same order of magnitude.

These harmonics can be interpreted due to primarily two reasons, the mechanical system of the gearbox with the gear contacts, and the piezo stack actuator nonlinearities, which also induces harmonics to the system. Although these nonlinearities may be undesirable in most of the mechanical systems, in this test-rig they are desired, as the harmonics of the signal are essential for the testing of the active vibration control system, that is going to be designed in the future.
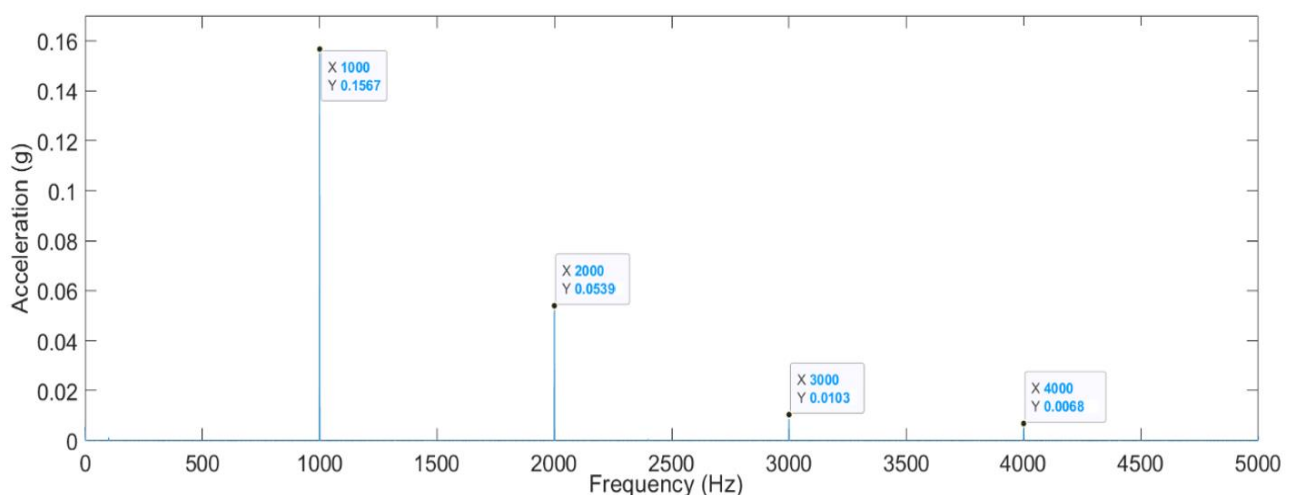
Figure 5: Acceleration spectrum showing harmonics captured on the housing with a 1000 Hz sine wave excitation using the piezo stack actuator.
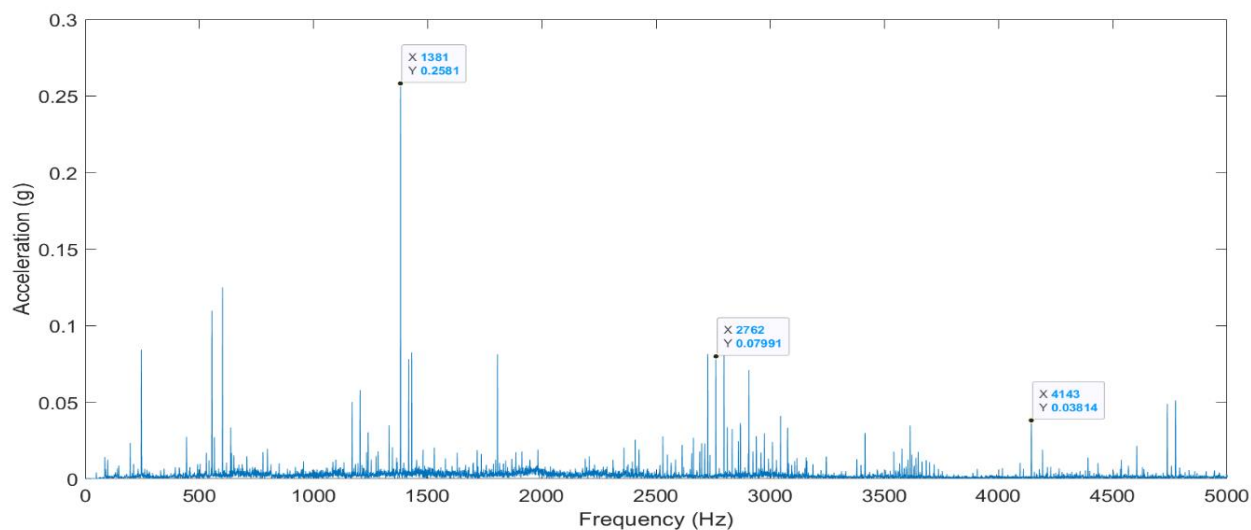
Figure 5: Acceleration spectrum showing harmonics captured on the housing with at a meshing frequency of 1381 Hz using the IMS CONNECT Test Bench.

The second set of investigation deals with correlation of noise with gearbox vibration, the microphone was used to capture the sound pressure level inside the housing. A sine sweep excitation signal is given to the piezo actuator, to determine the frequencies, that contribute to acoustical response of the gearbox. The recorded sound pressure is also compared to the housing accelerations and it can be seen from Fig. 7, that there is a correlation between the housing accelerations and the recorded sound pressure level, in the region that lies between approximately 1150 and 2300 Hz. This region can be related to the mode shapes that radiate the highest noise, which can be targeted with the active vibration control system to be developed.
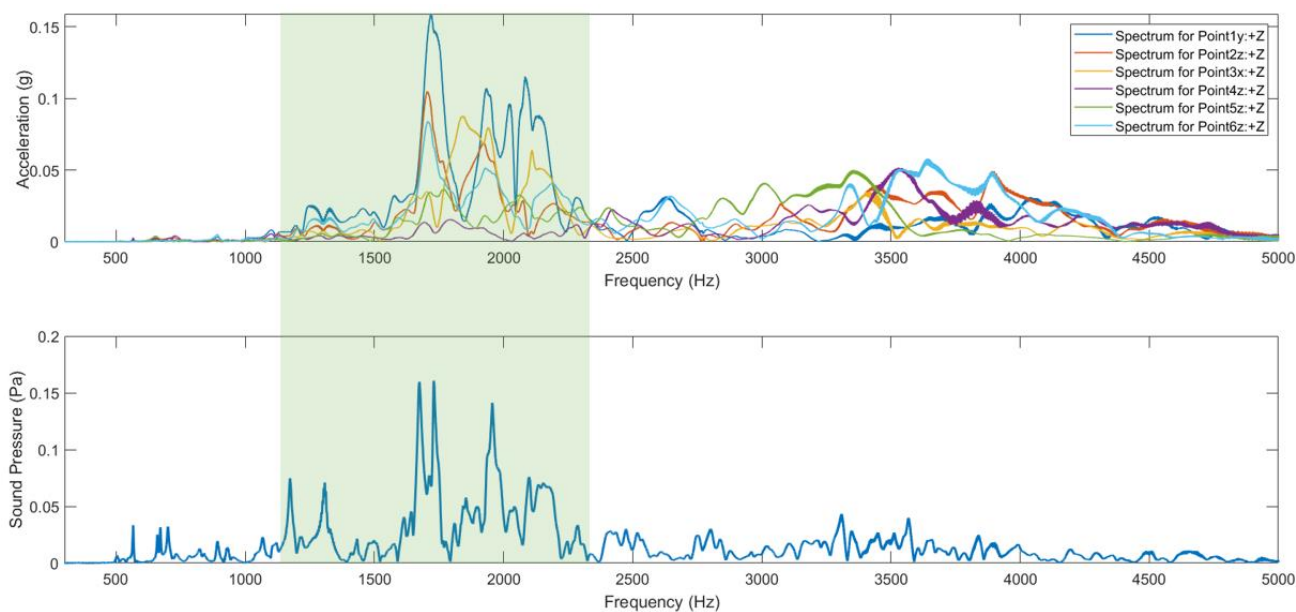
Figure 7: Acceleration spectrum (Top) compared to the measured sound pressure level (Bottom).

4. Conclusion

The designed test-rig successfully simulates the vibrations and noise of an automotive transmission system, by exciting the system using a piezo stack actuator. The vibrations through the gearbox housing include the harmonics of the exciting frequency, as well as amplitude values of acceleration close to the real running conditions. In addition, the sound pressure level is measured and a correlation is found between the housing accelerations and the sound pressure level, at a frequency region between 1150 and 2300 Hz. The exciting system shows great flexibility to induce excitations, that simulate any running speed and meshing frequency with its harmonics. This finding will be useful to develop an active vibration control system to mitigate the noise and vibrations emitted from the system.

5. Acknowledgments

6. References

[1] Tuma, Jiri. "Gearbox noise and vibration prediction and control." International Journal of Acoustics and Vibration 14, no. 2 (2009): 99-108.

[2] É. C. d. Lyon, "LIVE-I," 2020. [Online]. Available: https://livei.fr/. [Accessed 01 01 2022].

[3] TU-Darmstadt, „https://www.ims.tu-darmstadt.de/," TU, [Online]. Available: https://www.ims.tu-darmstadt.de/institut/aktuelles_6/ims_connect_1.en.jsp. [Data uzyskania dostępu: 13 April 2022].

[4] Rebbechi, Brian, Carl Howard, and Colin Hansen. "Active control of gearbox vibration." In INTER-NOISE and NOISE-CON Congress and Conference Proceedings, vol. 1999, no. 5, pp. 295-304. Institute of Noise Control Engineering, 1999.

[5] Guan, Yuan H., W. Steve Shepard Jr, Teik C. Lim, and Mingfeng Li. "Experimental analysis of an active vibration control system for gearboxes." Smart materials and structures 13, no. 5 (2004): 1230. [3]

[6] Sopouch, M., T. Resch, and P. Herster. "Analysis of Gearbox Acoustics with AVL EXCITE." In SIA Acoustic Simulation Workshop, France. 2011.

[7] Zech, P., D. F. Plöger, T. Bartel, T. Röglin, and S. Rinderknecht. "Design of an inertial mass actuator for active vibration control of a planetary gearbox using piezoelectric shear actuator." In Proceedings of ISMA2018 International Conference on Noise and Vibration Engineering, pp. 203-215. 2018.

[8] Wang, Han, Feng Zhang, Haiyan Li, Wenhao Sun, and Shunan Luo. "Experimental Analysis of an Active Vibration Frequency Control in Gearbox." Shock and Vibration 2018 (2018).

[9] Dion, Jean-Luc, Sylvie Le Moyne, Gaël Chevallier, and Hamidou Sebbah. "Gear impacts and idle gear noise: Experimental study and non-linear dynamic model." Mechanical Systems and Signal Processing 23, no. 8 (2009): 2608-2628.

[10] Barthod, M., B. Hayne, J-L. Tébec, and J-C. Pin. "Experimental study of dynamic and noise produced by a gearing excited by a multi-harmonic excitation." Applied Acoustics 68, no. 9 (2007): 982-1002.

NON-CONTACT NONLINEAR WAVE MIXING RESPONSE OF NARROWBAND LAMB WAVES GENERATED BY MAKING A LASER BEAM WITH LINE LASER ARRAY SOURCCES

Santhakumar Sampath[1], and Hoon Sohn[1]

[1]*Department of Civil & Environmental Engineering, KAIST, 291 Daehakro, Yuseong-gu, Daejeon 34141, Republic of Korea*
e-mail: hoonsohn@kaist.ac.kr

1. Background

A nonlinear ultrasonic wave mixing approach has recently been used to identify damage in plate-like materials. A damaged structure is subjected to two input Lamb waves in this method. Nonlinear mixed components at the sum and difference of the input frequencies are produced by the interaction between these waves [1]. However, the applicability of contact method to damage detection of plates is challenges mainly for the following three main reasons [2]. To begin with, it requires a coulpling medium which adds an additional nonlinearity to the output response. Second, it may not applicable under hazardous environments (e.g., high temperature). Third, it is challenging to acquire high spatial resolution (less than μm) enough to identify damage when the transducer can only be installed in a few distinct points.

2. Objective

In this study, a non-contact nonlinear Lamb wave mixing technique based on laser line-array excitation was developed for non-contact generation and detection of the nonlinear mixed components in plates. Specifically, a pulsed laser with a line-array pattern (LAP) source was created to generate two narrowband Lamb waves with distinctive frequencies; then, a laser Doppler vibrometer (LDV) was used to measure the corresponding ultrasonic responses. The uniqueness of this study is as follows: (1) A completely non-contact laser ultrasonic system equipped with a Sagnac interferometer was created for the generation of narrowband Lamb waves; additionally, an LDV was used to identify the mixed components.; (2) the proposed system allows two Lamb waves with different frequencies to be made at the same time by using a single pulse laser source; (3) it is possible to implement Lamb wave mode at a specific input frequency by simply altering an optical lens; and (4) unlike the slit mask method, the Sagnac interferometer produces laser LAP sources with sufficient energy (at least 80%) to generate input waves in structures.

3. Introduction

The nonlinear Lamb wave mixing technique has been widely used for nondestructive evaluation because of its advantages of a long propagation distance and high sensitivity to microstructural heterogeneity (e.g., microcrack) [3, 4]. These advantages include a long propagation distance and high sensitivity to microstructural heterogeneity (e.g., microcrack). In a nutshell, the nonlinearity of microcrack can be recognized by applying incident Lamb waves; this characteristic can then be used to detect microcracks. The detectable nonlinear effects are commonly exploited for applications in harmonics [5] and wave mixing [1] techniques, amongst other things. In the case of harmonics technique, the self-mixing of a single Lamb wave generates the harmonic components; alternatively, the wave mixing technique entails cross-mixing between two Lamb waves to generate the mixed components. In the case of the harmonics approach, the harmonic components are generated by the self-mixing of a single Lamb wave; in the case of the wave mixing technique, the mixed components are generated by the cross-mixing of two Lamb waves. Wave mixing has the following advantages over harmonics: I the amplitudes of the mixed components are only averaged within the wave mixing zone, which provides it with higher spatial resolution [6]; (ii) it is less sensitive to

nonlinearity introduced by instruments such as transducers and coupling media [7]; and (iii) the transmitter and receiver can remain fixed in place, as microcrack position detection is achieved by scanning the wave mixing zone [8]. As a result of these factors, the nonlinear Lamb wave mixing technique has gained popularity in recent years.

A contact method (e.g., the employment of a piezoelectric transducer) has traditionally been used to generate and sense mixed components in the use of the nonlinear Lamb wave mixing technique up to this point. While touch methods are effective for detecting microcracks, their usefulness is limited when used for microcrack detection. These four general reasons [18] can be summarized as follows: A coupling media (such as water or gel) is required between the transducer and specimen in touch techniques; nevertheless, the introduction of a coupling medium results in increased nonlinearity in the output response of contact methods. Another drawback of using contact transducers in tough conditions, such as high-temperature situations, is that they are difficult to maintain. Third, among all of the system components, contact transducers are frequently the most susceptible to damage; as a result, their employment has the potential to increase maintenance costs while simultaneously degrading system performance. Lastly, due to the limited number of contact transducers that have been put throughout the system, there are unavoidable restrictions in the spatial resolution. So non-contact laser ultrasonic systems, such as those used in the creation and detection of mixed components, are particularly significant for this application.

In this study, a laser ultrasonic system design that includes a Sagnac interferometer was newly developed to quantify the influence of microcrack on nonlinear mixed component generation. The system generates two narrowband Lamb waves with distinct frequencies by creating laser line-array pattern (LAP) sources. The uniqueness of this study is as follows: (1) A completely non-contact laser ultrasonic system equipped with a Sagnac interferometer was created for the generation of narrowband Lamb waves; additionally, an LDV was used to identify the mixed components.; (2) the proposed system allows two Lamb waves with different frequencies to be made at the same time by using a single pulse laser source; (3) it is possible to implement Lamb wave mode at a specific input frequency by simply altering an optical lens; and (4) unlike the slit mask method, the Sagnac interferometer produces laser LAP sources with sufficient energy (at least 80%) to generate input waves in structures.

3. Nonlinear ultrasonic Lamb wave mixing

Figure 1. Illustration of non-contact nonlinear ultrasonic wave mixing. (a) Linear structure and (b) nonlinear structure.

When two input waves a and b traveling at distinct frequencies f_a and f_b ($f_b < f_a$), respectively, are applied to a linear (ideal) structure, the structural response contains only the linear components corresponding to the input frequencies, as shown in Figure 1(a). Once the structure behaves nonlinearly (i.e., in the presence of a damage), the structural response undergoes a change that, in addition to the presence of the linear components and their harmonic components (i.e., $2 f_a$ and $2 f_b$), there is some indication of the presence of mixed components (i.e., $f_a \pm f_b$) (see Figure 1(b)) [7, 9]. Because these mixed components occur only if nonlinear sources exist, it can be considered an indication of the damage [6].

4. Developed laser non-contact Lamb wave mixing

Figure 2 depicts a schematic representation of the newly designed laser ultrasonic system, which is comprised of emission and sensor components. When generating laser LAP sources, the emission unit employs a Sagnac interferometer and laser beam polarization, which are both implemented in the emission unit. A Nd:YAG laser source produces a pulsed laser beam when it is turned on. In the first step, the laser beam is directed toward a quarter wave plate (QWP), which modifies the polarization components (s-polarized and p-polarized) of the incident laser beam. A 50/50 beam splitter divides a laser beam in half, resulting in two beams. A Lamb wave a is generated by the first laser beam and is referred to as Laser beam 1; an excited Lamb wave b is generated by the second laser beam and is referred to as Laser beam 2. The first polarized beam splitter divides laser beam 1 into s-polarized and p-polarized components, resulting in a total of two polarized components (PBS1). Following that, the p- and s-polarized components are transferred to the M2 and M4 amplifiers, respectively. After that, they are recombined using PBS1. PBS1 produces a laser LAP in accordance with the Fresnel-Arago equations, which is formed as a result of a polarization component interaction between two other polarization components [10]. The outputs from PBS1 are coupled to a beam expander (BE1), which generates a narrowband Lamb wave a on the surface of the specimen using the outputs from PBS1. BEs are utilized to change the size of the laser LAP in this instance. The designs of PBS1, M2, M3, and M4 are very similar to those of a Sagnac interferometer setup in terms of functionality. The setup for the Laser beam 2-derived creation of a laser LAP for the excitation of Lamb wave b at PBS2 is the same as it is for the excitation of Lamb wave b at PBS1.

Figure 2. Optical design of non-contact wave mixing. QWP- Quarter wave plate; BS- Beam splitter; PBS- Polarized beam splitter; M- Mirror; BE- Beam expander.

4. Experiments

In this section, the process of input Lamb wave selection for mixed component generation is described. The dispersion curves for the Lamb wave mode propagation through a 1-mm-thick aluminum plate. Guided by the internal resonance conditions, two input Lamb waves were chosen for mixed component generation [11, 12]. Accordingly, in this study, the two input modes S_0 and S_0 were selected for application at 1.02 MHz (f_a) and 0.46 MHz (f_b), respectively.

(a)   (b)
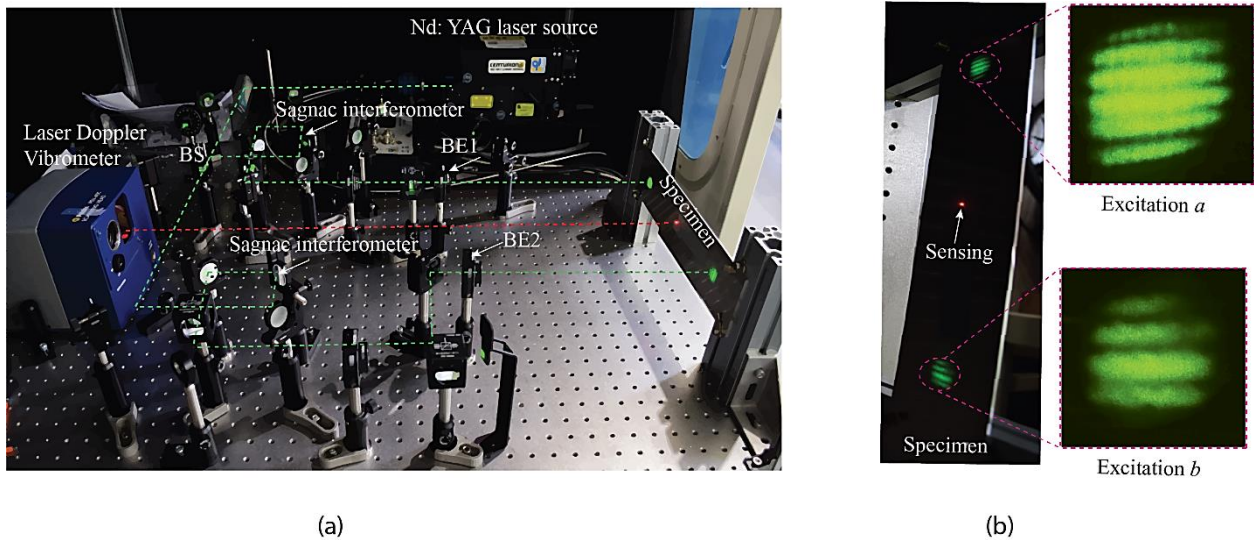
Figure 3. Proposed fully non-contact laser ultrasonic system for nonlinear Lamb wave mixing: (a) Experimental setup for the generation and detection of the mixed wave, and (b) an aluminum plate with excitations *a* and *b*.

Figure 3 depicts the suggested laser ultrasonic system that was created for the purpose of implementing the Lamb wave mixing technique. The system consisted of a pulsed laser source, a Sagnac interferometer, and an LDV, all of which were connected to a computer that controlled the system. As the illumination source, a Nd:YAG laser (Quantel Ultra Laser, pulse repetition rate: 10 Hz, pulse duration: 10 ns, wavelength: 532 nm, energy per pulse: 25 J) was employed. A beam splitter was used to divide the laser beam into two beams with equal levels of energy, each of which was produced by the same laser (BS). Following their passage through the Sagnac interferometer, the beams were combined to form a laser LAP source, which was then used to illuminate the surface of the target object. In Figure 3(b), the probe laser illumination on the specimen surface can be seen in conjunction with the specimen surface. A beam expander (BE) was utilized to reduce beam divergence to the bare minimum. Additionally, the pitches of 2.3 mm and 4 mm were maintained in order to excite the Lamb waves with frequencies of 1.02 MHz and 0.46 MHz, respectively, at the excitation frequencies.

5. Results

The performance of developed laser ultrasonic system is demonstrated experimentally by non-contact damage detection against an aluminum plate with varying damage sizes. The amplitude of mixed components obtained from the experiments is used to quantify the damage of test specimen. The test results indicate that the damaged specimen exhibits a larger amplitude value of mixed components than the intact specimen does.

In the initial experiment, the proposed system was applied to an intact plate and a plates with a 1.35 μm microcrack size under the conditions of excitation frequencies of $f_a = 1.02$ MHz and $f_b = 0.46$ MHz. Figures 4(a) and (b) show the ultrasonic responses respectively acquired in the time- and frequency- domains from the intact and microcracked plates. From the time-domain signals alone, it is difficult to determine whether microcrack-related nonlinearity produced any mixed components. However, analysis of the corresponding frequency spectra provided the evidence. In the case of the microcracked plate, the harmonic components (2 $f_a = 2.04$ MHz and 2 $f_b = 0.92$ MHz), mixed components ($f_a + f_b = 1.48$ MHz and $f_a - f_b = 0.56$ MHz), and input frequency components could be clearly distinguished. In contrast, only the input frequency components of the intact plate were observed. In addition, as can be seen in Figure 4(b), the amplitude of the mixed

components was higher than those of the harmonic components. This is because the applied input frequencies and modes satisfied the internal resonance conditions for mixed components. Thus, the strongest signal was obtained for the mixing frequency $f_a + f_b$ and $f_a - f_b$.
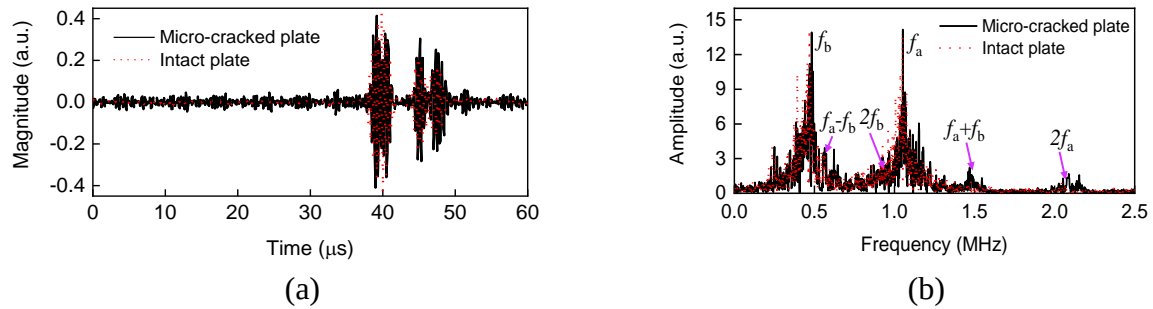
Figure 4. Nonlinear Lamb wave mixing responses from intact and microcracked (size: 1.35 µm) plates: (a) Time-domain signals, and (b) frequency spectra.
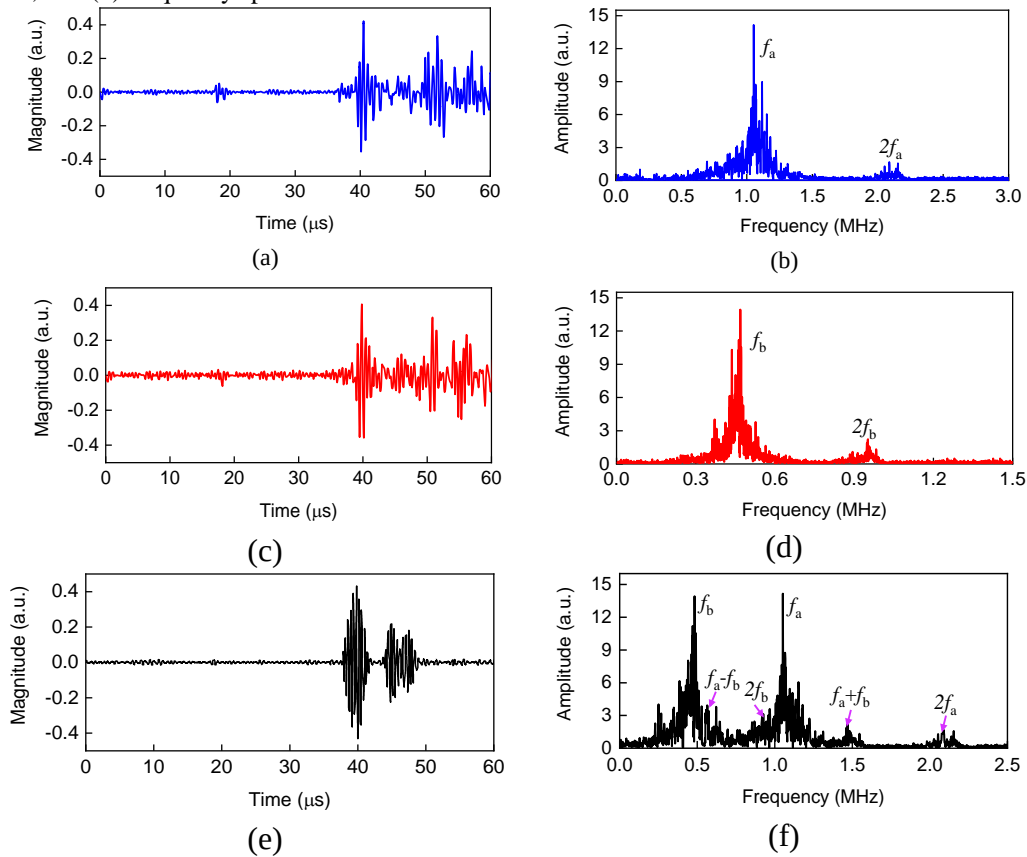
Figure 5. Nonlinear Lamb wave mixing responses from intact and microcracked (size: 1.35 µm) plates: (a) Time-domain signals, and (b) frequency spectra.

To further investigate the process of mixed component generation in the presence of a microcrack (size: 1.35 µm), we performed additional tests under the following three conditions: E_a (excitation of wave *a* only), E_b (excitation of wave *b* only), and E_{a+b} (simultaneous excitation of waves *a* and *b*). These three tests were performed under the condition that the LDV sensing position was distanced 110 mm from excitation *a*. The representative signal responses are shown in Figure 4. As can be ascertained from the time-domain results, it is generally difficult to discern any differences in amplitude due to the presence of the microcrack. Similarly, it is generally difficult to identify the nonlinear mixed waves that are directly related to the presence of a microcrack. When E_a and E_b were separately excited, only the input frequency components and their harmonic components were observed, as shown in Figure 5(b) and (d). In contrast, when E_a and E_b were

simultaneously excited (i.e., E_{a+b}), two mixed components with respective mixing frequencies of 1.48 MHz and 0.56 MHz were observed in addition to the input frequency components and harmonic components (Figure 5(f)). Because the experimental setup was the same for all three tests, the mixed components would have been observed in the results for all three tests if they were related to instrument nonlinearities, such as amplifiers, transducers, and coupling media. Thus, it is reasonable to conclude that the mixed components observed in the frequency spectra were only attributable to microcrack-related nonlinearity. Generally, the occurrence of nonlinear mixed components is a more accurate indicator of the presence of microcrack than the occurrence of harmonic components [13-15]. The reasons for this are as follows. First, the amplitude of the harmonic component is averaged over the entire distance between the transmitter and receiver (i.e., 215 mm in this study), whereas the amplitude of the mixed components is only averaged over the size of the wave mixing zone (i.e., 30 mm). Secondly, in addition to microcrack, instrument nonlinearities are known to affect harmonic component generation. Thus, analysis of the mixed components is a more effective way to detect microcrack.

6. Conclusion

In this study, a fully noncontact laser ultrasonic system was developed for generation and measurement of mixed components in an aluminum plate. With the help of developed laser-based optical Sagnac interferometer system, the location of the damage in an aluminum plate can be successfully detected. The laser LAP source, which created narrowband Lamb waves with separate frequencies (f_a = 1.02 MHz and f_b = 0.46 MHz), was supplied by a Nd:YAG pulse laser, which was used to generate the Nd:YAG pulse laser. By using a Lamb wave generator (LDV), the input Lamb waves were transmitted through a thin aluminum specimen, and the resulting ultrasonic responses were detected using an LDV. Experiments were conducted on six aluminum specimens with varying microcrack diameters in order to evaluate the efficacy of the proposed system.

References

[1] D.J. Lee, Y. Cho, W. Li, A feasibility study for Lamb wave mixing nonlinear technique, AIP Conference Proceedings, American Institute of Physics2014, pp. 662-666.

[2] L. Sun, S.S. Kulkarni, J.D. Achenbach, S. Krishnaswamy, Technique to minimize couplant-effect in acoustic nonlinearity measurements, The Journal of the Acoustical Society of America, 120 (2006) 2500-2505.

[3] N. Hosoya, T. Katsumata, I. Kajiwara, T. Onuma, A. Kanda, Measurements of S mode Lamb waves using a high-speed polarization camera to detect damage in transparent materials during non-contact excitation based on a laser-induced plasma shock wave, Optics and Lasers in Engineering, 148 (2022) 106770.

[4] X. Sun, G. Shui, Y. Zhao, W. Liu, N. Hu, M. Deng, Evaluation of early stage local plastic damage induced by bending using quasi-static component of Lamb waves, NDT & E International, 116 (2020) 102332.

[5] K.H. Matlack, J.-Y. Kim, L.J. Jacobs, J. Qu, Review of second harmonic generation measurement techniques for material state determination in metals, Journal of Nondestructive Evaluation, 34 (2015) 273.

[6] M. Sun, Y. Xiang, M. Deng, J. Xu, F.-Z. Xuan, Scanning non-collinear wave mixing for nonlinear ultrasonic detection and localization of plasticity, NDT & E International, 93 (2018) 1-6.

[7] J. Jingpin, M. Xiangji, H. Cunfu, W. Bin, Nonlinear Lamb wave-mixing technique for micro-crack detection in plates, Ndt & E International, 85 (2017) 63-71.

[8] S. Sampath, H. Sohn, Detection and localization of fatigue crack using nonlinear ultrasonic three-wave mixing technique, International Journal of Fatigue, (2021) 106582.

[9] A.J. Croxford, P.D. Wilcox, B.W. Drinkwater, P.B. Nagy, The use of non-collinear mixing for nonlinear ultrasonic detection of plasticity and fatigue, The Journal of the Acoustical Society of America, 126 (2009) EL117-EL122.

[10] M. Mujat, A. Dogariu, E. Wolf, A law of interference of electromagnetic beams of any state of

coherence and polarization and the Fresnel–Arago interference laws, JOSA A, 21 (2004) 2414-2417.

[11] M. Hasanian, C.J. Lissenden, Second order harmonic guided wave mutual interactions in plate: Vector analysis, numerical simulation, and experimental results, Journal of Applied Physics, 122 (2017) 084901.

[12] W. Li, M. Deng, N. Hu, Y. Xiang, Theoretical analysis and experimental observation of frequency mixing response of ultrasonic Lamb waves, Journal of applied physics, 124 (2018) 044901.

[13] G. Tang, M. Liu, L.J. Jacobs, J. Qu, Detecting localized plastic strain by a scanning collinear wave mixing method, Journal of Nondestructive Evaluation, 33 (2014) 196-204.

[14] Z. Chen, G. Tang, Y. Zhao, L.J. Jacobs, J. Qu, Mixing of collinear plane wave pulses in elastic solids with quadratic nonlinearity, The Journal of the Acoustical society of America, 136 (2014) 2389-2404.

[15] M. Sun, J. Qu, Analytical and Numerical Investigations of One-Way Mixing of Lamb Waves in a Thin Plate, Ultrasonics, (2020) 106180.

MRD Based Semi-active Robust Control of Civil Structures with Parametric Uncertainties

S. Vedat[1], T. Gürsoy[1], H. Anders[2], and A. Vortechz[3]

[1]*Izmir Institute of Technology, Urla, Izmir, Turkey*
[2]*Linköping University, Linkoping, Sweden*
[3]*Vortechz Research, Norrkoping, Sweden*

e-mail: vedatsenol@iyte.edu.tr

Abstract

In developing a mathematical model of a real structure, the model's simulation results may not match the real structural response. This issue is a general problem that arises during the dynamic motion of the structure, which may be modeled using parameter variations in the stiffness, damping, and mass matrices. These changes in parameters need to be estimated, and the mathematical model to be updated to obtain higher control performances and robustness. In this study, a linear fractional transformation (LFT) is utilized for uncertainty modeling. Further, a general approach to the design of a H_∞ control of a magneto-rheological damper (MRD) for vibration reduction in a building with mass, damping, and stiffness uncertainties is presented.

Keywords— uncertainty modeling, structural control, MR Damper, H_∞, robust control

1. Introduction

Civil structures can be modeled as second-order differential equations. However, due to the modeling and/or nonlinearity effects, it may not fully represent the physical systems and their behaviors. Hence, uncertainties should be considered in modeling so that the simulation behaviors cover the physical responses. For that reason, [1] inquired about the robust control approach with uncertainties in system matrices and control input matrices. Moreover, [2] designed a robust controller based on state-feedback control with a modified Kalman filter. Nevertheless, the parametric uncertainties were implemented as an increment of state-space representation matrices. Thus, uncertainties can't be recognized whether those are in mass, damping, or stiffness matrices.

In developing a mathematical model of a real structure, the simulation results may not match the real structural response. This matter is a general problem that arises during the structure's dynamic motion, which may be modeled by means of parameter variations in the stiffness, damping, and mass matrices. These changes in parameters need to be estimated within a bandwidth, and the mathematical model is updated to obtain higher control performances and robustness.

[3] modeled these uncertainties as distinguishable with reasonable percentages. Thanks to the LFT work of [4], upper linear fractional transformation (LFT) can be applied to civil structures uncertainties. In this part of the study, a magneto-rheological damper (MRD) device is implemented to stabilize the civil structure. Parametric uncertainties are used for mass, stiffness, and damping matrices.

2. System Dynamics

The structural system is modeled according to known geometry, material properties, and boundary conditions. This model will constitute the nominal model of the structure. Uncertainty of the structural system is considered to enter as variations in the nominal model, such as structural mass, damping, and stiffness matrices.

2.1. Nominal System with MRD

A civil structure system with an MRD, under earthquake excitation, as shown in Fig. 1, can be described as

$$(1) \qquad K_s\, x(t) + C_s \dot{x}(t) + M_s \ddot{x}(t) = \Gamma_u f_{MRD}(t) - M_s \Gamma_d \ddot{x}_g(t),$$
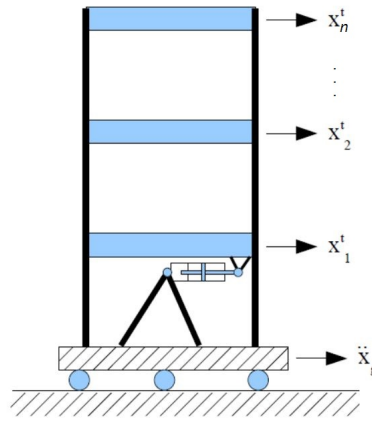
Figure 1: Shear building model with n floors

where $x(t)$ is the $n \times 1$ displacement vector of the structure relative to the ground, M_s, C_s and K_s are respectively the $n \times n$ mass, damping and stiffness matrices of the structure, Γ_d is the $n \times 1$ identity vector, $\ddot{x}_g(t)$ is the ground acceleration, $f_{MRD}(t)$ is the MRD control force applied to the structure, and Γ_u is the $n \times 1$ MRD location vector. The MRD control is modeled according to the modified Bouc-Wen model:
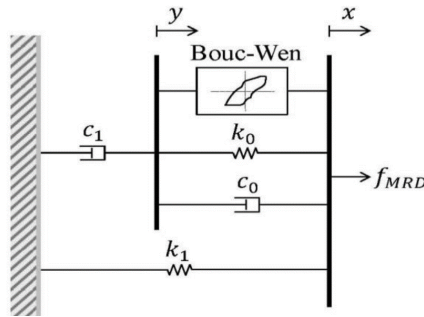

Figure 2: Modified Bouc-Wen model (Source: [5])

The modified Bouc-Wen model which was developed by [5] was used in numerical simulations of the present study. The Bouc-Wen model consists of springs, dash-pots and evolutionary variables to produce MRD behavior.

The MR damper force is calculated by using the equilibrium equation for the MR Damper model in Fig. 2 as

$$(2) \qquad f_{MRD}(t) = c_1 \dot{y}(t) + k_1(x(t) - x_0).$$

If this force is written for the upper part of the Modified Bouc-Wen model

$$(3) \qquad f_{MRD} = \alpha s + c_0(\dot{x} - \dot{y}) + k_0(x - y) + k_1(x - x_0).$$

Then the internal parameter, $\dot{y}$, can be obtained as follows.

$$(4) \qquad \dot{y} = \frac{1}{c_0 + c_1}[\alpha s + c_0\dot{x} + k_0(x - y)].$$

The evolutionary variable of the Bouc-Wen model is governed by

$$(5) \qquad \dot{s} = \gamma|\dot{x} - \dot{y}||s|^{p-1} - \beta(\dot{x} - \dot{y})|s|^p + A(\dot{x} - \dot{y}),$$

where k_1 is the stiffness of the accumulator within the damper casing, x_0 is the initial displacement of the piston. There are two damper models for low and high speeds, which are represented as c_0 and c_1, respectively. s represents the internal variable of the Bouc-Wen model. The shaping parameter of the hysteresis is defined with p.

2.2. Uncertain System Dynamics

Every mathematical model is an approximation of the true system. These models have always unmodeled effects such as neglected nonlinearity, deliberately reduced order modes and system parameter variations owing to environmental changes. These differences could adversely affect controller performance. In order to investigate uncertainty within the civil structure, the model is converted to state space representation. Subsequently, the relation of the uncertainty effect to the mathematical model is constructed. Fig. 3 shows the input-output relations of the 3-story building structure and
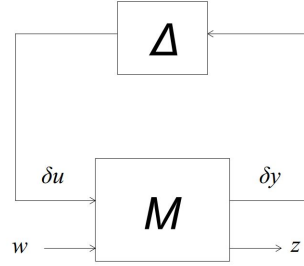

Figure 3: Standard M-Δ Configuration

its uncertainties. They are represented as two different systems. Here, w stands for the exogenous input which includes earthquake disturbance, measurement noise, and control input. z denotes the exogenous output to be controlled, which are selected as inter-story drifts and the control input. δu and δy are the input vector and output vector of uncertainties. The relation between δ_u and δ_y is

(6)
$$\delta_u = \Delta \delta_y.$$

The relation between the inputs and the outputs yields:

(7)
$$\begin{bmatrix} \delta_y \\ z \end{bmatrix} = \begin{bmatrix} M \end{bmatrix} \begin{bmatrix} \delta_u \\ w \end{bmatrix},$$

where M can be represented by subsystems,

(8)
$$M = \begin{bmatrix} M_{11} & M_{12} \\ M_{21} & M_{22} \end{bmatrix}.$$

The transfer function of exogenous input to exogenous output can be written as follows,

(9)
$$z = F_U(M, \Delta)w$$

Here, $F_U(M, \Delta)$ is the Linear Fractional Transformation (LFT), which can be derived as follows

(10)
$$F_U(M, \Delta) = M_{22} + M_{21}\Delta(I - M_{11}\Delta)^{-1}M_{12}.$$

In a real civil structure, the physical parameters of M_s, C_s, and K_s are not precisely known. It can be assumed that their actual values are varying with known intervals around nominal values.

(11)
$$M_s = \bar{M}_s + P_M\delta_M\bar{M}_s = (I + P_M\delta_M)\bar{M}_s,$$
$$C_s = \bar{C}_s + P_C\delta_C\bar{C}_s = (I + P_C\delta_C)\bar{C}_s,$$
$$K_s = \bar{K}_s + P_K\delta_K\bar{K}_s = (I + P_K\delta_K)\bar{K}_s,$$

where $\bar{M}_s$, $\bar{C}_s$, and $\bar{K}_s$ represent nominal values of M_s, C_s, and K_s. The possible perturbations are δ_M, δ_C, and δ_K

on model parameters. Further, P_M, P_C, and P_K represent the maximum ratio of differences between the real structure and the mathematical model. The matrices δ_M, δ_C and δ_K typically are diagonal matrices with uncertain varying values bounded within the range of $[-1, 1]$. These types of uncertainties are named structured uncertainties since they have zero off-diagonal elements. A brief description of the structured and the unstructured uncertainties was done by [?]. We note that M_s, C_s, and K_s could be represented as an LFT in δ_M, δ_C, and δ_K, respectively. Similar to the representation of the building model upper LFT, given in Eq. 11, M_M, M_C, and M_K are represented;

$$
(12) \qquad M_M = \begin{bmatrix} P_M & I \\ -\bar{M}_s^{-1} P_M & \bar{M}_s^{-1} \end{bmatrix}, \qquad M_C = \begin{bmatrix} 0 & \bar{C}_s \\ P_C & \bar{C}_s \end{bmatrix}, \qquad M_K = \begin{bmatrix} 0 & \bar{K}_s \\ P_K & \bar{K}_s \end{bmatrix}.
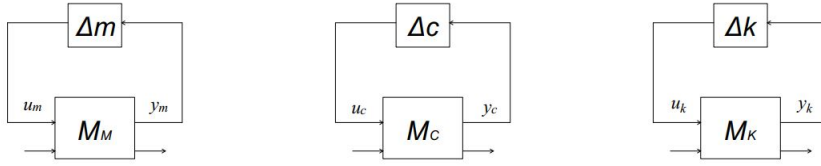$$

Figure 4: Representation of uncertainties as LFT

These matrices can be illustrated by standard $M - \Delta$ representation as shown in Fig. 4. It is noteworthy that M_M is given in the inverse form of M_s since it will be employed in that scheme while constructing the overall structural dynamics.
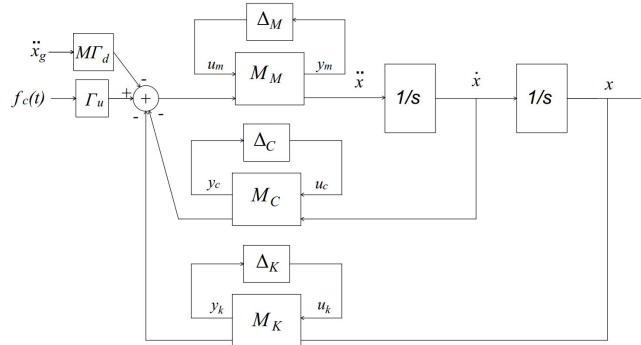

Figure 5: Block diagram of the control system with uncertainties

The uncertainties Δ_M, Δ_C and Δ_K shown in the block diagrams in Fig. 4 depict the inputs and outputs of δ_M, δ_C and δ_K as δu, and δy as shown in Fig. 5.

Let the states be $\begin{bmatrix} x \\ \dot{x} \end{bmatrix}$ and the measurement y be the story displacements of the structure and earthquake excitation $\ddot{x}_g$. The general state-space relation for Fig. 5 can be constructed as;

$$
(13) \qquad \begin{bmatrix} \dot{x} \\ \ddot{x} \\ \cdots \\ \delta y \\ \cdots \\ y \end{bmatrix} = \begin{bmatrix} A & \vdots & B_1 & B_2 \\ \cdots & \cdots & \cdots & \cdots \\ C_1 & \vdots & D_{11} & D_{12} \\ C_2 & \vdots & D_{21} & D_{22} \end{bmatrix} \begin{bmatrix} x \\ \dot{x} \\ \cdots \\ \delta u \\ \cdots \\ \ddot{x}_g \\ u \end{bmatrix},
$$

where

$$
A = \begin{bmatrix} 0 & I \\ -\bar{M}_s^{-1}\bar{K}_s & -\bar{M}_s^{-1}\bar{C}_s \end{bmatrix}, \qquad B_1 = \begin{bmatrix} 0 & 0 & 0 \\ -\bar{M}_s^{-1}P_M & -\bar{M}_s^{-1}P_C & -\bar{M}_s^{-1}P_K \end{bmatrix}, B_2 = \begin{bmatrix} 0 & 0 \\ -\Gamma_d & \bar{M}_s^{-1}\Gamma_u \end{bmatrix},
$$

and C_1, C_2, D_{11}, D_{12}, D_{21}, and D_{22} can be constructed according to measurements and exogenous outputs.

The input/output dynamics that take into account the uncertainty of the system parameters can be indicated by M, as shown in Fig. 6, housing all uncertainties and perturbations.

Figure 6: Input/output block diagram of the system

3. Robust Controller Design and Generalized Civil Structure Construction

In this section, a robust controller and how to construct the generalized civil structure will be explained, respectively.

The robust controller can be designed through small gain theorem [4]. According to the small gain theorem, generalized civil structure plant is internally stable for all Δ with

$$
\begin{aligned}
\|\Delta\|_\infty \leq 1/\gamma &\iff \|F_L(P,K)\|_\infty < \gamma, \\
\|\Delta\|_\infty < 1/\gamma &\iff \|F_L(P,K)\|_\infty \leq \gamma,
\end{aligned}
$$
(14)

where P represents the generalized civil structure plant. The value γ has the sense of energy ratio between exogenous outputs vector z and exogenous inputs vector w. As the γ tends to its minimal value, the above formulation can be also named as the optimal H_∞ control problem [6].

3.1. Generalized Civil Structure Plant

A block diagram representation of the civil structure system is depicted in Fig. 7. K represents the controller. The frequency domain weighted function W_g shapes the spectral content of the disturbance, $\ddot{x}_g$, modeling the earthquake excitation.The matrix W_p is weighting regulated response whereas W_u weighting the control signal. W_n is used to weight the measurement noise n. The input excitation w consists of earthquake excitation $\ddot{x}_g$ and measurement noise n. The output z is composed the frequency weighted regulated response and control force.
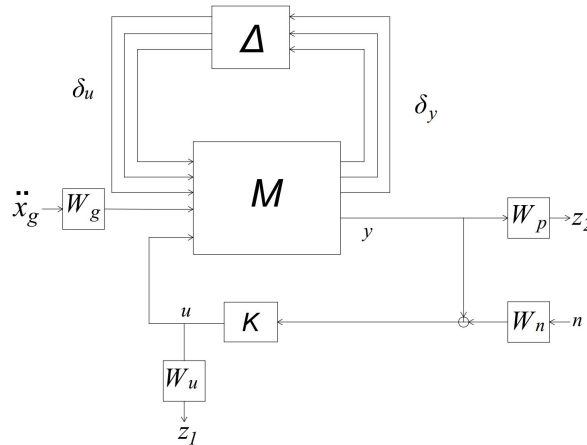
Figure 7: Control block diagram for a seismically excited civil structure.

Different control strategies can be utilized in order to find the control forces required for enhanced structural behavior. In the control algorithm, control forces that will cause the system to satisfy the desired exogenous output, and at the same time maximize or minimize a chosen cost function are determined. The cost function of the study is to minimize the introduced γ value.

In the present study, the controller consisted of two stages: a linear optimal control part and a modified clipped algorithm which is proposed by [8]. The required control force u was calculated by the controller. Then, the voltage to be applied was

Figure 8: MRD setup Source: [7]

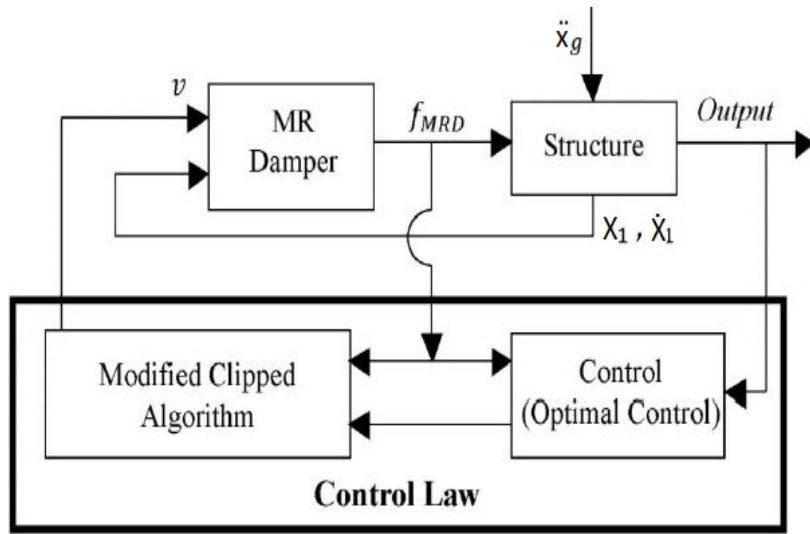determined by the modified clipped algorithm by comparing the required control force u and the damper force, f_{MRD}, of the previous time step. The block diagram representation of the system is presented in Fig. 8.
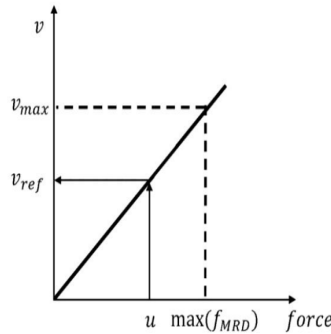

Figure 9: Graphical representation of modified clipped control algorithm (Source: [8])

The magnetic field in the damper is set to develop damping forces that are equal to those obtained by the H_∞ control. This part is performed by a clipped controller. The output of the feedback block in the block diagram representation in Fig. 8 is determined by the modified clipped control algorithm.(Fig. 9)

3.2. μ-Synthesis and D-K Iteration

The structured singular value μ is a powerful tool for the analysis of robust performance with a defined controller. Yet, one may also seek to find the controller that minimizes a defined μ-condition: the μ-synthesis problem ([9]).

$$(15) \qquad \mu\Delta\left(F_L(P,K)\right) = \frac{1}{\min\left\{\bar{\sigma}\left(\Delta\right)\big|\det\left(\mathbf{I}-F_L(P,K)\Delta\right)=0\right\}},$$

where $\bar{\sigma}\left(\Delta\right)$ is the largest singular value of Δ ; det is abbreviation of determinant. $\det\left(\mathbf{I}-F_L(P,K)\Delta\right)=0$ means that the uncertainty matrix Δ destabilizes $F_L(P,K)$. Eq. 15 shows that the largest singular value of $F_L(P,K)$ is, at the same, the reciprocal of smallest singular value for the uncertainty matrix Δ to destabilize $F_L(P,K)$.

Apparently, $\mu\Delta\left(F_L(P,K)\right)$ is linked the closed-loop (CL) and the structured uncertainties Δ. A robust controller can be designed by minimizing the largest value of $\mu\Delta\left(F_L(P,K)\right)$ to replace $\|F_L(P,K)\|_\infty$ in Eq. **??**. Nevertheless, there is no

available method to calculate $\mu\Delta\left(F_L(P, K)\right)$. Accordingly, an iterative method studied by [10] is utilized; D-K iteration.

$$(16) \qquad \mu_\Delta\left(F_L(P, K)(j\omega)\right) \leq \inf_{\mathbf{D}\in\Xi} \bar{\sigma}\left(\mathbf{D}F_L(P, K)\mathbf{D}^{-1}(j\omega)\right)$$

where D is a scaling matrix in Ξ which is a set of diagonal scaling matrices, the entries of which are a combination of system and constant matrices. The D-K iteration can use $\inf \bar{\sigma}\left(\mathbf{D}F_L(P, K)\mathbf{D}^{-1}\right)$ to replace $\mu\Delta\left(F_L(P, K)\right)$ and aims to solve the following optimization problem:

$$(17) \qquad \min_{\mathbf{K}(j\omega), \mathbf{D}\in\Xi} \bar{\sigma}\left(\mathbf{D}F_L(P, K)\mathbf{D}^{-1}(j\omega)\right).$$

If the D matrix is known, Eq.17 is a standard H_∞ optimization problem. After solving the given optimization problem over the interest frequency range with a known K, a series of $D(j\omega i)$ at every corresponding frequency point ωi will be formed by curve-fitting the rational transfer function matrix $D(j\omega i)$. Thereafter, $D(j\omega)$ is fixed to compute the controller K in the next iteration.

4. Simulation and Results

In this section, performance comparisons between the designed robust H_∞ controller considering the uncertainties and H_∞ controller without consideration of parametric uncertainties will be presented. A 3-storey civil structure with ideal MR damper, RD 1005-3 which was produced by Lord Co., was mounted to the first floor.

The nominal model parameters of the civil structure are $m_{s1} = m_{s2} = m_{s3} = 200$ kg, $k_{s1} = k_{s2} = k_{s3} = 156250$ N/m and C is calculated by Rayleigh Damping Criteria and first two modes damping ratios are $\zeta_1 = \zeta_2 = 0.02$. The uncertainty ratios were taken as 0.2, for mass and stiffness (P_M, P_K) and 0.6 for damping matrix, P_C.

In our model, to have the desired controlled structure response, the input disturbance was pre-multiplied by first order Tajimi Spectrum ([11]) ,W_g, to take into account stochastic earthquake excitation. The 1940 El Centro NS earthquake record is adopted as the ground excitation $\ddot{x}_g$. Further, white Gaussian noise is added to the measurements, y. The noise input was shaped by W_n filter.

Signal to noise ratio (SNR) and cut-off frequency were set as 10 and 100 Hz, respectively. Performance and control weights, W_p and W_u, are chosen after a few trial as, $W_p = diag([0, 5, 1, 1])$ and $W_u = 10e - 6$.
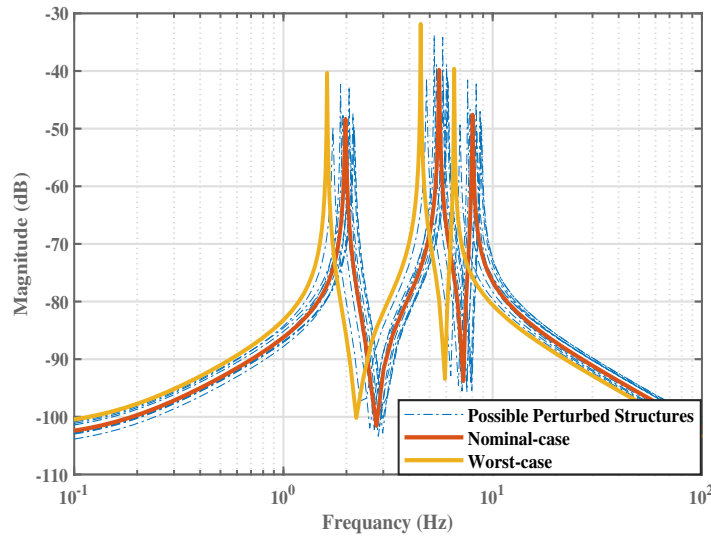

Figure 10: Singular values of possible perturbed structures

Uncertainties may change the model by a significantly. Fig. 10 shows the nominal and perturbed civil structure singular values. As can be seen in the figure, the singular values of the structures vary and deviate from the nominal value. Let us have a look at how to model the modal parameters having uncertainties.

(18)
$$K_s = \begin{bmatrix} 2k + P_k(\delta_{k1} + \delta_{k2})k & -k - P_k\delta_{k2}k & 0 \\ -k - P_k\delta_{k2}k & 2k + P_k(\delta_{k2} + \delta_{k3})k & -k - P_k\delta_{k3}k \\ 0 & -k - P_k\delta_{k3}k & k + P_k\delta_{k3}k \end{bmatrix},$$

$$C_s = \begin{bmatrix} 2c + P_c(\delta_{c1} + \delta_{c2})c & -c - P_c\delta_{c2}c & 0 \\ -c - P_c\delta_{c2}c & 2c + P_c(\delta_{c2} + \delta_{c3})c & -c - P_c\delta_{c3}c \\ 0 & -c - P_c\delta_{c3}c & c + P_c\delta_{c3}c \end{bmatrix},$$

$$M_s = \begin{bmatrix} m + P_m\delta_{m1}m & 0 & 0 \\ 0 & m + P_m\delta_{m2}m & 0 \\ 0 & 0 & m + P_m\delta_{m3}m \end{bmatrix}.$$

All the possible perturbed structures have uncertainties in their system matrix, A, with different ratios. The worst-case scenario is achieved through the maximum gain (the maximum singular value) computed according to the varying uncertainties. After the worst-case gain computations, the structure having worst uncertainties yields as;

(19)
$$K_s = \begin{bmatrix} 1.6k & -0.8k & 0 \\ -0.8k & 1.6k & -0.8k \\ 0 & -0.8k & 0.8k \end{bmatrix}, \qquad C_s = \begin{bmatrix} 0.8c & -0.4c & 0 \\ -0.4c & 0.8c & -0.4c \\ 0 & -0.4c & 0.4c \end{bmatrix},$$

$$M_s = \begin{bmatrix} 1.2m & 0 & 0 \\ 0 & 1.2m & 0 \\ 0 & 0 & 1.2m \end{bmatrix}.$$

$$k = k_{st} = 156250N/m, \qquad c = 42.25Ns/m, \qquad m = 200kg.$$

The structure having worst-case uncertainty has no instability issues for the structure without a controller. However, this does not mean that all structures will show small deformations under an earthquake. A controller aimed for a nominal structure may be destructive if existing uncertainties are not considered.

Figure 11: H_∞-controlled structure's responses
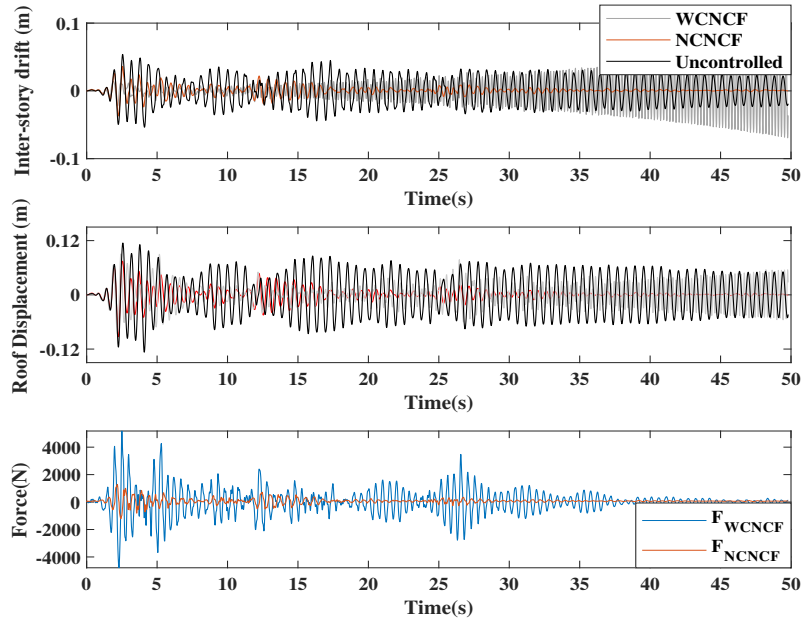
The roof displacements, the maximum inter-story drifts, and control forces for the nominally-controlled worst-case (WC-NCF) and nominal-case (NCNCF) structures are given in Fig. 11. The responses for the worst-case structure without a controller, which is depicted by a black line in the figure, are larger than the nominal-case responses given in the earlier chapters.

As seen in the figure, a nominal controller may cause instability if the designer neglects uncertainties. In other words, in control implementations, the uncertainties should be taken into account seriously. The control forces increase thoroughly since the controller computes the required force considering the nominal-case structure modal parameters. As a result, instability occurs.
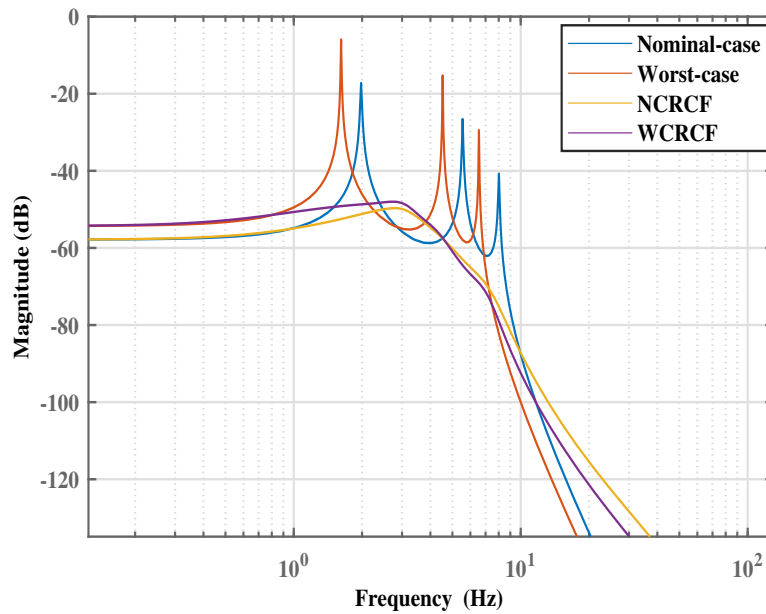

Figure 12: MRD-installed structure's bode diagram

Fig. 12 shows the uncontrolled and controlled structure frequency responses. The nominal-case robust control feedback (NCRCF) frequency magnitudes are reduced by around 30dB at the first mode. Similarly, the worst-case robust control feedback (WCRCF) response magnitudes are decreased by more than 30dB. The achieved robust controller can control both structures regardless of their modal parameters. Its stability margins are much wider than the nominal-case H_∞ controller.
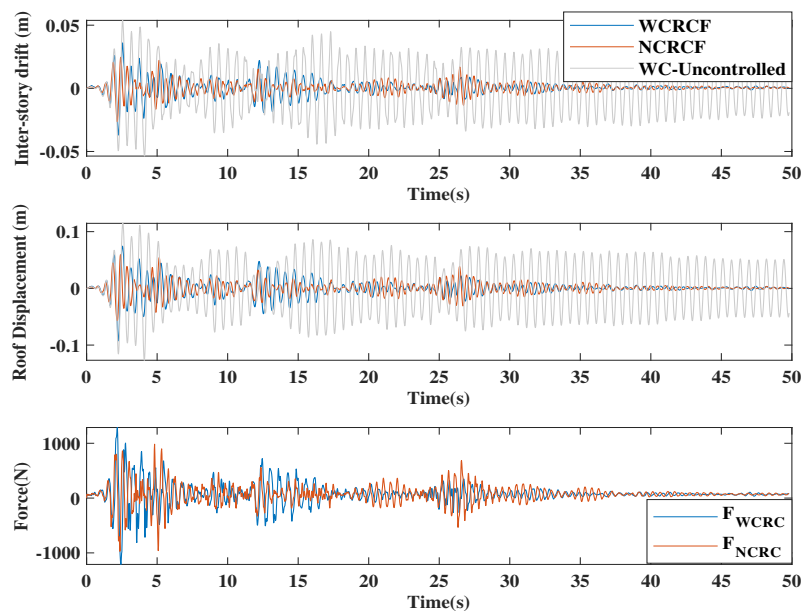

Figure 13: The robust controller-installed structure's responses

The robust controller decreases the frequency amplitudes at peaks, but at the same time, it causes around 5dB upthrusts in

between 2.5 and 5Hz. As a result, the closed-loop responses in the time domain increase.

Table 1: Performance indices of the robust controller

	J_1	J_2	J_3	J_4
Uncontrolled	1.0000	1.0000	1.0000	1.0000
NCRCF	0.7311	0.6690	0.3137	0.2637
WCRCF	0.4679	0.4578	0.2436	0.2280

Simulations for the structures equipped with the robust controller are undertaken. In these simulations, the MRD is employed as the control device. The roof displacements and maximum inter-story drifts of the 3-story structure are given in Fig. 13. According to Table 1, the indices J_1 and J_3 for the nominal-case structure are equivalent to 0.7311 and 0.3137, respectively. Besides, the indices with the same robust controller are decreased to 0.4679 and 0.2436 for the worst-case structure. It can be said that the robust controller shows a satisfactory performance for the structure within given uncertainties. J_2 and J_4 indices are 0.6690; 0.4578 and 0.2637;0.2280, respectively and these values represents the maximum inter-story drifts in infinity and 2-norm.

5 . Conclusion

The purpose of this study was to control a three story shear frame with model parameter uncertainties. For this purpose, the civil structure was modeled as uncertain in reasonable ranges regarding mass, stiffness, and damping. The nominal and worst-case uncertainty models were chosen to verify the designed controllers, based on H_∞ norm. It was observed that the controller reduces the response of the structure. However, the mere H_∞ controller's performances were not as satisfactory as expected. Besides, it amplified the oscillating responses and led the structure to fail.

A robust controller was designed by μ synthesis for selected possible perturbations and it covers all perturbations.

In conclusion, the proposed μ controller can be a solution to stabilize for the structure that has parametric uncertainties.

References

[1] I. N. Kar, T. Miyakura, and K. Seto, "Bending and torsional vibration control of a flexible plate structure using h_∞-based robust control law," *IEEE Transactions on Control Systems Technology*, vol. 8, no. 3, pp. 545–553, May 2000.

[2] S.-G. Wang, "Robust active control for uncertain structural systems with acceleration sensors," *Journal of Structural Control*, vol. 10, no. 1, pp. 59–76, 2003.

[3] L. Huo, C. Qu, and H. Li, "Robust control of civil structures with parametric uncertainties through d-k iteration," *The Structural Design of Tall and Special Buildings*, vol. 25, no. 3, pp. 158–176, 2016.

[4] K. Zhou and J. C. Doyle, *Essentials of robust control*. Prentice hall Upper Saddle River, NJ, 1998, vol. 104.

[5] B. Spencer Jr, S. Dyke, M. Sain, and J. Carlson, "Phenomenological model for magnetorheological dampers," *Journal of engineering mechanics*, vol. 123, no. 3, pp. 230–238, 1997.

[6] S. Skogestad and I. Postlethwaite, *Multivariable feedback control: analysis and design*. Wiley New York, 2007, vol. 2.

[7] F. Weber, S. Bhowmik, and J. Høgsberg, "Extended neural network-based scheme for real-time force tracking with magnetorheological dampers," *Structural Control and Health Monitoring*, vol. 21, no. 2, pp. 225–247, 2014.

[8] S. Dyke, B. Spencer Jr, P. Quast, M. Sain, D. Kaspari Jr, and T. Soong, "Acceleration feedback control of mdof structures," *Journal of Engineering Mechanics*, vol. 122, no. 9, pp. 907–918, 1996.

[9] A. K. Packard, "What's new with mu: Structured uncertainty in multivariable control." 1989.

[10] U. Mackenroth, "Robust control systems: theory and case studies," 2004.

[11] Y. Lin and Y. Yong, "Evolutionary kanai-tajimi earthquake models," *Journal of engineering mechanics*, vol. 113, no. 8, pp. 1119–1137, 1987.

OPTIMAL TUNING OF AN ADAPTIVE VIBRATION ABSORBER FOR VIBRATION CONTROL OF VEHICLE TRANSMISSION SYSTEM

S. Soleimanian[1,2], G. Petrone[1], A. Mroz[2], F. Franco[1], P. Kolakowski[2], S. De Rosa[1]

[1]*University of Naples Federico II, Naples, Italy*
[2]*Adaptronica sp. z o.o., R&D company, Łomianki, Poland*
e-mail: sina.soleimanian@unina.it

Abstract

Noise and vibration attenuation is a challenging topic in vehicle transmission systems. The objective of present study is to design an adaptive vibration absorber for vibration isolation of a transaxle of Getrag DC T300. The dynamic behavior of the transmission system is simulated through a conceptual model consists of 3D quadratic shell elements, linear spring element, mass points and appropriate boundary conditions. To design the vibration absorber, metal cushion is used which stiffness and damping properties can be adjusted by changing its density through pre-compressing of material. In this regard, the proper position of of absorber is decided, and a direct optimization is carried out following a sets of parametric studies. So that the optimum path for a wide frequency band is achieved offering optimum values of pre-compression rates (*C*). It is observed that this material can be adaptively tuned to isolate the vibration of automotive transmission system for the frequency range of 2000-3000 Hz with an acceptable effectiveness.

Keywords: Vibration control; finite element; transmission; metal cushion, smart material.

1. Introduction

Noise and vibration in automotive transmission systems has been a concrete engineering problem for decades [1]. Few efforts have been made by experts and scholars to suppress vibrations of this kind with the help of vibration controllers following semi-active working principle [2]. Semi-active systems require to adapt their properties lively to the host structure response or the excitation frequency. To make sure the vibration absorber is accurately adapted, optimal tuning is necessary. Some efforts have been made in previous research works in optimal design of adaptive vibration attenuators [3–5].

The present research offers an optimal tuning of a vibration absorber (VA) to isolate the vibration of a transaxle Getrag DC T300. Since the ultimate objective is to reduce whine noise for human comfort, the favorable frequency range is 2000 Hz to 5000 Hz. The VA is made of metal cushion, a smart material, which has a density dependent stiffness property providing the possibility to suppress many modes of vibration with a single absorber device. The main idea is to minimize the kinetic energy and prevent the energy flow propagation in the transaxle housing. A conceptual dynamic model using shell elements and mass compensating points, and a spring element is generated in this study which surpasses the numerical modeling of the whole transmission system which requires a heavy finite element discretization with more than one million elements as reported by Weis et al [6]. The results revealed an efficient vibration reduction in a wide frequency band by implementing a VA relying on its proper positioning and optimal tuning of its stiffness and damping properties.

2. Modeling strategy and probem formulation

Figure 1(a) introduces the transaxle Getrag DC T300 transmission model which consists of dynamic and static components. The housing shell and bearings are the static parts, while the internal components such as input, lay and differential shafts and associated gears are considered as the dynamic parts. The input and lay shafts are constrained by two sets of bearings hosted by two plates, at the front and back sides of the transmission housing (see Figure 1(a)). The source of structural noise is the internal parts which transmit the vibrational energy through the bearings to housing. The aforementioned plates which host the bearings play critical roles in vibration transmission from its source to the housing. In this regard, it is of our interest to constrain the VA

between these two plates. Since the back plate is fixed in reality, it is assumed that the VA is attached to the front plate from one side, and it is attached to a rigid media from other side.

To conduct the numerical analysis, a conceptual dynamic model is proposed including the circular plate with 3mm thickness with fixed boundary conditions as

(1) $$U_r = U_z = U_\theta = rot_{rz} = rot_{r\theta} = rot_{z\theta}$$

where U and rot refer to displacement and rotation degrees of freedom defined based on radial (r), axial (z), and tangential (θ) directions. In addition, the mass points A and B are devised at the location of bearings (see Figure 1(b)) to represent the mass of internal components which weight is applied on the corresponding bearings. The mass contributed to the weight force imposed on each bearing is estimated 4.4 kg by division of the whole dynamic components mass (26.5 kg) by total number of bearings (6). Besides, the circular plate is assumed to be made of aluminium alloy with the following properties.

Table 1. Material properties for aluminium alloy.

Density (kg/m³)	Elastic Modulus (GPa)	Poisson's Ratio	Damping Ratio (%)
2770	71	0.33	1

The target thin-walled plate is prone to vibration with out of plane modes. For this reason, an out of plane VA is considered to be connected from one side to the circular plate and from other side to the end plate.
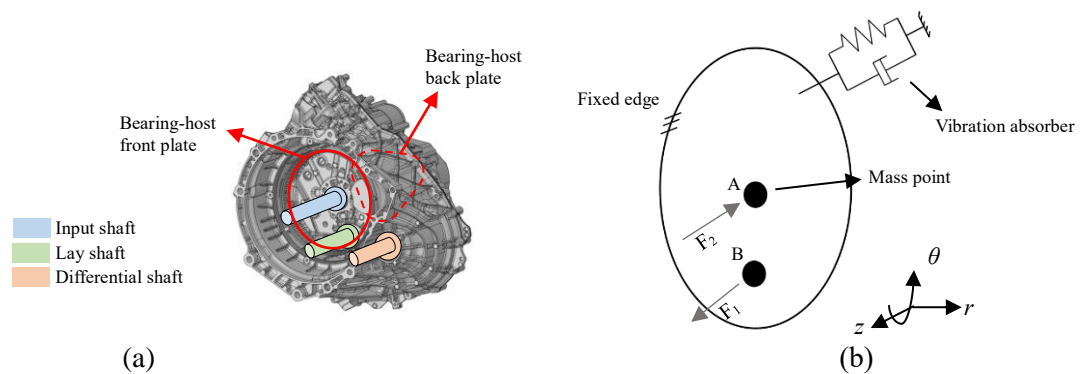

Figure 1. (a) transaxle Getrag DC T300, (b) conceptual dynamic model.

Considering metal cushion for the VA, the stiffness (K) and damping ratio (D) can be adjusted according to Table 2 measured by Rieß et al [7].

Table 2. Metal cushion properties at different pre-compression rates.

C (%)	K (N/mm)	D (%)
5	232	21
10	486	13.9
15	985	9
20	1880	4.4
25	4230	2.3
30	8370	1.25
35	15900	0.31
40	29100	0.14

The final important issue for dynamic modelling is the excitation which is applied on the bearings. By modelling the dynamic problem of transaxle using Romax Designer software, it is revealed that an average amplitude excitation force of $F_1=-F_0$ N and $F_2=2.33F_0$ ($F_0=234.34$N) is applied on the input and lay shaft bearings, respectively. These loads are obtained as a result of a harmonic analysis excited by a 1400 rpm and 20 N.m, input shaft rotation speed and torque amplitude, respectively. Hence, these forces are imposed on the mass points A and B harmonically as given by

$$F_{A\backslash B} = F_{1\backslash2}\sin(\omega t) \tag{2}$$

where ω is the frequency of harmonic load.

Since the in-plane components of bearing reaction force are not responsible for out of plane deformation modes, they are not included in this study.

The numerical design procedure for the adaptive VA is given by the flowchart in Figure 2. The first stage is to identify the natural frequencies, corresponding mode shapes, and the frequency response in the required frequency range. This evaluation is conducted by means of a finite element model built in ANSYS environment with quadratic shell elements solving the modal and harmonic analyses.

The next step is to locate the VA properly (i.e. where the efficiency is highest in terms of vibration amplitude reduction). In this regard, the VA is modelled through a linear spring element. After deciding the best position for the VA, the effect of absorber tuning property on KE (kinetic energy) in a wide frequency band should be studied. In this regard, a steady state forced vibration analysis should be based on full solution. Presenting the result of this analysis in the frame of response surface can determine whether the VA is adaptable to the frequency range of interest or not. In fact, the VA is adaptable if the frequency response demonstrates meaningful variations by changing the tuning variable, pre-compression rate C. If the VA works for the desired frequency band, the last step is to conduct narrow band optimizations to minimize the KE at specific frequencies which can be summarized as

$$\begin{cases} \text{optimization objective: min KE} \\ \text{optimization variable: } C \\ \text{optimization constraint: frequency interval including particular peaks} \end{cases} \tag{3}$$
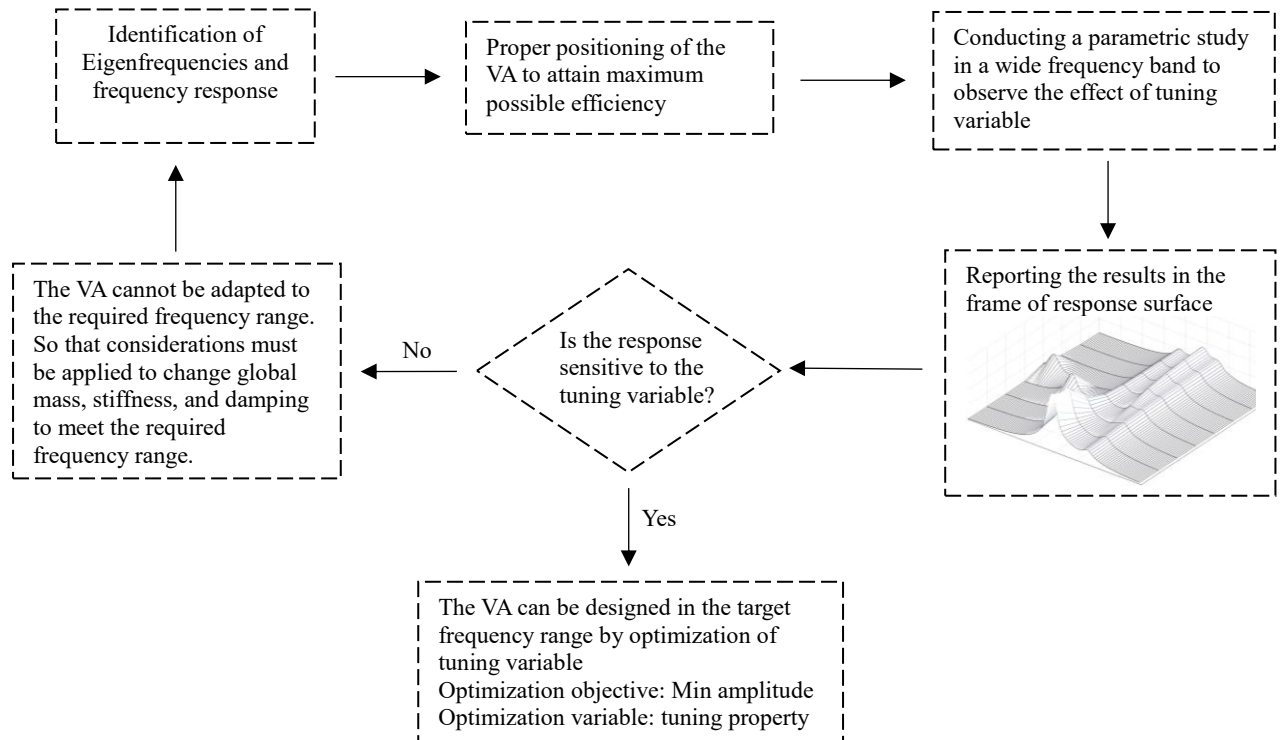

Figure 2. Numerical design procedure of the VA.

3. Results and discussion

The vibration analysis results can be evaluated in the form of maximum value, average value, summation, etc. However, the maximum value could be variable from one location to another when it comes to parametric studies. In addition, the average value could not show the variations clearly in a parametric study when the most of elemental values are close to each other but far from the maximum. Hence, the summation of KE among all elements is considered as the harmonic response variable. In addition, to make comparisons among different frequency response curves, the KE peaks and the area under the curve at the 60 Hz vecinity of resonance is evaluated.

3.1 Positining the VA

The KE frequency response is evaluated for a reference case where there is no treatment on the structure. For the frequency range of 2000 to 5000 Hz, the KE is plotted as represented by Figure 3. Among six number of peaks in the frequency response, four of them are selected for isolation.
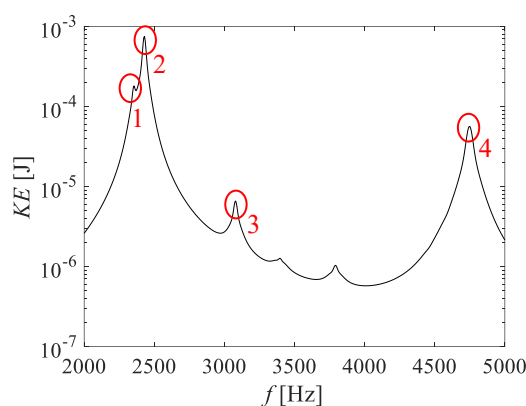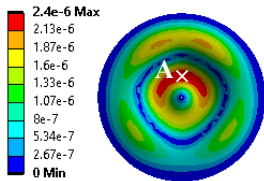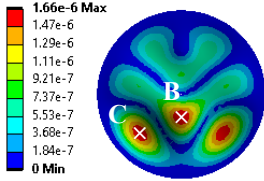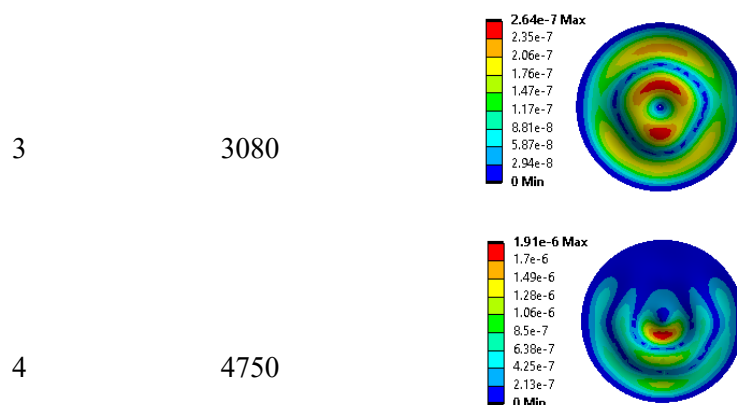

Figure 3. *KE* frequency response for the case without treatment.

The natural frequencies and mode shapes corresponding to the target peaks are presented in Table 3.

Table 3. The natural frequencies and corresponding mode shapes.

Peak no.	Natural frequency [Hz]	Mode shapes (deformation)
1	2350	
2	2400	

3	3080	
4	4750	

The cross marks show three candidate locations A, B and C to study the influence of VA on the system dynamic response. In order to find the best position for the VA, three different frequency intervals are considered including the target natural frequencies and setting the compression rate on 20%.

Figure 4 illustrates the effect of different VA positions on KE in the frequency interval [2200,2600] Hz including the first two target peaks.
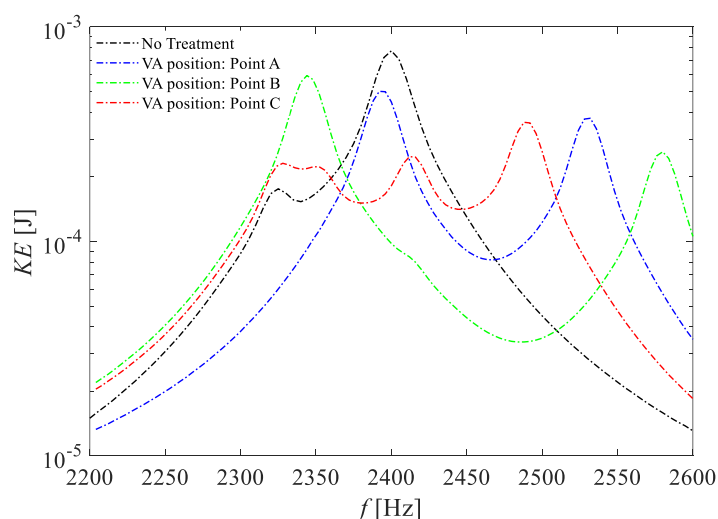

Figure 4. The effect of positions: *KE* frequency response (2200 Hz ≤*f*≤2600 Hz).

It can be observed that all candidate positions are in favour of vibration attenuation. However, their isolation effect is different offering the highest reduction of resonant peak and under the curve area by points C and B, respectively as reported by Table 4.

Table 4. Isolation rates obtained at different positions (2200 Hz ≤*f*≤2600 Hz)

position	$\dfrac{KE_T - KE_N}{KE_N} \times 100\,\%$	$\dfrac{\int (KE_T - KE_N)\,df}{\int KE_N\,df} \times 100\,\%$
A	35.24	7.85
B	23.28	10.09
C	53.54	5.05

Figure 5 indicates the influence of different VA positions on KE in the frequency interval [2950,3160] Hz including the third target peak.
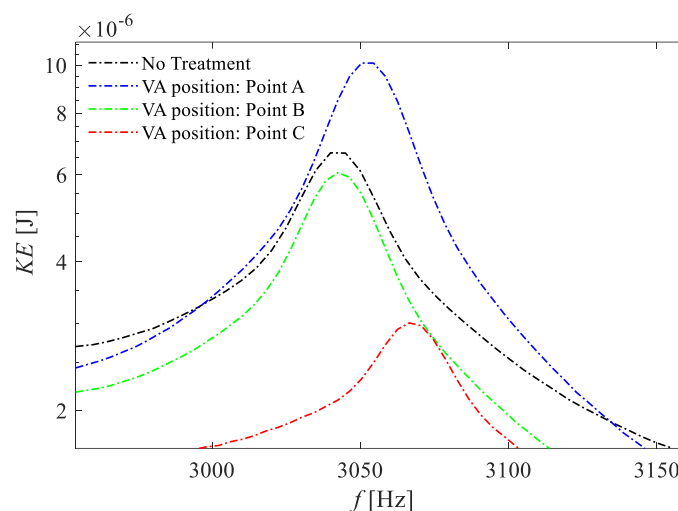

Figure 5. The effect of positions: *KE* frequency response (2950 Hz ≤*f*≤3160 Hz).

It can be figured out that points B and C are in favour of vibration reduction. However, point C offers a remarkable reduction in resonant peak and under the curve area as reported by Table 5.

Table 5. Isolation rates obtained at different positions (2950 Hz ≤*f*≤3160 Hz)

position	$\dfrac{KE_T - KE_N}{KE_N}$ $\times 100\ \%$	$\dfrac{\int (KE_T - KE_N)\, df}{\int KE_N\, df}$ $\times 100\ \%$
A	-	-
B	8.87	16.52
C	54.74	45.39

Figure 6 represents the effect of different VA positions on KE in the frequency interval [4500, 4950] Hz including the fourth target peak. What can be inferred from this diagram is that none of the candidate points is helpful for vibration attenuation in the investigated frequency range. However, tuning the material pre-compression rate which will be discussed in the next section could change this result. The shift on natural frequency is expectable since the system global stiffness changes by altering the position of absorber. An overall comparison of position effect results in different frequency bands (Figures 4-6) leads to selection of point C as the best position to attach the absorber.
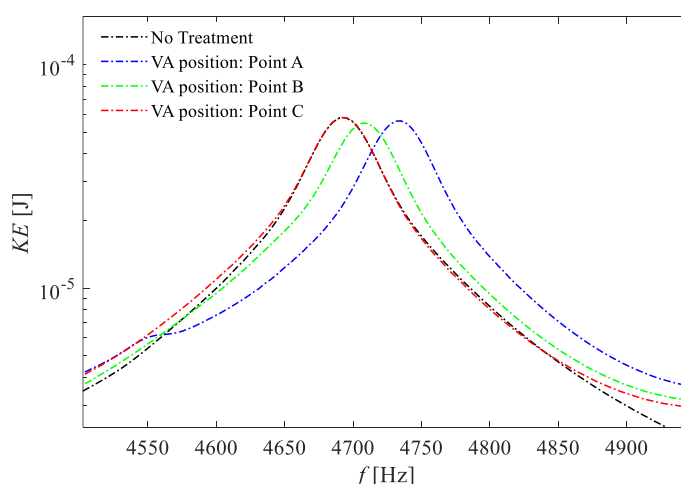
Figure 6. The effect of positions: *KE* frequency response (4500 Hz $\leq f \leq$ 4950 Hz)

3.2 Optimal tuning of pre-compression rate

To study the influence of material pre-compression rate (*C*) on KE frequency response, the same frequency intervals as Section 3.1 are taken. According to the results reported by Figures 7a, 8.a, and 9, it can be inferred that a non-uniform unpredictable variation of response is achieved for the first and second frequency intervals. Accordingly, it can be ensured that the VA is tuneable in the first and second frequency intervals. The results of tuning optimization is reported by red marks (—✱—) which means the optimal pre-compression rates are obtained at each frequency. The optimally tuned path is shown by Figures 7.b and 8.b. Regarding the third frequency interval, it can be figured out from Figure 9 that the VA is inside the frequency range but it exhibits a quite low effect. It should be noted that KE is plotted by exponential function, which means the variation response with respect to the tuning variable is negligible.

The consecutive increase and decrease observed in the frequency intervals [2250, 2300] Hz, and [3150, 3200] Hz is the result of a trade-off between stiffness and damping ratio of metal cushion which change reversely by pre-compressions rate.
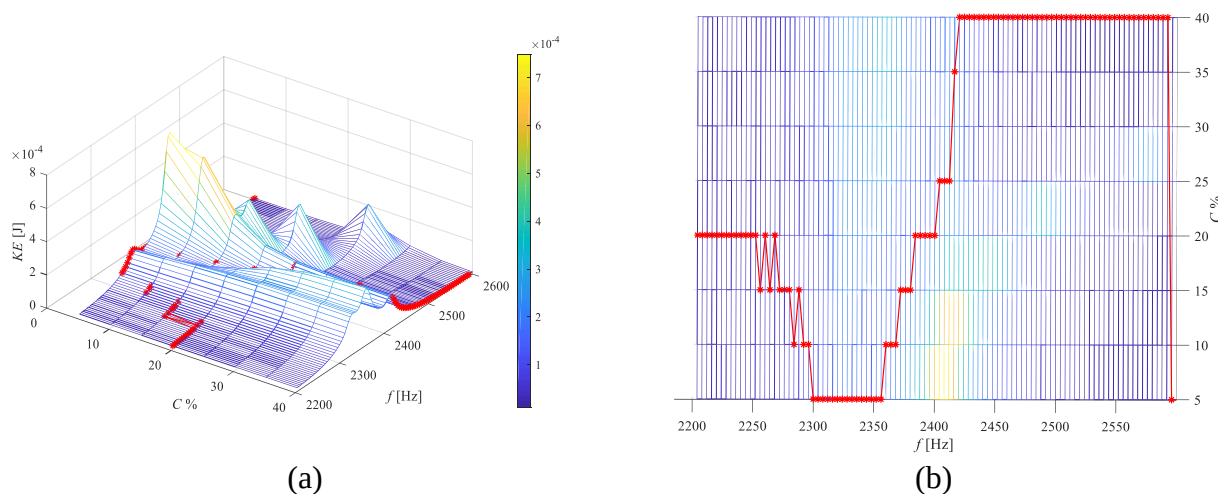

| (a) | (b) |

Figure 7. Frequency range of 2200 to 2600Hz: (a) *KE* over frequency and pre-compression rate, (b) pre-compression rate over frequency.
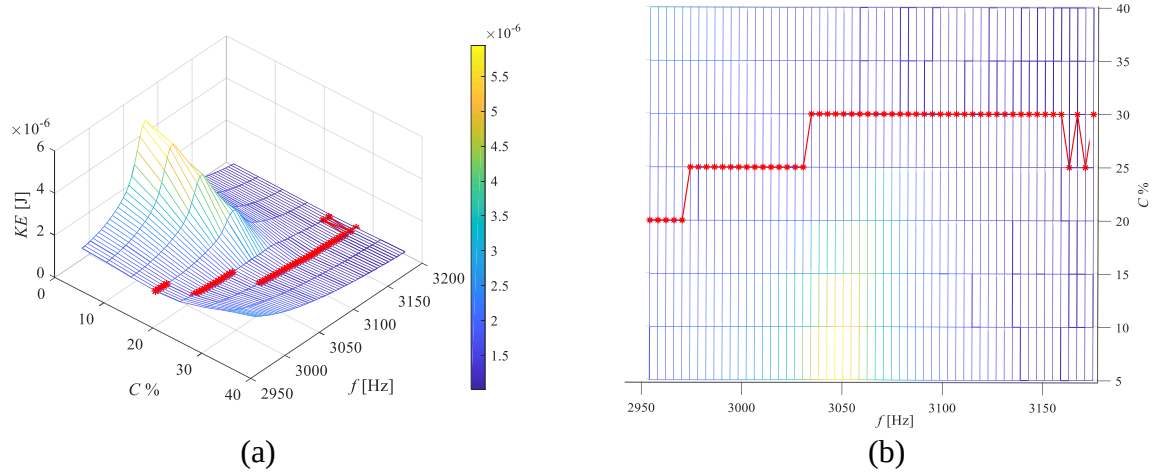
(a)   (b)

Figure 8. Frequency range of 2950 to 3200Hz: (a) *KE* over frequency and pre-compression rate, (b) pre-compression rate over frequency.
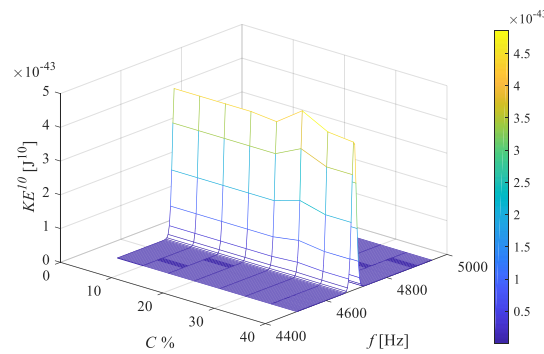

Figure 9. Frequency range of 4500 to 4950Hz: *KE* over frequency and pre-compression rate.

To observe the efficiency of the optimal tuning, the *KE* frequency response is compared for with and without treatment of vibration control in the frequency range of 2000 to 3200 Hz. The compression variable takes its optimum value according to results reported by Figures 7 and 8. It should be noted that the compression rate equals to 15% in the frequency ranges out of optimization design space. The effectiveness of this optimal treatment is well manifested by Figure 10 where the second (2400 Hz) and the third (3080 Hz) peaks are diminished by high rates as given by Table 6.
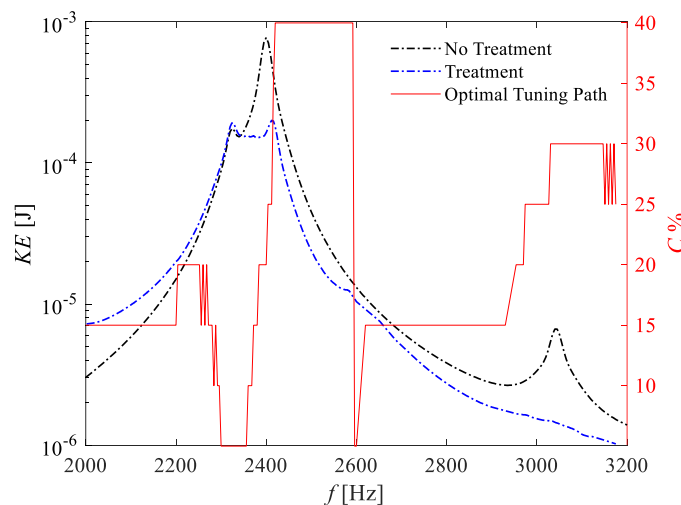

Figure 10.   (a) A comparison of *KE* frequency response with and without treatment (dashed lines), (b) The optimal tuning path (solid redline).

Table 6. Isolation rates obtained at different positions (2950 Hz $\leq f \leq$ 3200 Hz)

target peak	$\frac{KE_T - KE_N}{KE_N} \times 100\%$	$\frac{\int (KE_T - KE_N)\,df}{\int KE_N\,df} \times 100\%$
1	-	-
2	74.1	56.81
3	78.5	65.16

The prior comparison study (Figure 10) is carried out considering the excitations which are resulted from a typical shaft speed and torque condition described in Section 2. Yet, the loading condition could vary in reality due to several factors such as speeding, gear shifting, braking, and so on. In this regard, the effectiveness of the designed VA for different excitation forces ratios is studied. To change the ratio of excitation forces, it is persumed $\left|\vec{F_1}\right| = F_0 \cos\theta$, and $\left|\vec{F_2}\right| = F_0 \sin\theta$ where $0 \leq \theta \leq \pi/2$. So that a comprehensive study can be perfomed covering all contribution of loads acting on the bearings. Figure 12 reports the result of *KE* assessed at the 2nd target peak offering a remarkable effectiveness for the VA. However, it can be comprehended that minimum effectiveness is achieved in the absence of F_2.
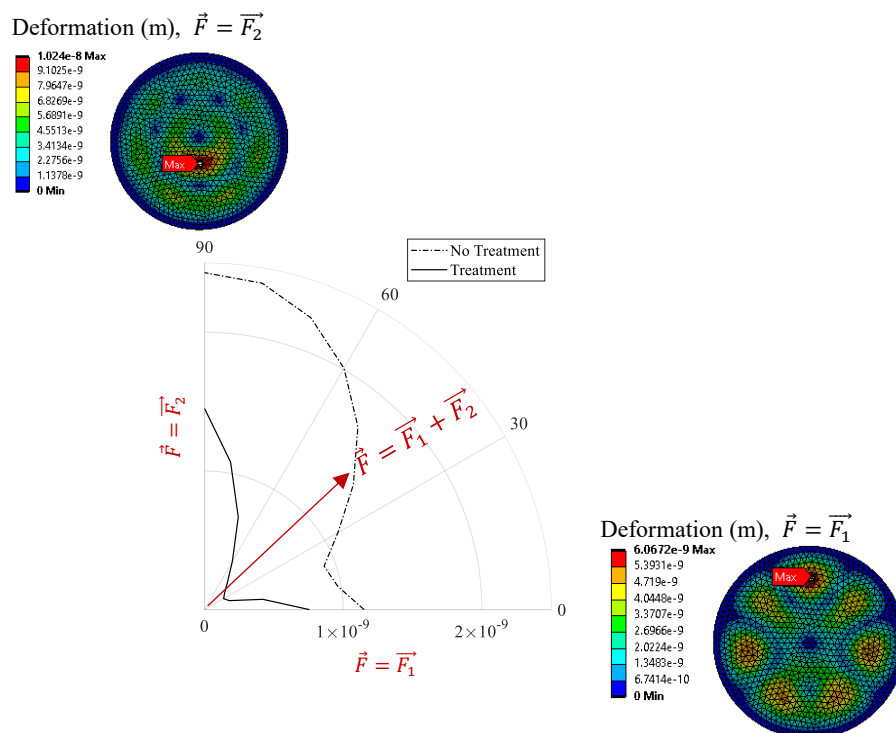

Figure 12. The influence of excitation forces ratio on KE at the 2nd target peak resonance

Figure 13 reports the result of *KE* assessed at the 3rd target peak offering a rewarding effectiveness which is highest in the absence of F_2, and decreases as F_1 decreases.
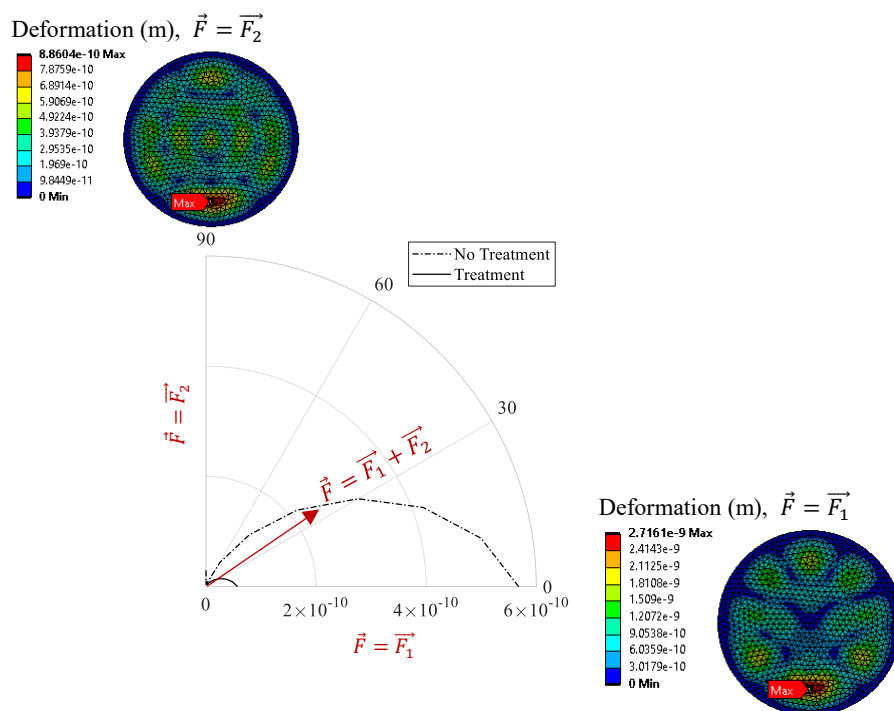
Figure 13. The influence of excitation forces ratio on KE at the 3rd target peak resonance

Conclusion

Noise and vibration in vehicle tranmission systems involves resnonts in a broad band of frequency. So that, isolation of this kind of vibration requires a vibration atenuator which not only suppresses several modes of vibration adaptively, but also is amenable to resonant modes far from each other. According to a recent research by scholars, a wide band frequency adaptability of metal cushion material is discovered. In this study the effect of position and pre-compression rate is investigated for a VA made of metal cushion. Accordingly, a response surface optimization is conducted to find the optimally tuned pathes.

An acceptable effectiveness is achieved using the optimally designed VA in the frequency range of 2000-3200 Hz. In fact, the amplitude of vibration and the are under the curve is reduced by 74.1% and 56.81% for the resonant peak at 2400 Hz, and 78.5% , 56.81% for resonant peak at 3080 Hz. Thus, it can be claimed that the optimally designed adaptive VA is helpful for noise and vibration isolation in a relatively wide frequency band.

Studying the effect of contribution of loads acting on the bearing revealed that vibration can be isolated by different effectiveness rates. So that it could be a suggestion for the future studies to reduce the dependency of VA efficiency by applying appropriate considerations.

The results of this research can be used as design references for developing the proccecor unit of a semi-active vibration controller. The processor unit produces the proper transfer function to isolate the vibration according to a sensed feedback which could be conducted in a live mode.

References

[1]   Y.H. Guan, M. Li, T.C. Lim, W.S. Shepard, Comparative analysis of actuator concepts for active gear pair vibration control, J. Sound Vib. 269 (2004) 273–294. https://doi.org/10.1016/S0022-460X(03)00072-5.

[2]   W. Li, X. Dong, J. Xi, X. Deng, K. Shi, Y. Zhou, Semi-active vibration control of a transmission system using a magneto-rheological variable stiffness and damping torsional vibration absorber, Proc. Inst. Mech. Eng. Part D J. Automob. Eng. 235 (2021) 2679–2698. https://doi.org/10.1177/0954407021999493.

[3]   P. Gao, H. Liu, P. Yan, C. Xiang, Optimization of the frequency tracking scheme for an adaptively tuned vibration absorber, J. Sound Vib. 512 (2021) 116376. https://doi.org/10.1016/j.jsv.2021.116376.

[4]   H. Kouhi, R. Ansari, E. Salahshoor, B.M. Fard, A Comparison Between the Linear and Nonlinear Dynamic Vibration Absorber for a Timoshenko Beam, 13 (2021) 448–459. https://doi.org/10.22034/jsm.2020.1905148.1625.

[5]   P. Gardonio, E. Turco, A. Kras, L. Dal, D. Casagrande, Semi-active vibration control unit tuned to maximise electric power dissipation, J. Sound Vib. 499 (2021) 116000. https://doi.org/10.1016/j.jsv.2021.116000.

[6]   P. Weis, Ľ. Kučera, P. Pecháč, M. Močilan, Modal Analysis of Gearbox Housing with Applied Load, Procedia Eng. 192 (2017) 953–958. https://doi.org/10.1016/j.proeng.2017.06.164.

[7]   S. Rieß, W. Kaal, Frequency-Adaptable Tuned Mass Damper Using Metal Cushions, Freq. Tuned Mass Damper Using Met. Cushions. 4 (2021) 77–90.

MODELLING OF TWO ANTAGONISTIC SHAPE MEMORY ALLOY WIRES

B. Stępniak[1], K. Falkowski[1]

[1] *Faculty of Mechatronics, Armament and Aerospace, Military University of Technology,*
Gen. Sylwestra Kaliskiego St. 2,00-908 Warsaw, Poland
e-mail: bartlomiej.stepniak@wat.edu.pl

Shape memory alloys (SMAs) are materials which can be classified as functional materials. The feature which distinguishes them from the other materials in this group is a shape memory effect. The aforementioned effect is connected with the direct and reverse martensitic transition. It means that the shape of an element which is made of this alloy can significantly change during these processes. The phenomenon has already been successfully applied in engineering and medicine where a part of applications are linear and rotary actuators. Such designs are driven by one, two or more shape memory alloy elements (in some cases with a bias spring or springs additionally applied). There is particular case the antagonistic work of two SMA elements is used.

There is a number of models of the behaviour of shape memory alloys which can be used to simulate SMA elements' actuation. They can be divided into three groups, as follows: thermal models, phase transition models and mechanical models. This paper presents some of the models belonging to three aforementioned groups. These considerations are followed by the author's approach to modelling of mechanical behaviour of antagonistic pair of shape memory alloy wires.

1. Introduction

Shape memory alloys (SMA) are materials which can be included in the group of functional materials [6]. The feature which distinguishes them is the shape memory effect which is connected with the phase transformation from martensite to austenite, and reversely [6]. There are three effects connected with such a material: one-way shape memory effect, two-way shape memory effect and pseudo-elasticity [5][6]. These effects occur due to the aforementioned phase transformations which are characterised with the phase transformation temperatures: M_s, M_f, A_s, A_f, which correspond with: martensite start, martensite finish, austenite start and austenite finish temperatures, respectively [5][6].

This work considers one-way shape memory effect. Mechanical loading applied to the SMA at temperature below M_f (when material is in martensitic phase) causes stable macroscopic deformation [5]. Heating the SMA above A_f triggers transformation to austenite and shape recovery [5]. Elements which are made of shape memory alloy can be used for actuation, damping and/or sensing [13]. SMA actuators can also generate large force per unit weight [13]. Hence, shape memory alloys actuators are expected to be one of the next generation actuators for aircraft [13].

This work focuses on shape memory alloys from modelling point of view. There are a lot of models of the behaviour of the SMAs which can be classified into different groups [1][12][14]. The first classification takes into account the scale of the model and distinguishes the following groups [14]:

- *micromechanical models,*
- *mesoscopic or lattice-level models,*
- *macroscopic models.*

The second classification refers to the assumption from [1], which constitute that the shape memory alloys behaviour can be modelled as a system consisting of three components [1] (Fig. 1):

- *thermal model,*
- *phase transformation model,*
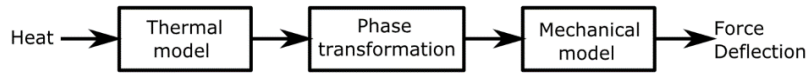- *mechanical model.*

Figure 1 The shape memory alloys behaviour model [1].

This division was also used by A. Pai in [12].

This study focuses only on the chosen macroscopic frameworks accordance with the latter of the aforementioned classifications.

1. Thermal models

Thermal models have been presented in various forms of thermal equilibrium as in the following works [1] [2] [3] [4] [12] [14]. Assuming that a wire made of SMA is modelled, a dedicated power balance should take into account the following characteristics [1] [2] [3] [4] [12] [14]:

- *internal energy change $\dot{Q}_w$,*
- *electrical power P_e (assuming the wire is being heated with an electric current),*
- *convection heat flow $\dot{Q}_k$.*

The publications mentioned above include also:

- *phase transformation P_{pf} (in [1] [3] [14] and implicitly in [4] by heat capacity value change),*
- *thermal radiation $\dot{Q}_p$ (in [3]),*
- *mechanical power P_w (in [3]).*

Based on the works mentioned above, the thermal equilibrium, which includes all of the above, may be expressed as:

(1)
$$\dot{Q}_w + \dot{Q}_k + \dot{Q}_p + P_{pf} + P_w = P_e,$$

where a type of phase transformation determines values (negative or positive) of P_{pf} and P_w.

Note that if balance's components enumerated above are provided, the equation can be formed as follows [1] [2] [3]:

(2)
$$\varrho V c_p \frac{dT}{dt} + hA(T - T_{ot}) + \varepsilon\sigma_{rad}A(T^4 - T_{ot}^4) + \varrho V \Delta H \frac{dR_m}{dt} + P_w = i^2 R,$$

with:
ϱ – SMA density,
c_p – SMA specific heat,
V – SMA volume,
T – SMA temperature,
t – time,
i – electrical current passing through SMA wire,
R – SMA wire resistivity,
h – convection heat transfer coefficient,
A – surface area of SMA wire,
T_{ot} – ambient temperature,
ΔH – latent heat defined on the transformation interval,
R_m – martensite fraction,
ε – SMA emissivity,
σ_{rad} – Stephan-Boltzman constant.

Furthermore, similarly as in mentioned sources, thermal model has been implemented into numeric computing software. For simplicity, thermal radiation and mechanical power has been neglected (free displacement). Exemplary response characteristic is shown on Figure 2.
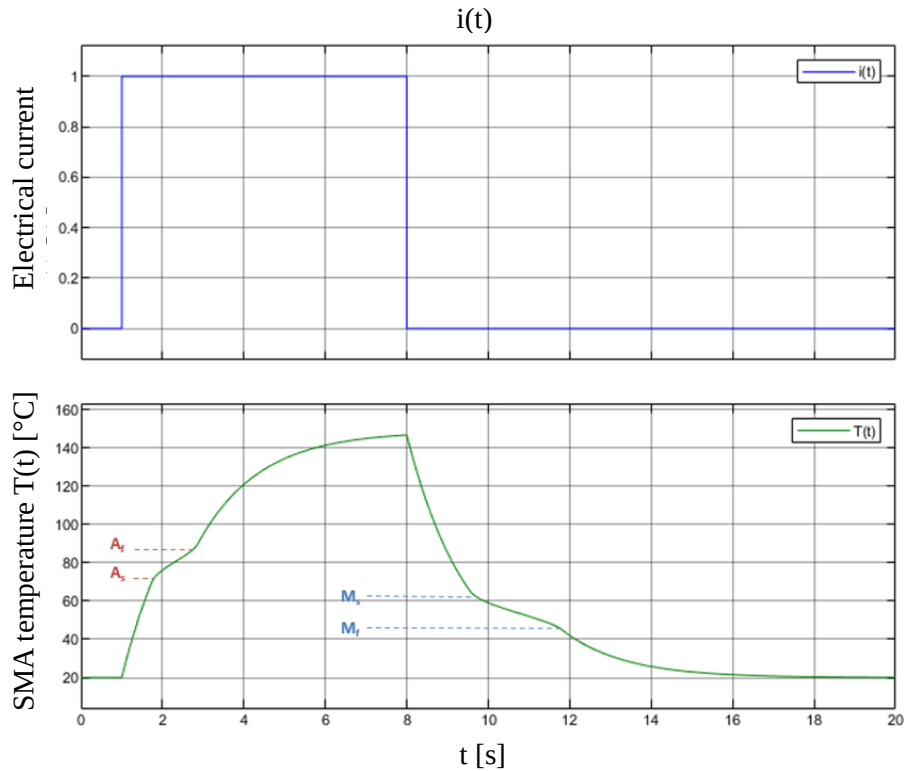

Fig. 2. Upper plot – excitation signal as an electrical current passing through SMA wire value change; lower plot – response signal as a SMA wire temperature value change.
A_s – martensite to austenite phase transformation start temperature;
A_f – martensite to austenite phase transformation finish temperature;
M_s – austenite to martensite phase transformation start temperature;
M_f – austenite to martensite phase transformation finish temperaturę (all temperatures are referred to no load condition).
Author's analysis based on [1]

2. Phase transformation models

This paragraph considers a phase transformation model as the second component of the SMA behaviour model. Such models have been discussed in works ([1] [2]), from simple to complex forms. At the beginning, a model from [1] will be presented. It determines martensite fraction in a SMA as the function of SMA temperature assuming a constant load condition. The model can be described by the following equations [1]:

- *for heating process:*

(3)
$$R_m = \begin{cases} 1 \; dla \; T < A_s^{\sigma} \\ \frac{1}{2}\left[cos\left(\pi \frac{T-A_s^{\sigma}}{A_f^{\sigma}-A_s^{\sigma}}\right) + 1\right] \; dla \; A_s^{\sigma} < T < A_f^{\sigma}, \\ 0 \; dla \; T > A_f^{\sigma} \end{cases}$$

- *for cooling process:*

$$(4) \qquad R_m = \begin{cases} 1 \ dla \ T < M_f^\sigma \\ \frac{1}{2}\left[cos\left(\pi \frac{T-M_f^\sigma}{M_s^\sigma - M_f^\sigma}\right) + 1\right] \ dla \ M_f^\sigma < T < M_s^\sigma. \\ 0 \ dla \ T > M_s^\sigma \end{cases}$$

where:

$A_s^\sigma, A_f^\sigma, M_s^\sigma, M_f^\sigma$ - phase transformation temperatures referred to determined stress σ.
More complicated model has been presented in [2], further used by A. Pai in [12]. Nevertheless, the following model description will be based on [2].

Regarding to heating or cooling process, the martensite fraction during phase transformation can be described by the undermentioned relations:

$$(5) \qquad R_m(\theta, t) = \begin{cases} R_m^C(\theta, t) \ for \ cooling \ process \\ R_m^H(\theta, t) \ for \ heating \ process \end{cases},$$

where:

$$(6) \qquad R_m^C(\theta, t) = \frac{R_{ma}^C(t)}{1 + e^{k_m^C(\theta - \beta^C)}} + R_{mb}^C(t),$$

$$(7) \qquad R_m^H(\theta, t) = \frac{R_{ma}^H(t)}{1 + e^{k_m^H(\theta - \beta^H)}} + R_{mb}^H(t),$$

$$(8) \qquad \theta = T - T_{ot},$$

with (^{C,H} superscripts have been omitted intentionally for simplicity):
$R_{ma}(t), R_{mb}(t)$ – model parameters,
k_m – temperature constant,
θ – difference between the wire temperature and ambient temperature,
β – „average" transformation temperature.

Note that there is a significant difference between this model and the one depicted previously. Modelling of martensite fraction value changes after reversing heating process into cooling process (and cooling into heating, as well) is allowed here. In case of only one of that processes, parameters $R_{ma}^C(t), R_{mb}^C(t), R_{ma}^H(t), R_{mb}^H(t)$ are constant. Under other conditions, these parameters are considered to be variables. Furthermore, in case of reversing heating or cooling process, before phase transformation is completed, the minor hysteresis loops are modelled. These loops occur for $R_{ma}^C(t) < 1$ or/and $R_{mb}^C(t) > 0$ (for heating $R_{ma}^H(t) < 1$ or/and $R_{mb}^H(t) > 0$). Major loops examples are shown in Fig. 3 and minor loops examples are presented in Fig. 4.
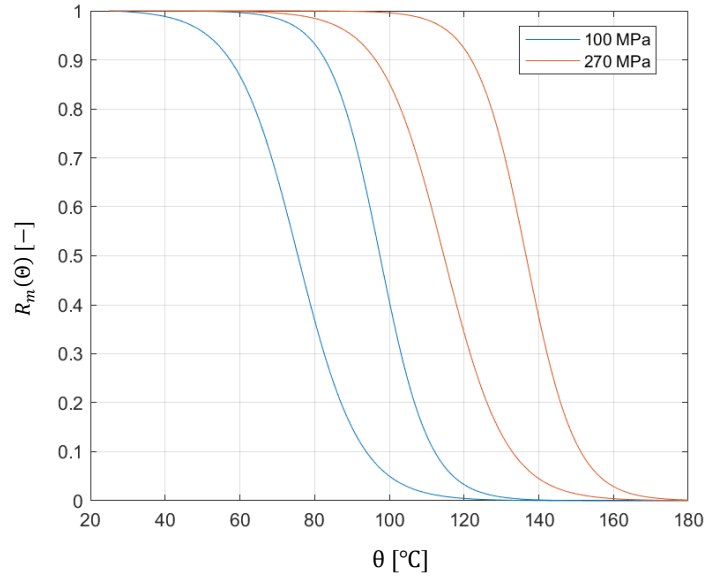
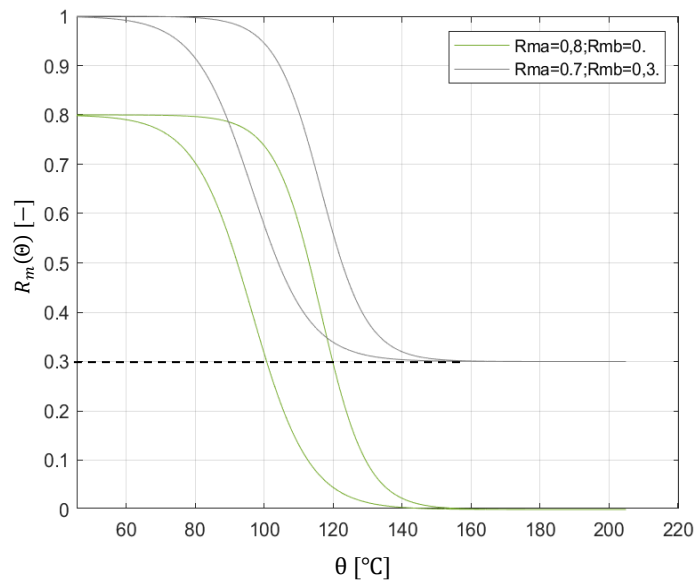Fig. 3. Major loops of R_m as a function of θ for different load condition. Author's analysis based on [2].

Fig. 4. Minor loops of R_m as a function of θ for:

a) $R_{ma}^C(t) = R_{ma}^H(t) = R_{ma}(t), = 0,8; R_{mb}^C(t) = R_{mb}^H(t) = R_{mb}(t) = 0$ – green,

b) $R_{ma}^C(t) = R_{ma}^H(t) = R_{ma}(t), = 0,7; R_{mb}^C(t) = R_{mb}^H(t) = R_{mb}(t) = 0,3$ – grey.

Author's analysis based on [2].

3. Mechanical models

There are a lot of models describing mechanical behaviour of shape memory alloys [5] [12] [14]. This work focuses on Preisach models mentioned in [14] and models publicated by A. Pai in [5] [12]. All the above are macroscopic phenomonological models [5] [12] [14]. The Preisach models has been used by a number of researchers [14]. It is not suprising due to their generality [14]. The models presented by Arathi Pai are also simple, especially model from [12]. Let us consider the first mechanical model from [12]. The author of [12] considers the wires as a 1D problem with uniaxial force. He reviews two options of the model – a parralel

model and a series one. The first one assumes that shape memory alloy is a compound of a parallel connection of martensite and austenite layers. The latter is similar but it assumes a series connection of the mentioned phases. Let us consider only the first one. The parallel configuration of layers means that the same strains apply to both martensite and austenite layers. It can be described as follows [12]:

(9) $$\varepsilon = \varepsilon_a = \varepsilon_m,$$

where:
ε – strain of the SMA,
ε_m – strain of the martensite layer,
ε_a – strain of the austenite layer.

Additionally, this configuration implies that a stress of the SMA is a weighted linear combination of the stresses of both layers, where martensite fraction (R_m) and ($1 - R_m$) are weights [12]:

(10) $$\sigma = R_m \sigma_m + (1 - R_m)\sigma_a,$$

where:
σ – stress of the SMA,
σ_m – stress of the martensite layer,
σ_a – stress of the austenite layer.
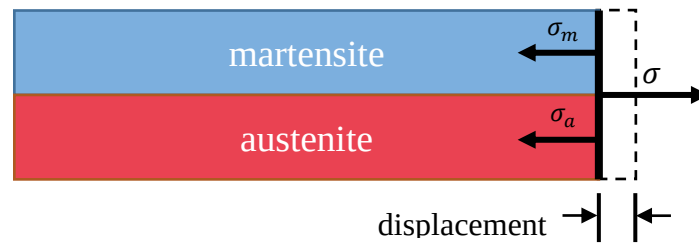
Fig. 5. Parallel mechanical model of SMA. Prepared based on [12]

The framework assumes modelling of stress vs. strain characteristics of pure martensite and pure austenite with the use of linear functions. It allows us to model curves for loading, unloading and reloading processes, and to determine σ_m and σ_a for a strain ε of the SMA, including its previous values. That data are sufficient to compute stress vs. strain curve of SMA for any martensite fraction value [12] . For more details, please see [12]. The exemplary simulated characteristics are shown in Figure 6.

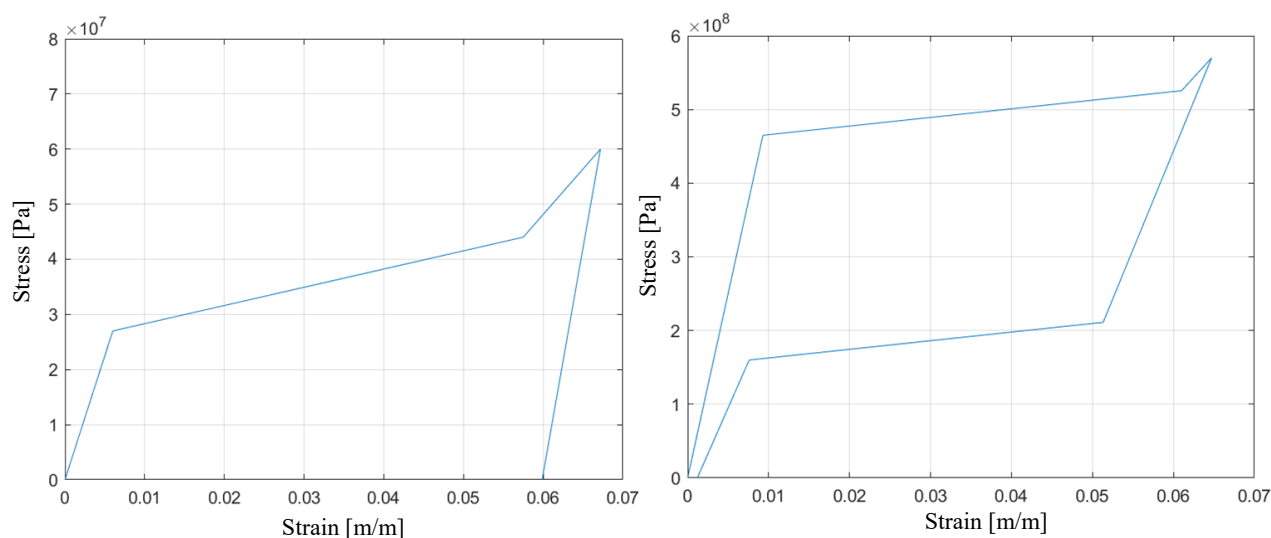Fig. 6. Simulated stress vs. strain loading and unloading curves for pure martensite and pure austenite for exemplary input data. Author's analysis based on [12].

The next model presented by Arath Pai in [5] is also used to model stress vs. strain characteristics of the martensite and austenite phases. However, it utilizes the continuous and differentiable equations. Exemplary plots for loading process are depicted in Figure 7 below. The considered framework allows to simulate a behaviour of martensite and austenite for both monotonic as well as cyclic loading and unloading [5]
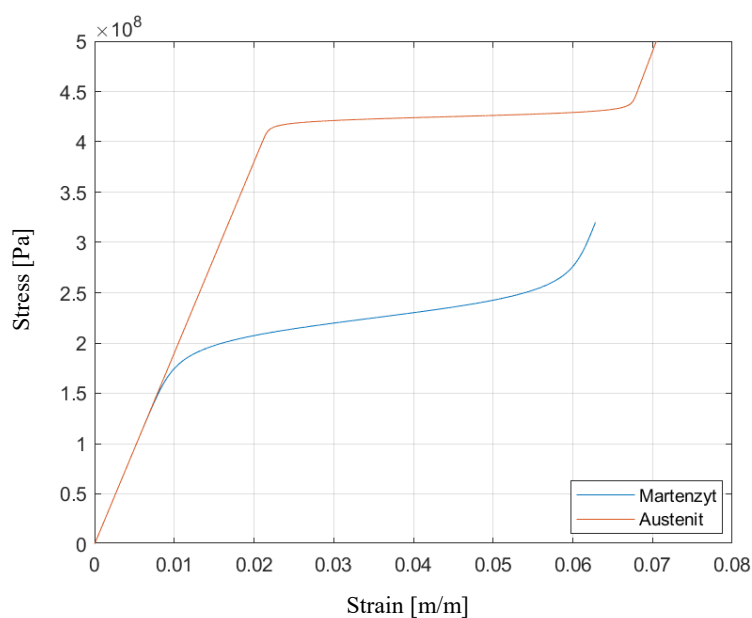

Fig. 7. Simulated stress vs. strain loading curves for pure martensite and pure austenite. Author's analysis based on [5].

4. Two antagonistic SMA wires model

The approach is similar to previously presented by T. Ikeda et al. in [13] but it exploits a parallel mechanical model of SMA form [12]. The SMA model under consideration assumes that:

- *SMA wires are heated and cooled down alternately,*
- $R_m^{SMA1} < 1 <=> R_m^{SMA2} = 1,$
- $R_m^{SMA2} < 1 <=> R_m^{SMA1} = 1.$

Fig. 8 presents a scheme of two SMA stress vs. strain characteristics. It distinguishes twelve phases while shape memory alloy wires are alternately heated and cooled down. During all the process, a pair of SMA wires changes their characteristics and equilibrium point is determined. The initial condition which defines the first phase (Fig. 8) assumes that two wires are in the martensite state. Moreover, the wire 1 is fully pre-strained and the wire 2 is unstrained. The equilibrium point is indicated by the red circle in Fig. 8. During Phase 2, the wire 1 is heated and its stress-strain curve rises up. Then the wire 1 shrinks and the wire 2 expands. In Phases 3 and 4, the heating of the wire 1 continues so that the thermal-induced martensite phase reorients into the stress-induced martensite phase and the wire 2 expands further.
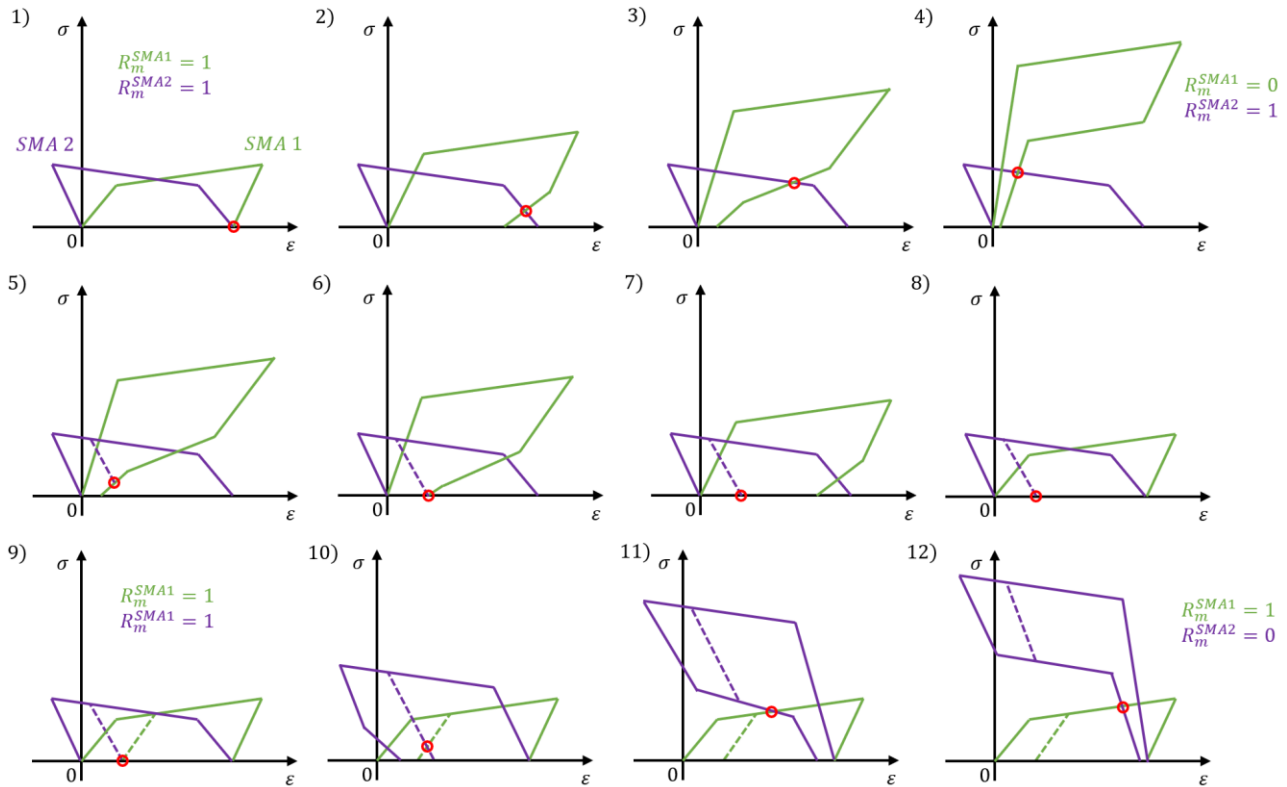

Fig. 8. Concept of the model of antagonistic pair of wires. The model includes twelve phases of alternating heating and cooling of the wires (1)-12))

Phase 5 presents cooling of the wire 1. Its curve falls, which causes expansion of the wire 1 and a shrinkage of the wire 2. The characteristic of the latter exhibits an inner hysteresis loop. This process lasts from Phase 5 to Phase 8 when the equilibrium point, which indicates a placement of the connection of the wires, moves a little to the right until the wire 2 is fully unstressed. Although the wire 1 backs to the martensite, it does not return to its initial condition.

Next, the wire 2 is heated. Its stress vs. strain curve rises up and the equilibrium point moves to the right through the inner hysteresis loops of both of the wires. The process lasts from Phase 9 to Phase 12, until heating

of the wire 2 finishes. Note that an analogous situation was observed in Phase 4. The alternating heating and cooling of the wires cause similar situation like shown already in Phases 5-12.

4. Results

The presented concept of the model of antagonistic work of two SMA wires was implemented into numeric computing software. The model had two inputs: a martensite fractions of first SMA wire R_m^{SMA1} and a martensite fraction of second SMA R_m^{SMA2}. Strains and stress for these two wires were outputs. To validate the model, the signals representing alternating heating and cooling of the SMAs (Fig. 9) were used as inputs. The results of this simulation were used to generate stress vs. strain characteristic of the wire 1, which represents a behaviour of the system of two wires. The depicted curves represent changes of the first SMA's strain after:

- *heating SMA wire 1 (Fig. 10a),*
- *heating and cooling SMA wire 1 (Fig. 10b)*
- *heating and cooling SMA wire 1 and then SMA wire 2 (Fig. 10c).*

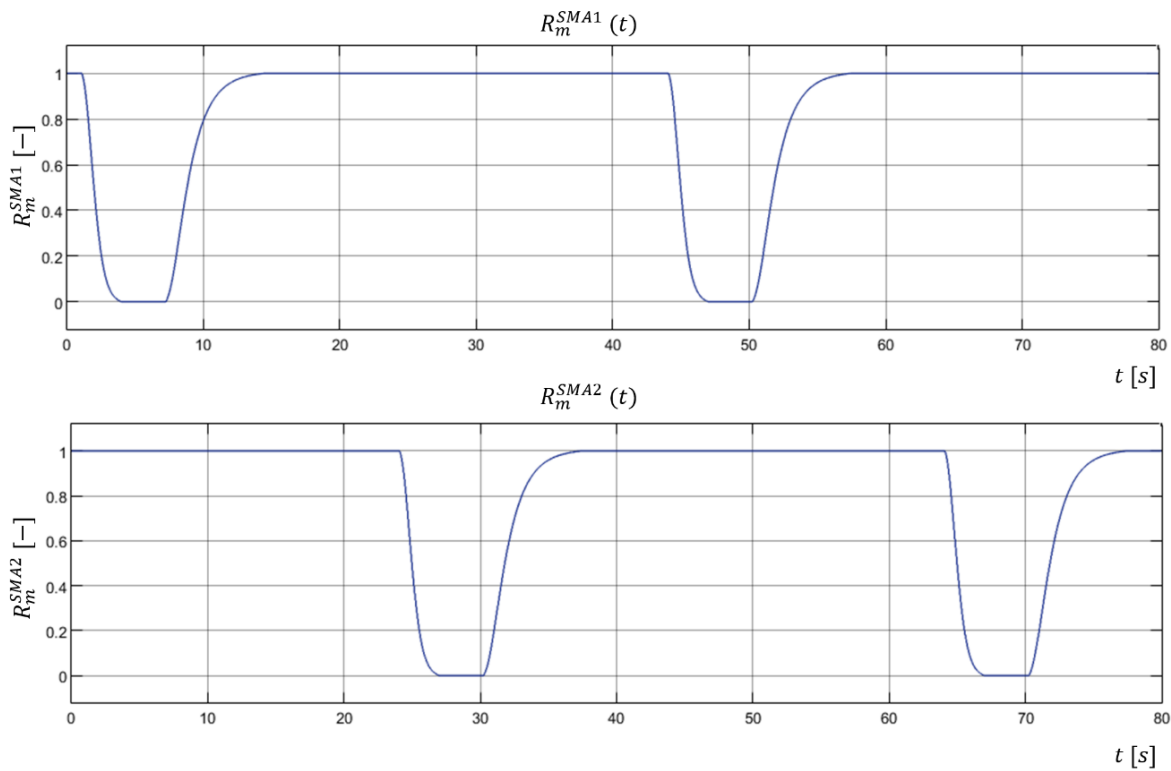Fig. 10d presents stress vs. strain curve for alternating heating and cooling of both wires.

Fig. 9 Exemplary input signals.

The results of the simulation are consistent with the description of the model which was discussed in the previous paragraphs. A further development of the model and its comparison with an experimental data are planned to be a subject of another study.
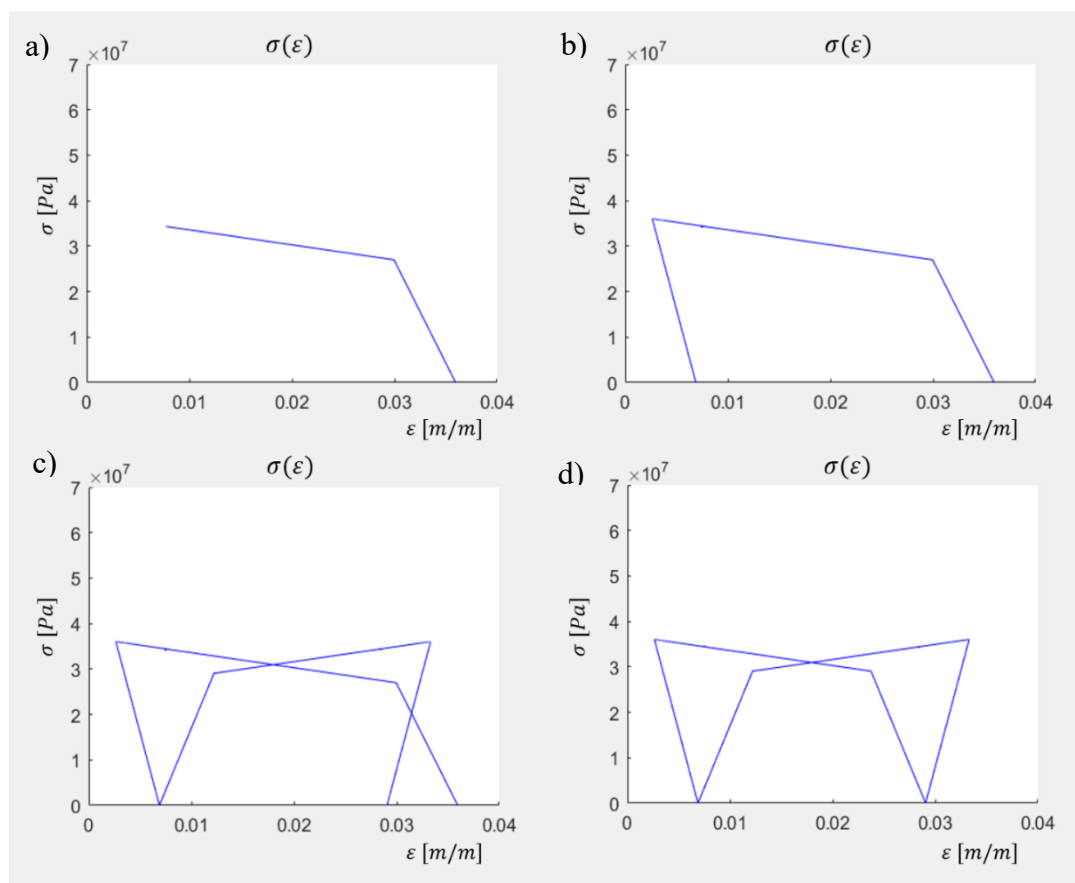
Fig. 10 Stress vs. strain curves as results of the simulation.

5. References

References

[1] R. Velázquez i E. E. Pissaloux, „Modelling and temperature control of shape memory alloys with fast electrical heating," International Journal of Mechanics and Control, tom 13, nr 2, 2012.

[2] D. R. Madill i D. Wang, „Modeling and L2-Stability of a Shape Memory Alloy Position Control System," IEEE Transactions on Control Systems Technology, tom 6, nr 4, pp. 473-481, 1998.

[3] H. Meier i L. Oelschläger, „Numerical modelling of the activation behaviour of SMA-actuator wires– application in an innovative drive system," Materials Science & Engineering Technology, tom 35, nr 5, 2004.

[4] H. Talebi, H. Golestanian , M. R. Zakerzadeh i H. Homaei , „Thermoelectric Heat Transfer Modeling of Shape Memory Alloy Actuators," The 22st Annual International Conference on Mechanical Engineering-ISME2014 , 2014.

[5] A. Pai et al., "Modelling the constitutive behaviour of martensite and austenite in shape memory alloys using closed-form analytical continuous equations", 7th ECCOMAS Thematic Conference on Smart Structures and Materials SMART 2015.

[6] H. Morawiec, „Metale z pamięcią kształtu i ich zastosowanie", Katowice: Wydawnictwo Uniwersytetu Śląskiego, 2014.

[7] K. Mehta i K. Gupta, „Fabrication and Processing of Shape Memory Alloys. SpringerBriefs in Applied Sciences and Technology," Springer, 2019, pp. 1-7.

[8] J. M. Jani, M. Leary, A. Subic i M. A. Gibson, „A review of shape memory alloy research, applications and opportunities," Materials & Design (1980-2015), pp. 1078-1113, Kwiecień 2014.

[9] H. Yuan, . J. Fauroux, F. Chapelle i X. Balandraud, „A review of rotary actuators based on shape memory alloys,"

Journal of Intelligent Material Systems and Structures, pp. 1863-1885, 2017.

[10] D. C. Lagoudas i P. K. Kumar, „Introduction to Shape Memory Alloys," w Shape Memory Alloys. Modeling and Engineering Applications, New York, Springer Science+Business Media, LLC, 2008, pp. 1-52.

[11] J. Strittmatter, P. Gümpel i M. Hiefer, „Intelligent materials in modern production – Current trends for thermal shape memory alloys," Procedia Manufacturing, pp. 347-356, 2019.

[12] A. Pai, "A phenomenological model of shape memory alloys including time-varying stress", 2007

[13] T. Ikeda et al. "Shape-retainment control using an antagonistic shape memory alloy system," Proc. SPIE 9431, Active and Passive Smart Structures and Integrated Systems 2015, 943117 (2 April 2015); doi: 10.1117/12.2084396

[14] Smith, Ralph C.. (2005). Smart Material Systems - Model Development. (pp. 241-274). Society for Industrial and Applied Mathematics (SIAM). Retrieved from https://app.knovel.com/hotlink/toc/id:kpSMSMD001/smart-material-systems/smart-material-systems

LASER MICRO BENDING MECHANISM
FOR HIGH-PRECISION ADJUSTMENT IN MECHATRONIC SYSTEMS

J. Widłaszewski[1]

[1]*Institute of Fundamental Technological Research PASc, Warsaw, Poland*
e-mail: Jacek.Widlaszewski@ippt.pan.pl

Abstract

The laser-based non-contact micro-adjustment method is widely applied in manufacturing and assembly of micro-electro-mechanical and micro-opto-electro-mechanical systems (MEMS and MOEMS). Due to miniaturization requirements and design considerations the access to these devices is frequently possible from one side only. This creates difficulties when laser-induced two-way micro-bending is needed – both towards, as well as away from the applied laser beam. Presented paper reports experimental and numerical investigations of a thermal micro-bending mechanism, which enables such adjustments, dependent on the applied processing parameters and using simple prismatic bar. A 3D finite element method (FEM) model has been developed to study the behaviour of a cantilever stainless steel beam heated with a stationary laser beam. Experimentally-validated numerical model allowed an analysis of temperature, strain and stress fields during the heating and cooling cycle to explain the mechanism of laser-induced micro-deformation.

Keywords:

laser forming, laser bending, non-contact adjustment, micro-adjustment, applied thermomechanics

1. Introduction

Application of laser technology makes it possible to perform highly accurate adjustment of components, which are difficult to access using traditional tools and are sensitive to mechanical forces. The energy input by the laser beam into the work-piece can be easily and precisely controlled. Since 1980's laser-induced micro-deformations are applied in manufacturing processes of the electrical and electronic industry, e.g. in production of miniature electric relays [1] and hard disk drives [2-4]. The leading companies of the sector have patented numerous practical solutions based on local laser heating of metallic and non-metallic materials that allow precise, non-contact (remote) and fast micro-scale shape corrections for positioning and alignment of parts and sub-assemblies, such as magnetic read/write heads, optical fibers, lenses and photodiodes [5-9].

Adjustment of critical dimensions with micrometer or milliradian accuracy in small metallic components is applied with laser-driven actuators during assembly stage in mass-production and it allows relatively large tolerances in the preceding production stages [10]. The high precision and cost-effectiveness in the assembly technology of micromechatronic systems is achievable due to the concept of the "on-board" (integrated) actuators, which are parts of the final product [10, 11]. The potential of the laser beam as a means of energy transport for optothermal microactuation is intensively investigated to expand practical applications of micro-opto-electro-mechanical systems (MOEMS) [12, 13]. Alignment accuracy 0.1 micrometer in mass-production of photonic devices operating in the near-UV wavelength range was addressed with the laser-driven three-bridge actuator concept [14, 15]. Effective analytical model was developed to describe behaviour of two-bridge actuators [16]. A separate direction in research on laser-controlled micro-adjustment is related to the application of shockwaves generated using nano-, pico- or femtosecond laser pulses [17-20],

The three fundamental mechanisms of laser thermal forming identified to date are: the temperature gradient mechanism (TGM), the upsetting mechanism (UM) and the buckling mechanism (BM) [21]. Dependent on laser processing parameters, part dimensions and topology, different shape changes are produced by pulsed

or continuous local heating of the material [22, 23, 24]. The temperature gradient mechanism has a drawback of producing bends always in one direction, i.e. towards the heat source (e.g. the laser beam). Such deformation is termed concave [25] or positive [26] bending in the literature and the related angular deformation is assumed positive in this work. The opposite deformation is termed convex [27] or negative [26] bending.

Lee and Lin [28] investigated deformation of a 304 stainless steel plate heated with a line-shaped CO2 laser beam. One case of negative bending was observed for a stainless steel specimen (0.5 mm thick, 150 mm long) in the cantilever arrangement, for laser power 1 kW and heating time 0.5 s, where material melting occurred.

Wang et al. [29] presented research on dynamic micro-deformations of cantilever beams made of St14 and C45 steels and heated with a CO2 laser beam of the Gaussian intensity distribution. They attributed the negative final angular deformation of a C45 carbon steel sample to the effect of the martensitic transformation and the involved volumetric expansion of the heat-affected region near the laser-heated surface.

Zhang and Xu [30] analysed laser bending of silicon microcantilevers, which are applied in extremely sensitive physical, chemical and biological sensors, e.g. in the atomic force microscopy. The laser beam of wavelength 524 nm (a frequency doubled Nd:YLF laser) operated with 20 ns pulses and 2 kHz repetition rate. The laser spot of diameter 8 micrometers traversed across 0.6 micrometer thick silicon cantilever. The obtained sensitivity of bending was 3.5 microradian. The microcantilever tip deflection was about 1.3 nm at 14 microradian bending angle. The authors indicated that such a technique is simple to implement and very useful for applications involving arrays of cantilevers for parallel chemical and biological sensing. However, its limitation is the one-directional bending only, always towards the laser beam.

A considerable difficulty in application of laser actuator technology arises when a component to be processed is accessible from one side only. To solve such a problem specially designed actuators were proposed [10, 31, 32]. In the so-called actuator with embossment, the positive or negative bending can be achieved dependent on the location of the thermal upsetting material region (above or below the neutral axis of the component cross-section) [10].

In order to achieve the bi-direction control of the bending deformation a two-stage technique has been invented by which the positive bending is produced with the temperature gradient mechanism, while the displacement in the opposite direction is produced due to laser-induced material annealing [33, 34]. However, such technique requires at least two applications of laser heating, using different processing parameters, and followed by cooling periods.

Presented paper reports experimental and numerical investigations on a thermal micro-bending mechanism, which enables deformation of a simple prismatic bar either towards or away from the laser beam, dependent on the applied processing parameters. A 3D finite element method (FEM) model has been developed to study the behaviour of a cantilever stainless steel beam heated with pulses of a stationary laser beam. Experimentally-validated numerical model allowed an analysis of temperature, strain and stress fields during the heating and cooling cycle.

2. Experiments

Samples of dimensions 50 x 4.05 x 0.55 mm made of 18-8 type stainless steel, clamped in the cantilever arrangement, were heated with a stationary Nd:YAG laser beam (Fig. 1). They were annealed prior to laser bending experiments in 400°C for a half an hour in order to reduce initial residual stresses and to increase coupling of laser radiation due to the created oxide layer. The transverse electromagnetic mode TEM_{mn} of the applied laser beam exhibited a multimode character. The laser beam was defocussed to obtain a spot of diameter 3.6 mm on the material surface. The spot was located on the longitudinal axis of symmetry of the

specimen (Fig. 2). Laser operated in the continuous wave (CW) mode. Fluctuations of the laser beam power were estimated as ±5% of the nominal value. Accuracy of pulse time duration was approximately ±0.05 s.
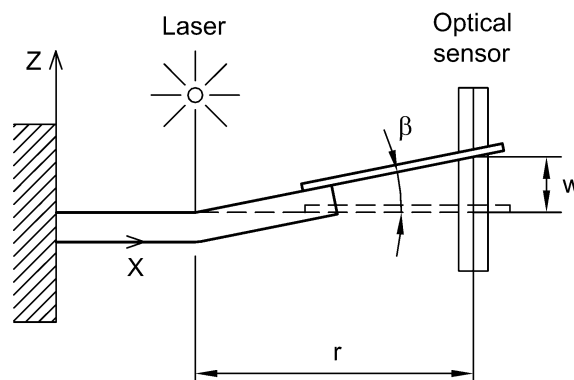

Fig. 1. Schematic of the laser bending experimental setup.
The definition of the positive angular deformation $\beta > 0$.

Non-contact deformation measurements were performed with a high-accuracy CCD micrometer Keyence LS-7070M. In order to achieve a high accuracy of optical measurements, an additional element of high-quality surface and low mass (a syringe needle) was attached to the specimen. Its displacement was measured and recorded during laser heating and after cooling down the sample to the initial material temperature. Fast deformation measurements were required during the phase of laser irradiation, while the highest accuracy was needed to precisely measure the final value of angular deformation. Both requirements were satisfied by dynamic control of the averaging number parameter of the optical micrometer.

Angle β of the bending deformation induced by the laser pulse was calculated from the linear vertical displacement w (Fig. 1) measured with the micrometer. The following formula was used: $\beta = \arctan(w/r)$, where r is the distance between the laser spot centre and the measurement location ($r = 48.8$ mm). Angular deformation is considered positive (concave) when the moving segment of the specimen rotates in the direction of the incident laser beam ($\beta > 0$), as show in Fig. 1.

3. Numerical simulation

Numerical simulations were conducted using the Finite Element Method (FEM). The thermal-mechanical sequentially coupled analysis was conducted in two separate steps: (1) determination of temperature field under prescribed heat load and boundary conditions, and (2) elastic-plastic incremental analysis of stress and strain due to the calculated temperature field. The calculations were performed with the ABAQUS system [35]. Energy input from the laser beam was treated as a surface heat source, since the absorption of the infrared radiation by metals is typically confined to a layer several tens of nanometres thick. Three-dimensional linear finite elements with 6 and 8 nodes were used: wedge elements DC3D6 and hexahedral DC3D8 for thermal problem, and compatible elements C3D6 and C3D8 for mechanical problem. Ten layers of elements were applied in the thickness direction of the specimen in order to accurately model the gradient of temperature and the bending effect. Only one half of the specimen was modelled taking the advantage of its symmetry. The spatial profile of power density over the laser beam transverse cross section was approximated by a top-hat model of constant intensity. The absorption coefficient of laser radiation by the material was assumed 0.77, as typical for the laser radiation of 1.06 micrometer wavelength incident on the stainless steel surface covered with oxide layer. The laser spot location is shown in Fig. 2, while Fig. 3 presents the mesh of finite elements in that region. Heat dissipation through free convection and radiation was taken into consideration in the numerical model.
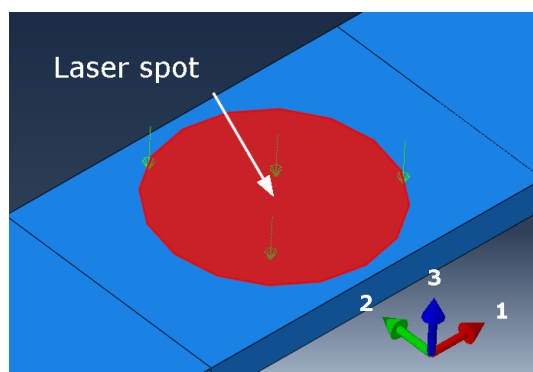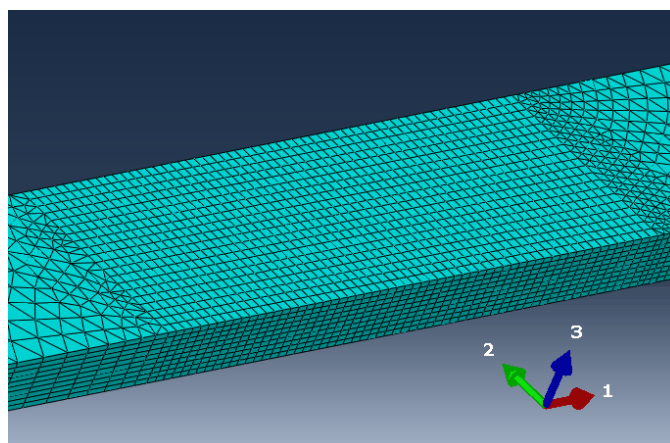
Fig. 2. Laser spot location.

Fig. 3. A mesh of finite elements in the laser spot region.

Thermal dependences of the following material properties were taken into consideration: thermal conductivity, specific heat, thermal expansion coefficient, Young's modulus, Poisson's ratio and density [36]. In order to achieve possibly high modelling accuracy, the yield stress dependence on temperature was based on data presented by Chen and Young [37] for the austenitic stainless steel. Their characteristics were recalculated using the room temperature yield stress value 234 MPa for the steel used in this research [38]. The Huber-Mises-Hencky yield criterion was employed in modelling of material behaviour.

5. Results and discussion

In order to clearly present the bend angle time-runs during laser heating and the subsequent material cooling, the logarithmic axis for the process time is employed in Fig. 4. During the phase of heating the specimen bends with negative angular deformation due to the presence of a high temperature gradient over the material thickness. Plastic (tensile) deformation starts to appear in the edge regions of the specimen after approximately 0.05 s of laser heating. The final bend angle values after laser irradiation for 1.05 s were: (1) positive for laser beam power 59 W, (2) close to zero for power 46.3 W and (3) negative when the power was 36.2 W. The comparison of experimental and numerical simulations results (Fig. 4) shows a good agreement.
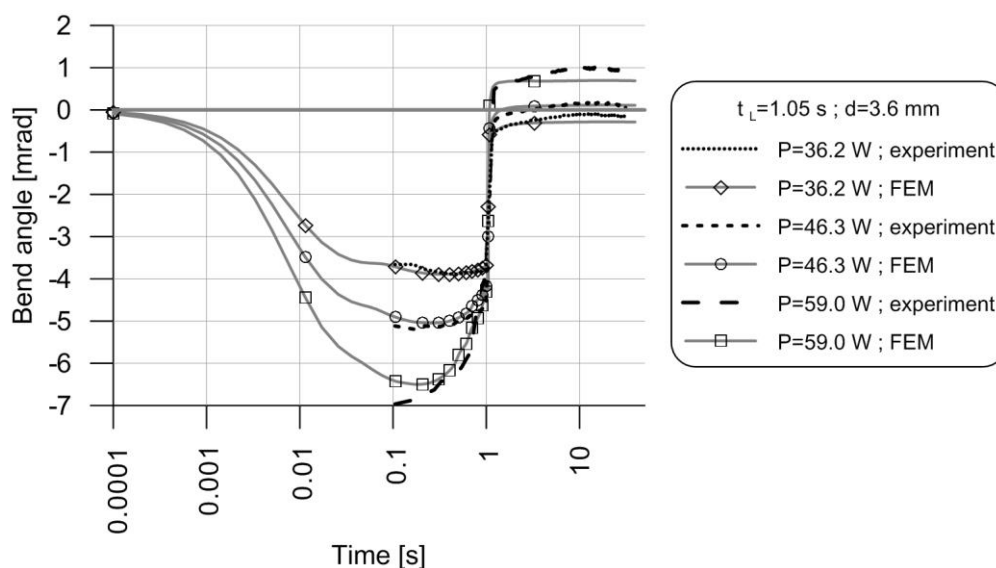

Fig. 4. A comparison of experimental and numerical time-runs of the bend angle for pulse length 1.05 s, laser spot diameter 3.6 mm and laser power 36.2, 46.3 and 59 W.

Using the experimentally-validated numerical model, the negative bending behaviour was further analysed in cases when the laser beam power was 36.2 W and the pulse length was 0.25, 0.5 and 0.75 s (Fig. 5). Results of numerical simulations show that the effect of negative bending can be achieved and controlled by suitable selection of laser beam power and the duration of the laser irradiation. A similar thermomechanical behaviour was observed and analyzed by Mucha at al. [39] and in a research with the moving laser beam [40, 41].
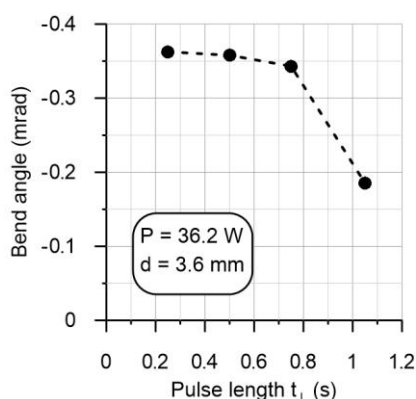

Fig. 5. Bend angle dependence on the pulse length for negative bending deformation cases.
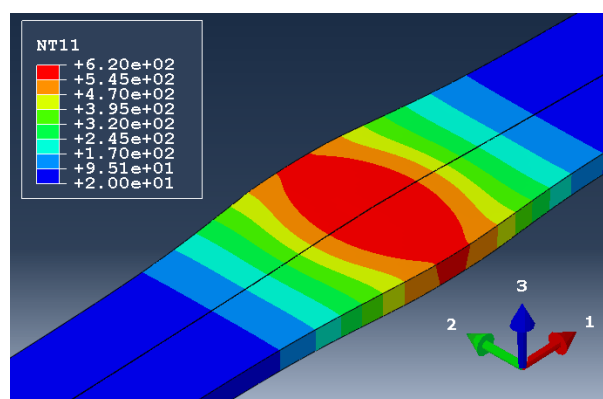

Fig. 6. Temperature distribution at time 1.05 s (power 36.2 W, deformation scale factor 20).

An example of the calculated distribution of material temperature is presented in Fig. 6 (power 36.2 W, pulse length 1.05 s). A similar distribution was obtained for laser beam power 59 W, but with the maximal temperature value 938 °C, while for power 36.2 W it was 635 °C.
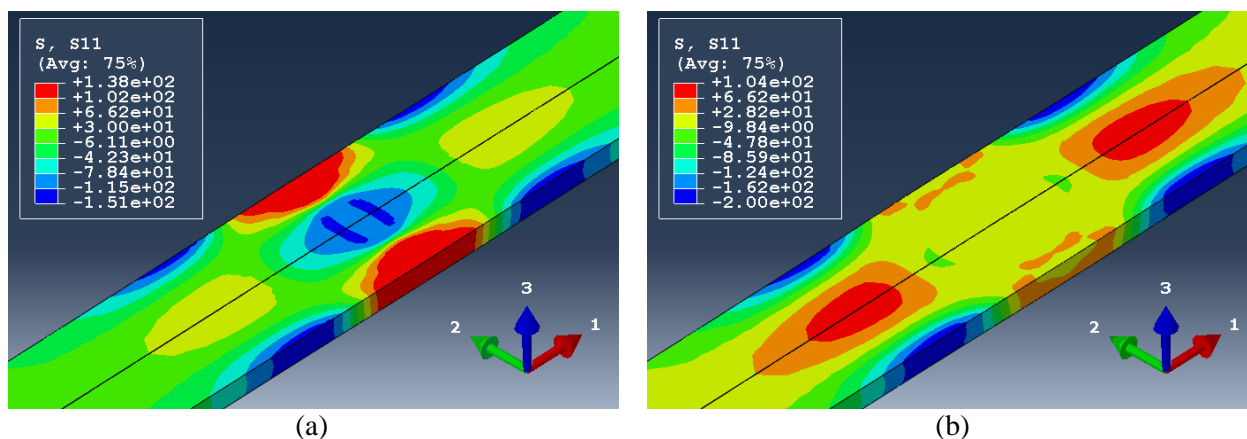

(a)

(b)

Fig. 7. Longitudinal stress component S11 at time 1.05 s: (a) power 36.2 W, (b) power 59 W. Deformation scale factor 1

Figures 7 (a) and (b) show differences in distribution of the longitudinal stress component S11 in the region of laser spot, at the end of laser pulse 1.05 s, for laser beam power 36.2 W and 59 W, respectively. The characteristic of thermomechanical response for the case of power 36.2 W is the occurrence of high tensile stress zones in the edge regions, while for the power 59 W such zones are located close to the longitudinal axis of symmetry. In both cases the central region located directly under the laser spot is initially under compression due to thermal expansion of the material, with gradually occurring effect of the yield stress decrease with the increase of temperature.
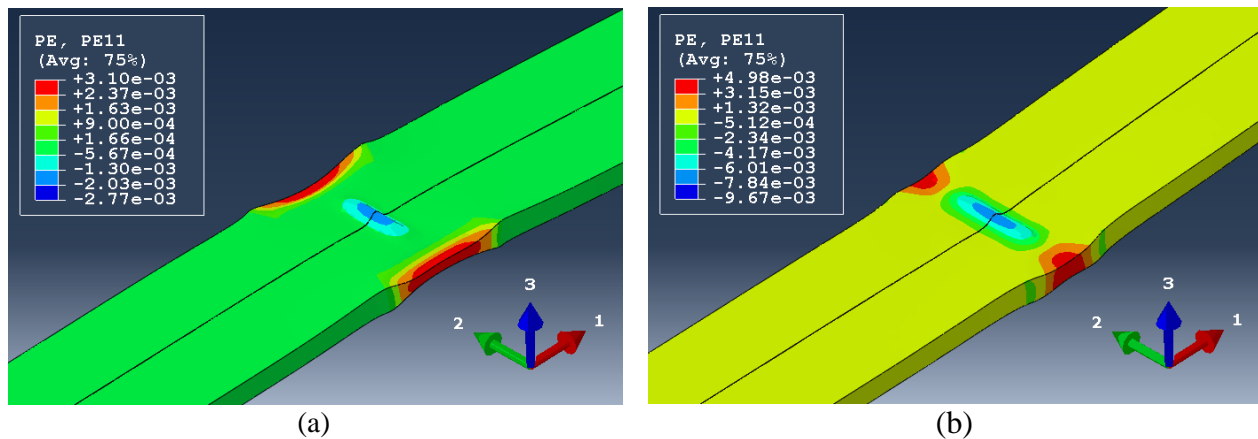
Fig. 8. Longitudinal plastic strain component PE11 in the final state:
(a) power 36.2 W, deformation scale factor 500, (b) power 59 W, deformation scale factor 100.

As a result of intense longitudinal stretching in the edge regions, long zones of positive longitudinal plastic strain component PE11 occur there for power 36.2 W, after laser heating for 1.05 s and subsequent cooling the material down to the initial (room) temperature (Fig. 8a). In the case of power 59 W, the material stretching regions are much smaller, while the central region of negative strain PE11 is considerably larger (Fig. 8b). In both cases the laser pulse length was 1.05 s, and the thermal load differentiated only in the applied power. The specimen behaviour in the case of the smaller heating power resembles the effects of the buckling mechanism, hence the final angular deformation is negative, while for the higher power the processing conditions favour the temperature gradient mechanism to play a more pronounced role in the deformation process. Maximal difference between temperatures of the upper and bottom specimen surface is 46 ºC for laser power 36.2 W, and 74 ºC for laser power 59W.

6. Conclusions

Presented experimental investigations and numerical simulations explained mechanism of bi-direction laser-induced micro-bending. It was found that the final angular deformation of a prismatic cantilever beam, heated from one side with a stationary laser beam, can be negative or positive, dependent on the applied laser power. The magnitude of angular deformation can also be controlled with the laser pulse duration. The studied mechanism of bending involves a significant positive longitudinal plastic strain in the edge regions of the beam. Final deformation of the beam is a combined result of the negative longitudinal strain in the central region and the positive strain close to the edges, with a contribution of the out-of-plane deformation due to the temperature gradient across the thickness direction. Negative laser micro-bending may find numerous practical applications in manufacturing of MEMS and MOEMS, as the miniaturization and integration requirements usually limit the access to these devices to one-side only.

References

[1] E. Steiger , *Führungsloses Justieren der Mittelkontaktfedern des Kleinrelais D2 in einem Pulslasersystem*. Siemens Components 22(3):135-137, 1984.

[2] N. Matsushita, *Laser micro-bending for precise micro-fabrication of magnetic disk drive components.* Proceedings of SPIE 5063:24-29, 2003.

[3] X. R. Zhang, X. Xu, *Laser bending for adjusting curvatures of hard disk suspensions*. Microsyst Technol 11:1197–1203, DOI 10.1007/s00542-005-0588-3, 2005.

[4] T. Sanada, H. Watanabe, A. Ushimaru, M. Nomura, *Development of high-speed and high-accuracy roll and pitch angle adjustment machine for HDD suspension*. J. Laser Micro Nanoeng. 4(2):141–143, 2009.

[5] G. Dearden, S. P. Edwardson, *Some recent developments in two- and three-dimensional laser forming for 'macro' and 'micro' applications*. J Optics A: Pure and Applied Optics, 5, pp. 8–15, 2003.

[6] J. Widłaszewski, *Applications of laser forming in micro technologies*. In: Adamczak S, Radziszewski L (eds) Selected problems of modeling and control in mechanics, Vol. M19. Wydawnictwo Politechniki Świętokrzyskiej, Kielce, pp. 96-106. PL ISSN 1897-2691, 2011.

[7] S. Maruyama, et al. (FUJITSU LIMITED), *Contactor having contact electrodes formed by laser processing*. Patent US6806723 B2, 2004.

[8] A.C. Tam, C.C. Poon, L. Crawforth, *Laser bending of ceramics and application to manufacture magnetic head sliders in disk drives.* Anal. Sci. 17 (special issue), 419–21, 2001.

[9] Ubl T. R., Balasubramaniam S., Koba H. T. (HUTCHINSON TECHNOLOGY INCORPORATED), *Method for adjusting a head suspension parameter*. Patent US6837092. 2005.

[10] W. Hoving, *Accurate manipulation using laser technology*, in: M. Geiger, A. Otto (Eds.), Proceedings of the 3rd LANE 2001 (Laser Assisted Net Shape Engineering 3, International Conference) Meisenbach Bamberg, pp. 113-124, 2001.

[11] M. Tichem, B. Karpuschewski, P.M. Sarro, *Self-adjustment of micro-mechatronic systems*. CiRP Annals - Manufacturing Technology. Vol. 52, issue 1, pp. 17–20, DOI:10.1016/S0007-8506(07)60520-4, 2003.

[12] X. Han, H. Zhang, R. Xu, S. Wang, C. Qin, *Theoretical model of an optothermal microactuator directly driven by laser beams*. J. Micromech. Microeng. 25(7) 075012. DOI: 10.1088/0960-1317/25/7/075012, 2015.

[13] S. Wang, Q. Chun, Q. You, Y. Wang, H. Zhang, *Dynamic modelling and experimental study of asymmetric optothermal microactuator*. Optics Communications 383, 566-570, 2017.

[14] K.G.P. Folkersma, *Laser forming for sub-micron adjustment*: with application to optical fiber assembly. Thesis. University of Twente. http://dx.doi.org/10.3990/1.9789036540186, 2015.

[15] K.G.P. Folkersma, D.M. Brouwer, G.R.B.E. Römer, J.L. Herder, Robust precision alignment algorithm for micro tube laser forming, Precision Engineering, Volume 46, 301-308, ISSN 0141-6359, https://doi.org/10.1016/j.precisioneng.2016.05.011, 2016.

[16] J. Widłaszewski, *The effects of design parameters on the laser-induced in-plane deformation of two-bridge actuators.* Int J Machine Tools and Manufacture 80-81C:30-38, 2014.

[17] J. Griffiths, S.P. Edwardson, G. Dearden, K.G. Watkins, *Thermal laser micro-adjustment using picosecond pulse durations.* Applied Surface Science 258, 7639–7643, 2012.

[18] Y. Sagisaka, M. Kamiya, M. Matsuda, Y. Ohta , *Thin-sheet-metal bending by laser peen forming with femtosecond laser.* J. Materials Processing Technology 210(15) 2304–2309, 2010.

[19] Y. Ye, Y. Feng, Z. Lian, Y. Hua, *Mold-free fs laser shock micro forming and its plastic deformation mechanism.* Optics and Lasers in Engineering 67, 74–82, 2015.

[20] Y. Sagisaka, K. Yamashita, W. Yanagihara, H. Ueta, *Microparts processing using laser cutting and ultra-short-pulse laser peen forming*. J. Materials Processing Technology, 219, 230–236, 2015.

[21] F. Vollertsen, *Mechanisms and Models for Laser Forming*, in: M. Geiger, F. Vollertsen (Eds.) Proceedings of the 26th International CIRP Seminar on Manufacturing Systems - LANE '94 (Laser Assisted Net Shape Engineering, International Conference) Meisenbach-Verlag, Bamberg, pp. 345-360, 1994.

[22] N. Lazarus, G. L. Smith, M. D. Dickey, *Self‐Folding Metal Origami*. Adv. Intell. Syst., 1: 1900059, https://doi.org/10.1002/aisy.201900059, 2019.

[23] A. L. Bachmann, M. D. Dickey, N. Lazarus, *Making Light Work of Metal Bending: Laser Forming in Rapid Prototyping*. Quantum Beam Science. 4(4):44. https://doi.org/10.3390/qubs4040044, 2020.

[24] X. Wang, Y. Shi, Y. Guo, Q. Wang, *Design of 3D surface laser forming process*. Journal of Manufacturing Processes, 73, 306-315, 2022.

[25] Y. Namba, *Laser Forming in Space*, in: Proceedings of the International Conference On Lasers '85, (Las Vegas, NV, USA. Soc. Opt. & Quantum Electron., 2-6 Dec. 1985), C. P. Wang (Ed.), STS Press, pp. 403-407, McLean, VA, USA, 1986.

[26] J. Liu, S. Sun, Y. Guan, Z. Ji, *Experimental study on negative laser bending process of steel foils*. Optics and Lasers in Engineering, 48, 83–88, 2010.

[27] W. Li, Y.L. Yao, *Buckling based laser forming process: concave or convex*, in: Proc. ICALEO 2000, P 506, 1-10, 2000.

[28] K.-C. Lee, J. Lin, *Transient deformation of thin metal sheets during pulsed laser forming*. Optics & Laser technology 34, 639-648, 2002.

[29] X.F. Wang, G.N. Chen, Sh.G. Hu, J. Takacs, Gy. Krallics, Y.P. Su, *Research on dynamic micro-deformation under laser point source*. International Journal of Machine Tools and Manufacture 45(12-13) 1515-1522, 2005.

[30] X.R. Zhang, X. Xu, *High precision microscale bending by pulsed and CW lasers*. ASME J. Manuf Sci Eng 125(3) 512– 518, 2003. DOI:10.1115/1.1580528

[31] M. Geiger *Laser forming - the forming of metal using a laser beam*. ICMEN 2002 - 1st International Conference on Manufacturing Engineering. Austrian Research Centre, Seibersdorf Research GmbH, 2002.

[32] P. Woizeschke, *Approach for bidirectional laser bending of sheet metal with one-sided accessibility*, CIRP Annals, Volume 68, Issue 1, 277-280, ISSN 0007-8506, https://doi.org/10.1016/j.cirp.2019.04.098, 2019.

[33] R. Jurgenson, R. C. Danielson, B. D. Lien, M. S. Lewandowski (HUTCHINSON TECHNOLOGY, USA), *In-stack adjustable magnetic head suspension*. Patent US5995335, 1999.

[34] P. Bechtold, M. Schmidt, *Non-thermal micro adjustment using ultrashort laser pulses*. JLMN-Journal of Laser Micro/Nanoengineering 2(3) 1, 83-188, 2007.

[35] Dassault Systèmes, *ABAQUS 6.12*, 2012.

[36] J. Widłaszewski, M. Nowak, Z. Nowak, P. Kurp, *Laser-assisted thermomechanical bending of tube profiles*. Arch. Metall. Mater. 64, 1, 421-430. DOI: 10.24425/amm.2019.126268, 2019

[37] J. Chen, B. Young, *Stress–strain curves for stainless steel at elevated temperatures*. Engineering Structures, 28, 229–239. https://doi.org/10.1016/j.engstruct.2005.07.005, 2006.

[38] Z. Nowak, M. Nowak, J. Widłaszewski, P. Kurp, *Experimental and numerical investigation on laser-assisted bending of pre-loaded metal plate*. AIP Conference Proceedings, American Institute of Physics, 1922, 140006. https://doi.org/10.1063/1.5019148, 2018.

[39] Z. Mucha, L. Gregova, R. Gradoń. *Permanent and non-permanent deformations in samples caused by CO_2 laser pulse*. Proc. SPIE, 6598, 1–10, 2007.

[40] Z. Mucha; M. Zawiliński, *Edge effects in laser bending of metal plates*. In Proceedings of the 2nd International Conference on New Forming Technology, Bremen, Germany, 20−21 September 2007; 201−211.

[41] J. Widłaszewski, Z. Nowak, P. Kurp, *Effect of Pre-Stress on Laser-Induced Thermoplastic Deformation of Inconel 718 Beams*. Materials, 14, 1847. https://doi.org/10.3390/ma14081847, 2021.

PERFORMANCE IMPROVEMENTS IN AN IN-WHEEL MOTOR SYSTEM INCORPORATING INERTERS

N. J. Wills[1], **Y-Y. Li**[1], **J. Z. Jiang**[1], **T. L. Hill**[1], **S. A. Neild**[1], and **M. Dhaens**[2]

[1]*Department of Mechanical Engineering, University of Bristol, Bristol, UK*
[2]*Tenneco, Sint-Truiden, Belgium*

e-mail: z.jiang@bristol.ac.uk, yiyuan.li@bristol.ac.uk, mdhaens@tenneco.com

Abstract

The in-wheel motor (IWM) is an encouraging development for the propulsion of electric vehicles since it provides improved torque vectoring capabilities and vehicle packaging efficiency than a more traditional motor mounted to the chassis. However, the increase in unsprung mass can increase body vertical acceleration (BVA, worsening ride comfort) and tyre dynamic load (TDL, worsening roadholding), thereby negatively affecting vehicle dynamics. Another consideration is that of the relative deflection between the motor stator and rotor, which is termed magnetic gap deformation (MGD). Reducing this improves the longevity and reliability of the motor. This study considers the reduction of BVA, TDL and MGD by including inerters in the strut and bushes. By optimising the bushes for MGD results in a reduction of deflection in excess of 80% without a compromise to the other performance indices. After this, inerter-based absorbers are included in both of the bushes and the strut and optimised as one. As a result of this, BVA and TDL show improvements of 20% and 8% respectively without worsening MGD. It is concluded that there are large potential improvements in performance where inerter-based absorbers are included in an in-wheel motor system.

1. Introduction

An EV is normally created by fixing the electric motor to the vehicle body or chassis (the sprung mass) and driving the wheels via driveshafts. This propulsion method is known as a chassis-mounted motor. The other method to power an EV is to use an in-wheel motor (IWM). The IWM is not a new idea. The original IWM patent was filed in 1884 [1], and the first IWM powered vehicle was the 1900 Lohner-Porsche [16].

The IWM can provide many benefits in comparison to the chassis-mounted motor. These include improved drivetrain efficiency after the removal of driveshafts, and more effective torque vectoring capabilities [16]. It also permits an improved efficiency of drivetrain packaging, which leads to greater vehicle interior space [16].

However, the primary disadvantage of the IWM is the increase in unsprung mass which occurs. Unsprung mass has a negative impact on system dynamics and driveability characteristics. Examples of these negative effects include worsening the ride comfort and road holding [2, 4]. As a result, it is important to reduce the negative impact the IWM can have to the vehicle dynamics through the design or optimisation of the IWM system itself.

Since the IWM was originally suggested, several studies have considered IWM modelling [3]. Examples of these include suggesting novel designs to counteract some of the downsides that the IWM has [15,17,18,23,25]. These have included reducing the unsprung mass through a reduction in the size of the motor body itself, without compromising performance [23]. Meanwhile, other papers considered isolating the stator and rotor from the system using rubber bushes [15, 25], or transferring the stator mass to the sprung mass [17, 18]. Various authors have also investigated active suspension systems to counter the impact that the IWM has on the dynamics of the vehicle [9, 11, 13, 27].

An important consideration when designing an IWM is magnetic gap deformation (MGD). This is defined as the relative deflection between the rotor and stator. This deflection will result in an unbalanced radial magnetic force being induced. This then acts, (in addition to the existing road input), as a destructive input to the system [26]. Therefore, reducing MGD is imperative to limit this unbalanced radial magnetic force. In doing this, a simplified modelling strategy (where the radial magnetic force is neglected) can be used (as in [25]). Reducing the MGD has also been considered by previous authors. An example of this is where Luo & Tan [15] found that through isolation of the rotor and stator from the unsprung and sprung masses respectively can reduce MGD when compared to a traditional three mass model (their proposed IWM model uses five masses). This study will

improve upon their solution of using rubber bushes by incorporating inerter-based absorbers into both the strut and the bushes.

The inerter is a recent development in passive vibration absorption. It provides a force which is proportional to the relative acceleration between its two endpoints, and as a result is the mechanical equivalent of an electrical capacitor [20]. The inerter has been successfully realised hydraulically as a fluid inerter [12,22]. The inerter can also be mechanically constructed as a ball-screw device [24] or a flywheel-based device [20]. These realisation methods allow the inerter to provide much higher inertance values than the mass of the device itself. This inertance affects the phase and magnitude of the system dynamics. The inerter has been successfully incorporated into the civil [6,14], automotive [21,24] and railway [5,7,8] industries. However, it has not yet been included into an IWM system. This study will focus on this application.

The Hall-Bush fluid integrated bush has been utilised in railway vehicles for several years, and can be modelled as a damper in parallel and series with a spring [7]. Additionally, Lewis et. al. [7] suggests an inerter-integrated bush for use in a railway application. This bush is shown to improve on the performance of the traditional Hall-Bush device. This study will build on this work, by proposing and numerically assessing a similar concept which is for use in an automotive IWM.

After the inerter was introduced, the force-current analogy between the mechanical and electrical domains could be completed. This meant that the complete range of network synthesis theories for electrical systems could then be applied directly to a given mechanical system. This then extended the number of possible absorber layouts, and increased their ability to change the system dynamics. The structure-immittance approach was proposed by [28] to permit this design methodology. This takes a set number of springs, dampers and inerter circuit elements and proposes a set of generic absorber networks. These networks give transfer functions, which can then be simplified to provide an individual transfer function for any given absorber network. This is particularly useful if several absorber layouts are to be considered and optimised - such as here. This method has been successfully used previously in an automotive context, and hence it is appropriate to adopt this methodology for this specific application [29].

This paper will utilise a completely passive vibration absorbing method for an IWM, where inerter-based absorbers are incorporated into the suspension strut and bushes. This then permits the consideration of some key issues apparent in an IWM system. The key issues selected for this study are the worsened ride comfort and roadholding that results when an IWM is included in a vehicle. This study will also focus on reducing MGD to improve the motor reliability and longevity.

2. Models and methodology

2.1. Introduction to the in-wheel motor model

The IWM considered here is an outer rotor IWM. This means it is direct drive, and hence is simpler and more robust than an inner rotor IWM, (which would require a reduction gear) [10]. The model used has the stator and rotor supported by rubber bushes. This means it differs from the more tradition IWM model which has these fixed rigidly to the wheel hub and rim respectively. These rubber bushes have been shown previously, by [15], to reduce MGD. This MGD can result in an additional source of excitation, in addition to the road input (x_0), being created. This is because it can generate a nonlinear unbalanced radial magnetic force, as discussed by [26], when the stator and rotor deflect relative to each other. Therefore it is useful to constrain or reduce MGD (see Section 2.2) to prevent the undesirable unbalanced radial magnetic force being induced.

The rubber bushes and suspension strut can be modelled as the parallel connection of a spring and damper. In Section 3.2, an inerter-based absorber will replace the damper. The bushes and strut are therefore modelled using a spring in parallel with a generic network, to allow this replacement to occur. This is shown in Figure 1, (with the parameters and corresponding values presented in Table 1).

The overall system static stiffness must be kept the same, regardless of the optimised parameter values. This is because the vehicle performance and response characteristics are determined by the static stiffness. As a
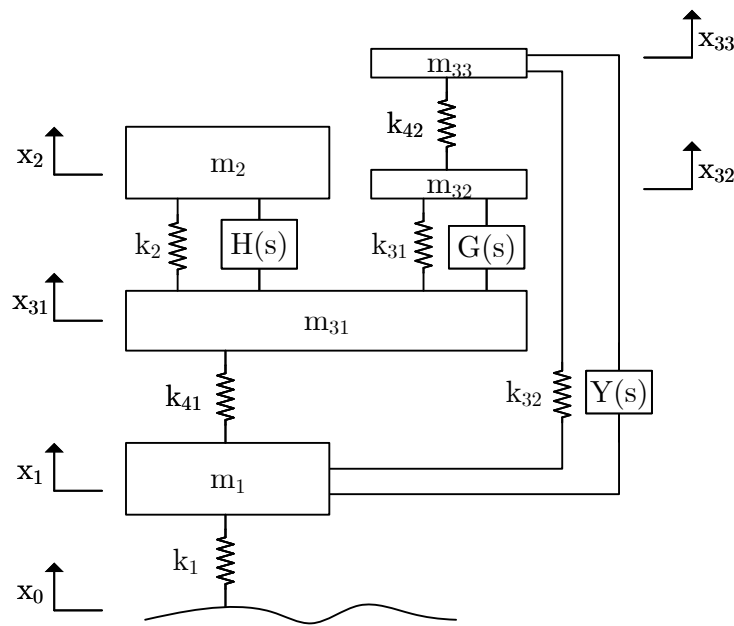
Figure 1: The IWM model considered in this study. This has been adapted from [15].

result of this, the static stiffness will remain fixed to the values shown in Table 1 throughout. This is the reason why generic networks replace the dampers alone, (and not the spring and damper together). This also requires layouts III-1 and III-8 (Figure 2) to have a stiffness (k) of zero. Due to the nature of their component layouts, any stiffness value reached would add to the (fixed) static stiffness of the system and increase it. As a result, they can be considered two element layout networks.

The generic networks represent the force-velocity structural-immittances of a given absorber network, through an approach first derived by [28]. It is these force-velocity admittances which permit the consideration of a complete range of alternative networks to the pure dampers, (as in the original model). In this study, up to three

Table 1: IWM parameter descriptions and corresponding values, reproduced from [15].

| Parameter	Value	Description
m_1	60 kg	Tyre mass and wheel rim (unsprung mass)
m_2	420 kg	Vehicle body (sprung mass)
m_{31}	20 kg	Wheel hub and brake calliper mass
m_{32}	30 kg	Stator mass
m_{33}	20 kg	Rotor mass
k_1	400 kN/m	Tyre stiffness
k_2	80 kN/m	Primary suspension strut stiffness
k_{31}/k_{32}	50 kN/m	Bush stiffness
k_{41}/k_{42}	5 MN/m	Bearing stiffness
$H(s)$	-	Suspension strut generic network
$G(s)$	-	Bush between stator and hub generic network
$Y(s)$	-	Generic network for the bushes between rotor and wheel rim (which results from the sum of two physical bush locations)
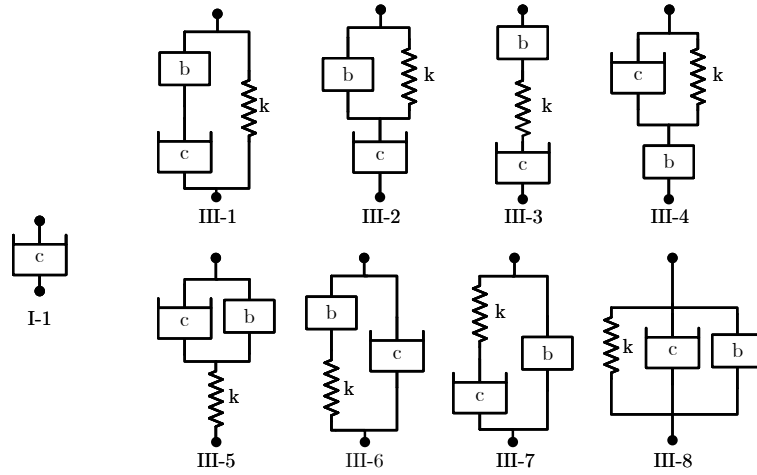
Figure 2: The absorber layouts considered which were derived through the structure-immittance approach [28].

elements will be considered in each case. These three elements are a single inerter, single damper and single spring. This results in eight unique networks (Figure 2, layouts III-1 to III-8). Figure 2 also shows a pure damper (I-1) which represents the baseline to be improved up. The primary reason for using generic networks, rather than deriving the individual equations of motion every time, is that of ease and simplicity. Changing a transfer function, rather than re-deriving the equations of motion, allows multiple layouts to be considered quickly in the optimisations.

The Laplace transformed equations of motion can be described as follows:

(1)

$$\hat{x}_1(m_1 s^2 + sY(s) + [k_1 + k_{32} + k_{41}]) - \hat{x}_0(k_1) - \hat{x}_{33}(sY(s) + k_{32}) - \hat{x}_{31}k_{41} = 0$$

$$\hat{x}_2(m_2 s^2 + sH(s) + k_2) - \hat{x}_{31}(sH(s) + k_2) = 0$$

$$\hat{x}_{31}(m_{31}s^2 + s[H(s) + G(s)] + [k_2 + k_{31} + k_{41}]) - \hat{x}_2(sH(s) + k_2) -$$
$$\hat{x}_1 k_{41} - \hat{x}_{32}(sG(s) + k_{31}) = 0$$

$$\hat{x}_{32}(m_{32}s^2 + sG(s) + [k_{31} + k_{42}]) - \hat{x}_{31}(sG(s) + k_{31}) - \hat{x}_{33}k_{42} = 0$$

$$\hat{x}_{33}(m_{33}s^2 + sY(s) + [k_{32} + k_{42}]) - \hat{x}_1(sY(s) + k_{32}) - \hat{x}_{32}k_{42} = 0$$

where $\hat{x}$ denotes the Laplace transformed x, s is the Laplace variable and all other terms are as previously defined. The Laplace transformed equations of motion are preferable for the analysis. This is because they allow for the frequency domain objective functions to be used (see Section 2.2).

2.2 . Performance indices

There are several different performance indices that could be used to define the performance quality when optimising a suspension system. Here body vertical acceleration and tyre dynamic load are taken as objective functions. They are described through the work of [21] as follows:

(2)
$$J_1 = 2\pi(V\kappa)^{\frac{1}{2}} \left\| sT_{\hat{x}_0 \to \hat{x}_2} \right\|_2$$

(3)
$$J_3 = 2\pi(V\kappa)^{\frac{1}{2}} \left\| \frac{1}{s} T_{\hat{x}_0 \to k_1(\hat{x}_1 - \hat{x}_0)} \right\|_2$$

where J_1 denotes the body vertical acceleration (the ride comfort metric) and J_3 the tyre dynamic load (a roadholding metric). Here $T_{\hat{a} \to \hat{b}}$ denotes the transfer function between $\hat{a}$ and $\hat{b}$, x_0 the road input, V the vehicle velocity and κ the road roughness parameter, $||\cdot||_2$ represents the standard $\mathcal{H}_2$ norm and all other terms are as

previously defined. The differentiator term (s) in J_1, and integrator ($\frac{1}{s}$) term in J_3 denotes that they correspond to relative acceleration and relative displacement respectively.

An equivalent metric for MGD, (termed J_m in this study for consistency to the J_1 and J_3 metrics) is also derived, as follows:

$$(4) \qquad J_m = 2\pi(V\kappa)^{\frac{1}{2}} \left|\left| \frac{1}{s} T_{\hat{x}_0 \rightarrow \hat{x}_{33} - \hat{x}_{32}} \right|\right|_2$$

where all terms are as previously defined. Road velocity profiles can be assumed to approximate a white noise input [19]. As a result, the vertical road velocity input $\hat{x}_0$ is taken to be white noise throughout this study.

The linear damping parameters (as well as the values in Table 1) are obtained from [15]. Additionally, the vehicle velocity ($V = 60$ kph) and road surface roughness ($\kappa = 5 \times 10^{-7}$ m^3/cycle) parameters are obtained from [21]. These are used to obtain the benchmark performance values. The default damping value is set at 5000 Ns/m for the strut, and 200 Ns/m for the bushes. The benchmark performance values are as follows:

$$
\begin{aligned}
J_1 &= 1.492\text{m/s}^2 \\
J_3 &= 953.9\text{N} \\
J_m &= 7.436\mu\text{m}
\end{aligned}
$$

(5)

which will be used as constraints in future optimisations.

3. Optimal absorber configurations identification

It is important to ensure a global minimum is found in any optimisation. Whilst it is difficult, and sometimes impossible, to guarantee that this has been found, there are a few techniques that can be used to reduce the chance of the global minimum being missed. Optimisation uses MATLAB and a 'sequential' approach.

The first optimisation step uses 'particleswarm', with the initial conditions spaced logarithmically through the boundaries provided to the solver. These solutions are then provided to 'patternsearch' before being given to 'fminsearch'. After each of these stages, the optimised solution gradually gets finer and closer to a global optimum.

3.1. Strut optimisation

Firstly, the strut is optimised for J_1 and J_3 across all the layouts shown in Figure 2 including the damper. When optimising for J_1, J_3 and J_m have constraints applied to them. Then, when J_3 is optimised, the constraints are applied to J_1 and J_m.
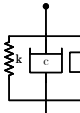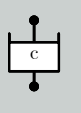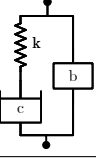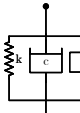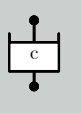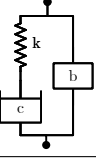
The strut optimisation results for both J_1 and J_3 only provided limited improvements over the pure damper. J_1 was reduced by 4.26%, and J_3 by 1.28%. In both situations, it was layout III-5 which provided the best performance improvement. Whilst it is clear that including an inerter can provide some performance benefit compared to a single damper (I-1), these benefits are only minimal. The damper alone was also optimised separately, and this provided no performance improvement over the default.

One important point to note is the value of J_m in both optimisations. The value for J_m was equal to that of the default (7.436 μm) for both. This suggests that the J_m constraint plays an important part in limiting the potential performance improvements to the system, and thus it should be a focus to control J_m.

3.2. Bush optimisation

Figure 1 showed that generic absorber networks were included in the place of the damper in the bushes ($G(s)$ and $Y(s)$). This section considers the optimisation of these bushes for J_m to see how far the deflection can be

Table 2: The results of optimising the bushes for J_m with all constraints applied. The bushes are individually optimised and then optimised together. Only inerter bushes are shown here to see the largest performance improvement possible.

Parameter Values		Default	Tune $G(s)$		Tune $Y(s)$		Tune $G(s)$ and $Y(s)$	
J1 (m/s^2)		1.492	1.471		1.487		1.461	
J3 (N)		953.9	944.5		952.5		953.9	
Jm (μm)		7.436	6.780	8.83%	5.251	23.4%	1.221	83.6%
$G(s)$	b (kg)	-	0.2527		-		2.907	
	c (Ns/m)	200.0	425.7		200.0		2351	
	k (N/m)	-	0		-		666800	
$Y(s)$	b (kg)	-	-		5.270		95.30	
	c (Ns/m)	200.0	200.0		287.9		1347	
	k (N/m)	-	-		12430		367.5	

reduced, based on conclusions made in Section 3.1.

As previously discussed, a railway Hall-Bush inspired fluid-based bush is proposed by [7]. This allows for inertance to be incorporated into the bush through careful design of the fluid channels inside the bush. To numerically compare the possible performance improvement which can be obtained by incorporating an inerter into the bush, initially the damper bush alone is optimised. Here the best possible performance improvement is 15.0% over the default if both bushes are optimised.

The results in Table 2 show a significantly more promising improvement in performance in comparison to only considering dampers. Here over 80% improvement can be provided compared to the default MGD value. This improvement in performance, from a 15% reduction to an 80% reduction neatly illustrates the benefit an inerter can provide to a system.
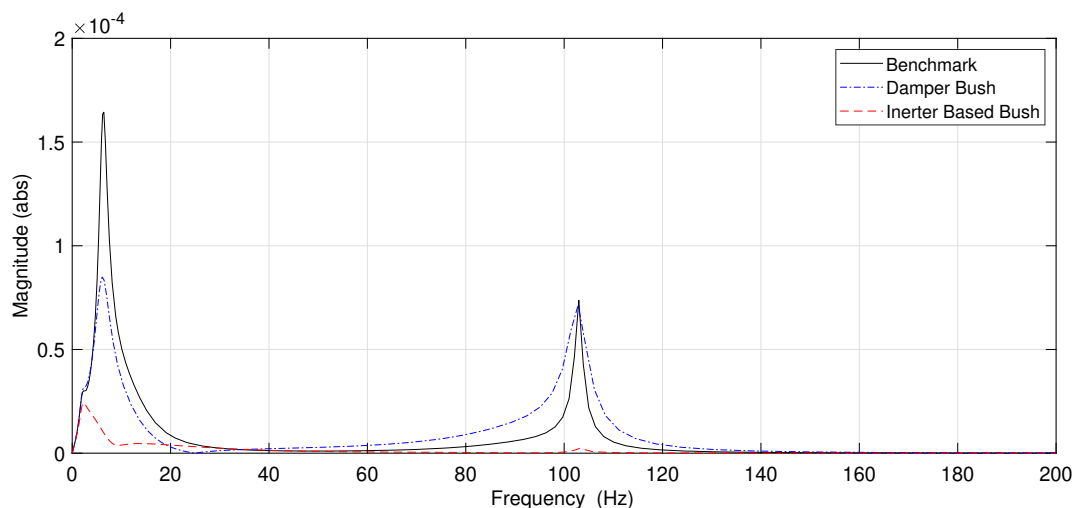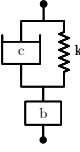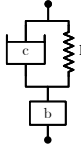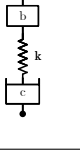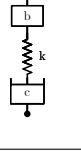

Figure 3: Frequency domain response for optimised bushes.

Table 3: The results of optimising all parameters in a single pass for J_1 and J_3 with all constraints applied. The bushes considered are the three best performing bush combinations from the previous step.

Parameter Values		Default	Optimised for J_1 J_3, J_m Constrained		Optimised for J_3 J_1, J_m Constrained	
J1 (m/s^2)		1.492	1.173	21.3%	1.195	
J3 (N)		953.9	883.0		871.4	8.66%
Jm (μm)		7.436	7.436		7.436	
H(s)	b (kg)	-	230.6		252.5	
	c (Ns/m)	5000	2416		2287	
	k (N/m)	-	26970		34720	
G(s)	b (kg)	-	285.9		107.3	
	c (Ns/m)	200.0	1256		1032	
	k (N/m)	-	208300		157900	
Y(s)	b (kg)	-	-		-	
	c (Ns/m)	200.0	568.1		488.0	
	k (N/m)	-	-		-	

Frequency domain analysis of the system is shown in Figure 3. It is clear to see how the significantly the response peaks can be reduced at both of the natural frequencies (at around 6.32 and 103 Hz).

This has proven that controlling J_m by optimising the bushes is not only possible, but that it can give excellent results. The three best performing combinations of inerter-based bushes can be taken and considered when optimising all of the parameters in a single pass[1]. This follows in Section 3.3.

3.3 . All parameter optimisation

Since it has been determined that J_m can be reduced through optimal bushes, the limitation on the strut optimisation should be reduced. This should permit greater improvements in J_1 and J_3, since the J_m constraint will not be so readily breached. In this step, all of the parameters for both bushes and the strut are optimised in a single pass.

Table 3 shows the results of this optimisation. One point of note is that the combination of bushes which provides the best performance is not the same as in Section 3.2. However, J_m is controlled sufficiently to permit significantly higher performance improvements when compared to optimising the strut alone. To contrast the previous optimisation results (Section 3.1), J_1 can improve by 21.3%, and J_3 by 8.66%.

The improvement in J_3 is smaller than the improvement in J_1. This is due to the definition of J_3 (Equation 3) combined with the bearing stiffness k_{41} (Figure 1). The unsprung mass (m_1) deflection will be mainly as a result of the force imparted on it by the bearing and the road input. Therefore, the comparatively smaller performance improvement possible for J_3 over J_1 follows where the bearing is left unoptimised. It is not advisable however to compromise the vertical stiffness of the bearing, and therefore this will not be changed or optimised in this study. As J_1 is defined as the acceleration of the sprung mass (m_2) relative to the acceleration of the road profile, it is possible to reduce its value more significantly since the strut ($H(s)$) lies on that force path.

---

[1]It is worth noting that only the single best performing combination of optimal $G(s)$ and $Y(s)$ is shown in this section.

4. Discussions and conclusions

This study has explored the validity of incorporating inerter-based absorbers into an in-wheel motor system. These were incorporated initially into the strut to control body vertical acceleration (denoted as J_1 here), and tyre dynamic load (termed J_3). The performance improvement was found at first to be limited. However, this was then related to the constraint applied to the magnetic gap deformation (termed J_m in this study).

After this, the bushes were updated to include inertance. They could then be optimised for J_m, which resulted in significant performance improvements (in excess of 80% over the default). Using the inertance based bushes, the entire system could be re-optimised for J_1 and J_3 to obtain performance improvements of 21.3% and 8.66% respectively. These both improve on the case where only the strut was optimised. This work has improved upon the model proposed by [15], and has addressed many of the issues that are inherent to the traditional in-wheel motor.

The most important result is the extent to which J_m can be reduced (over 80% compared to the default). Although this was not the original focus of this work it is still important. This is because the performance of J_1 and J_3 would not degrade beyond the default, since constraints were applied to them in the optimisation process. Meanwhile, the potential longevity and reliability of the motor itself would be improved by reducing the magnetic gap deformation.

References

[1] W. Adams. Electric motor, U.S. Patent US300827A. 24 June 1884.

[2] C Campbell. *Automobile Suspensions.* Chapman and Hall, 1st edition, 1981.

[3] E. Esmailzadeh, G.R. Vossoughi, and A. Goodarzi. Dynamic modeling and analysis of a four motorized wheels electric vehicle. *Vehicle System Dynamics*, 35(3):163–194, 2001.

[4] D. Hrovat. Influence of unsprung weight on ride quality. *Journal of Sound and Vibration*, 124:497–516, 1988.

[5] J.Z. Jiang, A.Z. Matamoros-Sanchez, R.M. Goodall, and M.C. Smith. Passive suspensions incorporating inerters for railway vehicles. *Vehicle System Dynamics*, 50(sup1):263–276, 2012.

[6] I.F. Lazar, S.A. Neild, and D.J. Wagg. Vibration suppression of cables using tuned inerter dampers. *Engineering Structures*, 122:62–71, 2016.

[7] T. D. Lewis, J. Z. Jiang, S. A. Neild, C. Gong, and S. D. Iwnicki. Using an inerter-based suspension to improve both passenger comfort and track wear in railway vehicles. *Vehicle System Dynamics*, 58(3):472–493, 2020.

[8] T. D. Lewis, Y. Li, G. J. Tucker, J. Z. Jiang, Y. Zhao, S. A. Neild, M. C. Smith, R. Goodall, and N. Dinmore. Improving the track friendliness of a four-axle railway vehicle using an inertance-integrated lateral primary suspension. *Vehicle System Dynamics*, 59(1):115–134, 2021.

[9] Z. Li, L. Zheng, Y. R., Y. Li, and Z. Xiong. Multi-objective optimization of active suspension system in electric vehicle with in-wheel-motor against the negative electromechanical coupling effects. *Mechanical Systems and Signal Processing*, 116:545–565, 2019.

[10] M. Liu, F. Gu, J. Huang, C. Wang, and M. Cao. Integration design and optimization control of a dynamic vibration absorber for electric wheels with in-wheel motor. *Energies*, 10(12), 2017.

[11] M. Liu, Y. Zhang, J. Huang, and C. Zhang. Optimization control for dynamic vibration absorbers and active suspensions of in-wheel-motor-driven electric vehicles. *Proceedings of the Institution of Mechanical Engineers, Part D: Journal of Automobile Engineering*, 234(9):2377–2392, 2020.

[12] X. Liu, J. Z. Jiang, B. Titurus, and A. Harrison. Model identification methodology for fluid-based inerters. *Mechanical Systems and Signal Processing*, 106:479–494, 2018.

[13] G. Long, F. Ding, N. Zhang, J. Zhang, and A. Qin. Regenerative active suspension system with residual energy for in-wheel motor driven electric vehicle. *Applied Energy*, 260:114180, 2020.

[14] J. Luo, J.H.G. Macdonald, and J.Z. Jiang. Use of inerter-based vibration absorbers for suppressing multiple cable modes. *Procedia Engineering*, 199:1695–1700, 2017.

[15] Y. Luo and D. Tan. Study on the dynamics of the in-wheel motor system. *IEEE Transactions on Vehicular Technology*, 61:3510–3518, 2012.

[16] S. Murata. Innovation by in-wheel-motor drive unit. *Vehicle System Dynamics*, 50(6):807–830, 2012.

[17] G. Nagaya, Y. Wakao, and A. Abe. Development of an in-wheel drive with advanced dynamic-damper mechanism. *JSAE Review*, 24(1):477–481, 2003.

[18] Y. Qin, C. He, X. Shao, H. Du, C. Xiang, and M. Dong. Vibration mitigation for in-wheel switched reluctance motor driven electric vehicle with dynamic vibration absorbing structures. *Journal of Sound and Vibration*, 419(1):249–267, 2018.

[19] W. Schiehlen. White noise excitation of road vehicle structures. *Sadhana*, 37(4):487–503, 2006.

[20] M. C. Smith. Synthesis of mechanical networks: The inerter. *IEEE Transactions on Automatic Control*, 47:1648–1662, 2002.

[21] M. C. Smith and F-C. Wang. Performance benefits in passive vehicle suspensions employing inerters. *Vehicle System Dynamics*, 42:235–257, 2004.

[22] S. J. Swift, M. C. Smith, A. R. Glover, C. Papageorgiou, B. Gartner, and N. E. Houghton. Design and modelling of a fluid inerter. *International Journal of Control*, 86(11):2035–2051, 2013.

[23] D. Tan, Y. Wu, J. Feng, K. Yang, X. Jia, and C. Ma. Lightweight design of the in-wheel motor considering the coupled electromagnetic-thermal effect. *Mechanics Based Design of Structures and Machines*, 0(0):1–19, 2020.

[24] F-C. Wang and W-J. Su. Impact of inerter nonlinearities on vehicle suspension control. *Vehicle System Dynamics*, 46(7):575–595, 2008.

[25] Q. Wang, R. Li, Y. Zhu, X. Du, and Z. Liu. Integration design and parameter optimization for a novel in-wheel motor with dynamic vibration absorbers. *Journal of the Brazilian Society of Mechanical Sciences and Engineering*, 42:459, 2020.

[26] Y. Wang, P. Li, and G. Ren. Electric vehicles with in-wheel switched reluctance motors: Coupling effects between road excitation and the unbalanced radial force. *Journal of Sound and Vibration*, 372:69–81, 2016.

[27] H. Wu, L. Zheng, and Y. Li. Coupling effects in hub motor and optimization for active suspension system to improve the vehicle and the motor performance. *Journal of Sound and Vibration*, 482(1):1–18, 2020.

[28] S. Y. Zhang, J. Z. Jiang, and S. A. Neild. Passive vibration control: a structure–immittance approach. *Proceedings of the Royal Society A*, 473(2201):20170011, 2017.

[29] S. Y. Zhang, M. Zhu, Y. Li, J. Z. Jiang, R. Ficca, M. Czechowicz, R. Neilson, S.A. Neild, and G. Herrmann. Ride comfort enhancement for passenger vehicles using the structure-immittance approach. *Vehicle System Dynamics*, 59(4):504–525, 2021.

7th European Conference on Structural Control

Book of Abstracts and Selected Papers